Soft Chemical Control of Layered Oxychalcogenides

Jack N. Blandy

A thesis submitted in part fulfilment of the requirements for the degree of Doctor of Philosophy at the University of Oxford

Trinity College

University of Oxford

September 2017



Abstract

Soft Chemical Control of Layered Oxychalcogenides

DPhil Thesis Jack N. Blandy September 2017

The structure, magnetic behaviour and chemistry of layered oxychalcogenides of composition $A_2MO_2X_2Ch_2$ (where *A* = Sr, Ba; *M* = Mn, Co, Ni, Cu, Zn; *X* = Cu, Ag and *Ch* = S, Se, Te) has been investigated by the synthesis of new compounds of this type and control of the properties of these compounds by oxidative deintercalation of Cu/Ag.

I_2 can be used to oxidatively deintercalate Cu from $Sr_2MnO_2Cu_{1.5}S_2$, forming $Sr_2MnO_2Cu_{1.33}S_2$, an incommensurately modulated compound, with a completely different Cu/vacancy ordering and antiferromagnetic ordering structure to the parent. This reaction is also probed in real-time, using *in situ* powder X-ray diffraction.

$Sr_2MnO_2Ag_{1.5}Se_2$ was found to have an *A*-type magnetic ordering structure, similar to $Sr_2MnO_2Cu_{1.5}Se_2$. $Sr_2MnO_2Cu_{1.8}Te_2$ on the other hand with a lower Mn oxidation state shows only two-dimensional magnetic correlations, rather than long-range order.

Extending the reaction with I_2 to several Co-containing analogues revealed that ~25% Ag could be removed from $Sr_2CoO_2Ag_2Se_2$, sufficient to observe a change in magnetic behaviour, from antiferromagnetic to ferromagnetic. By contrast only ~11% Cu can be deintercalated from $Sr_2CoO_2Cu_2S_2$ and even less (~5%) from $Sr_2CoO_2Cu_2Se_2$. Neutron diffraction was used to examine the resultant changes in magnetic ordering.

The novel compounds $Sr_2CuO_2Cu_2Se_2$ and $Ba_2CuO_{2-x}Cu_2Se_2$ are related by substitution of the alkali-earth metal, but while $Sr_2CuO_2Cu_2Se_2$ is a stoichiometric compound with metal-like character, $Ba_2CuO_{2-x}Cu_2Se_2$ is an oxygen-deficient semiconductor, with tuneable oxygen content.

Unusual features are observed in the magnetic susceptibility measurements of $Sr_2NiO_2Cu_2Se_2$ that appear unrelated to this compound's long-range magnetic ordering, as probed by neutron diffraction. Furthermore, unusual peak splitting is observed in low-temperature powder X-ray diffraction patterns of this compound; this may plausibly be due to a photon-induced effect arising from the use of a high-energy beamline; although further measurements are required to examine this.

Overall the work shows the flexibility and range of behaviour exhibited by a series of the transition metal oxide chalcogenides.

Acknowledgements

My first thanks must be to my supervisor, Prof. Simon Clarke, for providing ideas, enthusiasm and expertise to every aspect of this project. I am extremely grateful for the opportunity to have learnt so much.

I am extremely grateful to Drs Danny Woodruff and Simon "TOPAS wizard" Cassidy for their countless hours of help and support throughout my DPhil. Without their constant help and suggestions, this thesis would have taken much longer and been much lower quality. More importantly, both Danny and Simon have become great friends.

I particularly appreciate the many members of the Clarke group, former and present, that have made the experience so enjoyable: Pippa, Jacob, Fran, Archie, Michael, Thomas, Sophie, Abi, Andi, Toby, Jamie, Dom, Rob, Sonja, Partha, Cristina and Xiaoyu. I have many fun memories with many group members, both in and out of the lab. Xiaoyu, I hope life becomes a little bit more fair and a little bit less interesting.

Thank you to former MAH members, Drs Midori Amano Patiño and Ronghuan (Rona) Zhang: Midori, for constant willingness to help (and gossip); Rona, for keeping me entertained and her dexterity with thin wires.

Thank you to Drs Amber Thompson and Kirsten Christensen, who have been of great assistance with all matters single crystal. Amber's constant supply of board games made the many nights spent at I19 enjoyable.

I have been extremely fortunate over the course of my DPhil to have had access to an excessive number of beamlines at Diamond, ISIS, the ILL and the ESRF. Without the work of some excellent beamline scientists, this would not be possible: Prof. C. Tang, Dr A. Baker and Dr C. Murray (I11); Drs A. Fitch and C. Giacobbe (ID22); Drs M. Drakopoulos, S. Michalik and O. Magdysyuk (I12); Dr F. Demnel (OSIRIS); Drs D. Fortes and A. Gibbs (HRPD); Drs P. Manuel and F. Orlandi (WISH); Dr R. Smith (GEM XPress) and Dr E. Suard (D2B). Thanks to Dr P. Wiseman for maintenance of the powder diffractometers and SQUID magnetometers and T. Adams for flawless (and fast!) glass blowing. Also, thanks to Prof. J. Hadermann, Prof. A. Abakumov and Dr M. Batuk for electron diffraction and microscopy measurements and Dr N. Young for assistance with EDX measurements.

Finally, thanks to my friends, family and especially Sophia for support throughout.

Contents

1 Introduction 1

1.1 Solid state chemistry 1

1.2 Mixed-anion compounds 2

1.2.1 *Ln*OCu*Ch* compounds 3
1.2.2 *AMOCh* compounds 4
1.2.3 $A_2MO_2X_2Ch_2$ type compounds 7

1.3 Soft chemistry 11

1.3.1 CeOCuS and $CeOAg_{0.8}S$ 12
1.3.2 $Sr_4Mn_3O_{7.5}Cu_2S_2$ 12
1.3.3 FeSe 13
1.3.4 Reduction of $LaNiO_3$ 14
1.3.5 Reductive lithiation of $Sr_2MnO_2Cu_{1.5}S_2$ and $Sr_2MnO_2Cu_{3.5}S_3$ 14

1.4 Magnetic behaviour of solids 15

1.4.1 Diamagnetism 16
1.4.2 Paramagnetism 16
1.4.3 Pauli paramagnetism 18
1.4.4 Ferromagnetism 19
1.4.5 Antiferromagnetism 20
1.4.6 Spin-glass materials 21

1.5 Summary and project aims 22

2 Experimental Methods 24

2.1 Synthetic methods 24

2.1.1 Ceramic synthesis 24
2.1.2 Handling of air-sensitive materials 25
2.1.3 Oxidation using iodine 25
2.1.4 Synthesis of SrO 27
2.1.5 Synthesis of SrS 27

2.2 Diffraction 28

2.2.1 The Laue equations and Bragg's law 29
2.2.2 Structure factor 30
2.2.3 Aperiodic crystals 32

2.3 Powder X-ray diffraction 33

2.3.1 In-house powder X-ray diffraction 34
2.3.2 Synchrotron powder X-ray diffraction 35

2.4 Powder neutron diffraction 39

2.4.1 GEM 42
2.4.2 POLARIS 42

2.4.3 HRPD 42
2.4.4 WISH 43
2.4.5 OSIRIS 43
2.5 Analysis of powder diffraction data 44
2.6 Single crystal X-ray diffraction 46
2.7 Electron diffraction and microscopy 47
2.8 Magnetometry measurements 48
2.8.1 DC magnetometry measurements 49
2.8.2 AC magnetometry measurements 50
2.9 Electrical resistivity measurements 51

3 Structural and magnetic properties of $Sr_2MnO_2Cu_{1.5-x}S_2$, $Sr_2MnO_2Ag_{1.5}Se_2$ and $Sr_2MnO_2Cu_{1.8}Te_2$ 54
3.1 Introduction 54
3.2 Cu deintercalation from $Sr_2MnO_2Cu_{1.5}S_2$ using I_2 56
3.2.1 Synthesis of the parent compound and method of deintercalation 56
3.2.2 Room temperature powder X-ray diffraction 56
3.2.3 Structure and composition of the region "*C*" structure 60
3.2.4 Low temperature powder X-ray diffraction 68
3.2.5 Magnetometry 72
3.2.6 Powder neutron diffraction to probe changes in magnetic ordering 74
3.3 Synthesis, structure and magnetic behaviour of $Sr_2MnO_2Ag_{1.5}Se_2$ 88
3.3.1 Synthesis 88
3.3.2 Structure and composition 88
3.3.3 Magnetometry 92
3.3.4 Powder neutron diffraction 94
3.3.5 Discussion of magnetic behaviour 96
3.4 Synthesis, structure and magnetic behaviour of $Sr_2MnO_2Cu_{1.8}Te_2$ 97
3.4.1 Synthesis and composition 97
3.4.2 Magnetometry 99
3.4.3 Powder neutron diffraction to probe magnetic ordering 101
3.4.4 Discussion of magnetic behaviour 103
3.5 Conclusions 104

4 Investigating the reaction of $Sr_2MnO_2Cu_{1.5}S_2$ with iodine *in situ* 107
4.1 Introduction 107
4.1.1 Development of *in situ* powder X-ray diffraction 108
4.1.2 *In situ* investigation into the oxidative deintercalation of $Sr_2MnO_2Cu_{1.5}S_2$ 110

4.2 Method 111
4.2.1 General method 111
4.2.2 Design of reaction vessel 112
4.2.3 Cooling method 114
4.2.4 Data processing 117
4.3 Change in refined parameters 118
4.3.1 Lattice parameters 118
4.3.2 Copper site occupancy 120
4.4 Qualitative changes in peaks 121
4.5 Attempts to identify any phase gaps 125
4.6 Calculation of the activation energy 128
4.7 Improvements to the apparatus design 132
4.7.1 Design of reaction vessels 132
4.7.2 Gas-cooled box 133
4.8 Conclusions 134

5 Deintercalation of copper or silver from several cobalt-containing oxychalcogenides 135
5.1 Introduction 135
5.2 Cu deintercalation from $Sr_2CoO_2Cu_2(S/Se)_2$ using iodine. 137
5.2.1 Synthesis and deintercalation 137
5.2.2 Lattice parameters and composition 138
5.2.3 Magnetometry 144
5.2.4 Powder neutron diffraction to probe changes in magnetic ordering 148
5.2.5 Structural distortion at low temperature 174
5.3 Ag deintercalation from $Sr_2CoO_2Ag_2Se_2$ using iodine 183
5.3.1 Synthesis and deintercalation 183
5.3.2 Lattice parameters and composition 183
5.3.3 Magnetometry 194
5.3.4 Powder neutron diffraction to probe changes in magnetic ordering 197
5.3.5 Structural distortion at low temperature 201
5.3.6 Discussion of magnetic behaviour 203
5.4 Synthesis, composition and magnetic behaviour of $Sr_2CoO_2Cu_2Te_2$ 206
5.4.1 Synthesis and composition 206
5.4.2 Magnetometry measurements 208
5.4.3 Powder neutron diffraction to probe magnetic ordering 209
5.5 Discussion 212
5.5.1 Effect of substitutions on structure 212

5.5.2 Effect of substitutions on the extent of deintercalation 213
5.6 Conclusions 215

6 Synthesis and Characterisation of $Sr_2CuO_2Cu_2Se_2$ and $Ba_2CuO_{2-x}Cu_2Se_2$ ... 217
6.1 Introduction 217
6.2 Synthesis, Structure and composition of $Sr_2CuO_2Cu_2Se_2$ 219
6.2.1 Synthesis of $Sr_2CuO_2Cu_2Se_2$ 219
6.2.2 Powder X-ray and neutron diffraction analysis 219
6.3 Synthesis, Structure and Composition of $Ba_2CuO_{2-x}Cu_2Se_2$ 221
6.3.1 Synthesis of $Ba_2CuO_{2-x}Cu_2Se_2$ 221
6.3.2 Powder X-ray diffraction analysis 221
6.3.3 Single crystal X-ray diffraction analysis 222
6.4 Variable Temperature Powder X-ray Diffraction 229
6.4.1 $Sr_2CuO_2Cu_2Se_2$ 229
6.4.2 $Ba_2CuO_{2-x}Cu_2Se_2$ 229
6.5 Magnetometry measurements 232
6.6 Bulk resistivity measurements 236
6.6.1 $Sr_2CuO_2Cu_2Se_2$ 236
6.6.2 $Ba_2CuO_{2-x}Cu_2Se_2$ 237
6.7 Oxygenation of $Ba_2CuO_{2-x}Cu_2Se_2$ 238
6.8 Discussion 241
6.9 Conclusions 242

7 Synthesis and characterisation of $Sr_2NiO_2Cu_2Se_2$ 244
7.1 Introduction 244
7.2 Synthesis and composition of $Sr_2NiO_2Cu_2Se_2$ 245
7.2.1 Room temperature powder X-ray diffraction and powder neutron diffraction of JNB267B 248
7.3 Magnetometry and resistivity measurements 250
7.3.1 Magnetometry measurements 250
7.3.2 Resistivity measurements 251
7.4 Variable temperature diffraction 251
7.4.1 Changes in lattice parameters 251
7.4.2 Observation of peak splitting 253
7.5 Powder neutron diffraction to probe magnetic ordering 272

7.6 Treatment of $Sr_2NiO_2Cu_2Se_2$ with I_2 274
7.6.1 Method 275
7.6.2 Room temperature powder X-ray diffraction 275
7.6.3 Room powder neutron diffraction 277
7.6.4 Air sensitivity 277
7.6.5 Magnetometry measurements 278
7.6.6 Variable temperature powder X-ray diffraction 279
7.6.7 Discussion 280
7.7 Conclusions 281

8 Summary 282

References 290

A. Incommensurate Crystallography i

B. Magnetic structures and Symmetry-Mode Distortion Analysis v
B.1 Symmetry mode labels v
B.2 Magnetic space groups vi

C. Magnetic structures of $Sr_2CoO_2Cu_{2-x}Se_2$ and $Sr_2CoO_2Cu_{2-x}Se_{1.6}S_{0.4}$ modelled using model 1 viii
C.1 $Sr_2CoO_2Cu_{2-x}Se_2$ viii
C.2 $Sr_2CoO_2Cu_{2-x}Se_{1.6}S_{0.4}$ x

D. Energy Dispersive X-ray Spectroscopy of $Sr_2CoO_2Ag_{2-x}Se_2$ xiii

Chapter 1
1 Introduction

1.1 Solid state chemistry

This thesis investigates the structure and physical properties of crystalline solids. Crystalline solids have long-range periodic order, allowing the structure to be probed by diffraction methods. The properties of these solids are incredibly diverse, resulting in many different technological applications. Understanding the origin of these properties is key to the development of materials that are optimised for their application.

One such development is the discovery of superconductivity, compounds that exhibit zero resistance below a critical temperature (T_c). Bardeen, Cooper and Schrieffer developed an explanation for the mechanism of superconductivity, known as BCS theory, with an implied theoretical limit on the highest T_c obtainable (30 – 40 K).[1] However, the field of superconductivity was revolutionised by Bednorz and Müller when the first cuprate superconductor was discovered: the compound had a T_c of ~30 K and exhibited many characteristics that contradicted the BCS theory of superconductivity.[2] This discovery led to the discovery of many other cuprate superconductors, with even higher critical temperatures. In 2008 a second class of non-BCS superconductor, the iron-based superconductors, was reported.[3] Research into the mechanism by which the cuprates and iron-based compounds become superconductors is still ongoing.

Another technologically important discovery was the development of the lithium-ion battery. The discovery that the intercalation of Li into Li_xTiS_2[4] and later (and more famously) into Li_xCoO_2[5] could be used as a store of electrochemical energy led directly to the development of the Sony rocking-chair battery, announced in 1991, and therefore allowed a revolution in the development of portable electronics. Research into producing better battery materials is ongoing, to improve charge/discharge rates, cost-effectiveness and service life of batteries, so that they may be used for a wider variety of applications, such as battery powered cars and energy stores for the national grid.[6]

Other areas in which solid state chemistry has the potential for a significant technological impact, but which the research is ongoing include: thermoelectrics,

materials which convert a thermal gradient into electrical energy;[7] multiferroics, materials which have, for example, a superposition of ferromagnetic and ferroelectric behaviour, with potential applications in computer memory storage;[8] and photocatalysts, compounds which can be used to catalyse the water-splitting reaction from light.[9]

As well as directly researching potential applications of solid-state compounds, research on the fundamental structure and properties of solid-state compounds is also important. A lack of understanding of the structure-property relationship hinders the synthesis of compounds with properties optimised for their various applications. This thesis aims to explore the use of soft chemistry to control the composition of selected oxychalcogenides, providing another route to tune the structural, electronic and magnetic properties of these compounds.

This introduction will provide a basis for understanding the changes observed, by discussing the structure of mixed-anion compounds, the use of soft chemistry to produce compounds under kinetic, rather than thermodynamic control, as well as the magnetic behaviours of solids, as relevant to this thesis. Finally the aims of this thesis will be outlined.

1.2 Mixed-anion compounds

The chemistry of metal oxides has been widely explored for many years. This is because they are naturally extremely prevalent, stable in air (aiding preparation) and possess many interesting properties.[10-12] Traditionally, this left the study of compounds containing anions other than oxygen comparatively underdeveloped. However, the development and proliferation of methods and apparatus to treat compounds as air and moisture sensitive has allowed the synthesis of many compounds containing non-oxide anions.[13] Compounds that contain both oxide and non-oxide anions are of particular interest in this thesis.

When the non-oxide ion has a similar size and polarisability to the oxide ion, such as N^{3-} and F^{-}, the two different types of anions often occupy similar crystallographic sites.[14, 15] Here the effect of changing the compound from the pure oxide to a mixed anion compound influences the oxidation state of the transition metal, changing the

electronic and magnetic behaviour, but has comparatively little effect on the structure of the compound.[14]

However, in the case of the oxychalcogenides (chalcogen = S, Se, Te)[16-18] and the oxypnictides (pnictogen = P, As, Sb)[19, 20] there is both a large difference in size and polarisability between the non-oxide and the oxide anions. These anions will therefore bond preferentially to different metals: the oxide anions to small, charge dense cations and the non-oxide anions to large, sparsely charged metals. In most cases the different ions occupy different crystallographic sites, often manifesting as a layer-separated structure.[13]

1.2.1 *Ln*OCu*Ch* compounds

One such family of layered compounds are those based on *Ln*OCu*Ch* (where *Ln* = lanthanide La – Nd and *Ch* = S, Se, and Te).[21, 22] These compounds form in the ZrCuSiAs structure type[23] and are composed of alternating fluorite $[Ln_2O_2]^{2+}$ and antifluorite $[Cu_2Ch_2]^{2-}$ layers. *Ln*OCu*Ch* has been investigated due to its transparent *p*-type semiconductor properties,[24] which has led to the investigation of the use of LaOCuSe in light-emitting diodes (LEDs).[25] These compounds are also structurally related to the LaOFeAs-type superconductors.[3]

Substitution of one equivalent of Cu by 0.5 equivalent of a divalent transition metal, *M* (where *M* = Mn, Fe, Zn, Cd), to form $Ln_2O_2MSe_2$ leads to a compound with vacancies that are ordered at room temperature (RT). However, the ordering observed is dependent on the identity of *Ln* and *M*, as shown by the examples of $La_2O_2CdSe_2$ and $Ce_2O_2FeSe_2$ in Fig. 1.1.[26, 27] Work by Ainsworth *et al.* has shown that the ordering sequence can be tuned by the synthesis of various solid solutions.[28]

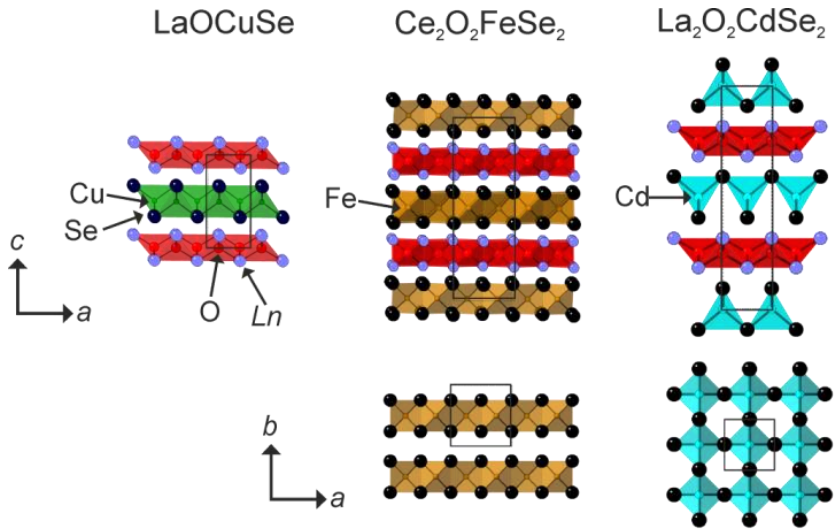


Fig. 1.1 The crystal structures of LaOCuSe which has a fully occupied selenide layer,[22] compared with the crystal structure of CeO_2FeSe_2[26] where the metals in the selenide layer are half occupied and adopt a "stripe" configuration of edge-shared $FeSe_4$ tetrahedra, as seen from the view down the c-axis, and the crystal structure of $La_2O_2CdSe_2$,[27] which is also half occupied but adopts a "checkerboard" pattern with verted-shared $CdSe_4$ tetrahedra, as shown from the view down the c-axis

However, some combinations of *Ln* and *M* do not form in the ZrCuSiAs structure type, instead adopting a "herringbone" structure, as is the case for $La_2O_2MnSe_2$, shown in Fig. 1.2.[29]

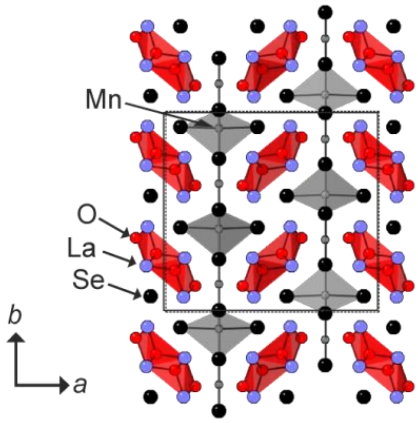


Fig. 1.2 The crystal structure of $La_2O_2MnSe_2$,[29] which adopts a "herringbone" structure

1.2.2 *AMOCh* compounds

The example of $La_2O_2MnSe_2$ shows that not all oxychalcogenides form with a total separation of the structure into discrete layers. As well as containing examples where there is layering, the *AMOCh* compounds contain further such examples where there is anion order, but discrete layers are not formed. The first compound to be reported with this composition was BaZnOS, in 2005.[30] Since then, a number of compounds with elements as diverse as *A* = Ca, Sr, Ba; *M* = Fe, Co, Zn and *Ch* = S, Se (for *AMOCh*)

have been reported. While holding structural similarities, the sulfur-containing compounds have been found to adopt two different structure types dependent on atom identity. The structure of CaFeOSe (the only known Se containing compound) is complex and was the subject of some debate, as is discussed below.

1.2.2.1 *BaZnOS-type compounds*

BaZnOS and BaCoOS have been found to adopt the structure shown in Fig. 1.3.[30, 31] It is shown that the coordination environment about *M* is a distorted tetrahedron in which two of the anions are O and two are S. The magnetic ordering structure of BaCoOS was determined using powder neutron diffraction by the author, but this work falls outside the scope of the thesis.[32]

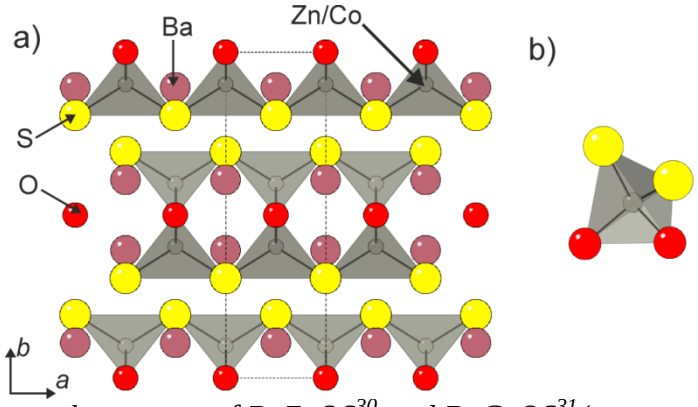


Fig. 1.3 a) The crystal structure of BaZnOS[30] and BaCoOS[31](space group: Cmcm) and b) the distorted tetrahedral environment of M (where M = Co, Zn) in these compounds

1.2.2.2 *CaZnOS-type compounds*

This structure type has been found to be adopted by CaZnOS,[33] SrZnOS,[34] CaCoOS[32] and CaFeOS.[35, 36] The structure differs from the BaZnOS structure in two key aspects: the structure type is polar (space group: $P6_3mc$) and the coordination environment around *M* is a distorted tetrahedron with three S and one O anions, as shown in Fig. 1.4 b).

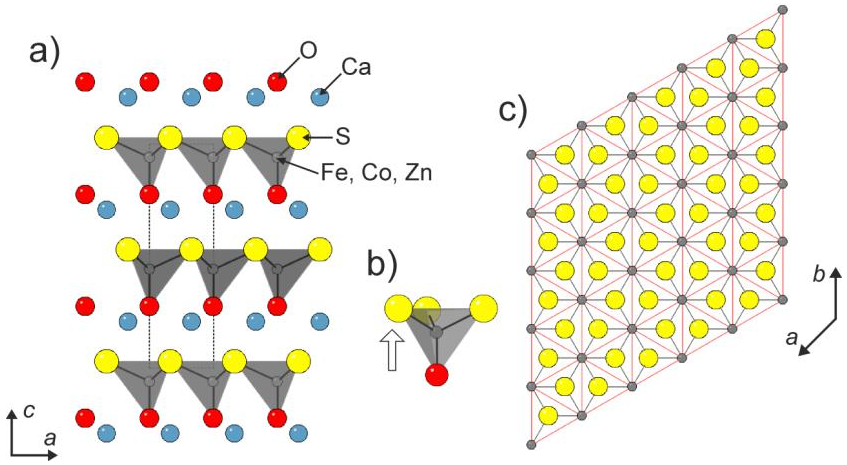


Fig. 1.4 a) The crystal structure of CaFeOS, CaCoOS and CaZnOS (space group: $P6_3mc$); b) the pseudo-tetrahedral environment of M (M = Fe, Co, Zn) in this compound, with arrow showing the direction of positive polarisation and c) the projection of these compounds down the c-axis, emphasising the triangular relationship between the M ions, all M ions are in the same plane

This structure is of particular interest in the case of CaCoOS and CaFeOS because it is a comparatively unusual example of the coexistence of polar structure with magnetically active ions. In both cases the compounds order antiferromagnetically at low temperatures, with interesting magnetic structures because the magnetic ions are based on a triangular lattice, leading to geometric frustration (see section 1.4 for a discussion of magnetic concepts).[32, 35, 36]

1.2.2.3 *CaFeOSe*

The synthesis of CaFeOSe was first reported by Han *et al.*, where the synthesis of an impure sample of the compound was reported and single-crystal X-ray diffraction (SCXRD) was used to solve the structure.[37] However, it was later found that CaFeOSe adopts two polymorphic structures, one of which is the structure reported by Han *et al.* Both these structures are distortions of the BaZnOS archetypal structure, as shown in Fig. 1.5. Electron microscopy and SCXRD measurements showed that this structure coexists in the same crystallites.[38, 39]

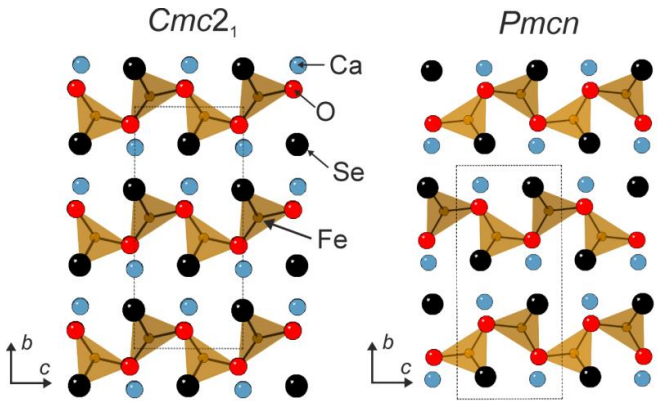


Fig. 1.5 Crystal structures of the two polymorphs of CaFeOSe: $Cmc2_1$ (layers related by C-centring) and Pmcn (layers related by inversion)[38, 39]

1.2.3 $A_2MO_2X_2Ch_2$ type compounds

Zhu and Hor discovered that the related $Sr_2Mn_3Sb_2O_2$ structure type[40] formed in quinary oxychalcogenides when they synthesised $Sr_2ZnO_2Cu_2S_2$, "$Sr_2MnO_2Cu_2S_2$" and $Sr_2CoO_2Cu_2S_2$.[41, 42] This structure type is fully crystallographically ordered, despite the many different types of atoms in the compound. This order arises, as in the case of the *Ln*OCu*Ch* series from differences in the size and polarisability of the ions, favouring the formation of layers, in this case alternating $[Sr_2MO_2]^{2+}$ and $[Cu_2S_2]^{2-}$ layers. Many compounds of this structure type have since been found (discussed in section 1.2.3.4 and throughout the rest of the thesis). It was also found that varying the element ratios and heating conditions allowed the synthesis of compounds with different thicknesses of the oxide and chalcogenide layers, as shown in Fig. 1.6, where *m* is the number of layers of *M* per layer and *n* is the number of layers of *X* per layer.[41, 43-46]

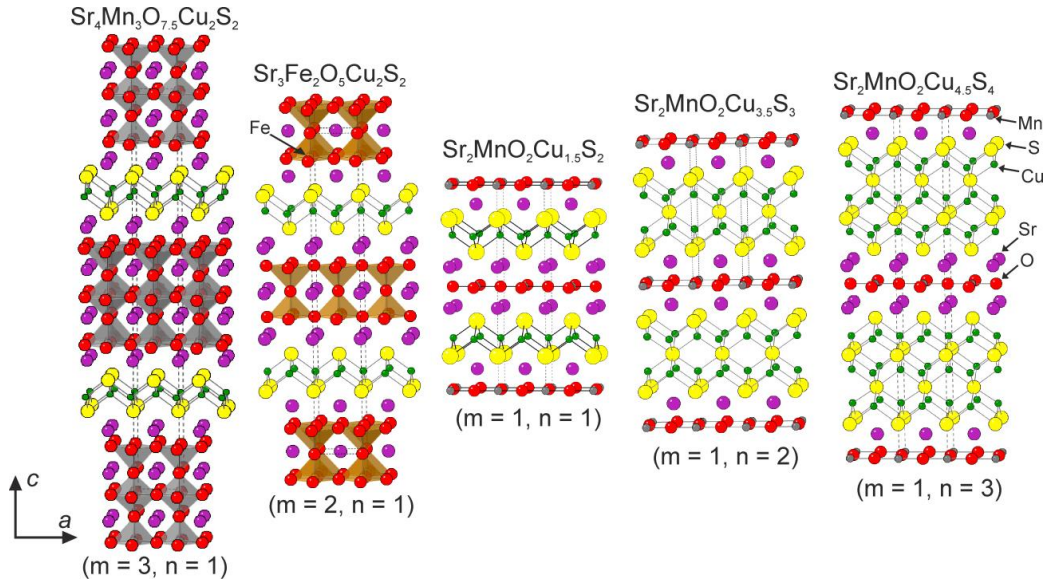


Fig. 1.6 The crystal structures of five related quinary oxysulfides: $Sr_4Mn_3O_{7.5}Cu_2S_2$,[44, 46] *$Sr_3Fe_2O_5Cu_2S_2$,*[43] *$Sr_2MnO_2Cu_{1.5}S_2$,*[41] *$Sr_2MnO_2Cu_{3.5}S_3$*[45] *and $Sr_2MnO_2Cu_{4.5}S_4$*[45]

While the $m = 1$, $n = 1$ structure type is incredibly compositionally abundant, only a few members of the other series are known.

1.2.3.1 *m = 3, n = 1*

$Sr_4Mn_3O_{7.5}Cu_2Ch_2$ (*Ch* = S, Se) are the only known $m = 3$ compounds.[46] These compounds (and the $m = 2$ compound) may be thought of as fragments of perovskite separated by the chalcogenide layers. Tuning of the fractional occupancy of the oxide position has been shown to be possible,[44] as is discussed in section 1.3.2.

1.2.3.2 *m = 2, n = 1*

Compounds of this structure type are only known for compounds where it is significantly more favourable for the transition metal, *M*, to be in the +3 oxidation state (as opposed to the +2 oxidation state). Hence known compounds are: $Sr_3Sc_2O_4Cu_2S_2$ and $A_3Fe_2O_4X_2Ch_2$ (where *A* = Sr, Ba; *X* = Cu, Ag and *Ch* = S, Se).[43, 47-50] In this structure *M* has 5 oxygen atom nearest-neighbours in a square-based pyramidal environment, as can be seen from Fig. 1.6,.

Aided by the fact that it only contains full-shell ions, $Sr_3Sc_2O_4Cu_2S_2$ is an example of a *p*-type transparent conducting material, with a large band gap (3.1 eV) but also a high electrical conductivity (2.8 S cm^{-1} at 300 K). These properties led to further investigation into the possibility of using this compound in optoelectronic applications.[51, 52]

1.2.3.3 *m = 1, n = 2, 3*

The multiple chalcogenide layered structure type is only known for Sr-Mn-O-Cu-S containing compounds. The double layered and triple layered compounds $Sr_2MnO_2Cu_{3.5}S_3$ and $Sr_2MnO_2Cu_{4.5}S_4$ are shown in Fig. 1.6, but another compound is known, the so-called "1.5" layer, which shows strict alternation between single and double chalcogenide layers.[45, 53] In all these compounds, Mn has a mixed oxidation state ~2.5, which leads to Cu vacancies for charge balance. The Cu ions are extremely mobile within the sulfide layer, so the vacancies are disordered at RT. However, these vacancies order when the sample is cooled significantly below RT. Interestingly, examination of the low temperature diffraction patterns of $Sr_2MnO_2Cu_{3.5}S_3$ revealed the presence of at least three different Cu/vacancy-ordering schemes dependent on the cooling rate.[54]

These compounds are metamagnetic, that is they order antiferromagnetically in a zero-field, but when a field larger than some critical field is applied, the magnetic behaviour switches from antiferromagnetic to ferromagnetic,[45] these magnetic ideas will be discussed further in section 1.4. It has also been found that these compounds are susceptible to oxidative deintercalation by I_2, causing dramatic changes in the Cu/vacancy-ordering scheme and magnetic behaviour of these compounds.[55, 56] This reaction will be studied in detail for selected $m = 1$, $n = 1$ compounds in this thesis.

1.2.3.4 *m = 1, n = 1*

This structure type may be written as $A_2MO_2X_2Ch_2$ where *A* = Sr, Ba; *M* = Mn, Co, Ni, Cu, Zn; *X* = Cu, Ag and *Ch* = S, Se, Te. This formula allows for up to 60 different permutations and each of the five elements in the compound occupies a distinct crystallographic site, offering a rich playground to explore the chemical and physical properties of these compounds. However, not all the possible permutations of this formula appear to be synthesisable, particularly those compounds containing both Ag and S. Boskovic attempted the synthesis of several compounds of this series: $Sr_2MnO_2Ag_2S_2$, $(Sr/Ba)_2CoO_2Ag_2S_2$ and $Sr_2ZnO_2Ag_2S_2$, none of these reactions resulted in the target phase, despite multiple attempts.[57] This leads to the likely conclusion that these compounds cannot be synthesised with Ag-S layers, as may be rationalised using steric arguments. It has also been found that attempts to synthesise compounds where *M* = Fe resulted in the formation of compounds of the $m = 2$ structure type, this is believed to be due to the favourability of the Fe^{3+} state in this environment.[48]

Central to this structure is the first-row transition metal in a distorted octahedral environment, shown in Fig. 1.7.

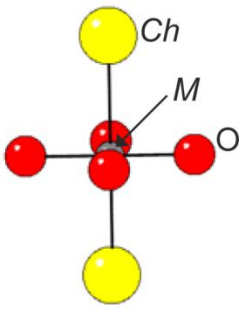


Fig. 1.7 The coordination environment of M in $A_2MO_2X_2Ch_2$, where A = *Sr, Ba;* M = *Mn, Co, Ni, Cu, Zn;* X = *Cu, Ag and* Ch = *S, Se, Te*

This environment leads to many interesting structural, electronic and compositional effects which are highly dependent on the identity of all five of the elements within the compound. Some of the products of high-temperature synthesis have been shown to have inherent deficiencies in *X* (the coinage metal in the chalcogenide layer), as in the case of most compounds where *M* = Mn, due to the Mn^{2+}/Mn^{3+} mixed oxidation state. It has been found that several *M* = Mn compounds containing Ba, such as $Ba_2MnO_2Cu_{1.8}Se_2$[58] and $Ba_2MnO_2Ag_{1.8}Se_2$[59] have a larger *X* fractional occupancy than their Sr containing analogues $Sr_2MnO_2Cu_{1.5}Se_2$[60] and $Sr_2MnO_2Ag_{1.5}Se_2$,[60] implying that the oxidation state of Mn is lower in the Ba analogues, most likely induced by the longer Mn-O bond. This is an example of the sensitivity of the properties of the transition metal to the whole chemical environment and not just the directly bonding atoms in this structure.

Compounds where *M* = Co appear to be the most widely formed, >95 wt% pure samples of: $Sr_2CoO_2Cu_2S_2$,[42, 58, 61] $Sr_2CoO_2Cu_2Se_2$,[58, 60] $Sr_2CoO_2Ag_2Se_2$,[60] $Ba_2CoO_2Cu_2S_2$,[42] $Ba_2CoO_2Cu_2Se_2$, [60] and $Ba_2CoO_2Ag_2Se_2$[59, 62] have all been reported. This contrasts with the cases where *M* = Ni, Cu, here the only reported compounds are $Sr_2NiO_2Cu_2S_2$ and $Sr_2CuO_2Cu_2S_2$, both of which appear to be metastable with maximum reported purities of ~90 wt% and ~75 wt% respectively.[47, 58]

The Zn containing analogues $Sr_2ZnO_2Cu_2S_2$ and $Sr_2ZnO_2Cu_2Se_2$, contain a d^{10} metal so, in contrast to their grey/black d^n ($n \neq 10$) cousins, are obtained as bright orange powders.[63, 64] This implies that the compounds are band-gap semiconductors with direct band gaps in the visible region.[41, 63]

It appears that increasing the size of the alkali-earth metal from Sr to Ba and the size of the coinage-metal ion from Cu to Ag puts significant strain on the Zn bonding environment. A small, but distinct, lowering of symmetry from the tetragonal *I4/mmm* to the orthorhombic *Cmca* was identified in $Ba_2ZnO_2Ag_2Se_2$ due to the formation of a linear O-Zn-O coordination environment of Zn^{2+},[62, 65] contrasting with the square-planar array observed for $Sr_2ZnO_2Cu_2Se_2$, as shown in Fig. 1.8. The single-crystal structure of the Cu-containing analogue $Ba_2ZnO_2Cu_2Se_2$ had oxygen thermal ellipsoids an order of magnitude larger along the Zn-O bond than $Sr_2ZnO_2Cu_2Se_2$, but no long-range ordering was observed.[62, 63] This was interpreted as the crystal-structure manifestation of localised pairing of the Zn-O bonds, as shown in Fig. 1.8.

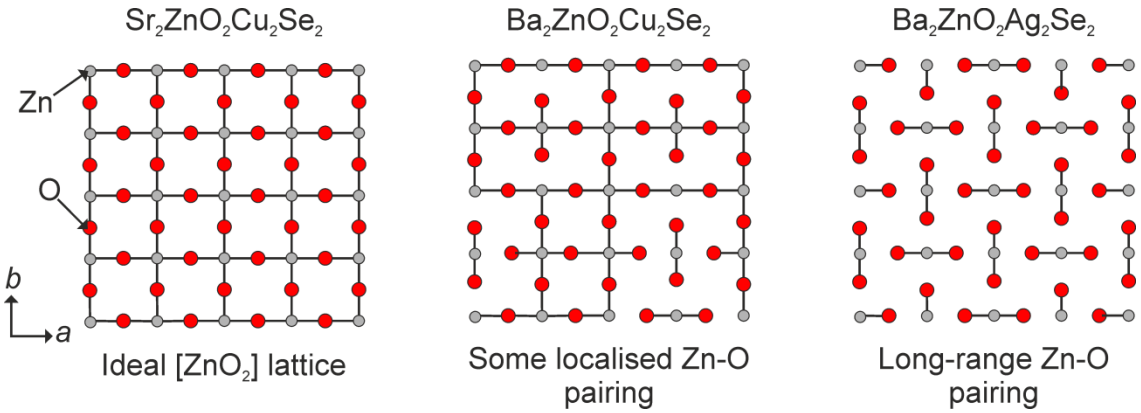


Fig. 1.8 Schematic of the position of the Zn and O atoms in $Sr_2ZnO_2Cu_2Se_2$ (ideal square-planar array),[63] $Ba_2ZnO_2Cu_2Se_2$ (some localised ordering of Zn-O pairs)[62, 63] and $Ba_2ZnO_2Ag_2Se_2$ (where long-range pairing of Zn-O has occurred)[65]

A brief review of the research into several of these compounds will be provided in the introduction to the relevant chapter.

Several of these compounds are reactive with respect to soft chemistry, be it oxidative deintercalation (a major focus of this thesis) or reductive intercalation of Li/Na. Some examples of this behaviour will be given in section 1.3.5.

1.3 **Soft chemistry**

The most common synthetic route in solid state chemistry is the ceramic method, in which the correct ratio of elements and simple oxides are mixed together and heated to a high temperature to synthesise the target compound. The use of high temperatures typically leads to the synthesis of the thermodynamic product. If this method is used alone then the compounds synthesised will necessarily be limited. This is contrasted with the products of organic chemistry, which are all kinetic products (the thermodynamic product of any organic compound in air being CO_2 and H_2O), so several different organic compounds with the same ratio of elements are often known.

Some methods can be employed to change the thermodynamic product in solid-state synthesis. Examples include quenching, to "freeze" the compound in the high-temperature thermodynamic state; use of evacuated silica tubes, to obtain the thermodynamic state when air is excluded from the reaction and high pressures, to obtain high-pressure states.

Soft chemistry, on the other hand, is used to reach the kinetic product of solid state compounds and has been used in many cases to synthesise compounds with interesting

properties, quite distinct from the parent, which could not be made using traditional methods. Properly understood, this chemistry may also provide a route for the targeted design of compounds with desired properties. In the following section, some examples will be discussed.

1.3.1 CeOCuS and $CeOAg_{0.8}S$

This compound is isostructural with LaOCuS (see section 1.2.1), but unlike La^{3+}, Ce^{3+} can be oxidised to Ce^{4+}. When CeOCuS was first synthesised, it was treated as air-stable and therefore thought to be either inherently Cu deficient ($CeOCu_{1-x}S$).[66-68] However, Pitcher *et al.* showed that if the compound was treated as air-sensitive, then stoichiometric CeOCuS could be synthesised. Stoichiometric CeOCuS is green, but rapidly turns black on exposure to air, as the compound oxidises to $CeOCu_{1-x}S$ and CuO.[69] Pitcher *et al*. forced this oxidation using a wet O_2 flow and showed that the oxidation could be reversed using a H_2/N_2 flow.[69]

By contrast the silver analogue, CeOAgS could never be made fully stoichiometric, the highest silver content found was ~0.8 ($CeOAg_{0.8}S$).[70] However, the Ag ions appear to be more mobile than in the case of CeOCuS because ^{n}BuLi could be used to fully lithiate the compound to CeOLiS, which could not be achieved with CeOCuS.[70] Further work showed that the Ce^{4+} compound CeOS could be formed, either by deintercalation of Li from CeOLiS, using excess I_2 dissolved in acetonitrile (MeCN),[70] or directly from $CeOAg_{0.8}S$ again using I_2/MeCN, but with the addition of excess NaI to prevent precipitation of AgI.[71] Neither CeOLiS nor CeOS can be made via a high-temperature route.

1.3.2 $Sr_4Mn_3O_{7.5}Cu_2S_2$

The structure of $Sr_4Mn_3O_{7.5}Cu_2S_2$ was discussed in section 1.2.3.1. The product from high-temperature synthesis contains Mn with average oxidation state Mn^{3+}. Hyett *et al.* found that the presence of oxygen vacancies made the compound labile to both oxidation and reduction.[44] Oxidation was achieved by filling the oxygen vacancies with F^-, using XeF_2 as the fluorination agent. Reduction was achieved using NaH to increase the concentration of oxygen vacancies. These three compounds are structurally similar to one another, but reducing the compound led to a dramatic reduction in the antiferromagnetic ordering temperature (T_N), while oxidation led to a small increase in

T_N, as observed by both magnetic susceptibility and powder neutron diffraction measurements.[44]

1.3.3 FeSe

Tetragonal FeSe is an unconventional (non-BCS) superconductor with transition temperature, T_c = 8.5 K.[72] However, T_c is highly sensitive to changes in composition. KFe_2Se_2, in which the alkali metal is positioned between the iron-selenide layers (see Fig. 1.9), has a significantly higher T_c of 30 K.[73] These discoveries led to significant research into the chemistry that is possible between the layers of this compound.

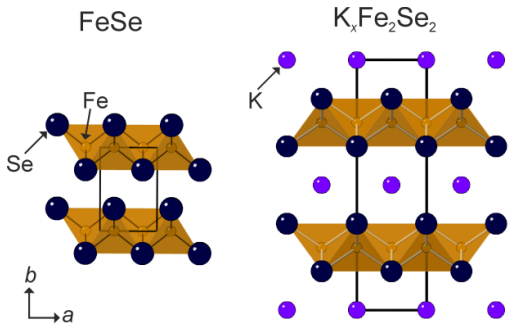


Fig. 1.9 The crystal structures of FeSe and $K_xFe_2Se_2$

One such example was the intercalation of Li into tetragonal FeSe using ammonia, producing a compound with T_c = 44 K.[74] This was initially reported as the synthesis of $Li_xFe_2Se_2$, but further work by the Clarke group demonstrated that intercalation of Li via this method also intercalated ammonia.[75] This work was followed up by an *in situ* experiment that showed that initial intercalation of Li using ammonia produced an ammonia-rich compound with T_c = 39(1) K, but applying dynamic vacuum for extended periods, in order to isolate the product as a dry powder produced the ammonia-poor compound with the increased T_c, as shown in Fig. 1.10.[76]

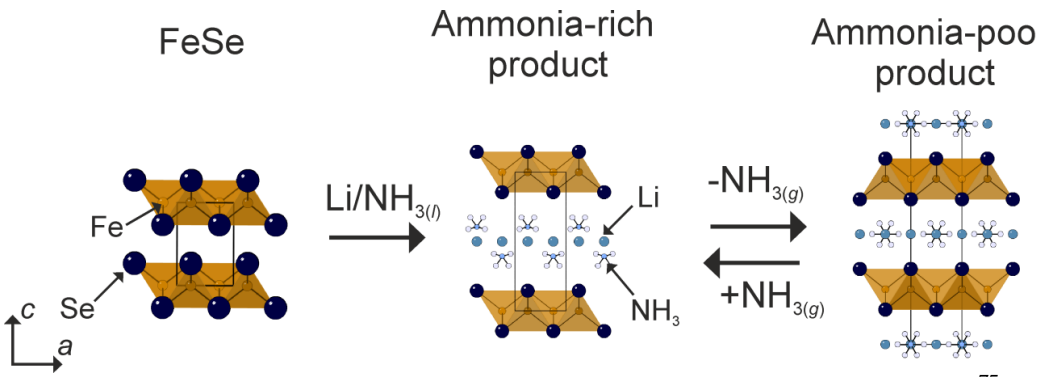


Fig. 1.10 Reaction scheme for the reaction of FeSe with Li and liquid ammonia[75]

1.3.4 Reduction of $LaNiO_3$

The formal oxidation state of Ni in $LaNiO_3$ is Ni^{3+}, but it was found that the compound could be reduced to $La_2Ni_2O_5$ (oxidation state: Ni^{2+}) by either flowing dilute H_2 at 390 °C or reacting it with an electropositive metal, such as Zr at similar temperatures.[77] Earlier reports suggested the existence of a third, Ni^+, phase $LaNiO_2$,[78, 79] but attempts to synthesise this phase by other groups were not successful until the work by Hayward *et al.* It was shown that if NaH was used, lower temperatures ($180 \leq T$ (°C) ≤ 210) could be used to reduce the parent compound, allowing for much greater control of the reduced products and allowing for the isolation of $LaNiO_{2+x}$ (where $x \sim 0.025$).[80]

This layered $LaNiO_2$ compound was of interest because it is isostructural and isoelectronic to $SrCuO_2$, the parent compound of several members of the high T_c cuprate superconductors. In the case of $LaNiO_{2+x}$ it was found that the compound had antiferromagnetic character (as observed from magnetic susceptibility data), but disorder in the Ni oxidation, caused by the presence of a few interstitial oxide ions (x), was sufficient to prevent observation of long-range ordering of the moments (see section 1.4.5 for discussion of antiferromagnetism).[80]

1.3.5 Reductive lithiation of $Sr_2MnO_2Cu_{1.5}S_2$ and $Sr_2MnO_2Cu_{3.5}S_3$

The Cu ions in $Sr_2MnO_2Cu_{1.5}S_2$ and $Sr_2MnO_2Cu_{3.5}S_3$ may be fully exchanged for Li using ^{n}BuLi, forming $Sr_2MnO_2Li_{1.86(3)}S_2$ and $Sr_2MnO_2Li_{3.8(1)}S_3$ respectively.[81] This resulted in the reduction of the Mn ion in both cases and therefore caused a change in the magnetic structure as observed in both magnetic susceptibility and PND data.[54]

It was found that the resultant sample, a mixture of the lithiated product and extruded copper, was air sensitive, which oxidised to the parent material ($Sr_2MnO_2Cu_{1.5}S_2$ or $Sr_2MnO_2Cu_{3.5}S_3$) and LiOH on exposure to air, as shown in the schematic in Fig. 1.11 for $Sr_2MnO_2Cu_{1.5}S_2$.

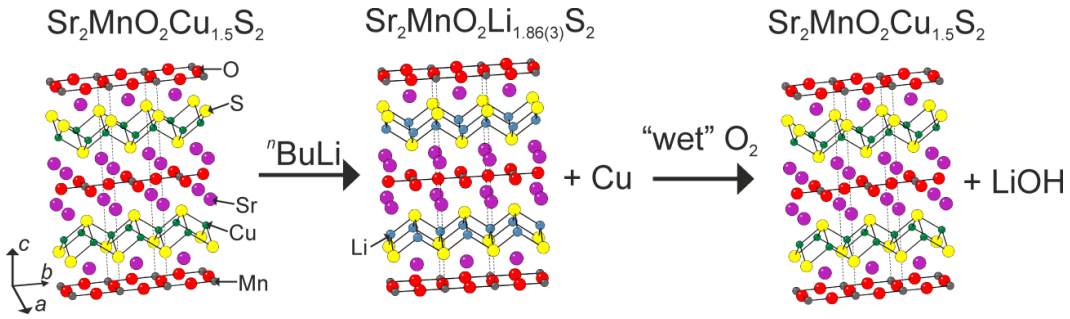


Fig. 1.11 Schematic of the reversible reaction of $Sr_2MnO_2Cu_{1.5}S_2$ to form $Sr_2MnO_2Li_{1.86(3)}S_2$;[81] the equivalent reaction is also possible with $Sr_2MnO_2Cu_{3.5}S_3$. Lithiation extrudes Cu as the element; when Li is then deintercalated in air the Cu on the surface of the particles reinserts, restoring the original compound

The demonstrable reversibility of the reaction led to the investigation of these compounds as battery materials. Indris *et al.* found that Li could be electrochemically intercalated into these compounds and that the reaction was partially reversible. Comparison of these compounds with the reaction of Cu_2S found greater reversibility in the oxychalcogenides, suggesting that the Sr_2MnO_2 layers play a role in the structural stability of the compounds.[82]

1.4 Magnetic behaviour of solids

Magnetism may be thought of as arising from the movement of current around a loop. On an atomic scale this translates to the movement of electrons within orbitals. The magnetic moment of an atom is determined by the combined total angular momentum of each electron, given by *l* (angular quantum number) and *s* (spin quantum number). For this the magnitude of orbit-orbit, spin-orbit and spin-spin couplings must be considered. However, in the case of the first-row transition metals, the magnetic atoms considered in this thesis, several of these effects may be disregarded in most cases. The magnitude of spin-orbit coupling is highly dependent on the charge of the nucleus and thus can often be neglected to a first-approximation for elements as light as the first-row transition metals, although it becomes more important towards the end of the series. It has also been shown that, due to the strong level of electronic interaction between the magnetic ion and its crystal lattice, the orbital contribution to the magnetic moment is quenched and therefore, as a first approximation, may be disregarded for first-row transition metals in many crystal environments. This leads to the spin-only approximation of the magnetic moment:

$$\mu_{eff} = g\sqrt{S(S+1)} \tag{1.1}$$

where μ_{eff} is the effective magnetic moment, S is the total spin and g is the free electron g-factor, when the orbital contribution to the magnetic moment is quenched $g \sim 2$. The spin-only approximation has been shown to offer better correlation (in most cases) with the empirically measured magnetic moments than the equivalent equation calculating the total magnetic moment including the full orbital contribution. However, there are many cases where the orbital contribution cannot be neglected in the first row, especially in Co^{2+} compounds.[83]

The lanthanides, the other major class of magnetic ions, exhibit very different magnetic behaviour. This is because the ligand field effects are much less important, so the magnetic moment may be approximated from the free-ion moment where both spin and orbital contributions are considered:

$$\mu_{eff} = g\sqrt{J(J+1)} \tag{1.2}$$

where J is the total magnetic moment, and the g-factor, g, is calculated by:

$$g = \frac{3}{2} + \frac{S(S+1) - L(L+1)}{2J(J+1)} \tag{1.3}$$

In extended solids, the magnetic moments of individual atoms interact in many ways, depending on the environment. The most basic interactions will be discussed below.

1.4.1 Diamagnetism

The diamagnetic effect is the phenomenon in which electrons work to oppose the magnetic field. This effect is present in all materials, but is sufficiently weak compared with other magnetic effects that it is only normally observed when other magnetic effects are not present, that is when all the orbitals are either filled or empty.

1.4.2 Paramagnetism

A paramagnet contains atoms with unpaired spin. The magnetic moment on each atom is randomly orientated and easily perturbed, so a paramagnet may be thought of as a spin-gas. These randomly orientated spins may be aligned by a magnetic field, H. The ease with which the magnetic spins may be aligned is called the magnetic susceptibility, χ and is calculated by:

$$\chi = \frac{M}{H} \tag{1.4}$$

where M is the magnetisation. The magnetic susceptibility decreases with increasing temperature because as temperature increases thermal fluctuations are more likely to perturb the spin. The magnetic susceptibility and inverse magnetic susceptibility of a representative paramagnet are shown in Fig. 1.12.

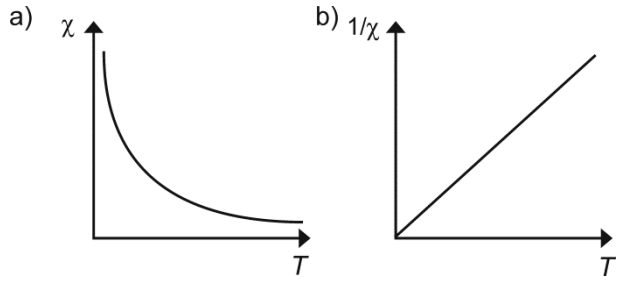


Fig. 1.12 a) the magnetic susceptibility and b) the inverse magnetic susceptibility of a typical paramagnet as a function of temperature

If the spins are not interacting, the relationship between χ and temperature, T, is considered in the Curie law:

$$\chi = \frac{C}{T} \tag{1.5}$$

where C is the Curie constant. The Curie constant is related to the effective magnetic moment, μ_{eff}, by:

$$\mu_{eff}{}^2 = \frac{3k}{N_A \mu_B{}^2} C \approx 8C \tag{1.6}$$

where k is the Boltzmann constant, N_A is Avogadro's constant and μ_B is the Bohr magneton.

The Curie law assumes that the moment of each atom is independent of the other. While this is the case in a true paramagnet, it is considered rare in solids where there are strong interactions between neighbouring atoms. Often coupling effects will act to align the moments in the same direction as one another (ferromagnetism) or will act to align the moments in the opposite direction to one another (antiferromagnetism). Each coupling interaction has a corresponding energy and therefore may be broken by sufficient thermal energy. This means that above some transition temperature the magnetic spins will act like paramagnet, this is called the Curie temperature (T_C) in a

ferromagnet and the Néel temperature (T_N) in an antiferromagnet. These phenomena will be discussed in greater detail in sections 1.4.4 and 1.4.5.

However, while above the transition temperature, where thermal fluctuations prevent the spins from freezing into a crystalline solid, the interactions still influence the susceptibility. This is taken into account in the Curie law by the addition of the Weiss temperature, θ, to form the Curie-Weiss law:

$$\chi = \frac{C}{T - \theta} \tag{1.7}$$

The inverse susceptibility of a ferromagnet, antiferromagnet and paramagnet are compared in Fig. 1.13, showing the relationship between θ and T_C and T_N in the ideal cases. $|\theta|$ generally compares well with T_C and T_N, though it may not in the case of more complex magnetic phenomena.

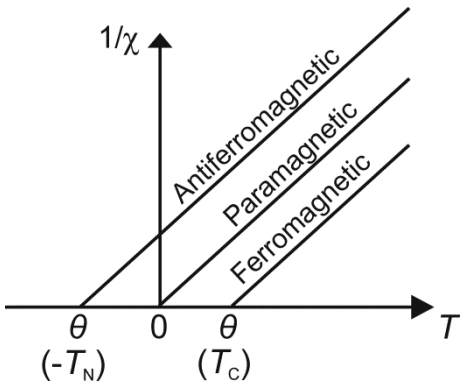


Fig. 1.13 Inverse magnetic susceptibilities of typical antiferromagnetic, paramagnetic and ferromagnetic materials as a function of temperature

1.4.3 Pauli paramagnetism

The previous description of paramagnetism assumed that electrons are localised to their individual atoms. This model is reasonable for insulators, but breaks down when the magnetic behaviour of metals is considered due to the significant delocalisation of electrons into bands. In this case, a free-electron model may be used to understand the results. Fig. 1.14 shows the density of states in a free-electron gas both before and after a field is applied. It shows that when a field is applied in the *up*-direction, that is parallel to the *down*-spin electrons, the energy of the *down*-spin electrons is reduced, while the energy of the *up*-spin electrons is increased.

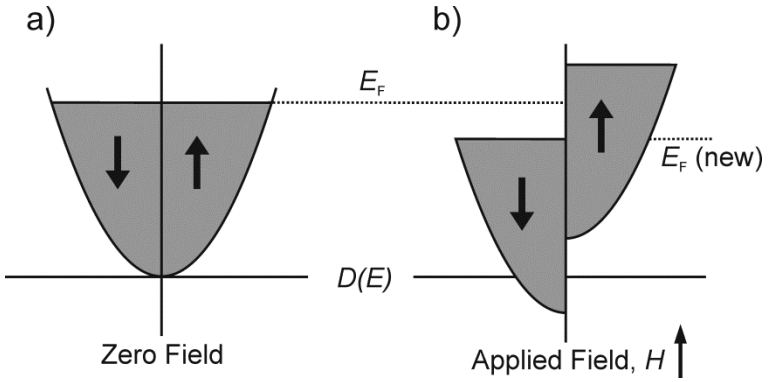


Fig. 1.14 The change in the density of states of a free electron gas when a magnetic field, H, is applied

The change in energy results in a change in the ratio of *up* and *down*-spin electrons until a new fermi level, E_F is obtained. The result apparent from this model is that the magnetic susceptibility is related to the density of states at E_F, $N(E_F)$, and is independent of temperature.

The magnetic susceptibility of a Pauli paramagnet is normally much smaller than that of a conventional (Curie) paramagnet. Therefore, often the diamagnetic susceptibility from the core electrons cannot be disregarded and require subtraction to produce the paramagnetic magnetic susceptibility, χ_P. A further discussion of Pauli paramagnetism is included in section 6.5.

1.4.4 Ferromagnetism

The temperature at which the spins in a ferromagnet "freeze" in the same direction is determined by the strength of the ferromagnetic coupling interactions.

Below T_C, although the magnetic moments are locally aligned to one another, the bulk material is often divided into domains, to minimise the total magnetic energy. The direction of the moment within each domain may be changed by the application of a magnetic field. This is demonstrated in the annotated hysteresis loop in Fig. 1.15.

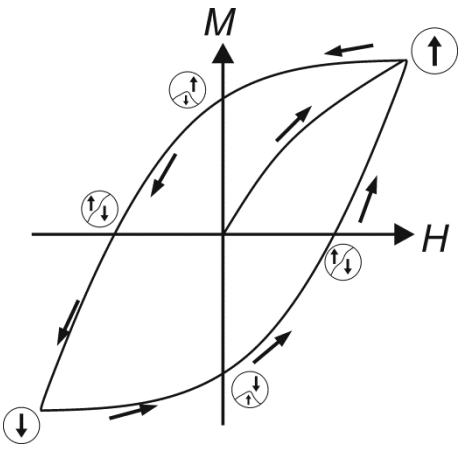


Fig. 1.15 Representative hysteresis loop of a ferromagnet, annotated with the representative behaviour of the magnetic domains. In this example, the ferromagnet is comparatively hard, that is the behaviour of the ferromagnetic domains is highly history dependent. Only a small rearrangement of the domains occurs on reduction of the field from the saturation field (H_s) to a zero field and a large negative field is required to reach zero magnetisation, where the domains are aligned equally in both directions

1.4.5 Antiferromagnetism

In an antiferromagnet, coupling interactions cause anti-alignment of neighbouring moments. The moments freeze in a long-range, fully anti-aligned structure below T_N, when the energy of the coupling interactions is larger than the thermal energy. Antiferromagnetism is generally more common than ferromagnetism.

The magnetic susceptibility of typical antiferromagnetic powder as a function of temperature is shown in Fig. 1.16. Note that paramagnetic behaviour is observed above T_N and below T_N the magnetic susceptibility decreases as temperature decreases.

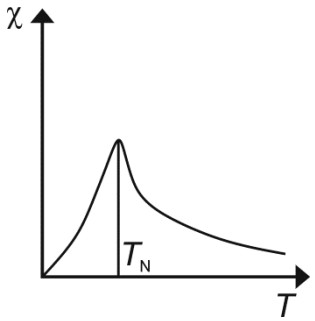


Fig. 1.16 The magnetic susceptibility of a typical antiferromagnet as a function of temperature

One such reason that coupling interactions between spins might cause them to anti-align is superexchange. In superexchange, the action of an intermediary orbital (e.g. an oxide 2p orbital in a covalent interaction with the metal d orbitals) causes the two magnetic ions to couple antiferromagnetically, as is shown in the schematic in Fig. 1.17. The

rules of these interactions were rationalised by the work of Goodenough and Kanamori,[84-86] although deviations from these rules are known.

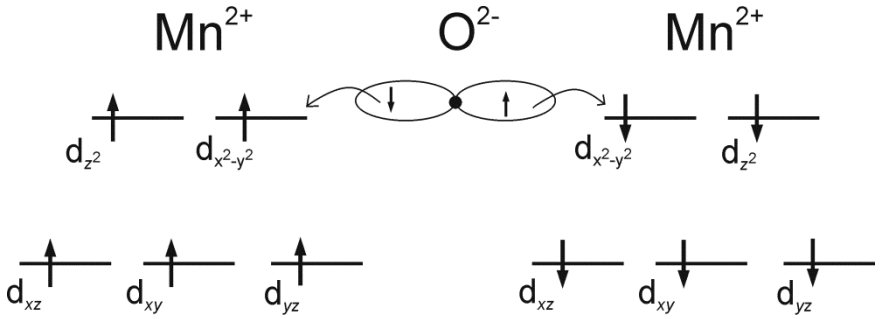


Fig. 1.17 Schematic of superexchange interactions causing antiferromagnetic coupling of two Mn^{2+} ions in an octahedral environment

1.4.6 Spin-glass materials

Spin-glass materials arise when there are strong interactions between magnetic spins, but competing interactions lead to frustration. An example of magnetic frustration is shown in Fig. 1.18 for the classical case of an equilateral triangle in which the favourable coupling interaction is for each spin to align antiparallel to its nearest neighbour. This type of magnetic frustration is called geometric frustration because the position of the magnetic spins in relation to one another prevents full satisfaction of the predominant magnetic interaction.

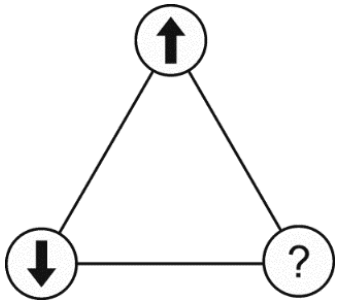


Fig. 1.18 Schematic demonstrating the geometric frustration of magnetic spins in a triangular lattice

This magnetic frustration means that there are several possible magnetic configurations, rather than a single low-energy state, as is the case for classical ferromagnets and antiferromagnets. If there is chemical disorder in the system, this often leads to the frustration of the interactions which prevents long range magnetic order, even below the temperature when the coupling interaction between spins is greater than the thermal energy. This temperature is known as the spin-glass freezing temperature, T_g, and the arrangement of spins below this temperature may be thought of as analogous to the

arrangement of atoms within a conventional glass: arranged randomly within a framework of strong interactions. Several experiments have been designed to further understand the properties of these materials.[87]

1.5 Summary and project aims

This introduction has introduced the $A_2MO_2X_2Ch_2$ class of compounds in the wider context of layered oxychalcogenides and has also shown the huge changes in physical properties that are achievable using soft chemistry.

The $A_2MO_2X_2Ch_2$ class of compounds is extremely large and diverse, in properties as well as in composition. Therefore, a significant fraction of this project has focussed on the synthesis of novel compounds of this type and understanding the physical properties of these compounds. A second strand of work has been investigation the effects on these compounds when they are topotactically oxidised, primarily using I_2 as an oxidant to remove some of the coinage metal, *X*.

It has been found that the primary determiner of a compound's properties for this class is the identity of *M*. To this end, the results chapters of this thesis are divided by the identity of *M*: manganese, cobalt, nickel and copper. An additional chapter explores the results when the reaction of $Sr_2MnO_2Cu_{1.5}S_2$ with I_2 was investigated *in situ*.

Chapter 3 describes the effects on the structure and magnetic behaviour of $Sr_2MnO_2Cu_{1.5-x}S_2$ when Cu is oxidatively deintercalated. It shows that the lowest-Cu-content compound: $Sr_2MnO_2Cu_{1.33}S_2$ is incommensurately modulated. Attempts are also made to characterise the behaviour of $Sr_2MnO_2Cu_{1.5-x}S_2$ at Cu occupancies intermediate between the parent and the lowest-Cu-content compound. The chapter also describes the magnetic ordering behaviour of $Sr_2MnO_2Ag_{1.5}Se_2$, which has been synthesised with high purity for the first time and the magnetic behaviour of $Sr_2MnO_2Cu_2Te_2$, a novel compound.

The next chapter describes the investigation of the reaction of $Sr_2MnO_2Cu_{1.5}S_2$ *in situ*. The development of equipment to carry out this investigation is reported, along with suggestions for further development. The results of this experiment are also analysed, showing the changes in lattice parameters and ordering behaviour over the course of the reaction.

Chapter 5 compares the behaviour of four cobalt-containing compounds: $Sr_2CoO_2Cu_2S_2$, $Sr_2CoO_2Cu_2Se_2$, $Sr_2CoO_2Cu_2Se_{1.6}S_{0.4}$ and $Sr_2CoO_2Ag_2Se_2$ when Cu/Ag is oxidatively deintercalated, also using I_2. Particular attention is paid to the changes in magnetic behaviour that occur as a result. The synthesis, structure and magnetic ordering behaviour of the novel compound $Sr_2CoO_2Cu_2Te_2$ is also reported here.

Chapter 6 describes the synthesis and behaviour of $Sr_2CuO_2Cu_2Se_2$ and $Ba_2CuO_{2-x}Cu_2Se_2$. These compounds are related by the isovalent substitution of the alkali-earth metal, but have very different observed behaviours. As is explained within the chapter, these are thought to arise from the changes in the Cu oxidation state from the expansion of the Cu-O-Se coordination environment, resulting from the use of the larger alkali-earth metal. It was found that the oxygen content of $Ba_2CuO_{2-x}Cu_2Se_2$ can be increased by heating the compound under a flow of O_2; the results of this experiment are discussed.

Chapter 7 details the synthesis and characterisation of $Sr_2NiO_2Cu_2Se_2$. The structural, magnetic and bulk resistivity behaviours are all analysed as a function of temperature, to understand the underlying electronic behaviour of this compound. This compound was also found to react with I_2 at low temperature and the observed changes in the compound that result from this are also described.

The final chapter concludes the findings from this thesis.

Chapter 2
2 Experimental Methods

In this thesis, samples were synthesised via high-temperature ceramic synthesis and then selected samples were chosen for titration against iodine, in which I_2 dissolved in acetonitrile (MeCN) was used to oxidatively deintercalate Cu/Ag from the chalcogenide layers of the synthesised $A_2M_2O_2X_2Ch_2$ (*A* = Sr, Ba; *M* = Mn, Co, Ni, Cu, Zn; *X* = Cu, Ag; *Ch* = S, Se, Te) compound.

The samples produced using these methods were then analysed using powder X-ray diffraction (PXRD), powder neutron diffraction (PND), single-crystal X-ray diffraction (SCXRD), electron diffraction, electron microscopy, magnetometry and bulk resistivity measurements.

2.1 Synthetic methods

2.1.1 Ceramic synthesis

The standard synthesis route for the quinary compounds discussed in this thesis was via the ceramic method. In the ceramic method, the reactants and products are in the solid state at all points in the reaction, this means that the reaction occurs at the interface between reactant grains and the rate-limiting step is often diffusion of reactants. To this end, it is important to minimise the distance between particles, when attempting to synthesise samples with high purity. It is also difficult to purify the products of a solid-state reaction, necessitating the use of the highest purity starting materials available.

For the ceramic-synthesis products described in this thesis, starting materials, normally elements and simple oxides and chalcogenides (such as SrO and SrS), were weighed out and ground in an agate pestle and mortar, mixing the reactants thoroughly. The reactants were then pelletised to maximise contact between grain boundaries. Then the pellets were loaded into an alumina crucible and sealed in an evacuated pre-dried silica tube. All the compounds described in this thesis contain S/Se/Te and Sr/Ba. S/Se/Te oxidise to sulfates/selenates/tellurates when heated in air, so it was necessary to heat these samples in an inert atmosphere, in this case provided by encasing the reactants in an evacuated silica tube. However, Sr/Ba containing samples react with silica, causing

the formation of impurities, so an alumina crucible was used to prevent direct contact between the reactants and the silica tube.

Once the sample had been prepared it was placed inside a furnace and heated to the reaction temperature; the standard heating rate used was 10 °C min^{-1} unless stated otherwise. The furnace was held at the synthesis temperature for a period of time determined by the requirements of the reaction. Then either the tube was cooled at the natural rate of the furnace or the sample was quenched to room temperature (RT) in a bucket of ice-water.

Samples were quenched using an ice-water bath if it was thought that the desired product was the thermodynamic product at the synthesis temperature, but that other phases were possible at temperatures in between the synthesis temperature and RT; quenching was therefore used to "freeze" the sample in the high temperature thermodynamic product. Otherwise the samples were cooled in the furnace.

2.1.2 Handling of air-sensitive materials

All products and starting materials described in this thesis were treated as air-sensitive as standard. All samples were therefore stored in an argon-filled dry glovebox. Argon was constantly circulated through a Dow Chemical copper catalyst to remove contaminating O_2 and a molecular sieve bed to remove contaminating H_2O that may have leaked into the glovebox. The O_2 concentration was monitored using an integral O_2 sensor that read below 1 ppm under normal working conditions.

When pressing pellets, it was necessary to do so outside of the glovebox. When this was done, the powder was loaded in the pellet die inside the glovebox and sealed inside an argon-filled polyethylene bag, removed from the glovebox in order to press the pellet and returned to the glovebox to extract the pellet.

Silica often retains moisture, even when appearing to be dry. Therefore, all silica tubes were stored in an 80 °C oven until required for use and then heated under dynamic vacuum using a butane/oxygen blowtorch for ~5 min to remove as much moisture as possible before exposing the sample to the silica tube.

2.1.3 Oxidation using iodine

Oxidative deintercalation of Cu/Ag from the compounds described in this thesis was performed using I_2 dissolved in acetonitrile (MeCN). Previous attempts to deintercalate

these elements from similar compounds using stronger oxidising agents, such as Br_2 or NO_2BF_4 had led to compound decomposition.[88] I_2 was therefore used as standard, due to its status as the strongest readily available oxidising agent that does not lead to sample decomposition.

For a standard reaction, small quantities of I_2 (99.99%, Alfa Aesar, precise mass determined by the reaction) was dissolved in approximately 30 cm^3 of MeCN. As the reactants and products were all treated as air-sensitive, the MeCN used was pre-dried using a commercial molecular-sieve-based solvent purification system and the I_2 was dried under dynamic vacuum for ~20 min prior to use. The I_2/MeCN solution was then cooled in an ice-water bath because Adamson and Cohen had previously found that a greater degree of oxidation was achieved in the removal of Cu from $Sr_2MnO_2Cu_{1.5-x}S_2$ when the reaction was performed below RT.[88, 89] This was thought to be because the lower temperature suppressed the domination of compound-destructive side-reactions.

Once cooled, the I_2 solution was transferred using a cannula and inert-gas overpressure to a precooled Schlenk flask containing the reactant compound. The reaction was then left to stir for a period determined by the reaction, but typically 1 – 2 days. The product was then filtered and washed three times in clean MeCN before drying for at least 20 min under dynamic vacuum and isolating in the glovebox.

When the most-oxidised product of the reaction of I_2 with the parent compound was targeted, an over-excess of 1.5 molar equivalents (equiv., I:Cu ratio) of I_2 was used to ensure the reaction went to completion. When a sample with Cu/Ag occupancy between that of the parent compound and the most-oxidised product was desired, smaller amounts of I_2 were used, typically ~0.1 equiv. However, it was difficult to quantify the amount of I_2 required to synthesise a specific product due to the difficulty with quantifying the effects of compound-destructive side-reactions,[89] amongst other effects, such as grain size. Therefore, several similar reactions were performed to produce a range of products.

2.1.3.1 *Deintercalation of Ag*

When first performing reactions in which Ag was deintercalated, it was found that the sample was contaminated by large quantities of AgI that could not be removed by repeated washings with MeCN. This was a similar problem to that identified by Lim, when using I_2 to deintercalate Ag from $CeAg_{1-x}OS$. Lim found that the addition of an

excess of NaI to the solution prevented the precipitation of AgI.[71] This is because NaI dissolves readily in MeCN, forming Na^+ and I^- ions. These released I^- ions react with AgI, forming complexes such as $[AgI_2]^-$ that are soluble in MeCN. This method was found to be extremely effective in preventing the precipitation of AgI.

2.1.4 Synthesis of SrO

SrO was synthesised by thermal decomposition of $SrCO_3$ under dynamic vacuum, as shown in eq. 2.1:

$$SrCO_3 \rightarrow SrO + CO_2 \quad (2.1)$$

Approximately 7 g of $SrCO_3$ was loaded into two alumina boats and placed inside a 25 mm diameter silica tube. The silica tube was sealed with two Swagelok endcaps, one of which was fitted with a Young's tap attachment. This attachment was connected to the vacuum line and left under dynamic vacuum. The tube was placed inside a split tube furnace and two fans were set up below the endcaps to prevent the rubber O-rings from overheating and damaging. Care was taken to ensure that the system was adequately sealed before the heating process was started. The setup is shown in Fig. 2.1.

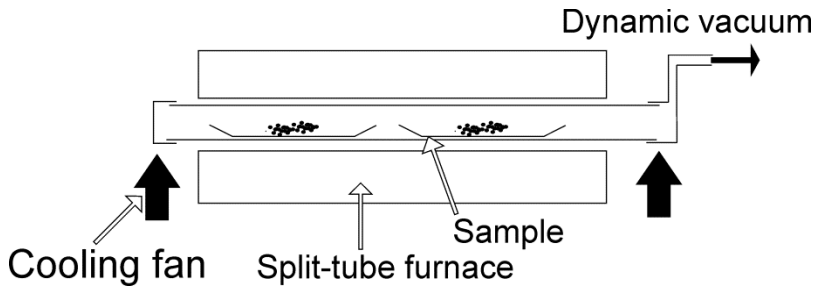


Fig. 2.1 Schematic of the setup used for synthesising SrO from $SrCO_3$

The furnace was heated to 837 °C (rate: 10 °C min^{-1}) for 18 h. The CO_2 produced from this reaction was condensed in the liquid-nitrogen-cooled trap attached to the vacuum line. Finally, to ensure that the reaction had gone to completion, the furnace was heated to 1100 °C (rate: 5 °C min^{-1}) for 4 h before allowing the sample to cool in the furnace. The sample, which is air-sensitive, was isolated in the glovebox and phase-purity assessed using in-house PXRD.

2.1.5 Synthesis of SrS

SrS was synthesised by the reaction of $SrCO_3$ with a continuous flow of CS_2 aerosolised in argon gas:

$$2SrCO_3 + CS_2 \rightarrow 2SrS + 3CO_2 \quad (2.2)$$

CS_2 is extremely toxic and flammable, therefore at all points of this reaction, extreme care was taken to ensure that the equipment was clean and in good repair. The reaction was also performed in a fume-hood. As with the synthesis of SrO, approximately 7 g of $SrCO_3$ was placed in alumina boats, which were themselves placed in an open-ended silica tube and Swagelok endcaps with Young's tap attachments were fitted to either end. The tube was then placed in a split-tube furnace, with cooling fans directed at the endcaps to prevent the rubber O-rings from overheating. A series of bubblers, shown in Fig. 2.2, was setup around the furnace, in which argon gas was directed into an empty bubbler, then a bubbler containing liquid CS_2, this flowed into the silica tube containing the reactants, the argon gas was then directed into an empty bubbler, followed by a bubbler of household bleach and a bubbler of H_2O_2 to destroy any remaining CS_2 before the gas was released at the back of the fume-hood.

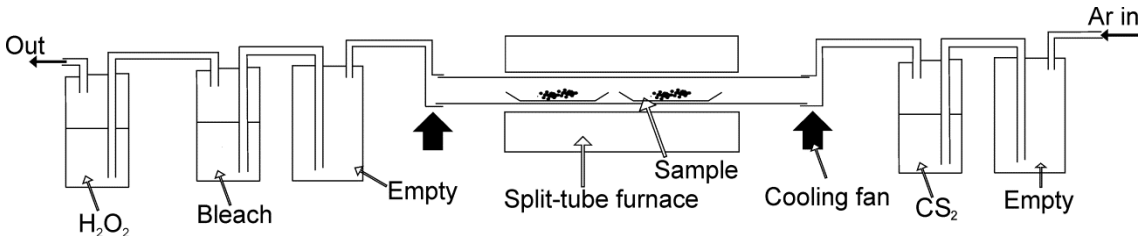


Fig. 2.2 Schematic of the setup used for the synthesis of SrS from $SrCO_3$ and CS_2

Once the Ar/CS_2 was flowing at a constant rate of 2 – 3 bubbles per second, the furnace was heated to 800 °C (rate: 10 °C min^{-1}) for 4 h before cooling in the furnace. This heating process was performed twice. The tube containing the sample was purged with clean argon before removal from the Ar/CS_2 line. The sample was then heated under dynamic vacuum to 700 °C (rate: 10 °C min^{-1}) and held at this temperature for 4 h. This vacuum heating step was performed to remove any elemental sulfur that may have formed from the decomposition of CS_2. SrS is air-sensitive, so the final product was isolated and stored in the glovebox. Phase purity was assessed by in-house PXRD.

2.2 **Diffraction**

Amorphous matter scatters radiation in all directions, with a broad distribution with respect to scattering angle. However, crystalline solids, which are translationally periodic, scatter radiation with wavelength comparable to the size of the crystal lattice (the diffraction grating) in a highly-structured way. The radiation is scattered strongly at

a few, specific angles and weakly at all others due to interference of the scattering from all the periodically-arranged atoms. When the scattered radiation is of the same energy as the incident radiation (elastic scattering), this process is called diffraction. This section will discuss the diffraction of X-rays, neutrons and electrons.

A lot of information may be obtained from the successful performance of a diffraction experiment: lattice parameters, unit cell symmetry, atom identity, position and thermal displacement. From these initial data, a great deal of secondary information can be inferred, such as interatomic distances and angles. The lattice parameters and symmetry are derived from the peak positions, while atomic information is derived from relative peak intensities. Peak positions are indexed using the Laue equations and Bragg's law, while the peak intensities are interpreted using the structure factor.

In commensurate crystallography, a unit cell is defined as the smallest volume three-dimensional unit that can be repeated by purely translational symmetry to comprise the whole crystal. This definition is complicated when a crystal is incommensurately modulated, as is described in section 2.2.3 and Appendix A.

2.2.1 The Laue equations and Bragg's law

Von Laue developed the theory of X-ray diffraction by considering crystals to be three dimensional networks of regularly spaced atoms. This theory is demonstrated in one direction in Fig. 2.3.

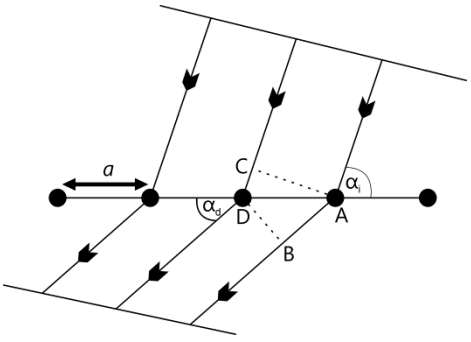


Fig. 2.3 Laue scattering of monochromatic radiation by a one-dimensional lattice

As parallel, monochromatic beams of radiation hit a crystalline lattice, each atom in the row acts like a point scatterer, elastically scattering the radiation with a spherical wave-front. Interference occurs between the scattered beams, which only interfere constructively if the path length differs by an integer number (h) of wavelengths (λ):

$$AB - CD = a(\cos\alpha_d - \cos\alpha_i) = h\lambda \tag{2.3}$$

If this theory is extended to a three-dimensional system, this produces three Laue equations, corresponding to the three orthogonal *x*, *y* and *z* axes, that must be satisfied simultaneously for constructive interference:

$$b(\cos\beta_d - \cos\beta_i) = k\lambda \tag{2.4}$$

$$c(\cos\gamma_d - \cos\lambda_i) = l\lambda \tag{2.5}$$

An alternative description arises from Bragg's law, in which diffraction is considered to arise from the reflection of planes of atoms, known as Miller planes, within a crystal. Miller planes are defined by the Miller indices, *h k l*, which for a unit cell with dimensions $a \times b \times c$ intersect the edges of the unit cell at $\frac{a}{h}$, $\frac{b}{k}$ and $\frac{c}{l}$, respectively. Fig. 2.4 shows the relationship between the difference in path length ($2r$) and the interlayer spacing d_{hkl}, from which Bragg's law can be derived (eq. 2.6).

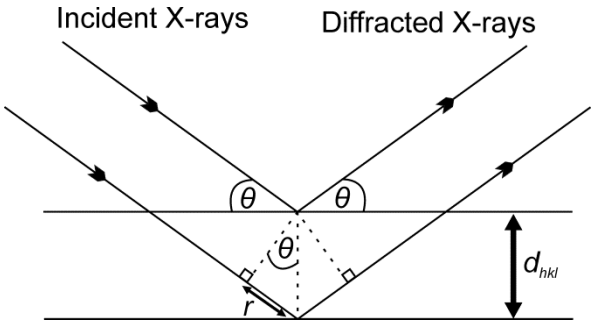


Fig. 2.4 Schematic showing the derivation of Bragg's law from scattering of the Miller planes in one dimension

$$n\lambda = 2d_{hkl}\sin\theta \tag{2.6}$$

2.2.2 Structure factor

As previously stated, while the unit cell lattice parameters are derived from peak positions, atomic information is derived from the peak intensities. This information is derived from the relationship:

$$I_{hkl} \propto |F_{hkl}|^2 \tag{2.7}$$

where I_{hkl} is the intensity of peak *hkl* and F_{hkl} is the structure factor, which is itself related to atomic information by:

$$F_{hkl} = \sum_{n=1}^{N} f_n(\theta)[\cos 2\pi(hx_n + ky_n + lz_n)]q \tag{2.8}$$

$$+ i \sum_{n=1}^{N} f_n(\theta)[\sin 2\pi(hx_n + ky_n + lz_n)]q$$

where x_n, y_n, z_n are the Cartesian coordinates of atom n in the unit cell; q is the Debye-Waller term (discussed below) and f_n is the form factor, which defines the contribution of an atom of an element to the structure factor. In X-ray diffraction, X-rays are diffracted by electron density, where a greater electron density scatters more strongly. Electron density and therefore f_n is dependent on atomic number, Z, and the angle of diffraction, θ:

$$f_n(\theta) \propto \frac{Z}{2}(1 + \cos 2\theta) \tag{2.9}$$

The dependence of f_n on Z makes it difficult to distinguish atoms with similar atomic number, it also means that light elements contribute little in X-ray diffraction. This is not the case in neutron diffraction because neutrons are diffracted by nuclei. The relationship between atom identity and f_n is more complex for neutron diffraction and will be discussed in greater detail in section 2.4.

The Debye-Waller term, q, accounts for the non-static nature of atoms when $T \neq 0$. Atomic vibrations lead to the dispersion of electron density, leading to the reduction in intensity as θ increases. This is because destructive interference increases due to a greater phase difference between scattered waves. The Debye-Waller term for isotropic thermal motion, q_{iso}, is given by:

$$q_{iso} = \exp\left(\frac{-8\pi^2 U_{iso} sin^2(\theta)}{\lambda^2}\right) \tag{2.10}$$

where U_{iso} is the experimentally determined isotropic temperature factor.

If the structure factor could be extracted directly from a diffraction experiment, then it would be computationally trivial to extract atomic information from the data, just as it is to extract lattice parameters from a SCXRD experiment. Unfortunately, I_{hkl} is proportional to $|F_{hkl}|$, not F_{hkl}; this means that, while the amplitude can be extracted from the peak intensities, the phase cannot. This is known as "the phase problem" and makes finding the structure from a diffraction experiment a complex process. Several computational methods, such as the Patterson method,[90] direct methods[91, 92] and, more recently, charge-flipping,[93] have been designed to circumvent this problem.

2.2.3 Aperiodic crystals

The conventional definition of a crystalline material is one where the crystal has a definable unit cell that can be repeated by purely translational symmetry in three dimensions to comprise the whole crystal. However, some materials which are clearly crystalline, giving diffraction patterns with sharp peaks, do not fall into this definition because the diffracted intensity cannot be indexed using a single unit cell in three dimensions. There are two main classes of aperiodic crystals: quasicrystals, which fall outside the remit of this thesis, and incommensurate crystals.

The average structure of an incommensurately modulated structure may be found using conventional periodic crystallography, but there is some feature, such as the position or fractional occupancy of specific atoms that does not change as a function of an integer number of any unit cell. This is called incommensurate modulation and is shown schematically for a one-dimensional array in Fig. 2.5.

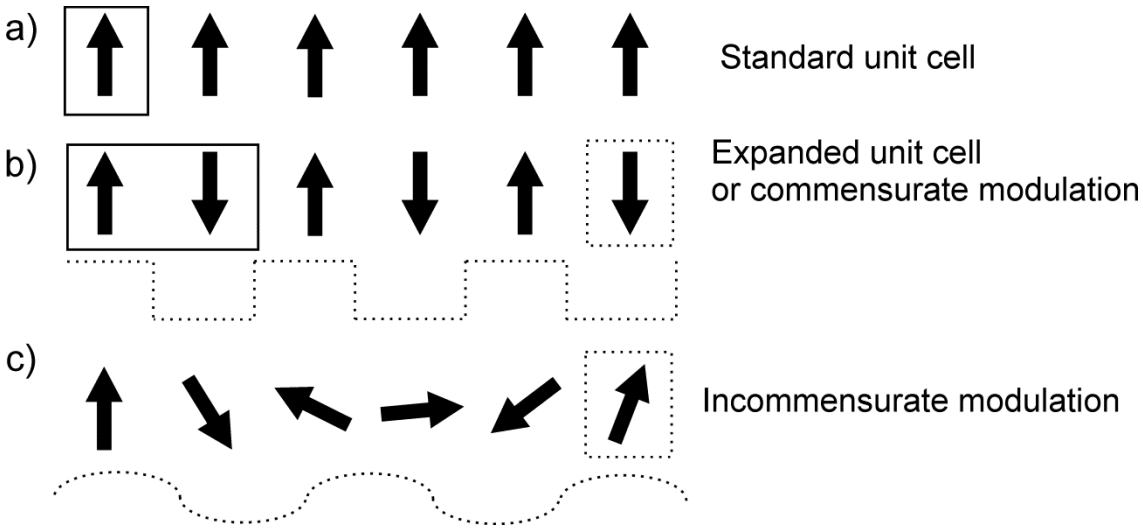


Fig. 2.5 Schematic showing how incommensurate modulation might arise from a one-dimensional array, here the vector represents some feature, such as atom occupancy or displacement that can be varied. a) shows an array where the unit cell is defined in the conventional way; b) shows the vector changing with a period of 2, this may be defined as an expanded unit cell or as the average unit cell convoluted with some function describing the modulation; c) shows that once this technique is employed, there is no reason that the period of modulation should be an integer number of the average unit cells, that is the modulation can be incommensurate

Modulated structures are indexed using the standard lattice parameters and then up to three modulations vectors, known as *q* vectors. The *q* vector is defined as the reciprocal of the modulation periodicity and has a component in *a*, *b* and *c* (though it may be zero). The symmetry is then defined by a new set of space groups, known as superspace

groups, necessitated by the additional dimensions used. Further detail on incommensurate crystallography is provided in Appendix A.

2.3 **Powder X-ray diffraction**

In a powder diffraction experiment, an arbitrarily large number of crystallites are measured at once. When the sample is irradiated, cones of intensity, rather than spots, are produced for each reflection. This is because every crystal orientation is sampled simultaneously. These cones, known as Debye-Scherrer cones, are shown in Fig. 2.6.

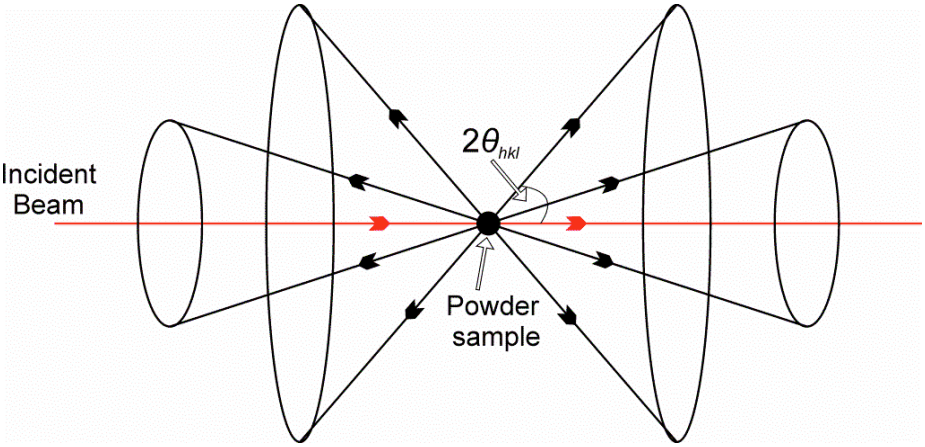


Fig. 2.6 Schematic of the formation of Debye-Scherrer cones from X-ray diffraction of a powder sample

In a standard PXRD experiment, the sample is illuminated with monochromatic X-rays and diffracted intensity is measured as a function of 2θ. In this way, all information is condensed into one dimension and *hkl* peaks with identical *d*-spacings overlap. The structure factor equation is modified to include a multiplicity factor, in which peak overlap due to symmetry rules is included.

However, an additional problem presents itself because peaks with similar (not identical) *d*-spacings may overlap due to the width of the peaks. This causes a problem because it makes it difficult to resolve the intensity of specific peaks, hindering structure solution.

Powder diffraction does have one inherent advantage over single-crystal diffraction - powder diffraction is a measurement of the bulk, while a single-crystal experiment measures one crystal, which is often then assumed to be representative of the bulk. In powder diffraction, if multiple phases are present in the sample, then they will appear in the diffraction pattern and can often be identified. In this way, although structure

solution is more difficult, a more thorough understanding of the sample is achieved with powder diffraction. Often the best results are produced when a combination of the two techniques are used.

The various powder diffractometers used in this thesis are described below.

2.3.1 In-house powder X-ray diffraction

The in-house powder X-ray diffractometers described in this thesis produce X-ray radiation from a copper anode. Electrons are produced by heating a tungsten filament and accelerated through a voltage of 40 kV, before being bombarded at the copper target. The incident electrons have enough energy to ionise 1s (K-shell) electrons from the Cu atoms, resulting in an excited ion. The core hole is quickly filled by a 2p or 3p electron. The energy gained by this relaxation is emitted by a photon of the same energy. The 2p → 1s transition produces K_α ($\lambda \sim 1.54$ Å) photons and the 3p → 1s transition produces K_β ($\lambda \sim 1.39$ Å) photons. Monochromatic radiation is required, so the K_α radiation is selected.

The wavelength of K_α is produced as a doublet due to spin-orbit coupling of the excited state. The two possible states: $^2P_{3/2}$ and $^2P_{1/2}$ are populated in a 2:1 ratio, these give rise to two wavelengths in a 2:1 ratio: $K_{\alpha1}$ ($\lambda = 1.54051$ Å) and $K_{\alpha2}$ ($\lambda = 1.54433$ Å).

Samples were prepared for in-house PXRD by scattering a small amount of powder on a glass slide that was coated with a thin layer of grease. The slide was then placed inside an airtight holder with Mylar windows to prevent the samples from decomposing over the course of the measurement. The setup of all the in-house diffractometers prevented spinning of the samples when an airtight holder was used.

In general, in-house diffractometers were used for phase-checking, lattice parameter analysis and initial structural analysis before samples selected for further analysis were measured using a synchrotron source.

2.3.1.1 *PANalytical X-Pert Pro and Empyrean diffractometers*

The PANalytical X-Pert Pro and PANalytical Empyrean diffractometers are very similar diffractometers, the Empyrean being a newer model of the X'Pert Pro. Both diffractometers were fitted with a germanium crystal based monochromator. This monochromator eliminates all the contribution from $CuK_{\alpha2}$, improving resolution and peak-shape, but also drastically reduces the intensity of $CuK_{\alpha1}$ radiation.

These diffractometers operate in Bragg-Brentano geometry with a fixed X-ray source and a moving detector and sample position. The detector is position sensitive over a 2θ range of 2.112°, which improves the effective time over which each value of 2θ is measured.

2.3.1.2 *Bruker d8 Advance Eco*

The Bruker d8 Advance Eco also operates in Bragg-Brentano geometry, but in this case the sample position is fixed and the X-ray source and detector move. This diffractometer is not equipped with a $CuK_{\alpha 2}$-excluding monochromator, reducing the resolution of the setup, but the increased intensity of the X-ray beam, along with the efficiency of the position-sensitive detector (2θ range of ~3°) allows patterns with a reasonable signal-to-noise ratio to be collected in ~20 min for $7 \leq 2\theta\ (°) \leq 70$. The detector used here is also energy sensitive, allowing for the suppression of fluorescence; an effect considered noise in a diffraction experiment.

2.3.2 Synchrotron powder X-ray diffraction

Synchrotrons are used to produce intense beams of wavelength-tuneable X-ray radiation. The emitted beam is also highly collimated and highly stable, allowing for data to be collected with high precision. This allows for a whole range of experiments to be performed that would not be otherwise possible.

Synchrotrons generate radiation when charged particles travelling at speeds close to the speed of light are forced to change direction by a magnetic field as they travel around a ring. In the case of X-ray generating synchrotrons, electrons are used. There are three stages to the generation of radiation from synchrotrons: electron generation, electron acceleration and radiation generation.

Electrons are generated using an electron gun, in which a metal, such as tungsten, is heated, forcing it to emit electrons. The electrons are then accelerated through a linear accelerator (a *linac*). The *linac* consists of a successive series of positive electric fields, to attract the electrons that oscillate to negative when the electron arrives to repel it on to the next electric field. The energy of the electrons is further increased in the booster ring, before being fed into the main storage ring, as shown in the schematic in Fig. 2.7. Quadrupole and Sextupole magnets are used to maintain a uniform electron beam within the storage ring, while radiofrequency (RF) cavities are used to replenish the energy lost to electromagnetic radiation. An extremely high vacuum (~10^{-13} bar) is

maintained throughout the *linac*, booster ring and storage ring to prevent loss of electron beam.

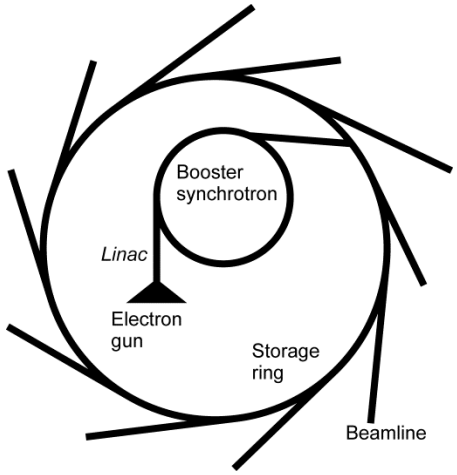


Fig. 2.7 Schematic of a synchrotron

The storage ring is a polygon, rather than a perfect circle. When the electron passes through the bending (dipole) magnets at the corners of the polygon, they are forced to change direction. This change in momentum causes electromagnetic radiation to be emitted. The wavelength of this emission is determined by both the magnetic field and the electron energy.

However, third generation synchrotrons (the type of synchrotron used in this thesis) use insertion devices, wigglers and undulators, in the straight sections of the storage ring to generate radiation. Both these types of insertion devices consist of an array of alternating pairs of magnets, which produce a series of oscillating electron accelerations; each acceleration causes the emission of radiation. A wiggler produces radiation that is directly superimposable, so that it has a similar profile to radiation emitted from a bending magnet, but with higher flux. An undulator produces a series of harmonic radiation that is not directly superimposable, but the radiation interferes producing high intensity peaks at wavelengths where the radiation is in-phase and low intensity at wavelengths where the radiation is out-of-phase.

The emitted radiation is then directed to individual beamlines where the beam is further primed (e.g. using a monochromator) before use.

Two synchrotrons were used for the work completed in this thesis: the Diamond Light Source (Diamond), located at the Harwell Science and Innovation Campus, UK and the European Synchrotron Radiation Facility (ESRF), located in Grenoble, France.

2.3.2.1 *I11 beamline, Diamond*

The I11 beamline is a high-resolution powder diffraction beamline.[94] The beamline uses an undulator source that produces X-rays of wavelength 0.4 – 2.5 Å, with optimum flux in the range $0.62 \leq \lambda$ (Å) ≤ 1.1. Monochromatic X-ray radiation is selected using a double-crystal monochromator. The wavelength selected for all the data obtained at I11 used in this thesis was $\lambda \sim 0.826$ Å. The precise wavelength used was obtained from refinement against a recent (same-day) silicon calibration measurement.

To prepare a sample for measurement at I11, samples were ground with an equi-volume quantity of either amorphous boron or ground-glass to reduce absorption and preferred orientation effects and packed into 0.5 mm diameter borosilicate capillaries (unless otherwise stated). These capillaries were glued into a brass ferrule that was screwed into a magnetic base. The magnetic base containing the capillary was then loaded into a carousel, allowing a programmable robot to select the capillary and load it onto the magnetic rotation stage that was situated so that the capillary would be in the path of the beam. The use of the carousel and robot setup significantly reduces the down-time between measurements and allows for the automation of several consecutive measurements.

I11 has several sample environments available: a N_2-based cryostream, allowing the samples to be cooled/heated in the range $100 \leq T$ (K) ≤ 500; a hot-air blower that could heat capillaries to 1000 °C; helium cryostats, capable of cooling samples to 5 K and a furnace capable of heating to 1500 °C. However, a significant disadvantage of the cryostats was that they required considerable assembly and the lack of antechamber meant that the rate of sample measurement would be limited to approximately 1 - 2 day^{-1}. For this reason, the I11 cryostat was not used.

I11 is equipped with both a Mythen position sensitive detector (PSD) and a MultiAnalyser Crystal (MAC) detector. The PSD is a strip detector comprised of 18 linear p-n junction strip detection modules arranged in a 90° arc. There is ~1 mm between modules that would leave uncollected gaps in the diffraction pattern; these can be removed by "rocking" the detector by 0.25° in 2θ and merging the two patterns. The PSD allows PXRD patterns with high signal-to-noise ratio to be collected very quickly ($t \sim 1$ s). The nominal resolution of the PSD is $\Delta d/d \sim 10^{-3} – 10^{-4}$.

The MAC detector consists of 5 separate arms, which are themselves comprised of nine Si(111) analyser crystals and detector combinations. This allows for 45 separate 2θ values to be collected simultaneously. The MAC produces higher resolution PXRD patterns and is less sensitive to imperfect sample alignment and preparation than the PSD, but the standard collection times required are significantly longer, often $t > 20$ min.

A common experiment performed on I11 was a variable temperature (VT) experiment, in which the cryostream or hot-air blower was used to cool/heat the sample at a constant rate (6 K min^{-1}) while short PSD scans were collected. This experiment allowed for lattice parameters and changes in symmetry to be examined as a function of temperature. The short scan times meant that the temperature resolution of any transition was ~1 K.

2.3.2.2 *ID22 and ID31 beamlines, ESRF*

The setup at ID22 was previously situated at ID31; both these beamlines are/were based at the ESRF. The X-ray source for this diffractometer is undulator based and the beamline is optimised for high-resolution PXRD. This beamline can access X-rays with energy 6 – 80 keV ($2.07 \geq \lambda$ (Å) ≥ 0.083), but in this this thesis the wavelength used was 0.3 – 0.4 Å. As with I11, the wavelength is selected by a double-crystal monochromator. The detector is comprised of nine Si(111) analyser crystal/scintillation detector combinations, in a similar manner to the MAC diffractometer at the I11 beamline.[95]

The main difference between the basic setup of I11 and ID22/ID31 is the optimum wavelengths for achieving the highest flux. The shorter wavelength of ID22/ID31 allows for higher-resolution measurements out to lower *d*-spacing, advantageous in the accurate determination of atomic coordinates and fractional occupancies; and sample absorption effects are reduced in most cases.

Amongst other sample environments (much the same as for I11), ID22/ID31 is equipped with a helium-based cryostat. This cryostat possesses a purge-able antechamber, allowing for samples to be changed over quickly (~5 min) and the measuring of multiple samples at low temperature in a single beam-time allocation. ID22/ID31 was therefore used when measurement temperatures below 100 K were desired.

2.3.2.3 *I12 beamline, Diamond*

I12 is the joint engineering, environment and processing (JEEP) beamline, located at Diamond.[96] I12 is fed X-ray radiation by a wiggler source, providing high-flux polychromatic and monochromatic radiation in the energy range 50 – 150 keV ($0.248 \geq \lambda$ (Å) ≥ 0.083). The beamline was designed to be as flexible as possible for different experimental setups; the beamline therefore has two experimental hutches, EH1 and EH2, 51 and 94 m from the source respectively. EH1 is configured for smaller experimental setups, while EH2 is designed for larger experimental setups and is equipped with heavy duty cranes. Various X-ray detectors are available. The high energy, high flux X-rays supplied to the beamline and flexible sample environment make it suitable for several applications: engineering, materials science, biomedical imaging, as well as tracking the progress of reactions *in situ*.

In this thesis, the I12 beamline was used for the *in-situ* measurement of reactions using monochromatic PXRD. For this purpose, X-rays with $\lambda = 0.15509$ Å were selected by a double-crystal monochromator. The diffracted X-rays were detected by a two-dimensional PIXIUM® image plate detector.[97] This detector has 2880 × 2881 pixels, each 148 × 148 μm. The sample-to-detector distance may be optimised as required by the experiment.

2.4 Powder neutron diffraction

Neutrons are particles that can be treated as waves via the de Broglie relationship:

$$\lambda = \frac{h}{p} = \frac{h}{m_n v} \tag{2.11}$$

where h is Planck's constant, p is momentum, m_n is the mass of the neutron and v is velocity. Therefore, a neutron moving slowly enough will have a wavelength comparable to that of the interatomic distances in a crystal and interact with the crystal via diffraction.

There are two methods of neutron generation for neutron diffraction: reactor sources and spallation sources. A reactor source generates neutrons from the radioactive decay of nuclear material. This reaction generates neutrons with wavelengths associated with the nuclear reaction. These neutrons are passed through a monochromator and

collimated before the beam is directed to the sample. The obtained diffraction pattern shows intensities as a function of 2θ, as for the diffraction of monochromatic X-rays.

The mechanism for the generation of neutrons from a spallation source is more complex. Hydride ions are generated by an ion source and accelerated through a radio frequency quadrupole (RFQ) and a *linac*. The high-energy hydride ions are stripped of their electrons to become protons, which are then accelerated around a synchrotron ring. The high-energy protons are then fired at a metal target, generating 15 – 20 neutrons per proton. The neutrons generated consist of a large range of wavelengths (called a "white" beam).

All the neutron diffraction experiments reported in this thesis were performed on instruments located at ISIS, Harwell Science and Innovation Campus, UK. ISIS is a spallation neutron source.

ISIS consists of two target stations: target station 1 (TS1) and target station 2 (TS2). The metal targets at both target stations are made of tantalum-coated tungsten. Once the neutrons are generated, they are moderated to slower speeds using various hydrogen-containing moderators. The type of moderator used is dependent on the individual instruments.

Although it is theoretically possible to produce a monochromatic beam of neutrons from a spallation source, it would be wasteful due to the large distribution in the wavelength of the neutrons. Therefore, a modification to the setup of the diffraction experiment is used, in which a "white" beam of neutrons is directed at the sample, which scatters the neutrons; these neutrons are then detected by one or more fixed-angle detectors, which record intensity as a function of time-of-flight (ToF). The ToF of the neutrons from the sample to the detector is a related to the neutron wavelength. Peaks are observed when they are the result of constructive interference (as determined by Bragg's law).

The resolution of a ToF neutron diffractometer is quoted in the uncertainty in the *d*-spacing as a function *d*: $\Delta d/d$. This is calculated by:

$$\frac{\Delta d}{d} = \sqrt{\Delta\theta^2 \cot^2\theta + \left(\frac{\Delta t}{t}\right)^2 + \left(\frac{\Delta L}{L}\right)^2} \tag{2.12}$$

where t is time of flight and L the distance from the sample to the detector. The equation shows that the uncertainty arising from uncertainty in θ ($\Delta\theta$) tends to 0 as θ tends to 90°. Therefore, higher angle banks (larger 2θ) have higher resolution. Increasing the related parameters L and t also increases the resolution, assuming Δt and Δl remain approximately constant.

As stated in section 2.2, neutron diffraction differs from X-ray diffraction in that neutrons are diffracted by nuclei, not by electron density (as is the case for X-rays). Therefore, the relationship between structure factor and element (indeed isotope) identity is determined by nuclear physics, not by Z. The result of this is that often elements that have similar Z need not have similar neutron scattering lengths. This is useful when trying to distinguish elements in a structure and aids the determination of the position and occupancy of lighter elements, which may contribute little to an X-ray diffraction pattern, but significantly to a neutron diffraction pattern.

Also of note, the form factor does not drop off as a function of Q (where $Q = 2\pi/d$), because the nuclei are significantly smaller than the wavelength. This means that neutron diffraction can often be helpful in high-resolution structural determination, even when resolution between different types of atoms is not a problem.

Neutrons also interact with unpaired spin via magnetic dipole interactions. This is because neutrons are spin-½ particles. When a material is magnetically ordered, neutrons are diffracted by the magnetic lattice to an extent proportional to the square of the ordered moment. This produces a second, magnetic, diffraction pattern that is superimposed onto the nuclear diffraction pattern. As the neutrons are interacting with the outermost electrons of the atom, the electron density is of a comparable size to the neutron wavelength, leading to a dramatic reduction in scattered magnetic intensity with increasing Q.

Unlike X-rays, neutrons only interact weakly with samples. This traditionally necessitated the use of significantly larger samples (> 1 g) and longer measurement times to obtain data with acceptable signal-to-noise ratios. While this is still largely the

case, the development of new generations of instruments (such as WISH, see section 2.4.4), using a higher neutron flux and more sensitive detectors, allows for the use of smaller sample sizes and shorter collection times.

Almost all the neutron diffraction experiments described in this thesis were performed on powders packed into airtight vanadium cans (6 or 8 mm diameter), sealed in an argon atmosphere with an indium gasket. A single sample measured on HRPD was packed into a "slab can" (see section 7.4). The neutron diffractometers used in this thesis are described below.

2.4.1 GEM

GEM is a diffractometer designed for GEneral Materials use, covering large *d*-spacing range with reasonable resolution and short collection times. GEM is equipped with six fixed-angle detector banks at 9°, 17°, 35°, 62°, 92° and 146°. The combination of these detector banks result in a reliable *d*-spacing coverage of ~0.4 – 25 Å, with $\Delta d/d > 0.3\%$ in the highest resolution (backscattering) bank. GEM is situated on TS1.

2.4.2 POLARIS

POLARIS was designed to be a high-flux medium-to-high resolution powder diffractometer, allowing for the measurement of small samples or short counting times. POLARIS is equipped with six fixed-angle detector banks at 9°, 26°, 48°, 90°, 139° and 155°. POLARIS has a reliable *d*-spacing coverage of ~0.25 – 20 Å, with $\Delta d/d > 0.3\%$ in the highest resolution (backscattering) bank.

2.4.3 HRPD

HRPD is designed to be used for the high-resolution characterisation of crystal structures from PND. It is not designed for the characterisation of magnetic ordering. As such, although HRPD is equipped with three fixed angle detector banks (30°, 90° and 168°). The signal-to-noise ratio of the 30° bank is very low indeed and the resolution relatively poor, and as such was excluded from all refinements because it did not provide useful data. The 168° bank is very high resolution, with reported $\Delta d/d > 0.04\%$. Combining data from the 90° and 168° banks provides a real reliable *d*-spacing coverage of ~0.25 Å – 5 Å.

2.4.4 WISH

WISH, in contrast to HRPD, is designed primarily for the characterisation of magnetic ordering. It is therefore optimised for high-resolution at medium-to-high *d*-spacings. The WISH detector bank is a continuous array of detectors, however the resolution of the detector changes as a function of angle, therefore the detector is divided into 10 banks; five either side. The data from each pair covering a given 2θ range are summed together to improve the signal-to-noise ratio, this results in five "effective banks". WISH has a high-resolution *d*-spacing range of 0.7 – 17 Å, but total coverage extends to up to 50 Å.

As previously stated, WISH is fed with an extremely high flux of neutrons, allowing for data with a good signal-to-noise ratio to be collected comparatively quickly.

2.4.5 OSIRIS

OSIRIS is fed with a high flux of long wavelength neutrons, providing a high resolution at long *d*-spacings. As with WISH, this makes OSIRIS useful for probing the magnetic ordering of a sample. However, in contrast to the other neutron diffractometers discussed, OSIRIS only features a single detector bank covering the backscattering angles 150 - 171°. This limited detector coverage is circumvented by adjusting the phases of two choppers. These choppers can be used to select neutrons of different wavelengths and therefore different *d*-spacing ranges. If a full range of *d*-spacing is required, then successive measurements with different phasing of the choppers are required to cover the full region of interest. After measurements are complete, the data are merged to form a single diffraction pattern.

It should also be noted that the data measured on OSIRIS and used in thesis were collected using an aluminium-tailed "orange" cryostat to control the temperature. This cryostat was used due to the superior signal-to-noise ratio that can be obtained, as contrasted with the vanadium-tailed cryostats available on OSIRIS, but led to a considerable sample environment contribution in the form of aluminium Bragg peaks.

2.5 Analysis of powder diffraction data

PXRD and PND data was analysed primarily using Pawley and Rietveld refinements. Both Pawley and Rietveld refinements proceed via the refinement of background parameters, peak positions, peak-shape parameters and intensities using a least-squares algorithm. In a Pawley refinement, the refined intensities are simply those that give the best fit; no atomic information is inputted into the refinement, so no atomic information may be obtained. A Rietveld refinement refines a structural model against the intensities of the peaks by the refinement of the scale factor and the refinement of the atomic positions, site occupancies and displacement parameters. This allows information on the atomic coordinates to be extracted from the refinement. To achieve a successful refinement, that is good agreement between the observed and calculated pattern, the initial model used must be a reasonable estimate of the true structure.

The Rietveld refinement was developed when it was found that overlapping peaks could be treated more easily if each point of data, rather than each peak, was treated as a separate observation.[98] For a given point *i* in the pattern, the intensity y_{ci} is calculated by combining all contributions of the Bragg reflections within a fixed range:

$$y_{ci} = s\sum_{hkl} L_{hkl}|F_{hkl}|^2\phi(2\theta_i - 2\theta_{hkl})P_{hkl}A + y_{bi} \quad (2.13)$$

where *s* is the scale factor, L_{hkl} is the Lorentz polarisation factor, F_{hkl} is the structure factor, ϕ is the reflection profile function that describes the peak shape, P_{hkl} is the preferred orientation function, *A* is the absorption factor and y_{bi} is the background intensity at point *i*. The calculated and observed intensities are compared using a cost function, called the residual, S_y:

$$S_y = \sum_i w_i(y_i - y_{ci})^2 \quad (2.14)$$

where y_i is the observed intensity at point *i* and w_i is the weighting factor, defined by $\frac{1}{y_i}$ to ensure each data point contributes equally to S_y. Once calculated, S_y is minimised using the least squares method, in which a small change in user-defined parameters is implemented and the new S_y is compared with the old S_y, if the change resulted in a

reduction in S_y, then the change is retained, if not then the old parameters are retained and a new change is implemented. The cycle is repeated until a minimum is found.

The quality of the refinement is assessed by visual inspection of the Rietveld plot, that is a plot of the overlaid calculated and observed patterns, with the difference between the two plotted below. It is also helpful to examine selected parameters that report the statistical quality of the fit, in this thesis the weighted profile R value, R_{wp} was used:

$$R_{wp} = \sqrt{\frac{S_y}{\sum_i w_i y_i^2}} \tag{2.15}$$

In a pattern in which the pattern has been perfectly fitted R_{wp} should approach the statistically expected R value, R_{exp}, in which all deviations of the calculated pattern from the observed pattern are due to statistical variations. R_{exp} is defined by:

$$R_{exp} = \sqrt{\frac{N_{obs} - N_{var}}{\sum_i w_i y_i^2}} \tag{2.16}$$

where N_{obs} and N_{var} are the number of observables and number of variables respectively. In a standard diffraction measurement and refinement, it is expected that $N_{obs} \gg N_{var}$. A goodness of fit parameter, χ^2, may also be derived from the ratio of R_{wp} and R_{exp}.

While it is generally considered that the lower the reported R_{wp}, the better the fit to the data, care should be taken to check the quality of the visual fit. It is also relatively difficult to accurately compare the fit of different datasets using R_{wp}, due to variations that occur for non-structural reasons. One such example of this is well-modelled high-intensity backgrounds can give a misleading low value of R_{wp}, even when the peaks are poorly fitted.

Pawley and Rietveld refinements were performed in TOPAS Academic, version 5.[99] JANA2006 was also used when the powder diffraction pattern was found to contain an incommensurately modulated phase.[100]

2.6 **Single crystal X-ray diffraction**

In a SCXRD experiment a single crystal is mounted onto a small nylon loop, often using a small quantity of oil. The loop is then centred in the centre of the path of the X-ray beam; during this process the crystal is rotated to ensure it is in the centre of rotation. The diffracted peaks resulting from this crystal are measured using an area detector. A series of scans are then collected at various angles, until a full, three-dimensional set of diffraction peaks in reciprocal space of data is collected. If the crystal is not triclinic, then there will be some redundancy in the data due to symmetry. This is beneficial because it allows the intensity of theoretically equivalent peaks that are to be compared or averaged, reducing error in the measurement.

Once the dataset is collected, the peaks are indexed using a unit cell and space group, unlike in the case for PXRD (see section 2.3), the three-dimensional nature of the data makes this a trivial, highly-automated task, provided the dataset collected does not consist of either twins or multiple crystals. The data is then integrated into a file which consists of a list of reflections (indexed using *hkl* and in the case of incommensurately modulated crystals *m*) and their associated intensities. The software used for integration in this thesis was CryAlisPro.[101]

The integrated file was then imported into either CRYSTALS[102] or JANA2006.[100] CRYSTALS was used for refining commensurate datasets and JANA2006 was used for refining incommensurate datasets. In both programmes an initial structure was found using a charge-flipping algorithm, implemented by Superflip.[103] The model was then then refined against the dataset, allowing for the refinement of atom positions, occupancies and thermal displacement parameters (*U*'s) using successive least-squares refinements until the minimum was found.

All the single-crystals used in this thesis were obtained from a powder, the crystals were therefore too small for a high-quality dataset to be collected easily using an in-house diffractometer. Instead the crystals were analysed on the I19 beamline (Diamond), where the use of high intensity and highly focussed synchrotron radiation allowed for the measurement of smaller crystals than would otherwise be possible.

I19 is an undulator sourced beamline, with a tuneable useable wavelength of 0.5 – 2.5 Å, however in all cases in this thesis a wavelength of 0.6889 Å was used. I19 is

equipped with a range of sample environments, including cryostreams, cryostats and furnaces. In the course of this thesis, two cryostreams were used: a nitrogen-based cryostream, allowing for the cooling of samples to 100 K and a helium-based cryostream (known as the HeLiX), allowing for samples to be cooled to 20 K.[104]

2.7 **Electron diffraction and microscopy**

As charged particles, the primary interaction of electrons with matter is through Coulombic forces. While the primary interaction of the incident electrons is with the nucleic protons, with the scattering amplitude increasing with increasing *Z*, an atom's electron density also plays a shielding role, this is related to the X-ray scattering factor, f_x. The combination of these two factors leads to the following relationship for the electron scattering factor (f_e):

$$f_e(\theta) \propto Z - f_x \tag{2.17}$$

A schematic of a transmission electron microscope (TEM) is shown in Fig. 2.8, it shows that the microscope measures both the transmitted beam, allowing for imaging of the material and the scattered beam, allowing for the electron diffraction pattern to be collected.

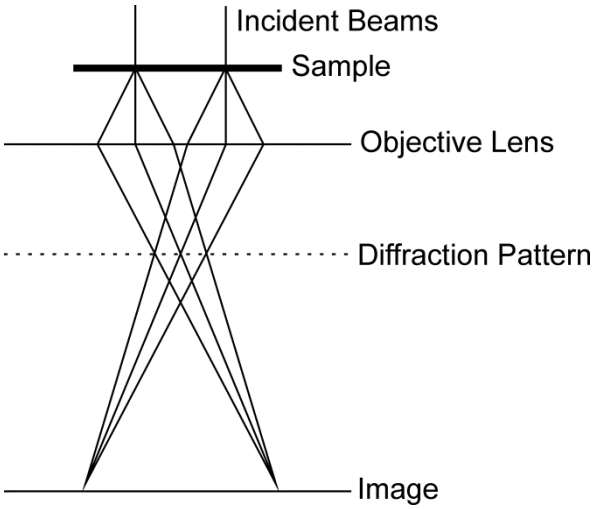


Fig. 2.8 Schematic of the electron beam bath of a transmission electron microscope (TEM)

Two primary advantages of electron diffraction over X-ray diffraction are: electrons are significantly easier to focus than X-rays and the increased scattering factor of electrons compared with X-rays. These advantages mean that the electron beam may be focussed so that a single-crystal diffraction pattern may be obtained from a grain of nanometre-

scale dimensions. This often makes it easier to find the space group of materials where it is impractical to grow a single-crystal. Another advantage arising from the short wavelengths used is that the correlation length of electron diffraction is significantly smaller than in X-ray diffraction, so localised correlations between atoms that appear as diffuse scattering in X-ray diffraction can appear as sharp diffraction spots in an electron diffraction pattern. The diffraction pattern is also concentrated over a very narrow 2θ range.

Electron microscopy can also be combined with energy dispersive X-ray spectroscopy (EDX), which is used as a method of elemental analysis.

Electron microscopy and diffraction measurements were performed and analysed by Prof. J. Hadermann, Prof. A. Abakumov and Dr M. Batuk, from the Electron Microscopy for Materials Science (EMAT), University of Antwerp, Belgium. EDX analysis of $Sr_2CoO_2Ag_{2-x}Se_2$ was performed in collaboration with Dr N. P. Young from the Department of Materials, University of Oxford.

2.8 Magnetometry measurements

The magnetic susceptibility measurements performed in this thesis were measured using either a Quantum design MPMS or a Quantum design MPMS XL magnetometer. The design of both these magnetometers is essentially the same, but the MPMS XL can perform alternating-current (AC), as well as direct-current (DC) measurements. A magnetometer measures magnetisation, M as a function of both field, H ($-5 \leq H\,(\mathrm{T}) \leq 5$) and temperature ($2 \leq T\,(\mathrm{K}) \leq 300$). The field is produced using a helium-cooled magnet and the temperature is controlled using a helium-supplied cryostat.

The magnetisation of the sample is measured under these conditions using a superconducting quantum interference device (SQUID). A SQUID is a closed ring of superconducting wire, divided by two thin layers of insulating material, called a Josephson junction.[105] When current is applied to the SQUID, Cooper pairs of electrons (from Bardeen-Cooper-Schrieffer (BCS) theory) can tunnel through the insulating material, creating a weak superconductor. However, if a current exceeding the critical current is applied to the Josephson junction, the ring has a non-zero resistance, which is measured as a voltage. The critical current of the Josephson junctions, and therefore the resistance, is affected by the magnetic field experienced by the junction. A SQUID

magnetometer is setup so the magnetic field experienced by the Josephson junction is directly related to the magnetisation of the sample, converting sample magnetisation to a read-out voltage.[105]

2.8.1 DC magnetometry measurements

DC Magnetic susceptibility measurements were performed using approximately 15 – 70 mg of sample, loaded into a gelatin capsule. Typically, the *M vs H* of a sample was measured at 300 K. If it was found that the relationship between the two was linear, even at very low fields, then it was assumed that the sample did not contain significant magnetic impurities and a low-field (normally 100 Oe) measurement was performed as a function of temperature. Magnetisation was measured as a function of temperature on warming twice. The first time the sample was cooled in the absence of a field (zero-field cooled (ZFC)), the second time the samples was cooled in the applied field (field-cooled (FC)). Differences between these two curves yielded additional information about the magnetic behaviour of the sample. The magnetisation was converted to molar magnetic susceptibility, χ_{mol}, so that results between different samples could be compared:

$$\chi_{mol} = \frac{M}{Hn} \tag{2.18}$$

where *n* is the amount of compound (units: mols).

However, it was found with some samples that the relationship between *M* and *H* was not linear at 300 K, due to a much larger gradient at low fields than high fields. This was normally attributed to a ferromagnetic impurity, which, due to the high sensitivity of the magnetometer, could be too small to be observed via PXRD but still contribute significantly to the measured *M*. Therefore, to accurately measure the magnetic susceptibility of the bulk compound, *M vs T* was measured twice at fields higher than the saturation field of the ferromagnetic impurities. The selected fields were typically 3 and 4 T (measured under FC conditions). χ_{mol} of the bulk sample was then calculated by:

$$\chi_{mol} = \frac{M(H_2) - M(H_1)}{(H_2 - H_1)n} = \frac{M(4\text{ T}) - M(3\text{ T})}{10000n} \tag{2.19}$$

Isotherms of *M vs H* were also measured in the range $-5 \leq H\,(\mathrm{T}) \leq 5$, these magnetisation isotherms are also known as hysteresis loops. Most commonly in this thesis those that were performed below 300 K were performed on cooling in a positive 5 T field. This was because, as discussed in section 1.4.6, materials with a component of spin-glass behaviour, often exhibit history-dependent behaviour. This is often exhibited in field-cooled hysteresis loops by a displacement from the origin towards the direction of the field that the sample was cooled in. This effect arises in spin-glass-like samples because cooling below the spin-glass freezing temperature (T_g), freezes the field-aligned spins in place, making it the energetically favourable configuration.

2.8.2 AC magnetometry measurements

In AC magnetometry, a low, fluctuating field is applied to the sample while magnetisation is measured. In this way, information about dynamics is collected, which is not possible in DC magnetometry, where a constant field is applied over the measurement period.

In the limiting case where the AC frequency (ω) is very low, the AC-induced magnetic moment (m_{AC}) will move with changing field, yielding similar results to those obtained from a DC experiment. m_{AC} is given by:

$$m_{\mathrm{AC}} = \left(\frac{dM}{dH}\right) H_{AC} \sin(\omega t) = \chi H_{AC} \sin(\omega t) \tag{2.20}$$

However, if the AC frequency is increased so that H_{AC} changes too quickly for the sample to respond, a phase shift (φ) develops between H_{AC} and m_{AC}. The susceptibility and phase shift are both measured by the magnetometer and are recorded in terms of the in-phase (real) component (χ') and the out-of-phase (imaginary) component (χ''):

$$\chi' = \chi \cos\varphi \tag{2.21}$$

$$\chi'' = \chi \sin\varphi \tag{2.22}$$

These two equations may be combined to find χ and φ:

$$\chi = \sqrt{\chi'^2 + \chi''^2} \tag{2.23}$$

$$\varphi = \arctan\left(\frac{\chi'}{\chi''}\right) \tag{2.24}$$

A common use of AC magnetometry measurements is the investigation of spin-glass behaviour. If the spin-glass freezing cusp observed in DC magnetometry measurements (and χ'(T)) is observed to be frequency dependent, then this confirms the spin-glass identity of the sample. In this thesis AC measurements were used in the preliminary investigation of the ferromagnetic behaviour of most-deintercalated $Sr_2CoO_2Ag_{1.5(2)}Se_2$ (see section 5.3.6.1).

2.9 Electrical resistivity measurements

Electrical resistance was measured on selected samples to measure resistivity as a function of temperature (15 – 300 K), using custom-built equipment. The equipment provided a constant (but adjustable) current to the sample, while measuring the voltage at 20 s intervals. A Gifford-McMahon closed-cycle refrigerator was used for cooling and a heater mounted on the sample holder was then used to control the temperature.

Before measurement samples were pressed into either 5 mm or 8 mm diameter pellets, which were sintered at the synthesis temperature to improve contact between grain boundaries. The pellets were then cut into a bar and thin copper wires were used to connect the sample to a small plastic chip that connected the sample to the current. A four-connection probe setup was used, shown as a schematic in Fig. 2.9.

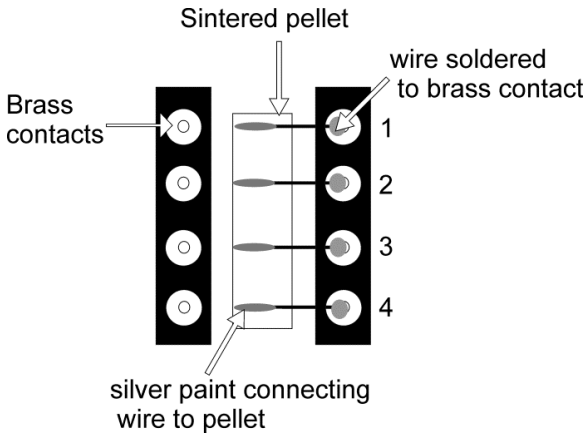


Fig. 2.9 Schematic of the four-connection probe setup used for measuring the electrical resistivity of sintered pellets

In a four-probe setup, a constant current is applied through the sample (contacts 1 and 4 in Fig. 2.9), while the voltage is measured across the sample (contacts 2 and 3 in Fig. 2.9). This method is applied in preference to a simple two-probe method to minimise the effect of contributions from the contacts and connecting wires to the measured

resistance and subsequently resistivity. Resistivity of the sample, ρ, is calculated from the measured parameters:

$$\rho = \frac{RA}{l} = \frac{VA}{Il} \tag{2.25}$$

Where A is the cross-sectional area of the pellet, l is the length between contact 2 and 3 (see Fig. 2.9), V is voltage, I is applied current, resistance R is given by V/I. This calculation of resistivity is only valid if the material is Ohmic, that is there is a linear relationship between V and I; this should be checked prior to measurement.

All samples were prepared in air and offcuts of the pellet were analysed via in-house PXRD to ensure the sintering process and exposure to air had not caused the sample to decompose.

One of two general behaviours is expected when the resistivity of a solid compound is measured as a function of temperature: metal-like behaviour or that of a semiconductor/insulator. The typical behaviour of these materials is shown in Fig. 2.10, along with a schematic of their corresponding density of states near the fermi level, E_F.

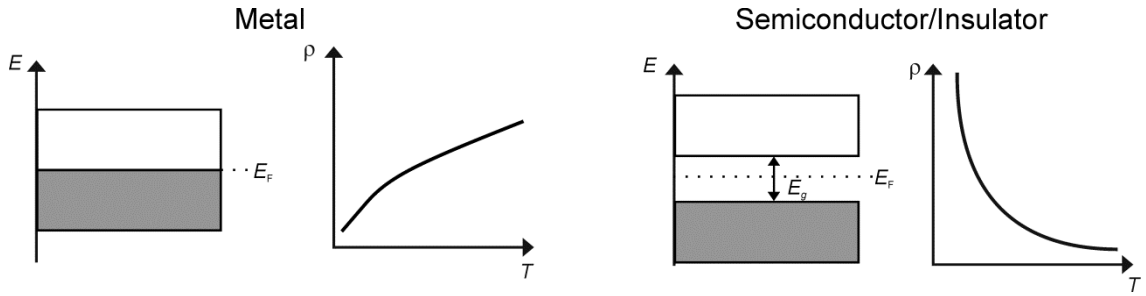


Fig. 2.10 Representative behaviour of the resistivity of a metal and a semiconductor or insulator as a function of temperature together with schematics of their corresponding density of states near the fermi level, E_F

These behaviours may be rationalised using simple band theory arguments. In a metal, the density of states is non-zero at the E_F, so electrons may flow freely from filled states to empty states with little energy cost. When a metal is cooled, the lattice vibrations are reduced, which reduces impedance on the movement of electrons, reducing the resistivity as temperature decreases.

In a semiconductor/insulator on the other hand, the density of states is zero at E_F, with an energy gap between the filled and empty bands (the band gap, E_g). For this type of material to conduct electricity, the electron must have sufficient energy to cross the

band gap, in order to flow in the high energy "conduction" band. In most cases electrons obtain the energy to cross the band gap from thermal energy. The number of electrons, *n*, in the conduction band is related to the temperature, *T* by:[106]

$$n \propto \exp\left(\frac{-E_g}{2k_B T}\right) \tag{2.26}$$

where k_B is the Boltzmann constant. The electrical conductivity of a semiconductor is dominated by *n*. This means that the resistivity of a semiconductor is inversely proportional to *n*, showing that resistivity increases exponentially with decreasing temperature in this case.

Chapter 3

3 Structural and magnetic properties of $Sr_2MnO_2Cu_{1.5-x}S_2$, $Sr_2MnO_2Ag_{1.5}Se_2$ and $Sr_2MnO_2Cu_{1.8}Te_2$

3.1 Introduction

$Sr_2MnO_2Cu_{1.5}S_2$ was amongst the first compounds of the $A_2MO_2X_2Ch_2$ (A = Sr, Ba; M = Mn, Co, Ni, Cu and Zn; X = Cu, Ag; Ch = S, Se, Te) series reported.[41] However, when first reported, the composition was incorrectly assumed to be stoichiometric $Sr_2MnO_2Cu_2S_2$.[41] When Gál *et al.* studied this material, they found that the material was copper deficient, with composition $Sr_2MnO_2Cu_{1.5}S_2$, reflecting that Mn was in the mixed oxidation state +2.5.[45] The copper vacancies are disordered at room temperature (RT), but order below ~250 K in a $2\sqrt{2}a \times \sqrt{2}a \times c$ expansion of the unit cell, as is shown in Fig. 3.1.[107]

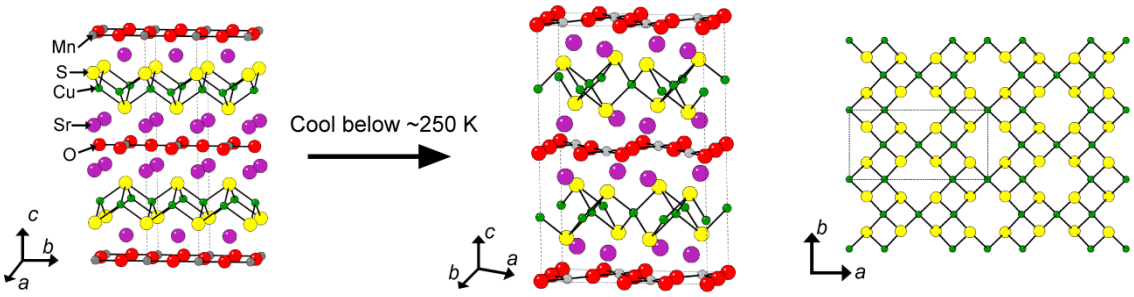


Fig. 3.1 The room temperature (RT) crystal structure of $Sr_2MnO_2Cu_{1.5}S_2$ and the idealised low-temperature Cu/vacancy ordering structure, in profile and also down the c-axis, showing just the Cu and S atoms to emphasise the ordering structure[107]

It was also shown, via a combination of magnetic susceptibility and low temperature powder neutron diffraction (PND) measurements that the compound orders antiferromagnetically below a Néel temperature, T_N ~30 K.[107] The magnetic ordering behaviour of this compound is unusual and is discussed further in section 3.2.6.1.

The mixed valent nature of this compound means that it is possible that ordering of the Mn^{2+}/Mn^{3+} charges occurs, as is observed in the mixed Mn^{3+}/Mn^{4+} perovskite $(La,Ca)MnO_3$ (amongst other compounds).[108] However, no long-range charge ordering has been observed in $Sr_2MnO_2Cu_{1.5}S_2$ thus far;[107] the work in this chapter further investigates any signs of charge ordering, in order to confirm this result.

Soft chemistry has been employed to tune the oxidation state of Mn in this compound. As was discussed in section 1.3.5, this compound has been lithiated, reducing the oxidation state, using both chemical (^{n}BuLi) and electrochemical means.[81, 82] It has also been found that I_2 could be used to topotactically remove Cu from the compound, producing a copper deficient compound, with vastly different copper-ordering and magnetic behaviour.[88, 89]

A large section of this chapter furthers this work. The structure, composition and magnetic behaviour of the lowest-Cu-content compound are confirmed and further analysed. The behaviour of the compound at Cu occupancies intermediate between that of the parent and most Cu-deficient phase is also analysed.

The behaviour of the double- and triple-layered analogues ($Sr_2MnO_2Cu_{3.5}S_3$ and $Sr_2MnO_2Cu_{5.5}S_4$) as Cu is oxidatively deintercalated is under investigation by other members of the Clarke group.[55]

Adamson found that the Se analogue of this compound, $Sr_2MnO_2Cu_{1.5}Se_2$, was unreactive with respect to oxidation using I_2.[88] It was also found that, despite having a large Cu deficiency, the Cu vacancies in $Sr_2MnO_2Cu_{1.5}Se_2$ do not order at low temperatures, although electron diffraction and imaging showed that some ordering occurs on a local scale.[58] The Ag-containing analogue $Sr_2MnO_2Ag_{1.5}Se_2$ has previously been reported, but attempts to synthesise this compound >90 wt% pure using a purely high-temperature route were not successful.[57, 60] In this work, I_2 dissolved in MeCN was used to remove almost all crystalline impurities from the sample. It is also established that $Sr_2MnO_2Ag_{1.5}Se_2$ is not active with respect to oxidation using I_2. The magnetic ordering of this structure is then analysed using PND.

Parker found that the stoichiometric compound $Ba_2MnO_2Cu_2Te_2$ could be synthesised, hitherto one of only two tellurides of the $A_2MO_2X_2Ch_2$ series known (the other being $Ba_2CoO_2Cu_2Te_2$, also synthesised by Parker).[109] Here the synthesis of $Sr_2MnO_2Cu_{2-x}Te_2$ is reported and the magnetic behaviour of this compound analysed using PND and magnetic susceptibility measurements.

Sections of this chapter have been published in *APL materials* (ref. 110) and the *Journal of Solid State Chemistry* (ref. 111).

3.2 Cu deintercalation from $Sr_2MnO_2Cu_{1.5}S_2$ using I_2

3.2.1 Synthesis of the parent compound and method of deintercalation

$Sr_2MnO_2Cu_{1.5}S_2$ was synthesised multiple times on the 5 g scale, using the method outlined by Rutt.[54] SrS, Mn, MnO_2 and CuO were weighed out in the molar ratio 2:0.25:0.75:1.5 and prepared as described in section 2.1.1. The reactants were heated to 900 °C (rate: 10 °C min^{-1}) for 48 h, before allowing the sample to cool in the furnace. Phase purity was checked by laboratory powder X-ray diffraction (PXRD). Small (< 3 wt%) SrS impurities were found to be difficult to remove by reheating.

Oxidation by I_2 was performed as described in section 2.1.3. Variable amounts of I_2 were used to produce products with variable copper occupancies. Unless otherwise stated, the reactions were left stirring for 1 – 4 days, with larger samples (intended for neutron diffraction experiments) typically left for longer. However, there appeared to be little, if any, correlation between the amount of time a reaction was left stirring and degrees of deintercalation. This was most-likely because the reaction occurred very fast. The rate of this reaction is discussed in Chapter 4, when the reaction is studied *in situ*.

While it was easy to target the most-deintercalated compound, by simply using a large excess of I_2 (typically 1.5 molar equivalents I_2), it was found to be much more difficult to target compounds with intermediate copper occupancy. This was due to the additional contribution of compound-destructive side-reactions,[89] which consumed some of the I_2 and prevented the quantitative reaction of $Sr_2MnO_2Cu_{1.5}S_2$ with I_2. It is also possible that different sized grains of $Sr_2MnO_2Cu_{1.5}S_2$ consumed I_2 at different rates, which also may have hindered the quantitative reaction with I_2. This difficulty was partially overcome by using multiple attempts to target an area of the phase diagram.

Several samples within this chapter were prepared by Prof. S. J. Clarke. These samples are indicated by a sample code with the prefix “SJC”. The variable temperature (VT) powder X-ray diffraction (PXRD) measurements at the ID31 beamline were performed by Drs S. J. Cassidy and S. J. Sedlmaier.

3.2.2 Room temperature powder X-ray diffraction

In the first analysis room temperature (RT) synchrotron powder X-ray diffraction (PXRD) was used to track the changes in lattice parameters that occur on

deintercalation of Cu and to check for any additional peaks present that could indicate RT ordering of the Cu vacancies. Fig. 3.2 shows the lattice parameters of samples of $Sr_2MnO_2Cu_{1.5-x}S_2$, along with annotations that indicate the phase assigned to the sections of the phase-diagram.

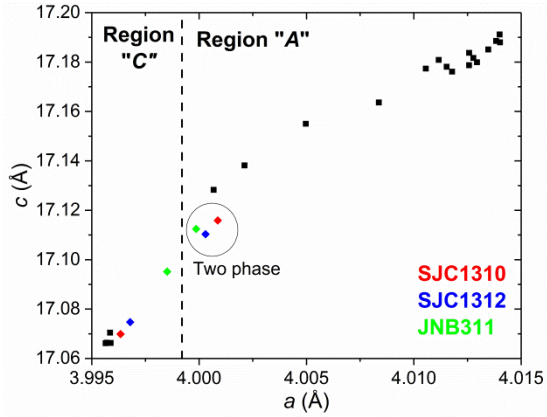


Fig. 3.2 Lattice parameters of various samples of $Sr_2MnO_2Cu_{1.5-x}S_2$, derived from Rietveld refinement against synchrotron PXRD data. The identified regions are discussed within the text and the error bars are smaller than the points on the graph

Removal of Cu from $Sr_2MnO_2Cu_{1.5-x}S_2$ was found to cause a reduction in both *a* and *c* in an approximately linear manner in relation to one another. This may be rationalised using space-filling arguments, in which the loss of Cu from the $[Cu_{1.5-x}S_2]$ layer causes contraction of the compound in both directions. A 0.75% reduction is observed in *c* and a 0.45% reduction observed in *a*.

Two regions are identified within Fig. 3.2, regions "*A*" and "*C*". In region "*A"*, the compounds are fully indexed by the tetragonal *I*4/*mmm* structure at RT, while in region "*C*" several additional peaks appear in the RT PXRD pattern and have been assigned to an incommensurately modulated ordering pattern that is fully described in section 3.2.3. Three samples (SJC1310, SJC1312 and JNB311) have also been highlighted. Close analysis of the PXRD patterns of these samples revealed that they were composed of two compounds with similar lattice parameters and structures, one within the circled area in region "*A*" and one in region "*C*". Therefore these samples contain some region "*C*" superstructure peaks. The two phased behaviour is shown in Fig. 3.3 for SJC1312.

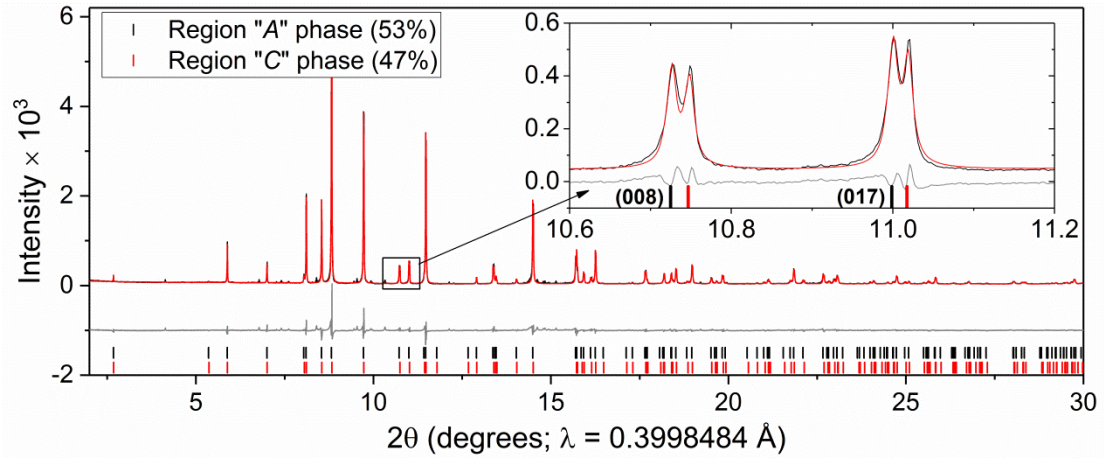


Fig. 3.3 Rietveld plot of SJC1312 ($Sr_2MnO_2Cu_{1.5-x}S_2$) measured at RT using the ID31 diffractometer. The inset emphasises the 008 and 017 peaks of the two phases identified within the sample. The sample was prepared by Prof. S. J. Clarke and the data collected by Drs S. J. Cassidy and S. J. Sedlmaier

This two-phased behaviour, observed in several samples, is suggestive of a phase-gap between the two regions. It is believed that region "*C*" is in fact a single low-copper phase with a negligible phase range and that the difference observed in the lattice parameters arises largely through systematic errors between different instruments.

It is noted that the lattice parameters of the phase of JNB311 that has been identified as region "*C*" are somewhat larger than the lattice parameters of other region "*C*" phases (see Fig. 3.2). It is possible that this is because the PXRD pattern of JNB311 was measured using the PSD (Mythen) on the I11 beamline, which has lower resolution, so some peaks which may have been resolved as double peaks using the MAC detector or ID31/ID22 appear as broadened peaks, as shown in Fig. 3.4. This may have led to small errors in the lattice parameters.

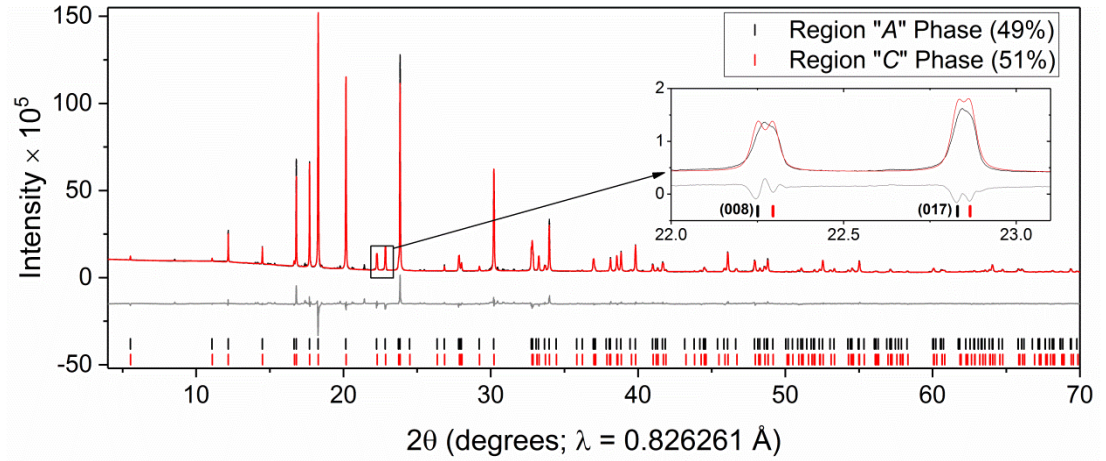


Fig. 3.4 Rietveld plot of JNB311 ($Sr_2MnO_2Cu_{1.5-x}S_2$) measured at RT using the PSD (Mythen) at the I11 beamline. The inset emphasises the 008 and 017 peaks of the two phases within the sample

Some samples were measured using either the ID31 diffractometer or the MAC detector on the I11 beamline. Both these diffractometers are high resolution at high *Q* (low *d*-spacings), allowing for the accurate determination of Cu site occupancy from PXRD data. The relationship between the Cu occupancy, as obtained from this data and the lattice parameters is shown in Fig. 3.5. The data from this figure was obtained by Rietveld refinement of the parent *I*4/*mmm* model for all samples.

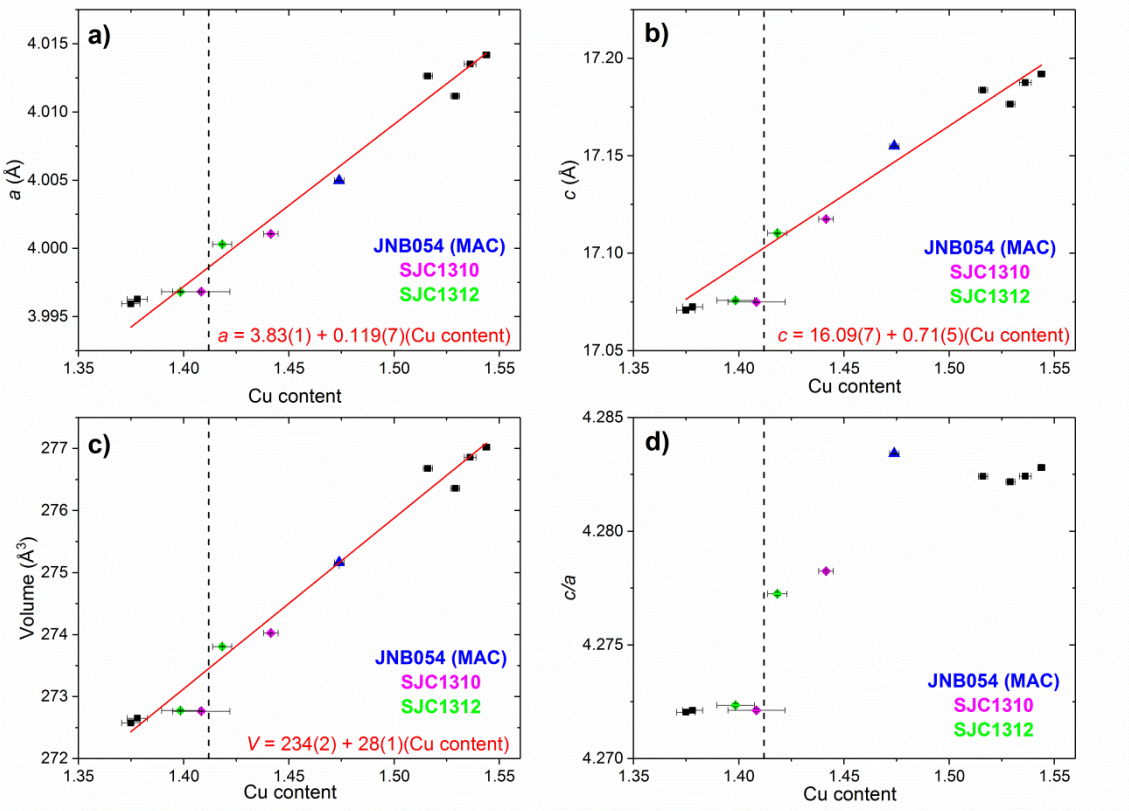


Fig. 3.5 The relationship between the Cu content of various samples of $Sr_2MnO_2Cu_{1.5-x}S_2$ and a) lattice parameter a, b) lattice parameter c, c) unit cell volume and d) the c/a ratio, with lines of best fit. All PXRD data collected using ID31 at RT, unless otherwise stated

The Cu content obtained from Rietveld refinement against these data appears to be systemically too high. Gál *et al.* established (using PND and single-crystal X-ray diffraction (SCXRD)) that the Cu content of the parent material was $Sr_2MnO_2Cu_{1.50(2)}S_2$[45] and in section 3.2.3 the occupancy of the lowest-obtainable phase is established as $Sr_2MnO_2Cu_{1.34(1)}S_2$ using single-crystal X-ray diffraction (SCXRD) and energy dispersive X-ray spectroscopy (EDX). However, the trend in the occupancies appears to be consistent, so it is thought that the Cu content is systematically over estimated by ~0.04.

Fig. 3.5 shows that the relationship between the lattice parameters and occupancies is approximately linear in both *a* and *c*. Two of the samples previously identified as two-phase are also analysed here, allowing for the identification of the postulated phase gap upon entering the region "*C"* regime at an approximate Cu content level of 1.41 using the Cu content values obtained directly from this analysis.

The apparent inconsistency in the trend in the *c/a* ratio of JNB054 is most likely because it is the sole sample measured using the MAC detector on I11. The *c/a* ratio does not change very much on removal of Cu; therefore the value is extremely sensitive to small changes that may arise from slight differences in the calibration of different instruments. It appears that crossing the phase boundary into region "*C*" causes the *c/a* ratio to drop significantly in a non-linear manner; this is likely to be a result of the ordering that will be described later.

3.2.3 Structure and composition of the region "*C*" structure

As previously discussed, when the lowest-copper-content phase of $Sr_2MnO_2Cu_{1.5-x}S_2$ was originally synthesised (by Adamson and Cohen),[88, 89] the RT PXRD pattern contained several small peaks that could not be indexed using either any known impurities or a reasonable expansion of the unit cell. Fig. 3.6 shows an attempted Rietveld fit of a most-oxidised sample indexed using the parent *I4/mmm* structure, emphasising the peaks not indexed by the model. The inability to index all the peaks in the pattern also prevented an accurate determination of the Cu occupancy. Attempts (by Cohen) to determine the Cu occupancy from titration of the amount of I_2 consumed in the reaction systematically overestimated the degree of deintercalation because some I_2 was consumed by compound-destructive side-reactions, even when the reaction was performed in an ice-bath.[89]

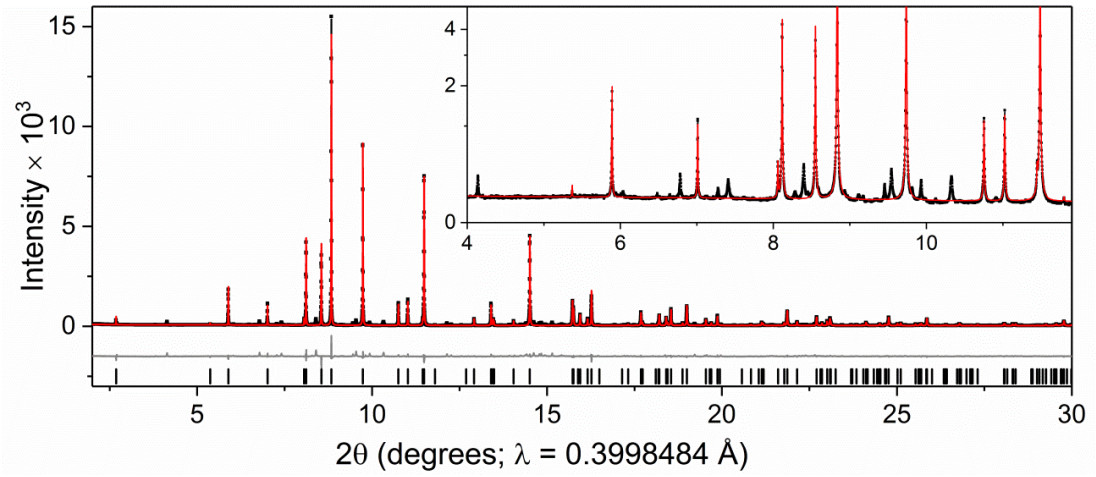


Fig. 3.6 Rietveld refinement against SJC1314 (most-oxidised $Sr_2MnO_2Cu_{1.5-x}S_2$), the data was collected using the ID31 diffractometer and refined using the parent I4/mmm structural model. The inset emphasises the peaks not indexed by the model. The sample was prepared by Prof. S. J. Clarke and the data collected by Drs S. J. Cassidy and S. J. Sedlmaier

Several methods were used to accurately determine the structure and composition of the most-oxidised $Sr_2MnO_2Cu_{1.5-x}S_2$ structure.

3.2.3.1 *Energy-dispersive X-ray analysis*

Energy-dispersive X-ray (EDX) analysis was performed by Prof. J. Hadermann to determine the Cu occupancy of the most-deintercalated compound; the data was calibrated against a well-characterised sample of composition $Sr_2MnO_2Cu_{1.5}S_2$. The following elemental ratios were deduced: Sr2.00(5):Mn1.0(1):Cu1.27(13):S2.0(2). This is in good agreement with the composition found from powder and single-crystal X-ray diffraction (see below).

3.2.3.2 *Electron diffraction and electron microscopy analysis*

The electron diffraction measurements were performed by Prof. J. Hadermann and analysed along with ID31 powder data in collaboration with Prof. A. Abakumov using a sample prepared by Dr P. Adamson. Prof. J. Hadermann and Prof. A. Abakumov are both from Electron Microscopy for Materials Science (EMAT), University of Antwerp, Belgium.

Electron diffraction showed that the reflections from the average structure (the main reflections) could be indexed using a body-centred tetragonal cell with a_t = 3.995 Å, c_t = 17.049 Å. However, as previously indicated, there were additional, smaller reflections (satellite reflections) present that could not be indexed using a rational unit cell. These

satellite reflections were therefore identified as the result of an incommensurately modulated cell and superspace concepts (see section 2.2.3 and Appendix A) were required to index them.

Prof. A. Abakumov found that a (3+1)D approach, using diffraction vector:

$$\mathbf{H} = h\mathbf{a^*} + k\mathbf{b^*} + l\mathbf{c^*} + m\mathbf{q} \quad (3.1)$$

was sufficient. The observed reflections were therefore indexed by: $a_o \approx b_o = \sqrt{2}a_t$, $c_o = c_t$, $\mathbf{q} \approx 0.24\mathbf{a^*} + \mathbf{c^*}$.

Analysis of reflection conditions allowed selection of the $Fmmm(\alpha 01)00s$ superspace group. The setting of the space group was refined to the non-standard setting $Xmmm(\alpha 00)00s$, where X represents the [½, ½, 0, 0], [½, 0, ½, ½], [0, ½, ½, ½] set of centring vectors. This change of the setting of the space group allowed the satellite reflections to be indexed using a single component: $\mathbf{q} \approx 0.24\mathbf{a^*}$. A short discussion of superspace groups is included in Appendix A.

3.2.3.3 *Powder X-ray diffraction analysis*

The unit cell parameters, space group and modulation vector obtained from electron diffraction were used by Prof. A. Abakumov to generate a starting model, allowing the Rietveld refinement against synchrotron PXRD data. This was initially performed on a sample synthesised by Dr P. Adamson (the same that was analysed by electron diffraction). Subsequently this model was used to characterise a synchrotron PXRD pattern of SJC1314, a higher quality, single-phased sample of the region "*C*" phase. The Rietveld plot of this model against the data for SJC1314 (Fig. 3.7) shows that all significant peaks were indexed using this model. This is in contrast to the model shown in Fig. 3.6.

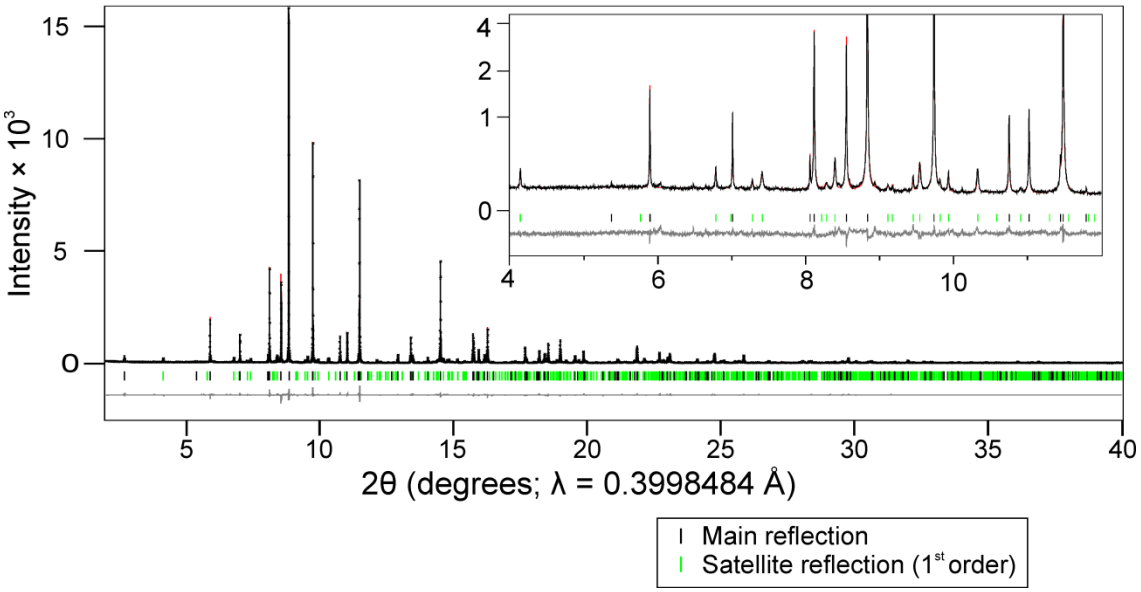


Fig. 3.7 Rietveld refinement against SJC1314 (most-oxidised $Sr_2MnO_2Cu_{1.5-x}S_2$), the data was collected using the ID31 diffractometer and refined using the incommensurately modulated Xmmm(α00)00s structural model. The inset, showing intensity on a square-root scale, emphasises the region where the satellite peaks are particularly large. The sample was prepared by Prof. S. J. Clarke and the data collected by Drs S. J. Sedlmaier and S. J. Cassidy

3.2.3.4 *Single crystal X-ray diffraction*

Although the structure of the most-deintercalated structure was already partially solved using a combination of electron diffraction and synchrotron PXRD data, SCXRD data was collected to confirm the structure obtained via other methods and to allow a more in-depth analysis of the structure. The single-crystal data was collected using the I19 single-crystal small molecule beamline.[104] The crystal, selected from sample SJC1310, was quenched to 100 K before measurement. This analysis was performed with significant assistance from Dr K. E. Christensen and Prof. A. Abakumov.

Reconstructed precession images (Fig. 3.8) confirmed the presence of small satellite peaks. It was found that the cell, including the satellite peaks, could be indexed using the setting obtained by electron diffraction. Therefore, this setting was retained in the analysis of SCXRD data.

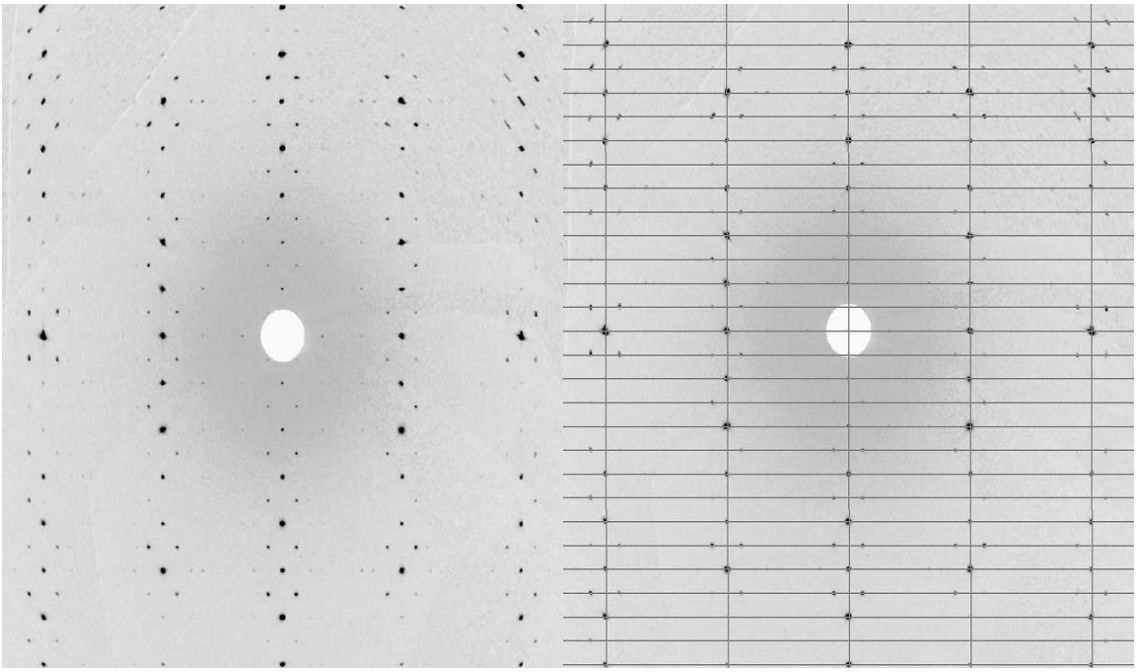


Fig. 3.8 Reconstructed hhl precession image of most-deintercalated $Sr_2MnO_2Cu_{1.5}S_2$, shown both without and with gridlines indicating the peaks indexed by the standard three-dimensional model

Although only satellite reflections of order one are visible in the reconstructed precession image, it was found that satellites of order two could be indexed as well, increasing the completion of the dataset.

The structure of the compound was initially solved using SUPERFLIP,[103] prior to iterative refinement of the model. The quality of the fit to the data was primarily assessed by examining the R_F value, but Fourier maps that plotted electron density as a function of superspace coordinates were also used to direct refinements. These showed that combinations of harmonic functions were more representative of the structure than "step" or "saw-tooth" functions. This is shown by a Fourier map with S as the central atom (Fig. 3.9), where there is a clear sine-wave-like positional modulation as a function of x_{s4}. See Appendix A for a description of the superspace coordinates x_{s1}, x_{s2}, x_{s3} and x_{s4}, as well as the harmonic functions used to describe the modulation.

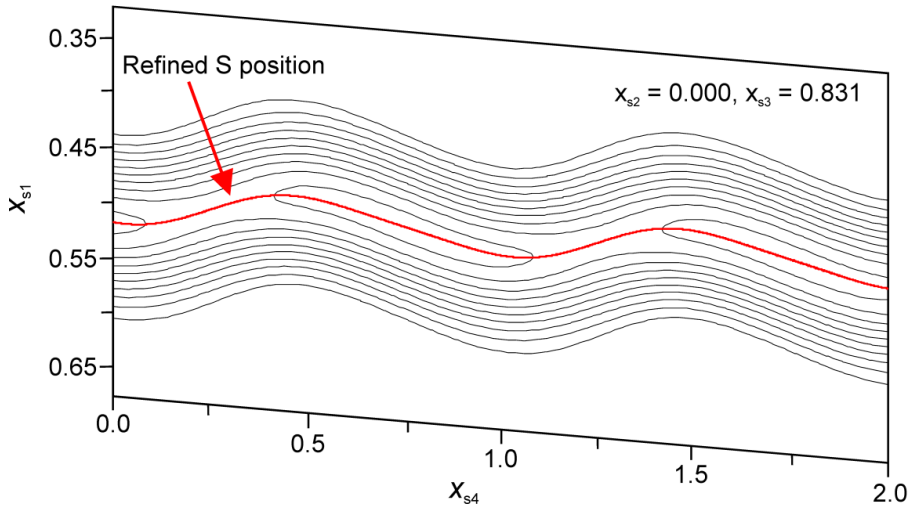


Fig. 3.9 Fourier map of observed electron density in superspace centred on the S atom, with the refined S position as a function of x_{s4} superimposed

The refined parameters from SCXRD analysis are shown in Table 3.1 – Table 3.3. See Appendix A for a definition of the displacement and occupational modulation functions used in the tables.

Table 3.1 Selected parameters for the SCXRD refinement of the structure of $Sr_2MnO_2Cu_{1.34}S_2$

Diffractometer	I19 beamline, λ = 0.6889 Å
Temperature (K)	100
Formula	$Sr_2MnO_2Cu_{1.341}S_2$
Space group	*Xmmm*(α00)00s *X* = [1/2,1/2,0,0], [1/2,0,1/2,1/2], [0,1/2,1/2,1/2]
a (Å)	5.6377(7)
b (Å)	5.6334(8)
c (Å)	16.9735(16)
q	0.2418**a***
Volume (Å^3)	539.07(11)
Z	4
Calculated density (g cm^{-3})	5.0705
GOF	3.36
R_F (all reflections) (%)	4.66
R_F (main reflections) (%)	4.17
R_F (satellites of order 1) (%)	5.21
R_F (satellites of order 2) (%)	9.82

Table 3.2 Atomic positions, isotropic displacement parameters and modulation parameters of $Sr_2MnO_2Cu_{1.34}S_2$, obtained from the SCXRD refinement

Atom	x_1	y	z	U_{iso} (Å^2)
Sr	0	0	0.89822(3)	0.0250(2)
$A_{z,1}$ = 0.01003(5), $B_{x,1}$ = 0.00949(13), $B_{z,2}$ = 0.00041(6)				
Mn	½	0	0	0.0255(5)
$A_{z,1}$ = 0.01253(10)				
Cu	¼	¼	¾	0.0238(4)
p_0 = 0.671(2), $p_{s,1}$ = 0.177(2), $p_{c,2}$ = 0.022(4), $B_{x,1}$ = 0.0213(4), $A_{x,2}$ = -0.0024(4)				
S	½	0	0.83050(5)	0.0220(6)
$A_{z,1}$ = 0.00227(9), $B_{x,1}$ = 0.0186(4), $A_{x,2}$ = -0.0027(6), $B_{z,2}$ = 0.00036(11)				
O	¾	¾	0	0.0252(17)
$A_{z,1}$ = 0.0065(3)				

Table 3.3 Anisotropic displacement parameters and their modulation for $Sr_2MnO_2Cu_{1.34}S_2$, obtained from the SCXRD refinement

Atom	U_{11} (Å^2)	U_{22} (Å^2)	U_{33} (Å^2)	U_{12} (Å^2)	U_{13} (Å^2)	U_{23} (Å^2)
Sr	0.0218(5)	0.0201(5)	0.0332(3)	0	0	0
$A_{U11,1}$ = -0.0031(3), $A_{U22,1}$ = -0.0014(3), $A_{U33,1}$ = -0.0078(3), $B_{U11,1}$ = 0.0030(3), $A_{U33,2}$ = -0.0009(4), $B_{U11,2}$ = 0.0004(7), $B_{U22,2}$ = 0.0002(6), $B_{U33,2}$ = -0.0083(4)						
Mn	0.0188(10)	0.0184(9)	0.0391(6)	0	0	0
Cu	0.0282(8)	0.0251(8)	0.0179(3)	0	0	0
S	0.0267(14)	0.0217(12)	0.0175(4)	0	0	0
O	0.030(4)	0.022(3)	0.0236(12)	-0.0024(11)	0	0

The modulation vector (**q** = 0.2418**a***) is close to ¼ in a_o and therefore the crystal structure can be represented reasonably well by an 8 × approximant, as is shown in Fig. 3.10.

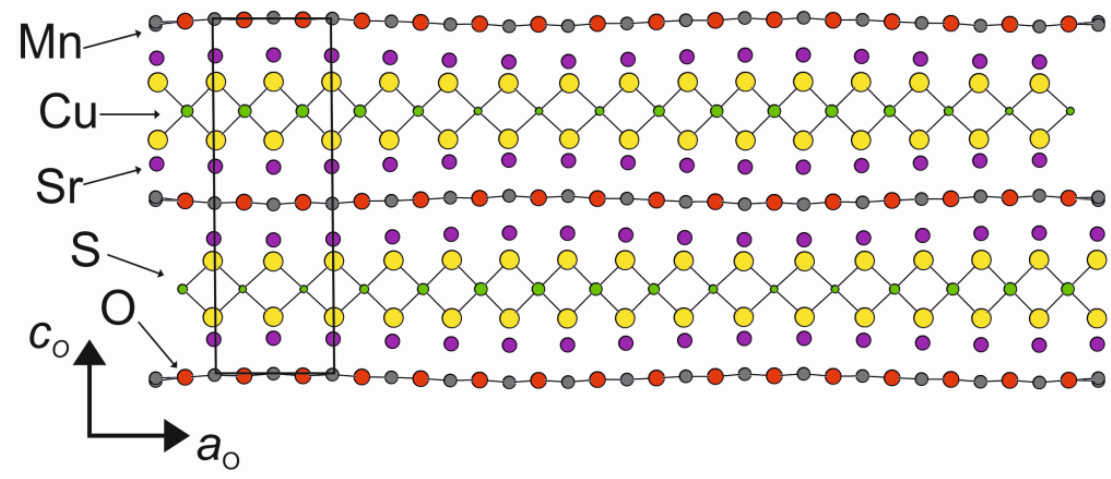


Fig. 3.10 An 8× approximant of the crystal structure of $Sr_2MnO_2Cu_{1.34}S_2$ (region "C" $Sr_2MnO_2Cu_{1.5-x}S_2$). The size of the green circles is used to represent the relative occupancy of the Cu sites

The model obtained from this crystal structure may also be represented by a series of graphs of selected parameters as a function of *t*, as shown in Fig. 3.11. Fig. 3.11 a), comparing the Mn-O distance with the Cu occupancy shows that the Mn-O distance changes little as a function of *t* (*t* may be thought of as the phase of the modulation, see Appendix A for further information), implying that any charge ordering that occurs is not a significant contributor to the modulation. The two graphs Fig. 3.11 b) and c) show the displacement of the $[Sr_2MnO_2]$ block towards the $[Cu_2S_2]$ block when the Cu occupancy is low to minimise under-bonding of sulfide ions. This displacement occurs mostly in the *c*-direction, but is also observed in the *ab*-plane. The diagram (Fig. 3.11 d)) is included to show that displacement of Sr in the *ab*-plane may cause some Sr-S distances to increase, while reducing others, hence the two more complex Sr-S distance curves seen in Fig. 3.11 b).

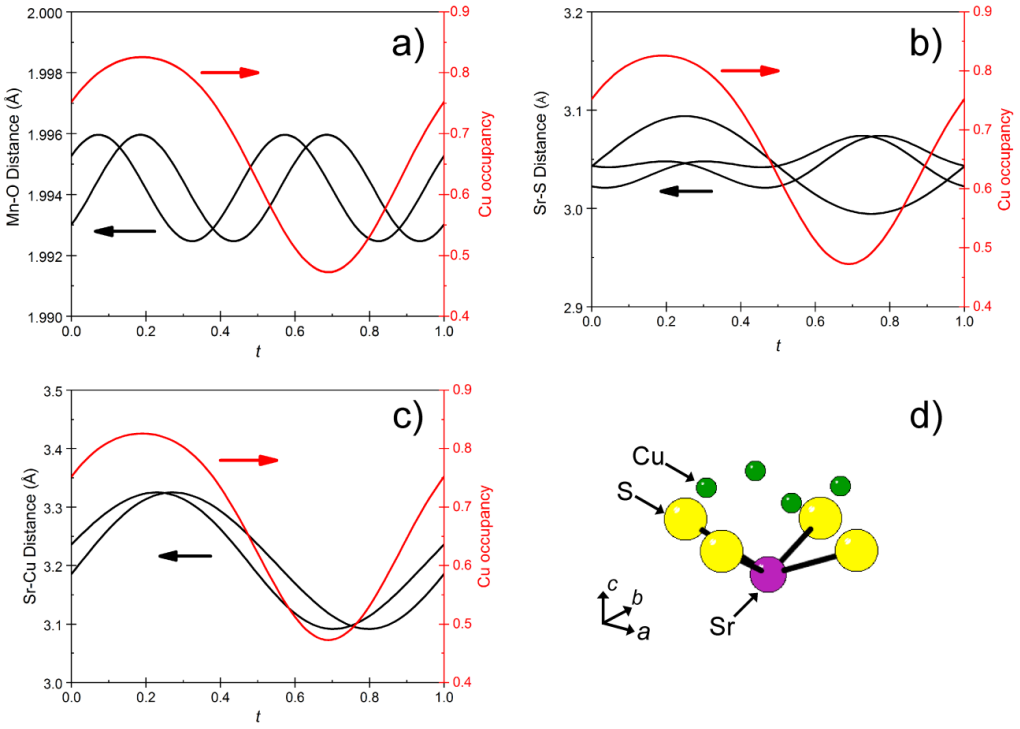


Fig. 3.11 a) Comparison of Cu occupancy and Mn-O bond distance; b) comparison of Cu occupancy and Sr-S distance; c) comparison of Cu occupancy and Sr-Cu distance, all as a function of t. d) shows the relationship between Sr and its nearest S and Cu neighbours

3.2.3.5 *Electron Microscopy*

High angle annular dark field scanning transmission electron microscopy (HAADF-STEM) images of $Sr_2MnO_2Cu_{1.33}S_2$ were collected and analysed by Prof. J. Hadermann,

as shown in Fig. 3.12. In this image, the movement of the [Sr_2MnO_2] blocks transverse to the plane in response to the changes in the Cu occupancy can be observed.

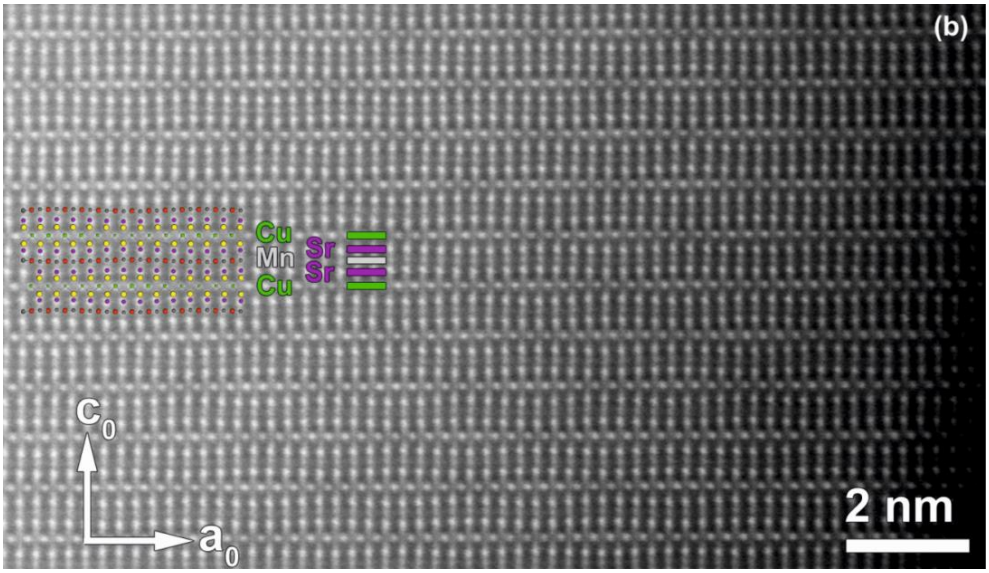


Fig. 3.12 Labelled high-angle annular dark field scanning transmission electron microscopy image of a sample of $Sr_2MnO_2Cu_{1.33}S_2$, measured and analysed by Prof. J. Hadermann (University of Antwerp)

3.2.4 Low temperature powder X-ray diffraction

When parent $Sr_2MnO_2Cu_{1.5}S_2$ is cooled below ~250 K, a phase change occurs with partial Cu/vacancy ordering, as outlined in section 3.1. The behaviour of the parent on cooling has already been well characterised;[107] therefore, this work focusses on the changes to the low temperature ordering that occur on removal of Cu from the system.

The modulated superstructure of compounds in region "*C*", described above in section 3.2.3, did not change as a function of temperature. Small peaks emerged in the PXRD patterns of samples with Cu occupancy and lattice parameters intermediate between the parent phase and region "*C*" on cooling, which couldn't be indexed using either the parent or region "*C*" ordering schemes. This regime was termed region "*B*". The peaks that arise from region "*B"* are demonstrated with reference to seven different samples, the lattice parameters of these samples are shown in Fig. 3.13. Note that several of the samples analysed have been identified as two-phased samples, with two distinct sets of lattice parameters and therefore composition.

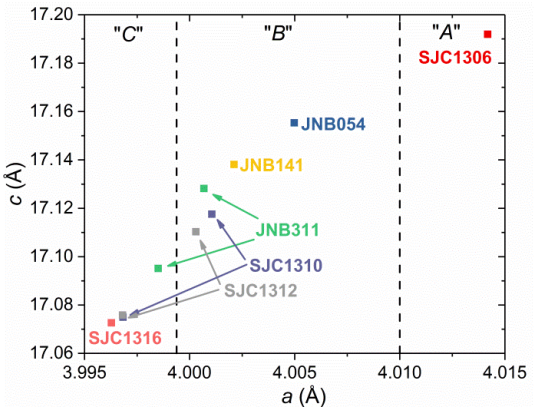


Fig. 3.13 Refined RT lattice parameters of seven samples of $Sr_2MnO_2Cu_{1.5-x}S_2$, three samples (JNB311, SJC1310 and SJC1312) have been refined as two similar phases. The error bars are smaller than the points on the graph

3.2.4.1 *Quenching and slow-cooling*

The PXRD patterns of selected samples of $Sr_2MnO_2Cu_{1.5-x}S_2$ were compared on quench cooling to low temperature (110 K) and on cooling slowly (rate: 6 K min^{-1}). It was found that the position of any low-temperature superstructure peaks was independent of cooling rate, but in the PXRD patterns of the quench-cooled samples the superstructure peaks were significantly smaller and broader. This behaviour was attributed to less complete ordering of the Cu vacancies, arising from the dramatically increased cooling rate. Fig. 3.14 compares the PXRD pattern of JNB141 (region "*B*" $Sr_2MnO_2Cu_{1.5-x}S_2$) when the sample has been cooled slowly and when it has been quench-cooled. Slow-cooled data was used when characterising the behaviour of these compounds as a function of Cu content.

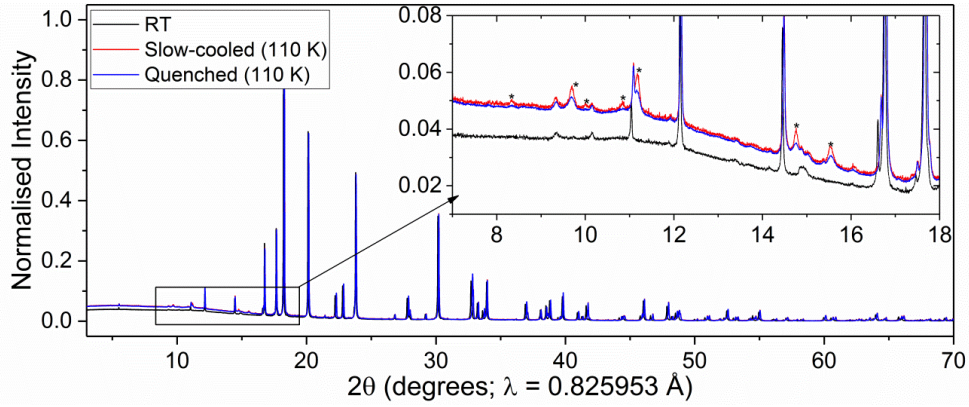


Fig. 3.14 Comparison of the low temperature superstructure peaks of JNB141 (region "B" $Sr_2MnO_2Cu_{1.5-x}S_2$) when the compound has been slow-cooled (rate: 6 K min^{-1}) and quench-cooled to 110 K

The behaviour observed here contrasts with that observed for the double-layered analogue $Sr_2MnO_2Cu_{3.5}S_3$, where different ordering schemes were observed as a function of cooling rate (see section 1.2.3.3).[54]

3.2.4.2 *Changes in low-temperature peaks*

The low-temperature ordering peaks that have been identified as belonging to region "*B*" are shown in Fig. 3.15 and compared to the region "*A*" low-temperature peaks. The peaks are sufficiently low in intensity compared with the substructure peaks that they are best shown using a square-root intensity scale.

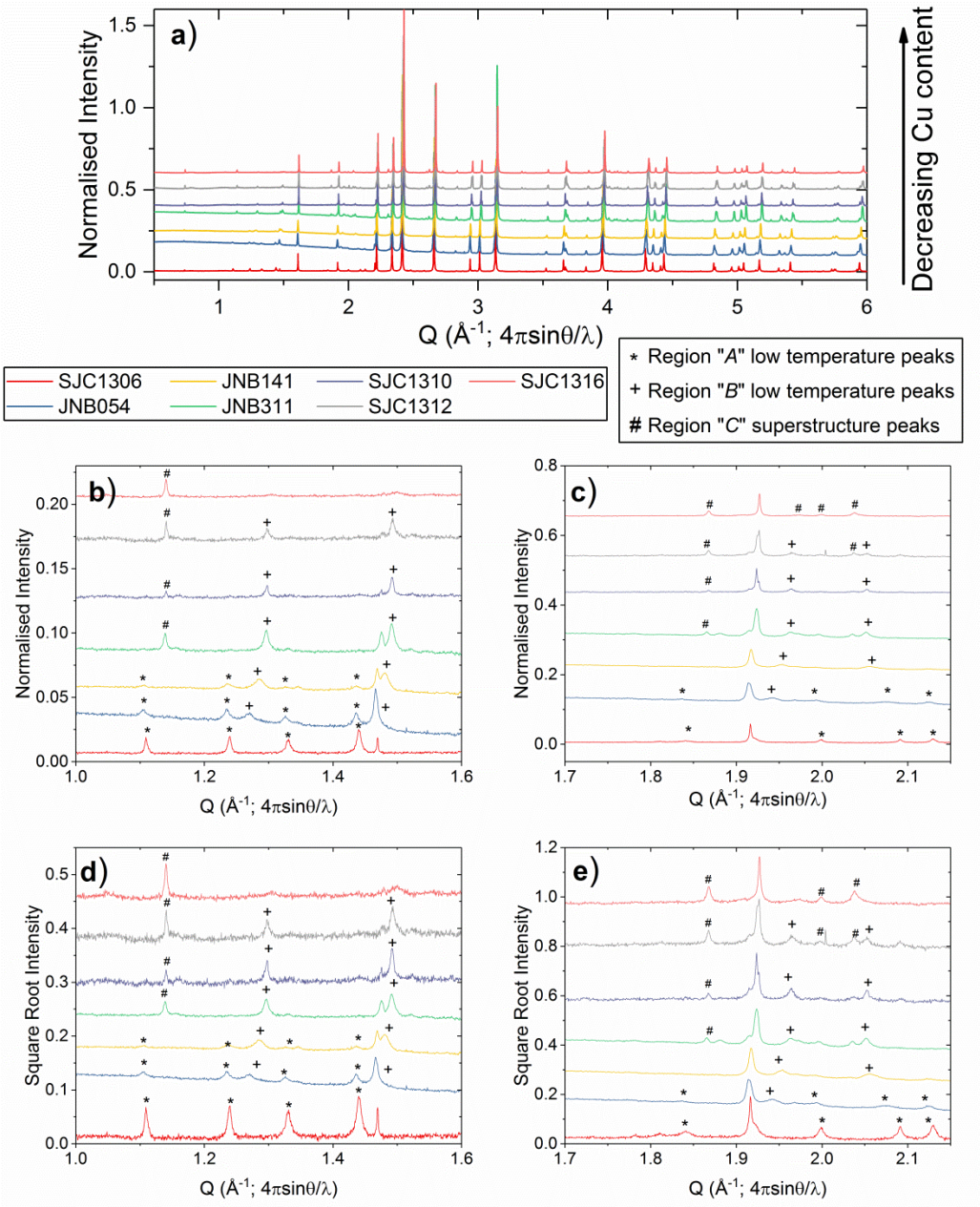


Fig. 3.15 Stacked PXRD patterns of SJC1306, JNB054, JNB141, JNB311, SJC1310, SJC1312 and SJC1316 all measured at 120 K, samples prefixed with SJC were measured using the ID31 diffractometer (data collected by Drs S. J. Sedlmaier and S. J. Cassidy), while samples prefixed with JNB were measured using the PSD on the I11 beamline. a) shows the full Q-range; b) and c) show 1.0 < Q (Å^{-1}) < 1.6 and 1.7 < Q (Å^{-1}) < 2.15 respectively using normalised intensity on a linear scale, while d) and e) show the same Q ranges on a square-root scale, allowing emphasis of smaller peaks. Symbols used are discussed within the body text

Fig. 3.15 highlights the four ordering peaks (indicated by + symbols) that appear on cooling for samples with lattice parameters within region "*B*" and shows that in all the samples that have been isolated, the ordering peaks coexist with either the region "*A*" ordering peaks (indicated by * symbols) or the region "*C*" peaks. When the region "*B*" peaks coexist with those from region "*C*" (indicated by # symbols), the sample is clearly two-phased, as has already been discussed. However, the same is not the case when region "*B*" and "*A*" peaks coexist (see JNB054 and JNB141 in particular). The superstructure peaks belonging to region "*B*" appear below ~250 K. This is the same ordering temperature as region "*A*".

Attempts to index the peaks assigned to region "*B*" using standard powder diffraction methods have been unsuccessful, hampered by the low intensity and low number of the peaks. Attempts were also made to characterise these peaks using electron diffraction, by Dr M. Batuk at EMAT, Antwerp. A sample of JNB141 was analysed, however the sample was found to be beam sensitive and the superstructure reflections characteristic of region "*B*" could not be identified in the crystallites of this sample that were probed. Further microscopy experiments, probably involving multiple crystallites would be required to explore this further.

3.2.4.3 *Changes in lattice parameters as a function of temperature*

Several samples were measured using the cryostat on ID31 in the range RT – 5 K to identify if any further phase changes beyond those described above occurred, as might be identified by the observation of further superstructure peaks, peak splitting or discontinuities in the refined lattice parameters. No changes in the peaks were observed in the PXRD patterns. The refined lattice parameters of SJC1306 (parent $Sr_2MnO_2Cu_{1.5}S_2$), SJC1310 (two phase region "*B*" and region "*C*" sample) and SJC1316 (region "*C*" sample) are shown in Fig. 3.16.

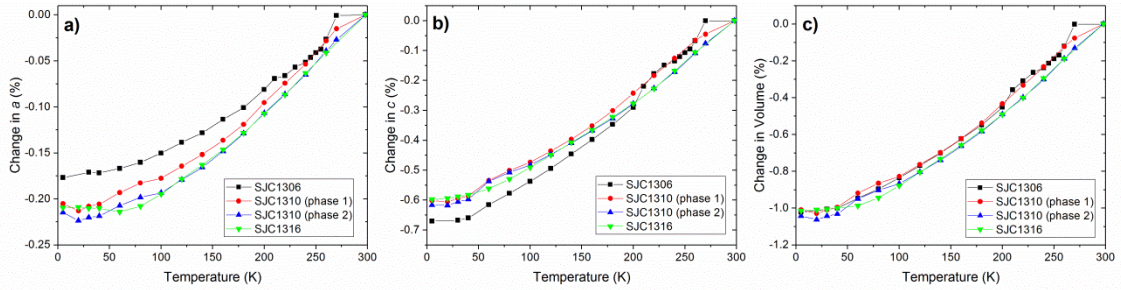


Fig. 3.16 The changes in lattice parameters a) a and b) c and c) the unit cell volume as a function of temperature for SJC1306 (parent $Sr_2MnO_2Cu_{1.5}S_2$), both phases of SJC1310 (two-phased sample) and SJC1316 (region "C" sample). All compounds were indexed using the parent I4/mmm model. The lines are guides to the eye and the error bars are smaller than the points on the graph. VT PXRD data obtained from ID31 (samples synthesised by Prof. S. J. Clarke and data collected by Drs S. J. Sedlmaier and Dr S. J. Cassidy)

A small discontinuity was observed in the lattice parameters of SJC1306 (parent $Sr_2MnO_2Cu_{1.5}S_2$), accompanying the *I4/mmm*-to-*Ibam* transition in this region. A local minimum is also observed in the *a* lattice parameter of SJC1316 (region "*C*" compound) at 60 K – 80 K, this accompanies the observed T_N of the compound (see section 3.2.5). It is more difficult to draw definitive conclusions from the inconsistencies in the lattice parameters of SJC1310 because of the uncertainty induced by the coexistence of two phases in one sample.

3.2.5 Magnetometry

Eight samples of $Sr_2MnO_2Cu_{1.5-x}S_2$ were selected for magnetometry measurements in order to examine the change in magnetic susceptibility as a function of copper occupancy. The lattice parameters of the eight samples are shown in Fig. 3.17 and the zero-field-cooled (ZFC) and field-cooled (FC) magnetic susceptibility curves of these samples are shown in Fig. 3.18.

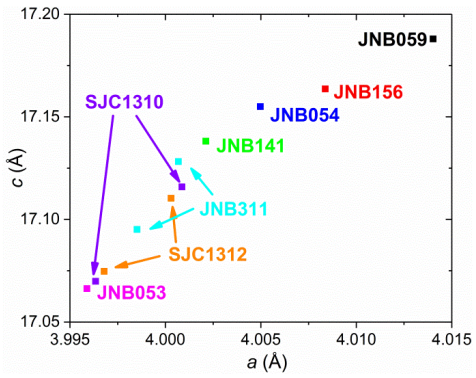


Fig. 3.17 Lattice parameters (derived from Rietveld refinement against synchrotron PXRD data) of the $Sr_2MnO_2Cu_{1.5-x}S_2$ samples that had their magnetic susceptibility measured. Some of the samples clearly contain two phases of $Sr_2MnO_2Cu_{1.5-x}S_2$. The error bars are smaller than the points on the graph

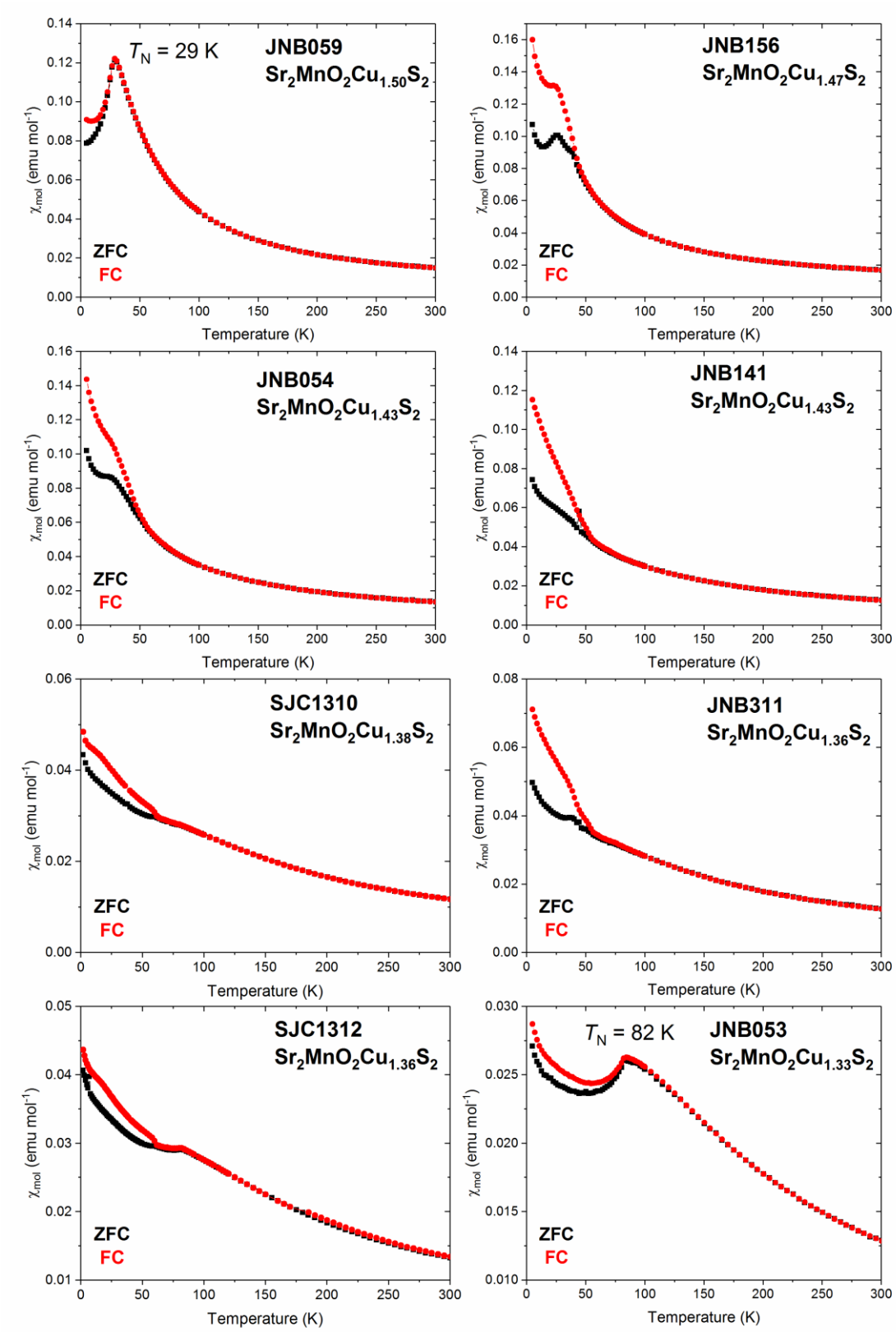


Fig. 3.18 The zero-field-cooled (ZFC) and field-cooled (FC) magnetic susceptibility curves of various samples of $Sr_2MnO_2Cu_{1.5-x}S_2$, all measured in a field of 100 Oe. The average compositions given for each sample are estimated from the refinement against synchrotron PXRD data from various sources (the systematic overestimation of Cu occupancy, when compared with PND and SCXRD data, has also been taken into account)

The ZFC/FC susceptibility curves (Fig. 3.18) show the evolution of the magnetic susceptibility from the parent magnetic antiferromagnetic behaviour, with a cusp identified as T_N = 29 K to the most-oxidised antiferromagnetic behaviour, with T_N = 82 K. Samples in between these two extremes appear to have a significantly larger divergence between the ZFC and FC susceptibility curves, indicating that there is a significant spin-glass component to the behaviour that is maximised in samples of intermediate copper occupancy. In these intermediate samples (JNB054, JNB141, SJC1310, JNB311 and SJC1312) the temperature at which the ZFC and FC susceptibility curves bifurcate is in the region 50 – 65 K.

Attempts to extract Curie and Weiss constants from linear regression of the inverse molar susceptibility led to unreasonably large effective magnetic moments and values for the Weiss temperatures that were inconsistent with values previously reported by Gál *et al.*[45] and Adamson *et al.*[107] This was attributed to small quantities of ferromagnetic impurities and therefore the extracted values were not compared. It is also noted that the Curie-Weiss law only applies at temperatures >> T_N. As T_N increases on oxidation, it is likely to become more difficult to extract reliable parameters from the Curie-Weiss law in the regime (< 300 K) that can routinely be measured using the available SQUID magnetometer.

3.2.6 Powder neutron diffraction to probe changes in magnetic ordering

This section aims to characterise the magnetic ordering behaviour of $Sr_2MnO_2Cu_{1.5-x}S_2$ as a function of Cu content and therefore the Mn oxidation state. The magnetic structure of the region "*A*" and region "*C*" phases are already known, having been solved by Adamson *et al.* and Prof. S. J Clarke (by comparison with the structure obtained for the analogous double-layered compound $Sr_2MnO_2Cu_{3.5}S_3$) respectively.[55, 107, 110] The magnetic ordering scheme of these sample is shown in Fig. 3.19.

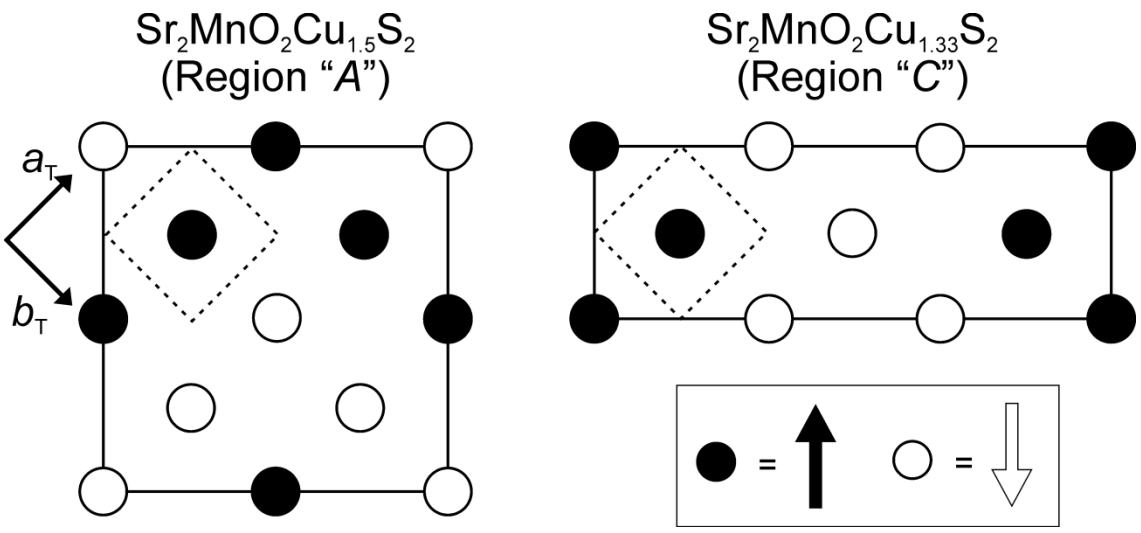


Fig. 3.19 The magnetic structure of (left) parent $Sr_2MnO_2Cu_{1.5}S_2$ and (right) most-oxidised $Sr_2MnO_2Cu_{1.33}S_2$. The magnetic moments are oriented perpendicular to the planes in both models. The only atoms shown are Mn, the only atoms with a magnetic moment associated with them.

Both these structures were solved using data obtained from the fixed-wavelength D2B diffractometer (λ = 1.593 Å) at the ILL (Grenoble, France). The resolution of a fixed wavelength diffractometer is reduced at high *d*-spacing because the ratio $\Delta d/\Delta 2\theta$ is increased, which may hinder the resolution of peaks that are close together in *d*-spacing, or hinder the observation of other features, such as anisotropic broadening of the peaks. Therefore, it was considered of interest to analyse the magnetic structure of these compounds using data from WISH, a time-of-flight diffractometer optimised for measurement of medium-to-high *d*-spacings. In this way the samples could be compared as part of a series, allowing investigation of the magnetic behaviour of phases with an intermediate Cu occupancy, and would offer an opportunity to search for additional features to the magnetic ordering, such as evidence for charge ordering of the Mn^{2+}/Mn^{3+} ions.

To this end four ~3 g samples of $Sr_2MnO_2Cu_{1.5-x}S_2$: JNB059 (region "*A*"), JNB054 (region "*B"*), JNB311 (two-phase region "*B*" and "*C*") and JNB053 (region "*C*"), were measured using WISH.

3.2.6.1 *JNB059 (parent $Sr_2MnO_2Cu_{1.5}S_2$)*

JNB059 was found to possess the same Cu/vacancy ordering and magnetic ordering behaviour as has previously been found for parent samples of $Sr_2MnO_2Cu_{1.5}S_2$. Fig. 3.20 shows Rietveld refinements for the samples measured at 270 K (well above the temperature at which any Cu/vacancy ordering or magnetic ordering occurs), 130 K

(below the Cu/vacancy ordering temperature but above the magnetic ordering temperature) and at 5 K (Cu/vacancy and magnetic ordering both observed).

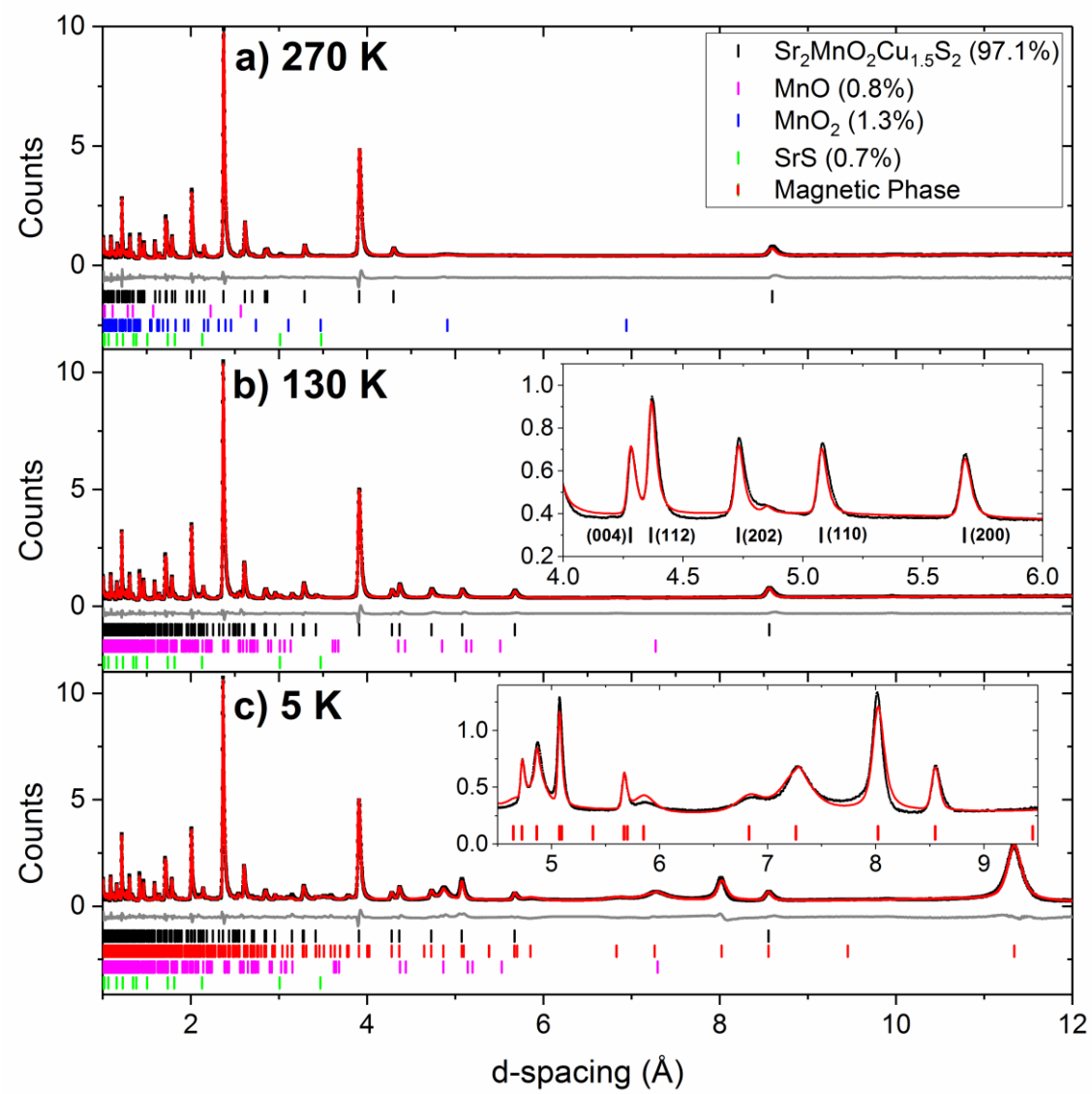


Fig. 3.20 Rietveld plot of JNB059 (parent $Sr_2MnO_2Cu_{1.5}S_2$) measured using the 2-9 (58.3°) bank of WISH at a) 270 K, b) 130 K (inset emphasises the low temperature copper-ordering peaks) and c) 5 K (inset emphasises a region dense with magnetic ordering peaks)

The magnetic peaks were indexed using a $a_O \times 2b_O \times c_O = 2\sqrt{2}a_T \times 2\sqrt{2}b_T \times c_T$ expansion of the nuclear unit cell (where a_O, b_O, c_O refer to the lattice parameters of the low-temperature, orthogonal *Ibam* unit cell and a_T, b_T and c_T refer to the lattice parameters of the tetragonal structural cell). Symmetry mode analysis, using ISODISTORT,[112] found that the intensity of the magnetic peaks could be predicted by relaxing the magnetic mDT4 symmetry modes, therefore a magnetic space group (P_cmn2_1 (31.130)) was selected that allowed refinement of these modes.

This space group allows for the refinement of the following magnetic Mn modes: mDT4 A'$_1$(a), mDT4 A'$_1$(b), mDT4 A'$_2$(a) and mDT4 A'$_2$(b). These modes are displayed in Fig. 3.21.

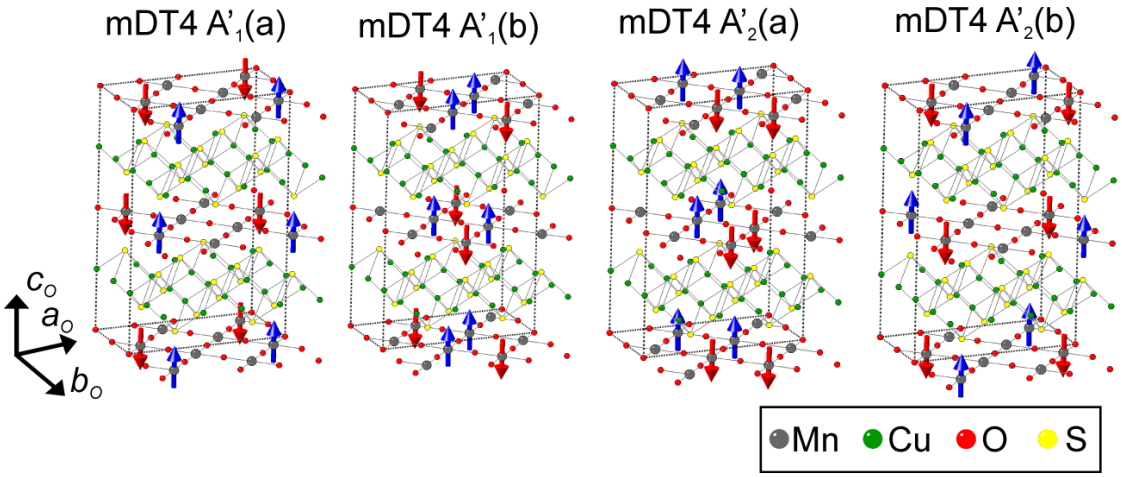


Fig. 3.21 The magnetic Mn symmetry modes allowed by the P_cmn2_1 (31.130) magnetic space group. Sr atoms omitted and relative ion size normalised for clarity. The dotted lines outline the nuclear Cu/vacancy-ordered cell

Since it is considered extremely unlikely that only half of the Mn atoms would carry a magnetic moment, only combinations of modes which resulted in magnetic moments on every magnetic ion were considered. It was also found that the following mode additions: mDT4 A'$_1$(a) + mDT4 A'$_2$(a) and mDT4 A'$_1$(b) + mDT4 A'$_2$(b) resulted in ferromagnetic-stripe magnetic ordering patterns (see Fig. 3.19) that had a unit cell that was smaller than that found for this compound and therefore did not predict intensity at all of the magnetic peaks. The mode additions mDT4 A'$_1$(a) + mDT4 A'$_1$(b) and mDT4 A'$_2$(a) + mDT4 A'$_2$(b) both successfully fitted the magnetic intensity, these are referred to as model 1 and model 2 respectively. It was found that the restraint mDT4 A'$_x$(a) = mDT4 A'$_x$(b) was required to prevent over-correlation between similar symmetry modes; this restricted the spin on each Mn ion to be of equivalent magnitude. The arrangement of these combinations of spins is shown in Fig. 3.22.

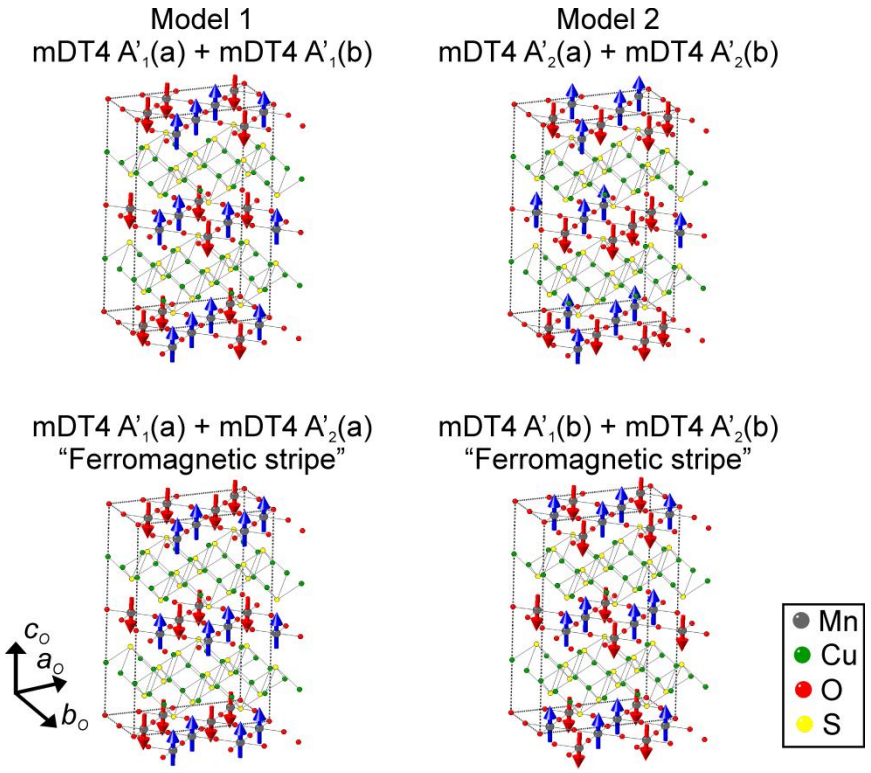


Fig. 3.22 The double combinations of mDT4 modes that were considered. The dotted lines outline the nuclear Cu/vacancy ordered cell

A fifth option is possible, in which all four mDT4 modes are activated, again with the restraints mDT4 A'$_1$(a) = mDT4 A'$_1$(b) and mDT4 A'$_2$(a) = mDT4 A'$_2$(b) to prevent errors in the refinement from over-correlation. Refinement with these modes allows some Mn ions to have different magnitude moments, which would be a possibility if the mixed oxidation state of Mn (Mn^{2+}/Mn^{3+}) led to charge ordering. This combination is shown schematically in Fig. 3.23

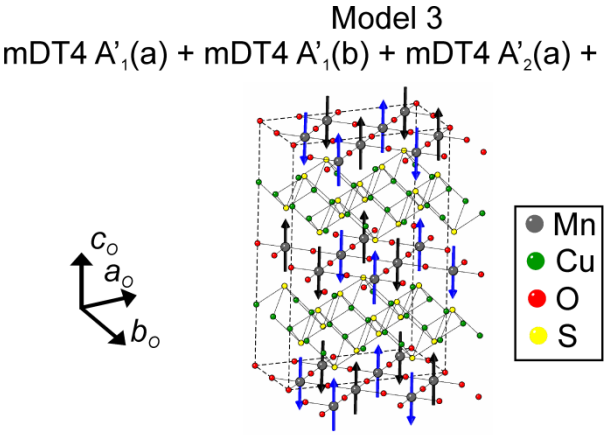


Fig. 3.23 The result of combining all four possible mDT4 modes (model 3), the different coloured vectors emphasise the two magnetic magnitudes possible

All three of these possible symmetry mode combinations were refined, in order to find the best model. The results of these refinements are compared in Table 3.4 – Table 3.5 and the Rietveld plots in Fig. 3.24.

Table 3.4 Definitions of the magnetic models compared

Model 1	mDT4 A'_1(a) + mDT4 A'_1(b)
Model 2	mDT4 A'_2(a) + mDT4 A'_2(b)
Model 3	mDT4 A'_1(a) + mDT4 A'_1(b) + mDT4 A'_2(a) + mDT4 A'_2(b)

Table 3.5 Comparison of selected refinement results using the different models. The models were refined against PND data collected for JNB059 (parent $Sr_2MnO_2Cu_{1.5}S_2$) using WISH at 5 K

Model	Model 1	Model 2	Model 3
a (Å)	11.3413 (4)		
b (Å)	5.6705(2)		
c (Å)	17.0997(2)		
Mn1 (0.1246, 0.1326, 0) (μ_B)	3.99(4)	4.14(4)	4.28(4)
Mn2 (0.3754, 0.3826, 0) (μ_B)	3.99(4)	4.14(4)	3.93(4)
Mn3 (0.8754, 0.8674, 0) (μ_B)	3.99(4)	4.14(4)	3.93(4)
Mn4 (0.6246, 0.1174, 0) (μ_B)	3.99(4)	4.14(4)	4.28(4)
R_{wp} (%)	6.495	6.356	6.425

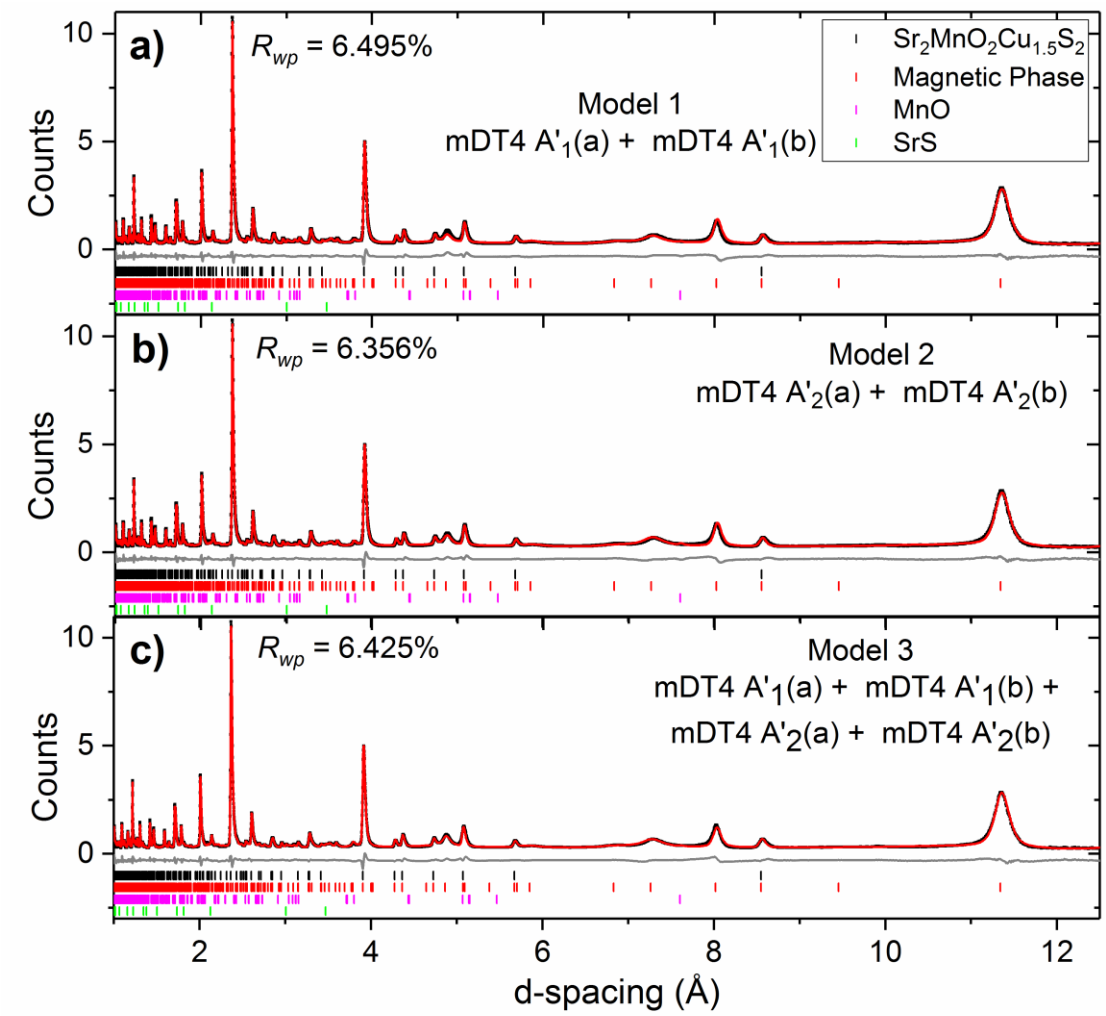


Fig. 3.24 Comparison of the Rietveld plots of JNB059 (parent $Sr_2MnO_2Cu_{1.5}S_2$) when different models are used a) model 1 (mDT4(a) + mDT4(b)); b) model 2 (mDT4(a) + mDT4(b)) and c)model 3 (mDT4(a) + mDT4(b) + mDT4(a) + mDT4(b)). Observed data shown is PND data collected at 5 K using the 2-9 (58.3°) bank of WISH

The results found here closely match those reported by Adamson *et al.*,[107] model 1 and 2 exhibit the *CE* magnetic structure, with equivalent ordered moments on each Mn. These two models are closely related to one another and very similar results are expected and obtained. Model 3 refines the magnetic moments of the two lattices to be within 3 standard deviations of one another, so the obtained ordered moments cannot be identified as statistically distinct from one another. This indicates that any charge ordering in this compound is likely to be incomplete.[107] This is in line with there being no clear evidence for a structural signature of charge order in high resolution PND or low temperature electron diffraction measurements.

3.2.6.1.1 **Variable temperature powder neutron diffraction measurements**

PND patterns were collected at 5, 15, 20, 25, 30, 35 and 40 K in order to model the change in magnetic behaviour from base temperature to above T_N. It was found that the ratio of the magnetic peak intensities remained the same but that the overall intensities decreased until they disappear above 30 K (as shown in Fig. 3.25). This matches the behaviour observed from the magnetic susceptibility measurement of JNB059 (see Fig. 3.18).

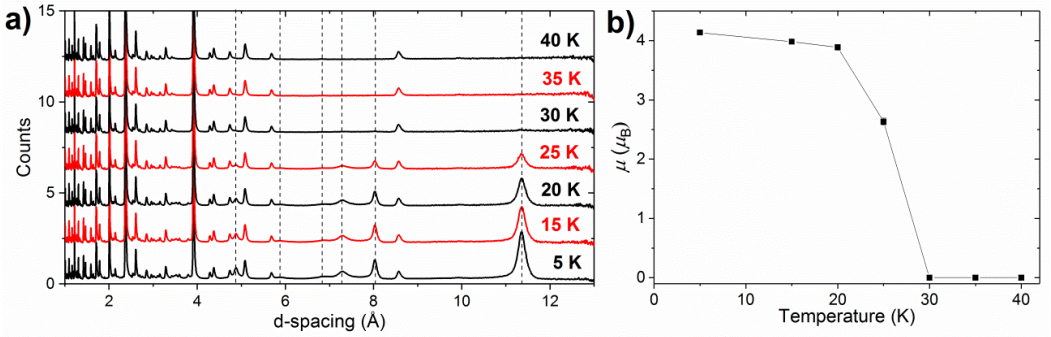


Fig. 3.25 a) PND patterns of JNB059 (parent $Sr_2MnO_2Cu_{1.5}S_2$) at various temperatures, showing the evolution of magnetic peaks as a function of temperature (data collected using the 2-9 (58.3°) bank of WISH) and b) showing the refined magnetic moment as a function of temperature, the line is a guide to the eye and the refined errors are smaller than the points on the graph

3.2.6.1.2 **Anisotropic broadening of magnetic peaks**

Full resolution of the parent magnetic structure was significantly hampered by the anisotropic broadening observed in the diffraction data. Peaks where $l \neq 0$ were significantly broader than peaks where l = 0. This broadening was successfully modelled by adding the term shown in eq. 3.2 to the standard time-of-flight peak-shape function.

$$\frac{c^* \times |l| \times d \times t_1 \times d^2}{\pi \xi_c} \tag{3.2}$$

Where *c** is the reciprocal-space equivalent of *c*, *l* the miller index perpendicular to the *c*-axis, *d* is the *d*-spacing, t_1 is the *d*-spacing independent parameter relating time of flight to *d*-spacing (known as DIFC in GSAS) and ξ_c is the *c*-axis correlation length. This term uses the rationale developed by Her *et al.*[113] and was developed by McCabe *et al.*[114]

Comparison of the Rietveld plots before and after anisotropic broadening is applied show the large improvement in the fit that is achieved (see Fig. 3.26). ξ_c is refined to

29.7(9) Å, a value that is less than two times *c*, suggesting a large degree of disorder occurs in the *c*-direction (i.e. between the layers).

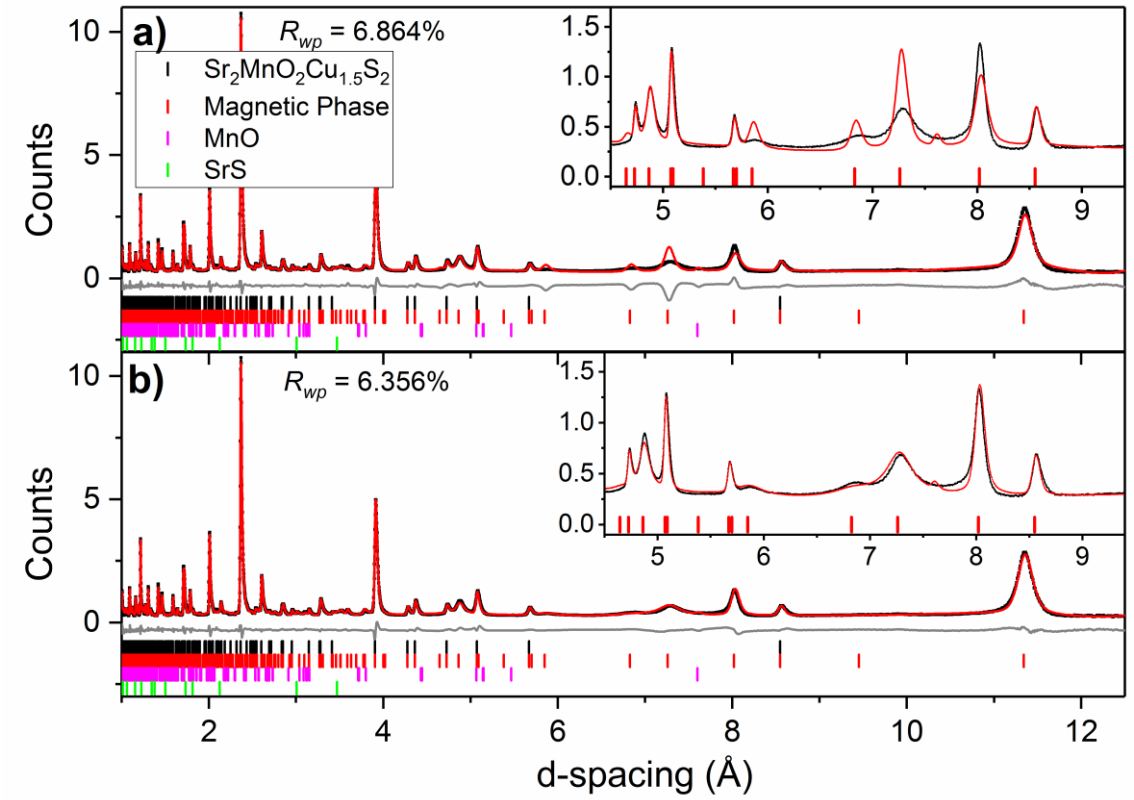


Fig. 3.26 Comparison of the Rietveld plots of JNB059 (parent $Sr_2MnO_2Cu_{1.5}S_2$) measured at 5 K using 2-9 (58.3°) bank of WISH, a) Model 3 without using anisotropic broadening terms and b) Model 3 with the previously described anisotropic broadening term incorporated into the peak-shape model

As previously discussed, the magnetic structure of region "*A*" $Sr_2MnO_2Cu_{1.5}S_2$ was previously solved using PND data obtained from D2B, a fixed wavelength diffractometer. With this data, it was found that using anisotropic broadening terms improved the fit, but the resolution of D2B at low angle was sufficiently reduced that it could not be unambiguously determined if this was the result of a real effect. The use of a time-of-flight diffractometer, which (unlike fixed-wavelength diffractometers) has constant $\Delta d/d$ in a single data bank, allowed resolution of this feature in the magnetic structure.

3.2.6.2 *JNB053 (region "C" $Sr_2MnO_2Cu_{1.33}S_2$)*

Attempts to refine the magnetic structure of JNB053 using the region "*C*" incommensurately modulated model proved to be extremely difficult with the multi-databank data obtained from WISH, due to problems using JANA2006. This is because JANA2006 is not as flexible as TOPAS when refining multiple phases and multiple

banks. However, TOPAS (version 5) cannot refine incommensurately modulated structures.[99] Therefore a commensurate 8 × approximant model, generated from the solution of the single-crystal dataset discussed in section 3.2.3 was used as the nuclear model. This model gave a reasonable fit to the nuclear structure, fitting most of the nuclear peaks, but was not a perfect fit, leading to small intensity discrepancies (most notably the 002 peak at ~8.46 Å) and therefore a relatively large R_{wp}, but the model was considered sufficient for examination of the magnetic structure.

It was confirmed that the magnetic structure of this phase was the same as that solved by Prof. S. J. Clarke (shown in Fig. 3.19). The Rietveld plot of this structure is shown in Fig. 3.27. The refined magnetic moment of the Mn ions is 4.11(3) μ_B. This value is within three standard deviations of the refined magnetic moment of JNB059 (parent $Sr_2MnO_2Cu_{1.5}S_2$), so is not considered to be significantly different, suggesting that region "*C*" is highly magnetically ordered, consistent with the high crystallinity observed. It is possible that the use of an approximant for the nuclear model led to small scaling inaccuracies, increasing the error in the refined magnetic moment beyond that calculated.

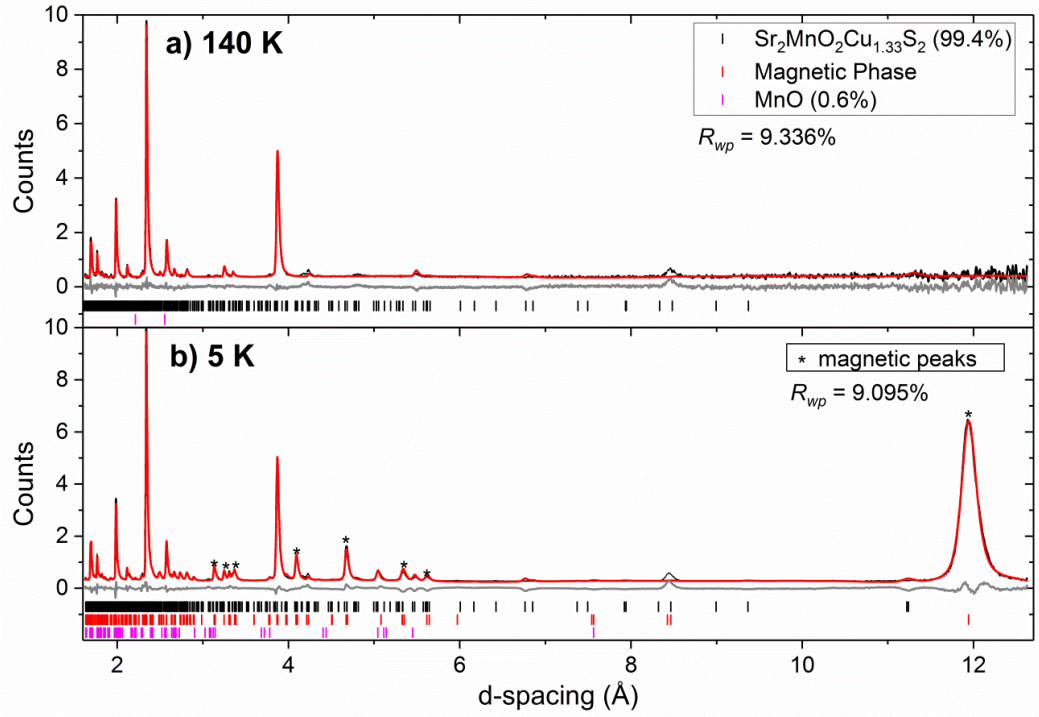


Fig. 3.27 Rietveld plots of the JNB053 (region "C" $Sr_2MnO_2Cu_{1.33}S_2$) measured at a) 140 K and b) 5 K using the 2-9 (58.3°) bank of WISH. The nuclear phase has been modelled using a × 8 approximant of the incommensurately modulated structure. The peak at 8.46 Å is indexed as the 002 peak using the × 8 approximant, but the intensity is poorly modelled

Unlike in the case of parent $Sr_2MnO_2Cu_{1.5}S_2$, it was found that all the magnetic peaks were of similar broadness to one another (anisotropic broadening terms were not required) and to the nuclear phase. It was therefore concluded that the region "*C*" magnetic structure is highly ordered in all directions.

Analysis of PND patterns collected as a function of temperature confirmed that the compound orders antiferromagnetically at ~85 K, which is approximately the temperature identified as T_N in the magnetic susceptibility data. No changes in the relative intensity of the magnetic peaks was identified that might have suggested a change in magnetic ordering as a function of temperature. The raw PND patterns and refined ordered moment as a function of temperature are shown in Fig. 3.28.

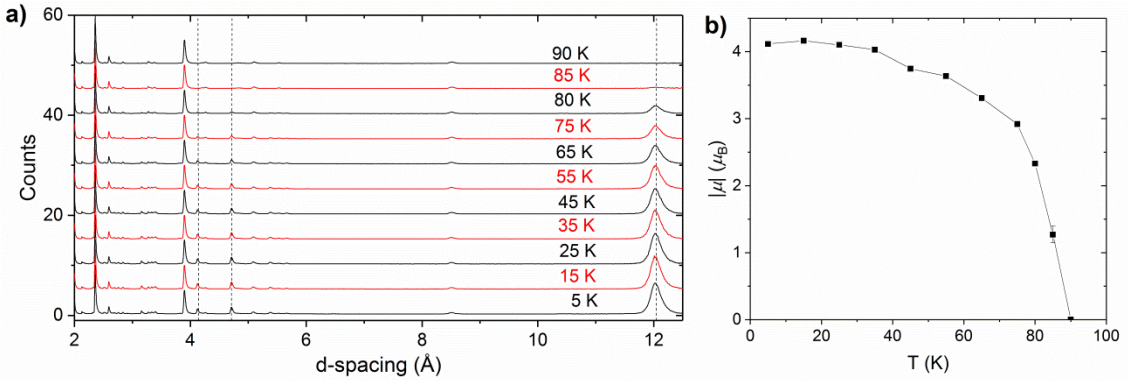


Fig. 3.28 a) Raw PND patterns of JNB053 (Region "C" $Sr_2MnO_2Cu_{1.33}S_2$) measured at various temperatures using the 2-9 (58.3°) bank of WISH, offset for clarity and with dotted lines emphasising the three largest magnetic peaks and b) the refined magnetic moment as a function of temperature, the line is a guide to the eye

3.2.6.3 *Region "B" $Sr_2MnO_2Cu_{1.5-x}S_2$*

The magnetic peaks of the two region "*B*" samples that were measured using PND (JNB054 and JNB311) are highlighted in Fig. 3.29 and compared with the magnetic peaks of the region "*A*" and region "*C*" samples (JNB059 and JNB053 respectively). These peaks were identified as magnetic because they only appear in PND data, not PXRD data and emerged at some temperature below 100 K, well below the temperature associated with ordering of the Cu-vacancies.

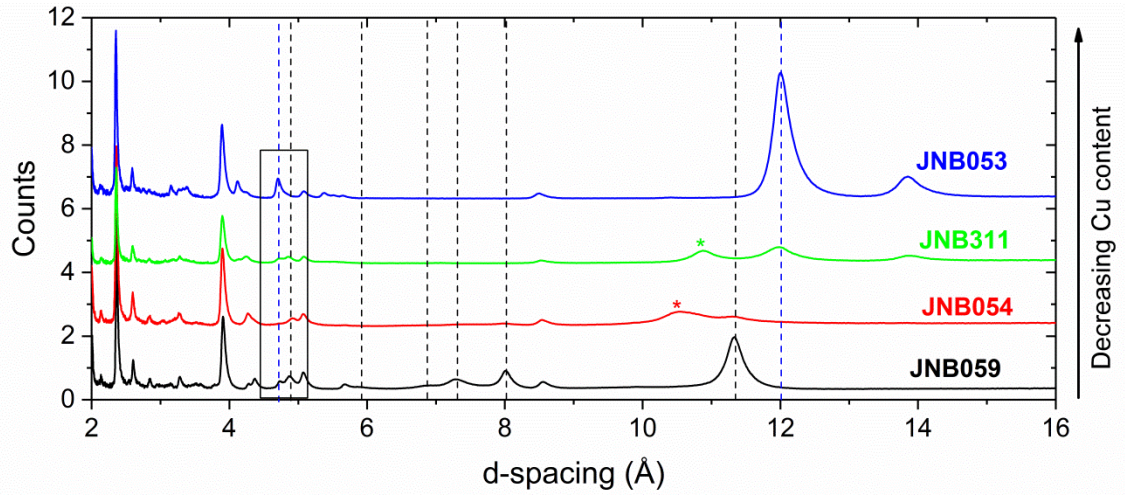


*Fig. 3.29 Offset raw PND patterns of JNB059 (region "A" $Sr_2MnO_2Cu_{1.5}S_2$), JNB054 (region "B" $Sr_2MnO_2Cu_{1.5-x}S_2$), JNB311 (region "B" $Sr_2MnO_2Cu_{1.5-x}S_2$) and JNB053 (region "C" $Sr_2MnO_2Cu_{1.33}S_2$), black dotted lines emphasise the region "A" magnetic peaks, blue dotted lines emphasise the region "C" magnetic peaks, while * symbols emphasise the unindexed magnetic peaks associated with region "B". The box highlights the region shown in Fig. 3.30. All samples were measured at 5 K using the 1-10 (27.1°) bank of WISH*

Fig. 3.29 shows that the PND pattern of JNB054 has magnetic peaks that correspond to the region "*A*" magnetic structure and one, or possibly two, broad peaks that correspond to a new, as yet unsolved, magnetic structure. JNB311, on the other hand, contains magnetic peaks associated with region "*C*" and an unsolved magnetic structure. These observations match the VT PXRD data for the two samples (see section 3.2.4).

The magnetic peaks of JNB054 and JNB311 that are believed to belong to an unsolved region "*B*" magnetic ordering scheme (or schemes) appear at slightly different *d*-spacings to one another, which might be evidence that this magnetic ordering scheme is incommensurate and varies as a function of Mn oxidation state within region "*B*". There is also some evidence for an additional magnetic peak associated with this magnetic phase at $d \sim 5$ Å, but resolution of this is hampered by the presence of magnetic peaks associated with region "*A*" and "*C*" in the same *d*-range, as is shown in the 3-8 (90°) bank data in Fig. 3.30.

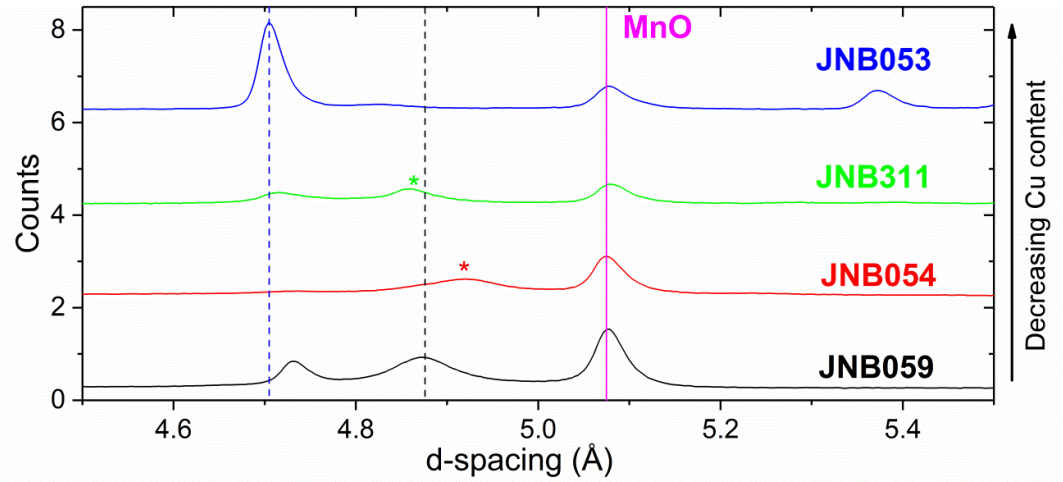


*Fig. 3.30 Offset raw PND patterns of JNB059 (region "A" $Sr_2MnO_2Cu_{1.5}S_2$), JNB054 (region "B" $Sr_2MnO_2Cu_{1.5-x}S_2$), JNB311 (region "B" $Sr_2MnO_2Cu_{1.5-x}S_2$) and JNB053 (region "C" $Sr_2MnO_2Cu_{1.33}S_2$) measured at 5 K using the 3-8 (90°) bank of WISH, black dotted lines emphasise the region "A" magnetic peaks, blue dotted lines emphasise the region "C" magnetic peaks, while * symbols emphasise the unindexed magnetic peaks associated with region "B"*

Examination of VT PND of JNB054 and JNB311 (Fig. 3.31) show that the magnetic peaks in these samples of intermediate composition that are associated with the region "*A*" and "*C*" behave as shown for the extreme members: JNB059 (parent) and JNB053 (most-oxidised) as a function of temperature. The unindexed magnetic peaks in JNB054 and JNB311 appear to disappear above 40 K and 50 K respectively. The difference in the presumed T_N between JNB054 and JNB311 is further evidence that the region "*B*" magnetic structure varies within region "*B*".

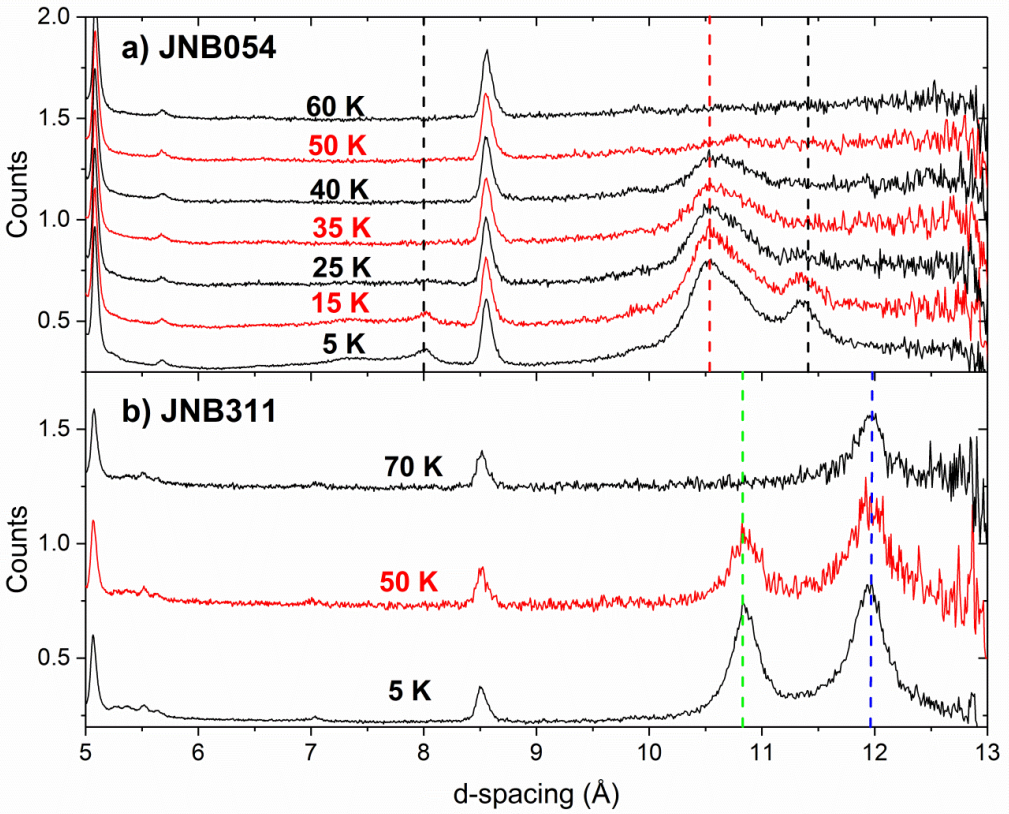


Fig. 3.31 VT PND patterns of JNB054 and JNB311 (both region "B" $Sr_2MnO_2Cu_{1.5-x}S_2$) samples measured using the 2-9 (58.3°) bank of WISH. The black dotted lines emphasise the largest region "A" magnetic peaks, the blue dotted line emphasises the largest region "C" magnetic peaks and the red and green dotted lines emphasise the main unindexed magnetic peaks in JNB054 and JNB311 respectively

Examination of the magnetic ordering behaviour of these region "*B*" samples has revealed the presence of a third magnetic ordering structure at Cu occupancy values intermediate between regions "*A*" and "*C*". It has also been shown that the magnetic ordering of JNB054 and JNB311 occurs at a temperature intermediate between the region "*A*" and "*C*" magnetic ordering temperatures. However, further work, perhaps measuring a greater range of samples, would be required to characterise this behaviour. Understanding the full details of this behaviour may be hampered by the possibility that the magnetic ordering is incommensurate and by the lack of magnetic peaks.

3.3 Synthesis, structure and magnetic behaviour of $Sr_2MnO_2Ag_{1.5}Se_2$

3.3.1 Synthesis

$Sr_2MnO_2Ag_{1.5}Se_2$ was synthesised on the 3 g scale from SrO, Mn, Ag, Se in the ratio 2:1:2:2. These reactants were prepared as described in section 2.1.1 and heated to 700 °C for 21 days, before being cooled to RT. A long heating period was used because Boskovic found that the highest sample purities were achieved when comparatively low temperatures and long reaction times were used.[57] The resulting product was tested for phase-purity by laboratory PXRD. The purity of the sample was significantly less than when the reaction was performed on a 1 g scale, so the sample was reground and reheated at 700 °C for 3 days. PXRD analysis showed this improved the purity of the sample to approximately 93 wt%, with SrSe and Ag as the dominant impurities.

The sample was then purified by stirring 2.5 g of sample in a solution containing I_2 (0.9979 g, 1.0 molar equivalent) and NaI (1.1786 g, 2.0 molar equivalents) dissolved in dry MeCN, in an ice-bath, as described in section 2.1.3. The suspension was left stirring for two days before removing the solution by filtration. 2.0 g of powder was isolated and this appeared phase-pure by laboratory PXRD analysis. I_2 was used to purify the sample because it has been found with similar samples that I_2 removes both SrSe and Ag from the sample. The reasons for the use of NaI are described in section 2.1.3.1. The addition of this purification step also allowed the reactivity of $Sr_2MnO_2Ag_{1.5}Se_2$ with respect to oxidation by I_2 to be assessed.

3.3.2 Structure and composition

3.3.2.1 *Refinement against MAC data*

Synchrotron PXRD data (using the MAC detector at I11) was used to confirm the structure and composition of purified $Sr_2MnO_2Ag_{1.5}Se_2$ (JNB148C). The Rietveld plot from this analysis is shown in Fig. 3.32 and the refined values in Table 3.6 and Table 3.7. The MAC detector was used to collect this data because, as discussed in section 2.3.2.1, this is the highest resolution detector available at the I11 beamline, allowing for the most reliable refinement of parameters, such as site occupancies, which are highly sensitive to changes in peak intensity.

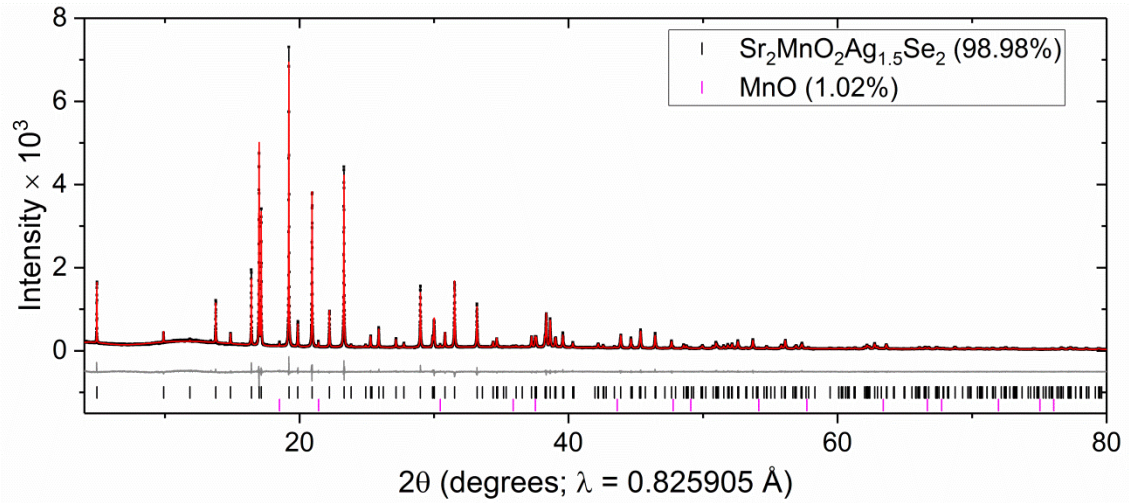


Fig. 3.32 Rietveld refinement against the PXRD pattern of the purified sample of $Sr_2MnO_2Ag_{1.5}Se_2$ (JNB148C), measured at RT using the MAC detector on the I11 beamline

Table 3.6 Refined parameters from Rietveld refinement against the PXRD pattern of the purified sample of $Sr_2MnO_2Ag_{1.5}Se_2$ (JNB148C), measured at RT using the MAC detector on the I11 beamline

Parameter	Value
Diffractometer	MAC (I11 beamline)
Wavelength (Å)	0.825905
R_{wp} (%)	5.892
χ^2	0.905
Crystal system	Tetragonal
Space group	*I*4/*mmm*
Formula weight (g mol^{-1})	585.46
Z	2
a (Å)	4.08798(1)
c (Å)	19.13391(9)
V (Å^3)	319.758(3)
Calculated density (g cm^{-3})	6.082(2)
Purity by mass (%)	98.98

Table 3.7 Atomic parameters derived from Rietveld refinement against the PXRD pattern of the purified sample of $Sr_2MnO_2Ag_{1.5}Se_2$ (JNB148C), measured at RT using the MAC detector on the I11 beamline

Atom	Site	*x*	*y*	*z*	Occupancy	U_{11}(Å^2)	U_{22}(Å^2)	U_{33} (Å^2)
Sr	4*e*	0	0	0.41081(3)	1	0.0077(2)	=U_{11}	0.0086(4)
Mn	2*a*	0	0	0	1	0.0059(4)	=U_{11}	0.0140(7)
O	4*c*	0	½	0	1	0.007(2)	0.010(2)	0.018(2)
Ag	4*d*	0	½	¼	0.7669(9)	0.0409(4)	=U_{11}	0.0150(5)
Se	4*e*	0	0	0.15497(3)	1	0.0085(2)	=U_{11}	0.0123(4)

The Rietveld refinement against this data shows that $Sr_2MnO_2Ag_{1.5}Se_2$ adopts the tetragonal *I*4/*mmm* structure, without any distortions or any RT ordering of vacancies. The site occupancy of the Ag site is refined to 0.7669(9), which corresponds to a

compound composition of $Sr_2MnO_2Ag_{1.534(2)}Se_2$. Refinement against PND data from WISH (discussed in section 3.3.4) produces a refined Ag site occupancy of 0.750(4). A composition of $Sr_2MnO_2Ag_{1.52(2)}Se_2$ may be deduced to reflect the realistic uncertainty on the refined composition from PXRD and PND measurements. Since this non-stoichiometric Ag occupancy is produced from a synthesis in which a stoichiometric amount of Ag was used (i.e. Sr:Ag ratio of 1:1), it may be assumed that the ~0.5 defect in the Ag occupancy is intrinsic to this compound.

Selected structural parameters are compared for $Sr_2MnO_2Cu_{1.5}S_2$, $Sr_2MnO_2Cu_{1.5}Se_2$ and $Sr_2MnO_2Ag_{1.5}Se_2$ in Table 3.8. As the sizes of the coinage metal and chalcogenide ions increase, the *c*/*a* ratio increases dramatically. This is due to a relatively small increase in *a* (which is equal to twice the Mn–O bond length), so consequently lattice parameter *c* increases disproportionately and expands by ~1.25 Å (~7%) as Cu^+ in $Sr_2MnO_2Cu_{1.5}Se_2$ is replaced by Ag^+ in $Sr_2MnO_2Ag_{1.5}Se_2$. This leads to a large distortion of the $AgSe_4$ tetrahedron in $Sr_2MnO_2Ag_{1.5}Se_2$ compared with the almost regular $CuSe_4$ tetrahedron in $Sr_2MnO_2Cu_{1.5}Se_2$.

Table 3.8 Comparison of selected structural parameters for $Sr_2MnO_2Cu_{1.5}S_2$ (synchrotron PXRD data, this thesis), $Sr_2MnO_2Cu_{1.5}Se_2$ (PND data, obtained from ref. 107), $Sr_2MnO_2Ag_{1.5}Se_2$ (synchrotron PXRD data, this thesis)

Compound	$Sr_2MnO_2Cu_{1.5}S_2$	$Sr_2MnO_2Cu_{1.5}Se_2$	$Sr_2MnO_2Ag_{1.5}Se_2$
a (Å)	4.01417(1)	4.06655(3)	4.08798(1)
c (Å)	17.19202(6)	17.8830(1)	19.13391(9)
c/*a* ratio	4.28282(2)	4.39759(4)	4.68053(3)
V (Å³)	277.026(2)	295.729(5)	319.759(3)
X occupancy	0.7733(9)	0.773(2)	0.770(3)
Mn–O distance (Å) [4]#	2.00709(1)	2.03328(1)	2.04399(1)
Mn–*Ch* distance (Å) [2]#	2.9172(7)	3.0002(3)	2.9652(5)
Mn–*Ch*/Mn-O ratio	1.4535(3)	1.4779(5)	1.4507(5)
X–*Ch* distance (Å) [4]#	2.4362(4)	2.5094(2)	2.7357(3)
Ch–*X*–*Ch* angle, *α** (°) [2]#	110.95(3)	108.25(5)	96.69(2)
Ch–*X*–*Ch* angle, *β** (°) [4]#	108.738(14)	110.09(5)	116.215(9)

*see Fig. 3.33 for definition of angle; #multiplicity in square brackets

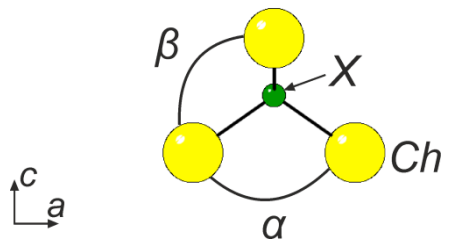


Fig. 3.33 Definition of the α and β tetrahedral angles

3.3.2.2 *Comparison of the compound before and after purification*

Synchrotron PXRD data (using the PSD on the I11 beamline) was used to compare the lattice parameters of $Sr_2MnO_2Ag_{1.5}Se_2$ before and after the I_2 purification step to check for any changes in the lattice parameters, which might indicate that the compound had reacted directly with I_2. The lattice parameters are compared in Table 3.9, the data is compared with the data reported by Jin *et al.*, who reported the structure of $Sr_2MnO_2Ag_{1.5}Se_2$ prior to this work.[60] The Rietveld plots are shown in Fig. 3.34.

Table 3.9 Refined parameters from Rietveld refinement against PXRD data of the $Sr_2MnO_2Ag_{1.5}Se_2$ samples before (JNB148B) and after (JNB148C) purification and comparison with data published by Jin et al.[60]

Sample	Before purification	After purification	Jin *et al.*[60]
Sample code	JNB148B	JNB148C	-
Diffractometer	PSD (I11 beamline)	PSD (I11 beamline)	Laboratory (Cu Kα)
Wavelength (Å)	0.826222	0.825953	1.5418
Purity by mass (%)	92	~99	90
Space group	*I*4/*mmm*	*I*4/*mmm*	*I*4/*mmm*
a (Å)	4.08973(2)	4.08771(1)	4.0882(1)
c (Å)	19.14709(9)	19.13087(8)	19.1179(2)
Volume (Å^3)	320.252(3)	319.664(3)	319.525(5)
Ag occupancy	0.7852(7)	0.7733(6)	0.720(2)
R_{wp} (%)	1.183	0.854	4.57

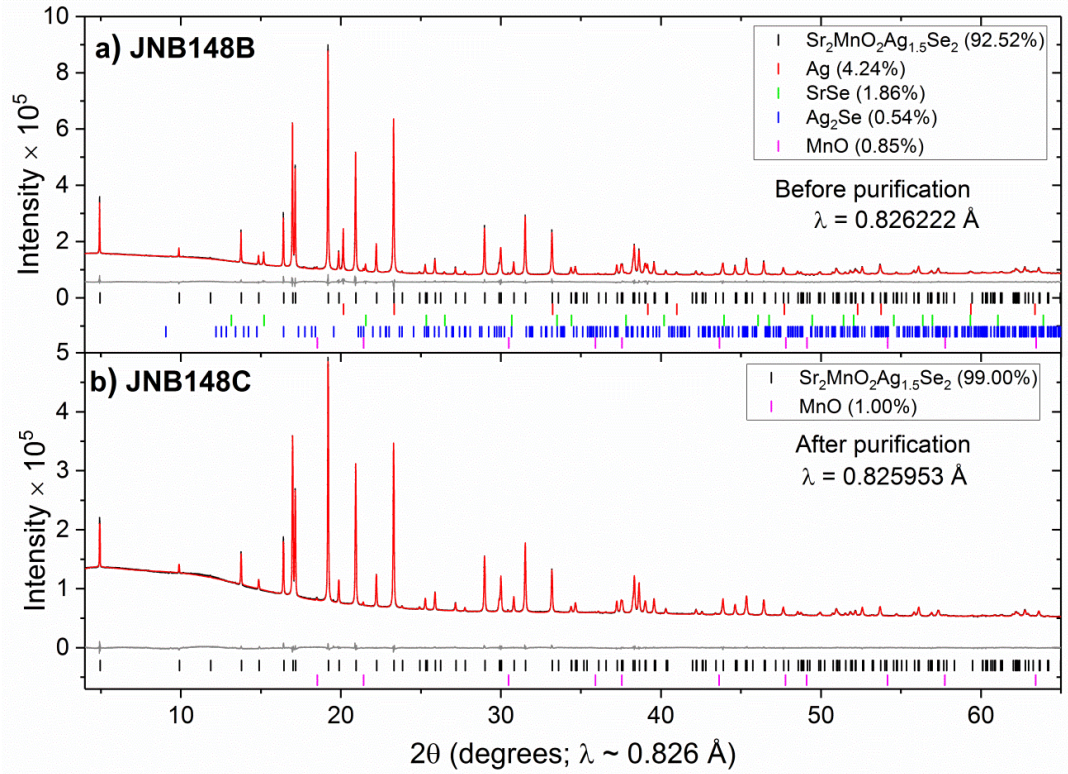


Fig. 3.34 Rietveld plot of the sample of $Sr_2MnO_2Ag_{1.5}Se_2$ a) before purification (JNB148B) and b) after purification (JNB148C), both were measured at RT using the PSD on the I11 beamline

Table 3.9 shows that the I_2 purification step reduces the unit cell volume by 0.588(6) $Å^3$ (0.18%), this is significantly larger than the difference in cell volume obtained in two separate measurements on the purified sample measured using the different detectors on I11 (compare Table 3.6 and Table 3.9; there is ~0.1 $Å^3$ (~0.03 %) apparent difference between the volumes measured using the Mythen PSD and the MAC detector for the purified sample), so may be judged to be the result of a real reduction in Ag occupancy which occurs during the reaction with I_2. In the $Sr_2MnO_2Cu_{1.5}S_2$ system described above, deintercalation of 11% of the Cu from $Sr_2MnO_2Cu_{1.5}S_2$ results in a 1.6% reduction in cell volume.[110] Extrapolating this trend to $Sr_2MnO_2Ag_{1.5}Se_2$ allows it to be estimated that only ~1% of the Ag in $Sr_2MnO_2Ag_{1.5}Se_2$ has been deintercalated in the I_2 purification step, and this is not contradicted by independent refinement of the Ag site occupancy before and after purification. It is noted that the cell volume after the purification step is marginally larger than that reported by Jin *et al.*, but the samples were not all measured on the same diffractometer, so further analysis of the differences in lattice parameters between samples cannot be made. It is concluded that a small reduction in Ag occupancy of about 1% is accessible using the purification with I_2/MeCN, but it cannot be ruled out that a similar variation in Ag occupancies is also accessible using a purely solid-state synthetic route, such as different heating conditions.

3.3.3 Magnetometry

Magnetic susceptibility measurements were performed on the sample before and after purification to assess whether the purification step caused a significant change in magnetic behaviour. The magnetic susceptibility measurements (Fig. 3.35) show that the sample is paramagnetic above 63(1) K, where an antiferromagnetic transition occurs.

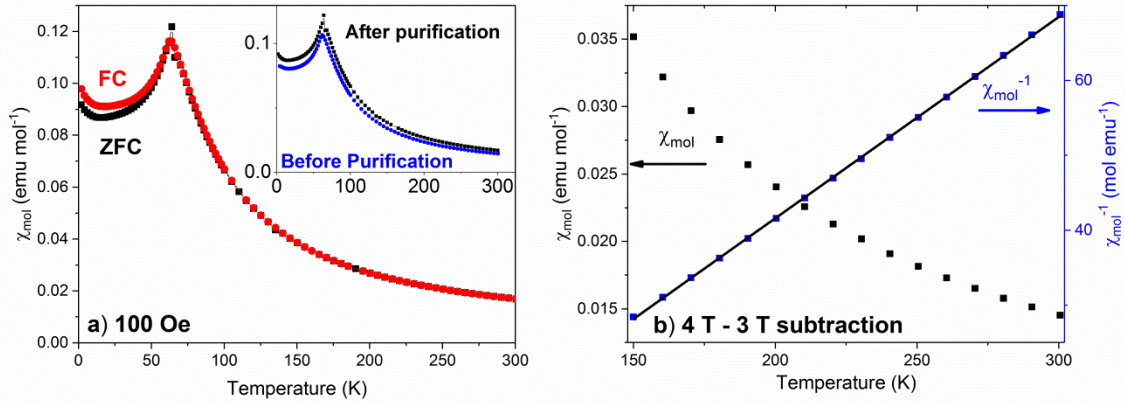


Fig. 3.35 a) The ZFC and FC magnetic susceptibility of the purified $Sr_2MnO_2Ag_{1.5}Se_2$ sample (JNB148C), using a measuring field of 100 Oe. The inset compares the ZFC magnetic susceptibility of $Sr_2MnO_2Ag_{1.5}Se_2$ before and after purification. b) The magnetic susceptibility of JNB148C obtained using a 4 – 3 T subtraction (as described in section 2.8) and the inverse magnetic susceptibility with line of best fit, from which the effective magnetic moment and Weiss temperature were derived.

Table 3.10 compares magnetometry data from $Sr_2MnO_2Ag_{1.5}Se_2$ before purification (JNB148B), after purification (JNB148C) with data from Jin *et al.*[12] The Weiss temperature (θ) and effective magnetic moment (μ_{eff}) were derived from the linear 150 – 300 K region of the inverse susceptibility (see Fig. 3.35 b)).

Table 3.10 Comparison of magnetometry data obtained from $Sr_2MnO_2Ag_{1.5}Se_2$ before purification (JNB148B), after purification (JNB148C) and the sample of $Sr_2MnO_2Ag_{1.5}Se_2$ described by Jin et al.[60]

Sample	Before purification (JNB148B)	After purification (JNB148C)	Jin *et al.*
Néel temperature, T_N (K)	63(1)	63(1)	67
Weiss temperature, θ (K)	+41(2)	+45(5)	+46.8
Effective moment, μ_{eff} (μ_B)	5.47(1)	5.45(1)	5.82(1)

The data show that T_N, the Weiss temperature and μ_{eff} are similar within the experimental uncertainty before and after purification. The calculated μ_{eff} is in between the values expected from the spin-only formula for high-spin octahedral Mn^{2+} (5.92 μ_B) and Mn^{3+} (4.90 μ_B), this reflects that Mn in the compound has an oxidation state between +2 and +3. Similar values of the effective moment were found for $Sr_2MnO_2Cu_{1.5}S_2$ (5.45(3) μ_B)[5] and $Sr_2MnO_2Cu_{1.5}Se_2$ (5.63(3) μ_B),[6] which are both closely related analogues of $Sr_2MnO_2Ag_{1.5}Se_2$.

The 100 Oe susceptibility data (Fig. 3.35 a)) reveal a slight divergence of ZFC and FC data below T_N, similar to that observed in parent $Sr_2MnO_2Cu_{1.5}S_2$ (see section 3.2.5).[2] The magnetisation isotherm (Fig. 3.36 a)), measured at 5 K, is slightly offset from the

origin. These observations suggest a small glassy element to the magnetism arising from some disorder and frustration of the magnetic interactions. It is possible that this arises from a slight inhomogeneity in the distribution of Mn^{2+} and Mn^{3+} ions, which itself may arise from the disorder in the distribution of Ag^{+} ions and Ag-site vacancies in the compound. The magnetisation isotherm at 5 K (Fig. 3.36 a)) also shows a slight upwards curvature in the magnetisation at high fields that is not evident in measurements of magnetisation against applied field above T_N (Fig. 3.36 b)); this suggests that the compound is metamagnetic, but that the field-induced antiferromagnetic-to-ferromagnetic transition would occur at much higher fields than 5 T. Metamagnetic behaviour has been observed in the series $Sr_2MnO_2Cu_{2m-x}S_{m+1}$, ($m$ = 2, 3),[5] which have a larger separation between MnO_2 layers. In those compounds the magnetic moments in the MnO_2 layers are coupled ferromagnetically, and the layers are coupled antiferromagnetically in low applied fields. The applied field required to drive the systems into the ferromagnetic state decreases as the separation of the layers increases.[5]

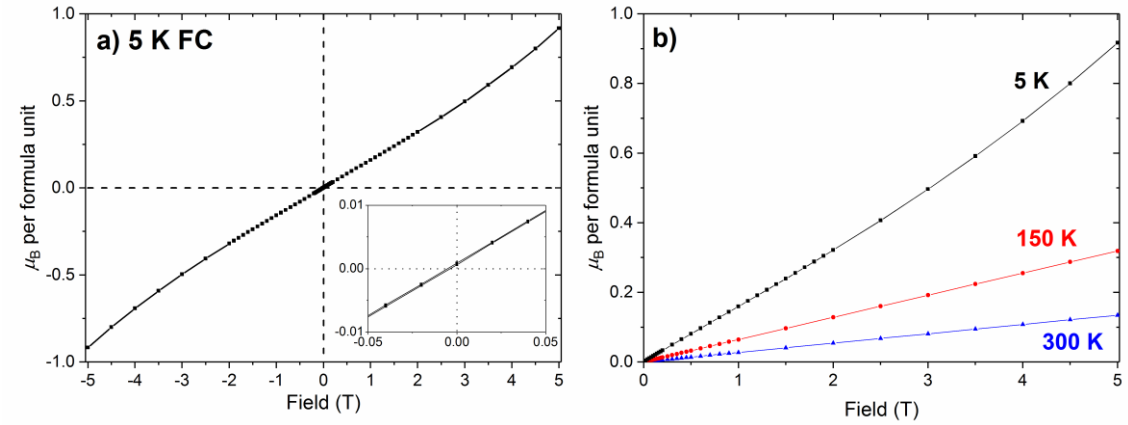


Fig. 3.36 a) M vs H isotherm of the purified sample of $Sr_2MnO_2Ag_{1.5}Se_2$ (JNB148C), measured at 5 K in the range -5 ≤ H (T) ≤ +5. The inset shows the slight offset from the origin. b) Comparison of magnetisation isotherms of $Sr_2MnO_2Ag_{1.5}Se_2$ (JNB148C) at 5, 150 and 300 K, measured in the range 0 ≤ H (T) ≤ 5

3.3.4 Powder neutron diffraction

Simultaneous refinements against four banks (2-9, 3-8, 4-7 and 5-6) of WISH data at 125 K (Fig. 3.37 a)) are in agreement with the structural model derived from PXRD analysis. No additional peaks from long-range ordering of Ag-vacancies were apparent. The reflection at d = 5.07 Å is indexed as the dominant magnetic reflection of MnO (< 1 wt%).[115] At 1.7 K additional reflections (see Fig. 3.37 b)) were evident, which diminished in intensity on warming and vanished above T_N (see Fig. 3.38), these were

therefore identified as magnetic peaks. These reflections were indexed on the nuclear unit cell, but with a breaking of symmetry from *I*4/*mmm*. ISODISTORT[112] was used to search for magnetic symmetry modes that could fit the intensity of these peaks, initially in magnetic space group *P*1 (1.1). It was found that all the magnetic intensity could be fitted using a single magnetic mode: $mM3^+(a)$ on the Mn sites. This magnetic mode corresponds to *A*-type antiferromagnetic order, in which the spins are aligned parallel in the *c*-direction within the MnO_2 planes, but anti-parallel in adjacent MnO_2 planes (see Fig. 3.37 inset). The highest-symmetry magnetic space group found that allowed for the refinement of $mM3^+(a)$ was P_I4/mnc (128.410).[116] This model gave a good fit to the data, as shown by the Rietveld fit in Fig. 3.37 (R_{wp} = 3.674%) and gives a refined ordered magnetic moment of 3.99(2) μ_B.

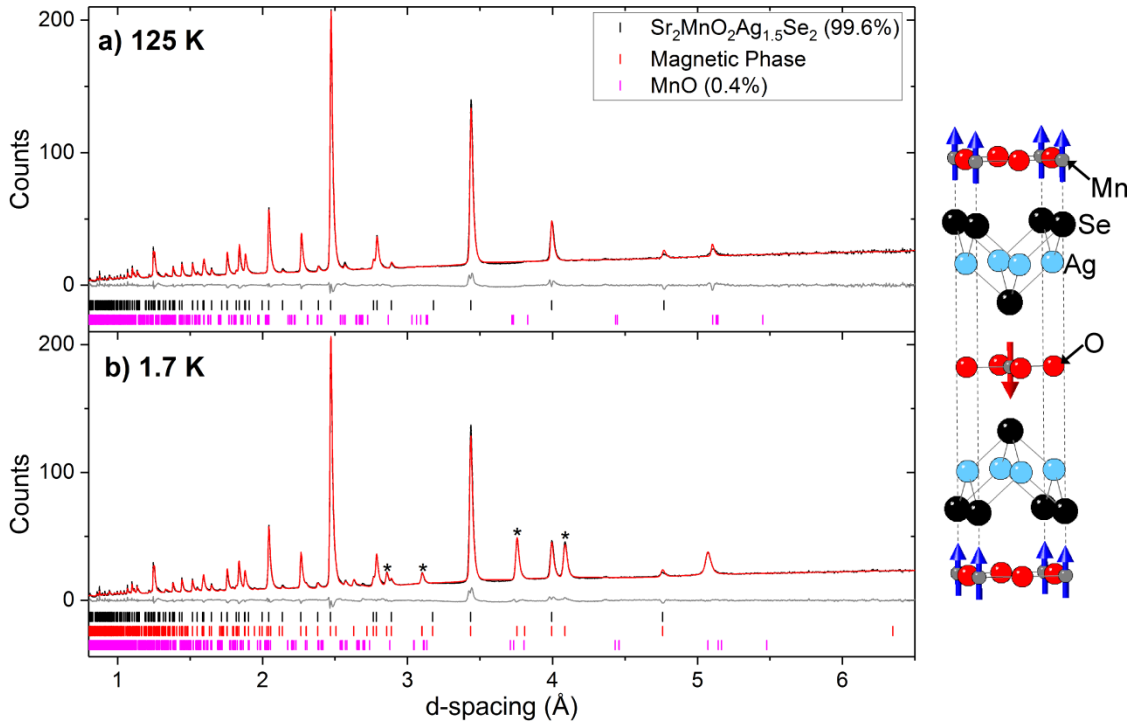


*Fig. 3.37 Rietveld plot of $Sr_2MnO_2Ag_{1.5}Se_2$ (JNB148C) measured at (a) 125 K and (b) 1.7 K on the 3-8 (90°) bank of WISH. The * symbols highlight the four main additional peaks arising from the magnetic structure. The inset shows the magnetic structure, Sr atoms have been omitted for clarity.*

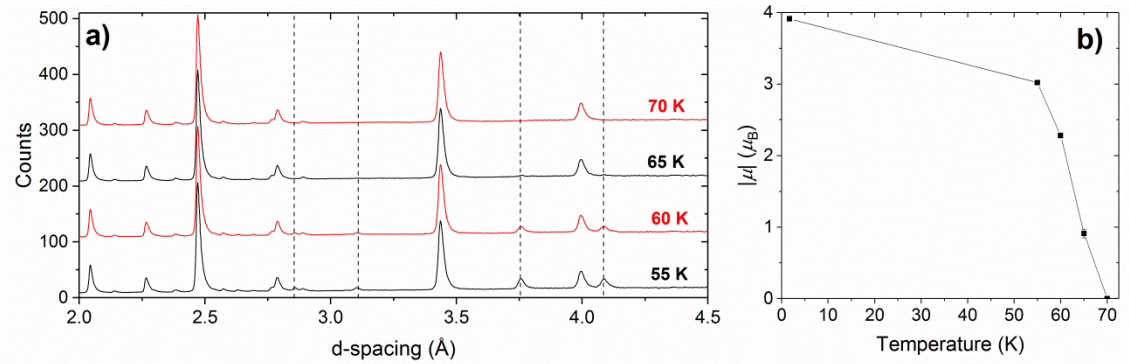


Fig. 3.38 a) PND patterns of $Sr_2MnO_2Ag_{1.5}Se_2$ (JNB148C) at 55 – 70 K, measured on the 3-8 bank (90°) of WISH. Dashed lines highlight the magnetic peaks, which disappear above 65 K. Successive diffractograms have been offset by 100 counts along the vertical axis for clarity and b) the ordered magnetic moment of JNB148C as a function of temperature obtained from PND measurements. The line is a guide to the eye

3.3.5 Discussion of magnetic behaviour

The magnetic structure adopted by $Sr_2MnO_2Ag_{1.5}Se_2$ is similar to that found for $Sr_2MnO_2Cu_{1.5}Se_2$[107] and the related sulfides $Sr_2MnO_2Cu_{3.5}S_3$ and $Sr_2MnO_2Cu_{5.5}S_4$.[5] The ordered magnetic moment of $Sr_2MnO_2Cu_{1.5}Se_2$ at base temperature is 4.1(1) μ_B;[107] it is therefore similar, within the experimental uncertainty, to that of $Sr_2MnO_2Ag_{1.5}Se_2$ (3.99(2) μ_B). These two compounds are isostructural, with similar refined coinage metal occupancies, indicative of similar Mn oxidation states (~+2.5). The Mn–O distances differ only by 0.01 Å (0.5%), indicating a similar degree of covalency in the compounds. These factors explain the similar ordered magnetic moments for the two phases. However, the T_N is ~10 K lower in $Sr_2MnO_2Cu_{1.5}Se_2$ (53 K) than in $Sr_2MnO_2Ag_{1.5}Se_2$ (63(1) K). Although lattice parameter *c* is significantly larger in $Sr_2MnO_2Ag_{1.5}Se_2$, due to the larger size of the coinage metal ion, the Mn–Se distance in $Sr_2MnO_2Ag_{1.5}Se_2$ is 0.04 Å (1.34%) shorter than in $Sr_2MnO_2Cu_{1.5}Se_2$; this, and the different shape of the coinage metal tetrahedron (see Table 3.8) may be the factors that lead to slightly stronger inter-plane exchange constants in $Sr_2MnO_2Ag_{1.5}Se_2$ than in $Sr_2MnO_2Cu_{1.5}Se_2$. The use of neutron spectroscopy to measure the inter-plane constants directly would enable this difference to be investigated in greater detail.

3.4 Synthesis, structure and magnetic behaviour of $Sr_2MnO_2Cu_{1.8}Te_2$

3.4.1 Synthesis and composition

The stoichiometric compound $Ba_2MnO_2Cu_2Te_2$ has previously been synthesised by heating a mixture of BaO, Mn, Cu and Te to 750 °C.[109] This synthesis route was used as the starting point for the synthesis of a compound of composition "$Sr_2MnO_2Cu_2Te_2$": SrO, Mn, Cu and Te were mixed in the ratio 2:1:2:2 and prepared using the solid-state synthesis route described in section 2.1.1, the sample was then heated to 750 °C at a rate of 5 °C min^{-1} for 72 h before quenching in ice-water. It was found that regrinding and reheating the product improved the purity of the sample, until a ~96 wt% pure sample was produced. This sample (JNB303B) was synthesised on a 4 g scale.

Attempts to make $Sr_2MnO_2Ag_2Te_2$ using this synthesis route failed.

Although "$Sr_2MnO_2Cu_2Te_2$" was synthesised assuming full occupation of the Cu site, it was considered likely that the compound was Cu deficient in a similar way to the S and Se analogues. High resolution synchrotron PXRD, using the MAC detector on the I11 beamline, was used to probe compound composition. Rietveld refinement against this data showed that the compound with nominal composition "$Sr_2MnO_2Cu_2Te_2$" was Cu deficient with refined composition $Sr_2MnO_2Cu_{1.798(4)}Te_2$. The Rietveld plot is shown in Fig. 3.39 and refined parameters are shown in Table 3.11 and Table 3.12. The high crystallinity of these compounds allowed high quality data to be collected at high angle, so it was judged that PXRD data was sufficient for a reasonable estimation of Cu occupancy. Unfortunately, some peaks proved difficult to index, despite a thorough database search. The two largest unindexed peaks are shown in the inset in Fig. 3.39. These peaks are thought to belong to a ~2 wt% impurity (wt% estimated by comparison of the intensity of these peaks with the intensity of the indexed Cu impurity peaks).

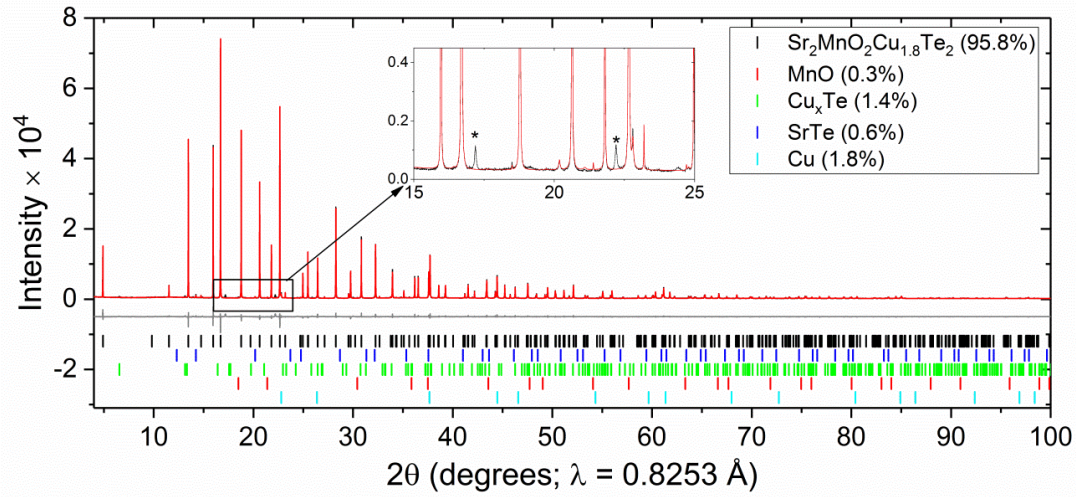


Fig. 3.39 Rietveld plot of $Sr_2MnO_2Cu_2Te_2$ (JNB303B), the synchrotron PXRD data was collected at RT using the MAC detector on the I11 beamline. The inset emphasises the two major unindexed peaks, assumed to be a ~2 wt% impurity

Table 3.11 Refined parameters from Rietveld refinement against synchrotron PXRD data for $Sr_2MnO_2Cu_{1.8}Te_2$ (JNB303B), measured at RT using the MAC detector on the I11 beamline

Parameter	Value
Diffractometer	MAC (I11)
Radiation	X-ray, λ = 0.853 Å
R_{wp} (%)	8.252
χ^2	2.478
Crystal system	Tetragonal
Space group	*I*4/*mmm*
Formula weight (g mol^{-1})	631.77
Z	2
a (Å)	4.200943(8)
c (Å)	19.28304(5)
Volume (Å^3)	340.306(2)
Calculated density (g cm^{-3})	6.164(2)
Purity by mass (%)	~95%

Table 3.12 Atomic parameters derived from Rietveld refinement against synchrotron PXRD data for $Sr_2MnO_2Cu_{1.8}Te_2$ (JNB303B), measured at RT using the MAC detector on the I11 beamline

Atom	Site	*x*	*y*	*z*	Occupancy	U_{11} (Å^2)	U_{22} (Å^2)	U_{33} (Å^2)
Sr	4*e*	0	0	0.41501(3)	1	0.0054(2)	$=U_{11}$	0.0080(3)
Mn	2*a*	0	0	0	1	0.0031(3)	$=U_{11}$	0.0150(7)
O	4*c*	0	½	0	1	0.006(2)	0.017(2)	0.014(3)
Cu	4*d*	0	½	¼	0.899(2)	0.0171(3)	$=U_{11}$	0.0158(6)
Te	4*e*	0	0	0.16659(2)	1	0.0066(1)	$=U_{11}$	0.0074(2)

The refined composition $Sr_2MnO_2Cu_{1.798(4)}Te_2$ suggests that the average oxidation of the Mn ions is +2.20, which is significantly smaller than the +2.5 oxidation found for

$Sr_2MnO_2Cu_{1.5}S_2$ (result of high-temperature synthesis) and $Sr_2MnO_2Cu_{1.5}Se_2$. Selected parameters of these compounds are compared in Table 3.13.

Table 3.13 Comparison of selected parameters of $Sr_2MnO_2Cu_{1.5}S_2$ (data from synchrotron PXRD, this thesis), $Sr_2MnO_2Cu_{1.5}Se_2$ (data from PND, obtained from ref. 107) and $Sr_2MnO_2Cu_{1.8}Te_2$ (data from synchrotron PXRD, this thesis)

Compound	$Sr_2MnO_2Cu_{1.5}S_2$	$Sr_2MnO_2Cu_{1.5}Se_2$	$Sr_2MnO_2Cu_{1.8}Te_2$
a (Å)	4.01417(1)	4.06655(3)	4.200943(8)
c (Å)	17.19202(6)	17.8830(1)	19.28304(5)
c/a	4.28282(2)	4.39759(4)	4.59017(1)
Volume (Å^3)	277.026(2)	295.729(5)	340.306(2)
Cu occupancy	0.7733(9)	0.773(2)	0.899(2)
Mn-O (Å)	2.00709(1)	2.03328(1)	2.10047(4)
Mn-*Ch* (Å)	2.9172(7)	3.0002(3)	3.2124(4)
Mn-*Ch*/Mn-O	1.4535(3)	1.4779(5)	1.5294(2)
Cu-*Ch* (Å)	2.4362(4)	2.5094(2)	2.6455(2)
Ch-Cu-*Ch*, α* (°) [2]$^{\#}$	110.95(3)	108.25(5)	105.12(1)
Ch-Cu-*Ch*, β* (°) [4]$^{\#}$	108.738(14)	110.09(5)	111.692(7)

*see Fig. 3.33 for definition of angle; $^{\#}$multiplicity in square brackets

The data in Table 3.13 shows that substituting Te for Se in $Sr_2MnO_2Cu_xCh_2$ causes a significantly larger increase in both *a* and *c* than the substitution of Se for S. This may be rationalised by considering that S (radius 1.7 Å) and Se (radius 1.84 Å) are a closer size match than Te (radius 2.07 Å).[117] As *a* is significantly larger in $Sr_2MnO_2Cu_{1.8}Te_2$, the Mn-O distance increases; it is likely that this is a significant factor in the reduction of the average Mn ion oxidation state from $Mn^{2.5+}$ in the sulfide and selenide analogues to $Mn^{2.2+}$ in the telluride. The increase in the *c/a* as the size of the chalcogenide ion increases causes the *Ch*-Cu-*Ch* bond angles to deviate from the ideal tetrahedral angle (109.5°), but the effect is much less significant than was observed in $Sr_2MnO_2Ag_{1.5}Se_2$ (see section 3.3).

3.4.2 Magnetometry

The magnetic susceptibility measurements of $Sr_2MnO_2Cu_{1.8}Te_2$ (JNB303B) show that the ZFC and FC curves diverge below ~41 K (see Fig. 3.40 a)), with behaviour akin to that of a spin-glass-freezing temperature (T_g). There is also a broad hump superimposed onto the otherwise paramagnetic-like curve at ~70 K. The three field-cooled magnetisation isotherms (measured at 5, 50 and 150 K) show that the feature at 70 K causes a large increase in the magnetic moment. The isotherms measured at 5 K and 50 K appear to be very similar to one another, but a larger degree of hysteresis is observed in the 5 K isotherm.

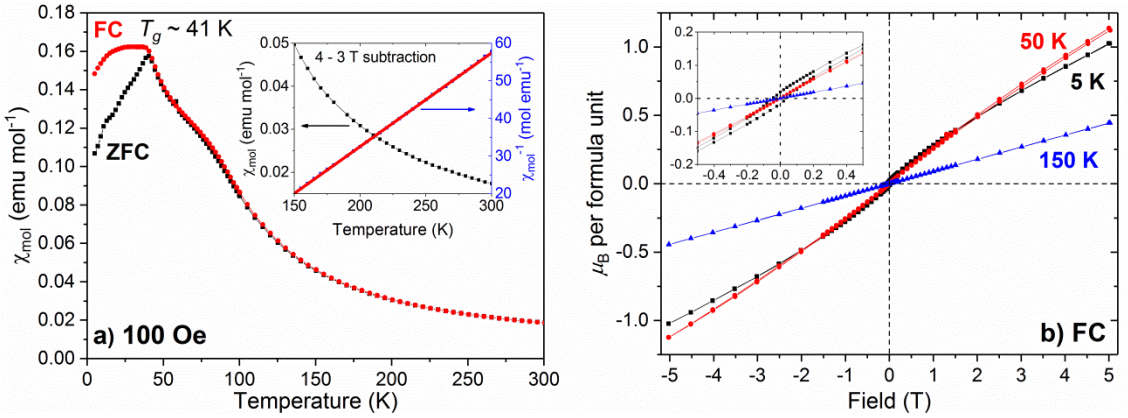


Fig. 3.40 a) ZFC and FC magnetic susceptibility curves of $Sr_2MnO_2Cu_{1.8}Te_2$ (JNB303B), measured at a field of 100 Oe and inset FC χ_{mol}, measured using a 4 – 3 T subtraction (as described in section 2.8), with corresponding inverse magnetic susceptibility, from which the effective magnetic moment and Weiss temperature were calculated. b) M vs H isotherms of $Sr_2MnO_2Cu_{1.8}Te_2$ (JNB303B), measured at 5, 50 and 150 K. The sample was cooled in a field of 5 T before each measurement and the inset emphasises the low field region

The magnetic susceptibility of $Sr_2MnO_2Cu_{1.8}Te_2$ (JNB303B) was also measured using a 3 T/4 T subtraction. This was done because the results of Curie-Weiss analysis on the low-field data were initially surprising (the magnitude of the Weiss temperature being significantly larger than 41 K), so a subtraction was used to ensure the effects of any ferromagnetic impurities in the sample were eliminated. The *M vs H* curve of this sample (measured at 300K) was linear between 3 and 4 T and the inverse magnetic susceptibility was linear in the region $150 < T$ (K) < 300, as shown in the inset in Fig. 3.40 a). This indicated that the Weiss temperature and μ_{eff} could be extracted reliably by linear regression (values shown in Table 3.14). The obtained μ_{eff} (5.67(1) μ_B) compares closely to the calculated spin-only magnetic moment of $Mn^{2.2+}$ ($\mu_{spin\text{-}only} = 5.71\ \mu_B$). The obtained Weiss temperature is positive, suggesting net ferromagnetic interactions and has a magnitude (70(1) K) corresponding to the feature at 70 K, not the feature at 41 K. The results of Curie-Weiss analysis from the high-field, subtracted data closely matched the results extracted from the low-field, unsubtracted data, further suggesting the absence of ferromagnetic impurities in the sample.

Table 3.14 Selected magnetic parameters of JNB303B ($Sr_2MnO_2Cu_{1.8}Te_2$), obtained both directly from the low-field ZFC and FC magnetic susceptibility curves and from the linear fit to the inverse high-field FC susceptibility (measured using 4 – 3 T subtraction)

Parameter	Value
T_g (K)	41
Curie Constant	4.016(7)
Weiss Temperature (K)	70(1)
μ_{eff} (μ_B)	5.67(1)

3.4.3 Powder neutron diffraction to probe magnetic ordering

Low-temperature PND was used to probe the magnetic ordering behaviour of $Sr_2MnO_2Cu_{1.8}Te_2$. A 3.29 g sample of $Sr_2MnO_2Cu_{1.8}Te_2$ (JNB303B) was measured using the WISH diffractometer at 1.7 and 100 K. Fig. 3.41 shows that all the peaks in the pattern at 100 K could be indexed by the RT structure of $Sr_2MnO_2Cu_{1.8}Te_2$ and known impurities, with no additional intensity from ordering of the Cu-vacancies. At 1.7 K some small, asymmetric features were observed, the most intense being a peak at d = 5.9 Å. These additional features were assumed to be magnetic in character.

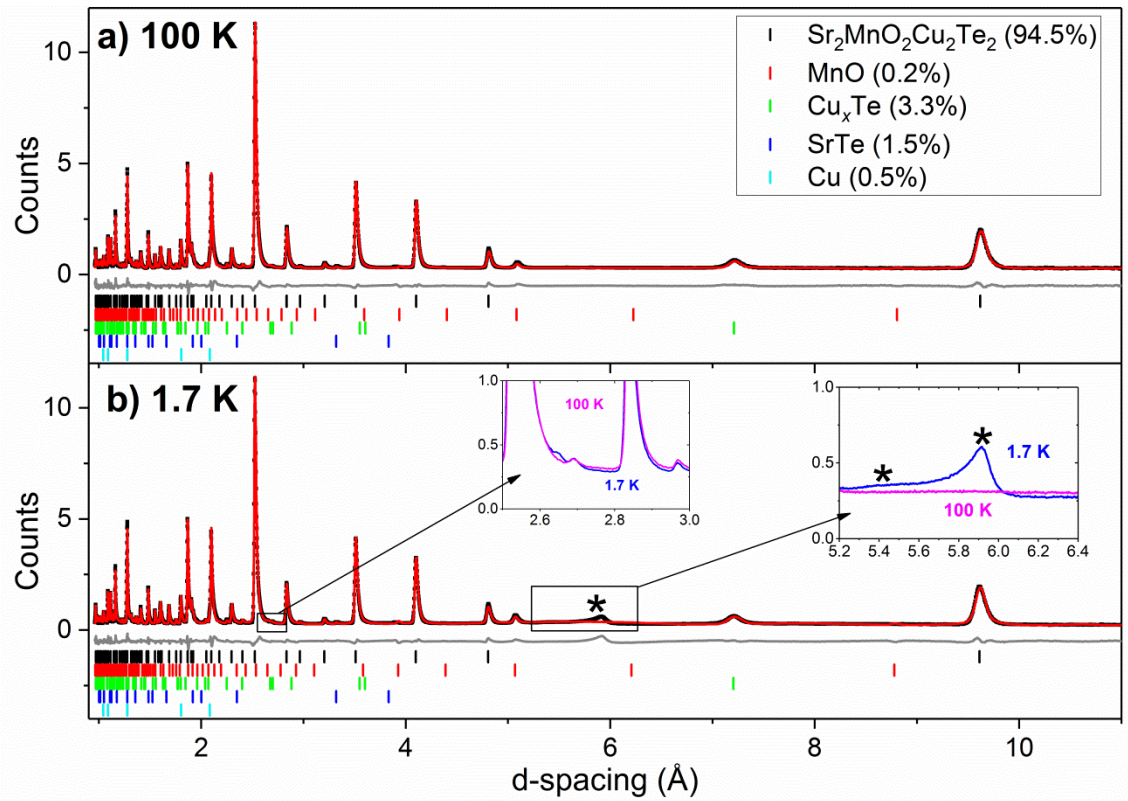


*Fig. 3.41 Rietveld plot of the 2-9 bank (58.3°, WISH) data of $Sr_2MnO_2Cu_{1.8}Te_2$ (JNB303B), when measured at a) 100 K and b) 1.7 K. The * symbols emphasise the peaks that appears on cooling and cannot be indexed using the nuclear model*

This peak was indexed as the 100 peak of a $\sqrt{2}a \times \sqrt{2}a \times c$ expansion of the unit cell. The shape of the peak, with a long "tail" at low *d*-spacing, was identified as similar in character to a Warren-like peak.[118]

The Warren-like peak-shape function was first used to describe the PXRD pattern of two-dimensional carbon black. This sample was extremely ordered in the *ab*-plane, but disordered in the *c*-direction.[118, 119] Since then, this peak-shape has been found to be a good descriptor for the magnetic peaks in a number of compounds including $Sr_2MnO_2Mn_2As_2$,[120] $La_2O_2Fe_2OSe_2$,[114] and $Sr_2F_2Fe_2OS_2$.[121] The development of a Warren-like peak shows that the magnetic ordering is two-dimensional and short-range in nature.

To model the magnetic ordering the data was converted to Q ($2\pi/d$) and the peak fitted using the following function:[118, 121]

$$S(\boldsymbol{Q}) = \frac{1}{2\pi\sigma_{\perp}^{2}} \exp[-\frac{1}{2}\left(\frac{|\boldsymbol{Q}-\tau|_{\perp}}{\sigma_{\perp}}\right)^{2}]\frac{\xi}{\pi}\frac{1}{1+(\xi|\boldsymbol{Q}-\tau|_{\parallel})^{2}} \quad (3.2)$$

where the Gaussian and Lorentzian parts describe the long-range in-plane correlation and short-range correlation along lattice parameter *c* respectively, $\sigma_{\perp}$ represents the in-plane peak width, ξ is the correlation-length and τ is the position of the centre of the peak. The result of this fitting is shown in Fig. 3.42.

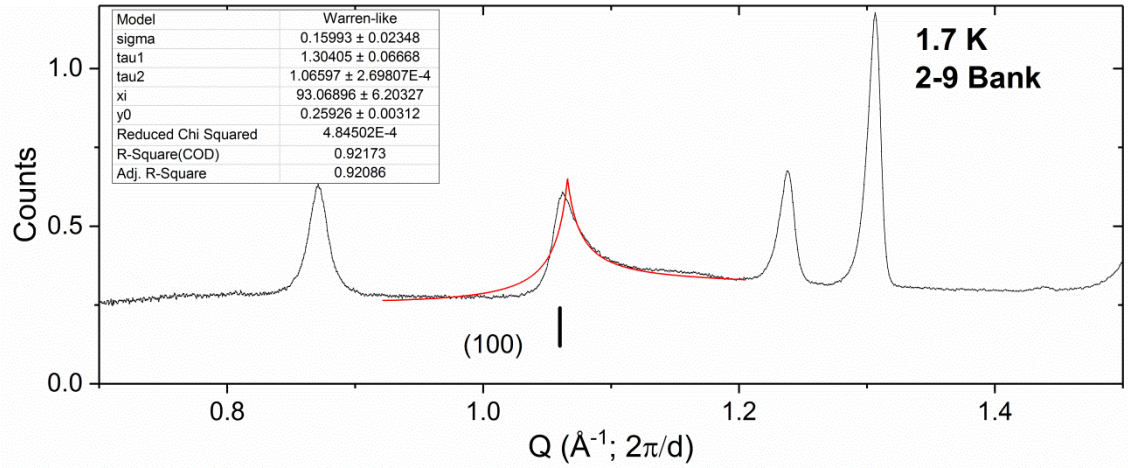


Fig. 3.42 The fit to the peak at Q ~ 1.07 Å^{-1} when a Warren-like peak-shape function is used. The data is from the measurement of $Sr_2MnO_2Cu_{1.8}Te_2$ (JNB303B) at 1.7 K using the 2-9 bank (58.3°) of WISH and the inset shows the numerical values extracted from the peak-fitting

The Warren-like peak-shape function gives a reasonable qualitative fit to the shape of the peak, fitting the high-*Q* asymmetry particularly well. However there are some discrepancies, these are thought to arise primarily because the region is relatively dense in peaks, making it difficult to resolve the intensity from this peak from the intensity of other peaks.

The magnetic behaviour of this compound as a function of temperature was not studied in detail using PND due to lack of beam time. Nonetheless, the compound was also measured on warming from 1.7 K at a nominal temperature of 55 K, but, due to the approaching end of the beam-time allocation, sufficient time was not given for the temperature of the sample to equalise fully with the temperature of the cryostat. This measurement (Fig. 3.43) shows that the magnetic peak has a smaller intensity but is still present, which would suggest that the appearance of the magnetic peak is associated with the feature in the magnetic susceptibility curve at ~70 K, not the feature at 41 K. However, there is a small possibility that the sample was below 41 K when measured without the normal temperature equilibration time.

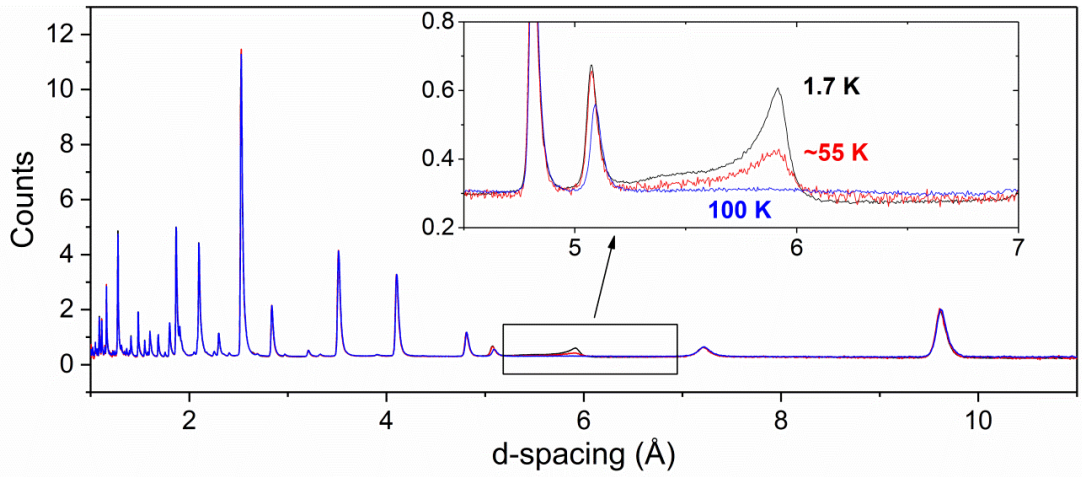


Fig. 3.43 Comparison of the raw PND plots of $Sr_2MnO_2Cu_{1.8}Te_2$ (JNB303B), when it was measured at 1.7 K, 55 K (temperature not equalised) and 100 K, when measured using the 2-9 bank (58.3°) of WISH

3.4.4 Discussion of magnetic behaviour

As described above, the largest observed magnetic peak was fitted using a Warren-like function and indexed using a $\sqrt{2}a \times \sqrt{2}a$ expansion of the unit cell. This suggests a model in which the primary magnetic interaction is the antiferromagnetic interaction of nearest-neighbour Mn ions, but that the presence of 20% Mn^{3+} ions (from average oxidation state $Mn^{2.2+}$) interrupts the antiferromagnetic ordering, causing spin disorder,

and indeed resulting in complete disorder in the out-of-plane direction, hence the lack of Bragg peaks resulting from long-range order, even at 1.7 K.

Magnetometry measurements suggested that two transitions occurred on cooling, one at ~70 K, the onset of short-range two-dimensional antiferromagnetic order and another at ~41 K, which appears to be a spin-glass-like transition.

3.5 Conclusions

The oxidative deintercalation of Cu from $Sr_2MnO_2Cu_{1.5-x}S_2$ causes a dramatic change in structure and magnetic properties. The incommensurately modulated structure of the region "*C*" phase ($Sr_2MnO_2Cu_{1.33}S_2$) has been analysed in detail, showing that the wavelike fractional occupancy of Cu is complemented by displacements in the $[Sr_2MnO_2]$ layer to prevent under-bonding of the S atoms when the Cu occupancy is low.

A third region of the $Sr_2MnO_2Cu_{1.5-x}S_2$ phase diagram has been identified, with a small number of peaks appearing at low temperature, suggesting the presence of a Cu/vacancy ordering scheme not corresponding to the region "*A*" or "*C*" schemes. Further characterisation of this phase has been hampered by the paucity, low intensity and broad character of the associated superstructure peaks. It is possible that further low-temperature electron diffraction measurements may assist in characterising this behaviour, but it appears that the samples are relatively unstable in the electron beam.

PND measurements have confirmed and described in greater detail the magnetic structure of the region "*A*" and "*C*" $Sr_2MnO_2Cu_{1.5-x}S_2$ compounds. These results, combined with the low-temperature PXRD measurements (using ID31) have shown that there is no evidence for charge-ordering of Mn in these compounds. The anisotropic broadening of the magnetic peaks evident in the region "*A*" sample (JNB059) showed that the ordering structure has a short correlation length in the *c*-direction. The presence of antiferromagnetic ordering peaks in two samples within region "*B*" (JNB054 and JNB311) that did not correspond to either the region "*A*" or "*C*" ordering structure suggested the presence of a third, possibly incommensurate, magnetic ordering structure.

$Sr_2MnO_2Ag_{1.5}Se_2$ has been synthesised with > 99 wt% purity, although an ambient-temperature purification step using a solution of I_2 in MeCN was required to remove small amounts of impurity phases. This I_2 purification step results in an extremely small (~1%) reduction in Ag occupancy through oxidative deintercalation, showing that only a very narrow phase width is accessible using this soft chemical approach in this case. Magnetic susceptibility measurements in the Curie-Weiss regime produce an effective moment of 5.45(1) μ_B per Mn ion, consistent with the mixed valence (Mn oxidation state of +2.5), and a positive Weiss temperature suggesting that the strongest interactions between Mn moments are ferromagnetic. Below the Néel temperature of 63(1) K the magnetic structure of the compound was accordingly found to be *A*-type antiferromagnetic (with ferromagnetic coupling of nearest neighbour Mn moments), with a long range ordered moment of 3.99(2) μ_B per Mn ion, similar to that of $Sr_2MnO_2Cu_{1.5}Se_2$.[107]

In $Sr_2MnO_2Ag_{1.5}Se_2$ there is no evidence for a superstructure arising from long range crystallographic ordering of coinage metal ions and vacancies, nor is the coinage metal readily extracted by reaction with iodine. This behaviour is similar to the case of $Sr_2MnO_2Cu_{1.5}Se_2$, but contrasts with the case of $Sr_2MnO_2Cu_{1.5}S_2$ where there is long-range Cu/vacancy order and ~11% of the Cu ions may readily be extracted by oxidative deintercalation. The coinage ion mobilities[122] and the distribution of the ions[123] in antifluorite type $Cu_{2-x}S$ and $Cu_{2-x}Se$ ($0 \leq x \leq 0.2$) are reportedly similar. The different behaviours of the oxide sulfide $Sr_2MnO_2Cu_{1.5}S_2$, and the oxide selenides $Sr_2MnO_2Cu_{1.5}Se_2$ and $Sr_2MnO_2Ag_{1.5}Se_2$ with antifluorite-type coinage metal chalcogenide layers are presumably due to small differences in the thermodynamic driving force for cation/vacancy order or cation deintercalation, and to small differences in ionic mobility.

The synthesis of $Sr_2MnO_2Cu_{1.8}Te_2$ has been reported for the first time. As with $Sr_2MnO_2Cu_{1.5}Se_2$ and $Sr_2MnO_2Ag_{1.5}Se_2$ there is no evidence for the long-range ordering of vacancies at low temperature, though the lower concentration of Cu-vacancies makes this less surprising. Substituting Te^{2-} into the chalcogenide site expands the Mn-O bond distance and Te is less oxidising than either Se or S, both these factors result in the stabilisation of a reduced average oxidation state of $Mn^{2.2+}$ and therefore an increased Cu occupancy (1.8).

Curie-Weiss analysis of magnetometry measurements of $Sr_2MnO_2Cu_{1.8}Te_2$ extracts an effective moment of 5.67(1) μ_B, which compares well with expected value from spin-only calculations. However, low-temperature PND measurements revealed the absence of magnetic Bragg peaks and the presence of a Warren-shaped magnetic peak, characteristic of short-range two-dimensional magnetic ordering. Magnetometry measurements also revealed the presence of what appeared to be a spin-glass freezing transition, T_g ~41 K. This was attributed to the disorder induced by doping 20% Mn^{3+} ions into the [MnO_2] planes, leading to frustration of the magnetic interactions.

Chapter 4

4 Investigating the reaction of $Sr_2MnO_2Cu_{1.5}S_2$ with iodine *in situ*

4.1 Introduction

It is often extremely informative to observe the progress of a reaction while it is in progress, that is "*in situ*". This allows better understanding of the mechanism and kinetics and the presence of any intermediates may be identified. In many cases, the identification of these intermediates has led to their subsequent isolation. Some examples of these reactions, such as the intercalation of Li/NH_3 into FeSe, were discussed in Chapter 1. *In-situ* investigations have allowed reaction mechanisms to be proposed and in the case of $Li/NH_3/FeSe$ a new ammonia-rich $Li\text{-}NH_3\text{-}FeSe$ phase was identified.[76]

In situ measurements have also proven to be vital in understanding the mechanism of potential battery materials, such as the intercalation of Li into MnOOH to form $LiMnO_2$,[124] the electrochemical deintercalation of Li from $Li_{1-x}CoO_2$, eventually to form CoO_2,[125] and the cyclic intercalation/deintercalation of Li from $LiFePO_4$.[126] Each of these studies revealed information about the behaviour of the materials as they would be when they were in use.

During an *in situ* measurement, a non-invasive technique, such as diffraction (X-ray or neutron), nuclear magnetic resonance (NMR) or spectroscopy, is used to track the progress of the reaction by the use of multiple scans, measured as a function of time. However, this presents a considerable technical challenge for two primary reasons: the measurement time of each scan must be short with respect to the timescale of the reaction and secondly contributions from the experimental apparatus must be taken into account and preferably minimised. Powder X-ray diffraction (PXRD) had been a highly informative characterisation technique for all the compounds described in this thesis and was therefore the natural choice for the investigation of the reaction of these compounds *in situ*.

4.1.1 Development of *in situ* powder X-ray diffraction

As was discussed in 2.3.1, the traditional design of a laboratory diffractometer (still widely used) is that of a point detector which tracks along an arc of 2θ, measuring intensity at each data point. This detection method presents an inherent issue for *in-situ* work, since the sample will evolve from the beginning to end of the scan. This means that the scan time must be minimised such that the sample is effectively static over the measurement, which must be done at the expense of signal-to-noise, resolution, or 2θ range.

However, in-house diffractometers have been used to good effect to measure reactions *in situ* when the rate is slow enough that a typical in-house powder X-ray diffraction (PXRD) scan duration may be considered short. One such example where in-house diffractometers were used was the measurement of the electrochemical intercalation of Cs/H_2O into NbS_2 to form $Cs_{0.27}(H_2O)_yNbS_2$ via intermediates with smaller Cs occupancies.[127] Electrochemical reactions lend themselves relatively well to *in situ* measurements because the cell may be constructed with relatively little amorphous media, but several other reactions of interest require a comparatively large volume of solvent. It is also common that reactions occur fast enough that a scan time on the scale of seconds, rather than minutes, is required to monitor the progress of reaction. In such cases it is important that a large *Q*-range can be measured at once and a high flux of X-rays is required in order to achieve reasonable signal-to-noise ratios, especially if the reaction requires penetration through a large amount of amorphous media. In these cases synchrotron sources can be highly advantageous.

Synchrotron sources offer many advantages in the field of *in situ* PXRD. As discussed in section 2.3.2, synchrotrons generate a highly intense beam of X-rays with a range a wavelengths, a "white" beam. This beam has a higher-energy profile than that offered by laboratory sources. Both the higher flux and the higher-energy profile provide a greater signal-to-noise ratio for *in-situ* diffraction: the higher flux because a greater number of photons incident on the sample will mean a greater number of photons hitting the detector and the higher-energy profile because a higher-energy beam is more penetrating, so a greater number of photons will be able to penetrate the amorphous media.

In standard high-resolution powder diffraction the "white" beam generated by the synchrotron source is monochromated. This monochromation disperses all X-rays with a wavelength that is not equal to the target wavelength, at a significant cost to the flux. For earlier generations of synchrotrons, such as the Synchrotron Radiation Source (SRS) in Daresbury (UK), the overall flux available was not sufficient to produce PXRD patterns with sufficient signal-to-noise ratios over the short timescales desired. Therefore, an alternative technique was developed: energy dispersive X-ray diffraction (EDXRD).[128] During an EDXRD measurement, the sample is illuminated with a white beam of X-rays, which diffract to a fixed-angle, energy-sensitive detector. Intensity is then measured as a function of wavelength, contrasting with conventional X-ray diffraction, where intensity is measured as a function of angle.

When EDXRD is used for *in-situ* experiments, an additional benefit is that a comparatively confined geometry can be used because only one diffracted angle needs to be accessed. For this reason, this method continues to be used extensively, particularly when extreme conditions, such as high temperatures and pressures are required. One such example of this is the Oxford-Diamond *in-situ* cell, developed by Moorhouse *et al.*, which uses an infrared furnace to heat reactions up to 1200 °C, while allowing simultaneous EDXRD measurement.[129] A schematic of this setup is shown in Fig. 4.1.

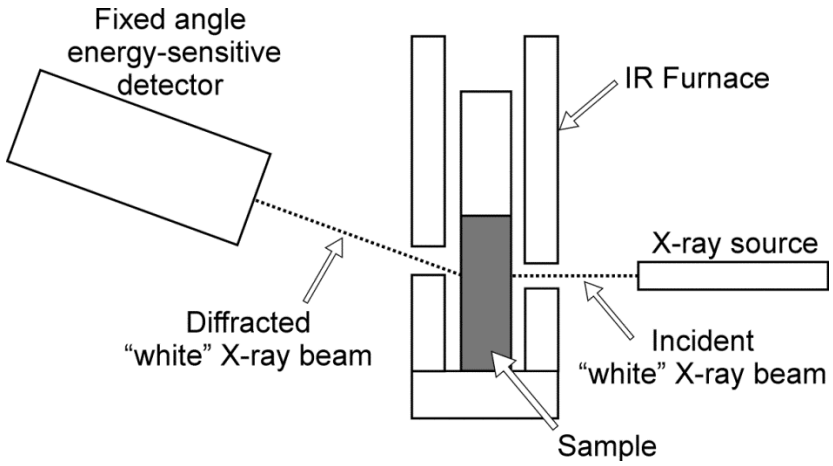


Fig. 4.1 Schematic of the setup used for in-situ energy-dispersive X-ray diffraction (EDXRD) of samples using the Oxford-Diamond in-situ cell developed by Moorhouse et al.[129]

The development of a new generation of higher-flux synchrotrons, such as Diamond, and of position sensitive area detectors has allowed for high signal-to-noise *in-situ* measurements to be collected using monochromatic radiation. This is advantageous

because, in general, energy-sensitive detectors (used in EDXRD) have been found to be lower in resolution than position-sensitive detectors (used in monochromatic PXRD). Therefore, the use of monochromatic PXRD allows smaller changes in lattice parameters to be detected, widening the scope of *in-situ* diffraction.[130]

Both EDXRD and monochromatic PXRD remain useful techniques for *in-situ* PXRD experiments. If both methods were considered workable, monochromatic PXRD would probably be the method of choice, due to the higher resolution of this technique. However, if a large volume of liquid or other amorphous media is required for the reaction, it may be necessary to use EDXRD so the higher flux from a white beam may be used, though in these cases the absorption profile of the setup may not be flat as a function of λ and would therefore require due consideration.

4.1.2 *In situ* investigation into the oxidative deintercalation of $Sr_2MnO_2Cu_{1.5}S_2$

The results of the reaction of $Sr_2MnO_2Cu_{1.5}S_2$ with I_2 when it was studied *ex situ* are discussed in detail in Chapter 3. Although these *ex-situ* studies have identified a lot of information about the end product (the most-deintercalated phase, termed region "*C*" in Chapter 3), significantly less is known about compounds with an intermediate Cu occupancy ($Sr_2MnO_2Cu_{1.5-x}S_2$, termed region "*B*" in Chapter 3). The presence of phase-gaps in the copper occupancies has also been observed, but the precise region where they arise is unknown. Successive short reaction time experiments established that the reaction had gone to completion within ~1 h. This established the reaction as a suitable candidate for study by *in-situ* PXRD because several reactions could be performed in the space of a two day reaction period, with clear objectives.

This chapter discusses the study of the reaction of $Sr_2MnO_2Cu_{1.5}S_2$ with I_2 when it was performed at ~294 K, ~279 K and ~242 K. In all cases the change in peak positions and emergence/disappearance of superstructure peaks is analysed to identify changes in structure, rate of reaction and activation energy, accompanied by a discussion of the kinetics of the reaction. A temperature below 250 K was selected so that changes in the low temperature copper vacancy ordering could be probed directly.

These experiments were also intended to further develop the scope of *in-situ* experiments that were possible at the I12 beamline on Diamond,[96] by building on previous work at this beamline.[76, 129, 131] To this end, new apparatus was developed,

tested and reviewed for both the controlled cooling and remote mixing of reactants. Further developments to this apparatus are suggested at the end of this chapter.

These experiments were performed with significant assistance from Drs D. N. Woodruff and S. J. Cassidy.

4.2 Method

4.2.1 General method

This experiment was performed on the I12 (Joint Engineering, Environment and Processing (JEEP)) beamline (Diamond).[96] This beamline was selected because the beamline was designed with an open, highly customisable environment and also importantly, the X-rays are high-flux and highly-penetrating, allowing for measurements with relatively good signal-to-noise ratio to be made with short collection times (1 s scans). The I12 beamline is discussed further in section 2.3.2.3. The general setup of the experiment is shown in Fig. 4.2. Data were collected using a PIXIUM® image plate detector. The detector distance (2067.13 mm), wavelength (0.15509 Å) and detector deviation from vertical alignment were calibrated using a standardised calibration routine with a CeO_2 standard.

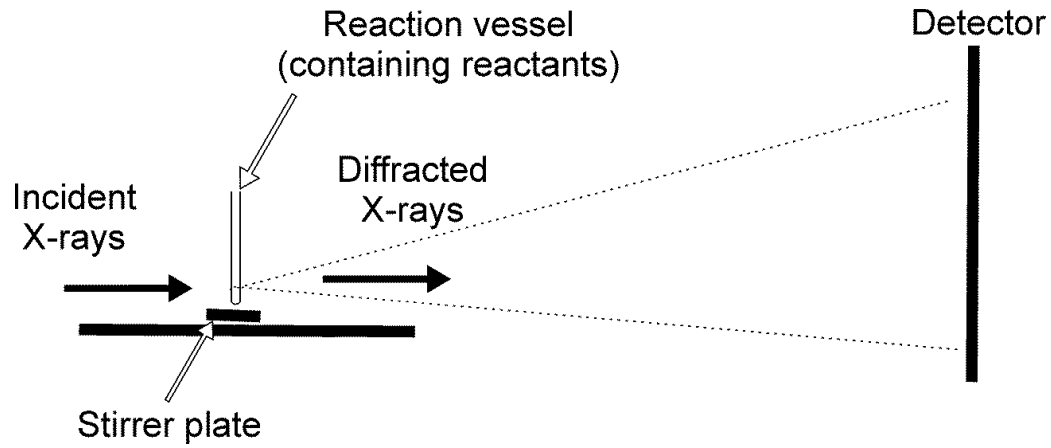


Fig. 4.2 Schematic showing the overall experimental setup

To enable observation of the reaction from its initiation, the two reactants were loaded into two separate chambers of a custom-designed reaction vessel. The reaction vessel was then attached to an arm that could be rotated remotely, the reaction vessel was aligned in the beam and the stirrer plate underneath was switched on so that the powder would remain suspended in the solution by stirring. The beam was switched on and data collection started before the arm was rotated. Then the arm was rotated, mixing the two

reactants. The short scan duration meant that the progress of the reaction could be tracked in real time, by observing changes in the diffraction peaks. After ~10 min, diffraction patterns collected ~1 min apart were examined to see if any significant changes had occurred, if they had not then the scan duration was increased to 5 s to improve the signal-to-noise ratio (this generated another scan series number). The experiment was stopped when the reaction was judged to be finished by examining several scans that had been measured at time intervals that were far apart, but for which the peak positions and intensities were unchanging.

300 mg of $Sr_2MnO_2Cu_{1.5}S_2$ (JNB347) was loaded into one of the arms, ~4 cm^3 of 0.16 mol dm^{-3} I_2 in acetonitrile solution was loaded under air-sensitive conditions into the other.

4.2.2 Design of reaction vessel

Two designs of reaction vessel were used: the "powder-tip" and the "solution-tip" vessels.

The "powder-tip" vessels, shown in Fig. 4.3, are identical to those that were designed for investigating the *in-situ* intercalation of Li/NH_3 into FeSe.[76] These reaction vessels work well because the part of the tube that will be measured throughout the reaction remains in the centre of rotation, so it is easy to align in the tube. A second benefit is that the solution is allowed to stir in the setup section of the experiment; this makes it easy to check that the solution is stirring sufficiently well before the reaction is begun. However, there were two main flaws identified in this setup, the first was that the glass used was designed to withstand high pressures, associated with liquid ammonia reactions. This meant that the glass was thicker than was necessary for the current experiment. The other flaw was that, as the setup required the powder to fall into the solution, there was a risk, previously observed, that significant amounts of the powder would get stuck on the sides of the vessel, dramatically reducing the amount of powder taking part in the reaction and reducing the diffracted intensity. Although it is noted that this effect is powder and solvent dependent, when FeSe was tipped into liquid ammonia, this was not found to be a significant problem.[76]

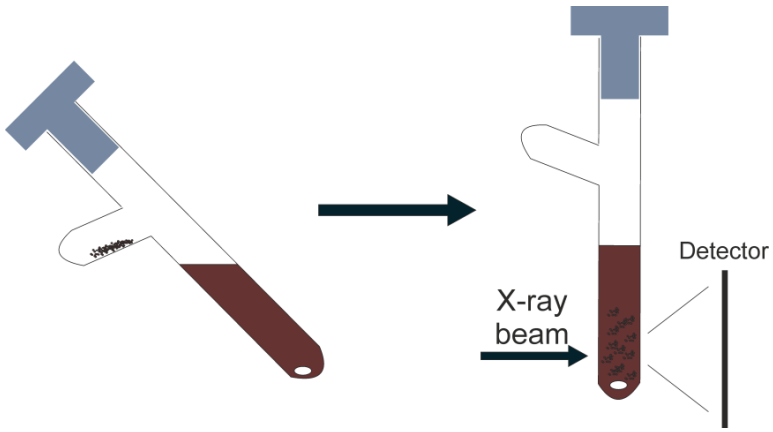


Fig. 4.3 Schematic of the design and mechanism of the "powder-tip" reaction vessel

Therefore a second vessel type was designed, as shown in Fig. 4.4. This reaction vessel was designed with thinner glass, to reduce background effects, and for the solution to tip into the powder, so that all powder would take part in the reaction. However, this reaction-vessel type encountered two separate, but related, problems of its own. It was difficult to align the reaction vessel so that after the reactants had mixed, the arm that contained the reaction mixture was in the X-ray beam. Related to this, since the solution was not stirring in the pre-mixing setup phase, the effectiveness of the stirring mechanism could not be checked. The result of these problems was that when the experiment was attempted with this setup, it was often found that no diffraction pattern was observed. When this occurred, it resulted in the crucial first few minutes of a reaction been missed while the reaction vessel was re-orientated.

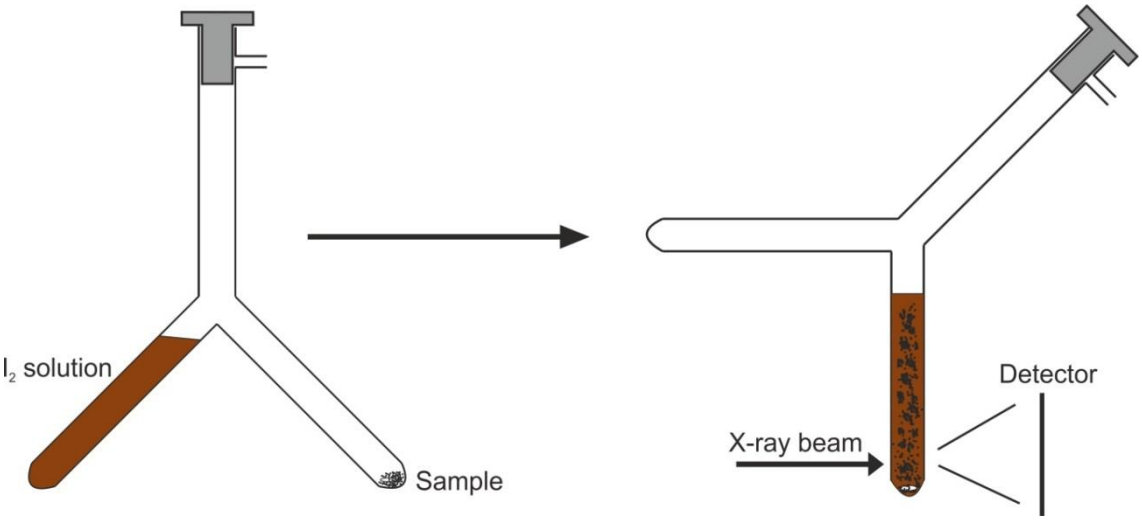


Fig. 4.4 Schematic of the design and mechanism of the "solution-tip" reaction vessel

It was therefore decided that the original "powder-tip" reaction vessel should be used for the *in-situ* experiment, because this method was the most consistently reliable of the

two methods tested. Further refinement of the reaction vessels are planned for subsequent beam time allocations and potential modifications are discussed in section 4.7.1.

4.2.3 Cooling method

As stated above, it was chosen to perform the reaction at room temperature (RT), 280 K and 240 K. In order to do this, a cooling method needed to be found that would cool the sample to these low temperatures, deliver reasonable temperature control and contribute relative minimally to the sample environment.

During previous similar experiments, an isopropanol bath was used. This isopropanol bath was cooled using either dry ice or a closed circulation chiller (CC-chiller), capable of cooling to temperatures as low as ~200 K. As this dramatically increased the volume of liquid in the beam pathway, this substantially increased the sample environment contribution to the background. When the CC-chiller was used, the container was changed from a double-walled borosilicate Dewar to a double-walled plastic Dewar, in order to accommodate the CC-chiller coils; these plastic walls contributed peaks to the PXRD pattern, degrading the quality of the diffraction pattern yet further.

Therefore, a development to enable gas-based cooling of the apparatus was investigated. Preliminary investigations of improvised cryostream-like systems showed that if the entire system was not covered in dry air, then water in the air would condense on the reaction vessel. If the reaction vessel was below 273 K, then the water would freeze. This icing is a significant problem because the ice-crystals contribute unwanted peaks to the diffraction pattern and it also has an insulating effect, preventing the system from reaching temperatures significantly below 273 K.

Accordingly, it was decided to use a polystyrene box filled with a dynamic flow of cooled argon to cool the system. As the box was filled with dry, inert gas, icing was not a problem. The box was equipped with double-walled borosilicate windows, so that the laser used to align the X-ray beam could still be seen. The cavity between the walls of the windows was evacuated to prevent them icing. The argon gas was cooled by passing it through a long copper coil submerged in an isopropanol bath; the isopropanol bath itself was cooled by the CC-chiller system, allowing the temperature of the gas going in to be adjusted. A schematic of the box is shown in Fig. 4.5 and a labelled photograph is shown in Fig. 4.6.

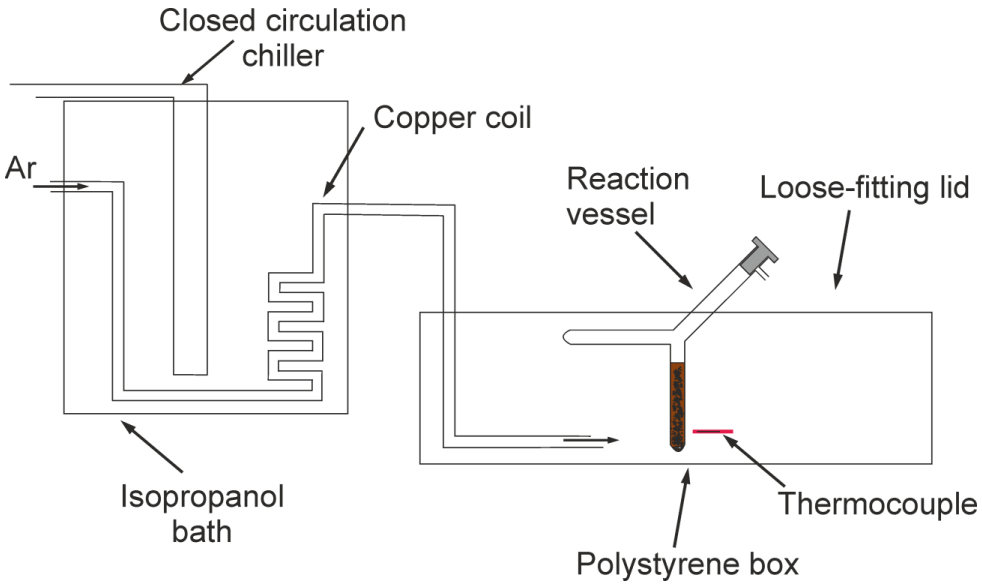


Fig. 4.5 Schematic of the gas-filled-box cooling system

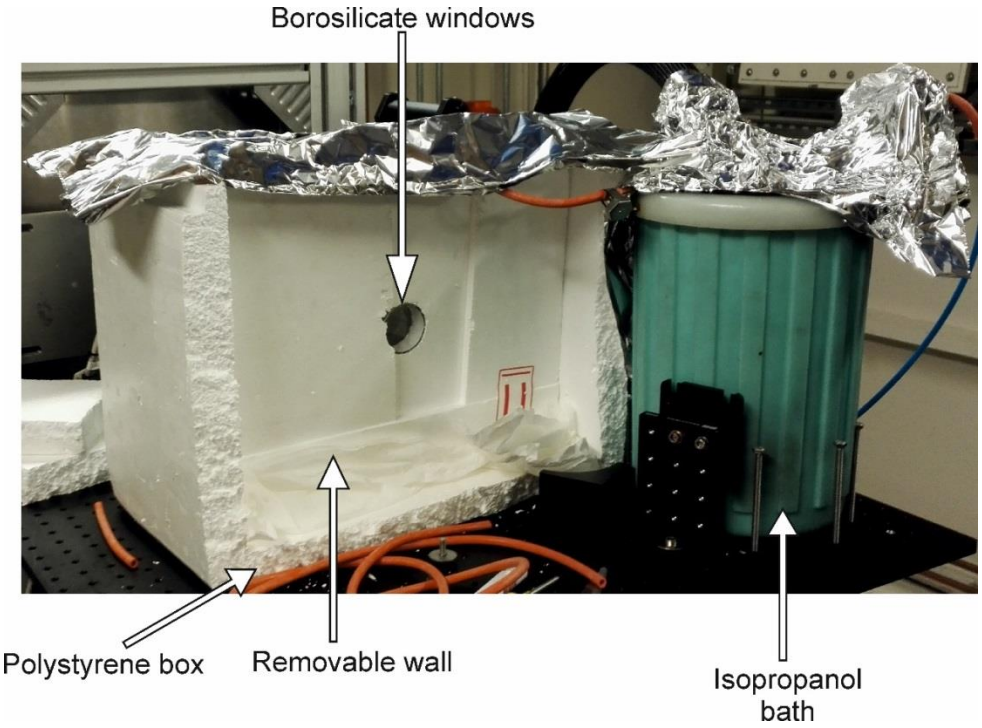


Fig. 4.6 A labelled photograph of the gas-filled-box cooling system

The gas-filled box technique was moderately successful in cooling the sample. It was found that one of the walls needed to be removable in order to align the reaction vessels and the fit of the removable wall to the rest of the polystyrene box was not perfect, allowing gas to flow out. This meant that significantly more argon than anticipated was required to perform this experiment. Small quantities of dry-ice at the bottom of the gas-bath were used to cool the apparatus faster. Some temperature control during the reaction was achieved by altering the gas-flow rate from outside of the beamline hutch.

1.1.1.1 Temperature tracking

The temperature of the gas surrounding the reaction vessel was recorded throughout the experiment using a thermocouple; therefore each scan has a temperature associated with it. It is recognised that the temperature of the liquid inside the reaction vessel did not instantaneously change with the temperature of the gas, but since the reaction vessel was left to equilibrate in the gas-filled box for ~15 min before the reaction was begun and since the temperature of the gas did not change too much, the thermocouple temperature (shown in Table 4.1) is thought to be a good approximation. The thermocouple temperature as a function of time is shown in Fig. 4.7 for each experiment (JNB348, JNB349 and JNB350).

Table 4.1 Average temperature of the reactions described in this chapter, only the scan series which were included in the calculation of the activation energy were averaged

Experiment code	Scan Series	Average temperature (K)
JNB348	68407	293.8(1)
JNB349	68411	279(2)
JNB350	68415, 68416, 68417	242(2)

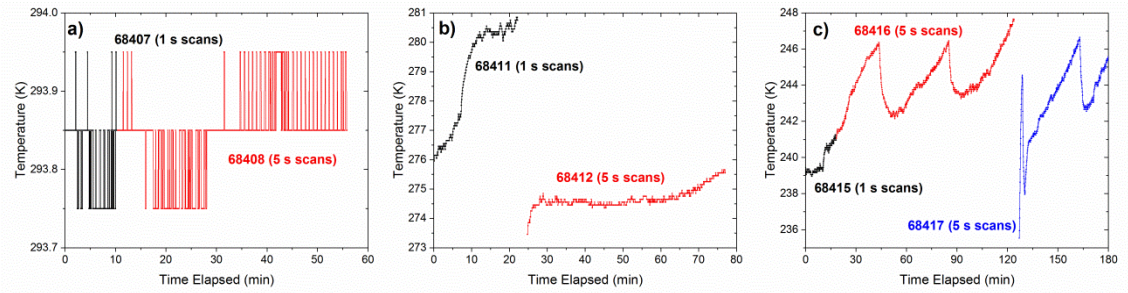


Fig. 4.7 Temperature as a function of time for the following in-situ reactions a) JNB348, b) JNB349 and c) JNB350

The temperature profiles shown in Fig. 4.7 arise from the treatment of the apparatus in each case. As might be expected, the temperature did not vary when the reaction was performed at RT (JNB348). When the reaction was performed with a target temperature of ~275 K (JNB349), the temperature was relatively unstable, with a gradual rise as a function of time. When the reaction had proceeded far enough that it was judged that a ~2 min gap in the data would not be a severe hindrance to data analysis, the experimental hutch was opened (closing the shutter and therefore halting measurements) and small quantities of dry-ice were placed in the polystyrene box to aid temperature control. It is for this reason that the temperature profile of scan series 68412 is lower and more stable. The temperature profile of JNB350 (average temperature: 242(2) K) is characterised by a general rise in temperature followed by a

sudden drop. The sudden drops in temperature mark the times when the argon gas flow was increased (which could be done from outside the experimental hutch). It was found increasing the gas flow increased the cooling power of the apparatus, causing a drop in temperature. When increasing the gas flow was no longer effective in keeping the apparatus at the desired temperature, the experimental hutch was opened and further quantities of dry-ice added to the gas-filled box.

The degree of temperature control achieved was judged sufficient for the experiment in question, where three reaction temperatures that are far apart from one another were required. Although the precise temperature achieved was not important (within a range), it was important that the average temperature of the reaction was known, particularly when interpreting the reaction kinetics (see section 4.6). Therefore the use of a thermocouple that monitored the reaction temperature was crucial. Further suggestions for the improvement of this apparatus are suggested in section 4.7.2.

4.2.4 Data processing

Each scan image was integrated twice, once for Rietveld refinement analysis and once for qualitative graphical display. Data suitable for Rietveld refinement were integrated using DAWN 2.[132] Data suitable for graphical display were integrated to one-dimensional powder diffraction pattern files using FIT2D.[133]

Data for graphical display was background subtracted using a program written by Dr A. Jupe, which implements the Bruckner background subtraction method.[134] All Rietveld refinements were performed on unsubtracted data with the background fitted in the Rietveld refinement. Rietveld fits of the first and last scans of JNB349 (reaction performed at 279 K) are shown in Fig. 4.8. This demonstrates the sizable background associated with these PXRD patterns and also the differences in intensity between scans collected for 1 s and 5 s.

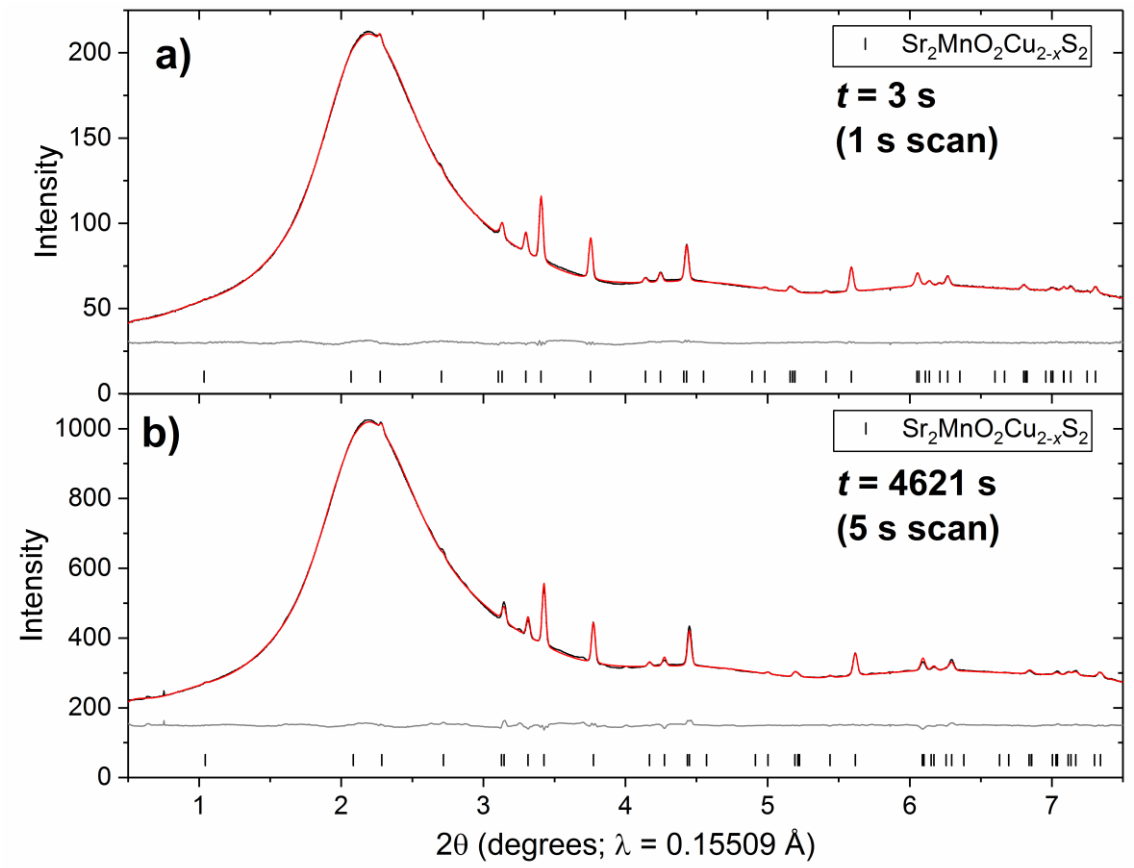


Fig. 4.8 Rietveld plots of the a) first and b) last complete scans of JNB349 (reaction performed at 279 K)

4.3 Change in refined parameters

A sequential Rietveld refinement routine implemented in TOPAS[99] (known as "multitopas") was used to calculate lattice parameters as a function of time elapsed from the beginning of the reaction. The sequential refinement routine modelled $Sr_2MnO_2Cu_{1.5-x}S_2$ as a single phase, using the *I4/mmm* model, throughout the reaction. The peaks were modelled using a modified Thompson-Cox-Hastings pseudo-Voight function with freely refining parameters.[135] Within the atomic model, the atom positions were fixed at the values obtained from refinement against the first scan and isotropic thermal parameters were fixed to prevent over-parameterisation of the model. Superstructure peaks were not modelled in these refinements.

4.3.1 Lattice parameters

The results of these *in-situ* experiments (shown graphically in Fig. 4.9 – Fig. 4.11) show that at every temperature measured the compound reaches lattice parameters associated the lowest-copper-content phase (region "*C*"), described in section 3.2.3. This result is relatively unexpected because when I_2 deintercalations of $Sr_2MnO_2Cu_{1.5}S_2$ were

performed *ex situ*, it was found that the temperature had to be depressed below RT for the lowest-copper-content product (region "*C*" $Sr_2MnO_2Cu_{1.33}S_2$) to form. The differences in the behaviour observed are perhaps due to the long duration (> 1 day) of the *ex situ* RT reactions, which may be sufficient time for the region "*C*" phase to form and then be destroyed by the I_2 solution. However, this is unlikely to be a complete explanation because full deintercalation is observed *in situ*, but *ex situ* the obtained product has lattice parameters smaller than but close to those of the parent. This would suggest that when the deintercalated product is left stirring in CuI/I_2/MeCN solution for too long a reaction that reinserts Cu into the compound occurs. There is some precedent for this – when the lowest-copper-content phase ($Sr_2MnO_2Cu_{1.33}S_2$) is exposed to air, the products are $Sr_2MnO_2Cu_{1.5}S_2$ and some decomposition products.[88] The behaviour of $Sr_2MnO_2Cu_{1.5}S_2$ at RT over a longer timescale could be resolved by continuing to measure the reaction mixture for significantly longer (>1 day), but this may not be considered efficient use of beam-time.

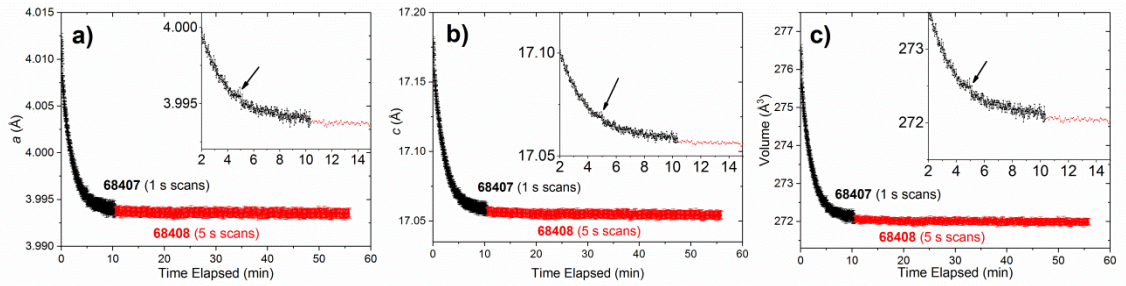


Fig. 4.9 Refined lattice parameters a) a and b) c and c) the unit cell volume of $Sr_2MnO_2Cu_{1.5-x}S_2$ as a function of time elapsed for the reaction JNB348 (RT). Scan series 68407 (black) was a series of 1 s scans and 68408 (red) was a series of 5 s scans. The arrows indicate a small discontinuity in the data

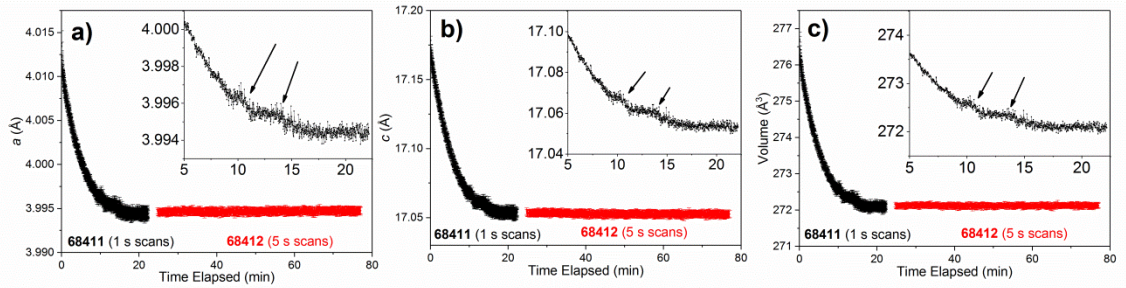


Fig. 4.10 Refined lattice parameters a) a and b) c and c) the unit cell volume of $Sr_2MnO_2Cu_{1.5-x}S_2$ as a function of time elapsed for the reaction JNB349 (279 K). Scan series 68411 (black) was a series of 1 s scans and 68412 (red) was a series of 5 s scans. The arrows indicate a small discontinuity in the data

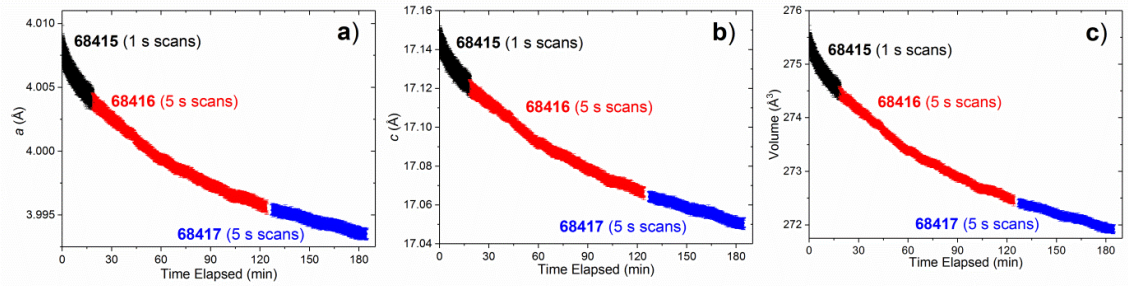


Fig. 4.11 Refined lattice parameters a) a and b) c and c) the unit cell volume of $Sr_2MnO_2Cu_{1.5-x}S_2$ as a function of time elapsed for the reaction JNB350 (242 K). Scan series 68415 (black) was a series of 1 s scans and scan series 68416 (red) and 68417 (blue) were a series of 5 s scans

While reactions JNB348, JNB349 and JNB350 all reach completion, a large change in rate of reaction is observed, when the reaction is performed at RT (JNB348), the reaction reaches completion in just ~7 min, this takes ~180 min at 242 K (JNB350). This change in rate is expected from the ~50 K change in reaction temperature and the observed change is used to extract a value for the activation energy (E_a) of the reaction (described in section 4.6).

The insets and arrows in Fig. 4.9 and Fig. 4.10 show a small discontinuity in the change in the lattice parameters, this occurs at lattice parameter values where a possible phase-gap was identified in section 3.2.2; the work performed to identify this phase gap is reported in section 4.5.

4.3.2 Copper site occupancy

Attempts were also made to refine the fractional copper site occupancy as a function of time for each dataset. It was found in each case that the refined change in copper occupancy was less than the standard uncertainty, as shown in Fig. 4.12, error bars shown are a single standard deviation. The errors are particularly large for the data collected at ~242 K (JNB350); this is unsurprising because at this temperature there are large superstructure peaks unindexed by the *I*4/*mmm* model.

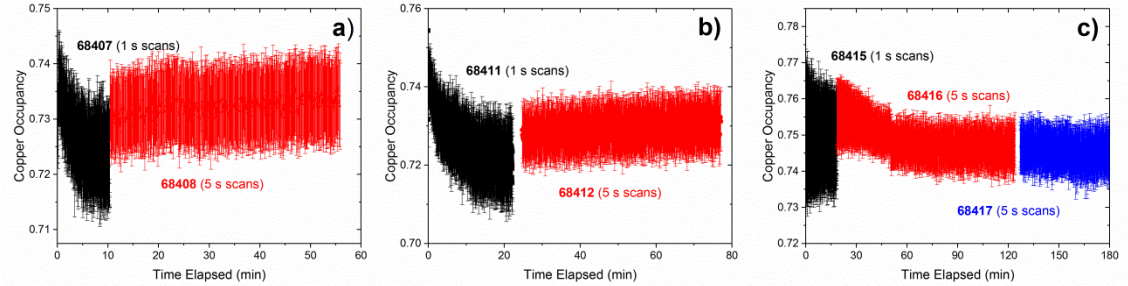


Fig. 4.12 Refined copper occupancy of $Sr_2MnO_2Cu_{1.5-x}S_2$ as a function of time when the reaction was performed at a) RT (JNB348), b) 279 K (JNB349) and c) 242 K (JNB350)

4.4 Qualitative changes in peaks

Qualitative changes in peaks are examined using contour maps that were constructed from data that had been background subtracted and normalised so that the largest peak in each diffraction pattern was equal to 1. Three types of change are observed as a function of time: structural peaks drifting to higher angle, indicating the contraction of lattice cell parameters; superstructure peaks shrinking (for JNB350, T = 242 K), indicating the loss of the copper-vacancy ordering scheme that has previously been described in this compound; and superstructure peaks growing-in, indicating the appearance of a new superstructure (region "*C*" phase with incommensurate superstructure, described in section 3.2.3 and ref. 110).

Contour maps of reaction JNB348 (RT) (Fig. 4.13) show that while the reaction takes ~7 min to reach completion, superstructure peaks corresponding to the region "*C*" phase begin to appear within ~2 min. It is observed that the region "*C*" phase superstructure peaks do not appear to change position throughout the reaction, so it is thought that (as was found from *ex situ* experiments) that the peaks belong to a phase with a very small, rather than broad, range of lattice parameters. The difference between the time when the superstructure peaks are first observed and the average lattice parameters are within the region "*C*" phase range may be reconciled by assuming different sized grains react at different rates. This hypothesis is supported by the observation that the intensity of the superstructure reflections appears to increase as a function of time. However, a further experiment in which the effect of the $Sr_2MnO_2Cu_{1.5}S_2$ particle size on the rate of reaction was investigated would be required to confirm this.

Interestingly, the 1161 peak (2θ = 4.0°) seems to grow in ~1 min before the 116-1 peak (2θ = 3.7°) amongst other superstructure peaks. The paucity of data prevents further investigation of this phenomenon, but it may suggest that the long-range ordering scheme develops in a multi-step process.

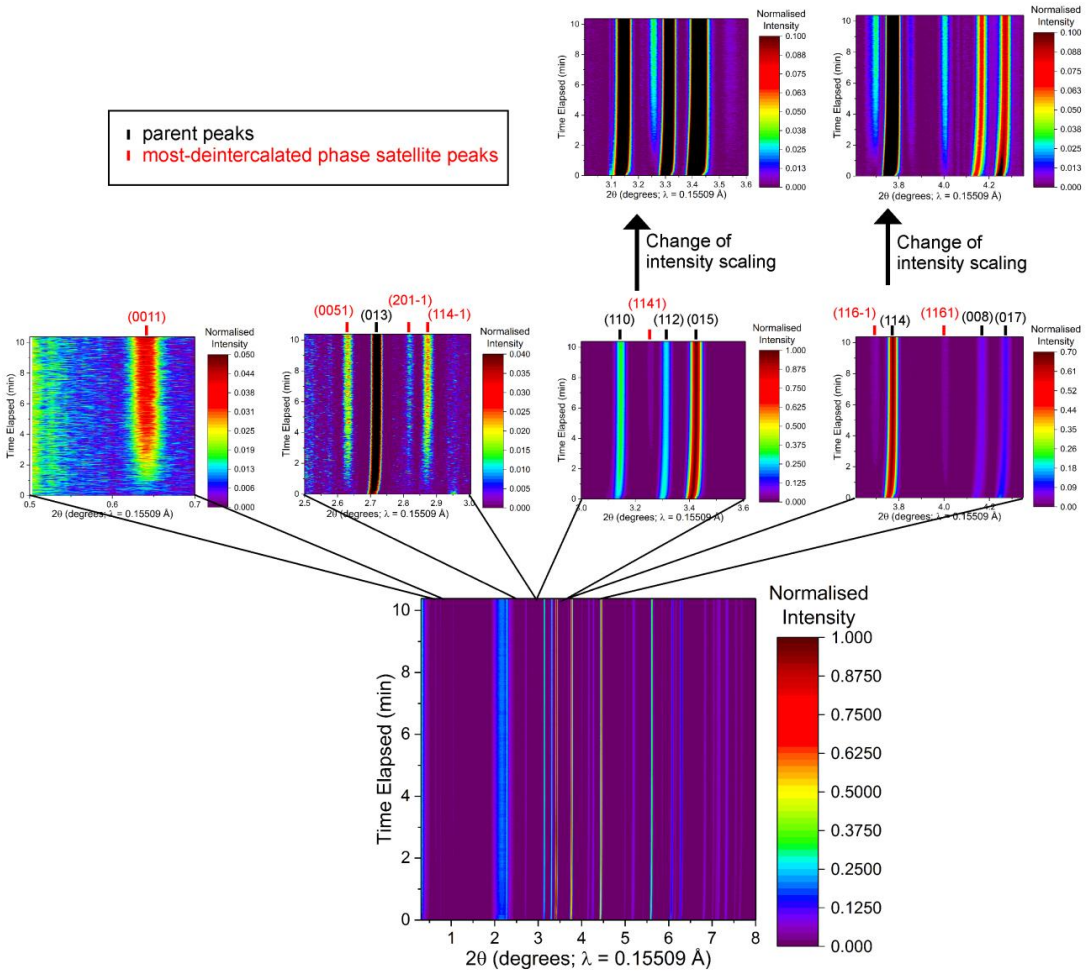


Fig. 4.13 Contour plots showing the evolution of peaks as a function of time for reaction JNB348 (scan series 68407, RT). Tick-marks in black indicate peaks belonging to the parent phase (indexed using the parent unit cell), tick-marks in red indicate peaks belonging to the lowest-copper-content phase characterised structurally in section 3.2.3 and ref. 110 and are indexed using that unit cell

The changes observed in JNB348 (RT) are largely repeated in JNB349 (279 K) (Fig. 4.14) but as previously stated, the reaction is observed to take ~17 min to reach completion.

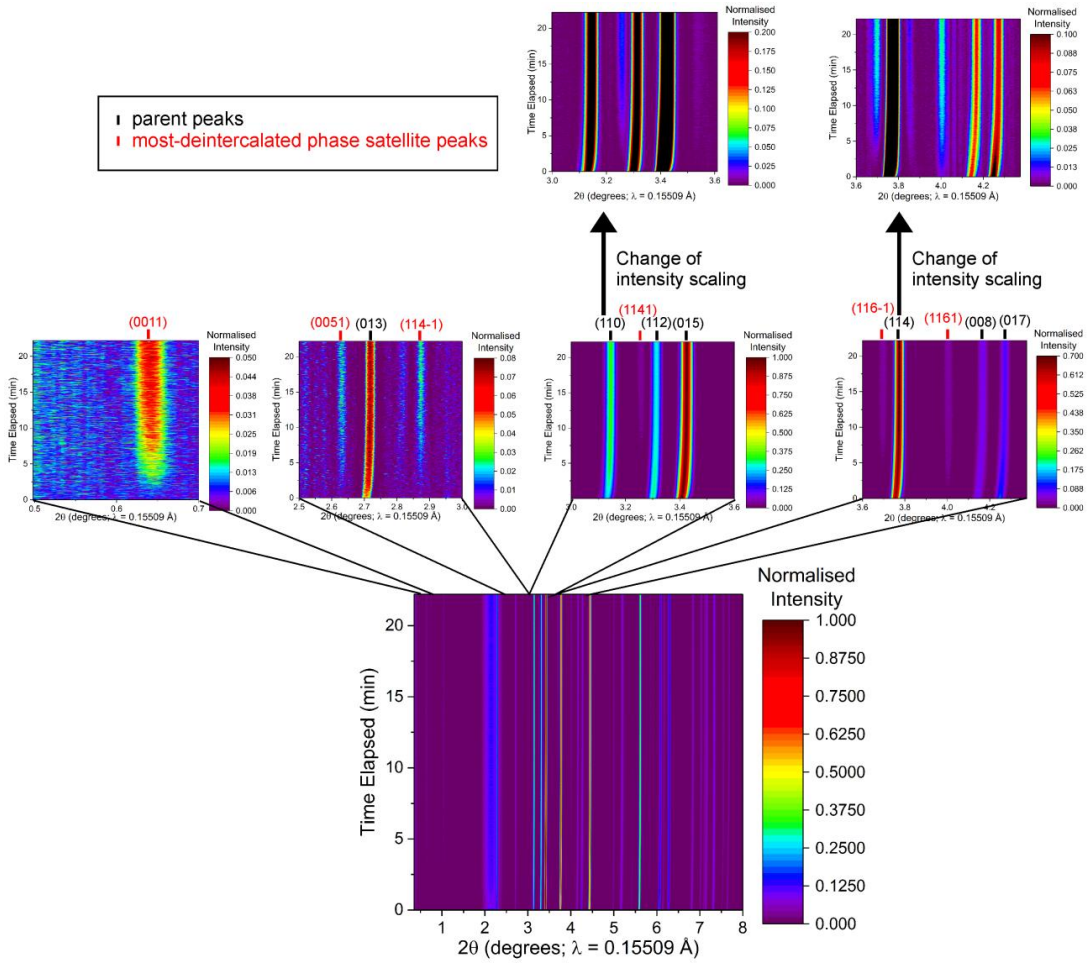


Fig. 4.14 Contour plots showing the evolution peaks as a function of time for JNB349 (scan series 68411, 279 K, 1 s scans). Tick-marks in black indicate peaks belonging to the parent phase, tick-marks in red indicate peaks belonging to the lowest-copper-content phase characterised structurally in section 3.2.3 and ref. 110 and are indexed using that unit cell

The contour maps of JNB350 (242 K) (shown in Fig. 4.15) are qualitatively different from those of JNB348 (RT) and JNB349 (279 K) due to the presence of copper ordering peaks arising from the parent (region "*A*") structure at low temperature that shrink as a function of reaction progress. There is a ~30 – 60 min time-gap between the near disappearance of the parent ordering peaks and the appearance of region "*C*" phase superstructure peaks of significant intensity. This suggests that there is a region where neither the parent nor the most-deintercalated superstructure applies. The region corresponds with region "*B*" identified in section 3.2.4, therefore the peaks identified as belonging to a region "*B*" ordering phase may be observable in the *in-situ* data.

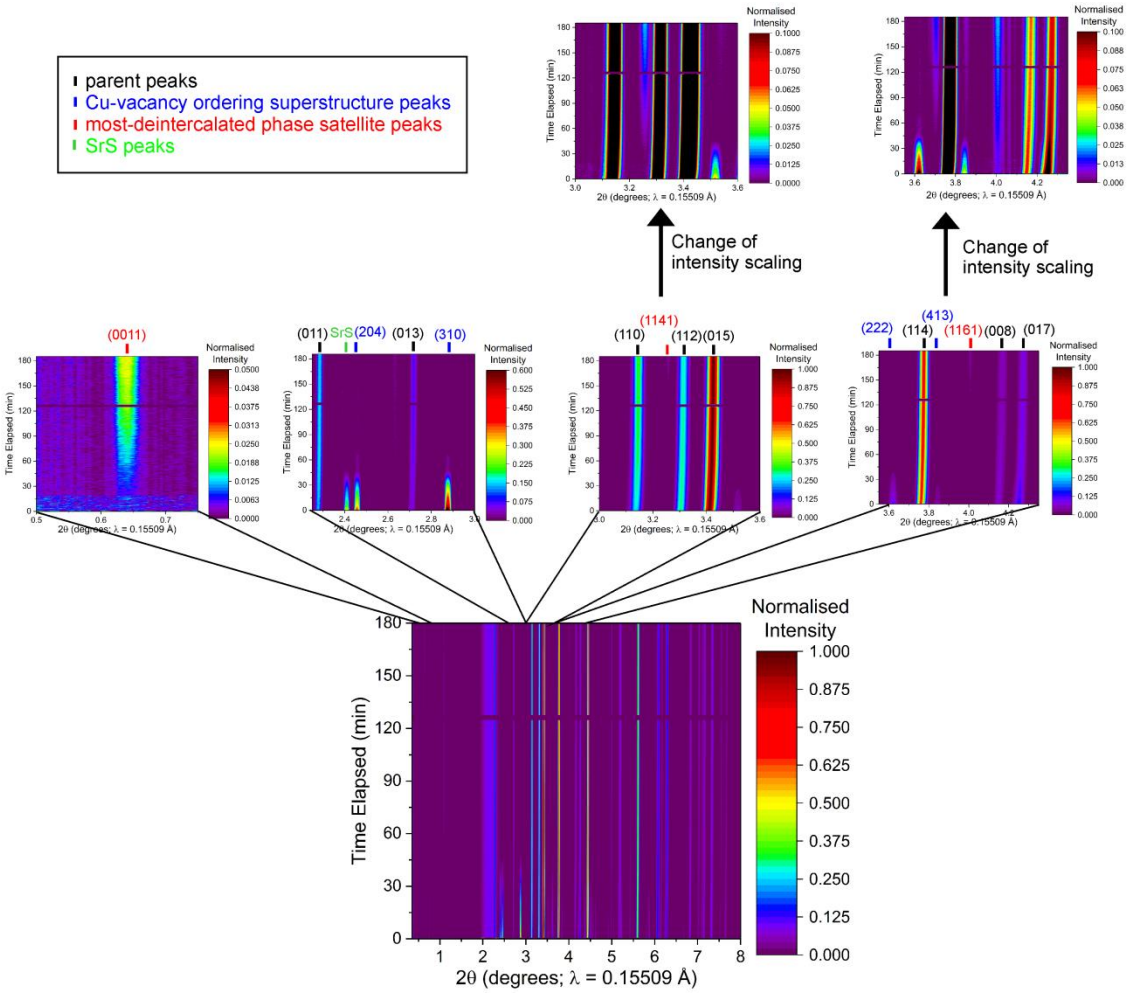


Fig. 4.15 Contour plots showing the evolution peaks as a function of time for JNB350 (scan series 68415, 68416 and 68417, 242 K) Tick-marks in black indicate peaks belonging to the parent phase, tick-marks in red indicate peaks belonging to lowest-copper-content-phase superstructure and blue ticks indicate parent phase Cu/vacancy ordering superstructure peaks

Attempts to find evidence of the region "*B*" low-temperature vacancy ordering structure were hampered generally by the low intensity and broad character of the ordering peaks associated with this phase and specifically because the largest peak associated with this phase (Q = 1.5 Å^{-1}, marked with a '+' in Fig. 3.15) coincides with a region where the background contribution to the pattern is very large, making it particularly difficult to resolve small and broad peaks in this region, even after background subtraction.

Therefore, the region where Q ~ 2.0 Å^{-1} (2θ ~ 2.8° when λ = 0.15509 Å), as shown in Fig. 4.16 was examined. This region contains a region "*A*" low-temperature ordering peak at the start of the reaction and a region "*C*" phase superstructure peak at the end of the reaction. From *ex-situ* work, a region "*B*" phase peak would also be expected in this region. The region "*A*" low-temperature ordering peak is easily resolved because it has

significantly more intensity than the daughter-compound peaks in the region, but the region "*B*" and "*C*" superstructure peaks overlap and cannot be resolved from one another. However, if the peak consisted solely of a peak from the region "*C*" phase, it would be expected (as is observed for other region "*C*" superstructure peaks) that the peak angle would not change as a function of time. Fig. 4.16 seems to show a small change in angle as a function of time, which suggests that the single observed peak is two peaks, with the region "*C*" peak growing in intensity as the reaction completes.

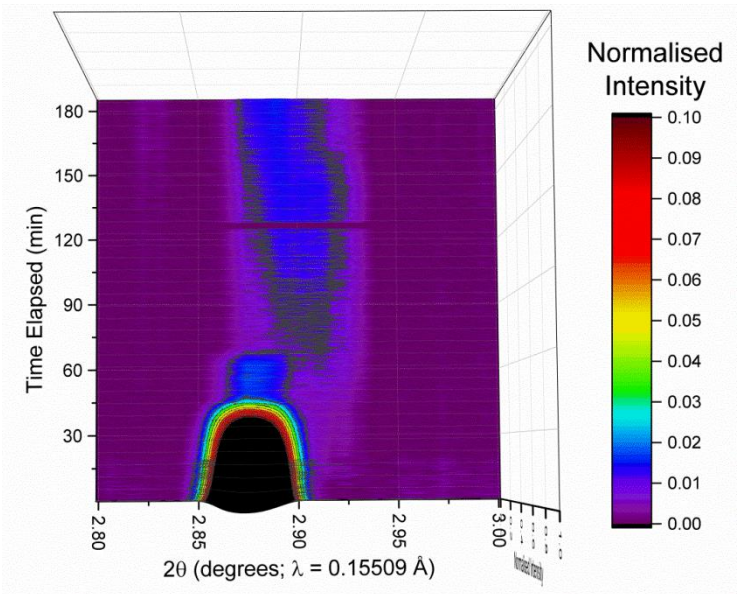


Fig. 4.16 Colour surface map showing the evolution of peaks as a function of time in the range 2.80 ≤ 2θ (°) ≤ 3.00 for JNB350 (242 K)

While consistent with the presence of a region "*B*" ordering phase in the *in-situ* reaction, this is not considered to be conclusive proof. It also may be that there is a small phase-width within region "*C*", allowing for a small change in modulation vector, which is most apparent in this part of the diffraction pattern.

4.5 **Attempts to identify any phase gaps**

A phase gap between region "*B*" and "*C*" has been proposed because some samples have been isolated in which two clearly distinct phases are present in the same sample, as shown in section 3.2.2 and in ref. 110. It was found by careful examination of the *in-situ* data that no splitting of the peaks is observed, even as a shoulder. This is shown in Fig. 4.17, which compares the background subtracted patterns of JNB349 (279 K) at various stages of reaction with the ID31 synchrotron data of SJC1312, which is the

sample where the largest degree of peak splitting has been observed. It can be seen that the peaks from the *in situ* data are too broad to resolve the two phases.

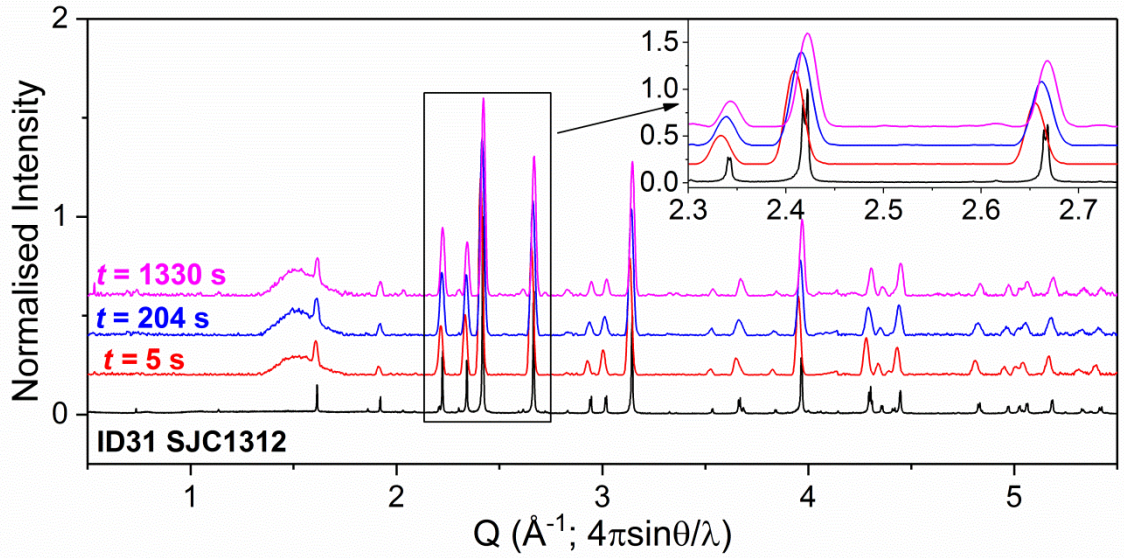


Fig. 4.17 Comparison of the diffraction pattern of SJC1312 (measured at 280 K using ID22) with background subtracted data (n = 40) for reaction JNB349 (279 K) at t = 5, 204 and 1330 s (data collected at I12).

Changes in the peak-shape as a function of time were analysed to deduce if the proposed phase gap could be identified from this information. Selected peaks were modelled using a standard Gaussian peak-shape function, with refined peak position, intensity and full-width-half-maximum (FWHM). This peak-shape function fitted individual peaks well at every stage of the reaction, as shown by the representative fits in Fig. 4.18.

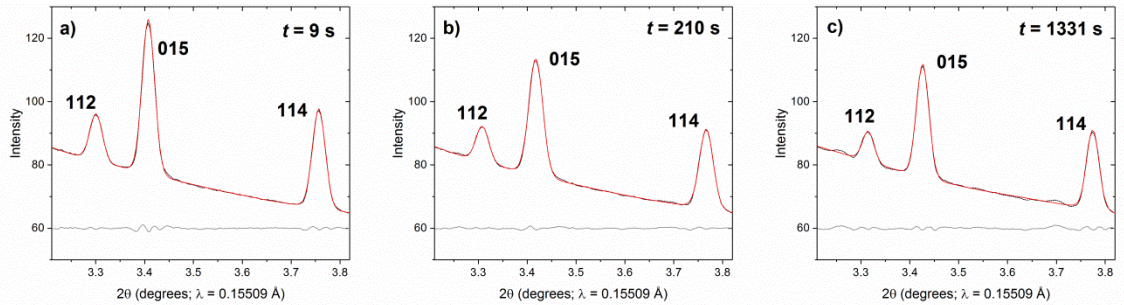


Fig. 4.18 Gaussian fits to the 112, 015 and 114 peaks of $Sr_2MnO_2Cu_{1.5-x}S_2$ for JNB349 (279 K), when time elapsed was 9, 210 and 1331 s.

Three peaks (the 112, 015 and 114) were selected for analysis as a function of time for each reaction (JNB348, JNB349 and JNB350). The refined parameters from this peak fitting are shown in Fig. 4.19 – Fig. 4.21. The peaks were selected because they are

relatively high intensity peaks and reasonable peak splitting could be observed in the two-phased sample SJC1312.

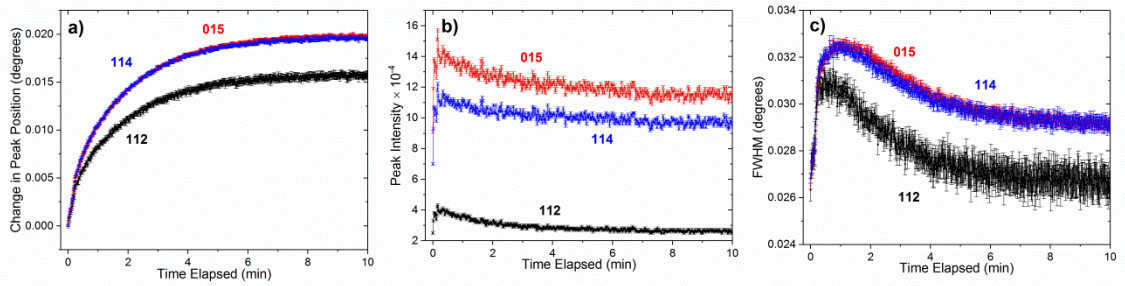


Fig. 4.19 a) The refined change in peak position, b) peak intensity and c) FWHM of the 112, 015 and 114 peaks of the $Sr_2MnO_2Cu_{1.5-x}S_2$ phase for the reaction JNB348 (RT)

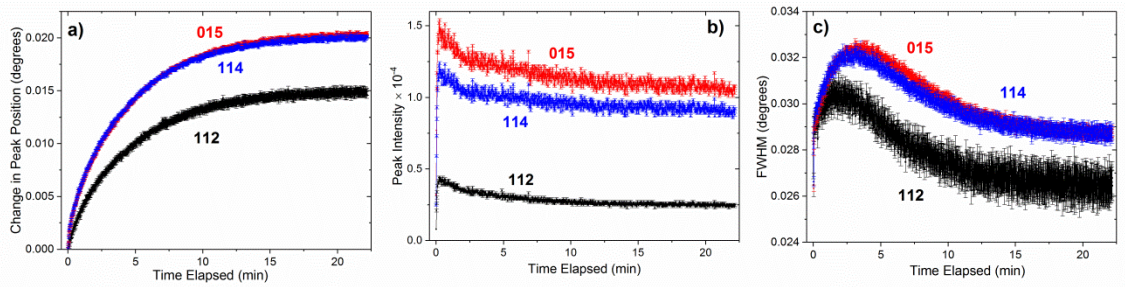


Fig. 4.20 a) The refined change in peak position, b) peak intensity and c) FWHM of the 112, 015 and 114 peaks of the $Sr_2MnO_2Cu_{1.5-x}S_2$ phase for the JNB349 (279 K)

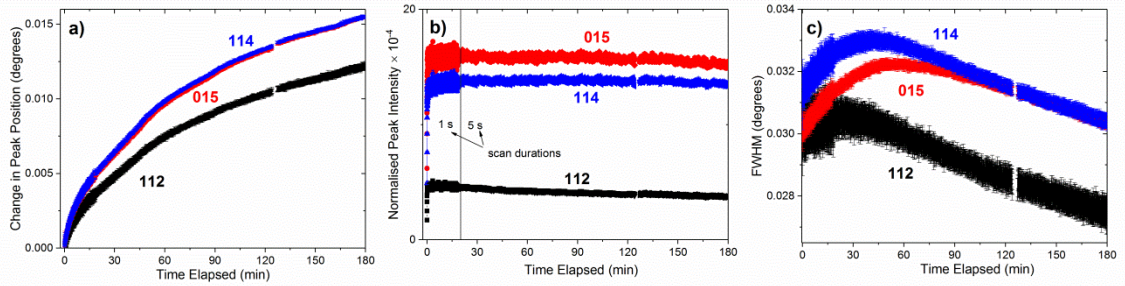


Fig. 4.21 a) The refined change in peak position; b) peak intensity and c) FWHM of the 112, 015 and 114 peaks of the $Sr_2MnO_2Cu_{1.5-x}S_2$ phase for JNB350 (242 K)

This data shows that in each reaction and for each peak analysed, the FWHM is at its maximum at approximately the point *t* where the phase-gap is expected to occur, which may suggest the presence of two phases in this regime. However, it appears that the FWHM of the 112 peaks reaches a maximum slightly before the 015 and 114 peaks, which may suggest that the observed peak broadening is due to another effect.

The most common causes of peak broadening are size and strain effects. The observed increase in the FWHM is unlikely be due to a reduction in the size of the grains as a function of time because the FWHM decreases once a maximum is reached. However, the effect of particle strain on the peak width cannot be ruled out.

4.6 Calculation of the activation energy

In this section the change in the rate of reaction as a function of temperature (RT, 279 K and 242 K) is used to calculate the activation energy (E_a) of the reaction studied. This is obtained from the Arrhenius equation:

$$\frac{d\alpha}{dt} = Aexp\left(-\frac{E_a}{RT}\right)f(\alpha) \tag{4.1}$$

where α is the conversion fraction, describing the extent of the reaction; A is the pre-exponential factor; R is the gas constant; $f(a)$ is the reaction model. α and $f(\alpha)$ must be considered before E_a may be calculated. In this reaction the change in unit cell volume was chosen as a proxy for reaction conversion. *Ex-situ* work described in section 3.2.2 showed that there is a good linear relationship between unit cell volume and Cu occupancy, so this was considered a reasonable method for estimating α:

$$\alpha_{unnorm} = \frac{V_{max} - V_i}{V_{max}} \tag{4.2}$$

where V_{max} is the unit cell volume of the compound before the reaction has begun, while V_i is the unit cell volume at point i. α_{unnorm} is then normalised between 0 and 1 to produce α, where 1 represents the largest change in volume and 0 represents no change in volume. For these calculations it was assumed in each case (JNB348, JNB349 and JNB350) that the reaction had reached completion.

To consider the reaction model ($f(\alpha)$) it is first useful to examine plots of reaction coordinate against time and reduced time: $(t - t_{\text{ind}})/t_{0.5}$; where t_{ind} is the time it takes the reaction to start (in this case approximated to zero) and $t_{0.5}$ is the time at which $\alpha = 0.5$. These plots are shown in Fig. 4.22.

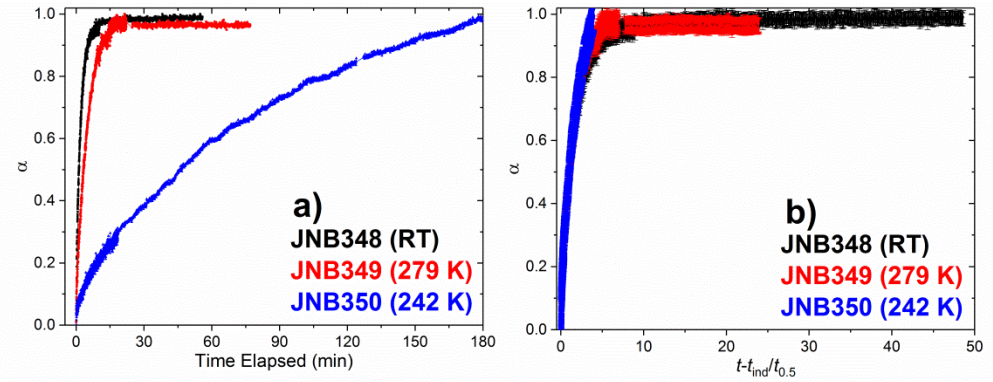


Fig. 4.22 Reaction coordinate as a function of a) time elapsed and b) reduced time for JNB348 (RT), JNB349 (279 K) and JNB350 (242 K)

Plotting in reduced time effectively removes the rate constant hence reactions at different temperatures should show the same conversion ratio as a function of reduced time if the mechanism is the same. The plots of reduced time *vs* α are close to superimposable for each temperature, this is a good indicator that the reactions proceed via the same mechanism, an expected result.

The form that $f(\alpha)$ takes is dependent on the type of reaction described, but Avrami-Erofe'ev kinetics[136-139] are the most widely applied in solid-state chemistry. This kinetic model has successfully been applied to describe reactions as diverse as the thermal decomposition of $BaCO_3$,[140] the crystallisation of gibbsite (γ-$Al(OH)_3$) from supersaturated solutions of $NaAl(OH)_4$,[141] the intercalation of $Co(Cp)_2$ (where Cp = η-C_5H_5) in layered SnS_2,[142] and the intercalation of Na/NH_3 into FeSe.[143] Most pertinently, this model was used to calculate the activation energy of the ion exchange of Cu for Li in $Sr_2MnO_2Cu_{3.5}S_3$ and $Sr_2MnO_2Cu_{5.5}S_4$, systems closely related to $Sr_2MnO_2Cu_{1.5}S_2$ (see section 1.2.3).[54, 81] The wide applicability of Avrami-Erofe'ev kinetics and its success with related reactions suggest that it would be a useful model in this case.

The Avrami-Erofe'ev model considers solid-state reactions as nucleation, the formation of product at the reactive points of the reactants. Neglecting complicating factors, this obeys eq. 4.3:

$$\alpha = kt^n \tag{4.3}$$

where k is the rate of reaction and n is a power exponent, calculated by:

$$n = \beta + \lambda \tag{4.4}$$

where β is the number of steps required to form the nucleus and λ is the number of dimensions the nuclei grow in.

Eq. 4.3 implies constant and continuous nucleus growth because it neglects two major factors: coalescence (merging of growing nuclei, resulting in the loss of reaction interface) and ingestion (blocking of potential reaction interfaces by other nuclei). In the Avrami-Erofe'ev model this is treated by considering α', which is an idealised α, neglecting coalescence and ingestion. The model relates α and α' by:

$$\alpha' = -\ln(1 - \alpha) \tag{4.5}$$

This is substituted into eq. 4.3 to obtain:

$$[-\ln(1-\alpha)]^{1/n} = k(t - t_0) \tag{4.6}$$

n and k may be extracted using a Sharp-Hancock[140] plot of ln[-ln(1-α)] *vs* ln(t), shown in Fig. 4.23 for JNB348 (RT), JNB349 (279 K) and JNB350 (242 K), the parameters derived from this plot are shown in Table 4.2. The approximate linearity of the plots over a reasonable range suggests that the model is a reasonable first approximation.

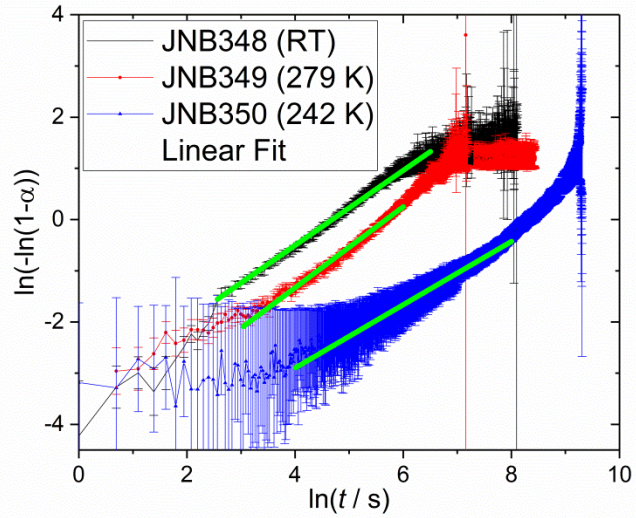


Fig. 4.23 Sharp-Hancock plot for JNB348 (RT), JNB349 (279 K) and JNB350 (242 K)

Table 4.2 Kinetic parameters for the fitting of the reaction conversion ratio, α, to a refineable rate constant, k, at three temperatures

Temperature (K)	*n*	*k* ($\times 10^{-3}$ s^{-1})
294	0.732(4)	9.2(7)
279	0.791(4)	3.4(3)
242	0.617(2)	0.17(2)

While theoretically information could be extracted from *n*, it is in practice very difficult to separate the contribution from β and λ, unless significantly more information about the mechanism is known than is the case for this reaction. *k* is inputted into the Arrhenius equation (eq. 4.7) to obtain E_a by linear regression, as shown in Fig. 4.24.

$$k = A \exp\left(-\frac{E_a}{RT}\right) \tag{4.7}$$

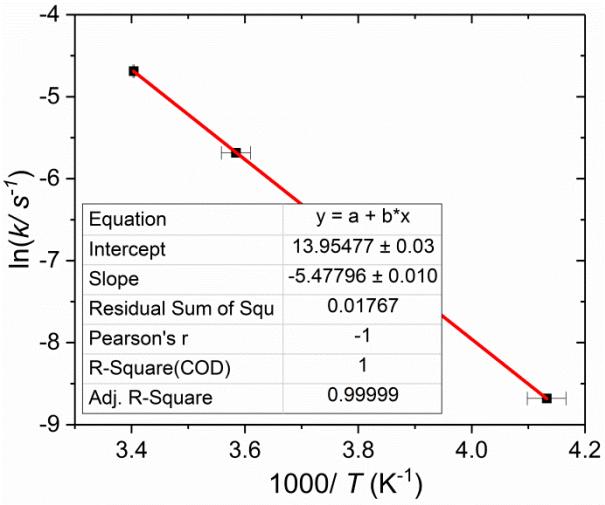


Fig. 4.24 ln(k) vs 1000/T, inset showing the results of linear regression. This data is used to calculate E_a

The calculated E_a value is therefore 45.54(8) kJ mol^{-1}. The error shown here is that calculated by linear regression. It is thought that the calculated error is too small for a value obtained from three data points and numerous approximations and is therefore likely to be significantly larger. An error of 10% is thought to be a reasonable estimation, leading to E_a = 46(5) kJ mol^{-1}. This value is comparable with those values obtained for the reaction of $Sr_2MnO_2Cu_{3.5}S_3$ and $Sr_2MnO_2Cu_{5.5}S_4$ with ^{n}BuLi (58(8) and 55(16) kJ mol^{-1} respectively)[54, 81] and also the reaction of Na/NH_3 with layered FeSe (26(2) kJ mol^{-1}).[143]

4.7 Improvements to the apparatus design

4.7.1 Design of reaction vessels

The design of the reaction vessels could be improved. Before each experiment was initiated there was always a degree of doubt that it would start successfully. The doubt primarily arose from uncertainty associated with alignment of the sample in the beam and problems associated with the powder getting stuck as it was tipped, when using the "powder-tip" vessel. These problems could be counteracted by designing a new reaction vessel, based on injection of the solution into a vessel containing the powder, rather than a tipping mechanism.

In this design, shown in Fig. 4.25, the syringe is attached to the body of the reaction by a screw sealed with a rubber O-ring. A rubber septum separates the body reaction vessel from the syringe and allows the two sections to be connected without exposing the sample to air. The plunger could be depressed remotely.

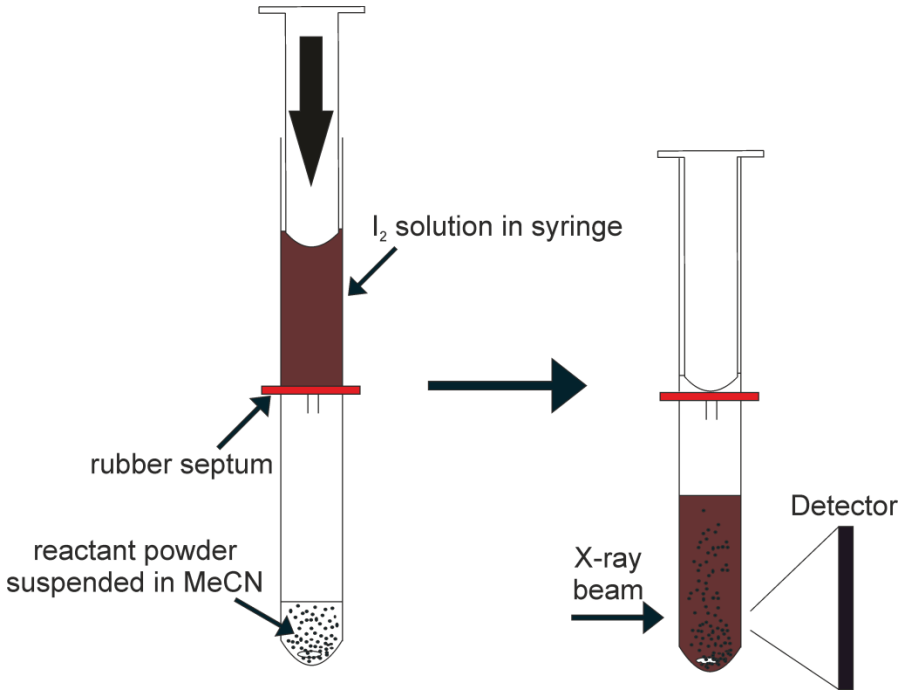


Fig. 4.25 A schematic of the proposed injection-based-mixing reaction vessel

The "powder-tip" vessel was originally designed by Sedlmaier *et al.* for a reaction where the solvent was liquid ammonia. Ammonia has an extremely high vapour pressure at RT, making the use of an injection system difficult; therefore, the reactants were required to be sealed in a single piece of thick-walled glass.[76] There is no such requirement for I_2/MeCN based reactions because the solution is comparatively non-

volatile. Accordingly, it is believed that the injection-based design would be more appropriate for this type of reaction.

The additional step of suspending the powder in MeCN prior to injection of the I_2 solution has also been suggested to ensure that the powder stirs well prior to initiation of the reaction.

4.7.2 Gas-cooled box

The basic mechanism of the gas-cooled box worked well. The major advantage of this system of cooling compared with the direct use of an isopropanol bath is the reduction in the contribution from the amorphous background. Fig. 4.26 compares the raw PXRD patterns of JNB348 (RT) and JNB349 (279 K, cooled using gas-based cooling), showing that there is little increase in the background when the gas-cooled box is used.

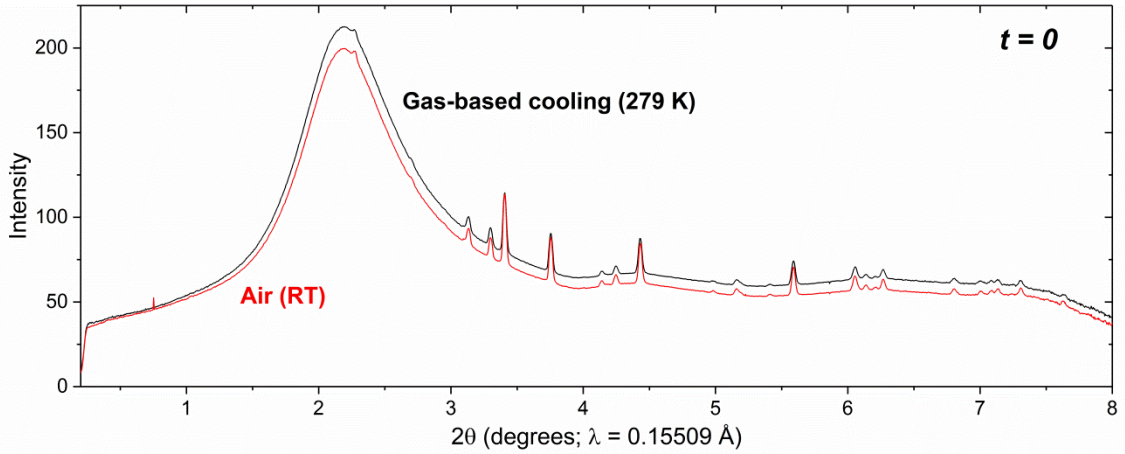


Fig. 4.26 Comparison of the raw PXRD patterns of JNB348 (RT) and JNB349 (279 K, cooled using gas-based cooling)

However, the box was made of several pieces of polystyrene, leading to several holes in the structure. These holes leaked gas, slowing down the cooling process. Originally, it was anticipated that the pieces of the polystyrene would be sealed together using a silicone-based sealant, but when performing the experiment, it was found to be necessary to remove one of the walls to correctly align the reaction vessel. This prevented any permanent sealant being used. If a tipping mechanism is used in future, then one of the walls of the gas-cooled box could be fitted with a hinge and rubber seals to reduce gas leakage, while allowing access.

However, if an injection-based reaction vessel were used, then several improvements to the gas-cooled box could be realised. As the main body of the reaction vessel would not

need to move, the box could be smaller and a more tightly fitting lid could be used, greatly improving efficiency.

One problem that is harder to overcome is that it is significantly more difficult to reach stable intermediate temperatures than it is to stabilise apparatus at its base temperature. It is hoped that this problem may be overcome by use of a smaller, better insulated box and careful calibration of the gas flow and temperature of the isopropanol bath.

4.8 Conclusions

The reaction of $Sr_2MnO_2Cu_{1.5}S_2$ with I_2 appears to proceed extremely quickly at ambient temperatures. It is also noted that although the rate decreases, the reaction still occurs below the temperature where the phase has changed from *I4/mmm* to *Ibam* and the Cu vacancies have ordered. While surprising, this was a useful result because it allowed the transformation between the parent and intermediate low-temperature Cu/vacancy ordering scheme to be probed directly.

Through analysis of the peak broadening, it is believed that the presence of at least one phase-gap has been established. However, little information was obtained about the intermediate Cu occupancy phase because the peaks associated with this phase are small, broad and appear to be transient.

Apparatus has been developed for the *in-situ* measurement of mixed solution-solid phase reactions below ambient temperatures, but, as discussed in section 4.7, further work is required.

Chapter 5

5 Deintercalation of copper or silver from several cobalt-containing oxychalcogenides

5.1 Introduction

The cobalt analogues of $A_2MO_2X_2Ch_2$ (*A* = Sr, Ba; *M* = Co; *X* = Cu, Ag; *Ch* = S, Se, Te) are an abundant class of compounds, as previously discussed in section 1.2.3.4. These compounds hold several features in common. In contrast to the manganese analogues, these compounds are synthesised with stoichiometric Cu/Ag content, representative of an oxidation state of $Co^{2.0+}$.[42, 58, 60-62] As a result, there are no vacancies to order at low temperature, so the compounds retain the *I*4/*mmm* space group until very low temperatures (where there is a small orthorhombic distortion, not driven by Cu/vacancy ordering and discussed within this chapter).

However, when $Sr_2CoO_2Cu_2S_2$ was first reported, it was noted that the compound was slightly Cu deficient when treated as air stable.[42] Further work revealed that this compound could be synthesised with the Cu sites fully occupied, but when exposed to moist O_2, Co^{2+} oxidised slightly, releasing Cu to maintain charge balance, yielding a compound of composition $Sr_2CoO_2Cu_{1.89(2)}S_2$.[58, 61] Harris extended this work, using I_2 to oxidise $Sr_2CoO_2Cu_2S_2$, producing a compound, $Sr_2CoO_2Cu_{1.78}S_2$, that had a lower copper occupancy than could be achieved by moist O_2 alone.[144] No ordering of the Cu-vacancies was observed using powder neutron diffraction (PND), even at very low temperatures, likely because the concentration of the Cu vacancies (~11%) was not high enough for long-range ordering to be favourable.

This chapter extends the oxidative deintercalation work performed on $Sr_2CoO_2Cu_2S_2$ to $Sr_2CoO_2Cu_2Se_2$, $Sr_2CoO_2Cu_2Se_{1.6}S_{0.4}$ and $Sr_2CoO_2Ag_2Se_2$. This is done to further understand the changes in the behaviour of the compound when *X* and *Ch* are changed. In order to do this, the data collected by Smura and Harris for $Sr_2CoO_2Cu_2S_2$ is re-evaluated to allow like-for-like comparisons to be made between compounds.[58, 144]

As well as structural comparisons, the magnetic behaviour of these compounds as a function of Cu/Ag occupancy is studied in detail. The interactions of Co^{2+} (d^7) cations in a square plane separated by an oxide anion are predicted to have antiferromagnetic

coupling of nearest neighbours from Goodenough-Kanamori superexchange rules.[84-86] This has been found to hold true for all the $A_2CoO_2X_2Ch_2$ compounds where the magnetic ordering has already been reported.[58, 62]

The magnetic ordering behaviour of the solid solution $Sr_2CoO_2Cu_2S_{2-x}Se_x$ was studied by Smura. It was found that, while all the magnetic peaks observed in $Sr_2CoO_2Cu_2S_2$ could be indexed on a $\sqrt{2}a \times \sqrt{2}a \times c$ expansion of the nuclear cell, when $x > \sim 0.5$, a larger magnetic cell, doubled in the c-direction ($\sqrt{2}a \times \sqrt{2}a \times 2c$) was required to index all of the magnetic peaks.[58]

While all the peaks could be indexed using a single expansion ($\sqrt{2}a \times \sqrt{2}a \times 2c$), it was found that no single, reasonable magnetic structure could fit all the intensity from the magnetic peaks. Therefore, the magnetic behaviour was modelled as emerging from two magnetic structures with different unit cells, one that was a $\sqrt{2}a \times \sqrt{2}a \times 2c$ expansion and one that was a $\sqrt{2}a \times \sqrt{2}a \times c$ expansion of the nuclear cell. These were termed the "2c" and "c" magnetic structures respectively and are shown schematically in Fig. 5.1. This model was found to fit the intensity of the magnetic peaks well.[58]

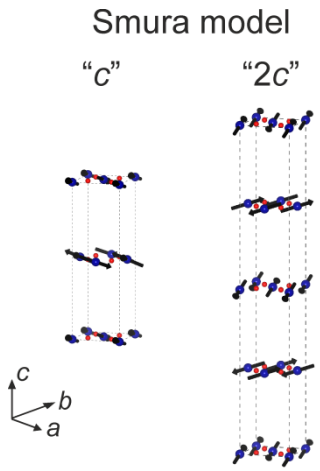


Fig. 5.1 Schematic of the two-phase magnetic structure of $Sr_2CoO_2Cu_2Se_2$ proposed by Smura,[58] for clarity only the Co (blue) and O (red) atoms are shown. The dotted black lines outline the expanded magnetic unit cells

The magnetic intensity of $Sr_2CoO_2Cu_2S_{2-x}Se_x$ in the region $1.5 \leq x \leq 1.7$ could be fitted using the "2c"-magnetic structure only. Surprisingly, $Sr_2CoO_2Cu_2Se_2$, which does not contain a solid solution of anions, required both magnetic structures to give a good fit to the magnetic intensity.[58] The presence of two magnetic structures in the same compound might be justified by assuming that the two structures are sufficiently close

together in energy that small changes (e.g local variations in the S:Se ratio) could cause different regions to magnetically order in different ways.

However, this model is somewhat dissatisfactory in the absence of further evidence of phase separation in $Sr_2CoO_2Cu_2Se_2$, where there is only one chalcogenide. It is also noted that several samples of $Sr_2CoO_2Cu_2Se_2$ were measured using low temperature PND and the resulting diffractograms revealed that the relative intensity of all the magnetic peaks remained approximately constant.[58] If the magnetic peaks were the result of two magnetic structures, changes in the proportion of each phase observed might be expected.

Here an alternative model, using a single magnetic structure is presented in the context of understanding the magnetic structure of $Sr_2CoO_2Cu_2Se_2$ and $Sr_2CoO_2Cu_2Se_{1.6}S_{0.4}$ as a function of Cu occupancy. $Sr_2CoO_2Cu_2Se_{1.6}S_{0.4}$ was selected for study to examine the effects of oxidation on the magnetic structure of a compound with solely the "2*c*" magnetic structure peaks, using the Smura notation.[58]

The novel compound $Sr_2CoO_2Cu_2Te_2$ has also been synthesised. This chapter reports the structure of the compound and the magnetic ordering behaviour of the compound as a function of temperature. This allows further comparisons in the behaviour of these compounds as a function of chalcogenide ion to be made.

5.2 Cu deintercalation from $Sr_2CoO_2Cu_2(S/Se)_2$ using iodine.

$Sr_2CoO_2Cu_2Se_2$ reacted with I_2 to form $Sr_2CoO_2Cu_{2-x}Se_2$ in a similar manner to $Sr_2CoO_2Cu_2S_2$, though in general the compound was less reactive, with smaller observed changes in Cu occupancy and lattice parameters.

In this section, the work performed by Smura,[58] Smura *et al.*[61] and Harris[144] is reviewed and extended, so that the oxidation behaviour of $Sr_2CoO_2Cu_2S_2$ may be compared reliably to $Sr_2CoO_2Cu_2Se_2$. Another compound, $Sr_2CoO_2Cu_2Se_{1.6}S_{0.4}$ was synthesised and Cu deintercalated using I_2, so that (as previously discussed) the behaviour of a phase with a mixed S/Se site could be compared.

5.2.1 Synthesis and deintercalation

$Sr_2CoO_2Cu_2S_2$ was synthesised on the 5 g scale by mixing SrS, Co and CuO in the molar ratio 2:1:2 and preparing them as described in section 2.1.1. The prepared

reactants were heated to 825 °C, at a rate of 10 °C min^{-1}, for 48 h before cooling in the furnace.

$Sr_2CoO_2Cu_2Se_2$ was synthesised (again on the 5 g scale) by reacting SrO, Co, Cu and Se in the molar ratio 2:1:2:2. The reactants were heated to 825 °C, using the same heating regime as for $Sr_2CoO_2Cu_2S_2$. $Sr_2CoO_2Cu_2Se_{1.6}S_{0.4}$ was synthesised by the reaction of SrS, SrO, Co, Cu, CuO and Se in the molar ratio 0.4:1.6:1:1.6:0.4:2, prepared and heated (825 °C) as described for $Sr_2CoO_2Cu_2S_2$.

All compounds were tested for phase purity by laboratory powder X-ray diffraction (PXRD) before reacting further. Small (< 3 wt%) Sr(S/Se) impurities could not eliminated by repeated heating and regrinding. Synchrotron PXRD showed that $Sr_2CoO_2Cu_2Se_{1.6}S_{0.4}$ was obtained as a single phase, without ordering of the chalcogenide ions.

I_2 oxidations were performed as described in section 2.1.3. In general, reactions were performed on either a 0.5 g scale, to prepare samples intended for standard analysis, or on a 4 g scale, to prepare samples intended for PND. Various concentrations of I_2 were used to produce samples of $Sr_2CoO_2Cu_{2-x}Ch_2$ with various values of *x*.

5.2.2 Lattice parameters and composition

5.2.2.1 *Room temperature powder X-ray diffraction*

For each of $Sr_2CoO_2Cu_2S_2$, $Sr_2CoO_2Cu_2Se_{1.6}S_{0.4}$, $Sr_2CoO_2Cu_2Se_2$, the primary change observed in the PXRD after reaction with I_2 was a reduction in the lattice parameters. No additional peaks, which may have indicated the presence of some Cu/vacancy ordering, were apparent at room temperature (RT). In the first instance, the changes in lattice parameters were used to compare the extent of reaction in each case, as shown in Fig. 5.2.

The lattice parameters shown in Fig. 5.2 were derived from Rietveld refinement against synchrotron PXRD data obtained from the MAC detector and PSD of the I11 beamline).

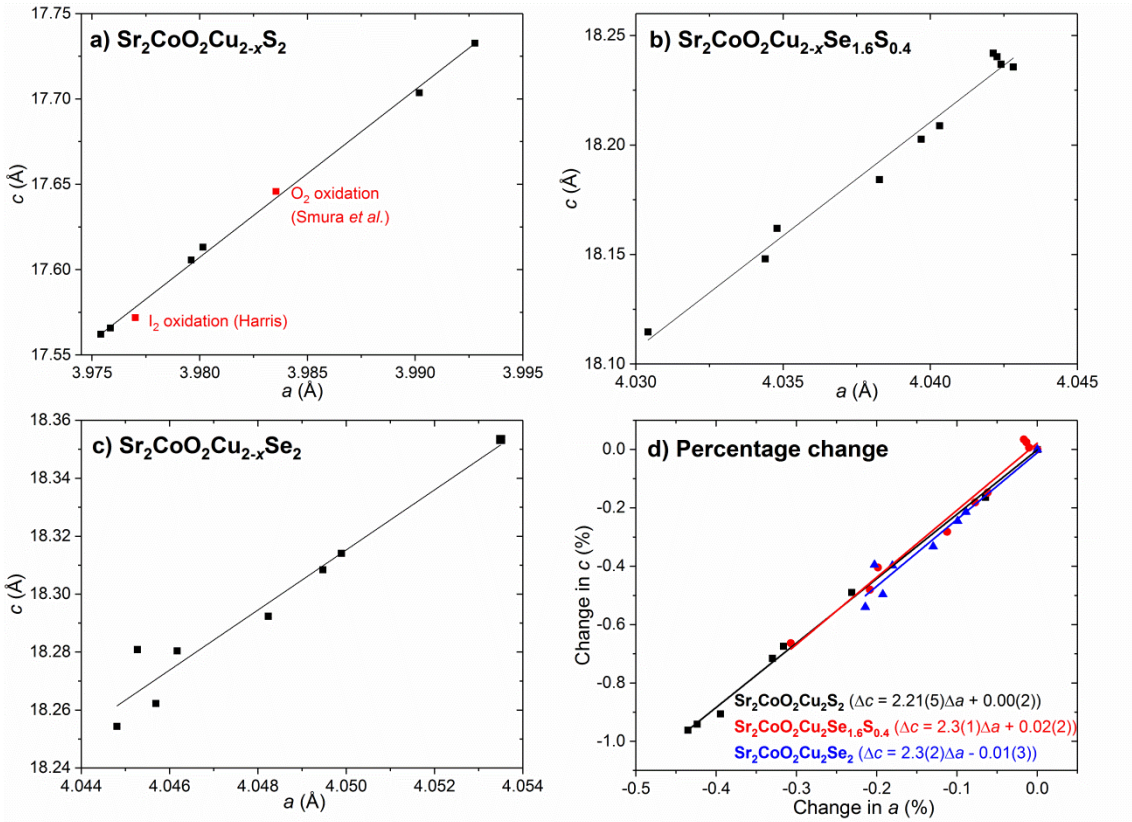


Fig. 5.2 The changes in lattice parameters that occur on reaction with I_2 for each of a) $Sr_2CoO_2Cu_{2-x}S_2$ (some data points from ref. 61 (Smura et. al) and ref. 144 (Harris)); b) $Sr_2CoO_2Cu_{2-x}Se_{1.6}S_{0.4}$ and c) $Sr_2CoO_2Cu_{2-x}Se_2$; d) shows the percentage change in a and c for each of these compounds, with a linear fit. The error bars are smaller than the points on the graph

Fig. 5.2 shows that for the gradient of the change in *c* as a function of the change in *a* is the same within error of each of these compounds ($\Delta c = 2.3(2)\Delta a$). The most significant observed difference is that a much larger change in lattice parameters is possible in $Sr_2CoO_2Cu_2S_2$ than $Sr_2CoO_2Cu_2Se_2$, both in percentage and absolute terms. This is because more Cu may be removed from $Sr_2CoO_2Cu_2S_2$ than $Sr_2CoO_2Cu_2Se_2$, as shown below.

Synchrotron PXRD (obtained using the PSD at the I11 beamline) was also used to extract refined Cu occupancy values, as shown in Fig. 5.3. In these refinements the Cu occupancy of the stoichiometric product of high-temperature synthesis (termed the "parent") was fixed at one and the anisotropic thermal displacement parameters (ADPs) allowed to refine, these ADPs were then exported to the Rietveld refinement of the daughter compounds where the Cu occupancy was refined freely, but the ADPs were fixed. This method was used to prevent over-correlation between ADPs and occupancy values. The three parent samples used for each of the $Sr_2CoO_2Cu_{2-x}S_2$ (JNB051),

$Sr_2CoO_2Cu_2Se_{1.6}S_{0.4}$ (JNB236A) and $Sr_2CoO_2Cu_2Se_2$ (JNB149A) series were also defined as the point of zero change in lattice parameters, it is for this reason that each of the graphs has three data points superimposed at the position (1, 0).

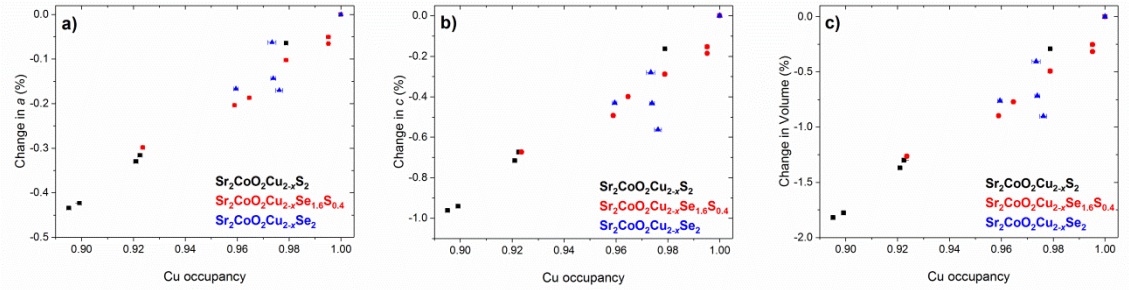


Fig. 5.3 Percentage change in a) lattice parameter a; b) lattice parameter c and c) unit cell volume as a function of Cu occupancy, values have been extracted from Rietveld refinement against synchrotron PXRD data obtained from the PSD at the I11 beamline. Error bars shown are the standard uncertainties calculated during the Rietveld refinement

A strong linear trend is observed between Cu occupancy and lattice parameters *a* and *c* and also the unit cell volume for each of $Sr_2CoO_2Cu_{2-x}S_2$, $Sr_2CoO_2Cu_{2-x}Se_{1.6}S_{0.4}$ and $Sr_2CoO_2Cu_2Se_2$. Some anomalous results appear in the data for $Sr_2CoO_2Cu_{2-x}Se_2$; the origin of these discrepancies is unclear.

5.2.2.2 *Room temperature powder neutron diffraction*

RT PND was used to obtain good structural models of the $Sr_2CoO_2Cu_2Ch_2$ compounds as a function of Cu occupancy. In particular PND was used to confirm the Cu occupancy values obtained from PXRD data. Three large samples (4 g) of both $Sr_2CoO_2Cu_2Se_2$ and $Sr_2CoO_2Cu_2Se_{1.6}S_{0.4}$ were synthesised each and reacted with I_2, so that the samples obtained had lattice parameters of the parent, the smallest achievable lattice parameters and those that were intermediate between the two. Samples of $Sr_2CoO_2Cu_{2-x}S_2$ had already been measured using high-resolution PND by Smura *et al.* and Harris, so this data has been used to compare behaviour between compounds.[61, 144] The data obtained from Rietveld refinement against this data is tabulated in Table 5.1 – Table 5.3. The Rietveld fits of the data shown in Table 5.2 and Table 5.3 are shown in Fig. 5.4.

The samples of $Sr_2CoO_2Cu_{2-x}S_2$ evaluated in Table 5.1 were synthesised in the following way: DRP053 (unexposed) is the product of high-temperature synthesis that was then kept in an inert environment prior to all measurements; DRP053AE was synthesised in the same batch as DRP053 (unexposed), but subsequently exposed to a

flow of moist O_2; LH999 was a sample of $Sr_2CoO_2Cu_2S_2$ that was reacted with an over-excess of I_2, using a method similar to that discussed in this thesis.[61, 144]

Table 5.1 Comparison of refined parameters from RT PND data of as-synthesised $Sr_2CoO_2Cu_2S_2$ (DRP053, data from ref. 61); $Sr_2CoO_2Cu_{2-x}S_2$ that has been oxidised by exposure to air (DRP053AE, data from ref. 61) and $Sr_2CoO_2Cu_{2-x}S_2$ that has been oxidised by excess I_2 (LH999, data from ref. 144)

Sample	DRP053 (unexposed)	DRP053AE (moist O_2 exposed)	LH999 (I_2 oxidised)
Radiation	Neutron, ToF		
Diffractometer	POLARIS	POLARIS	HRPD
a (Å)	3.99129(2)	3.98354(2)	3.97647(1)
c (Å)	17.71555(9)	17.6458(1)	17.5675(1)
Volume (Å^3)	282.216(2)	280.014(2)	277.783(2)
z(Sr)	0.40767(1)	0.40646(1)	0.40530(5)
z(S)	0.17119(3)	0.17072(3)	0.1703(1)
Cu occupancy	0.990(1)	0.945(1)	0.889(5)
Sr U_{iso} (Å^2)	0.0071(1)	0.0075(1)	0.0095(4)
Co U_{iso} (Å^2)	0.0091(2)	0.0096(2)	0.0026(9)
O U_{iso} (Å^2)	0.0076(1)	0.0080(1)	0.0093(7)
Cu U_{iso} (Å^2)	0.0173(1)	0.0176(1)	0.0212(6)
S U_{iso} (Å^2)	0.0081(1)	0.0084(1)	0.009(1)
R_{wp} (%)	1.44	1.16	2.35

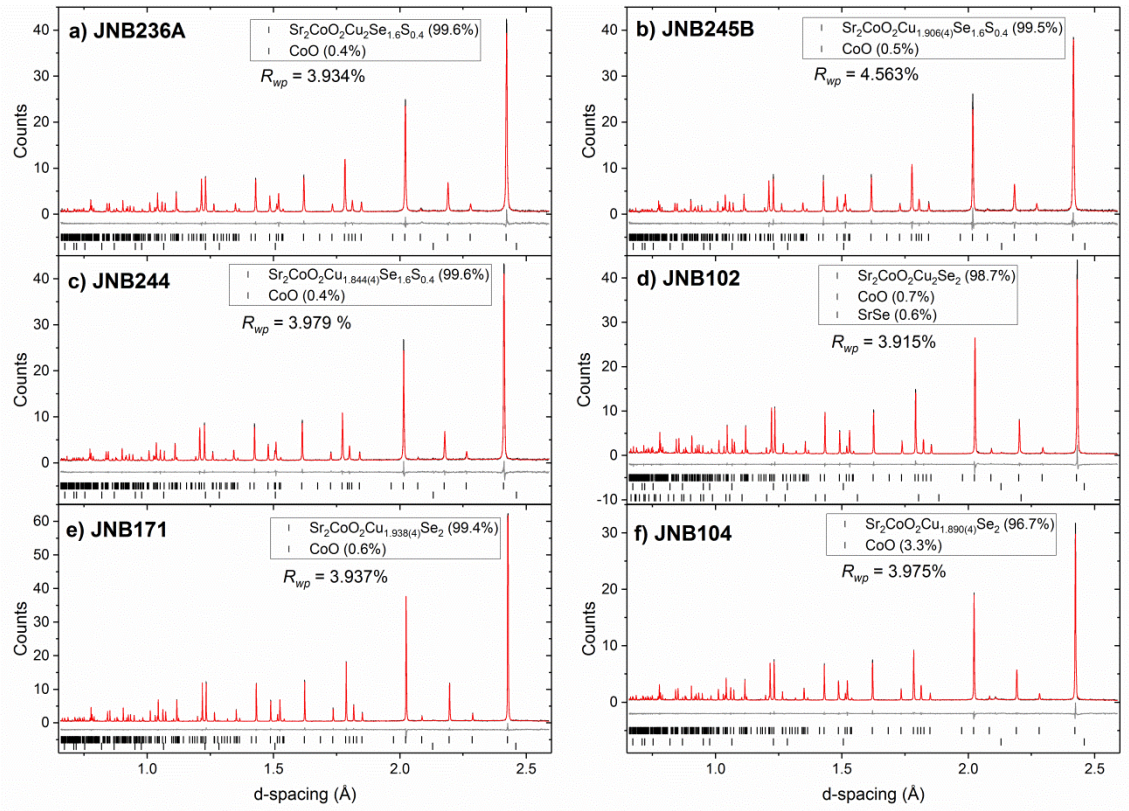


Fig. 5.4 Rietveld plots of various samples of $Sr_2CoO_2Cu_2Se_{1,6}S_{0.4}$ and $Sr_2CoO_2Cu_2Se_2$, measured using the backscattering (168.6°) bank of HRPD at RT

Table 5.2 Comparison of refined parameters for three samples of $Sr_2CoO_2Cu_{2-x}Se_{1.6}S_{0.4}$, data obtained from refinement against RT HRPD PND data. The S/Se sites were restricted to have equivalent positions and ADPs, with relative occupancy Se:S 0.8:0.2

Sample	JNB236A	JNB245B	JNB244
Radiation	Neutron, ToF		
Diffractometer	HRPD		
a (Å)	4.03900(3)	4.03183(3)	4.02608(3)
c (Å)	18.2245(1)	18.1485(2)	18.0964(1)
Volume (Å^3)	297.306(5)	295.015(6)	293.330(4)
z(Sr)	0.41107(3)	0.40996(3)	0.40915(3)
z(Se/S)	0.16859(3)	0.16837(4)	0.16819(3)
Cu occupancy	1*	0.953(2)	0.922(2)
Sr U_{11} (Å^2)	0.0082(3)	0.0082*	0.0082*
Sr U_{33} (Å^2)	0.0119(5)	0.0119*	0.0119*
Co U_{11} (Å^2)	0.0030(8)	0.0030*	0.0030*
Co U_{33} (Å^2)	0.021(2)	0.021*	0.021*
O U_{11} (Å^2)	0.0099(6)	0.0099*	0.0099*
O U_{22} (Å^2)	0.0072(6)	0.0072*	0.0072*
O U_{33} (Å^2)	0.0144(6)	0.0144*	0.0144*
Cu U_{11} (Å^2)	0.0193(5)	0.0193*	0.0193*
Cu U_{33} (Å^2)	0.0174(5)	0.0174*	0.0174*
Se/S U_{11} (Å^2)	0.0083(3)	0.0083*	0.0083*
Se/S U_{33} (Å^2)	0.0102(5)	0.0102*	0.0102*
R_{wp} (%)	3.943	4.563	3.979
χ^2	1.488	1.366	1.494

*not refined

Table 5.3 Comparison of refined parameters for three samples of $Sr_2CoO_2Cu_{2-x}Se_2$, data obtained from refinement against RT HRPD PND data

Sample	JNB102	JNB171	JNB104
Radiation	Neutron, ToF		
Diffractometer	HRPD		
a (Å)	4.04780(5)	4.04533(7)	4.04207(4)
c (Å)	18.3404(2)	18.2855(3)	18.2420(2)
Volume (Å^3)	300.501(9)	299.24(1)	298.044(4)
z(Sr)	0.41189(3)	0.41108(3)	0.41032(3)
z(Se)	0.16798(2)	0.16788(2)	0.16764(3)
Cu occupancy	1*	0.969(2)	0.945(2)
Sr U_{11} (Å^2)	0.0066(3)	0.0066*	0.0066*
Sr U_{33} (Å^2)	0.0077(5)	0.0077*	0.0077*
Co U_{11} (Å^2)	0.0020(8)	0.0020*	0.0020*
Co U_{33} (Å^2)	0.012(1)	0.012*	0.012*
O U_{11} (Å^2)	0.0054(5)	0.0054*	0.0054*
O U_{22} (Å^2)	0.0069(5)	0.0069*	0.0069*
O U_{33} (Å^2)	0.0102(6)	0.0102*	0.0102*
Cu U_{11} (Å^2)	0.0158(4)	0.0158*	0.0158*
Cu U_{33} (Å^2)	0.0141(5)	0.0141*	0.0141*
Se U_{11} (Å^2)	0.0059(3)	0.0059*	0.0059*
Se U_{33} (Å^2)	0.0086(4)	0.0086*	0.0086*
R_{wp} (%)	3.915	3.937	3.975
χ^2	1.860	1.462	1.674

*not refined

The relationship between the change in lattice parameters and Cu occupancy is shown in Fig. 5.5 (lattice parameters derived from PND data are used). The results shown here are largely analogous with the data obtained from synchrotron PXRD data.

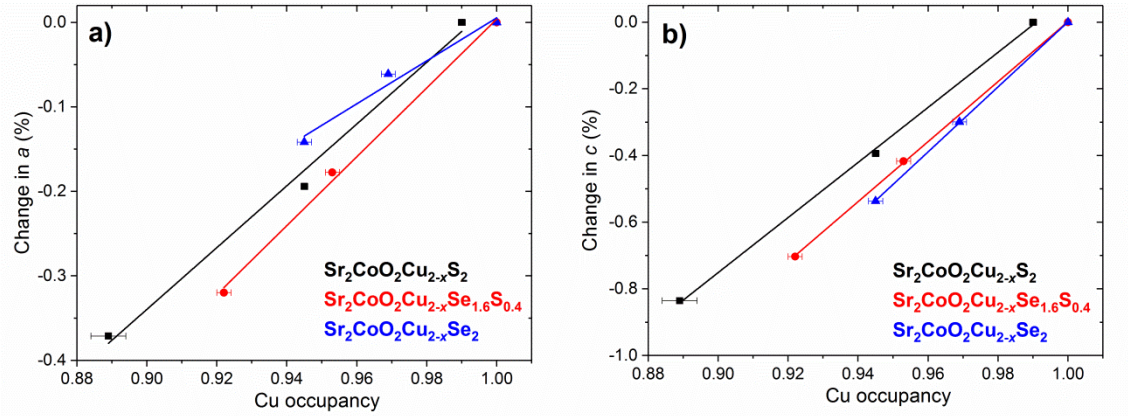


Fig. 5.5 The changes in a) lattice parameter a and b) lattice parameter c as a function of refined Cu occupancy obtained from Rietveld refinement against RT PND data, with linear fit

5.2.3 Magnetometry

Magnetometry measurements were performed on these samples to examine the effect of oxidative deintercalation on the magnetic behaviour. The changes in behaviour are likely to derive primarily from the increase in the formal Co oxidation state, but secondary effects may also follow from the small changes in geometry associated with the removal of Cu from these compounds.

The magnetic susceptibility of three samples of each of $Sr_2CoO_2Cu_{2-x}S_2$, $Sr_2CoO_2Cu_{2-x}Se_{1.6}S_{0.4}$ and $Sr_2CoO_2Cu_{2-x}Se_2$ were measured using a 3 T/4 T subtraction, as described in section 2.8. This method was used to eliminate the effects of small ferromagnetic impurities observed from the non-linearity at low field of isotherms of *M vs H* measured at 300 K. The curve was always linear above ~500 Oe, suggesting the curve had saturated, therefore this subtraction approach is likely to be a good approximation. This approach was used for all data, to make the data as comparable as possible.

All the samples described in this section have a Néel temperature (T_N) sufficiently close to room temperature that reliable Curie-Weiss analysis of the paramagnetic regime cannot be performed, using the standard magnetometer setup.

5.2.3.1 $Sr_2CoO_2Cu_{2-x}S_2$

As previously discussed, in this thesis some of the work previously performed on the $Sr_2CoO_2Cu_{2-x}S_2$ series is re-evaluated so direct comparisons with the selenide analogues can be made. As well as re-evaluating data that had already been collected, some new measurements were also performed. These were performed on three freshly prepared samples of $Sr_2CoO_2Cu_{2-x}S_2$, with lattice parameters as shown in Table 5.4. The sample JNB051 is a stoichiometric parent that has not been exposed to air (a close equivalent to DRP053, see section 5.2.4.1) and JNB086 has been treated with I_2 to remove the maximum possible amount of Cu from the system (a close equivalent to LH999, see section 5.2.4.1). JNB087 has a fractional Cu occupancy intermediate between the two.

Table 5.4 Refined lattice parameters and composition (values obtained from refinement against data from the PSD at the I11 beamline) of the samples of $Sr_2CoO_2Cu_{2-x}S_2$ which were measured using magnetic susceptibility

Sample	*a* (Å)	*c* (Å)	Volume (Å)	Composition
JNB051	3.99277(2)	17.73266(7)	282.698(2)	$Sr_2CoO_2Cu_{2.00}S_2$
JNB087	3.98014(3)	17.6132(1)	279.020(4)	$Sr_2CoO_2Cu_{1.85}S_2$
JNB086	3.975401(6)	17.56210(4)	277.548(1)	$Sr_2CoO_2Cu_{1.79}S_2$

The magnetic susceptibility of these samples is compared in Fig. 5.6.

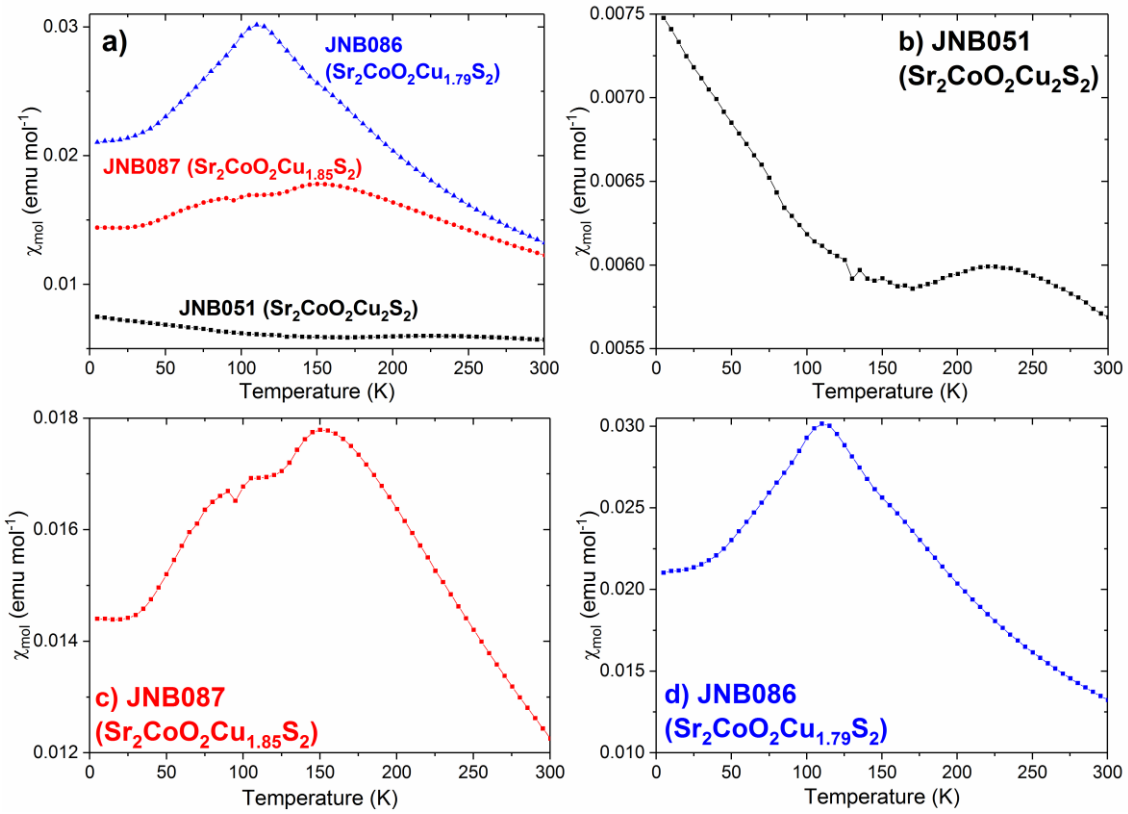


Fig. 5.6 (a) Field-cooled magnetic susceptibility of selected samples of $Sr_2CoO_2Cu_{2-x}S_2$, measured using a 4 – 3 T subtraction (described in section 2.8). The magnetic susceptibility of each sample is also shown in a separate graph (b) – d)) for clarity

Two trends are observed as a function of Cu occupancy. Firstly the temperature of the broad hump in the susceptibility, that in the parent material corresponds to T_N, appears to decrease as the Cu occupancy decreases, from ~225 K in JNB051 (parent) to ~110 K in JNB086 (most-deintercalated). It appears that JNB087 has two cusps that may correspond to two distinct magnetic ordering transitions: one at ~150 K and one at ~100 K. This may suggest that JNB087 is a mixed phase, containing a small range of Cu occupancies.

The other trend observed is that the magnitude of the magnetic susceptibility increases dramatically on removal of copper. It is possible that this is related to the magnetic disorder in the compound. It is presumed that the interactions between Co atoms in this compound are predominantly antiferromagnetic, therefore the larger the number of moments involved in long range magnetic order the lower the magnetic susceptibility will be. So, increased disorder, resulting in paramagnetic-like behaviour, may lead to the observed increase in the magnitude of magnetic susceptibility.

The magnetic susceptibility trends observed here match those previously observed by Smura *et al.*, which also shows a shift in the local susceptibility maximum from ~220 to ~100 K, when the parent sample is exposed to a flow of moist O_2.[61]

5.2.3.2 $Sr_2CoO_2Cu_{2-x}Se_{1.6}S_{0.4}$

The refined lattice parameters and composition of the $Sr_2CoO_2Cu_{2-x}Se_{1.6}S_{0.4}$ samples discussed here are shown in Table 5.5. The magnetic susceptibility of these compounds is shown in Fig. 5.7.

Table 5.5 Refined lattice parameters (obtained from refinement against synchrotron PXRD data) and composition (obtained from refinement against PND data) of the samples of $Sr_2CoO_2Cu_{2-x}Se_{1.6}S_{0.4}$ which were measured using magnetic susceptibility

Sample	*a* (Å)	*c* (Å)	Volume (Å)	Composition
JNB236A	4.04240(1)	18.23684(6)	298.009(2)	$Sr_2CoO_2Cu_{2.00}Se_{1.6}S_{0.4}$
JNB245B	4.03480(2)	18.1620(1)	295.669(4)	$Sr_2CoO_2Cu_{1.91}Se_{1.6}S_{0.4}$
JNB244	4.03041(2)	18.11465(9)	294.258(3)	$Sr_2CoO_2Cu_{1.84}Se_{1.6}S_{0.4}$

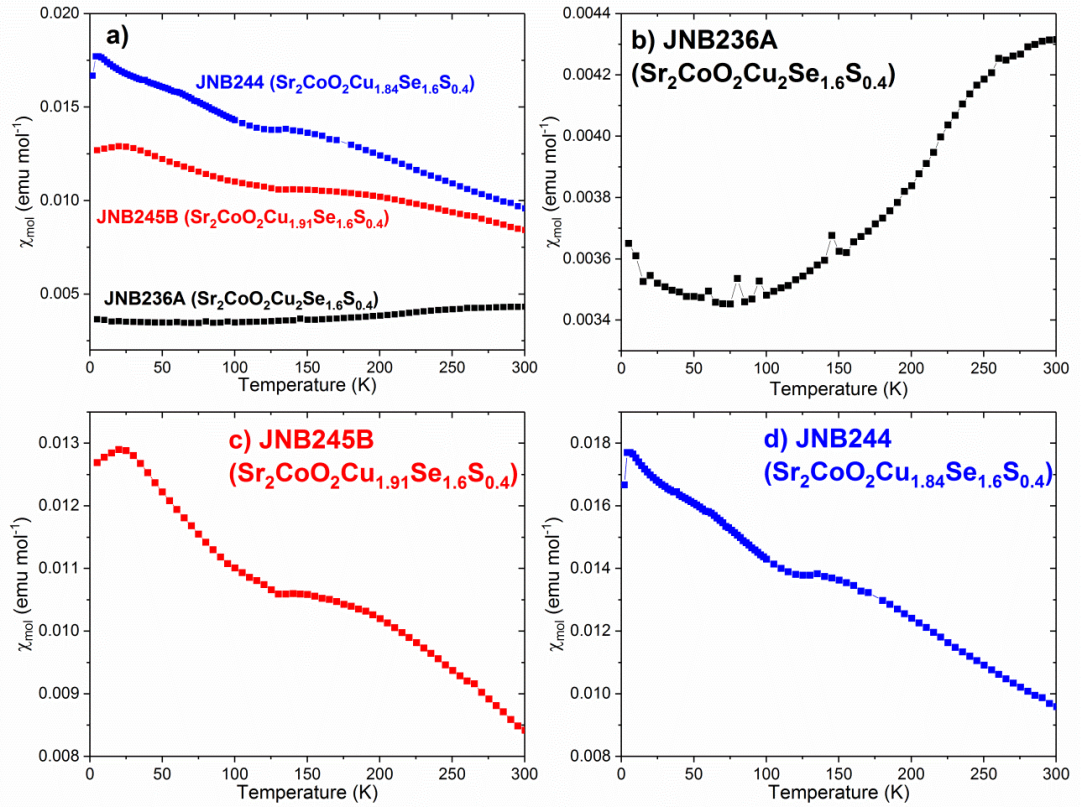


Fig. 5.7 Field-cooled magnetic susceptibility of selected samples of $Sr_2CoO_2Cu_{2-x}Se_{1.6}S_{0,4}$ measured using a 4 – 3 T subtraction (described in section 2.8). The magnetic susceptibility of each sample is also shown in a separate graph (b) – d)) for clarity

Similar trends in the magnetic susceptibility are observed as for $Sr_2CoO_2Cu_{2-x}S_2$, where the temperature where the broad maximum, suggestive of T_N, is observed decreases from >250 K in JNB236A ($Sr_2CoO_2Cu_{2.00}Se_{1.6}S_{0.4}$) to ~150 K in JNB245B ($Sr_2CoO_2Cu_{1.91}Se_{1.6}S_{0.4}$) and JNB244 ($Sr_2CoO_2Cu_{1.84}Se_{1.6}S_{0.4}$). Here, the magnetic susceptibility curves of JNB245B and JNB244 appear to be qualitatively very similar, suggesting that the two samples are magnetically very similar. The cause of the increase in the magnitude of the magnetic susceptibility is again attributed to an increase in magnetic disorder, caused by the doping of Co^{3+} ions into the Co^{2+} lattice. The data obtained for the parent is similar to that obtained by Smura for the same compound.[58]

5.2.3.3 *$Sr_2CoO_2Cu_{2-x}Se_2$*

The refined lattice parameters and compositions of the $Sr_2CoO_2Cu_{2-x}Se_2$ samples discussed here are shown in Table 5.6. The magnetic susceptibility of these compounds is shown in Fig. 5.8.

Table 5.6 Refined lattice parameters (obtained from refinement against synchrotron PXRD data) and composition (obtained from refinement against PND data) of the samples of $Sr_2CoO_2Cu_{2-x}Se_2$ which were measured using magnetic susceptibility

Sample	*a* (Å)	*c* (Å)	Volume (Å)	Composition
JNB149A	4.052021(9)	18.36000(6)	301.451(2)	$Sr_2CoO_2Cu_{2.0}Se_2$
JNB171	4.04947(1)	18.30843(6)	300.226(2)	$Sr_2CoO_2Cu_{1.94}Se_2$
JNB104	4.04513(1)	18.25662(7)	298.734(2)	$Sr_2CoO_2Cu_{1.89}Se_2$

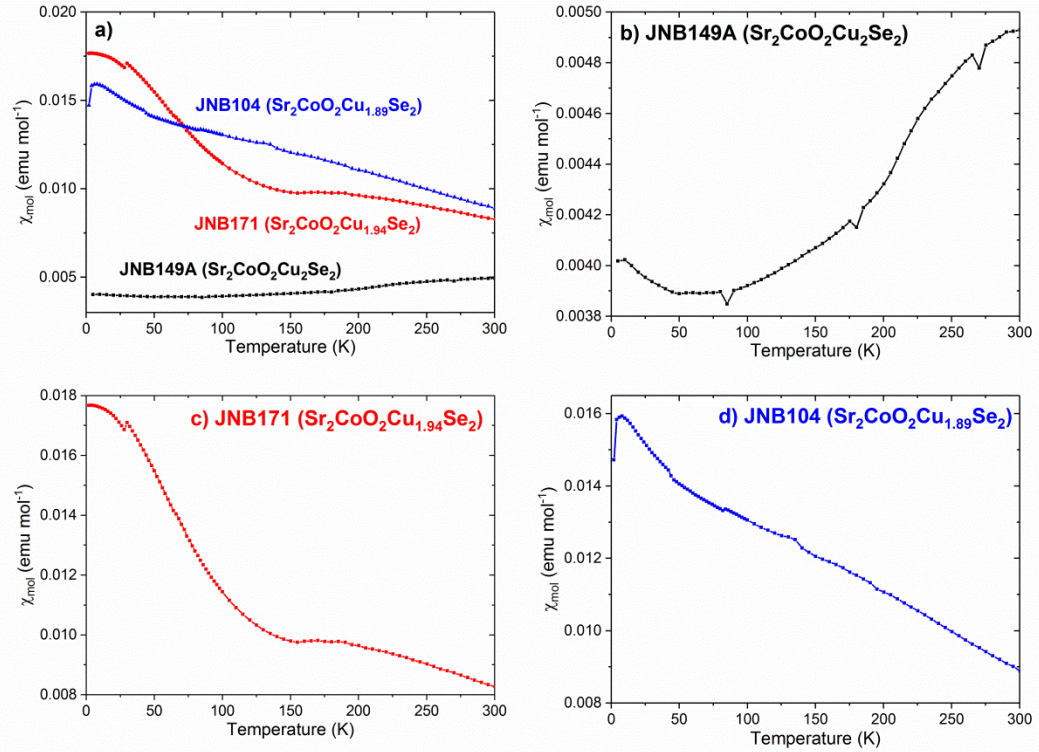


Fig. 5.8 Field-cooled magnetic susceptibility of selected samples of $Sr_2CoO_2Cu_{2-x}Se_2$, measured using a 4 – 3 T subtraction (described in section 2.8). The magnetic susceptibility of each sample is also shown in a separate graph (b) – d)) for clarity

The magnetic susceptibility of $Sr_2CoO_2Cu_{2-x}Se_2$ shows similar trends to those observed in $Sr_2CoO_2Cu_{2-x}S_2$. The broad maximum (most likely indicating T_N) shifts to lower temperature as Cu occupancy decreases, however in this case no maxima can be observed in the magnetic susceptibility curve of the most-deintercalated sample (JNB104). There is a small increase in the magnitude of the magnetic susceptibility on oxidation, though this trend is less dramatic in $Sr_2CoO_2Cu_{2-x}Se_2$ than $Sr_2CoO_2Cu_{2-x}S_2$. This may be related to the observation that significantly less Cu is removed from $Sr_2CoO_2Cu_{2-x}Se_2$, resulting in smaller changes to the average Co oxidation state.

5.2.4 Powder neutron diffraction to probe changes in magnetic ordering

As discussed in section 5.1, all the compounds described in this chapter have an ordered magnetic structure based on a $\sqrt{2}a \times \sqrt{2}a$ expansion of the nuclear unit cell in the *ab*-

plane, with the primary interaction being antiferromagnetic coupling of nearest-neighbour atoms within the CoO_2 planes. The magnetic structures of parent $Sr_2CoO_2Cu_2S_2$, $Sr_2CoO_2Cu_2Se_2$ and $Sr_2CoO_2Cu_2Se_{1.6}S_{0.4}$ were originally solved by Smura.[58] Here the magnetic ordering behaviour of several samples of each of $Sr_2CoO_2Cu_{2-x}S_2$, $Sr_2CoO_2Cu_{2-x}Se_2$ and $Sr_2CoO_2Cu_{2-x}Se_{1.6}S_{0.4}$ are compared as a function of Cu occupancy using low-temperature PND. This allows the effect of Cu occupancy on the magnetic behaviour of the compounds to be analysed further.

Smura found that the magnetic moment of these compounds had a significant component in the *ab*-plane.[61] A problem often encountered in these cases is that it becomes difficult to distinguish related magnetic models using powder diffraction, particularly when two or more directions are indistinguishable by symmetry.[145]

A famous case to consider is that of La_2CuO_4 and La_2NiO_4. In this case, shown in Fig. 5.9, the two models are identical, except that La_2CuO_4 has all magnetic spins aligned parallel to the (100) plane and in La_2NiO_4 the spins are aligned perpendicular to this plane.[146, 147]

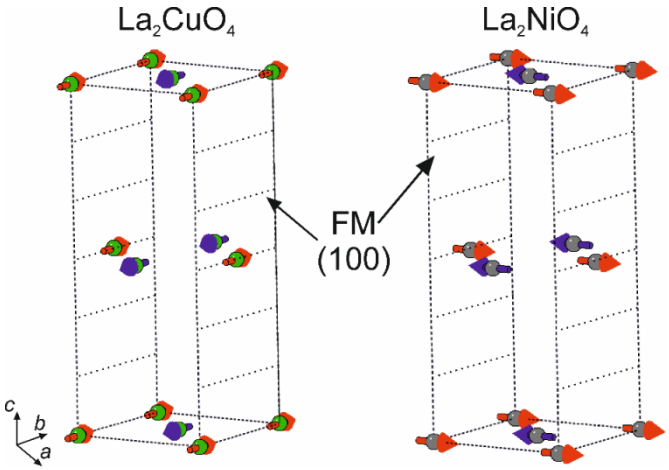


Fig. 5.9 Comparison of the magnetic structures of La_2CuO_4 and La_2NiO_4; [146, 147] *for clarity only the magnetic ions (Cu and Ni respectively) are shown*

When the spins are aligned parallel to the 100 plane, the 100 peak is present in the PND pattern; the peak is absent when the spins are aligned perpendicular to the plane. However, Smura found that although the 100 peak was present in the diffraction pattern, a La_2CuO_4-type model alone was insufficient to give a good fit to the data for $Sr_2CoO_2Cu_2S_2$.[58] Knee and Weller observed a similar phenomenon in the related compounds $Sr_2CoO_2X_2$ (where X = Br, I), here they modelled the magnetic intensity as a mixture of the La_2CuO_4 and La_2NiO_4 models.[148] However, Smura found that the

magnetic intensity could be modelled by refining the moment to have magnitude in both the *a* and *b* directions.[58] This model allows the magnetic intensity to be fitted with a single magnetic structure, greatly simplifying magnetic PND refinements; this approach is used in this chapter.

However, Smura also notes that the use of collinear spin arrangements, in which all spins are either parallel or antiparallel to one another breaks the 4-fold rotation-axis, therefore breaking tetragonal symmetry. This problem is overcome in a large number of cases where the cell is tetragonal, such as La_2CoO_4,[149] Pr_2CuO_4,[150] $NdCuO_4$[151] and $SmCuO_4$,[151] by using a non-collinear model. A non-collinear model is obtained from combination of a collinear magnetic model with a version of itself that has been rotated by 90°, as shown in Fig. 5.10. This results in a 4_2 axis and the model is thus compatible with tetragonal symmetry.

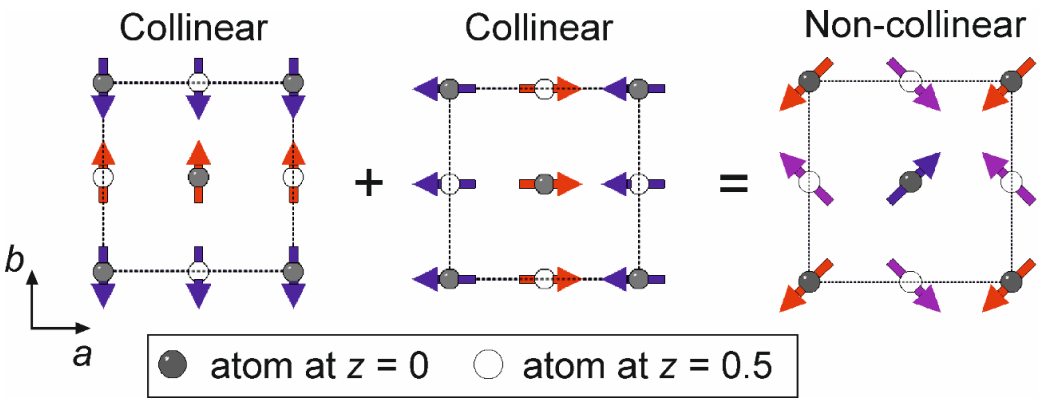


Fig. 5.10 Formation of the non-collinear magnetic model from the linear combination of two identical collinear magnetic models rotated 90° with respect to one another; for clarity, only the magnetic ions are shown and the compound is viewed down the c axis

The collinear and non-collinear spin arrangements are indistinguishable by PND; therefore, a single-crystal neutron diffraction experiment would be required to distinguish whether the magnetic arrangements of $Sr_2CoO_2Cu_2S_2$ and related compounds are collinear or non-collinear. In this thesis, the non-collinear model is used in the final analysis.

As in the rest of this thesis, the magnetic behaviour of these compounds has been modelled by the refinement of symmetry modes, using ISODISTORT,[112] interfaced with TOPAS.[99]

5.2.4.1 $Sr_2CoO_2Cu_{2-x}S_2$

The PND data analysed here was originally collected, analysed and reported by Smura *et al.*[61] and Harris.[144] It has been re-evaluated for this thesis, using symmetry mode analysis, for direct comparison with $Sr_2CoO_2Cu_{2-x}Se_2$ and $Sr_2CoO_2Cu_{2-x}Se_{1.6}S_{0.4}$.

As previously found,[58, 61] all peaks identified as magnetic peaks could be indexed using a $\sqrt{2}a \times \sqrt{2}a \times c$ expansion of the unit cell. The cell was reduced to *P*1 (1.1) symmetry and the magnetic Co symmetry modes evaluated using the data collected for DRP053 (parent $Sr_2CoO_2Cu_2S_2$, D2B data), before this model was transposed to the other two datasets (DRP053AE and LH999, see section 5.2.2.2 for composition). Initial analysis showed that the $mX2^+$, $mX3^+$ and $mX4^+$ modes added intensity to the magnetic peaks without predicting intensity where there was none in the observed diffraction pattern. These modes represented nearest-neighbour antiferromagnetic interactions in the *c*, *a* and *b* direction respectively, as shown in Fig. 5.11.

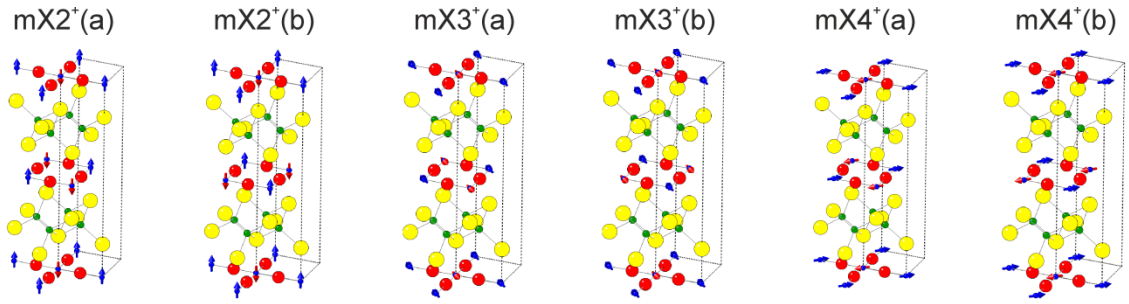


Fig. 5.11 Symmetry modes evaluated when attempting to solve the magnetic structure of $Sr_2CoO_2Cu_2S_2$; Sr atoms omitted for clarity, the dotted line outlines the nuclear unit cell

Each of $mX2^+$, $mX3^+$ and $mX4^+$ have two symmetry modes associated with them, (a) and (b), representing whether the modes are ferromagnetically coupled along the 001 plane (the (a) modes) or antiferromagnetically coupled (the (b) modes). The two $mX2^+$ modes are related to one another by a 90° rotation. As the pairs of modes gave equivalent fits to one another, only the (a) modes were evaluated further. The $mX3^+$ and $mX4^+$ modes are closely related to one another, but $mX3^+$ leads to magnetic moment with a component in the *a*-direction and $mX4^+$ leads to magnetic moment with a component in the *b*-direction.

No single mode ($mX2^+$(a), $mX3^+$(a) or $mX4^+$(a)) gave a good fit to the data alone, so combinations of modes were evaluated. The best fit to the magnetic intensity was achieved when both the $mX3^+$(a) and $mX4^+$(a) modes were refined. Little improvement to the fit was achieved when $mX2^+$(a) was also refined, as is shown in Table 5.7 and the

refined magnitude of the magnetic moment was the same within error. Therefore, $mX3^+(a)$ and $mX4^+(a)$ were refined alone. This contrasts with the magnetic structure found by Smura *et al.*[61], which refined a small moment in the *c*-direction, analogous to the "$mX2^+(a)$ + $mX3^+(a)$ + $mX4^+(a)$" model, as shown in Table 5.7.

Table 5.7 Contrasting refined parameters when the $mX2^+(a)$ symmetry mode is fixed at zero and when it is refined for DRP053 (parent $Sr_2CoO_2Cu_2S_2$, data obtained from ref. 61). This is also compared with the values obtained for refinement against the same data when the analysis was performed by Smura et al.[61]

Sample	DRP053 unexposed		
Composition	$Sr_2CoO_2Cu_{1.980(2)}S_2$		
Radiation	Neutron, λ = 1.593 Å		
Diffractometer	D2B		
Temperature (K)	5		
Symmetry modes refined	$mX3^+$ + $mX4^+$	$mX2^+$ + $mX3^+$ + $mX4^+$	Smura *et al.*[61] Analysis
μ_a (μ_B)	2.74(6)	2.66(7)	2.85(7)
μ_b (μ_B)	2.32(6)	2.24(8)	2.42(7)
μ_c (μ_B)	0*	0.8(2)	0.9(2)
$\|\mu\|$ (μ_B)	3.59(6)	3.57(9)	3.85(6)
R_{wp} (%)	6.092	6.087	-
χ^2	0.658	0.657	-

*not refined

Refining only the $mX3^+(a)$ and $mX4^+(a)$ modes allows the magnetic structure of DRP053 (parent $Sr_2CoO_2Cu_2S_2$) to be refined in the P_C4_2/n (86.73) magnetic space group. This space group is tetragonal and therefore refines the magnetic moment in a non-collinear manner, as shown in Fig. 5.12.

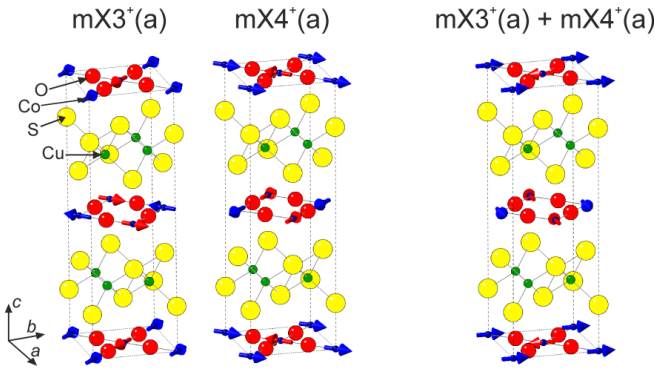


Fig. 5.12 The symmetry modes refined in the P_C4_2/n (86.73) magnetic space group; the dotted lines outline the expanded magnetic cell and the Sr atoms have been omitted for clarity. The diagram on the right hand side represents the magnetic model used for this series

This model was also used to fit the PND data for DRP053AE ($Sr_2CoO_2Cu_{1.89(1)}S_2$) and LH999 ($Sr_2CoO_2Cu_{1.78(1)}S_2$), achieving a good fit. The Rietveld plots of these refinements are shown in Fig. 5.13 and the refined parameters compared in Table 5.8.

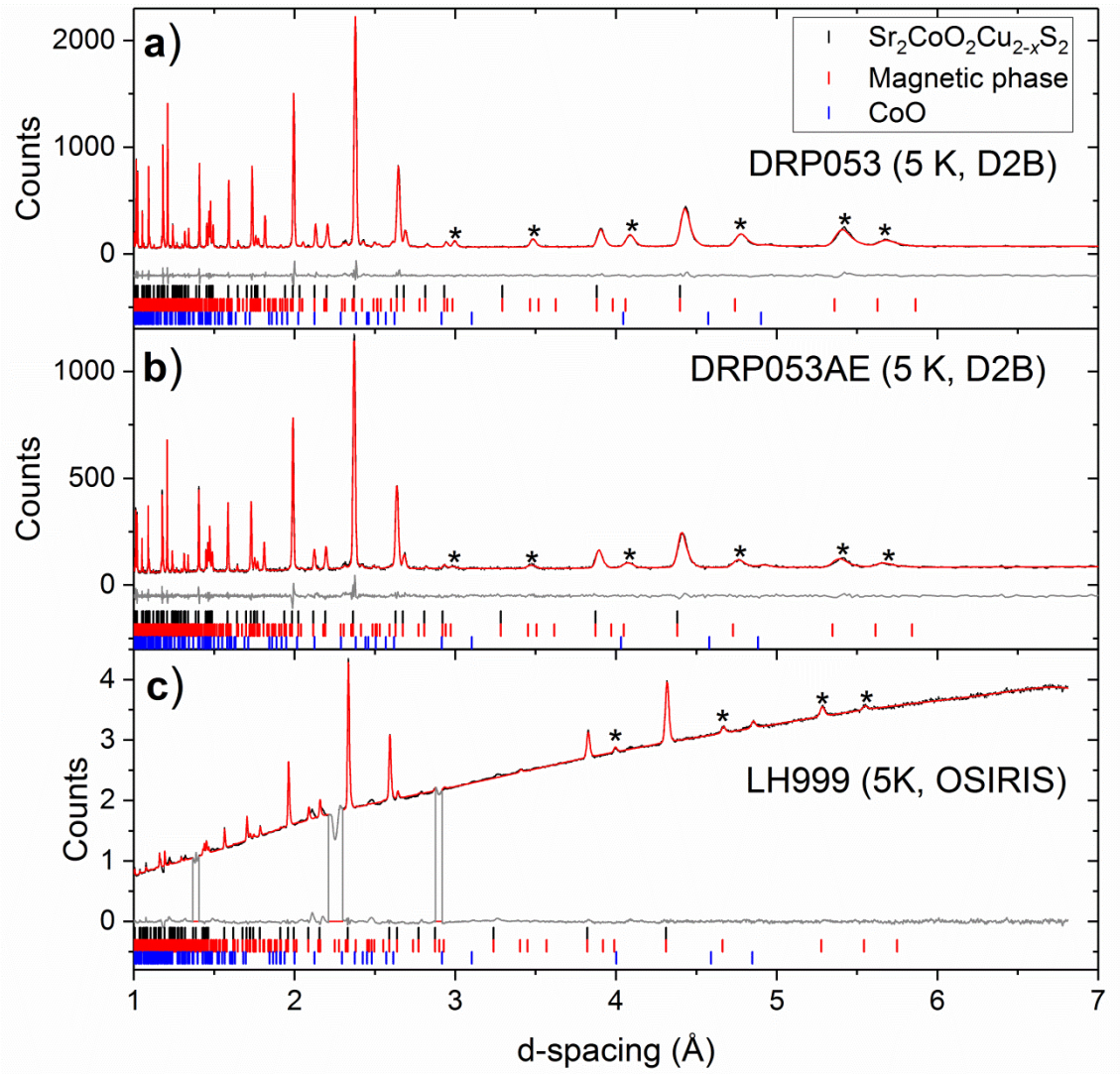


*Fig. 5.13 Rietveld plots of the refinement of the magnetic structure of various samples of $Sr_2CoO_2Cu_{2-x}S_2$ measured using PND: a) DRP053 (parent $Sr_2CoO_2Cu_{1.980(2)}S_2$), measured using D2B at 5 K, b) DRP053AE ($Sr_2CoO2Cu_{1.89(1)}S_2$), measured using D2B at 5 K and c) LH999 ($Sr_2CoO_2Cu_{1.78(1)}S_2$), measured using OSIRIS at 5 K. Magnetic peaks are emphasised by * symbols*

Table 5.8 Refined Co^{2+} magnetic moment components of $Sr_2CoO_2Cu_{2-x}S_2$ from PND data measured at 5 K. Data obtained from ref. 61 and ref. 144

Sample	DRP053 unexposed	DRP053 moist O_2 exposed	LH999
Composition	$Sr_2CoO_2Cu_{1.980(2)}S_2$	$Sr_2CoO_2Cu_{1.890(2)}S_2$	$Sr_2CoO_2Cu_{1.78(1)}S_2$
Radiation	Neutron, λ = 1.593 Å	Neutron, λ = 1.593 Å	Neutron, ToF
Diffractometer	D2B	D2B	OSIRIS
Temperature (K)	5	5	5
μ_a (μ_B)	0.30(6)	0.0(1)	0.14(1)
μ_b (μ_B)	3.59(6)	2.6(1)	1.74(3)
$\lvert\mu\rvert$ (μ_B)	3.60(6)	2.6(1)	1.75(3)
R_{wp} (%)	6.040	5.545	0.941
χ^2	0.652	0.538	-

As observed from the Rietveld fit in Fig. 5.13 c), the PND data obtained for LH999 from OSIRIS is of comparatively poor quality. However, it is considered to be good enough to compare trends of overall ordered magnetic moment in these compounds.

The overall loss of ordered magnetic moment from the parent sample (DRP053 unexposed) to the I_2 oxidised sample (LH999) is ~50%, accompanying the small change in the formal oxidation state of the Co ions from $Co^{2.0+}$ in DRP053 (unexposed) to $Co^{2.2+}$ in LH999 (value obtained from Cu occupancies). This suggests that loss of ordered moment is not solely due to loss of unpaired spin from oxidation of some of the Co^{2+} to Co^{3+} ions. A standard magnetic Rietveld refinement constrains the magnetic phase fraction to be equal to the phase fraction of the nuclear sample, preventing over-correlation of parameters in the refinement. However, as suggested by the magnetic susceptibility measurements in section 5.2.3.1, it is also possible that the introduction of different oxidation states into the $[CoO_2]$ planes introduces disorder and therefore regions where long-range magnetic ordering is not observed.

If it assumed that the parent compound (DRP053, unexposed) is 100% ordered and that the magnetic moment of each Co ion is the same in every compound (a reasonable approximation given the small degree of oxidation that has occurred), then the relative "total ordered phase fraction" of the deintercalated compounds may be calculated by:

$$Total\ ordered\ phase\ fraction\ (\%) = 100\ \times \left(\frac{|\mu|}{|\mu|_{parent}}\right)^2 \qquad (5.1)$$

This is because the intensity of magnetic peaks scales with the square of the magnetic moment, but linearly with the percentage of the phase that is magnetically ordered. The results of this treatment are shown in Table 5.9.

Table 5.9 Comparison of the "total ordered phase fraction" for samples of $Sr_2CoO_2Cu_{2-x}S_2$

Sample	DRP053 (unexposed)	DRP053AE (moist O_2 exposed)	LH999
Composition	$Sr_2CoO_2Cu_{1.980(2)}S_2$	$Sr_2CoO_2Cu_{1.890(2)}S_2$	$Sr_2CoO_2Cu_{1.78(1)}S_2$
Total ordered phase fraction (%)	100	52(4)	24(1)

This model is thought to simulate the real magnetic behaviour of these samples more closely and shows the sharp drop off in ordered magnetic behaviour as a function of the decrease in Cu occupancy.

5.2.4.2 $Sr_2CoO_2Cu_{2-x}Se_2$

Three 3 – 4 g samples of $Sr_2CoO_2Cu_{2-x}Se_2$ were measured at 5 K on OSIRIS and HRPD. The samples measured were the same as those measured using HRPD at RT (see section 5.2.2.2).

Additional peaks were present in the low temperature PND pattern of samples of $Sr_2CoO_2Cu_{2-x}Se_2$ that were not present in equivalent PXRD patterns. These were assigned as magnetic peaks. All these peaks could be indexed using a $\sqrt{2}a \times \sqrt{2}a \times 2c$ expansion of the nuclear cell.

5.2.4.2.1 Magnetic structure of parent $Sr_2CoO_2Cu_2Se_2$

As described in section 5.1, Smura indexed the magnetic intensity of parent $Sr_2CoO_2Cu_2Se_2$ using a two-magnetic-phase model, in which one phase was modelled using a $\sqrt{2}a \times \sqrt{2}a \times 2c$ expansion of the nuclear cell (the "$2c$" model) and one phase was modelled using a $\sqrt{2}a \times \sqrt{2}a \times c$ expansion (the "c" model).[58] However, here ISODISTORT,[112] interfaced with TOPAS[99] is used to solve the magnetic structure of $Sr_2CoO_2Cu_2Se_2$ using a single magnetic model. The quality of the refinement using this model is then compared with the Smura model before analysis of the low-temperature PND patterns of the deintercalated $Sr_2CoO_2Cu_{2-x}Se_2$ samples.

The structure was initially analysed in magnetic space group $P1$ (1.1) with a $\sqrt{2}a \times \sqrt{2}a \times 2c$ expansion of the nuclear cell so that all possible magnetic modes and combination of modes could be considered. No single mode could be used to fit the magnetic

intensity of all the peaks satisfactorily; therefore, various combinations of modes were considered. It was found that five sets of modes resulted in non-zero intensity on the magnetic peaks of $Sr_2CoO_2Cu_2Se_2$ without modelling additional intensity where no peak intensity is observed in the measured pattern. These modes were the $mX2^+$, $mX3^+$, $mX4^+$ (analogous to the modes used to model the magnetic structure of $Sr_2CoO_2Cu_2S_2$), mP4 and mP5 modes. These modes are shown schematically in Fig. 5.14.

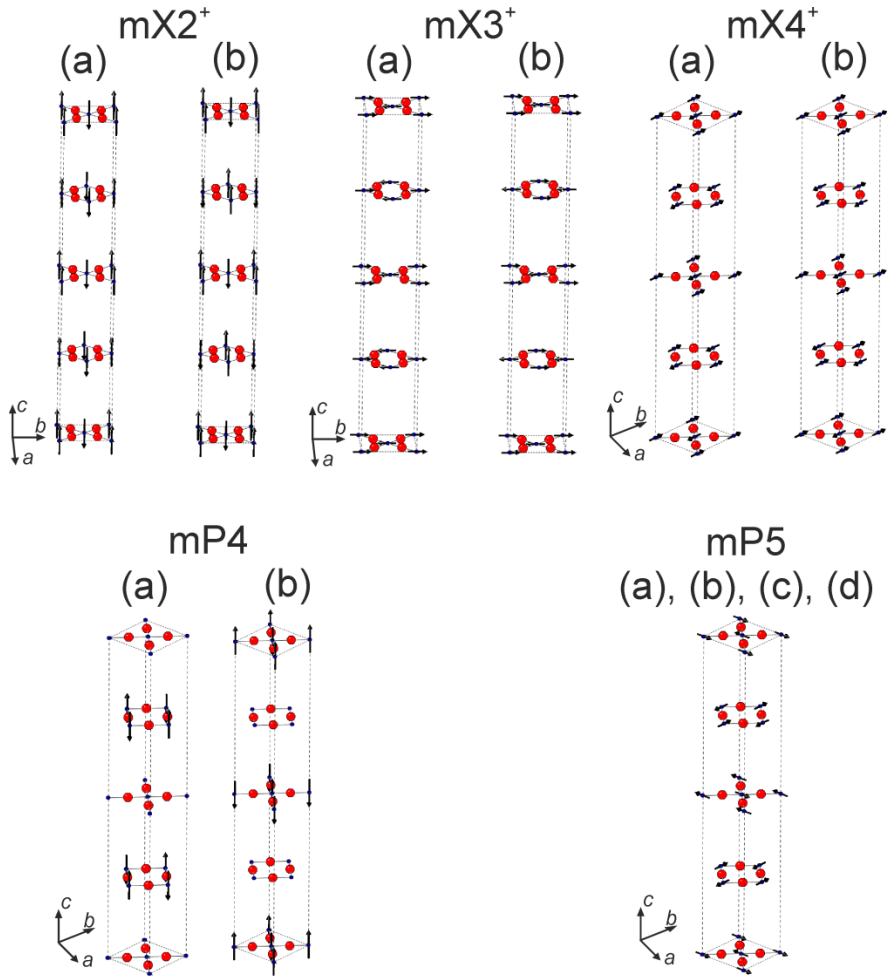


Fig. 5.14 Schematic of the magnetic symmetry modes considered in the refinement of the magnetic structure of $Sr_2CoO_2Cu_2Se_2$. For clarity only the Co (blue) and O (red) atoms are shown. The dotted lines outline the expanded magnetic unit cell

As was the case with $Sr_2CoO_2Cu_2S_2$, the pairs of modes mXn^+(a) and mXn^+(b) (where n = 2, 3, 4) were found to give equivalent fits to one another, so only the (a) modes were evaluated further. Refinement of the mP4(a) and mP4(b) modes separately led to over-correlation between the modes, therefore these modes were refined with the constraint mP4(a) = mP4(b). As previously stated for $Sr_2CoO_2Cu_2S_2$, $mX3^+$ and $mX4^+$ are closely related symmetry modes, but one mode leads to a magnetic component in the *a*-direction and the other in the *b*-direction.

The four possible mP5 modes (mP5 (a), (b), (c) and (d)) are equivalent, but rotated by 90° with respect to one another. Therefore, only one mP5 mode was used in the refinement.

The first model considered was that where all possible modes that added intensity to the magnetic peaks (without over-correlating with one another) were refined simultaneously, i.e. the following modes and constraints: $mX2^{+}$(a), $mX3^{+}$(a), $mX4^{+}$(a), mP4(a) = mP4(b) and mP5(a). This model was called model 1 and refinement of these modes led to a good fit to the data. The Rietveld fit obtained using this model and a representative magnetic structure is shown in Fig. 5.15. The resultant refined magnetic parameters are shown in Table 5.10.

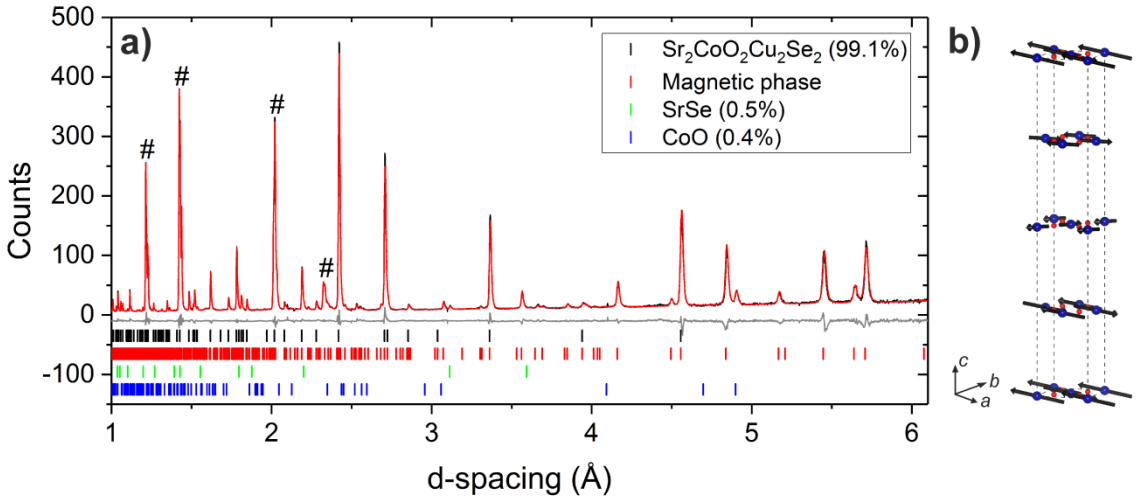


Fig. 5.15 a) Rietveld plot of JNB102 (parent $Sr_2CoO_2Cu_2Se_2$) measured using OSIRIS at 5 K and refined using model 1 (all reasonable magnetic symmetry modes relaxed). The four main peaks arising from the sample environment (primarily the Al-tailed cryostat) are indicated by # symbols. b) Shows the refined magnetic structure of model 1, for clarity only the Co (blue) and O (red) atoms are shown and the dotted lines outline the expanded magnetic unit cell

Table 5.10 Results of Rietveld refinement of the magnetic structure of $Sr_2CoO_2Cu_2Se_2$ (JNB102) using model 1 (all reasonable magnetic symmetry modes refined). The model was refined against combined HRPD/OSIRIS data, measured at 5 K

Atom	μ_a (μ_B)	μ_b (μ_B)	μ_c (μ_B)	$\|\mu\|$ (μ_B)
Co1 (0, 0, 0)	1.84(3)	-4.02(5)	1.1(2)	4.55(6)
Co2 (0.5, 0.5, 0)	-1.84(3)	4.02(5)	-1.1(2)	4.55(6)
Co3 (0, 0.5, 0.25)	3.20(6)	-2.65(3)	1.1(2)	4.30(6)
Co4 (0.5, 0, 0.25)	-3.20(6)	2.65(3)	-1.1(2)	4.30(6)
Co5 (0, 0, 0.5)	1.84(3)	-1.29(5)	0.1(2)	2.25(4)
Co6 (0.5, 0.5, 0.5)	-1.84(3)	1.29(5)	-0.1(2)	2.25(4)
Co7 (0, 0.5, 0.75)	0.47(6)	-2.65(3)	0.1(2)	2.70(3)
Co8 (0.5, 0, 0.75)	-0.47(6)	2.65(3)	-0.1(2)	2.70(3)
R_{wp} (%)	4.095			
χ^2	2.208			

It seems unreasonable that there would be such large differences between the magnitudes and directions of the magnetic moments in a compound that nominally consists of chemically identical $Co^{2.0+}$ ions. These differences arise due to the relationship between different types of modes (such as the mP4 and $mX2^+$ modes) that result in components in the same direction (in this case the *c*-direction).

Therefore, a second model (model 2) was considered in which the $mX2^+$(a) and mP5 modes were fixed at zero. In this way, refinement of the mP4 modes led to the magnetic component in *c*, while refinement of the $mX3^+$ and $mX4^+$ modes led to the magnetic component in the *ab*-plane and therefore constraining the magnitude of the magnetic moments to be identical for every Co ion in the model. This gave a good fit, shown in Fig. 5.16 (with representative magnetic structure) and Table 5.11, but the R_{wp} is slightly higher than model 1, arising from imperfect fitting of the high *d*-spacing magnetic peaks.

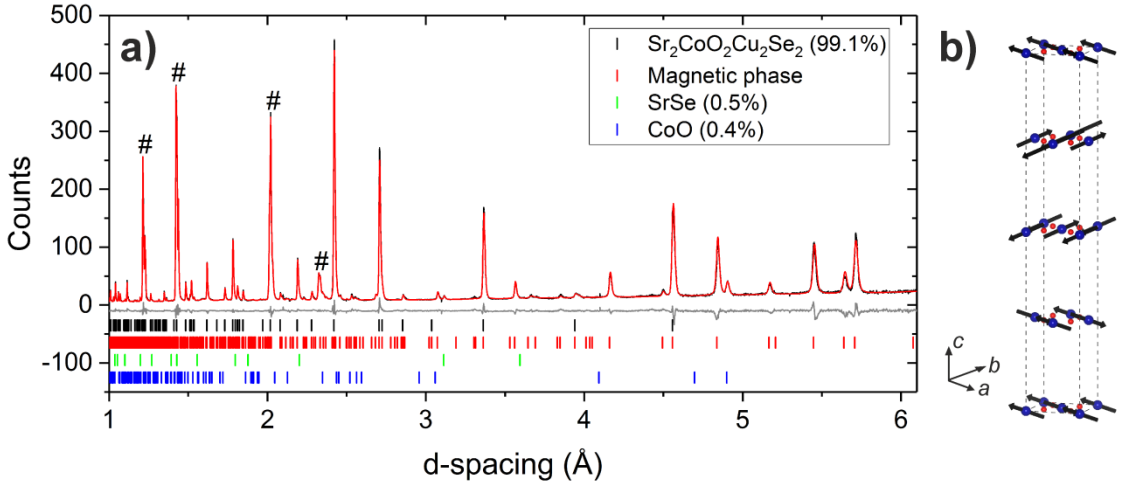


Fig. 5.16 a) Rietveld plot of $Sr_2CoO_2Cu_2Se_2$ (JNB102) refined using model 2 ($mX3^+(a)$ + $mX4^+(a)$ + mP4). The sample was measured using OSIRIS at 5 K. The four main peaks arising from the sample environment (primarily the Al-tailed cryostat) are indicated by # symbols. b) Shows the refined magnetic structure of model 2, for clarity only the Co (blue) and O (red) atoms are shown and the dotted lines outline the expanded magnetic unit cell

Table 5.11 Results of Rietveld refinement of the magnetic structure of $Sr_2CoO_2Cu_2Se_2$ (JNB102) using model 2 ($mX3^+(a)$ + $mX4^+(a)$ + mP4). The model was refined against combined HRPD/OSIRIS data, measured at 5 K

Atom	μ_a (μ_B)	μ_b (μ_B)	μ_c (μ_B)	$\lvert\mu\rvert$ (μ_B)
Co1 (0, 0, 0)	1.87(3)	-2.67(2)	1.24(2)	3.49(2)
Co2 (0.5, 0.5, 0)	-1.87(3)	2.67(2)	-1.24(2)	3.49(2)
Co3 (0, 0.5, 0.25)	1.87(3)	-2.67(2)	1.24(2)	3.49(2)
Co4 (0.5, 0, 0.25)	-1.87(3)	2.67(2)	-1.24(2)	3.49(2)
Co5 (0, 0, 0.5)	1.87(3)	-2.67(2)	-1.24(2)	3.49(2)
Co6 (0.5, 0.5, 0.5)	-1.87(3)	2.67(2)	1.24(2)	3.49(2)
Co7 (0, 0.5, 0.75)	1.87(3)	-2.67(2)	-1.24(2)	3.49(2)
Co8 (0.5, 0, 0.75)	-1.87(3)	2.67(2)	1.24(2)	3.49(2)
R_{wp} (%)	4.139			
χ^2	2.231			

The difference in the fit between model 1 and model 2 is shown in Fig. 5.17. It shows that the use of model 2 leads to imperfect fitting of the 011 and 015 magnetic peaks compared with model 1.

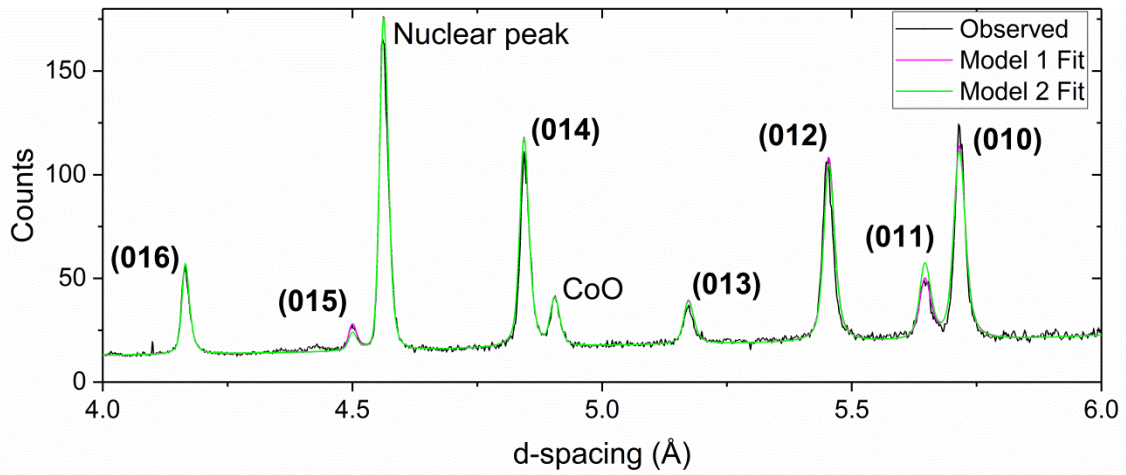


Fig. 5.17 Comparison of the fit to the high d-spacing magnetic peaks of JNB102 ($Sr_2CoO_2Cu_2Se_2$, measured at 5 K using OSIRIS) when model 1 and model 2 are used

Attempts to fit the data using models with a single mXn^+ (n = 3, 4) mode, or in which just the mX2$^+$ and mP5 modes (or a combination of) were used led to a poorer fit to the data. No further improvement to the fit to the data could be found without causing large differences in the magnitude of different magnetic moments in the same model (as was observed for the model 1 fit). Therefore, model 2 was chosen as the most reasonable model (with equal magnetic moment on each Co ion) that gave an acceptable fit to the data, although the possibility of a further nuance in the magnetic structure, unaccounted for in model 2, cannot be ruled out.

A higher symmetry magnetic space group was searched for, in which the desired magnetic modes could be relaxed. The highest symmetry space group found was P_C4_1 (76.11). This space group allows the refinement of three magnetic modes: mX3$^+$, mX4$^+$ and mP4, shown schematically in Fig. 5.18. The origin of the unit cell is shifted by (0, ½, 0). This model was called model 3.

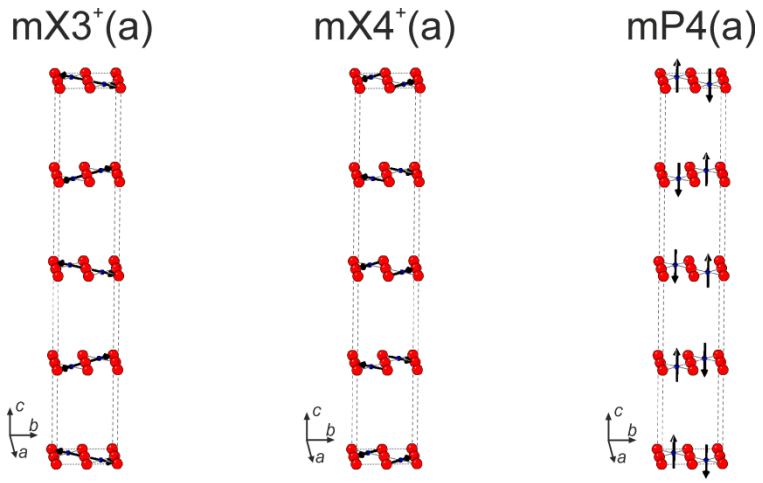


Fig. 5.18 Schematic of the possible magnetic symmetry modes in the magnetic space group P_C4_1 (76.11), for clarity only the Co (blue) and O (red) atoms are shown. The dotted lines outline the expanded magnetic unit cell

Refining the magnetic structure of $Sr_2CoO_2Cu_2Se_2$ (JNB102) in this magnetic space group produced an equivalent fit and equivalent results as when the refinement was performed in *P*1 (1.1) (i.e. model 2), as shown in Table 5.12.

Table 5.12 Results of Rietveld refinement of the magnetic structure of $Sr_2CoO_2Cu_2Se_2$ (JNB102) using model 3 ($mX3^+(a)$ + $mX4^+(a)$ + mP4 in magnetic space group P_C4_1 (76.11)). The model was refined against combined HRPD/OSIRIS data, measured at 5 K

Atom	μ_a (μ_B)	μ_b (μ_B)	μ_c (μ_B)	$\lvert\mu\rvert$ (μ_B)
Co1 (0.75, 0.75, 0)	3.22(2)	-0.56(2)	1.25(2)	3.50(2)
R_{wp} (%)	4.139			
χ^2	2.231			

The PND pattern (HRPD and OSIRIS) of $Sr_2CoO_2Cu_2Se_2$ was also analysed using the model devised by Smura (here called the Smura model) in order to compare the quality of the fit with the new model.[58] In order to directly compare the two models, all other parameters, such as the nuclear cell, impurities indexed and the peak-shape functions used were kept the same. In this model, two magnetic structures are constructed in *P*1 (1.1) symmetry with the constraints shown in Table 5.13. These two magnetic structures were initially modelled as if both structures were fully ordered over the whole of the nuclear phase.

This initial refinement produced a good fit to the data, but is physically meaningless. Therefore the two structures were scaled so that the "*c*":"2*c*" phase fraction could be refined iteratively until the phase fraction where $|\mu|_{\text{“}c\text{”}} = |\mu|_{\text{“}2c\text{”}}$ was found. This was considered to be the end point of the refinement because it was assumed that the

magnitude of the magnetic moment would be approximately the same in both magnetic structures. The Rietveld fit of this refinement is shown in Fig. 5.19 and the results of the model shown in Table 5.13.

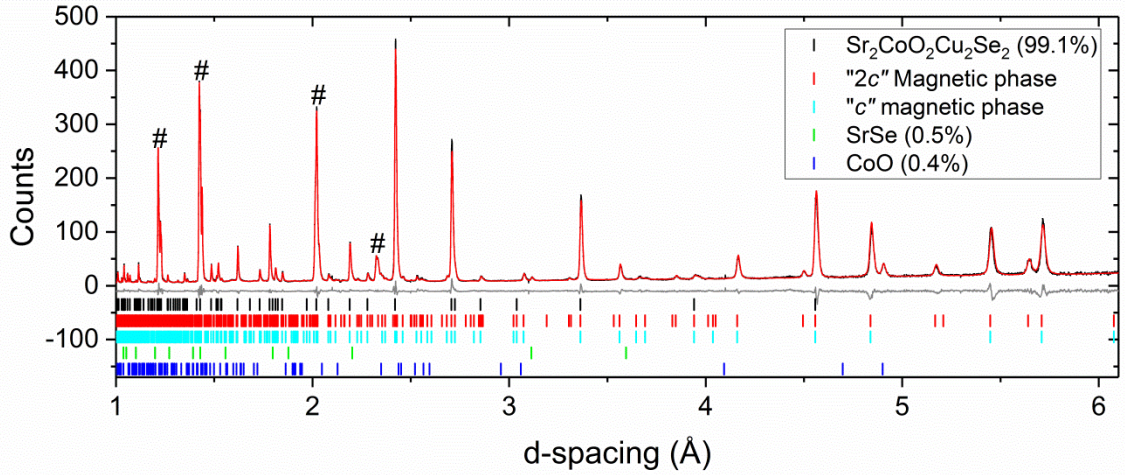


Fig. 5.19 Rietveld plot of $Sr_2CoO_2Cu_2Se_2$ (JNB102) refined using the Smura two-phase model.[58] The sample was measured using OSIRIS at 5 K. The four main peaks arising from the sample environment (primarily the Al-tailed cryostat) are indicated by # symbols

Table 5.13 Results of Rietveld refinement of the magnetic structure of $Sr_2CoO_2Cu_2Se_2$ (JNB102) using the Smura two-phase model.[58] The model was refined against combined HRPD/OSIRIS data, measured at 5 K

Atom	μ_a (μ_B)	μ_b (μ_B)	μ_c (μ_B)	$\lvert\mu\rvert$ (μ_B)
"*c*" magnetic structure (72% of sample)				
Co1 (0, 0, 0)	3.14(3)	2.18(4)	0.7(2)	3.88(4)
Co2 (0.5, 0.5, 0)	-3.14(3)	-2.18(4)	-0.7(2)	3.88(4)
Co3 (0.5, 0, 0.5)	3.14(3)	2.18(4)	0.7(2)	3.88(4)
Co4 (0, 0.5, 0.5)	-3.14(3)	-2.18(4)	-0.7(2)	3.88(4)
"2*c*" magnetic structure (28% of sample)				
Co1 (0, 0, 0)	-2.59(9)	0*	0.9(2)	3.9(2)
Co2 (0.5, 0.5, 0)	2.59(9)	0*	-0.9(2)	3.9(2)
Co3 (0, 0.5, 0.25)	0*	2.59(9)	0.9(2)	3.9(2)
Co4 (0.5, 0, 0.25)	0*	-2.59(9)	-0.9(2)	3.9(2)
Co5 (0, 0, 0.5)	2.59(9)	0*	-0.9(2)	3.9(2)
Co6 (0.5, 0.5, 0.5)	-2.59(9)	0*	0.9(2)	3.9(2)
Co7 (0, 0.5, 0.75)	0*	-2.59(9)	-0.9(2)	3.9(2)
Co8 (0.5, 0, 0.75)	0*	2.59(9)	0.9(2)	3.9(2)
R_{wp} (%)	4.095			
χ^2	2.207			

*not refined

These results show that the Smura model produces an equivalent fit to that obtained for model 1. The refined ratio of the phases is 72% "*c*" magnetic structure and 28% "2*c*" magnetic structure.

At this point it is useful to contrast the three models presented here: model 1, model 2/3 (models 2 and 3 are equivalent, but in different magnetic space groups) and the Smura model. To do this, the magnetic structures arising from the different models are compared in Fig. 5.20.

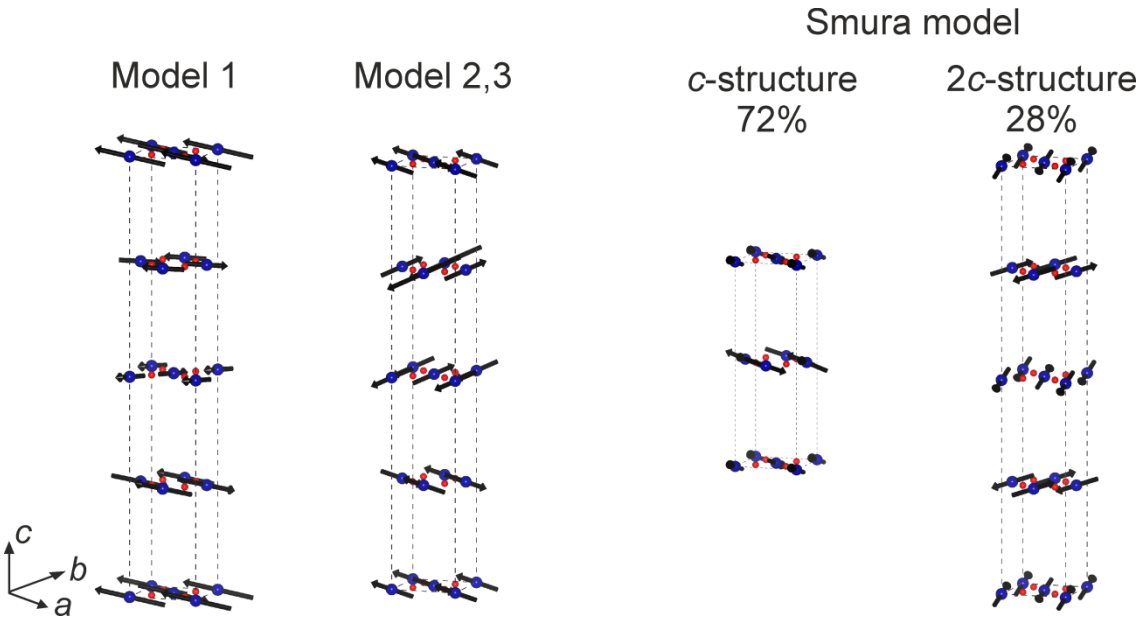


Fig. 5.20 Comparison of the possible magnetic ordering structures of $Sr_2CoO_2Cu_2Se_2$: Model 1 (all reasonable modes) Model 2, 3 ($mX3^+$, $mX4^+$ and mP4 modes) and the Smura model (two magnetic structures with different sized unit cells)

These models may also be compared in terms of the symmetry modes activated to make up the model, as is shown in Table 5.14. The symmetry modes that comprise the two magnetic structures described by the Smura model were also found using ISODISTORT.[112]

Table 5.14 Comparison of the magnetic symmetry modes used to construct the various magnetic models used to describe the magnetic ordering behaviour of $Sr_2CoO_2Cu_2Se_2$

Magnetic Model	Unit cell expansion	Symmetry modes
Model 1	$\sqrt{2}a \times \sqrt{2}a \times 2c$	$mX2^+(a) + mX3^+(a) + mX4^+(a) + mP4(a) + mP4(b) + mP5(a)$
Model 2, 3	$\sqrt{2}a \times \sqrt{2}a \times 2c$	$mX3^+(a) + mX4^+(a) + mP4(a) + mP4(b)$
Smura model	$\sqrt{2}a \times \sqrt{2}a \times c$ (72%)	$mX2^+(a) + mX3^+(a) + mX4^+(a)$
	$\sqrt{2}a \times \sqrt{2}a \times 2c$ (28%)	$mP4(a) + mP4(b) + mP5(a)$

Table 5.14 shows that model 1 and the Smura model are likely closely related models, because they activate the same symmetry modes, although in the Smura model the modes are separated into two separate magnetic structures, depending on the period of the symmetry mode (c for the mXn^+ modes and $2c$ for the mPn modes). This is possible

because activation of the mXn^+ modes and the mP*n* modes leads to intensity on different magnetic peaks, as shown in Fig. 5.21.

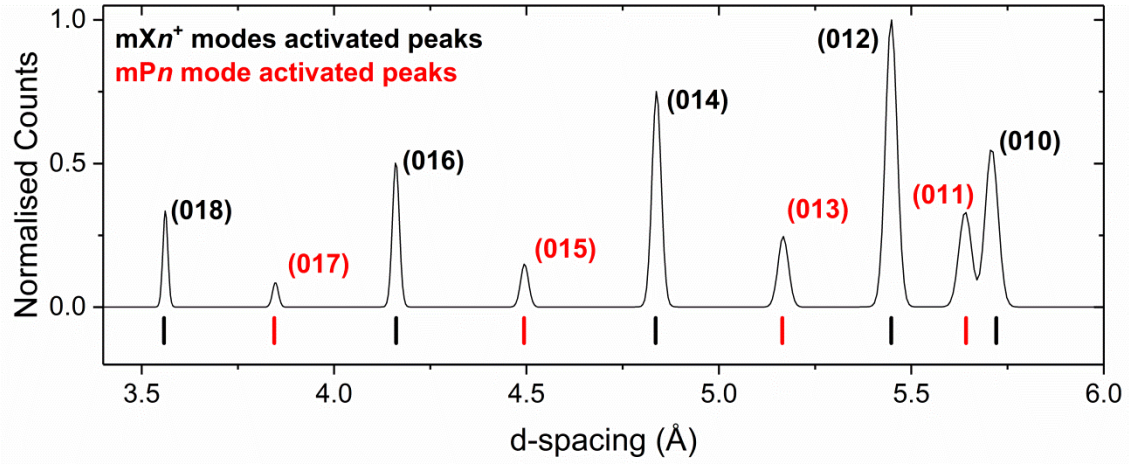


Fig. 5.21 Simulated PND pattern of the magnetic peaks of $Sr_2CoO_2Cu_2Se_2$, distinguishing those peaks that can be modelled using mXn^+ modes and those that can be modelled using mPn modes in the range 3.4 ≤ d (Å) ≤ 6.0. For clarity only magnetic peaks are shown. The peaks are indexed using the expanded magnetic unit cell (√2a ×√2a × 2c)

Combining the Smura model into a single magnetic structure (by multiplication of the different components of the magnetic moment of equivalent atoms with one another, weighted by the refined phase fractions) indeed results in a magnetic structure that has very similar character to model 1, as shown in Fig. 5.22.

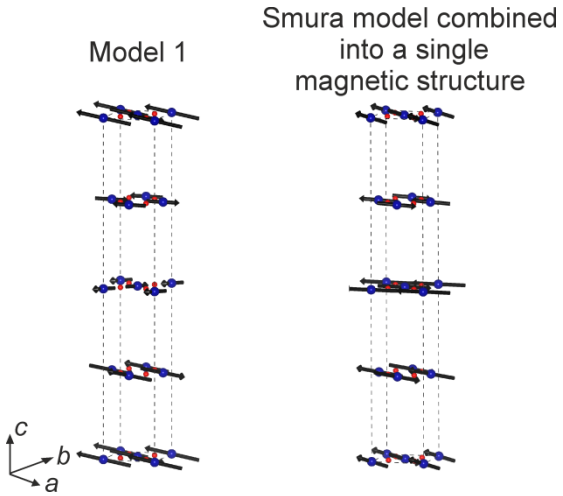


Fig. 5.22 Comparison of model 1 and the Smura model when it is combined into a single magnetic structure (the method of combining the magnetic structures is described in the text). For clarity only the Co (blue) and O (red) atoms are shown. The dotted lines outline the expanded magnetic unit cell

Model 1 and the Smura model are both considered to be unusual descriptors of the magnetic structure of $Sr_2CoO_2Cu_2Se_2$. Model 1 is considered unusual because

nominally chemically, and apparently crystallographically, identical Co ions are modelled as having very different magnetic moments, while the Smura model is considered unusual because it requires the coexistence of two different magnetic structures when there is no further evidence of phase separation in $Sr_2CoO_2Cu_2Se_2$. Both these models only lead to a small improvement to the fit to the data compared with models 2 and 3; therefore, model 3 (the high-symmetry equivalent of model 2) was chosen for the comparison of the magnetic behaviour of samples of $Sr_2CoO_2Cu_{2-x}Se_2$ with different Cu occupancies.

5.2.4.2.2 **Changes to the magnetic ordering on removal of Cu from $Sr_2CoO_2Cu_{2-x}Se_2$**

Model 3 was applied to JNB171 ($Sr_2Co_2O_2Cu_{1.94}Se_2$) and JNB104 ($Sr_2CoO_2Cu_{1.89}Se_2$) to assess changes in the magnetic structure as a function of Cu occupancy. The Rietveld fits from this analysis (including parent $Sr_2CoO_2Cu_2Se_2$ (JNB102)) are shown in Fig. 5.23 and the results compared in Table 5.15. Model 3 was found to be satisfactory for all three samples.

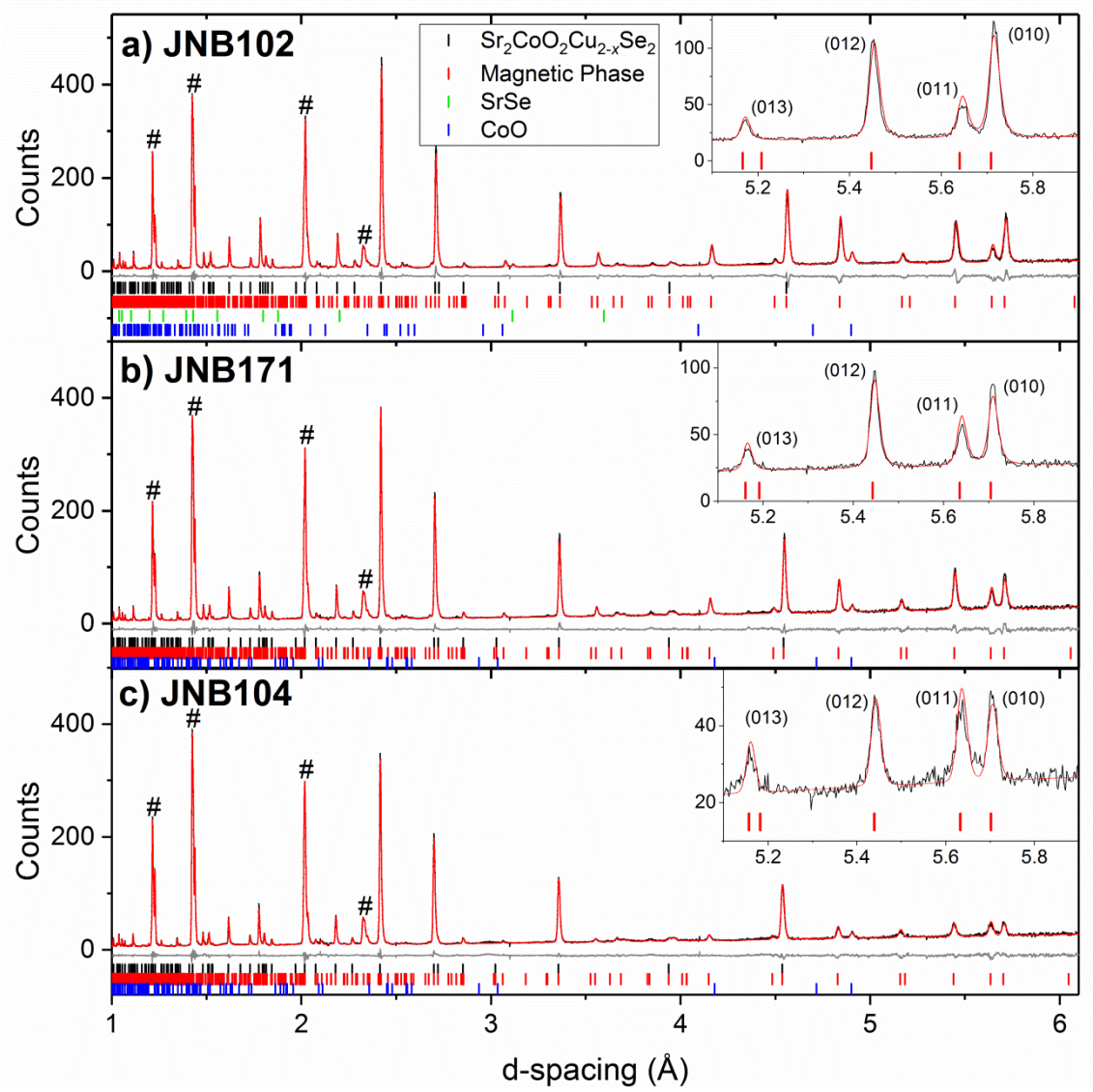


Fig. 5.23 Rietveld plots of three samples of $Sr_2CoO_2Cu_{2-x}Se_2$ measured using OSIRIS at 5 K a) JNB102 ($Sr_2CoO_2Cu_2Se_2$), b) JNB171 ($Sr_2Co_2O_2Cu_{1.94}Se_2$) and c) JNB104 ($Sr_2CoO_2Cu_{1.89}Se_2$), all magnetic intensity was refined using model 3 (P_c4_1 (76.11) model). The four main peaks arising from the sample environment (primarily the Al-tailed cryostat) are indicated by # symbols

Table 5.15 Comparison of the refined ordered moment of samples of $Sr_2CoO_2Cu_{2-x}Se_2$, data obtained from combined refinement against HRPD and OSIRIS data measured at 5 K using model 3 (P_c4_1 (76.11) model)

Sample	JNB102	JNB171	JNB104
Composition	$Sr_2CoO_2Cu_{2.0}Se_2$	$Sr_2CoO_2Cu_{1.94}Se_2$	$Sr_2CoO_2Cu_{1.89}Se_2$
Diffractometer	OSIRIS/HRPD	OSIRIS/HRPD	OSIRIS/HRPD
Radiation	Neutron, ToF	Neutron, ToF	Neutron, ToF
μ_a (μ_B)	3.22(2)	2.59(3)	1.55(3)
μ_b (μ_B)	-0.56(2)	-0.23(3)	0.18(3)
μ_c (μ_B)	-1.25(2)	-1.24(2)	-1.00(2)
$\lvert\mu\rvert$ (μ_B)	3.50(2)	2.88(2)	1.85(3)
R_{wp} (%)	4.139	3.826	4.084
χ^2	2.231	2.032	2.009

The Rietveld plot of JNB104 ($Sr_2CoO_2Cu_{1.89}Se_2$) in the inset of Fig. 5.23 c) shows that there is some unindexed intensity in the proximity of the 011 peak, this could be evidence of diffuse magnetic scattering arising from the disorder in the magnetic ions induced in this compound. It also appears that the slightly poor modelling of the 011 and 013 peaks observed for stoichiometric $Sr_2CoO_2Cu_2Se_2$ (JNB102) when model 3 was used is also observed for JNB171 ($Sr_2CoO_2Cu_{1.94}Se_2$) and JNB104 ($Sr_2CoO_2Cu_{1.89}Se_2$). Modelling this data using model 1 (see Appendix C) improves the fit to the data somewhat, but requires the magnetic moments on crystallographically equivalent ions to be different, as previously discussed.

A reorientation of the magnetic moment into the *c*-direction accompanies the general loss of ordered moment observed on oxidation, as shown by the change in the μ_c/μ_{ab} ratio (see Table 5.17).

Table 5.16 Comparison of the μ_c/μ_{ab} ratio for samples of $Sr_2CoO_2Cu_{2-x}Se_2$

Sample	JNB102	JNB171	JNB104
Composition	$Sr_2CoO_2Cu_{2.0}Se_2$	$Sr_2CoO_2Cu_{1.94}Se_2$	$Sr_2CoO_2Cu_{1.89}Se_2$
μ_c/μ_{ab}	0.382(7)	0.48(1)	0.64(2)

The loss of ordered moment is far greater than can be accounted for by simple loss of unpaired spin; therefore, the changes in the ordered moment have therefore been modelled as loss of the "total ordered phase fraction" relative to stoichiometric $Sr_2CoO_2Cu_2Se_2$ (JNB102) using eq. 5.1, as shown in Table 5.17.

Table 5.17 Comparison of the calculated "total ordered phase fraction" for samples of $Sr_2CoO_2Cu_{2-x}Se_2$

Sample	JNB102	JNB171	JNB104
Composition	$Sr_2CoO_2Cu_2Se_2$	$Sr_2CoO_2Cu_{1.94}Se_2$	$Sr_2CoO_2Cu_{1.89}Se_2$
Total ordered phase fraction (%)	100	67(1)	28(1)

These results show the loss of 72(1)% of the ordered phase fraction from only ~5% oxidation. The magnetic peaks in JNB104 ($Sr_2CoO_2Cu_{1.89}Se_2$) are not substantially broader than those in the parent (JNB102), suggesting that large regions within JNB104 are still ordered. There also does not appear to be any sign of significant anisotropic broadening, which might have suggested that order was lost in one direction, but retained in another.

5.2.4.3 $Sr_2CoO_2Cu_{2-x}Se_{1.6}S_{0.4}$

As discussed in section 5.1, $Sr_2CoO_2Cu_2Se_{1.6}S_{0.4}$ was selected for study because Smura identified that the parent material adopts solely the "2*c*" magnetic structure, unlike $Sr_2CoO_2Cu_2Se_2$, which adopts a mixed ("*c*"/"2*c*") structure using the Smura two-phase model;[58] it was therefore considered interesting to study the changes in magnetic behaviour as a function of deintercalation for comparison with the work carried out on $Sr_2CoO_2Cu_2Se_2$.

The same three samples that were measured using RT PND (section 5.2.2.2) were measured at 5 K using OSIRIS and HRPD and analysed by combined refinement against these datasets. Surprisingly, it was found that deintercalation of Cu caused the *c*-magnetic structure to appear at low temperature, as is shown in Fig. 5.24.

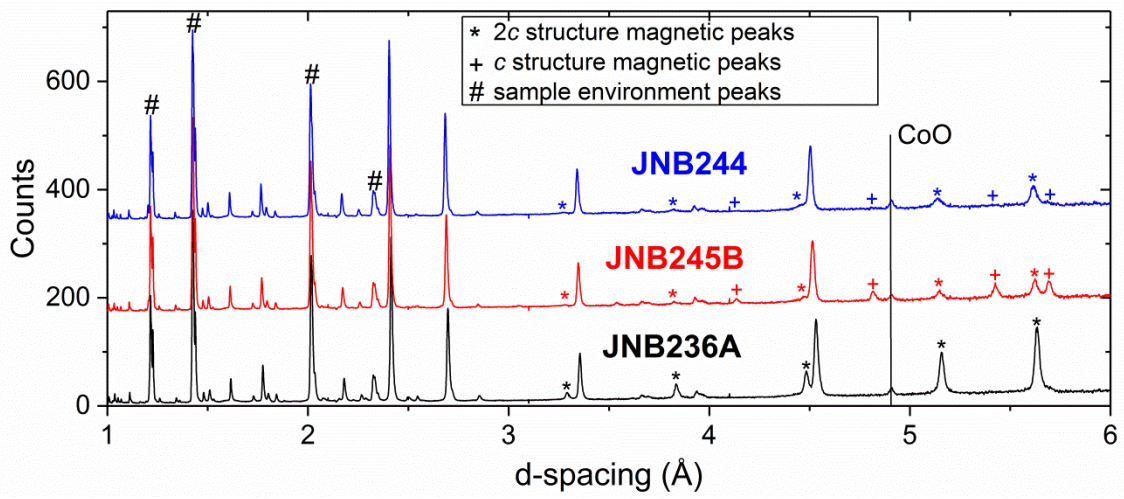


*Fig. 5.24 Raw PND plots of JNB236A (parent $Sr_2CoO_2Cu_2Se_{1.6}S_{0.4}$), JNB245B ($Sr_2CoO_2Cu_{1.93(1)}Se_{1.6}S_{0.4}$) and JNB244 ($Sr_2CoO_2Cu_{1.86(1)}Se_{1.6}S_{0.4}$), magnetic peaks have been highlighted using * and + symbols for the 2c- and c-magnetic structures (using the Smura two-phase model)[58] respectively. The four main peaks arising from the sample environment (primarily the Al-tailed cryostat) are indicated by # symbols*

In order to produce three large samples for neutron diffraction experiments, the deintercalated samples JNB245B and JNB244 were synthesised from different parent batches to JNB236A, where JNB236A showed the same magnetic ordering behaviour as the samples of $Sr_2CoO_2Cu_2Se_{1.6}S_{0.4}$ synthesised by Smura.[58] However, to minimise the differences between the samples, all the parent samples were produced at the same time under similar conditions and using the same furnace. Despite this, due to the unexpected changes observed in the magnetic ordering pattern, the three parent samples JNB236A, JNB236B (parent of JNB244) and JNB236C (parent of JNB245B) were

analysed by Rietveld refinement against synchrotron PXRD data (using the PSD on the I11 beamline) to compare refined lattice parameters (Table 5.18). This was done to ensure the observed differences in the magnetic ordering structures were due to differences in Cu occupancy and not variations, such as the S:Se ratio, between parent samples.

Table 5.18 Comparison of the refined lattice parameters (obtained from refinement against data from the PSD at the I11 beamline) of the three parent samples used to produce the daughter compounds described in this section

Sample	JNB236A	JNB236B	JNB236C
Daughter	-	JNB244	JNB245B
a (Å)	4.04239(1)	4.04212(1)	4.04238(2)
c (Å)	18.23689(6)	18.24190(7)	18.24091(9)
Volume (Å^3)	298.007(2)	298.049(2)	298.071(3)
R_{wp} (%)	0.901	1.189	1.062
χ^2	2.708	3.257	2.612

Table 5.18 shows that the maximal difference between the lattice parameters of the three samples is ~0.005 Å in the *c* direction. Smura reported that compounds with composition $Sr_2CoO_2Cu_2Se_{1.5-1.7}S_{0.5-0.3}$ ordered with only the 2*c*-magnetic structure. The changes in the lattice parameters observed in the parent here are not sufficient for the sample to fall outside this Se:S ratio range; therefore, analysis of the magnetic structure of $Sr_2CoO_2Cu_{2-x}Se_{1.6}S_{0.4}$ is continued with the assumption that the differences observed in the magnetic structure are due to the change in Cu occupancy as a result of the oxidation with I_2, not differences in the composition of the parent compound.

Attempts were made to characterise the magnetic structure of parent $Sr_2CoO_2Cu_2Se_{1.6}S_{0.4}$ (JNB236A) using the same set of magnetic symmetry modes as were used to characterise $Sr_2CoO_2Cu_2Se_2$, but this led to a poor fit to the data (Fig. 5.25a)). It was found that combined refinement of the mP4 and mP5 modes (but no mXn^+ modes were required) was necessary to fit the data (Rietveld plot shown in Fig. 5.25 b)). The highest symmetry magnetic space group that allowed refinement of these modes was I_aba2 (45.240), shown schematically in Fig. 5.26. The I_aba2 (45.240) model is a high-symmetry analogue of the "2*c* only" model proposed by Smura.[58] In the I_aba2 magnetic model the origin has been shifted by (-5/8, 7/8, 1/4).

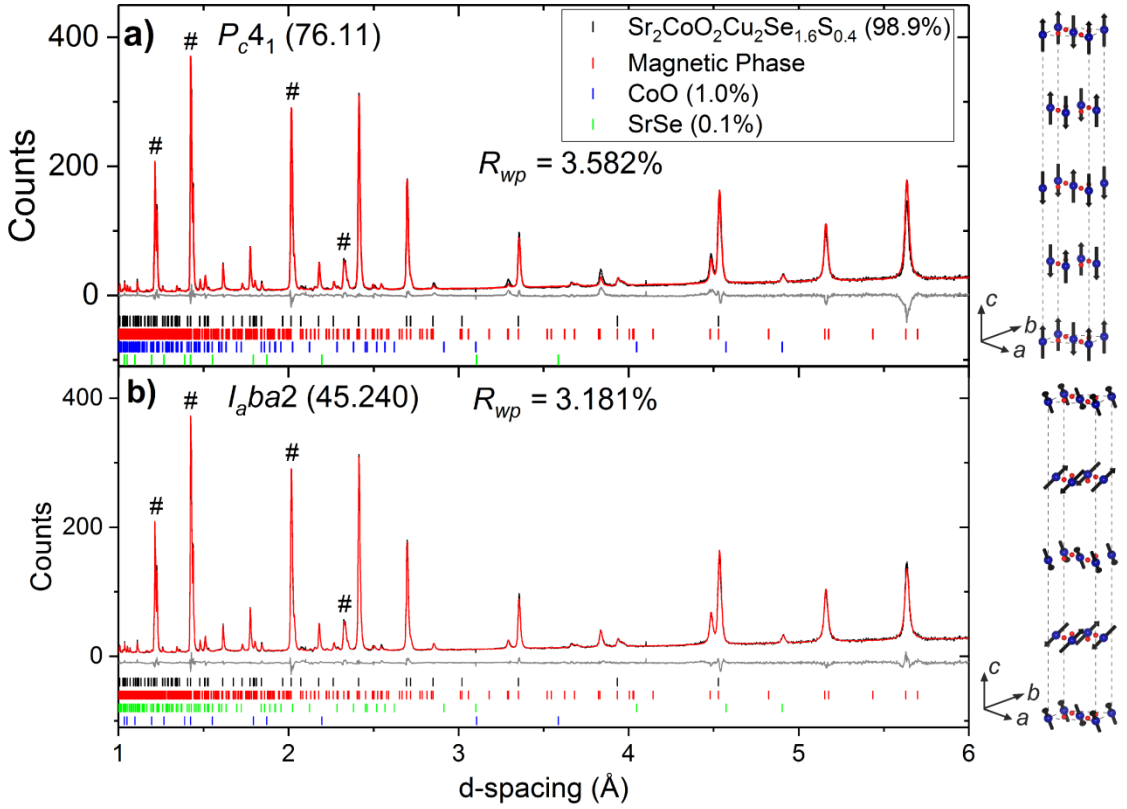


Fig. 5.25 Comparison of the Rietveld plots of parent $Sr_2CoO_2Cu_2Se_{1.6}S_{0.4}$ (JNB236A) measured using OSIRIS at 5 K when the following magnetic models are used: a) model 3 (P_c4_1 (76.11) model) and b) the I_aba2 (45.240) model. The four main peaks arising from the sample environment (primarily the Al-tailed cryostat) are indicated by # symbols. Representative models of the magnetic structure refined in each case are shown to the right.

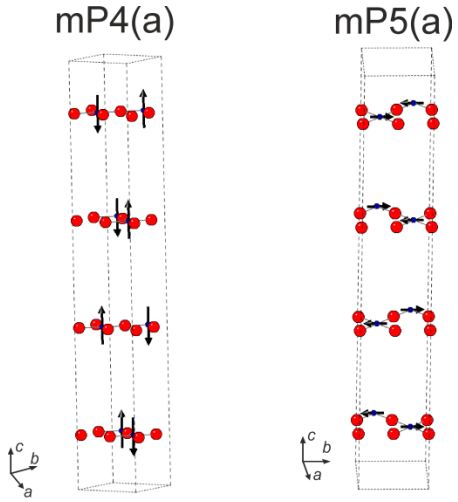


Fig. 5.26 Schematic of the magnetic symmetry modes possible in the magnetic space group I_aba2 (45.240), for clarity only the Co (blue) and O (red) atoms are shown. The dotted lines outline the expanded magnetic unit cell

Due to the presence in the oxidised sample JNB245B of magnetic peaks that could be indexed using the "*c*"-magnetic structure using the Smura model (or otherwise, peaks

that require activation of the mXn^+ modes to acquire intensity), the magnetic structure of JNB245B was refined using "$Sr_2CoO_2Cu_2Se_2$ model 3" (P_C4_1 (76.11) model). There were also some small features hinting at the presence of very weak peaks corresponding to the Smura "*c*"- structure in the PND of the more highly oxidised JNB244, so the magnetic structure of JNB244 was also refined using this model. The Rietveld plots of these refinements are shown in Fig. 5.27 and the refined magnetic moments compared in Table 5.19.

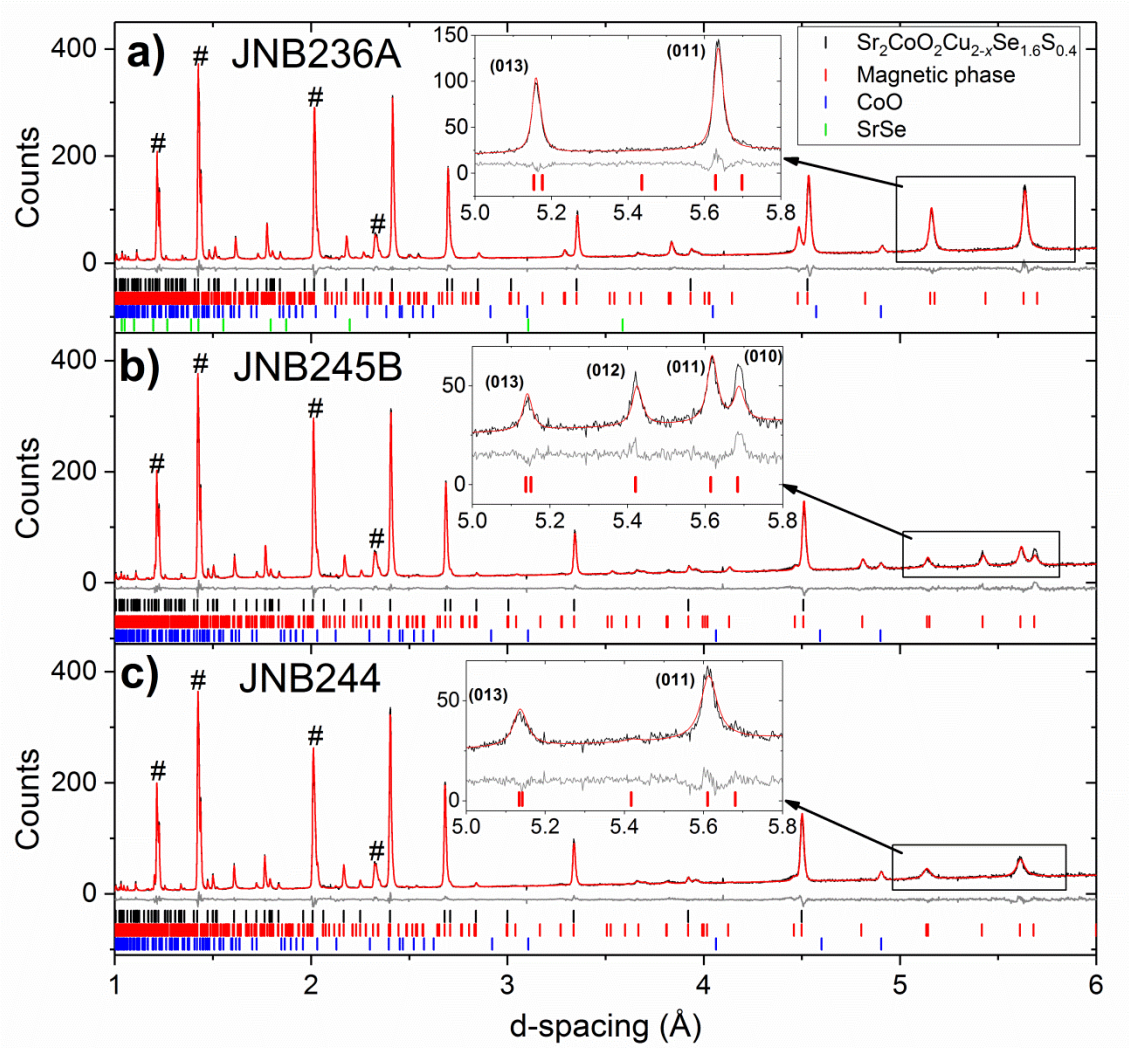


Fig. 5.27 Rietveld plots of JNB236A (parent $Sr_2CoO_2Cu_2Se_{1.6}S_{0.4}$), JNB245B ($Sr_2CoO_2Cu_{1.93(1)}Se_{1.6}S_{0.4}$) and JNB244 ($Sr_2CoO_2Cu_{1.86(1)}Se_{1.6}S_{0.4}$) measured using OSIRIS at 5 K and modelled using the magnetic models described in the text, the insets emphasise the fit at high d-spacing. The four main peaks arising from the sample environment (primarily the Al-tailed cryostat) are indicated by # symbols

Table 5.19 Comparison of the refined ordered moment of samples of $Sr_2CoO_2Cu_{2-x}Se_{1.6}S_{0.4}$, data obtained from combined refinement against HRPD and OSIRIS data measured at 5 K and refined using the magnetic models stated in the text

Sample	JNB236A	JNB245B	JNB244
Composition	$Sr_2CoO_2Cu_2Se_{1.6}S_{0.4}$	$Sr_2CoO_2Cu_{1.93}Se_{1.6}S_{0.4}$	$Sr_2CoO_2Cu_{1.86}Se_{1.6}S_{0.4}$
μ_a (μ_B)	3.08(4)	1.74(2)	0.4(1)
μ_b (μ_B)	0*	-0.18(3)	0.1(1)
μ_c (μ_B)	1.04(8)	-1.42(2)	-1.73(3)
$\lvert\mu\rvert$ (μ_B)	3.25(4)	2.25(2)	1.78(4)
R_{wp} (%)	3.181	2.925	2.924
χ^2	1.319	1.267	1.379

*not refined

The insets in Fig. 5.27 show that the fit to the data is very good at high *d*-spacing for JNB236A (parent $Sr_2CoO_2Cu_2Se_{1.6}S_{0.4}$). However, a significant discrepancy in the intensity of the 010 peak (indexed using the magnetic unit cell) is observed in the PND pattern of JNB245B ($Sr_2CoO_2Cu_{1.930(8)}Se_{1.6}S_{0.4}$). This is a feature that is also observed in the low-temperature PND patterns of the pure selenide analogues, albeit to a lesser extent. The fit shown in Appendix C (Fig. C.2) shows that the fit can be improved somewhat by use of model 1, but does not remove the discrepancy entirely and leads to what are deemed to be unrealistic differences in the magnetic moments of different Co ions in the model.

The removal of Cu from $Sr_2CoO_2Cu_{2-x}Se_{1.6}S_{0.4}$ causes a large change in magnetic structure. The peaks identified as belonging to the "*c*" phase by Smura reappear, suggestive of a large reorientation. One observable feature of the reorientation is that the oxidised samples (JNB245B and JNB244) have a significantly larger component in the *c*-direction (in relative terms). The ratio between the component in the *c*-direction (μ_c) and the component in the *ab*-plane (μ_{ab}) is shown in Table 5.20.

Table 5.20 Comparison of the μ_c/μ_{ab} ratio for samples of $Sr_2CoO_2Cu_{2-x}Se_{1.6}S_{0.4}$

Sample	JNB236A	JNB245B	JNB244
Composition	$Sr_2CoO_2Cu_2Se_{1.6}S_{0.4}$	$Sr_2CoO_2Cu_{1.93}Se_{1.6}S_{0.4}$	$Sr_2CoO_2Cu_{1.86}Se_{1.6}S_{0.4}$
μ_c/μ_{ab}	0.34(3)	0.81(1)	3.46(7)

Since it was observed that the reduction of ordered moment was far larger than would be expected from the loss of magnetic spin, this reduction was also modelled as the loss of "total ordered phase fraction", using eq. 5.1, assuming the parent (JNB236A) was fully ordered. The results of these calculations are shown in Table 5.21, revealing a very large loss of the total ordered phase fraction.

Table 5.21 Comparison of the calculated "total ordered phase fraction" of samples of $Sr_2CoO_2Cu_{2-x}Se_{1.6}S_{0.4}$

Sample	JNB236A	JNB245B	JNB244
Composition	$Sr_2CoO_2Cu_2Se_{1.6}S_{0.4}$	$Sr_2CoO_2Cu_{1.93}Se_{1.6}S_{0.4}$	$Sr_2CoO_2Cu_{1.86}Se_{1.6}S_{0.4}$
Total ordered phase fraction (%)	100	48(1)	30(2)

5.2.4.4 *Discussion*

The "total ordered phase fraction" for $Sr_2CoO_2Cu_2S_2$, $Sr_2CoO_2Cu_2Se_2$ and $Sr_2CoO_2Cu_2Se_{1.6}S_{0.4}$ is compared as a function of the average Co oxidation state (assumed from Cu occupancy values) in Fig. 5.28. The rate of loss of the "total ordered phase fraction" appears to be higher at lower oxidation states. This is consistent with what might be expected from modelling the random insertion of Co^{3+} ions into a Co^{2+} lattice.

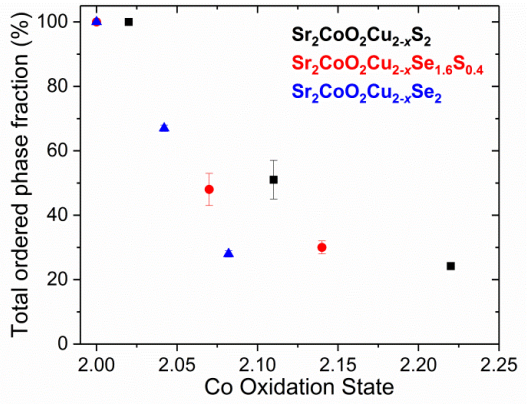


Fig. 5.28 Relationship between the Co oxidation state and the "total ordered phase fraction" for the compound series $Sr_2CoO_2Cu_{2-x}S_2$, $Sr_2CoO_2Cu_{2-x}Se_{1.6}S_{0.4}$ and $Sr_2CoO_2Cu_{2-x}Se_2$

It is a relatively common observation that the ordered phase fraction (or ordered moment) is suppressed by the introduction of ions of a different oxidation state into the compound. A famous example is that of $La_{2-x}Sr_xCuO_4$ (a parent of one of the original cuprate high-T_c superconductors[2]), the antiferromagnetic order observed in La_2CuO_4 is fully suppressed with just 3% Cu(III) centres.[152] The antiferromagnetic order of the $Sr_2CoO_2Cu_{2-x}(S/Se)_2$ compounds in question is comparatively robust.

The single-structure model (model 3) proposed here with equal moment magnitudes on crystallographically equivalent Co ions does not appear to model the magnetic intensity of $Sr_2CoO_2Cu_2Se_2$ quite as well as the Smura model or model 1. This might suggest that

there are additional features to the magnetic structure of this compound that are not modelled using model 3.

It would be intellectually satisfying if all the magnetic structures of the solid-solution series $Sr_2CoO_2Cu_2S_{2-x}Se_2$ could be refined with a single model. Due to the overlap in the magnetic symmetry modes used, it would be trivial to index $Sr_2CoO_2Cu_2S_2$ with the model obtained for $Sr_2CoO_2Cu_2Se_2$, simply fixing mP4 to zero. However, the $Sr_2CoO_2Cu_2Se_2$ magnetic model cannot be transposed to $Sr_2CoO_2Cu_2Se_{1.6}S_{0.4}$. This is because in order to model the magnetic peaks of $Sr_2CoO_2Cu_2Se_{1.6}S_{0.4}$ satisfactorily one of the four possible mP5 symmetry modes must be activated. These modes cannot be activated in "$Sr_2CoO_2Cu_2Se_2$ model 3" because mP5 is active in *ab*-plane and would interfere with the $mX3^+$ and $mX4^+$ modes causing large differences in the magnitude of magnetic moments of different Co ions in the same structure. It was this problem that led to the rejection of "$Sr_2CoO_2Cu_2Se_2$ model 1" as a potential magnetic model.

The fact that the magnetic structure of $Sr_2CoO_2Cu_2Se_2$ cannot be used to model the magnetic intensity of $Sr_2CoO_2Cu_2Se_{1.6}S_{0.4}$ is taken to be further evidence that the magnetic structure of $Sr_2CoO_2Cu_2Se_2$ is not quite the correct model, especially in the light that only a small (5%) oxidation of the Co^{2+} ions is required for the $Sr_2CoO_2Cu_2Se_{1.6}S_{0.4}$ "2*c*" magnetic structure to convert to a magnetic structure more closely resembling that of $Sr_2CoO_2Cu_2Se_2$; this is highly suggestive of a close relationship between the two.

$Sr_2CoO_2Cu_2Se_2$ is an interesting case where several different magnetic structures may be modelled from the available PND data. Single-crystal neutron diffraction may be a useful technique for further understanding the magnetic structure.

5.2.5 Structural distortion at low temperature

Smura *et al.* noted from high-resolution synchrotron PXRD data (ID31) that parent $Sr_2CoO_2Cu_2S_2$ (DRP051) undergoes a small orthorhombic distortion below ~150 K, as observed by broadening of specific peaks, particularly the 200/020 peak. The magnitude of the orthorhombic distortion was found to increase dramatically as a function of x in the solid solution $Sr_{2-x}Ba_xCoO_2Cu_2S_2$.[61] It was suggested that the orthorhombic distortion may arise when ordered moments with an orbital contribution couple to the lattice, resulting in magnetoelastic coupling. The collinear ordering of the

magnetic moments in the *ab*-plane would then lead to the orthorhombic distortion.[153] The magnetic moment of $Sr_{2-x}Ba_xCoO_2Cu_2S_2$ increased as a function of x, which was attributed to an increase in the orbital contribution to the ordered magnetic moment and hence the increase in the orthorhombic distortion.[61]

When evidence of a distortion was searched for in the copper-deficient air-exposed sample of $Sr_2CoO_2Cu_{2-x}S_2$ (DRP051_AE), it could not be resolved because the method of deintercalation (moist-O_2 exposure) led to significant peak broadening, suggestive of a phase-width arising from an inhomogeneous Cu distribution.[61] Therefore, in this thesis, three samples of both $Sr_2CoO_2Cu_{2-x}S_2$ and $Sr_2CoO_2Cu_{2-x}Se_2$ (the same samples that were measured using magnetic susceptibility) were measured using PXRD at ID22 as a function of temperature below 100 K, so the effect of removal of copper and the resultant changes in magnetic behaviour could be correlated with changes to the low-temperature structure.

Peak splitting, characteristic of an orthorhombic distortion, was observed in both $Sr_2CoO_2Cu_{2-x}S_2$ and $Sr_2CoO_2Cu_{2-x}Se_2$. Surprisingly, a larger orthorhombic distortion was observed in the more Cu-deficient samples, contradicting the previous hypothesis that a larger ordered moment would result in a larger orthorhombic distortion.

No additional peaks that might indicate the appearance of a superstructure due to Cu/vacancy ordering or similar appeared at low temperature. It is also of note that very little rearrangement of atoms is allowed by the lowering of symmetry from *I*4/*mmm* to *Immm*: the Sr, Co and S atoms all retain their single crystallographic sites; while the *z*-position of the Cu site may be refined in the lower-symmetry space group, it has little real effect (see Table 5.22 and Table 5.23 below) and while the O site divides into two separate crystallographic sites, it does not directly affect the structure.

5.2.5.1 $Sr_2CoO_2Cu_{2-x}S_2$

The refined parameters from Rietveld refinement against the ID22 data for JNB051, JNB087 and JNB086 (the same samples that were analysed using magnetic susceptibility) are shown in Table 5.22. Peak-splitting was observed in peaks where $h, k \neq 0$, most markedly in the 200/020 peak. This was identified as an orthorhombic distortion and indexed using the *Immm* space group, as reported by Smura *et al*.[61] The relative difference between *a* and *b* as a function of temperature has been plotted for each compound in Fig. 5.29 with a representative fit of the 200/020 peak at 5 K. It was

found that a better fit to the data (as assessed by examination of the R_{wp}) was obtained for JNB051 (parent $Sr_2CoO_2Cu_2S_2$) when the tetragonal space group *I*4/*mmm* was used, this is discussed further below.

Table 5.22 Comparison of refined parameters for three samples of $Sr_2CoO_2Cu_{2-x}S_2$, values obtained from Rietveld refinement against synchrotron PXRD data collected at 5 K using ID22

Sample	JNB051	JNB087	JNB086
Radiation	X-ray λ = 0.33502512 Å		
Diffractometer	ID22		
Temperature (K)	5		
Space group	*I4/mmm*	*Immm*	*Immm*
a (Å)	3.98272(2)	3.96904(2)	3.96464(1)
b (Å)	≡ *a*	3.97284(2)	3.96984(1)
c (Å)	17.61784(9)	17.50556(7)	17.45156(5)
Volume (Å^3)	279.456(3)	276.034(2)	274.670(1)
z(Sr)	0.40761(3)	0.40575(3)	0.40496(3)
z(S)	0.17059(7)	0.17032(7)	0.17006(7)
z(Cu)	0.75*	0.7499(1)	0.74981(1)
Cu occupancy	0.970(2)	0.914(2)	0.881(1)
Sr U_{11} (Å^2)	0.0000(1)	0.0011(1)	0.0008(2)
Sr U_{33} (Å^2)	0.0037(2)	0.0071(2)	0.0128(3)
Co U_{11} (Å^2)	0.0000(3)	0.0003(3)	0.0000(3)
Co U_{33} (Å^2)	0.0071(6)	0.0181(6)	0.0307(8)
O U_{11} (Å^2)	0.000(2)	0.007(3)	0.007(3)
O U_{22} (Å^2)	0.005(2)	0.007(3)	0.007(3)
O U_{33} (Å^2)	0.010(2)	0.007(2)	0.016(2)
Cu U_{11} (Å^2)	0.0011(2)	0.0042(3)	0.0039(3)
Cu U_{33} (Å^2)	0.0022(4)	0.0013(4)	0.0049(5)
S U_{11} (Å^2)	0.0042(5)	0.0046(5)	0.0052(5)
S U_{33} (Å^2)	0.0004(6)	0.0007(6)	0.0037(7)
R_{wp} (%)	8.545	8.950	9.783
χ^2	3.047	3.153	3.626

*not refined by symmetry

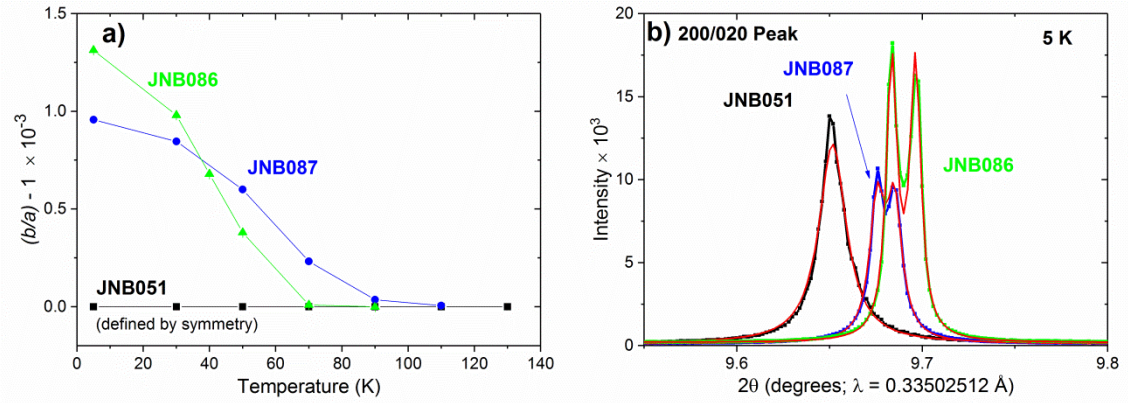


Fig. 5.29 a) Orthorhombic distortion of three samples of $Sr_2CoO_2Cu_{2-x}S_2$ as a function of temperature (the line is a guide to the eye and the error bars are smaller than the points on the graph) and b) the splitting of the 200/020 peak at 5 K for the same three samples

As previously stated, no measurable orthorhombic distortion was observed in parent $Sr_2CoO_2Cu_2S_2$ (JNB051), but Smura *et al.* observed a small orthorhombic distortion in nominally the same compound (DRP051) from an increase in broadening of the 200/020 peak at low temperatures. Comparison of the full-width-half-maximum of JNB051 and DRP051 at 130 K and at base temperature (5 K for JNB051 and 10 K for DRP051) in Fig. 5.30 shows that the increase in the broadening of the 200/020 peak in DRP051 on cooling from 130 K to 10 K is of the order of the amount that the 200/020 peak is broader in JNB051 at 130 K than DRP051. This suggests that the comparative broadness of the peaks in JNB051 could be obfuscating a small orthorhombic distortion.

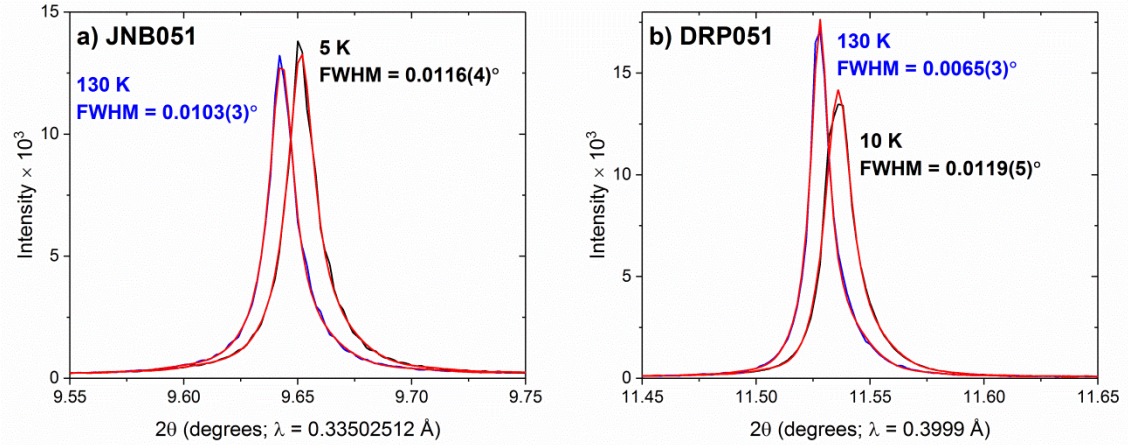


Fig. 5.30 Comparison of the full-width-half-maximum (FWHM) of a) JNB051 and b) DRP051 at 130 K and either 5 or 10 K. PXRD data collected at ID22 (the data for DRP051 were collected when the diffractometer system was situated at ID31) and the FWHM were obtained using a Lorentzian peak-shape function

The orthorhombic distortions described here are parameterised as *b/a* - 1, for direct comparison with the orthorhombic distortion in the $Sr_{2-x}Ba_xCoO_2Cu_2S_2$ solid solution described by Smura *et al*.[61] The distortion observed in JNB086 ($Sr_2CoO_2Cu_{1.79}S_2$*) at 5 K, 1.3×10^{-3}, is less than half the distortion observed in $Ba_2CoO_2Cu_2S_2$ at 4 K (3.43×10^{-3}).[61]

The plot in Fig. 5.29a) shows that the orthorhombic distortion in JNB086 ($Sr_2CoO_2Cu_{1.79}S_2$*) decreases faster as temperature increases than JNB087 ($Sr_2CoO_2Cu_{1.85}S_2$*). It has been shown from magnetometry measurements that the broad cusp in the magnetic susceptibility measurements of JNB086 occurs at a lower temperature than in JNB087, so this might be considered evidence linking the orthorhombic distortion to magnetic ordering in some way. This is further discussed in section 5.2.5.3.

A small intensity mismatch is observed in the splitting of the 200/020 peaks (see Fig. 5.29 b), JNB087 and JNB086), in which the peak at low angle has a slightly higher intensity. This feature is not allowed by the symmetry of the space group. Efforts to model this distortion using ISODISTORT[112] were not successful, although the use of orthorhombic Stephens' anisotropic broadening terms[154] (used in the final refinement) did reduce the discrepancy somewhat. However, there is a small degree of peak asymmetry at low angle in 00*l* reflections (Fig. 5.31), which suggests that both samples have a small phase-width, primarily containing phases with larger than average lattice parameters for the sample, presumably arising from an inhomogeneous Cu distribution. It was found that orthorhombic Stephens' anisotropic peak broadening terms[154] partially compensated for this feature in the data.

* Cu occupancy values from Rietveld refinement against RT PSD (I11) data, see section 5.2.2.1

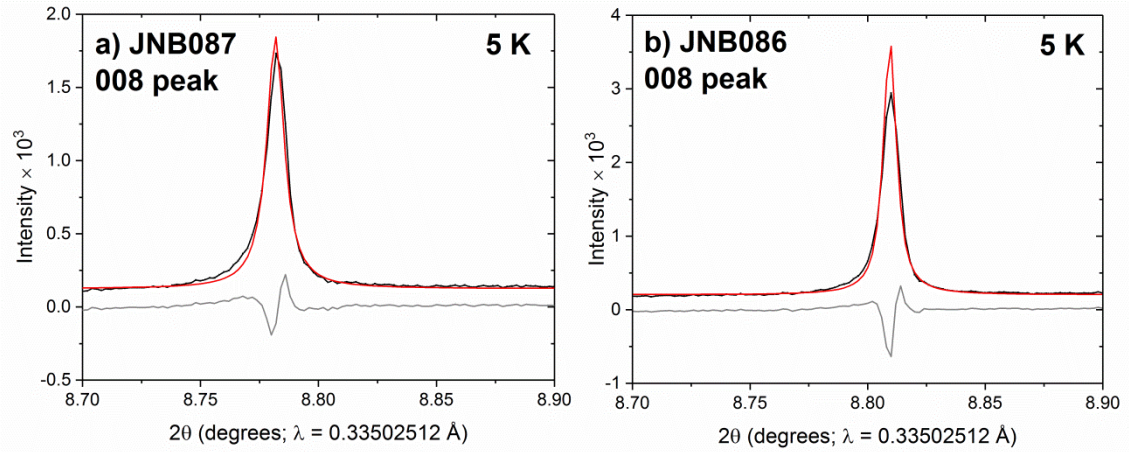


Fig. 5.31 Rietveld plot of a) JNB087 ($Sr_2CoO_2Cu_{1.79}S_2$) and b) JNB086 ($Sr_2CoO_2Cu_{1.85}S_2$) of data collected at 5 K using ID22. Only the 008 peak is shown, emphasising a small degree of peak asymmetry

5.2.5.2 $Sr_2CoO_2Cu_{2-x}Se_2$

The refined parameters of three sample of $Sr_2CoO_2Cu_2Se_2$, measured at 5 K using ID22 are shown in Table 5.23. It was found, as for $Sr_2CoO_2Cu_2S_2$, that while parent $Sr_2CoO_2Cu_2Se_2$ (JNB149A) fitted best to a tetragonal space group (*I*4/*mmm*), the deintercalated daughter samples (JNB171 and JNB104) showed splitting of peaks that was consistent with an orthorhombic distortion, using the *Immm* space group. The size of the orthorhombic distortion as a function of temperature and the splitting of the 200/020 peak of each sample at 5 K is shown in Fig. 5.32.

Table 5.23 Comparison of refined parameters for three samples of $Sr_2CoO_2Cu_{2-x}Se_2$, values obtained from Rietveld refinement against synchrotron PXRD data collected at 5 K using ID22

Sample	JNB149A	JNB171	JNB104
Radiation	X-ray, λ = 0.39996825 Å		
Diffractometer	ID22		
Temperature (K)	5		
Space group	*I*4/*mmm*	*Immm*	*Immm*
a (Å)	4.043240(7)	4.04053(1)	4.03292(1)
b (Å)	≡ *a*	4.03757(1)	4.03711(1)
c (Å)	18.26119(5)	18.19848(5)	18.15097(5)
Volume (Å^3)	298.530(1)	296.888(1)	295.522(1)
z(Sr)	0.41165(2)	0.41095(4)	0.41025(3)
z(Se)	0.16806(2)	0.16795(4)	0.16777 (3)
z(Cu)	0.75*	0.7502(2)	0.7497(2)
Cu occupancy	1.018(1)	0.977(2)	0.950(2)
Sr U_{11} (Å^2)	0.0019(1)	0.0067(3)	0.0020(2)
Sr U_{33} (Å^2)	0.0001(2)	0.0070(4)	0.0013(3)
Co U_{11} (Å^2)	0.0016(3)	0.0082(6)	0.0038(5)
Co U_{33} (Å^2)	0.0045(5)	0.008(1)	0.0065(9)
O U_{11} (Å^2)	0.004(1)	0.002(4)	0.018(4)
O U_{22} (Å^2)	0.001(1)	0.033(5)	0.001(4)
O U_{33} (Å^2)	0.006(2)	0.003(3)	0.000(3)
Cu U_{11} (Å^2)	0.0077(2)	0.0110(4)	0.0049(3)
Cu U_{33} (Å^2)	0.0035(3)	0.0060(6)	0.0017(5)
Se U_{11} (Å^2)	0.0023(2)	0.0077(3)	0.0031(2)
Se U_{33} (Å^2)	0.0000(2)	0.0060(5)	0.0003(4)
R_{wp} (%)	6.879	12.979	9.445
χ^2	2.202	4.473	3.008

*not refined by symmetry

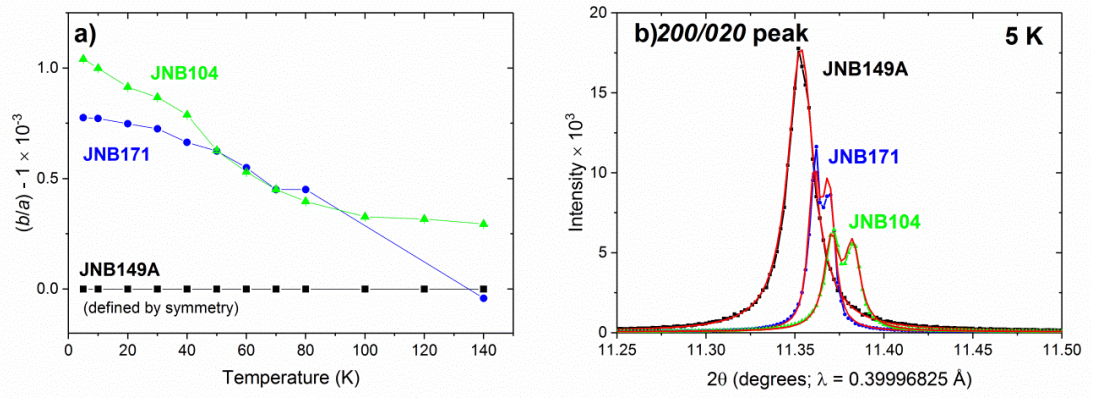


Fig. 5.32 a) Orthorhombic distortion of three samples of $Sr_2CoO_2Cu_{2-x}Se_2$ as a function of temperature (the line is a guide to the eye and the refined errors are smaller than the points on the graph); b) the splitting of the 200/020 peak at 5 K for the same three samples

The general trends in the low temperature behaviour of $Sr_2CoO_2Cu_{2-x}Se_2$ closely match those observed for $Sr_2CoO_2Cu_{2-x}S_2$: an orthorhombic distortion that increases as

temperature decreases is observed. This distortion also increases as Cu occupancy decreases, seemingly from an undistorted stoichiometric "parent" (JNB149A, $Sr_2CoO_2Cu_2Se_2$), which was fitted using the RT tetragonal model at all temperatures.

The distortions in the deintercalated samples are of comparable magnitude in the selenide and sulfide series, but are slightly larger in the most-deintercalated sulfide analogue (JNB086) than the equivalent selenide (JNB104). This difference is attributed to the lower copper fractional occupancy in JNB086 than JNB104.

When splitting is observed, the lower angle peak of the 200/020 doublet has a larger intensity than the higher angle peak, this is particularly apparent for JNB171 ($Sr_2Co_2O_2Cu_{1.94}Se_2$[*]). As with $Sr_2CoO_2Cu_{2-x}S_2$, this asymmetry is justified by examination of the phase-width within the sample; i.e. the sample contained a slightly inhomogeneous Cu distribution. Anisotropic broadening terms could only partially model this discrepancy, but were used in the model shown in Table 5.23 and Fig. 5.32.

JNB171 ($Sr_2Co_2O_2Cu_{1.94}Se_2$[*]) visibly consists of several closely related phases of $Sr_2CoO_2Cu_{2-x}Se_2$, as shown in Fig. 5.33, suggesting a small Cu inhomogeneity between different grains. It was this that led to the poorer fit to the data when a single phase was used (observed from the slightly larger R_{wp} value for this sample in Table 5.23). It was chosen to model JNB171 as a single phase so that directly comparable data for the orthorhombic distortion could be used.

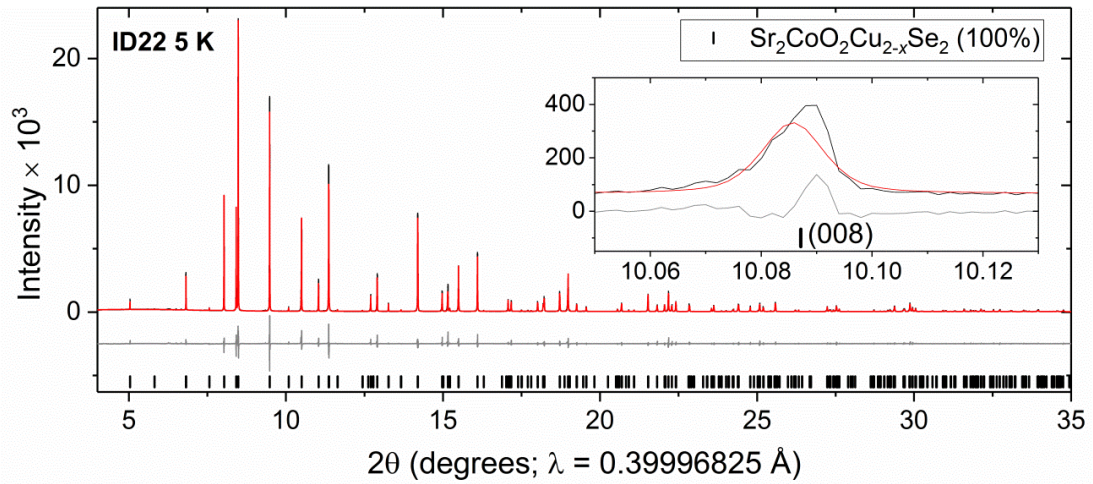


Fig. 5.33 Rietveld plot of JNB171 ($Sr_2Co_2O_2Cu_{1.94}Se_2$[*]) measured at 5 K using ID22, the inset emphasises the 008 peak, showing that the sample consists of multiple similar phases

[*] Cu occupancy values from Rietveld refinement against RT PND (HRPD) data, see section 5.2.2.2

5.2.5.3 *Discussion*

The low-temperature orthorhombic distortion increases as the Cu-deficiency increases in both $Sr_2CoO_2Cu_{2-x}S_2$ and $Sr_2CoO_2Cu_{2-x}Se_2$. However, section 5.2.4 showed that the ordered magnetic moment decreases with reduced Cu occupancy. This suggests that the orthorhombic distortion in the $Sr_2CoO_2Cu_{2-x}S_2$ and $Sr_2CoO_2Cu_{2-x}Se_2$ series is not directly related to magnetostriction, as was hypothesised to be the cause of the orthorhombic distortion in $Sr_{2-x}Ba_xCoO_2Cu_2S_2$ by Smura *et al*.[61]

It is possible that the causes of the orthorhombic distortion in the two series $Sr_{2-x}Ba_xCoO_2Cu_2S_2$ and $Sr_2CoO_2Cu_{2-x}S_2$ are different. Comparison of the Co-S/Co-O bond distance ratios of $Sr_2CoO_2Cu_2S_2$ (JNB051), $Sr_2CoO_2Cu_{1.79}S_2$ (JNB086) and $Ba_2CoO_2Cu_2S_2$ (CFS044, data from ref. 61) in Table 5.24, shows that a large elongation of the Co-S bond occurs on substitution of Sr for Ba. The opposite effect occurs on removal of Cu. As is shown in Fig. 5.34, changes in the geometry of the bonding environment can have a large effect on the energy of the d-orbitals, so the electronic environment of $Sr_2CoO_2Cu_{1.79}S_2$ and $Ba_2CoO_2Cu_2S_2$ are likely to be very different. The presence of mixed Co^{2+}/Co^{3+} ions in the system is also likely to have an effect on the most energetically favourable geometry.

Table 5.24 Comparison of the Co-O and Co-S bond distances in parent $Sr_2CoO_2Cu_2S_2$ (JNB051) and most-deintercalated $Sr_2CoO_2Cu_{2-x}S_2$ (JNB086) (data obtained from Rietveld refinement against PXRD data from the PSD at the I11 beamline) with $Ba_2CoO_2Cu_2S_2$ (CFS044, values obtained from PND data, from ref. 61)

Sample	JNB051	JNB086	CFS044
Compound	$Sr_2CoO_2Cu_2S_2$	$Sr_2CoO_2Cu_{1.79}S_2$	$Ba_2CoO_2Cu_2S_2$
Co-O (Å)	1.99639(1)	1.98770(3)	2.03210(2)
Co-S (Å)	3.0322(4)	2.9838(7)	3.3721(9)
Co-S/Co-O	1.5188(2)	1.5011(4)	1.6594(4)

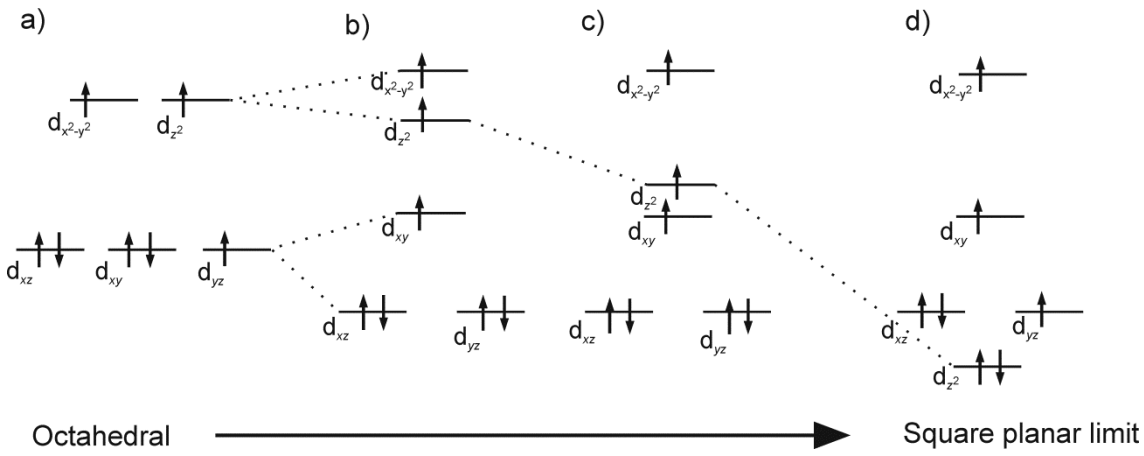


Fig. 5.34 Cartoon showing the d orbital splitting for high-spin Co^{2+} from a perfect octahedral (a) to a purely square-planar field (d), via a slightly (b) and highly (c) tetragonal distorted octahedron. Computational calculations suggested that scheme c) most-closely resembles the d-orbital environment of $Sr_2CoO_2Cu_2S_2$[61]

Further work is required to understand the cause of this low-temperature orthorhombic distortion. If $Ba_2CoO_2Cu_2S_2$ was reactive with respect to I_2, then it would be of interest to examine the effect of oxidation on the low temperature structure of $Ba_2CoO_2Cu_{2-x}S_2$.

5.3 Ag deintercalation from $Sr_2CoO_2Ag_2Se_2$ using iodine

5.3.1 Synthesis and deintercalation

$Sr_2CoO_2Ag_2Se_2$ was synthesised on the 5 g scale by weighing out SrO, Co, Ag and Se in the ratio 2:1:2:2, preparing them using the solid state method outlined in section 2.1.1 and heating to 835 °C (ramp rate: 10 °C min^{-1}), after 48 h the sample was allowed to cool in the furnace. Phase purity was assessed via in-house PXRD.

I_2 dissolved in MeCN was used to remove Ag from $Sr_2CoO_2Ag_2Se_2$, forming $Sr_2CoO_2Ag_{2-x}Se_2$, this was performed on samples that were either 0.5 g (for standard analysis) or ~4 g (for samples intended for PND), using the method described in section 2.1.3. However, AgI, a by-product of this reaction, is insoluble in MeCN. This was counteracted by adding a large excess of NaI, as described in section 2.1.3.1. Various concentrations of I_2 were used to produce $Sr_2CoO_2Ag_{2-x}Se_2$ samples with various values of *x*.

5.3.2 Lattice parameters and composition

As with the Cu analogues, the changes that occurred on oxidation were initially assessed by analysis of the change in lattice parameters derived from Rietveld refinement against PXRD data. The data was fitted using the standard *I*4/*mmm* model.

This gave a good fit to the data for all samples except those samples where an excess of I_2 had been used to remove the maximum amount of Ag. A representative fit is shown for a parent sample of $Sr_2CoO_2Ag_2Se_2$ in Fig. 5.35.

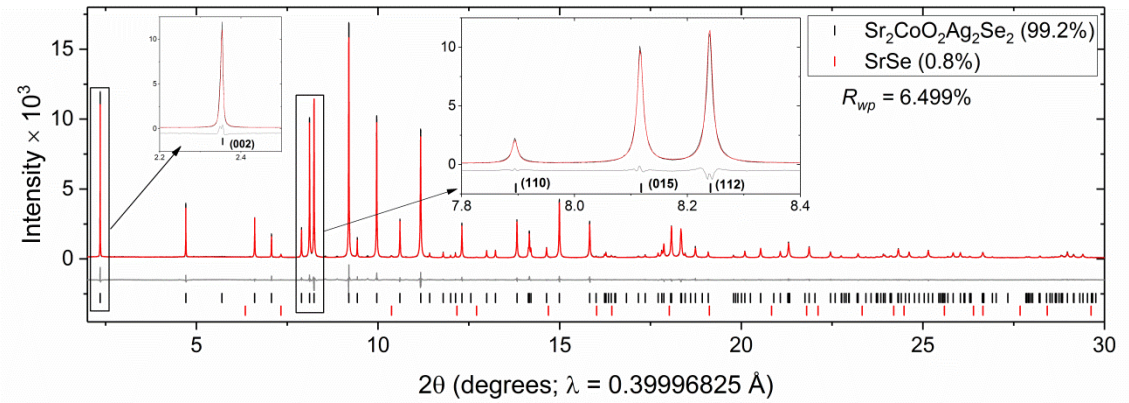


Fig. 5.35 Rietveld plot of parent $Sr_2CoO_2Ag_2Se_2$ (JNB043), synchrotron PXRD data measured at RT using ID22. The insets emphasise the fit to the data of the 002, 110, 015 and 112 peaks

The change in the lattice parameters of $Sr_2CoO_2Ag_{2-x}Se_2$ as Ag is deintercalated is very different from the relationship observed in the Cu analogues. While both *a* and *c* decrease as *x* increases, the relationship between the two is not linear over the whole range, as shown in Fig. 5.36. This relationship can be divided into two regions: "*A*" and "*B*". In region "*A*", the reduction in lattice parameter *a* dominates; in region "*B*", the reduction in lattice parameter *c* dominates.

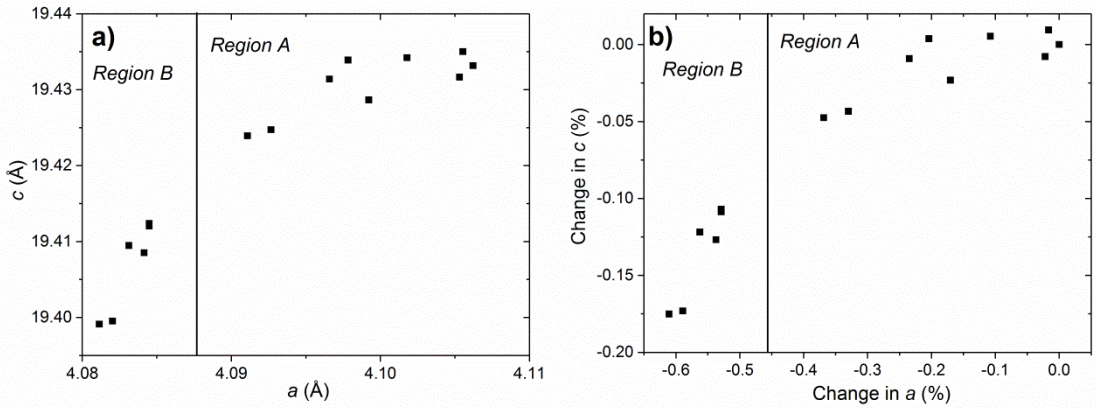


Fig. 5.36 Refined lattice parameters of various samples of $Sr_2CoO_2Ag_{2-x}Se_2$ in terms of a) absolute values and b) percentage change from the parent. Values obtained from Rietveld refinement against synchrotron PXRD data collected at the I11 beamline (using both the MAC detector and PSD). The error bars are smaller than the points on the graph

It is unusual that the change in *a* is significantly larger than the change in *c* (in percentage terms), this contrasts with the Cu-containing cases described above. It is

possible that this is related to the large amount of strain on the $AgSe_4$ tetrahedra, as is further discussed in section 5.5.2.

More significant is that the behaviour of $Sr_2CoO_2Ag_{2-x}Se_2$ may be divided into two regions, dependent on the extent of deintercalation. This suggests the onset of a phase change. Changes in the magnetic behaviour (discussed in sections 5.3.3, 5.3.4 and 5.3.6) and some changes in the structural behaviour (discussed in section 5.3.2.1) accompany the transition from region "*A*" to region "*B*".

5.3.2.1 *Stacking fault model for the most-deintercalated phase*

The stacking faults model described here was calculated by Dr S. J. Cassidy, using TOPAS Academic Version 6.[155]

Peak asymmetry was observed in samples where the compound had been reacted with a large excess of I_2, producing compounds with the smallest achievable lattice parameters and are therefore presumed to have the lowest Ag occupancy. Initially it was thought that this peak asymmetry was due to a phase-width within the sample, due to incomplete oxidation of the entire sample. However, the synthesis of several samples (JNB106, JNB130, JNB306) with similar peak shapes showed that this was a feature inherent to the most-oxidised compound. The character of the peak asymmetry was not consistent with a model in which several similar phases of $Sr_2CoO_2Ag_{2-x}Se_2$ were used, which might have resulted from an inhomogeneous Ag distribution. Therefore, it was hypothesised that the peak asymmetry arose from stacking faults.

Several stacking fault models were attempted, including several models that hypothesised that the stacking faults arose from different amounts of Ag in different $[Ag_{2-x}Se_2]$ layers within the compound. However, these models did not achieve as good a fit to the data as the turbostratic stacking fault model described here. This model divided the compound into two layers, A and B, which were stacked upon one another in an A-B-A-B formation, but with a refineable shift in the *a*, *b* and *c* directions, as shown in Fig. 5.37. The Ag fractional occupancy was modelled to be the same in every layer.

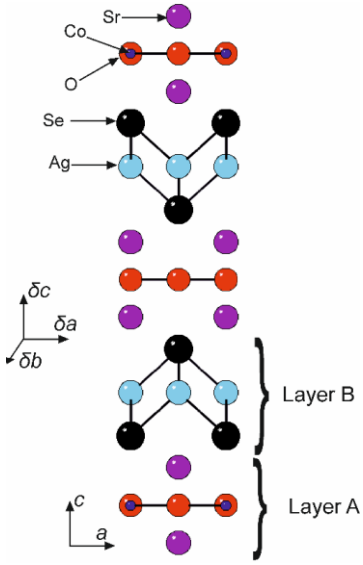


Fig. 5.37 The stacking fault model used to describe the behaviour of most-deintercalated $Sr_2CoO_2Ag_{2-x}Se_2$

It was found that increasing the total number of layers beyond 200 (50 unit cells), did not improve the fit to the data further. The Rietveld fit of JNB130 (most-deintercalated $Sr_2CoO_2Ag_{2-x}Se_2$) using the stacking fault model is compared to the fit using the simple *I*4/*mmm* model in Fig. 5.38. It shows a significant improvement to the fit is achieved using the stacking faults model, as also shown by comparison of the obtained R_{wp} values.

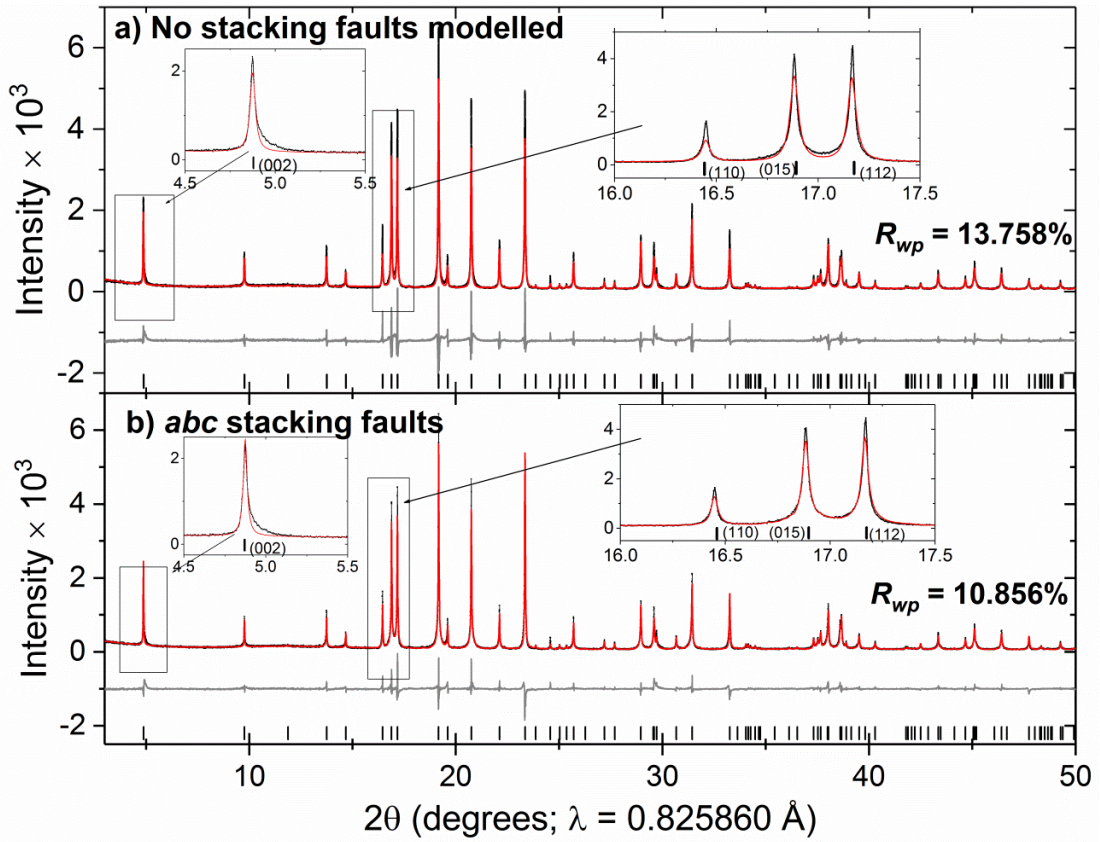


Fig. 5.38 Comparison of the fit to JNB130 (most-deintercalated $Sr_2CoO_2Ag_2Se_2$) a) a standard I4/mmm model is used and b) when xyz stacking faults are modelled. In both a) and b) the tick marks indicate peak positions as expected from the I4/mmm model. The synchrotron PXRD data was collected at RT using the MAC detector at the I11 beamline

The results of the modelling on the calculated structure are displayed in Fig. 5.39, in which each point represents the deviation of a layer from the previous layer *a*, *b* and *c* directions (δa, δb, δc).

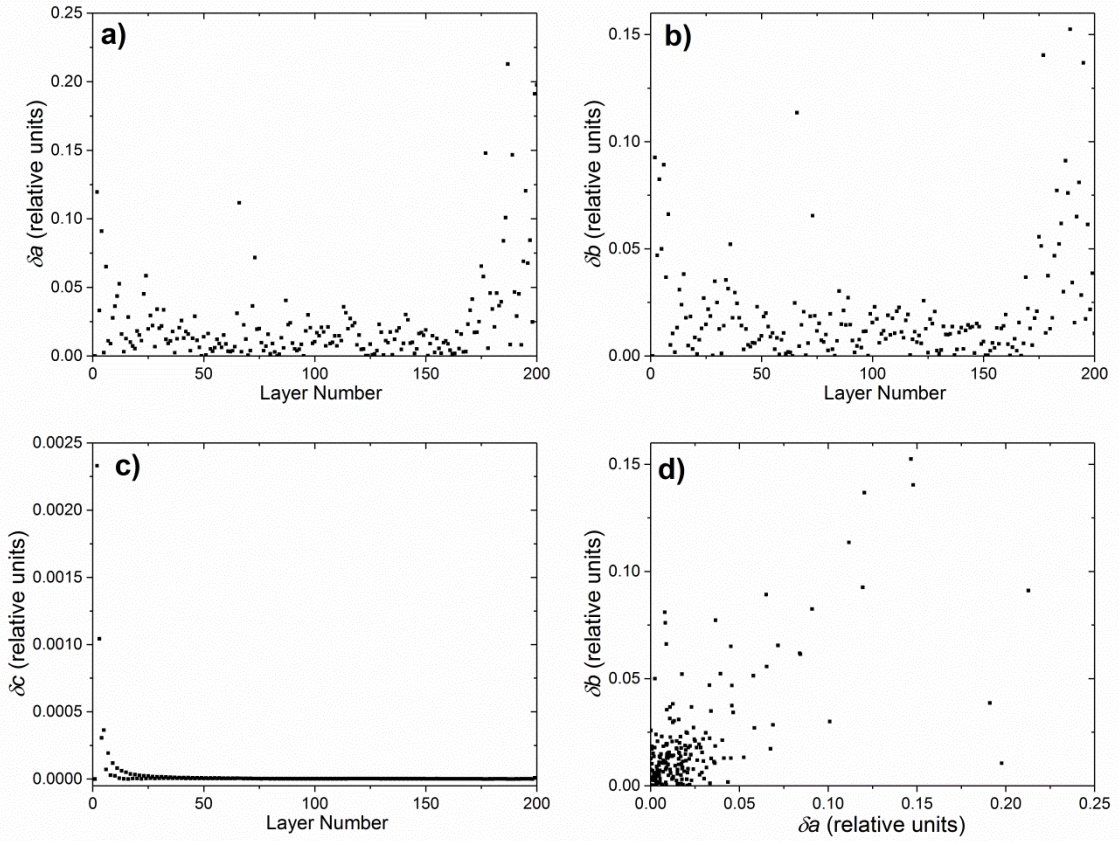


Fig. 5.39 The deviation of the layer from the previous layer in the a) a, b) b and c) c directions; d) shows the correlation between the layer deviations in the a and b directions. δa, δb and δc are in relative units, where a δx of 1 represents a shift of the layer from its ideal position relative to the previous layer by one unit cell in the x direction

Fig. 5.39 shows that the layer-to-layer changes are generally small, but that in some regions of the model, the layer-to-layer shifts are much larger in the *a* and *b* directions. At low values of *δa* and *δb* (< 0.05) there appears to be no correlation between *δa* and *δb*, but there is a small positive correlation between the two at larger values. Allowing refinement of the layer positions in the *c*-direction improved the quality of the fit, despite Fig. 5.39 c) showing that the refined shift in *c* was very small.

This model provides a significant improvement to the fit of data obtained for most-deintercalated $Sr_2Co_2O_2Ag_{2-x}Se_2$. It is likely that the observed shifts in the layers relative to one another arise from small inhomogeneity in the Ag content, perhaps from localised clustering or ordering that cannot be observed crystallographically. The use of high-resolution electron microscopy (e.g. HAADF-STEM imaging) could further improve understanding of the structure of this compound.

5.3.2.1.1 **Annealing experiment**

An annealing experiment was performed on a sample of most-deintercalated $Sr_2CoO_2Ag_{2-x}Se_2$ to investigate if the stacking faults observed were an artefact of the low temperature method used to produce the samples and could be removed by annealing.

5 × 0.3 g portions of JNB306 (most-deintercalated $Sr_2CoO_2Ag_{2-x}Se_2$) were sealed in separate silica ampoules. The ampoules were put in a hot furnace, heated to 100 °C, 200 °C, 250 °C, 300 °C and 400 °C respectively. The samples were left in the furnace for 16 h before quenching in ice-water. No crucible was used; this aided fast-cooling of the samples. Then each sample was isolated and examined by laboratory PXRD (Empyrean or ICL X'Pert), the results are shown in Fig. 5.40.

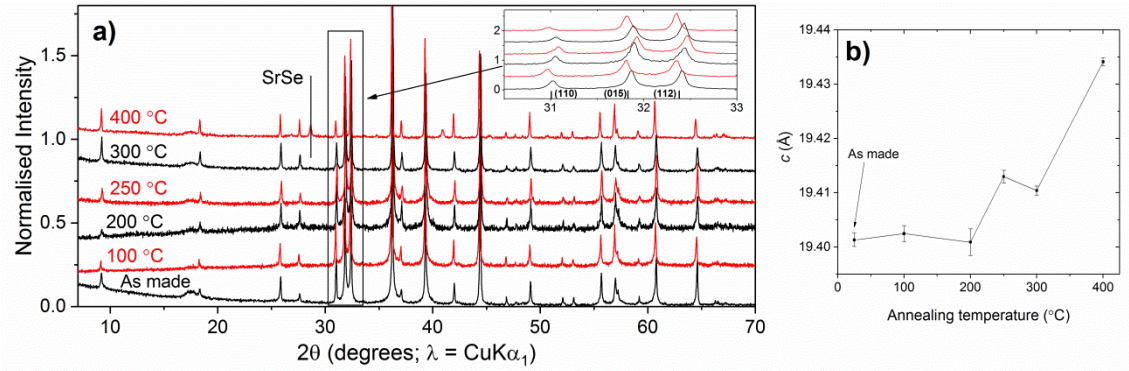


Fig. 5.40 a) Comparison of the normalised PXRD patterns of annealed samples of JNB306 (most-deintercalated $Sr_2CoO_2Ag_{2-x}Se_2$) with inset showing that the shape of the peaks does not change until there has been a large change in lattice parameters. b) The lattice parameter c as a function of annealing temperature ("as-made" sample showed with annealing temperature of 25 °C for clarity)

It was found that heating up to 200 °C had no measurable effect on the peak-shapes or positions, but heating beyond this caused decomposition of the most-deintercalated $Sr_2CoO_2Ag_{2-x}Se_2$ phase to the stoichiometric $Sr_2CoO_2Ag_2Se_2$ "parent" phase plus the corresponding decomposition products according to eq. 5.2, most notably (in the diffraction pattern) SrSe. This is shown in Fig. 5.40 by the appearance at high temperatures of additional peaks (indexed as known impurities) and by the shift of the *c* parameter to larger values at higher annealing temperatures. This suggests annealing cannot be used to remove stacking faults in the most-deintercalated $Sr_2CoO_2Ag_{2-x}Se_2$ samples without causing decomposition.

$$(1 + \delta)Sr_2CoO_2Ag_{2-x}Se_2 \longrightarrow Sr_2CoO_2Ag_2Se_2 + 2\delta SrSe + \delta CoO + (\delta/2)O_2 \qquad (5.2)$$

5.3.2.2 *Room temperature powder neutron diffraction*

Three 3 – 4 g samples of $Sr_2CoO_2Ag_{2-x}Se_2$ were measured at RT using HRPD to confirm the structure and composition of the compounds as a function of lattice parameters. The three samples were JNB101 (parent $Sr_2CoO_2Ag_2Se_2$), JNB243 (I_2 treated, region "*A*" intermediate) and JNB106 (most-deintercalated $Sr_2CoO_2Ag_{2-x}Se_2$).

In the first instance, all of the samples were refined using the standard *I*4/*mmm* model; the results of these refinements are shown in Table 5.25. Although this produced satisfactory Rietveld fits for JNB101 and JNB243, the presence of stacking faults in JNB106 severely lowered the quality of the fit, as shown in Fig. 5.41.

Table 5.25 Comparison of refined parameters for three samples of $Sr_2CoO_2Ag_{2-x}Se_2$, data obtained from refinement against RT HRPD PND data

Sample	JNB101	JNB243	JNB106
a (Å)	4.10271(2)	4.08922(4)	4.0856(2)
c (Å)	19.4290(1)	19.4084(2)	19.407(1)
Volume (Å^3)	327.033(4)	324.541(1)	323.95(4)
z(Sr)	0.41700(3)	0.41627(4)	0.4157(1)
z(Se)	0.15525(3)	0.15512(4)	0.1539(1)
Ag occupancy	1.000(4)	0.963(5)	0.76(2)
Sr U_{11} (Å^2)	0.0308(6)	0.0102(4)	0.038(3)
Sr U_{33} (Å^2)	0.0315(6)	0.0091(6)	0.109(4)
Co U_{11} (Å^2)	0.0246(9)	0.004(1)	0.034(5)
Co U_{33} (Å^2)	0.039(2)	0.012(2)	0.19(2)
O U_{11} (Å^2)	0.0301(6)	0.0099(7)	0.056(3)
O U_{22} (Å^2)	0.0278(6)	0.0110(6)	0.066(3)
O U_{33} (Å^2)	0.0343(7)	0.0101(7)	0.039(3)
Ag U_{11} (Å^2)	0.0396(7)	0.0251(9)	0.040(3)
Ag U_{33} (Å^2)	0.0419(8)	0.0197(9)	0.114(6)
Se U_{11} (Å^2)	0.0306(5)	0.0097(3)	0.048(2)
Se U_{33} (Å^2)	0.0333(6)	0.0107(5)	0.066(3)
R_{wp} (%)	3.888	4.181	10.801
χ^2	1.523	1.374	3.907

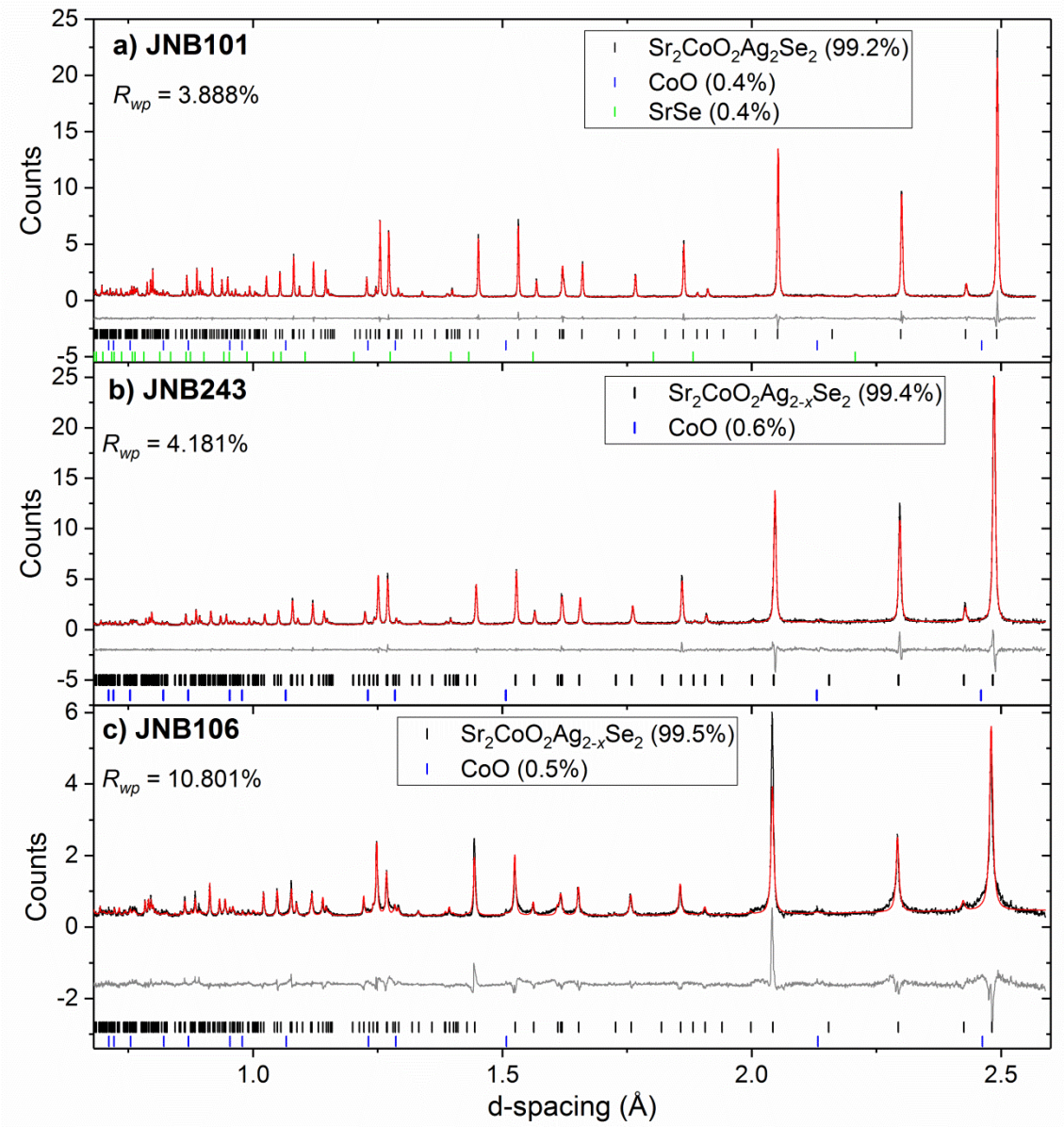


Fig. 5.41 Rietveld plots of a) JNB101 (parent $Sr_2CoO_2Ag_2Se_2$), b) JNB243 ($Sr_2CoO_2Ag_{1.93(1)}Se_2$) and c) JNB106 (most-deintercalated $Sr_2CoO_2Ag_{2-x}Se_2$). The PND data was measured using the backscattering bank of HRPD at RT

The poor quality of the fit to JNB106 (most-deintercalated $Sr_2CoO_2Ag_{2-x}Se_2$) using this model prevents a reliable value for the Ag occupancy from being extracted. Attempts were therefore made to fit the data with the stacking fault model described in section 5.3.2.1, the result of this Rietveld fit is shown in Fig. 5.42.

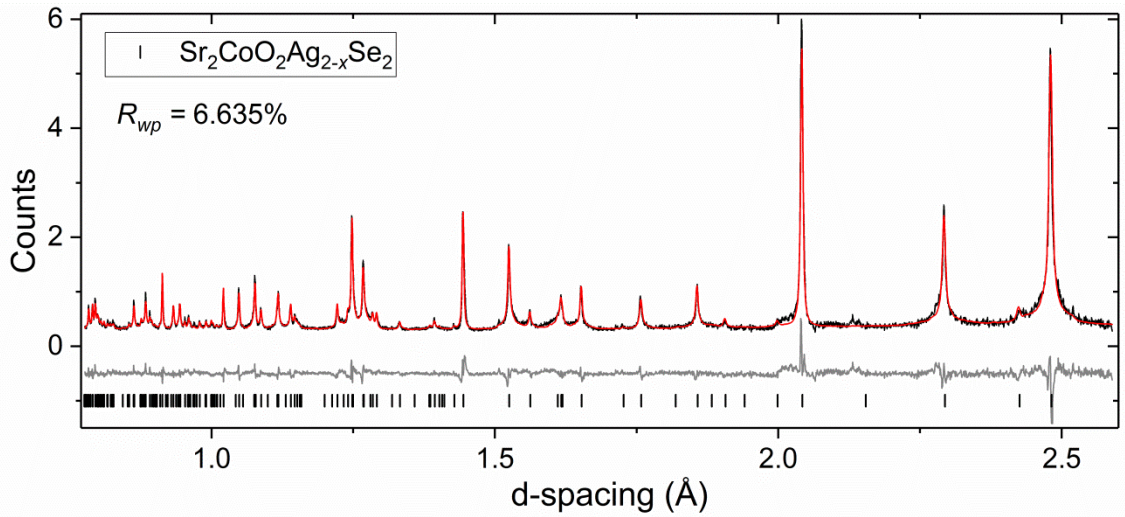


Fig. 5.42 Rietveld fit of JNB106 (most-deintercalated $Sr_2CoO_2Ag_{2-x}Se_2$), refined using the abc-stacking fault model described in section 5.3.2.1. The PND data was measured using the backscattering bank of HRPD at RT

Refining the PND data using the stacking fault model led to a refined Ag occupancy of 0.77(8), which is very similar to the value obtained when no stacking faults are modelled, and to the result from PXRD. However, as shown in Fig. 5.42, there are still significant discrepancies between the measured pattern and the fit, therefore the obtained Ag occupancy is of limited reliability and carries a large uncertainty.

5.3.2.3 *Energy dispersive X-ray spectroscopy*

The EDX data was collected and analysed in collaboration with Dr N. P. Young from the Department of Materials, University of Oxford.

EDX was performed in an attempt to confirm the Ag occupancy value obtained from refinement against PND data. Two samples of $Sr_2CoO_2Ag_{2-x}Se_2$: JNB010 (parent $Sr_2CoO_2Ag_2Se_2$) and JNB130 (most-deintercalated $Sr_2CoO_2Ag_{2-x}Se_2$) were analysed. EDX was performed on samples using a JEOL JEM-2100 transmission electron microscope (TEM). Spectra were collected from six different areas on the TEM grid for each sample. The spectra were integrated to produce atomic molar percentages of each of the elements: Sr, Co, O, Ag and Se in the sample. These values are tabulated in Appendix D, along with details of sample preparation and images of the area from which each spectrum was measured.

The values obtained for the O atomic percentages were extremely unreliable for both samples and generally much lower than expected. EDX is generally less reliable for atoms with a smaller atomic number (Z), but this was judged not to account fully for the

observed unreliability of the data. When a sample is measured using TEM, the sample is under a high vacuum, with a beam of electrons directed at it. This is a rather reducing environment, which may affect the obtained O atomic percentage. The O atomic percentage data was excluded from analysis due to its unreliability.

The rest of the data was normalised with respect to atomic percentage of the Sr atom, to produce atomic ratios, as shown in Table 5.26 for JNB010 (parent $Sr_2CoO_2Ag_2Se_2$) and Table 5.27 for JNB130 (most-deintercalated $Sr_2CoO_2Ag_{2-x}Se_2$). Also shown are the mean atomic ratios and the mean atomic ratios when specific spectra, considered to be outliers due to their large deviation from the mean, were excluded. Spectrum 1 was excluded from the JNB010 data and spectra 1 and 2 were excluded from the JNB130 data.

Table 5.26 Atomic ratios obtained from EDX analysis of JNB010 (parent $Sr_2CoO_2Ag_2Se_2$); data is normalised with respect to the Sr atom

Spectrum	Sr	Co	Ag	Se
1	1	0.841	1.615	1.003
2	1	0.553	0.928	0.994
3	1	0.544	1.146	1.011
4	1	0.588	1.177	1.088
5	1	0.754	1.125	0.976
6	1	0.866	1.121	0.959
Mean(su)	1	0.7(1)	1.2(2)	1.01(4)
Mean(su) (excluding outliers)	1	0.7(1)	1.10(9)	1.01(4)

Table 5.27 Atomic ratios obtained from EDX analysis of JNB130 (most-deintercalated $Sr_2CoO_2Ag_{2-x}Se_2$); data is normalised with respect to the Sr atom

Spectrum	Sr	Co	Ag	Se
1	1	0.536	0.577	0.980
2	1	0.595	1.083	1.034
3	1	0.567	0.815	1.040
4	1	0.581	0.770	1.088
5	1	0.612	0.971	1.152
6	1	0.564	0.722	1.093
Mean(su)	1	0.58(2)	0.8(2)	1.06(5)
Mean(su) (excluding outliers)	1	0.58(2)	0.82(9)	1.09(4)

The results of this analysis lead to an atomic composition of 2Sr:1.4(2)Co:2.2(2)Ag:2.02(8)Se for JNB010 (parent $Sr_2CoO_2Ag_2Se_2$) and 2Sr:1.16(4)Co:1.6(2)Ag:2.18(8)Se for JNB130 (most-deintercalated $Sr_2CoO_2Ag_{2-x}Se_2$). The Ag occupancy is overestimated by ~10% in JNB010 from the stoichiometric value

(2.0) (this sample is effectively being used as a calibration in this EDX experiment), if a similar overestimation of the Ag occupancy can be assumed in JNB130, then the obtained Ag occupancy would be 1.45. However, due to the large errors observed in this analysis, as observed not just from variations in the Ag ratios, but also in the Co and Se ratios lead to the conclusion that an error of a minimum 10% must be assumed, resulting in a composition of $Sr_2CoO_2Ag_{1.5(2)}Se_2$.

However, this value is in good agreement with the Ag occupancy obtained independently from Rietveld refinement against PND and PXRD data ($Sr_2CoO_2Ag_{1.5(2)}Se_2$), so can be considered a best estimate of the Ag composition.

5.3.3 Magnetometry

Magnetometry measurements were performed on four samples of $Sr_2CoO_2Ag_{2-x}Se_2$ to observe the changes in magnetic behaviour that occurred on removal of Ag. The lattice parameters of these samples are shown in Fig. 5.43. Two of the samples are in region "*A*" and two are in region "*B*".

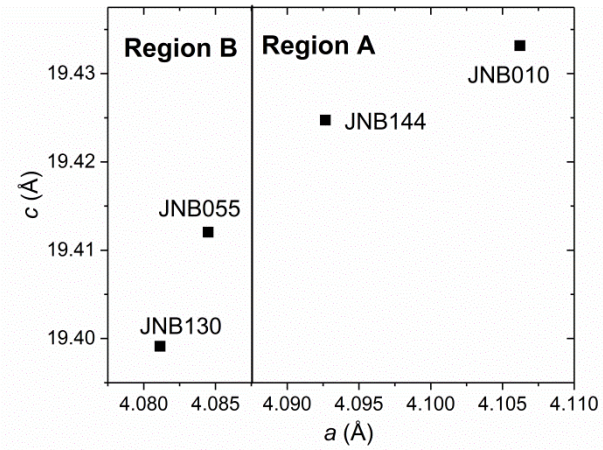


Fig. 5.43 Refined lattice parameters of the four samples of $Sr_2CoO_2Ag_{2-x}Se_2$ that were measured using magnetic susceptibility. The error bars are smaller than the points on the graph

The magnetic susceptibility measurements (Fig. 5.44) show that samples with lattice parameters in region "*A*" appear to be antiferromagnetic, while the two samples with lattice parameters in region "*B*" have magnetic susceptibility curves consistent with the onset of a ferromagnetic component below 75 K. This implies that a magnetic phase transition occurs on removal of Ag.

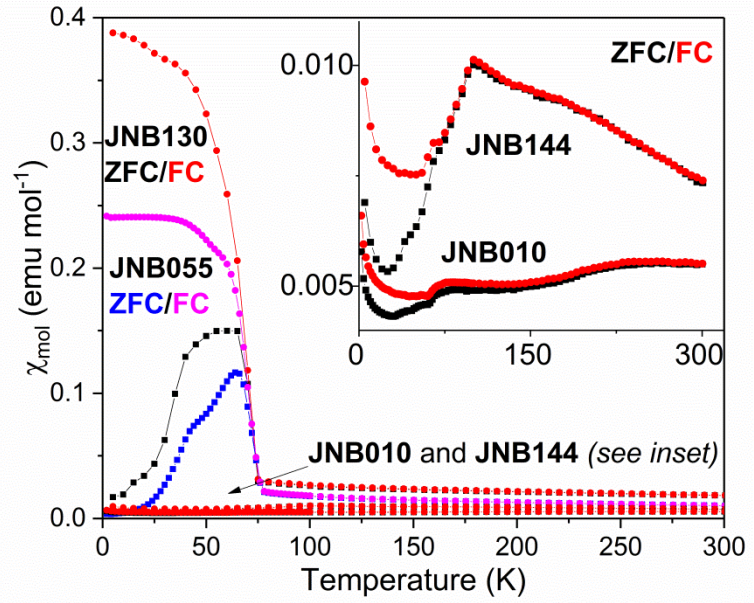


Fig. 5.44 Zero-field-cooled (ZFC) and field-cooled (FC) magnetic susceptibility measurements of selected samples of $Sr_2CoO_2Ag_{2-x}Se_2$

The magnetic susceptibility curve of JNB010 (parent $Sr_2CoO_2Ag_2Se_2$) I_2 is consistent with the magnetic susceptibility previously reported for the stoichiometric compound.[60, 62] There is a broad transition in the range 200 – 300 K, which has been identified as T_N and divergence of the zero-field-cooled (ZFC) and field-cooled (FC) curves below ~70 K, suggestive of a degree of magnetic disorder in the compound leading to glassy behaviour. The magnetic susceptibility behaviour of JNB144 (region "*A*" intermediate) is like that of JNB010, but the divergence of the ZFC and FC curves is significantly larger, suggesting that the compound is even more magnetically disordered. This would be consistent with the partially oxidised compound now containing a mix of Co^{2+}/Co^{3+} ions, with no charge ordering.

Field-cooled *M vs H* isotherms, measured at 5 K, were used to investigate the spin-glass behaviour of the region "*A*" samples further (Fig. 5.45). The magnetisation isotherms of both the region "*A*" samples measured are predominantly linear, consistent with antiferromagnetic behaviour. However, both samples, but particularly JNB144 (region "*A*" intermediate), exhibit hysteresis at low fields, with significant displacement from the origin also observed in JNB144. The hysteresis in JNB010 (parent $Sr_2CoO_2Ag_2Se_2$) is most likely due to a small elemental Co impurity, present below the limit that can be observed by diffraction. However, the sizable displacement from the origin of the hysteresis loop in JNB144 is further evidence of a significant spin-glass component to

the magnetic ordering in this sample, which is introduced in the early stages of oxidation.

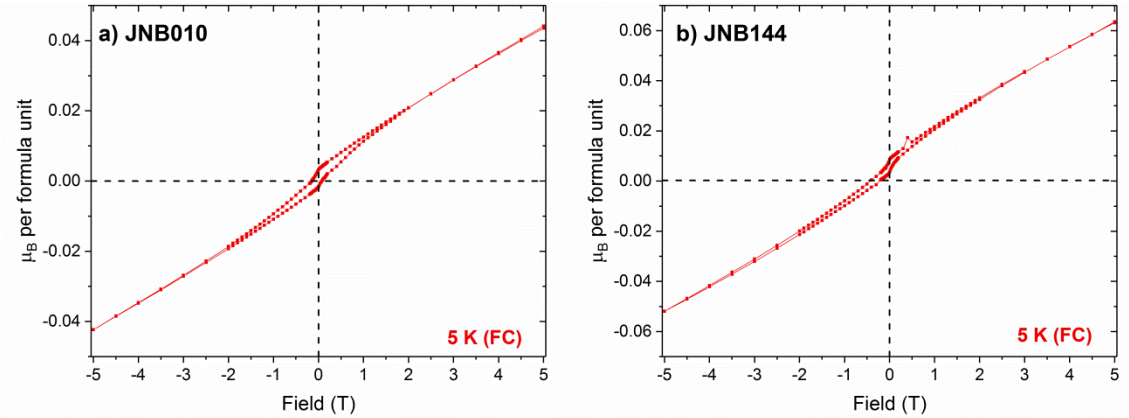


Fig. 5.45 M vs H isotherms of a) JNB010 (parent $Sr_2CoO_2Ag_2Se_2$) and b) JNB144 (region "A" intermediate); measured at 5 K after cooling in a 5 T field

Magnetisation isotherms of two region "*B*" samples: JNB055 (region "*B*" intermediate) and JNB130 (most-deintercalated $Sr_2CoO_2Ag_{1.5(2)}Se_2$), were measured at several temperatures. These isotherms (Fig. 5.46) demonstrate that up to three transitions occur below 150 K. The isotherms of JNB130 show that at 80 K above ~2.5 T the magnetic susceptibility increases more rapidly than at low fields and a small amount of hysteresis is observed, characteristic, perhaps, of field-induced ferromagnetism (metamagnetic behaviour) at higher fields. The hysteresis loops measured at 65, 50 and 30 K are characteristic of a "soft" ferromagnet, which saturates at relatively low field and with only a small amount of hysteresis. The saturated moment of JNB130 at 30 K is ~0.5 μ_B per Co, significantly below that predicted by the spin-only value expected for high-spin Co^{2+} (3 μ_B), even if the oxidation results in some low-spin Co^{3+}. The isotherm measured at 5 K, while still retaining a large ferromagnetic component is highly asymmetric, suggesting that the compound has undergone a spin-glass-like transition.

The two isotherms of JNB055 (Fig. 5.46 a)) indicate that similar magnetic behaviour might be expected in this compound. The isotherm at 5 K is very displaced from the origin and asymmetric, again indicating spin-glass behaviour. The isotherm at 50 K seems characteristic of a soft ferromagnet, analogous to JNB130, except the saturation moment is lower (~0.2 μ_B per Co). Above ~2.5 T the magnetic susceptibility is linear and positive suggesting that not all the moments are aligned ferromagnetically. The hysteresis loop is also not closed, which suggests that a glassy component to the

magnetism is present in this case also. This might suggest there are mixed ferromagnetic/antiferromagnetic regions in JNB055.

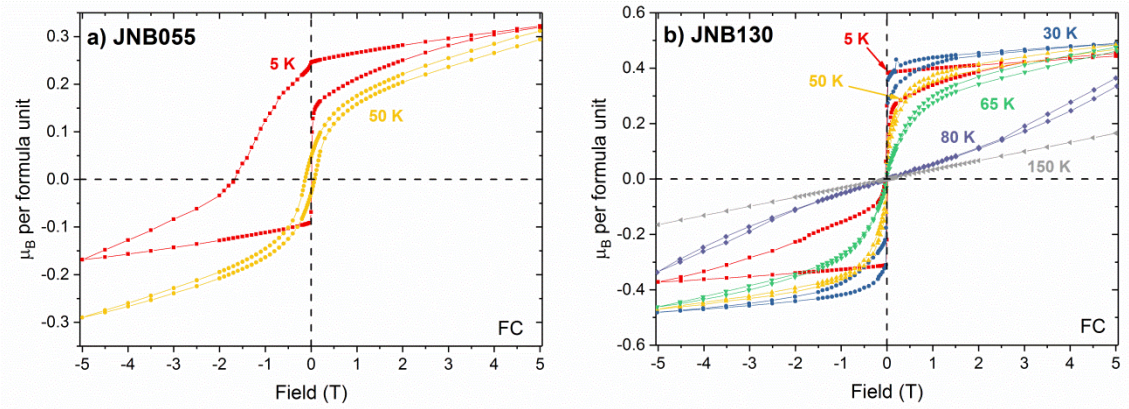


Fig. 5.46 M vs H isotherms, measured at various temperature for a) JNB055 (region "B" intermediate) and b) JNB130 (most-deintercalated $Sr_2CoO_2Ag_{1.5(2)}Se_2$). Before each measurement the sample was cooled from 300 K in a 5 T field

5.3.4 Powder neutron diffraction to probe changes in magnetic ordering

The magnetic structure of stoichiometric $Sr_2CoO_2Ag_2Se_2$ has previously been solved by Herkelrath.[62] $Sr_2CoO_2Ag_2Se_2$ was shown to adopt an antiferromagnetic structure based on a $\sqrt{2}a \times \sqrt{2}a \times c$ expansion of the unit cell, with antiferromagnetic coupling of nearest-neighbour spins. Herkelrath refined the crystal structure of $Sr_2CoO_2Ag_2Se_2$ using a collinear model, with a non-zero component in each of the *a*, *b* and *c* directions.[62]

The same three samples of $Sr_2CoO_2Ag_{2-x}Se_2$ that were measured at RT using HRPD were also measured using OSIRIS and HRPD at 5 K, allowing combined refinement against these datasets. This was done so that the changes in magnetic structure as a function of Ag occupancy could be analysed.

Comparison of the raw PND patterns (Fig. 5.47) showed a general reduction in the intensity of the magnetic peaks from the parent (JNB101) to $Sr_2CoO_2Ag_{1.93(1)}Se_2$ (JNB243, region "*A*"). No additional peaks were observed for JNB106 (most-deintercalated $Sr_2CoO_2Ag_{1.5(2)}Se_2$, region "*B*"). This showed that the ferromagnet-like behaviour observed from the magnetic susceptibility measurement does not arise from long-range canted antiferromagnet or ferrimagnetic ordering.

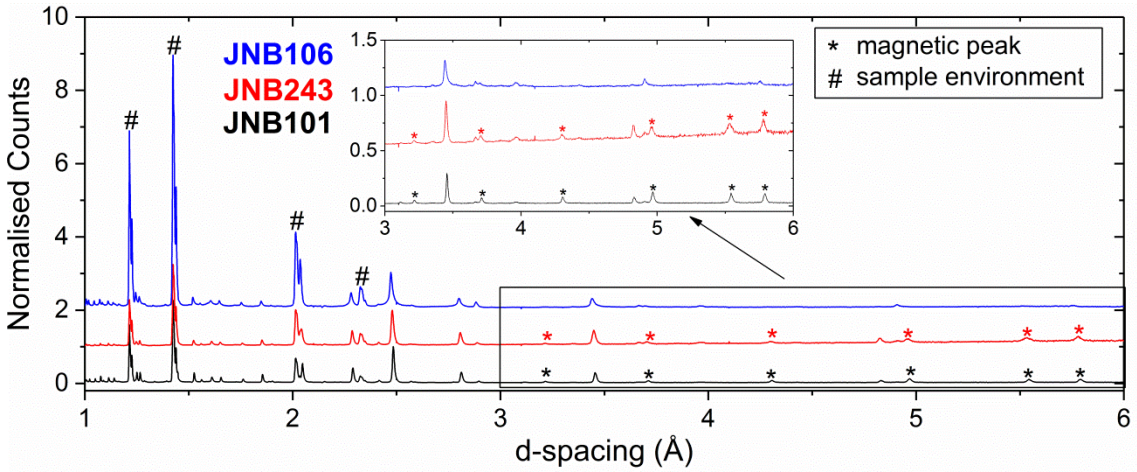


*Fig. 5.47 Offset PND patterns of JNB106 ($Sr_2CoO_2Ag_2Se_2$), JNB243 ($Sr_2CoO_2Ag_{1.93(1)}Se_2$) and JNB106 (most-deintercalated $Sr_2CoO_2Ag_{2-x}Se_2$) measured using OSIRIS at 5 K. The * symbols highlight the main peaks arising from antiferromagnetic ordering and the # symbols highlight the four main peaks arising from the sample environment (primarily the Al-tailed cryostat)*

Since no additional peaks were observed in the PND pattern of JNB106 (most-deintercalated $Sr_2CoO_2Ag_{1.5(2)}Se_2$), the nuclear peaks were examined to see if there was additional intensity on these peaks that may have indicated long-range ferromagnetic ordering. To aid this search, three PND patterns were simulated to show the effect of a 0.5 μ_B moment in either the *c* or *a* direction, as shown in Fig. 5.48. This analysis indicated that, within the *d*-spacing range that was measured, additional intensity would be observed primarily on the 006 and 011 peaks. 0.5 μ_B is the upper bound of the saturated ferromagnetic moment indicated by the hysteresis loop measurements in Fig. 5.46 b).

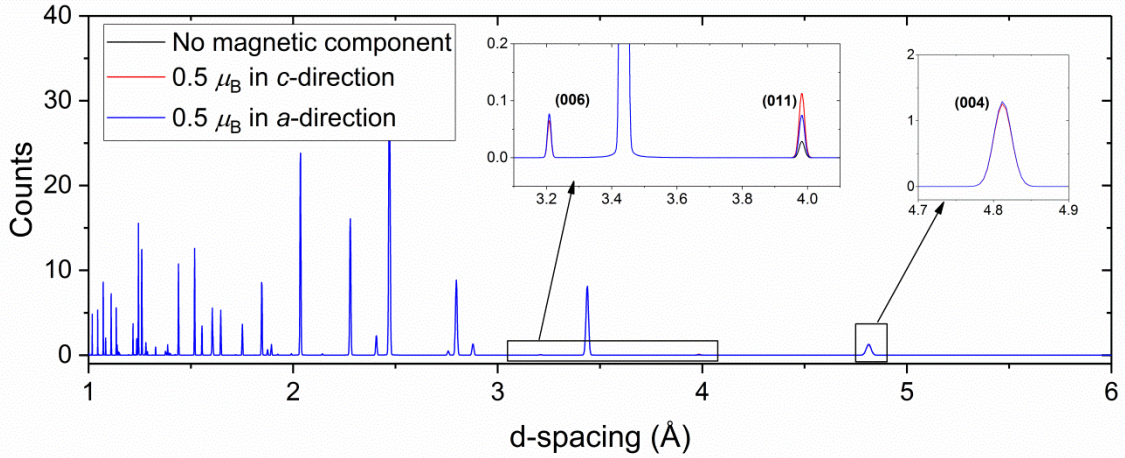


Fig. 5.48 Comparison of simulated PND patterns of $Sr_2CoO_2Ag_2Se_2$ when there is no magnetic intensity, a 0.5 μ_B ferromagnetic component in the c-direction and a 0.5 μ_B ferromagnetic component in the a-direction. The insets emphasise areas where changes in the intensity are observed

Comparison of the PND patterns measured at 5 K (significantly below T_C) and 100 K (above T_C) (see Fig. 5.49) showed no significant differences in the intensity around these peaks. However, it is difficult to be conclusive due to the small intensity changes expected from a comparatively small ferromagnetic component, compared with the low signal-to-noise ratio of the data. It is also noted that the 011 peak is coincident with a peak arising from the sample environment, hindering analysis of this peak.

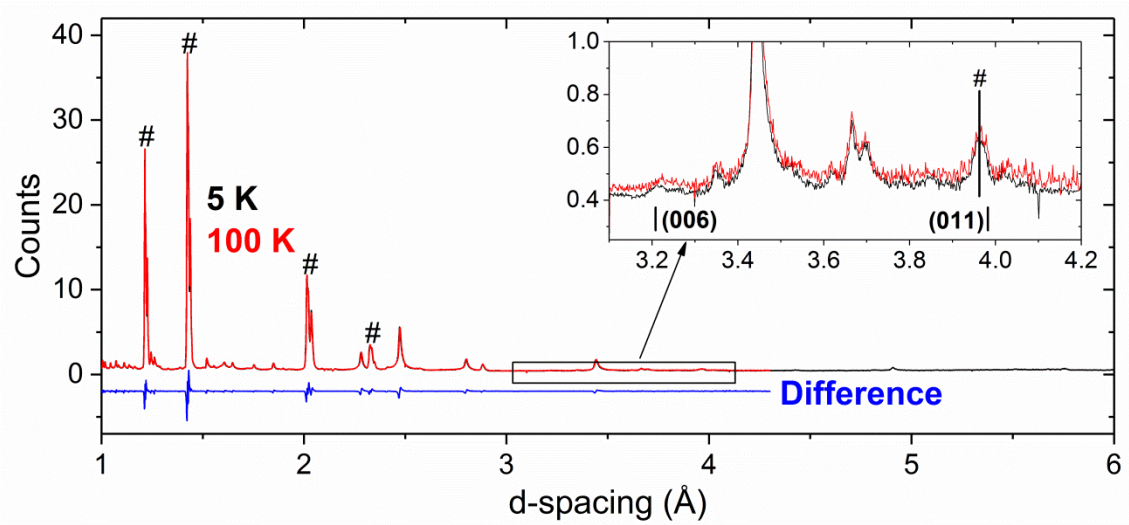


Fig. 5.49 Comparison of the PND pattern of JNB106 (most-deintercalated $Sr_2CoO_2Ag_{1.5(2)}Se_2$) when measured using OSIRIS at 5 and 100 K, with a curve of the difference between the two. The inset emphasises the region where additional intensity from ferromagnetic ordering might be expected and the # symbols highlight the four main peaks arising from the sample environment (primarily the Al-tailed cryostat)

The magnetic structures of JNB101 and JNB243 were initially refined in magnetic space group *P*1 (1.1), using refinement of the mX2$^+$(a), mX3$^+$(a) and mX4$^+$(a) modes, as are described for $Sr_2CoO_2Cu_2S_2$ (see Fig. 5.11). As for $Sr_2CoO_2Cu_2S_2$, it was found that it was necessary to refine the mX3$^+$(a) and mX4$^+$(a) modes but not the mX2$^+$(a) mode to achieve a good fit to the data. Therefore the P_C4_2/n (86.73) magnetic space group was used, with structure as shown in Fig. 5.12 for $Sr_2CoO_2Cu_2S_2$. This magnetic structure differs from that found by Herkelrath, in that it was not found necessary to have a non-zero μ_c component.[62] Rietveld plots of this data are shown in Fig. 5.50 and the refined magnetic moments are shown in Table 5.28.

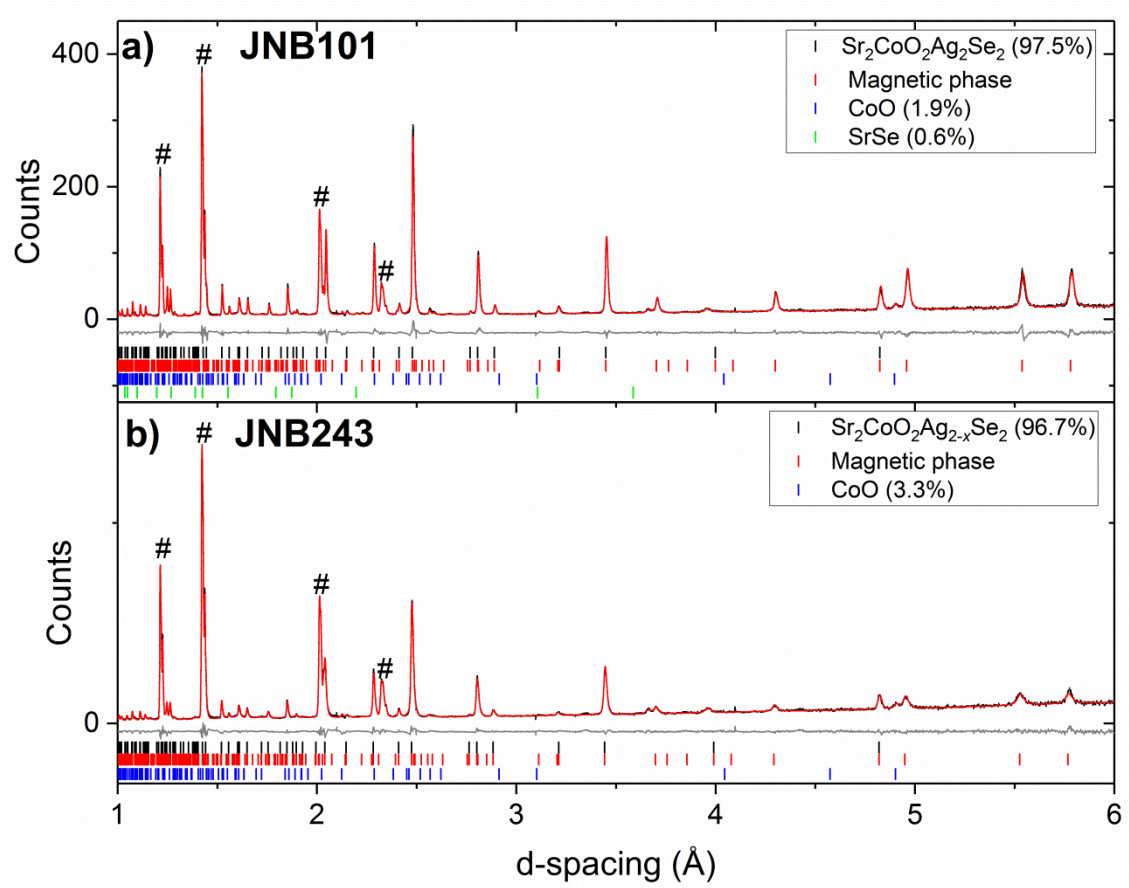


Fig. 5.50 Rietveld plot of a) JNB101 (parent $Sr_2CoO_2Ag_2Se_2$) and b) JNB243 ($Sr_2CoO_2Ag_{1.93(1)}Se_2$) measured at 5 K using OSIRIS. The # symbols indicate the four main peaks arising from the sample environment (primarily the aluminium-tailed cryostat).

Table 5.28 Comparison of the refined ordered moment of samples of $Sr_2CoO_2Ag_{2-x}Se_2$, data obtained from combined refinement against HRPD and OSIRIS data measured at 5 K

Sample	JNB101	JNB243	JNB106
Composition	$Sr_2CoO_2Ag_2Se_2$	$Sr_2CoO_2Ag_{1.93(1)}Se_2$	$Sr_2CoO_2Ag_{1.5(2)}Se_2$
Temperature (K)	5	5	5
Radiation	Neutron, ToF	Neutron, ToF	Neutron, ToF
Diffractometer	OSIRIS/HRPD	OSIRIS/HRPD	OSIRIS/HRPD
μ_a (μ_B)	0.53(2)	0.30(7)	0*
μ_b (μ_B)	3.10(2)	2.34(7)	0*
μ_c (μ_B)	0*	0*	0*
$\lvert\mu\rvert$ (μ_B)	3.56(4)	2.5(1)	0*
R_{wp} (%)	3.095	3.440	-
χ^2	1.390	1.560	-

*not refined

The results of these Rietveld refinements show that oxidation of Co from Co^{2+} in JNB101 (parent $Sr_2CoO_2Ag_2Se_2$) to $Co^{2.07(1)+}$ in JNB243 ($Sr_2CoO_2Ag_{1.93(1)}Se_2$) causes a ~30% loss of ordered magnetic moment. As in the case of the Cu-containing analogues

(see section 5.2.4), this was considered to be too large to arise solely by loss of unpaired spin from oxidation. Therefore, the ordered magnetic moment was analysed in terms of ordered phase fractions, using eq. 5.1. The results of this analysis are shown in Table 5.29. The magnetisation isotherms, suggestive of a large increase in the spin-glass behaviour of the compound as a function of deintercalation support the analysis of these compounds in these terms.

Table 5.29 Comparison of the calculated "total ordered phase fraction" of samples of $Sr_2CoO_2Ag_{2-x}Se_2$

Sample	JNB101	JNB243
Composition	$Sr_2CoO_2Ag_2Se_2$	$Sr_2CoO_2Ag_{1.93(1)}Se_2$
Total ordered phase fraction (%)	100	49(4)

Although this magnetic model generally produces a good fit to the data, a small discrepancy in the peak position of the 110 peaks (indexed using the magnetic unit cell) was observed in the PND pattern of JNB101, shown in Fig. 5.51. It is possible that this is due to a structural distortion at low temperature, causing a shift in the position of the magnetic peaks. However, attempts to model this distortion did not improve the fit to the data.

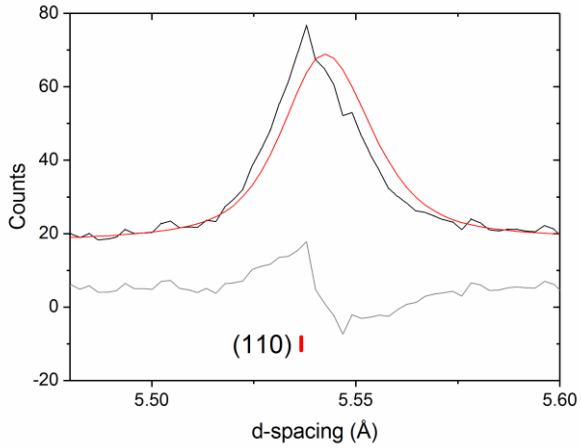


Fig. 5.51 The quality of the fit to the 110 peak (indexed using the magnetic unit cell) of JNB101 (parent $Sr_2CoO_2Ag_2Se_2$*) in the model. The PND data was measured at 5 K using OSIRIS*

5.3.5 Structural distortion at low temperature

Three samples of $Sr_2CoO_2Ag_{2-x}Se_2$ were measured using PXRD in the temperature range 5 – 100 K using ID22 to observe if any structural distortion, beyond the stacking faults that have already been discussed, accompany the transition from region "*A*" to region "*B*". Any distortions that appeared below the temperature of a known magnetic

transition may have provided evidence for the mechanism by which the observed change in magnetic behaviour occurred (discussed further in section 5.3.6).

A small orthorhombic distortion in parent $Sr_2CoO_2Ag_2Se_2$ (JNB043) was observed at low temperatures. It is possible that this orthorhombic distortion is present in JNB144 (region "*A*" intermediate) and JNB130 (most-deintercalated $Sr_2CoO_2Ag_{2-x}Se_2$), however analysis of these low temperature distortions was obfuscated by the stacking faults that appear in JNB130 and the broadness of the peaks in JNB144. For this reason, only the parent compound (JNB043) was analysed quantitatively. Fig. 5.52 shows the change in the distortion of JNB043 as a function of temperature and also compares the 200/020 peak of the three samples at 5 K; Table 5.30 shows the refined parameters of JNB043 using the *Immm* model and compares it to the data for JNB144 and JNB130, which for simplicity were both indexed using a model utilising a single phase with *I4/mmm* symmetry. The size of the orthorhombic distortion of JNB043 at 5 K (~0.7×10^{-3}) is of a comparable size to the orthorhombic distortion in most-deintercalated $Sr_2CoO_2Cu_{1.89}Se_2$ (JNB104, ~1.0×10^{-3}, see section 5.2.5).

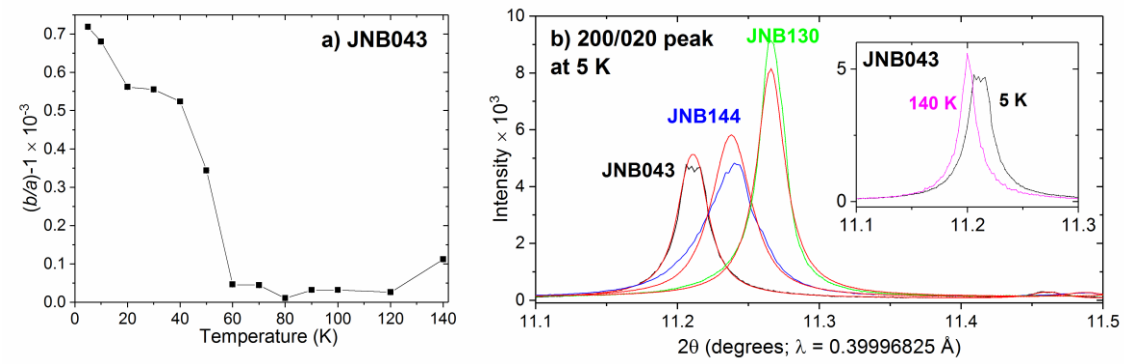


Fig. 5.52 a) Orthorhombic distortion of JNB043 (parent $Sr_2CoO_2Ag_2Se_2$) as a function of temperature (the line is a guide to the eye and error bars are smaller than the points on the graph); b) the splitting of the 200/020 peak at 5 K for JNB043, JNB144 (region "A" intermediate) and JNB130 (most-deintercalated $Sr_2CoO_2Ag_{1.5(2)}Se_2$). The inset shows the difference in the 200/020 peak of JNB043 at 5 K and 140 K

Table 5.30 Comparison of refined parameters for three samples of $Sr_2CoO_2Ag_{2-x}Se_2$, values obtained from Rietveld refinement against synchrotron PXRD data collected at 5 K using ID22. JNB130 has been refined without reference to stacking faults

Sample	JNB043	JNB144	JNB130
Radiation	X-ray, λ = 0.39996825 Å		
Detector	ID22		
Temperature (K)	5		
Space group	*Immm*	*I4/mmm*	*I4/mmm*
a (Å)	4.09592(4)	4.08464(2)	4.07469(2)
b (Å)	4.09298(3)	≡ *a*	≡ *a*
c (Å)	19.31980(5)	19.3160(1)	19.2937(1)
Volume (Å^3)	323.886(4)	322.273(3)	320.335(3)
z(Sr)	0.41669(3)	0.41607(4)	0.41482(5)
z(Se)	0.84479(3)	0.15522(4)	0.15468(5)
z(Ag)	0.7489(1)	0.75*	0.75*
Ag occupancy	1.017(1)	0.962(1)	0.881(2)
Sr U_{11} (Å^2)	0.0000(2)	0.0009(3)	0.0000(3)
Sr U_{33} (Å^2)	0.0000(3)	0.0000(5)	0.0029(5)
Co U_{11} (Å^2)	0.0022(4)	0.0025(6)	0.0003(7)
Co U_{33} (Å^2)	0.0000(6)	0.000(1)	0.001(1)
O U_{11} (Å^2)	0.002(7)	0.008(4)	0.008(4)
O U_{22} (Å^2)	0.002(7)	0.008(4)	0.009(4)
O U_{33} (Å^2)	0.000(2)	0.008(3)	0.021(5)
Ag U_{11} (Å^2)	0.0066(2)	0.0144(3)	0.0149(4)
Ag U_{33} (Å^2)	0.0000(3)	0.0000(4)	0.0071(6)
Se U_{11} (Å^2)	0.0000(2)	0.0020(3)	0.0026(4)
Se U_{33} (Å^2)	0.0000(3)	0.0000(5)	0.0053(6)
R_{wp} (%)	7.424	10.422	12.457
χ^2	2.658	4.281	5.536

*not refined

Qualitative comparison of the 200/020 peaks at 5 K reveals that the orthorhombic distortion appears to decrease as a function of deintercalation. However, further measurements on more samples would be required to confirm this trend. This is the reverse of the trend observed for $Sr_2CoO_2Cu_{2-x}S_2$ and $Sr_2CoO_2Cu_{2-x}Se_2$.

5.3.6 Discussion of magnetic behaviour

The initial reduction of ordered magnetic moment as Ag is removed from $Sr_2CoO_2Ag_{2-x}Se_2$ might be expected from the disorder induced by introduction of Co^{3+} centres into the lattice of Co^{2+} ions, as discussed in section 5.2.4.4 for the Cu-containing analogues. The antiferromagnetic-to-ferromagnetic transition as a function of *x* observed here was not observed in the Cu analogues; this is likely because significantly more Ag has been deintercalated from $Sr_2CoO_2Ag_{2-x}Se_2$ than Cu was deintercalated from $Sr_2CoO_2Cu_{2-x}Ch_2$ (*Ch* = S, Se).

A possible cause of the change in magnetic behaviour is that enough Co ions have been oxidised from Co^{2+} to Co^{3+} that the primary interaction between nearest-neighbour Co ions is ferromagnetic, rather than antiferromagnetic, superexchange, as determined by Goodenough-Kanamori rules and shown in Fig. 5.53.[84-86]

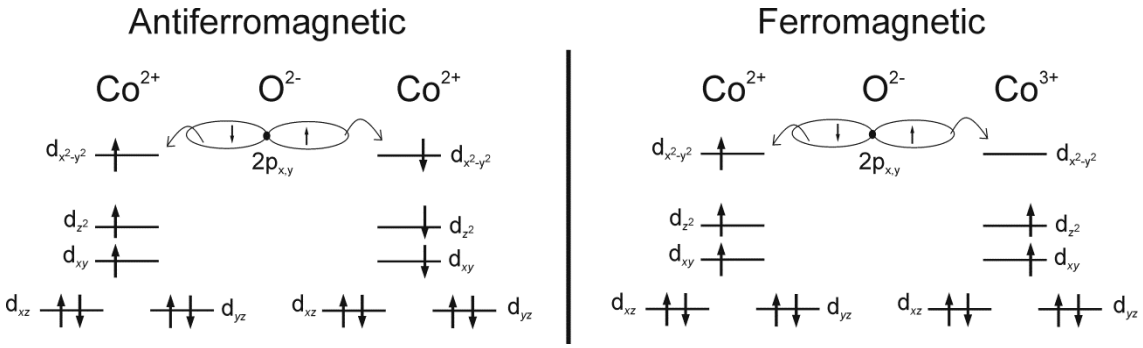


Fig. 5.53 Schematic of superexchange interactions that may lead to nearest-neighbour antiferromagnetic and ferromagnetic interactions in the [CoO_2] planes

However, if this model were correct, saturated ferromagnetic moments as high as 2.5 μ_B, assuming the spin states shown in Fig. 5.53, would be expected, when the highest saturated magnetic moment found in most-deintercalated $Sr_2CoO_2Ag_{1.5(2)}Se_2$ (JNB130) is ~0.5 μ_B (at 30 K), and there is no sign of any long-range order in the PND patterns at low temperatures. Evidence of charge ordering in the nuclear structure may also be expected, which was not observed from low temperature PXRD measurements, although subtle effects may have been obfuscated by the broadness of the peaks, caused by stacking faults, in most-deintercalated $Sr_2CoO_2Ag_{2-x}Se_2$.

Another model to consider is itinerant ferromagnetism. In this model the unpaired electrons are delocalised into bands, which then split spontaneously to produce a net ferromagnet if the increase in kinetic energy from this splitting is less than the reduction in potential energy from a reduction in the number of electron-electron exchange interactions. The magnitude of the magnetic moment is therefore dependent on this energy difference and thus the degree to which the band structure is spin-polarised and not solely the amount of unpaired spin (as is the case when ferromagnetism arises from localised interactions).

Since a premise of itinerant ferromagnetism is the delocalisation of electrons into bands, this would imply that region "*B*" $Sr_2CoO_2Ag_{2-x}Se_2$ is metallic below T_C. This could be confirmed by conductivity measurements. These measurements have not been performed because in most cases a sintered pellet or single crystal is required and, as

shown in section 5.3.2.1.1, most-deintercalated $Sr_2CoO_2Ag_{2-x}Se_2$ decomposes above ~250 °C, well below the temperature required to achieve good grain-to-grain contact in a sintered pellet of this compound. If large (~1 mm) single crystals of most-deintercalated $Sr_2CoO_2Ag_{2-x}Se_2$ could be synthesised, it may be possible to perform conductivity measurements. However, since the process of removing Ag causes microstructural stacking faults, this is likely to result in macrostructural fracturing of the crystallites, which would hinder accurate conductivity measurements.

5.3.6.1 *AC magnetic susceptibility measurements*

AC magnetic susceptibility measurements were performed on most-deintercalated $Sr_2CoO_2Ag_{1.5(2)}Se_2$ (JNB130) to further investigate the ferromagnetic transition. The AC magnetic susceptibility was measured in the temperature range 2 – 80 K at multiple frequencies and is shown in Fig. 5.54. Two frequency-dependent transitions can be observed, one at ~20 K and a significantly larger transition at ~70 K. Comparison of this AC magnetometry data with the magnetisation isotherms shown in Fig. 5.46 b) suggests that the transition at ~20 K can be identified as the spin-glass transition temperature, T_g, and the transition at ~70 K can be identified as T_C.

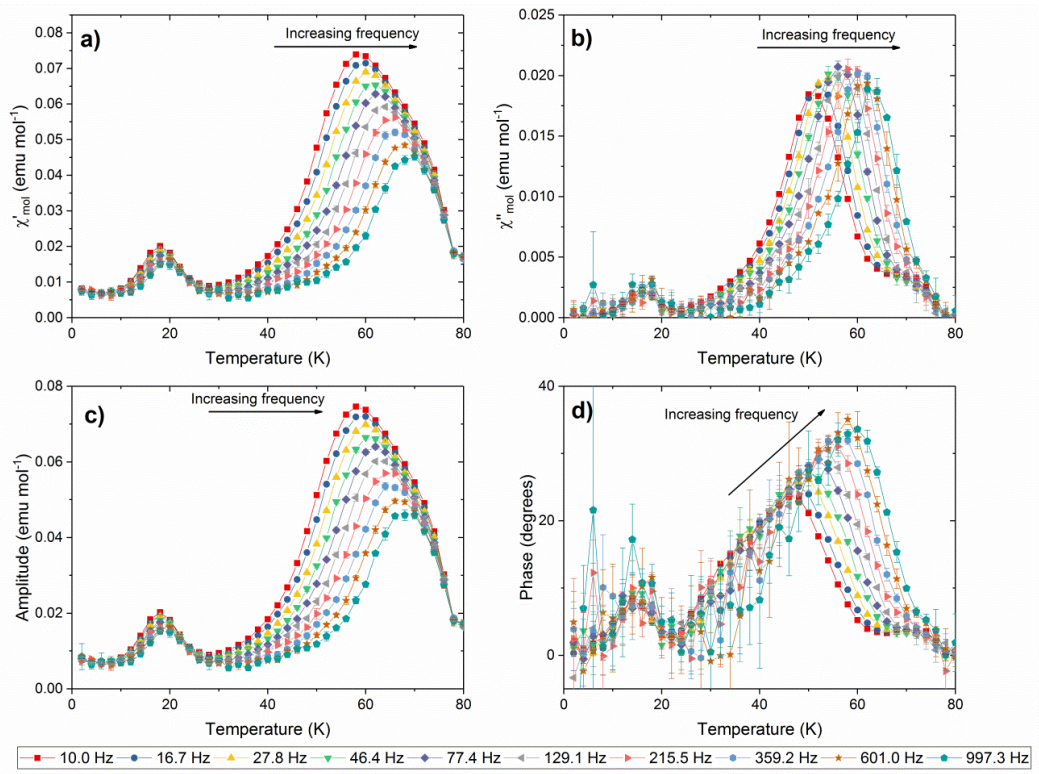


Fig. 5.54 Results of the AC measurements of JNB130 (most deintercalated $Sr_2CoO_2Ag_{1.5(2)}Se_2$), the measurements used a 4 Oe alternating field, and were measured in the absence of a direct current field. Showing a) χ'; b) χ''; as well as the derived values: c) the amplitude and d) the phase

The transition identified as T_C is rather broad. When ferromagnetism arises from the ordering of localised moment, the peak in χ' is normally very sharp, while ferromagnetism arising from an itinerant ferromagnet normally presents as a broad feature below T_C.[156, 157] This could be further evidence that $Sr_2CoO_2Ag_{1.5(2)}Se_2$ is an itinerant ferromagnet, but further AC magnetometry measurements as a function of DC field would be required to prove this. The change in AC susceptibility behaviour of localised-moment and itinerant ferromagnets has been shown to be quite different on the application of fields.[156, 157]

5.4 Synthesis, composition and magnetic behaviour of $Sr_2CoO_2Cu_2Te_2$

5.4.1 Synthesis and composition

A high-purity 3 g sample of the novel compound $Sr_2CoO_2Cu_2Te_2$ (JNB288) was synthesised by mixing SrO, Co, Cu and Te in the ratio 2:1:2:2 and preparing them using the solid-state synthesis method described in section 2.1.1. The reactants were heated to 750 °C at a rate of 5 °C min^{-1} and the temperature was maintained for 72 h before quenching in ice-water.

Analysis of $Sr_2CoO_2Cu_2Te_2$ (JNB288) by synchrotron PXRD (I11 beamline, using the MAC detector) and PND (WISH) showed that the compound, like the other compounds discussed in this thesis, belonged to the $Sr_2Mn_3Sb_2O_2$ structure type[40] (space group: *I*4/*mmm*). Refinement of the fractional occupancies of each element in the structure revealed the possibility that this compound is 5 – 10% Co deficient. However, analysis of the impurities visible in the PXRD pattern showed only very small quantities of CoO and Cu_xTe, which would not necessarily suggest a Co deficiency in the main phase. There was also comparatively little improvement in the R_{wp} on refinement of the Co fractional occupancy (10.162% *vs* 10.209%). Therefore, in the Rietveld analysis of the PXRD and PND data shown in Fig. 5.55 and Fig. 5.56 and Table 5.31, $Sr_2CoO_2Cu_2Te_2$ has been modelled as stoichiometric. The possibility of a small Co deficiency cannot be ruled out, but further analysis using PND with high resolution at low *d*-spacings (such as HRPD or GEM) or EDX analysis would be required to investigate this further.

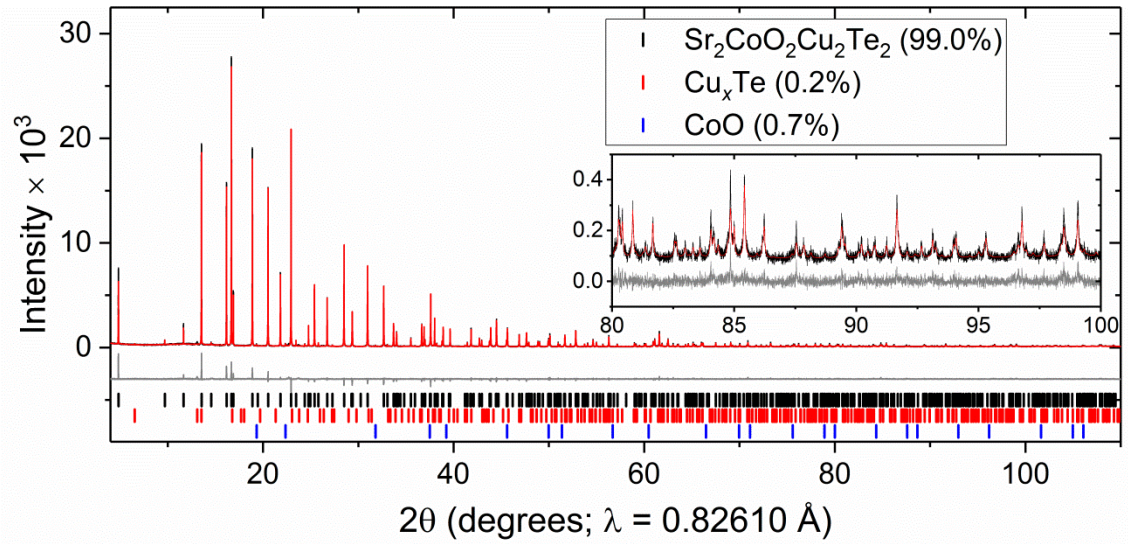


Fig. 5.55 Rietveld plot of $Sr_2CoO_2Cu_2Te_2$ (JNB288), synchrotron PXRD data measured at RT using the MAC detector on the I11 beamline. The inset emphasises the comparatively high signal-to-noise ratio at high angle

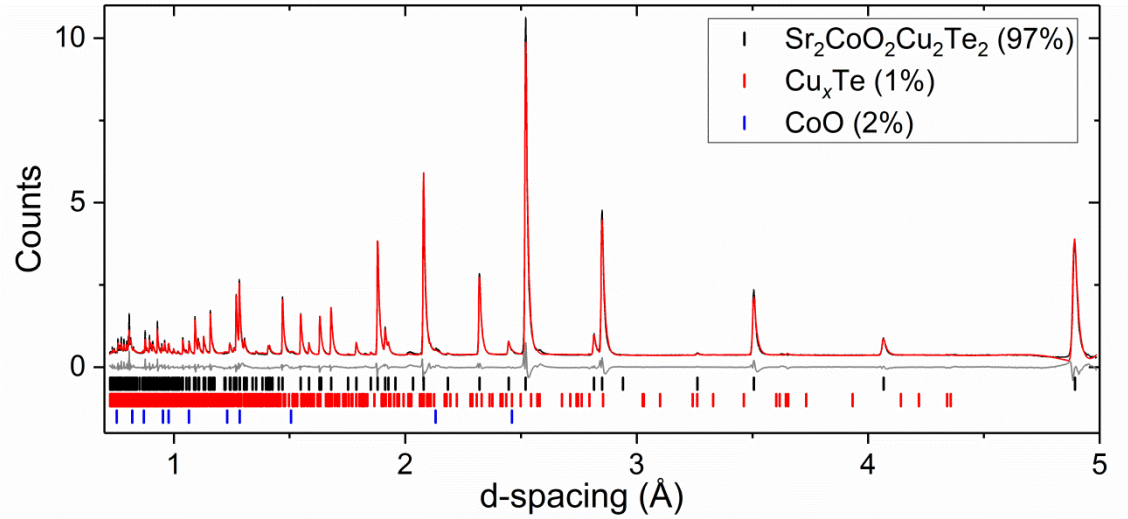


Fig. 5.56 Rietveld plot of $Sr_2CoO_2Cu_2Te_2$ (JNB288), PND data measured at RT using the 5-6 detector bank of WISH

Table 5.31 Refined parameters from measurement of $Sr_2CoO_2Cu_2Te_2$ (JNB288) at RT using both PXRD and PND

Sample	JNB288	
Compound	$Sr_2CoO_2Cu_2Te_2$	
Radiation	X-ray, λ = 0.82610 Å	Neutron, ToF
Diffractometer	MAC (I11)	WISH
Temperature (K)	RT	300
Purity (wt%)	99.0	97.0
Impurities	Cu_xTe, CoO	Cu_xTe, CoO
Space group	*I*4/*mmm*	
a (Å)	4.15268(1)	4.15754(4)
c (Å)	19.54824(6)	19.5738(3)
Volume (Å^3)	337.104(2)	337.104(3)
z(Sr)	0.41819(3)	0.41751(4)
z(Te)	0.16575(2)	0.16552(4)
Sr U_{11} (Å^2)	0.0038(2)	0.0105(9)
Sr U_{33} (Å^2)	0.0086(4)	0.007(2)
Co U_{11} (Å^2)	0.0034(4)	0.018(2)
Co U_{33} (Å^2)	0.0179(9)	0.051(5)
O U_{11} (Å^2)	0.019(3)	0.018(2)
O U_{22} (Å^2)	0.022(3)	0.015(1)
O U_{33} (Å^2)	0.008(3)	0.011(3)
Cu U_{11} (Å^2)	0.0171(3)	0.016(1)
Cu U_{33} (Å^2)	0.0225(7)	0.037(2)
Te U_{11} (Å^2)	0.0052(2)	0.016(1)
Te U_{33} (Å^2)	0.0092(2)	0.008(2)
R_{wp} (%)	10.209	5.647
χ^2	2.012	-

5.4.2 Magnetometry measurements

JNB288 ($Sr_2CoO_2Cu_2Te_2$) contained small ferromagnetic impurities, possibly small quantities of elemental Co, that prevented accurate measurement of the magnetic susceptibility using a small field, so a 3 T/4 T subtraction experiment was performed (see Fig. 5.57). The *M vs H* curve of the sample at 300 K was linear in this regime, showing that the contribution from the ferromagnetic impurity had saturated. The magnetic susceptibility curve showed a broad antiferromagnetic transition at $250 \leq T\,(\mathrm{K}) \leq 300$, which is comparable to the feature found in the related stoichiometric compounds discussed above. In common with the other compounds discussed in this chapter, the observed T_N is too high for Curie or Weiss constants to be extracted from this temperature regime.

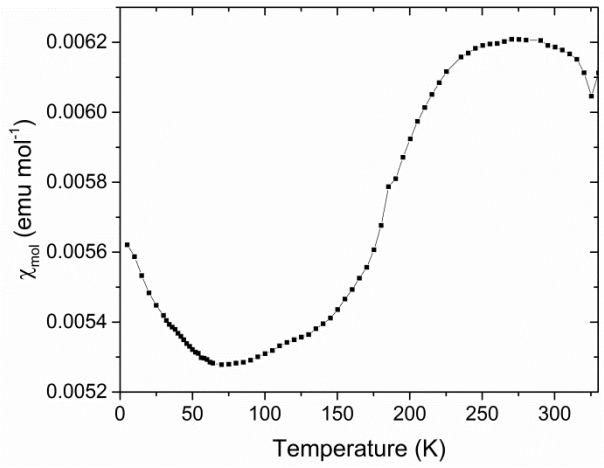


Fig. 5.57 Field-cooled magnetic susceptibility of $Sr_2CoO_2Cu_2Te_2$ (JNB288), measured using a 4 – 3 T subtraction (as described in section 2.8)

5.4.3 Powder neutron diffraction to probe magnetic ordering

2.0 g of JNB288 ($Sr_2CoO_2Cu_2Te_2$) was measured using PND (WISH) at a large number of different temperatures in the range 1.7 – 300 K in order to understand this compound's magnetic ordering behaviour as a function of temperature.

Antiferromagnetic ordering peaks appeared on cooling, as suggested by the magnetic susceptibility measurements. These peaks could be indexed on a $\sqrt{2}a \times \sqrt{2}a \times c$ expansion of the unit cell, suggesting that the primary interaction between the spins was nearest-neighbour antiferromagnetic coupling within the $[CoO]_2$ planes.

The data was initially evaluated using symmetry mode analysis in magnetic space group *P*1 (1.1), before using this information to search for a higher symmetry space group. As with $Sr_2CoO_2Cu_2S_2$, all the magnetic intensity could be accounted for using the mX3$^+$(a) and mX4$^+$(a) modes (shown in Fig. 5.11 for $Sr_2CoO_2Cu_2S_2$), representing antiferromagnetic alignment of spins along the *ab*-plane. Analysis was therefore continued using the tetragonal P_C4_2/n (86.73) magnetic space group (see Fig. 5.12). Fig. 5.58 shows the Rietveld plot of a magnetic refinement using this space group at 1.7 K and a table of refined magnetic parameters is given in Table 5.32.

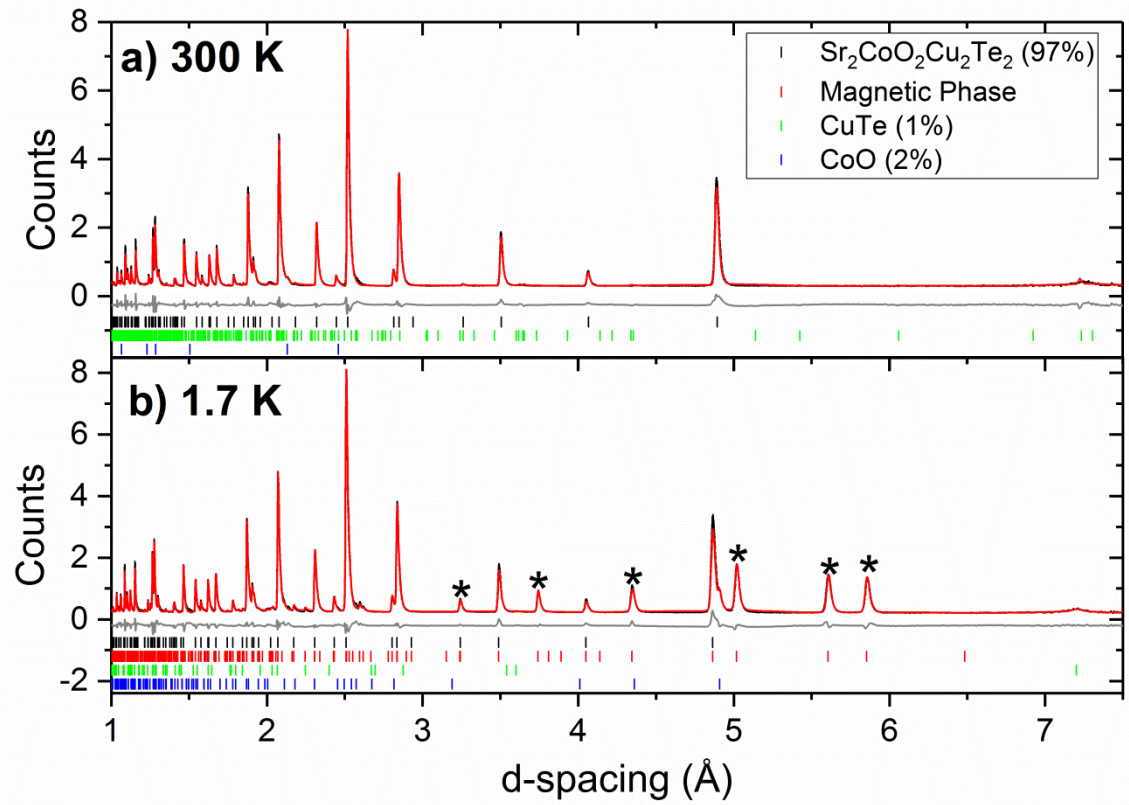


*Fig. 5.58 Rietveld plots of $Sr_2CoO_2Cu_2Te_2$ (JNB288), PND data measured using the 3-8 (90°) bank of WISH at a) 300 K and b) 1.7 K; the * symbols indicate the main magnetic peaks that appear on cooling*

Table 5.32 Refined parameters for the magnetic ordering of $Sr_2CoO_2Cu_2Te_2$ (JNB288) when it was measured at 1.7 K using PND

Radiation	Neutron, ToF
Diffractometer	WISH
Temperature (K)	1.7
Magnetic space group	P_C4_2/n (86.73)
μ_a (μ_B)	0.56(2)
μ_b (μ_B)	3.65(2)
$\|\mu\|$ (μ_B)	3.69(2)
R_{wp} (%)	6.913

However, the stacked raw plots in Fig. 5.59 show that the peaks do not lose intensity at the same rate when temperature increases, some peaks reduce in intensity on warming faster than others. This suggests that the magnetic spins reorientate as a function of temperature.

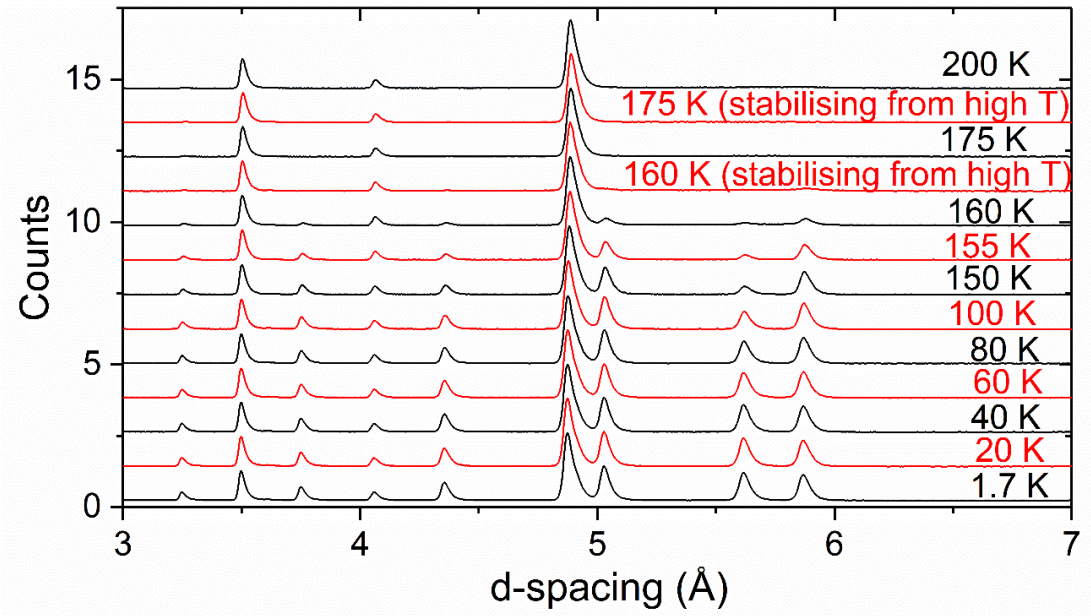


Fig. 5.59 Raw powder neutron diffraction patterns of $Sr_2CoO_2Cu_2Te_2$ (JNB288), measured as a function of temperature using the 2-9 (53.1°) databank of WISH. Successive diffractograms set off by 1.2 counts from the origin for clarity

This was modelled in the magnetic refinements as a change in the ratio of the two activated distortion modes, which results in a small change in the ratio of the magnetic component parallel to the *a* direction and the *b* direction (here *a* and *b* refer to the parameters of the magnetic supercell). The results of this are shown in Fig. 5.60.

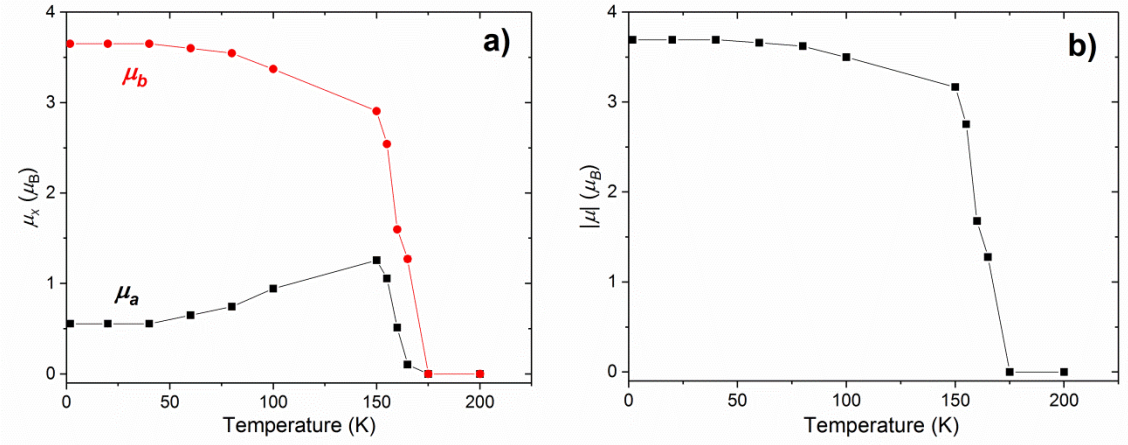


Fig. 5.60 a) The refined magnetic moment of each component a and b (in the magnetic supercell) as a function of temperature and b) the magnitude of magnetic moments as a function of temperature for $Sr_2CoO_2Cu_2Te_2$ (JNB288). Data obtained from refinement against WISH data; the refined error values are smaller than the points on the graph; the line is a guide to the eye

The T_N observed from PND data is significantly lower than that indicated by magnetic susceptibility measurements, suggesting that short-range magnetic ordering (detected as

the broad maximum in the magnetometry measurements) occurs at a higher temperature than long-range magnetic ordering (detected by PND).

5.5 Discussion

5.5.1 Effect of substitutions on structure

All the compounds discussed in this chapter adopt the same crystal structure modelled in space group *I4/mmm*. However, substituting different sized *X* and *Ch* ions has a significant effect on the lattice parameters, atom positions, bond lengths and bond angles. Some of these changes have been discussed in previous work,[58, 62] but here will be discussed to inform the discussion on the effect of substitutions on the amount of *X* that may be removed (section 5.5.2) and to allow comparisons with the newly-synthesised compound $Sr_2CoO_2Cu_2Te_2$. The RT structural parameters of $Sr_2CoO_2Cu_2S_2$, $Sr_2CoO_2Cu_2Se_2$, $Sr_2CoO_2Ag_2Se_2$ and $Sr_2CoO_2Cu_2Te_2$ are shown in Table 5.33.

Table 5.33 Comparison of selected structural parameters for $Sr_2CoO_2Cu_2S_2$ (from PND data, obtained from ref. 61), $Sr_2CoO_2Cu_2Se_2$ (PND data, this thesis), $Sr_2CoO_2Ag_2Se_2$ (PND data, this thesis) and $Sr_2CoO_2Cu_2Te_2$ (synchrotron PXRD data, this thesis)

Compound	$Sr_2CoO_2Cu_2S_2$[61]	$Sr_2CoO_2Cu_2Se_2$	$Sr_2CoO_2Ag_2Se_2$	$Sr_2CoO_2Cu_2Te_2$
a (Å)	3.99129(2)	4.04826(4)	4.10271(2)	4.15268(1)
c (Å)	17.71555(9)	18.3425(2)	19.4290(1)	19.54824(6)
c/a	4.43855(3)	4.53096(7)	4.73565(3)	4.70738(2)
Volume ($Å^3$)	282.216(2)	300.603(6)	327.033(4)	337.104(2)
z(Sr)	0.40767(1)	0.41193(3)	0.41700(3)	0.41819(3)
z(*Ch*)	0.17119(3)	0.16798(2)	0.15525(3)	0.16575(2)
Co-O (Å)	1.99565(1)	2.02413(2)	2.05136(1)	2.07634(1)
Co-*Ch* (Å)	3.0327(5)	3.0812(5)	3.0163(5)	3.2401(4)
Sr-O (Å)	2.5803(2)	2.5897(3)	2.6093(3)	2.6209(4)
Sr-*Ch* (Å)	3.1491(3)	3.2160(3)	3.2228(3)	3.3637(4)
X-*Ch* (Å)	2.4356(3)	2.5220(3)	2.7563(3)	2.6502(3)
Ch-*X*-*Ch*, *α** (°) [2]#	110.04(2)	106.756(17)	96.19(2)	103.16(2)
Ch-*X*-*Ch*, *β** (°) [4]#	109.19(1)	110.846(9)	116.493(9)	112.718(8)

*see Fig. 3.33 for definition of angle; #multiplicity in square brackets

Table 5.33 shows increasing the size of *Ch* and *X* has an elongating effect on the compounds, increasing the *c/a* ratio. Increasing the size of *X* from Cu to Ag appears to increase the *c/a* ratio more than increasing the size of *Ch*, which leads to a larger increase in the deviation of the *Ch*-*X*-*Ch* bond angles from the ideal tetrahedral angle (109.5°). It is perhaps not surprising that a substitution in *X* has a greater effect; Table 5.34 compares the ionic radii of Cu, Ag, S, Se and Te; showing that substituting Ag for

Cu constitutes a 54% increase in ion size, while substituting Te for S constitutes a comparatively small 22% increase in size of the anion.

Table 5.34 Comparison of the size of selected ionic radii; data extracted from ref. 117

Ion	Radius (Å)
Cu^{+}	0.74
Ag^{+}	1.14
S^{2-}	1.7
Se^{2-}	1.84
Te^{2-}	2.07

The increase in ion size lead largely to an increase in the *c* (interlayer) parameter because *a* is defined as twice the Co-O bond distance, so the energy cost of expanding *c* is comparatively smaller.

5.5.2 Effect of substitutions on the extent of deintercalation

This chapter has shown that several $Sr_2CoO_2X_2Ch_2$ compounds are active with respect to topotactic oxidation using I_2/MeCN, contrasting with the *M* = Mn analogues, where the only compound known to participate in this reaction is $Sr_2MnO_2Cu_{1.5}S_2$ (see Chapter 3). The number of Co-containing compounds that react with I_2 allows comparison of behaviour to be made on substitution of *X* and *Ch*.

5.5.2.1 *Effect of Ch*

It was found that significantly more Cu may be removed from $Sr_2CoO_2Cu_2S_2$ than from $Sr_2CoO_2Cu_2Se_2$. The proportion of Cu that may be removed from $Sr_2CoO_2Cu_2Se_{1.6}S_{0.4}$ lies at an intermediate point between these extremes, as is shown in the graphs in Fig. 5.61.

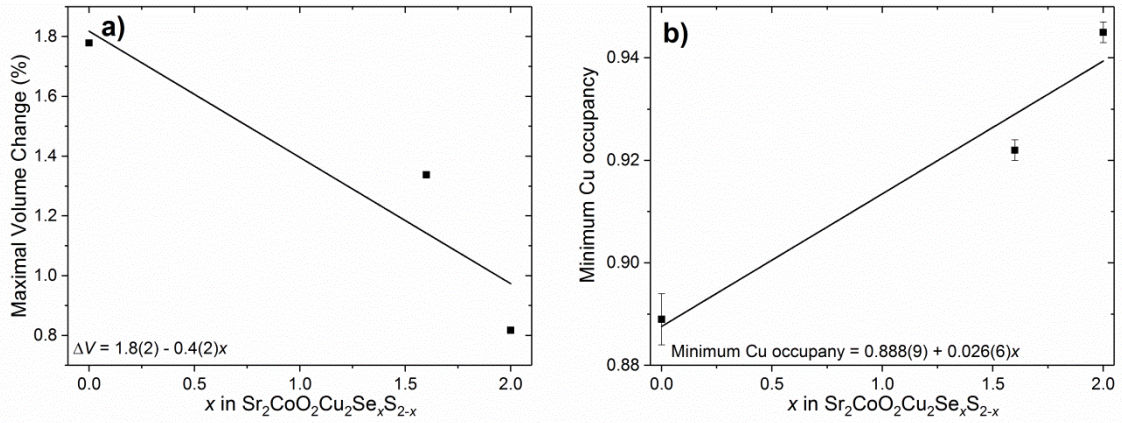


Fig. 5.61 a) Relationship between maximum volume change and chalcogenide identity (error bars smaller than points on the graph) and b) relationship between minimum Cu occupancy and chalcogenide identity when $Sr_2CoO_2Cu_2Se_xS_{2-x}$ is reacted with I_2/MeCN. Data obtained from refinement against PND data

It would be of interest to test if $Sr_2CoO_2Cu_2Te_2$ is active with respect to oxidation by I_2 to observe if the trend that larger chalcogenide ions lead to a smaller possible change in the Cu occupancy is continued when *Ch* = Te.

5.5.2.2 *Effect of X*

Far more Ag could be removed from $Sr_2CoO_2Ag_2Se_2$ than Cu from any of the Cu-containing analogues discussed in this chapter, showing that here the identity of *X* has a greater effect than the identity of *Ch*.

It was hypothesised that more Ag could be removed because the [$AgSe_4$] tetrahedra are particularly distorted and removal of Ag may allow for relaxation of the tetrahedra. However, Table 5.35, comparing the structural parameters of the three $Sr_2CoO_2Ag_{2-x}Se_2$ measured using HRPD (see section 5.3), shows that the average [$AgSe_4$] tetrahedron deviates more from the ideal tetrahedral angle as Ag-deficiency increases. Note that the data shown for JNB106 is obtained from Rietveld refinement without accounting for stacking faults and is therefore of limited reliability.

Table 5.35 Comparison of selected structural parameters of three samples of $Sr_2CoO_2Ag_{2-x}Se_2$; values obtained from PND (HRPD) data

Sample Code	JNB101	JNB243	JNB106
Composition	$Sr_2CoO_2Ag_2Se_2$	$Sr_2CoO_2Ag_{1.93(6)}Se_2$	$Sr_2CoO_2Ag_{1.5(2)}Se_2$
a (Å)	4.10271(2)	4.08922(4)	4.0856(2)
c (Å)	19.4290(1)	19.4084(2)	19.407(1)
c/a	4.73565(3)	4.74624(7)	4.7501(3)
Volume (Å^3)	327.033(4)	324.541(1)	323.95(4)
z(Sr)	0.41700(3)	0.41627(4)	0.4157(1)
z(*Ch*)	0.15525(3)	0.15512(4)	0.1539(1)
Co-O (Å)	2.05136(1)	2.04461(2)	2.04281(1)
Co-*Ch* (Å)	3.0163(5)	3.0105(7)	2.987(3)
Sr-O (Å)	2.6093(3)	2.6118(5)	2.6177(2)
Sr-*Ch* (Å)	3.2228(3)	3.2063(5)	3.1890(2)
X-*Ch* (Å)	2.7563(3)	2.7517(5)	2.7659(2)
Ch-*X*-*Ch*, *α** (°) [2]$^{\#}$	96.19(2)	95.98(2)	95.22(9)
Ch-*X*-*Ch*, *β** (°) [4]$^{\#}$	116.493(9)	116.609(12)	117.03(5)

*see Fig. 3.33 for definition; $^{\#}$multiplicity in square brackets

The difference in reactivity of $Sr_2CoO_2Cu_2Se_2$ and $Sr_2CoO_2Ag_2Se_2$ could be due to differences in the ion mobility. Oliveria, McMullan and Wuensch used a single-crystal neutron diffraction study to show that the Ag^+ ions in Ag_2Se were significantly more delocalised than the Cu^+ ions in Cu_2Se.[123] This delocalisation could be related to the ion

mobility, allowing more transport of the ions near to the surface of the powder grains and therefore allowing reaction with I_2.

The observation that a greater *X*-deficiency (*X* = Cu, Ag) may be achieved when removing Ag is not unprecedented. This has also been found to be the case with CeO*XCh* (*X* = Cu, Ag; *Ch* = S, Se), as also discussed in section 1.3.1.[70, 71, 158] The *XCh* layers in CeO*XCh* are analogous to those in $Sr_2CoO_2X_2Ch_2$, so it is unsurprising that similar trends in reactivity are observed when the identity of *X* and *Ch* are changed.

However, the behaviour observed here contrasts with the behaviour observed for $Sr_2MnO_2Ag_{1.5}Se_2$, which is not active with respect to oxidation by I_2. There appear to be inconsistencies in the deintercalation behaviours of these compounds from transition metal to transition metal; further studies are required to fully understand these differences.

5.6 **Conclusions**

This chapter has shown that several analogues of $Sr_2CoO_2X_2Ch_2$ are susceptible to oxidative deintercalation by I_2, albeit to different extents. This chapter has also shown that, for the compounds tested, identity of *X* is a more significant factor in determining the reactivity of the compounds with respect to I_2 than the identity of *Ch*. Unfortunately, far fewer compounds where *X* = Ag are reported in the literature, making it difficult to test this behaviour with more compounds.

An alternative magnetic-ordering scheme for $Sr_2CoO_2Cu_2Se_2$ has been proposed (model 3). This model contrasts with the two-phase model previously proposed by Smura,[58] because this scheme hypothesises that the magnetic ordering arises from a single magnetic structure. However, it appears that the proposed magnetic structure leads to a slightly poorer fit to the data, suggesting that this model might oversimplify the magnetic ordering behaviour somewhat. Nonetheless this model was considered sufficiently good to model the changes in magnetic intensity as a function of the Co oxidation state, showing that the reduction in the ordered moment was also accompanied by a reorientation of the moment into the *c*-direction.

Deintercalation of Ag from $Sr_2CoO_2Ag_{2-x}Se_2$ causes an antiferromagnetic-to-ferromagnetic ordering transition. The ferromagnetism in most-deintercalated

$Sr_2CoO_2Ag_{1.5(2)}Se_2$ is currently poorly understood, but there appear to be many complex interactions, which change dramatically as a function of temperature. The magnetisation isotherms in Fig. 5.46 b) indicate at least four regimes in most-deintercalated $Sr_2CoO_2Ag_{1.5(2)}Se_2$ as a function of temperature: paramagnetic, metamagnetic, soft ferromagnetic and ferromagnetic with a large spin-glass component. Further experiments, such as conductivity measurements and field-dependent AC magnetometry measurements, are required to probe the mechanism by which the ferromagnetic behaviour occurs, but the working hypothesis is that this material is an itinerant ferromagnet.

The novel compound $Sr_2CoO_2Cu_2Te_2$ was also found to crystallise in the same structure as the analogues with space group *I*4/*mmm*; the refined lattice parameters are a = 4.15268(1) Å and c = 19.54824(6) Å. The magnetic structure of $Sr_2CoO_2Cu_2Te_2$ is similar to that reported for $Sr_2CoO_2Cu_2S_2$ and $Sr_2CoO_2Cu_2Se_2$, but a small rearrangement of magnetic moment was observed on warming. It is possible that a similar rearrangement occurs in $Sr_2CoO_2Cu_2S_2$ and $Sr_2CoO_2Cu_2Se_2$, but VT PND measurements would be required to examine this.

The refined magnetic moments at 5 K of all the parent compounds discussed in this chapter are compared in Table 5.36.

Table 5.36 The refined magnetic moments of several related Co-containing compounds discussed in this chapter. All data obtained from PND data discussed in this chapter

Compound	Magnetic moment (μ_B)
$Sr_2CoO_2Cu_2S_2$	3.59(6)
$Sr_2CoO_2Cu_2Se_{1.6}S_{0.4}$	3.25(4)
$Sr_2CoO_2Cu_2Se_2$	3.50(2)
$Sr_2CoO_2Ag_2Se_2$	3.56(4)
$Sr_2CoO_2Cu_2Te_2$	3.69(2)

The magnetic moments of these compounds are all larger than 3 μ_B, the spin-only value expected from high-spin Co^{2+}, suggesting that all in these cases the orbital contribution to the magnetic moment is significant. The slightly smaller refined moment in $Sr_2CoO_2Cu_2Se_{1.6}S_{0.4}$ may be due to a small amount of disorder arising from the mixed S:Se site in this compound. However, it is also possible that the reduction in moment is related to the different magnetic structures observed for $Sr_2CoO_2Cu_2Se_{1.6}S_{0.4}$ and $Sr_2CoO_2Cu_2Se_2$.

Chapter 6

6 Synthesis and Characterisation of $Sr_2CuO_2Cu_2Se_2$ and $Ba_2CuO_{2-x}Cu_2Se_2$

6.1 Introduction

Compounds of composition $A_2CuO_2X_2Ch_2$ are of particular interest because they contain infinite CuO_2 planes, a feature characteristic of the high-temperature cuprate superconductors. Previous attempts to synthesise these compounds have focused on $Sr_2CuO_2Cu_2S_2$, which has been shown to be exceedingly difficult to synthesise phase pure.[47, 58]

Smura found that during the attempted synthesis of $Sr_2CuO_2Cu_2S_2$, the use of temperatures above ~500 °C or heating for longer than ~30 h caused $Sr_2CuO_2Cu_2S_2$ to disproportionate to $SrSO_4$, as facilitated by the reduction of Cu to its elemental state:[58]

$$[Sr_2CuO_2Cu_2S_2] \rightarrow 3Cu + (1.5)SrS + (0.5)SrSO_4 \quad (6.1)$$

Smura also found that the use of a halide flux was required to facilitate this reaction, suggesting that $Sr_2CuO_2Cu_2S_2$ was a kinetic product of the reaction. This was believed to be because Cu favoured Cu^0 in the elemental state over the distorted octahedral Cu^{2+} configuration, when synthesised in a reducing environment. Smura was only able to synthesise $Sr_2CuO_2Cu_2S_2$ approximately 75 wt% pure.[58]

$Sr_2CuO_2Cu_2S_2$ is not the only known oxychalcogenide containing infinite Cu-O planes. The synthesis of $Na_{1.9}Cu_2OCu_2Se_2$ has also been reported. This structure is analogous to the structure of the compounds discussed in this chapter, but the position of the Cu and O atoms have switched, as shown in Fig. 6.1.[159]

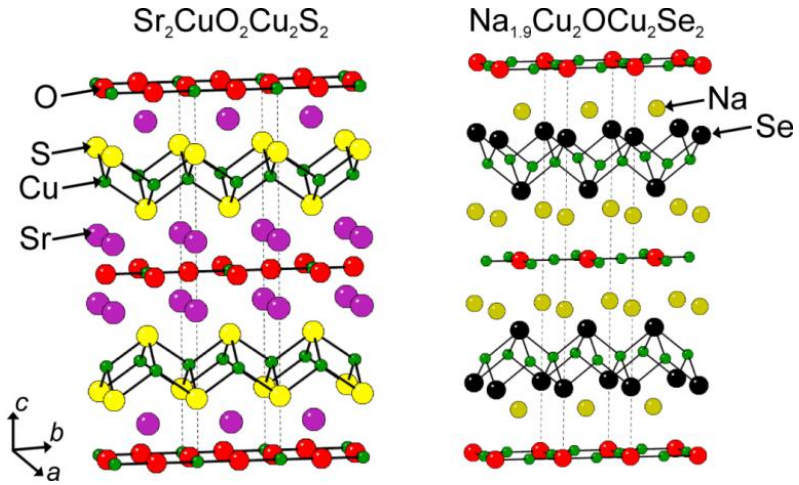


Fig. 6.1 Comparison of the crystal structures of $Sr_2CuO_2Cu_2S_2$[58] and $Na_{1.9}Cu_2OCu_2Se_2$[159]

This compound was originally thought to have composition $Na_2Cu_2OCu_2Se_2$, but after resistivity measurements showed that the compound was metallic, the fractional occupancies of the compound were evaluated using single-crystal X-ray diffraction (SCXRD) and showed that the compound was slightly Na-deficient, which is likely to lead to a partially-filled valence band, providing an explanation for the observed metallic behaviour.[159]

This chapter shows that the phase-pure synthesis of the selenide analogue $Sr_2CuO_2Cu_2Se_2$ may be achieved through a simple synthetic route. The magnetic and electronic properties of this compound are then investigated.

It was also found that a compound of composition $Ba_2CuO_{2-x}Cu_2Se_2$ could be synthesised using a similar synthesis route. However, unlike the Sr analogue, $Ba_2CuO_{2-x}Cu_2Se_2$ appears to be oxygen-deficient and the phase-pure synthesis of this compound could not be achieved due to the presence of an unindexed and possibly novel impurity or impurities. The structure and composition of this compound have been investigated using a combination of powder X-ray diffraction (PXRD) and SCXRD at different temperatures. The electronic behaviour of this compound has been probed using a combination of magnetic susceptibility and bulk resistivity measurements.

It was found that the product of high-temperature synthesis of $Ba_2CuO_{2-x}Cu_2Se_2$ produced several compounds with similar compositions, but slightly different oxygen occupancies in the same sample. Therefore, attempts to control the oxygen occupancy using a flow of $O_{2(g)}$ are reported.

6.2 Synthesis, Structure and composition of $Sr_2CuO_2Cu_2Se_2$

6.2.1 Synthesis of $Sr_2CuO_2Cu_2Se_2$

$Sr_2CuO_2Cu_2Se_2$ (JNB112B) was prepared on a 5 g scale by mixing SrO, Cu and Se in the molar ratio 2:3:2 and preparing them as discussed in section 2.1.1. The reactants were heated to 500 °C at 10 °C min^{-1} for 48 h. The sample was then allowed to cool in the furnace, before isolating the product. Laboratory PXRD after this step revealed that the sample was contaminated with significant SrO, SrSe, Cu_2Se and Cu_2O impurities, so the sample was prepared and reheated as before. This produced a sample that was phase-pure by laboratory PXRD.

6.2.2 Powder X-ray and neutron diffraction analysis

The composition of $Sr_2CuO_2Cu_2Se_2$ (JNB112B) was probed using synchrotron PXRD (MAC detector on the I11 beamline) and PND (GEM). Refinement against both datasets showed that the sample was stoichiometric with *I*4/*mmm* symmetry and the same $Sr_2MnO_2Mn_2Sb_2$ structure[40] as has been reported for other members of the $A_2MO_2X_2Ch_2$ class. Rietveld plots from synchrotron PXRD and PND are shown in Fig. 6.2 and Fig. 6.3 respectively. The refined parameters are collated in Table 6.1.

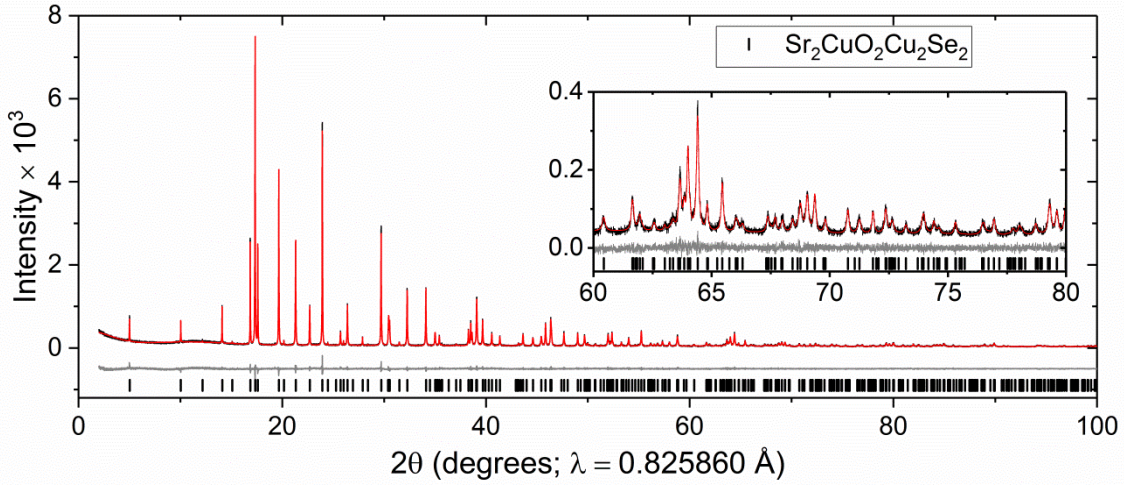


Fig. 6.2 Rietveld plot of $Sr_2CuO_2Cu_2Se_2$ (JNB112B) against synchrotron PXRD data measured at room temperature (RT) using the MAC detector at the I11 beamline; the inset emphasises the quality of the fit at high angle

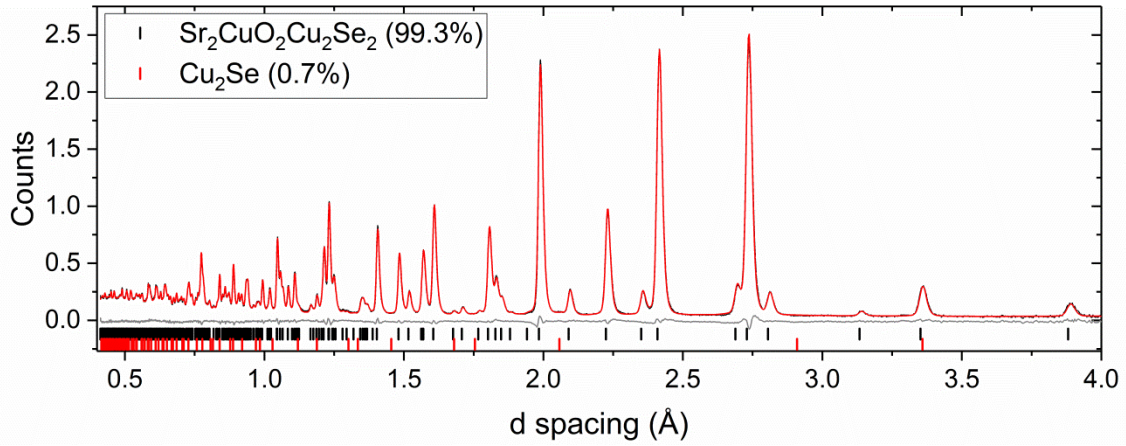


Fig. 6.3 Rietveld plot of bank 4 (63.62°) of GEM for $Sr_2CuO_2Cu_2Se_2$ (JNB112B)

Table 6.1 Refined parameters from the Rietveld refinement against synchrotron PXRD and PND measurements of $Sr_2CuO_2Cu_2Se_2$ (JNB112B)

Sample	JNB112B ($Sr_2CuO_2Cu_2Se_2$)	
Radiation	X-ray, λ = 0.825860 Å	Neutron, time of flight
Diffractometer	MAC, I11	GEM
Temperature	Room temperature	
Space group	*I*4/*mmm*	
Impurities	Nil	Cu_2Se (0.7 wt%)
a (Å)	3.98212(4)	3.97116(4)
c (Å)	18.8686(2)	18.8198(2)
Volume (Å)	299.205(6)	296.791(7)
z(Sr)	0.41207(3)	0.41190(3)
z(Se)	0.16845(3)	0.16838(2)
U_{11}(Sr) (Å^2)	0.0014(2)	0.007(2)
U_{33}(Sr) (Å^2)	0.0021(3)	0.0086(4)
U_{11}(Cu(1)*) (Å^2)	0.0000(3)	0.0033(2)
U_{33}(Cu(1)*) (Å^2)	0.0032(6)	0.0118(5)
U_{11}(O) (Å^2)	0.007(2)	0.0072(4)
U_{22}(O) (Å^2)	0.000(2)	0.0054(4)
U_{33}(O) (Å^2)	0.001(2)	0.0097(6)
U_{11}(Cu(2)*) (Å^2)	0.0116(3)	0.0151(3)
U_{33}(Cu(2)*) (Å^2)	0.0115(5)	0.0177(5)
U_{11}(Se) (Å^2)	0.0022(2)	0.0055(3)
U_{33}(Se) (Å^2)	0.0012(3)	0.0109(4)
R_{wp} (%)	8.221	3.683

*where Cu(1) is at Wyckoff position 2*a* (0, 0, 0) and Cu(2) is at Wyckoff position 4*d* (0, ½, ¼)

Refinement against both synchrotron PXRD and PND data indicates that $Sr_2CuO_2Cu_2Se_2$ is stoichiometric; this suggests that at least partial oxidation of the Cu ion in the oxide layer beyond Cu^+ has occurred. This is discussed further in section 6.8, where the compound is compared with $Ba_2CuO_{2-x}Cu_2Se_2$ and in Chapter 8 where

$Sr_2CuO_2Cu_2Se_2$ is compared with other compounds of composition $Sr_2MO_2Cu_2Se_2$ (*M* = Mn, Co, Ni, Cu, Zn).

6.3 Synthesis, Structure and Composition of $Ba_2CuO_{2-x}Cu_2Se_2$

6.3.1 Synthesis of $Ba_2CuO_{2-x}Cu_2Se_2$

The synthesis of $Ba_2CuO_2Cu_2Se_2$ proved to be significantly more difficult than for $Sr_2CuO_2Cu_2Se_2$. It was found that the range of heating temperatures (600 – 900 °C) and heating conditions (heating times, rate of cooling) used made little difference to the purity of the overall product. The powder sample discussed most extensively in this chapter is JNB128C, this was synthesised on the 1 g scale by mixing BaO, Cu and Se in the molar ratio 2:3:2 and preparing them as described in section 2.1.1. The reactants were then heated to 600 °C (rate: 10 °C min^{-1}) for 48 h and allowed to cool at the rate of the furnace. The sample was ground and purity was assessed by in-house PXRD. The sample was then prepared as before and heated using the same regime twice, in an effort to increase the purity of the sample. Significant impurities remained at the end of this process. Other samples of "$Ba_2CuO_2Cu_2Se_2$" are also discussed in this chapter, with slightly different synthesis routes, described below, when relevant.

6.3.2 Powder X-ray diffraction analysis

$Ba_2CuO_{2-x}Cu_2Se_2$ (JNB128C) was measured using synchrotron PXRD (using the PSD on the I11 beamline) in an attempt to resolve the structure and composition of the compound. This was hindered by two related but separate problems evident in PXRD patterns of multiple samples of this compound. Firstly, the sample contained a significant number of unindexed peaks (shown in Fig. 6.4 a)), which could not be indexed with any known impurity, despite a thorough database search. Secondly, the use of synchrotron radiation showed, from the shapes of the peak profiles, that the sample was composed of a range of compounds with slightly different lattice parameters and (thus) compositions. Here this was modelled as two phases, as shown in Fig. 6.4 b) and c), the refined parameters are shown in Table 6.2.

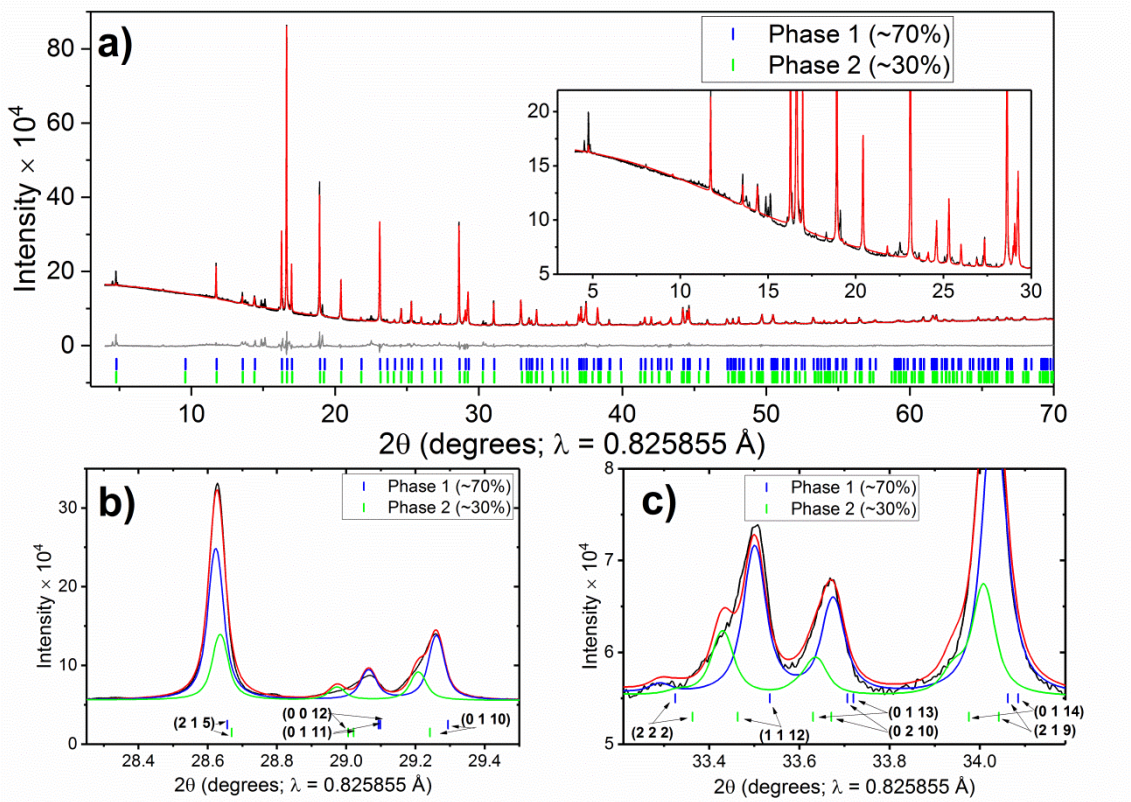


Fig. 6.4 Rietveld plots of JNB128C ($Ba_2CuO_{2-x}Cu_2Se_2$) measured using the PSD on the I11 beamline, the inset emphasises the region where the unindexed peaks are most prominent, while b) and c) emphasise regions where the two-phase character of JNB128C is particularly prominent

Table 6.2 Refined parameters from the modelling of two phases in JNB128C ($Ba_2CuO_{2-x}Cu_2Se_2$); PXRD data obtained using the PSD on the I11 beamline

Sample	JNB128C ($Ba_2CuO_{2-x}Cu_2Se_2$)	
Radiation	X-ray, λ = 0.825855 Å	
Diffractometer	PSD, I11	
Phase fraction (%)	70.2(2)	29.8(2)
a (Å)	4.11742(6)	4.11244(7)
c (Å)	19.7250(3)	19.7865(5)
Volume (Å^3)	334.40(1)	334.63(1)
R_{wp} (%)	2.455	

6.3.3 Single crystal X-ray diffraction analysis

This data was analysed with significant assistance from Dr K. E. Christensen.

It was possible that some of the unindexed peaks in the PXRD pattern of $Ba_2CuO_{2-x}Cu_2Se_2$ samples were due to long-range ordering of vacancies in "$Ba_2CuO_2Cu_2Se_2$". Therefore, a sample was prepared from which small single crystals could be selected for SCXRD analysis and three single-crystal datasets were collected from this sample.

The sample (JNB237) was prepared on a 1 g scale from the reaction of BaO, Cu and Se in the same ratios as before but with the addition of 0.2533 g of KI flux. The sample was not pelletised, but heated to 400 °C (rate: 10 °C min^{-1}) for 15 h, before raising the temperature to 850 °C (rate: 10 °C min^{-1}), where it dwelt for 48 h before cooling slowly in the furnace (rate: 0.1 °C min^{-1}). The modifications were made to this method in order to produce crystals that were big enough for analysis by SCXRD.

The measurement conditions of the three SCXRD datasets are shown in Table 6.3.

Table 6.3 The conditions under which each single-crystal dataset of JNB237 ("$Ba_2CuO_2Cu_2Se_2$") was collected

Dataset	034jnb16	040jnb16	041jnb16
Sample	JNB237 (crystal A)	JNB237 (crystal B)	JNB237 (crystal B)
Temperature (K)	100	100	30
Diffractometer	I19, λ = 0.6889 Å	I19, λ = 0.6889 Å	I19, λ = 0.6889 Å
Completion	Full sphere	Full sphere	Full sphere

For each of these datasets it was found the crystal could be indexed using a tetragonal unit cell (where $a \sim 4.1$ Å and $c \sim 19.7$ Å) and space group *I*4/*mmm*. It was therefore concluded that the unindexed peaks in the PXRD pattern were due to some unindexed impurity. However, examination of reconstructed precession images of these datasets revealed the presence of structured diffuse scattering along the ($h + ½\ k\ l$) and ($h\ k + ½\ l$) planes, as shown in Fig. 6.5. This indicates that some local ordering likely occurs in these compounds.

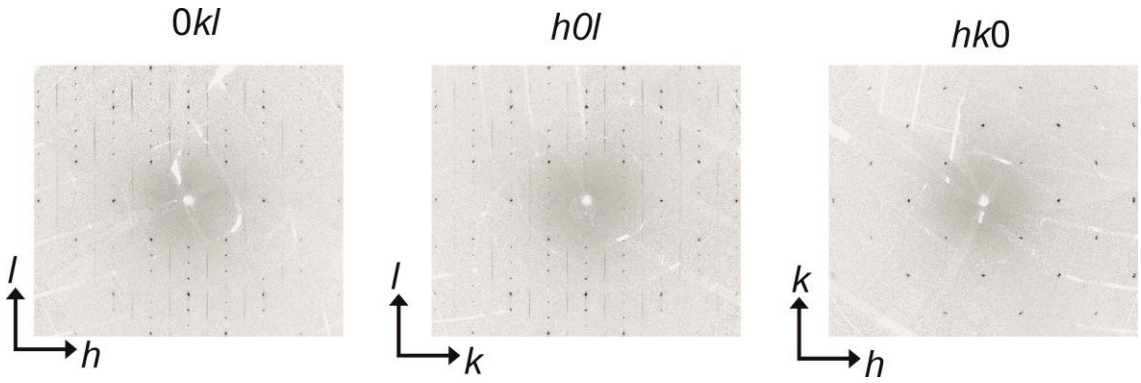


Fig. 6.5 Reconstructed precession images of the SCXRD dataset 040jnb16 (a crystal from JNB237 ("$Ba_2CuO_2Cu_2Se_2$")), the sample was quenched to 100 K before measurement began

It was thought possible that the diffuse scattering lines, indicating local ordering, may lead to long-range ordering at temperatures lower than 100 K, so a crystal dataset of the

same crystal was collected after the crystal had been cooled slowly from 100 K to 30 K (041jnb16). However, no change in the reconstructed precession images was observed.

The fractional occupancies of each atom in the crystal structure were refined in turn to assess if this was a viable avenue of investigation. It was found that two of the atoms in the unit cell possibly had non-unitary site occupancies: Cu(1) (2*a* 0, 0, 0) and O(1) (4*c* 0, ½, 0). Single crystal data still suffers from correlation effects between refined occupancies and thermal displacements parameters, although the effects are reduced compared with powder data. Therefore, the results of refining the three datasets when just the O(1) occupancy was refined is shown in Table 6.5, when just the Cu(1) occupancy was refined is shown in Table 6.6 and when both the O(1) and Cu(1) occupancy were refined is shown in Table 6.7; to allow for comparison of the fits. Table 6.4 shows the atomic positions and occupancies of the described structure.

Table 6.4 Atomic positions and occupancies of the compound "$Ba_2CuO_2Cu_2Se_2$", values that were refined may be found in Table 6.5 – Table 6.7

Atom	*x*	*y*	*z*	Occupancy
Ba(1)	0	0	*z*Ba(1)	1
Cu(1)	0	0	0	*o*Cu(1)
O(1)	0	½	0	*o*O(1)
Cu(2)	0	½	¼	1
Se(1)	0	0	*z*Se(1)	1

Table 6.5 Refined parameters from analysis of the three single-crystal datasets collected of JNB237 ("$Ba_2CuO_2Cu_2Se_2$") when the O(1) occupancy was refined but the Cu(1) occupancy was not; positions of any atoms referred to is in Table 6.4

Dataset	034jnb16	040jnb16	041jnb16
a (Å)	4.09110(10)	4.08380(10)	4.0840(3)
c (Å)	19.6746(7)	19.6645(11)	19.669(2)
Volume (Å^3)	329.296(16)	327.95(2)	328.06(5)
Space group	*I*4/*mmm*		
*z*Ba(1)	0.40764(4)	0.40754(3)	0.40753(4)
*z*Se(1)	0.17579(7)	0.17590(6)	0.17576(6)
*o*Cu(1)	1*	1*	1*
*o*O(1)	0.72(4)	0.74(3)	0.77(4)
U_{11}(Ba(1)) (Å^2)	0.0239(5)	0.0143(4)	0.0167(4)
U_{33}(Ba(1)) (Å^2)	0.0318(6)	0.0190(6)	0.0163(5)
U_{11}(Cu(1)) (Å^2)	0.0420(11)	0.0336(11)	0.0353(10)
U_{33}(Cu(1)) (Å^2)	0.0290(13)	0.0172(11)	0.0141(11)
U_{11}(O(1)) (Å^2)	0.038(9)	0.047(11)	0.046(11)
U_{22}(O(1)) (Å^2)	0.107(19)	0.12(2)	0.12(2)
U_{33}(O(1)) (Å^2)	0.018(5)	0.005(4)	0.002(5)
U_{11}(Cu(2)) (Å^2)	0.0263(6)	0.0170(5)	0.0170(5)
U_{33}(Cu(2)) (Å^2)	0.0287(8)	0.0136(6)	0.0107(7)
U_{11}(Se(1)) (Å^2)	0.0219(5)	0.0124(4)	0.0147(4)
U_{33}(Se(1)) (Å^2)	0.0270(7)	0.0127(6)	0.0103(6)
GOF	1.0992	1.0500	1.0284
R_F (%)	7.18	6.65	5.69

*not refined

Table 6.6 Refined parameters from analysis of the three single-crystal datasets collected of JNB237 ($Ba_2CuO_2Cu_2Se_2$) when the Cu(1) occupancy was refined but the O(1) occupancy was not. The positions of the atoms referred to is in Table 6.4.

Dataset	034jnb16	040jnb16	041jnb16
a (Å)	4.09110(10)	4.08380(10)	4.0840(3)
c (Å)	19.6746(7)	19.6645(11)	19.669(2)
Volume (Å^3)	329.296(16)	327.95(2)	328.06(5)
Space group	*I*4/*mmm*		
*z*Ba(1)	0.40763(4)	0.40754(3)	0.40752(3)
*z*Se(1)	0.17577(6)	0.17590(6)	0.17576(6)
*o*Cu(1)	0.885(16)	0.888(13)	0.891(13)
*o*O(1)	1*	1*	1*
U_{11}(Ba(1)) (Å^2)	0.0234(4)	0.0138(4)	0.0162(4)
U_{33}(Ba(1)) (Å^2)	0.0315(6)	0.0187(5)	0.0161(5)
U_{11}(Cu(1)) (Å^2)	0.0374(13)	0.0292(12)	0.0307(11)
U_{33}(Cu(1)) (Å^2)	0.0242(14)	0.0127(12)	0.0097(12)
U_{11}(O(1)) (Å^2)	0.047(8)	0.052(10)	0.052(9)
U_{22}(O(1)) (Å^2)	0.128(18)	0.130(18)	0.135(18)
U_{33}(O(1)) (Å^2)	0.030(5)	0.015(4)	0.011(4)
U_{11}(Cu(2)) (Å^2)	0.0258(6)	0.0165(5)	0.0165(5)
U_{33}(Cu(2)) (Å^2)	0.0281(8)	0.0165(5)	0.0102(6)
U_{11}(Se(1)) (Å^2)	0.0214(5)	0.0119(4)	0.0143(4)
U_{33}(Se(1)) (Å^2)	0.0268(7)	0.0126(5)	0.0102(5)
GOF	1.1036	1.0547	1.0237
R_F (%)	7.24	6.71	5.62

*not refined

Table 6.7 Refined parameters from analysis of the three single-crystal datasets collected of JNB237 ("$Ba_2CuO_2Cu_2Se_2$") when both the O(1) and Cu(1) occupancies were refined simultaneously. The positions of the atoms referred to is in Table 6.4

Dataset	034jnb16	040jnb16	041jnb16
a (Å)	4.09110(10)	4.08380(10)	4.0840(3)
c (Å)	19.6746(7)	19.6645(11)	19.669(2)
Volume (Å^3)	329.296(16)	327.95(2)	328.06(5)
Space group	*I*4/*mmm*		
*z*Ba(1)	0.40764(4)	0.40754(3)	0.40752(3)
*z*Se(1)	0.17579(6)	0.17591(6)	0.17577(6)
*o*Cu(1)	0.91(2)	0.918(19)	0.909(18)
*o*O(1)	0.88(6)	0.89(5)	0.93(5)
U_{11}(Ba(1)) (Å^2)	0.0236(4)	0.0140(4)	0.0163(4)
U_{33}(Ba(1)) (Å^2)	0.0316(6)	0.0188(5)	0.0162(5)
U_{11}(Cu(1)) (Å^2)	0.0386(14)	0.0304(13)	0.0315(12)
U_{33}(Cu(1)) (Å^2)	0.0254(15)	0.0139(13)	0.0104(13)
U_{11}(O(1)) (Å^2)	0.043(8)	0.049(10)	0.050(9)
U_{22}(O(1)) (Å^2)	0.117(18)	0.122(18)	0.130(18)
U_{33}(O(1)) (Å^2)	0.025(6)	0.011(4)	0.008(5)
U_{11}(Cu(2)) (Å^2)	0.0259(6)	0.0166(5)	0.0166(5)
U_{33}(Cu(2)) (Å^2)	0.0283(8)	0.0132(6)	0.0103(6)
U_{11}(Se(1)) (Å^2)	0.0216(5)	0.0121(4)	0.0144(4)
U_{33}(Se(1)) (Å^2)	0.0269(7)	0.0127(5)	0.0102(5)
GOF	1.0884	1.0506	1.0267
R_F (%)	7.19	6.67	5.58

The results of these refinements may be compared by analysing the thermal displacement parameters, R_F values and the likelihood of the values obtained. 034jnb16 was selected for this analysis because the crystal dataset was assessed to be the highest quality in terms of completion. Fig. 6.6 compares the crystal structures obtained.

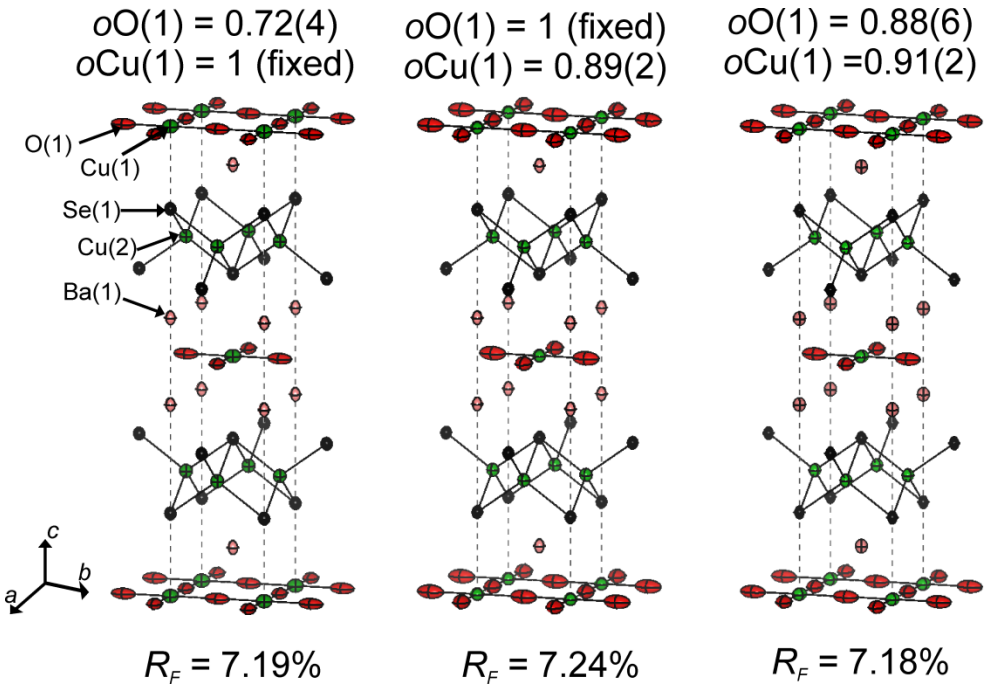


Fig. 6.6 The refined crystal structure models obtained when different occupancy constraints are applied. The models were refined against the 034jnb16 (JNB237, "$Ba_2CuO_2Cu_2Se_2$") dataset

Although refining both the Cu(1) and O(1) occupancy produces the lowest R_F value, the difference is marginal compared with refinement of the O(1) occupancy alone and the thermal displacement parameters (particularly those of O(1)) increase in size when *o*Cu(1) is refined. It is also noted that *o*Cu(1) is within 10% of fully occupied, which is generally considered to be the margin of error when finding fractional occupancies using SCXRD, particularly when the other atoms in the unit cell are particularly heavy (Ba, Se). Therefore, the chosen model was that where the O(1) occupancy is partially occupied and the Cu(1) occupancy is fixed at one. However, it is understood that the possibility of a small Cu(1) deficiency cannot be excluded.

Examination of the O(1) occupancy across the three datasets in Table 6.5 suggests a reasonable estimate is *o*O(1) = 0.74(5). This suggests that the composition is $Ba_2CuO_{1.5}Cu_2Se_2$ and can be understood in terms of all the Cu ions being Cu^+ with no oxidation of selenide. The Cu^I ions in the oxide layers would be three coordinate by oxide on average.

It is likely that the local ordering identified from the diffuse scattering in the reconstructed precession images arises from local ordering of the O(1) atoms in the copper-oxide layers. Electron diffraction, which has a shorter correlation length than

X-ray diffraction, may allow for a greater understanding of the nature of this observed ordering. Alternatively, a total scattering experiment may provide similar insights.

6.4 Variable Temperature Powder X-ray Diffraction

6.4.1 $Sr_2CuO_2Cu_2Se_2$

$Sr_2CuO_2Cu_2Se_2$ (JNB112B) was measured using VT PXRD on the PSD at the I11 beamline. It was found that JNB112B exhibited the expected cell contraction on cooling to 100 K, with no features in the lattice parameters observed that might suggest a phase-transition (Fig. 6.7). The small feature present in each of the refined parameters at ~150 K is an artefact of the experiment, arising from activation of the "turbo" setting on the cryostream. Careful examination of the PXRD pattern on cooling showed that all peaks could still be indexed using the same *I*4/*mmm* model and no splitting of these peaks was observed.

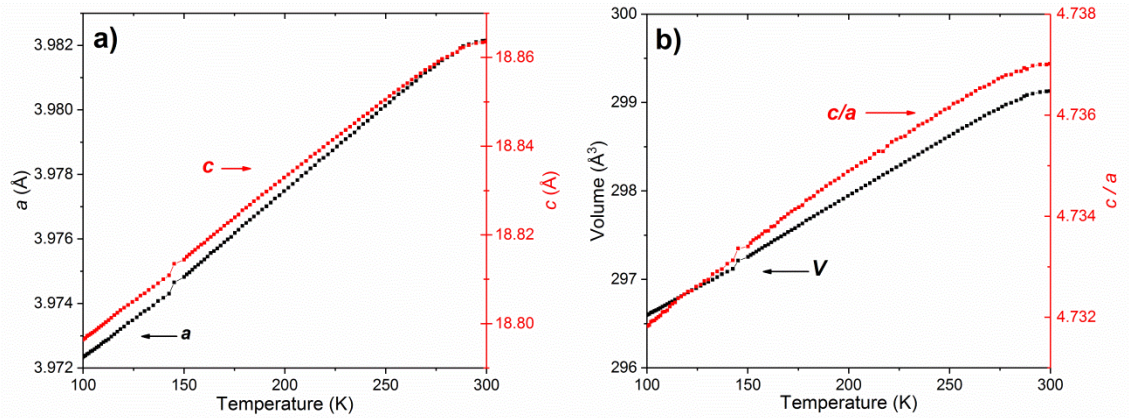


Fig. 6.7 Refined lattice parameters of $Sr_2CuO_2Cu_2Se_2$ (JNB112B) as a function of temperature: a) lattice parameters a and c; b) unit cell volume and the c/a ratio. The small feature at ~150 K is an artefact of the experiment (from activation of the "turbo" cooling setting). The error bars for each dataset are smaller than the points on the graph

6.4.2 $Ba_2CuO_{2-x}Cu_2Se_2$

A sample of $Ba_2CuO_{2-x}Cu_2Se_2$ (JNB128C) was heated to 500 K, using VT PXRD, to examine if any of the unindexed peaks disappeared on heating, which might indicate that these peaks were the result of some temperature dependent ordering (this experiment was performed before the SCXRD experiment). This did not occur. Instead, a change in the ratio of the two phases (discussed in section 6.3.2) was observed, with more of the phase with a larger *a* and smaller *c* forming. It was found that this change was maintained on cooling the sample back to room temperature (RT), indicating that

the change that had occurred was a chemical reaction and not a phase transition. The changes observed in the diffraction pattern are shown in Fig. 6.8.

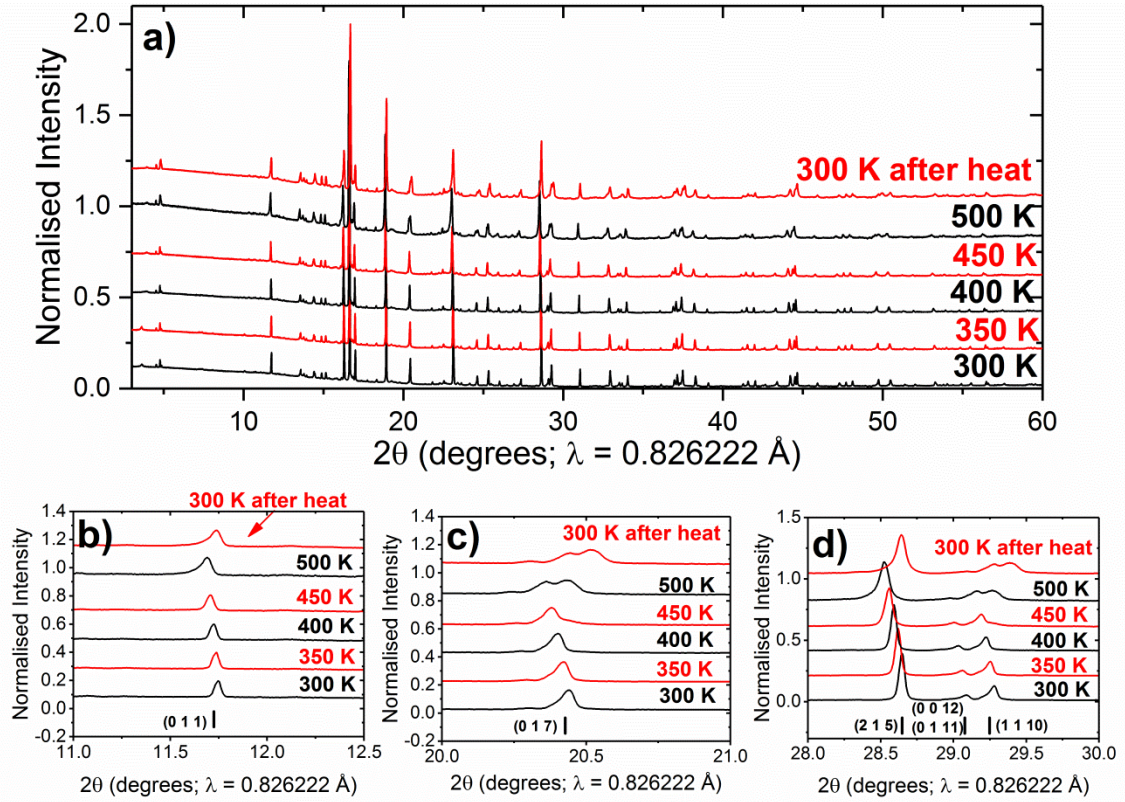


Fig. 6.8 Offset normalised PXRD patterns of $Ba_2CuO_{2-x}Cu_2Se_2$ (JNB128C) as it is heated from 300 K to 500 K and also the resulting 300 K PXRD pattern after heating. b), c) and d) emphasise the observed changes to the 011, 017 and 215 peaks (indexed using a single I4/mmm unit cell) respectively

Fig. 6.9 shows the refined changes in lattice parameters as a function of temperature. It shows that when the temperature at which the reaction can occur is reached (~450 K) a large contraction in *c* occurs. However, these values should be treated with caution because, as is shown in Fig. 6.9 c), the quality of the fit deteriorates significantly when the reaction begins.

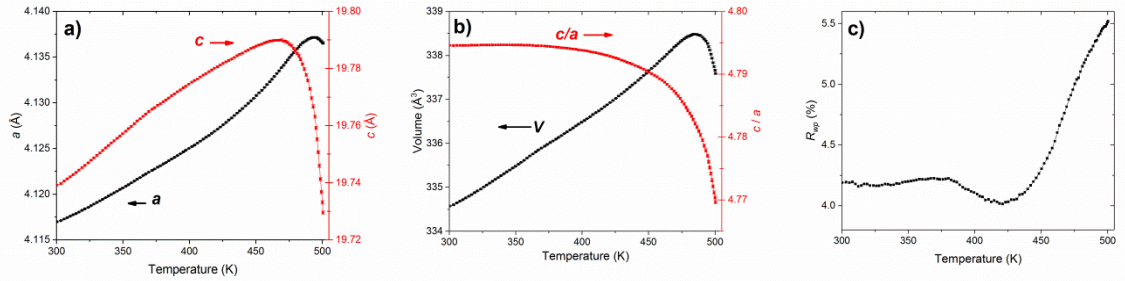


Fig. 6.9 Refined parameters of $Ba_2CuO_{2-x}Cu_2Se_2$ (JNB128C) when it is heated from 300 K to 500 K: a) lattice parameters a and c; b) unit cell volume and c/a; c) R_{wp}. The error bars associated with the lattice parameters are smaller than the data points

The lattice parameters of JNB128C before and after heat treatment are compared in Table 6.8, showing that the changes in the refined lattice parameters are within reasonable estimates of the error, considering the quality of the fit, but that the proportion of the sample that is phase 1 has increased.

Table 6.8 Comparison of refined lattice parameters of JNB128C ($Ba_2CuO_{2-x}Cu_2Se_2$) before and after the sample was heated to 500 K in a capillary filled with boron

Sample	JNB128C (as-synthesised)		JNB128C (after capillary heating)	
Radiation	X-ray, λ = 0.826222 Å			
Diffractometer	PSD, I11			
Phase	1	2	1	2
Phase fraction (wt%)	71.0(3)	29.0(3)	77.6(4)	22.4(4)
a (Å)	4.11828(3)	4.11295(4)	4.11921(3)	4.11398(5)
c (Å)	19.7285(2)	19.7924(3)	19.7306(2)	19.7906(4)
Volume (Å^3)	334.600(5)	334.815(9)	334.787(5)	334.95(1)
R_{wp} (%)	2.986		2.760	

Three possible causes of this observed change were identified:

1. Heating above 450 K causes phase conversion
2. There was a small hole in the capillary allowing the reaction of $Ba_2CuO_{2-x}Cu_2Se_2$ with O_2 above 450 K
3. $Ba_2CuO_{2-x}Cu_2Se_2$ has reacted with boron in the capillary (used as a dilutant)

The reaction of $Ba_2CuO_{2-x}Cu_2Se_2$ with an active flow of O_2 is discussed further in section 6.7, where it is shown that heating in the presence of O_2 leads to a contraction of the lattice parameters of $Ba_2CuO_{2-x}Cu_2Se_2$. It is therefore a reasonable conclusion that the presence of a small amount of oxygen has caused some conversion of the large-lattice-parameter phase to the small-lattice-parameter phase, presumably by filling of O vacancies. However, further studies, such as heating with undiluted capillaries are required to rule out the possibility that reaction with boron has occurred.

A sample of $Ba_2CuO_{2-x}Cu_2Se_2$ (JNB128C) was also measured on cooling (using ID22 below 100 K and the PSD on I11 above 100 K). No additional peaks were observed in the temperature range 300 – 5 K. The refined lattice parameters of these results are shown in Fig. 6.10.

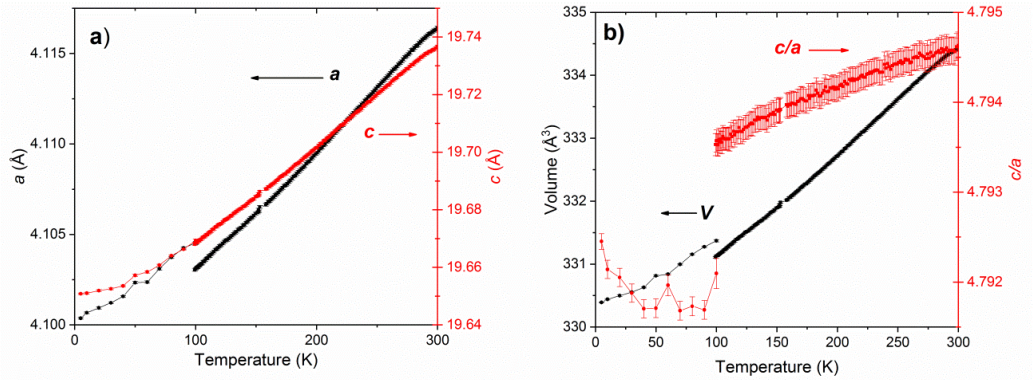


Fig. 6.10 Refined unit cell parameters of $Ba_2CuO_{2-x}Cu_2Se_2$ (JNB128C) in the temperature range 5 – 300 K. Data below 100 K was collected using ID22 and data above 100 K was collected using the PSD on the I11 beamline. a) shows lattice parameters a and c, b) shows the unit cell volume and c/a ratio. With the exception of the c/a data (where the error bars are visible), the error bars are smaller than the points on the graph

The refined lattice parameters indicate a small discontinuity in the refined lattice parameters at ~50 K (most obvious in the *c/a* ratio), which closely matches an observed feature in the bulk resistivity measurements (see section 6.6), but the cause of this feature is unknown.

The refined lattice parameters obtained from the ID22 and PSD (I11) data are not quite the same, most likely due to small systematic errors between the two diffractometers. This causes a large relative change in the *c/a* ratio because this parameter does not appear to change very much with temperature. As discussed with the VT PXRD data obtained for $Sr_2CuO_2Cu_2Se_2$ (JNB112B), the small feature in the lattice parameters at ~150 K is an experimental artefact arising from switching the cryostream to "turbo" mode.

6.5 Magnetometry measurements

Magnetic susceptibility data collected for $Sr_2CuO_2Cu_2Se_2$ and $Ba_2CuO_{2-x}Cu_2Se_2$ has been treated in a slightly different way to equivalent data in other chapters. This is because RT magnetometry measurements showed that the bulk magnetic property of both compounds was net diamagnetic. This can arise when the sample is actually diamagnetic or when a Pauli paramagnetic magnetic susceptibility is smaller than diamagnetic effects from the core electrons.

In materials conventionally considered magnetic (Curie paramagnets, ferromagnets and antiferromagnets) the diamagnetic susceptibility contribution of core electrons (χ_D) to

the measured magnetic susceptibility (χ_{meas}) can often be disregarded. However, the magnetic susceptibility of Pauli paramagnets is small enough that χ_{D} is considered significant. The effect of χ_{D} may be removed by simple subtraction:

$$\chi_{\text{meas}} = \chi_{\text{P}} + \chi_{\text{D}} \tag{6.2}$$

where χ_{D} is obtained by the addition of tabulated constants.[160] If the sample was intrinsically diamagnetic (i.e. a band gap insulator with only closed-shell ions), then it follows that:

$$\chi_{\text{meas}} = \chi_{\text{D}} \tag{6.3}$$

i.e. there is zero paramagnetic contribution to χ_{meas}. When a sample is a Pauli paramagnet, χ_{P} may be used to calculate the density of states at the Fermi level ($N(E_{\text{F}})$):

$$N(E_{\text{F}}) = \frac{10e\chi_P}{2\mu_{\text{B}}^2 N_{\text{A}}} \tag{6.4}$$

where e is the electronic charge (1.60219×10^{-19} C), N_{A} is Avogadro's constant, μ_{B} is the Bohr magneton and χ_{P} is the Pauli susceptibility in c.g.s. units, with all the constants expressed in SI units. The factor of 2 in the denominator arises because the total number of states is twice the number of orbital states. The factor of 10 in the numerator is a conversion factor between c.g.s and SI units. The units of $N(E_{\text{F}})$ are orbital states per eV per formula unit.

Movement of conduction electrons in a field induces a diamagnetic effect called Landau diamagnetism. For free electrons the Landau magnetic susceptibility (χ_{Landau}) is modelled as:

$$\chi_{Landau} = -\frac{1}{3}\chi_P \tag{6.5}$$

In a metal where the electrons may be considered fully delocalised, this correction should be applied before calculation of $N(E_{\text{F}})$. However, the effect is reduced in such cases where the electrons are not entirely free; therefore, the reduction in χ_P from χ_{Landau} has been disregarded in the calculation of $N(E_{\text{F}})$, but the calculated values should be considered a lower bound.

The *M vs H* isotherms of $Sr_2CuO_2Cu_2Se_2$ (JNB112B) and $Ba_2CuO_{2-x}Cu_2Se_2$ (JNB128C) (Fig. 6.11 a) and b)) show that in both cases there appears to be a minuscule ferromagnetic component, ascribed to impurities, that saturates above 1 – 2 T. At larger fields than this, the magnetic susceptibilities are negative, characteristic of net diamagnetic materials and believed to be the property of the bulk of the sample.

The linear behaviour of the magnetic susceptibility at high fields allowed measurement of the magnetic susceptibility as a function of temperature using a 3 T/4 T subtraction (Fig. 6.11 c) and d)). However, these plots are extremely noisy; this is thought to be because in both cases the measured longitudinal moment was close to zero. The magnetic susceptibility of both samples is largely temperature independent above ~50 K. Temperature independent behaviour is characteristic of both Pauli paramagnetic and diamagnetic behaviour. The rise in the susceptibility in $Sr_2CuO_2Cu_2Se_2$ below ~50 K is likely due to a small Curie tail, often observed in Pauli paramagnetic materials. The similar rise in the magnetic susceptibility of $Ba_2CuO_{2-x}Cu_2Se_2$ could be due to further ferromagnetic impurities with a low (< 100 K) T_C as is discussed below or, equally, it could be due to a Curie tail.

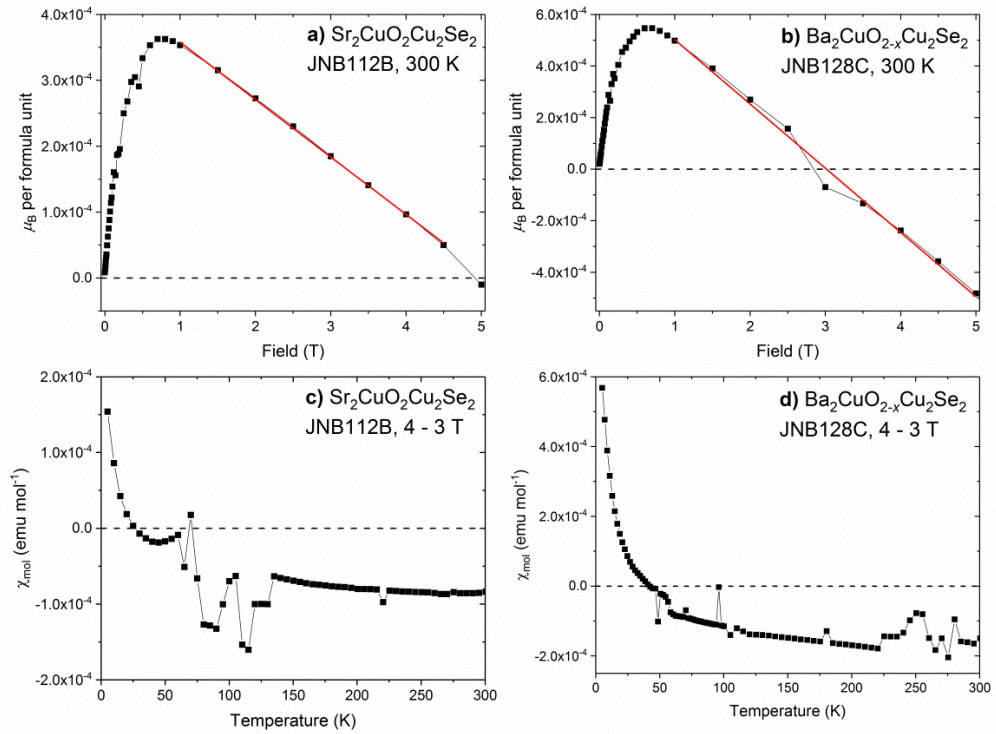


Fig. 6.11 M vs H isotherms of a) $Sr_2CuO_2Cu_2Se_2$ (JNB112B) and b) $Ba_2CuO_{2-x}Cu_2Se_2$ (JNB128C) measured at 300 K; and variable temperature magnetic susceptibility of c) JNB112B and d) JNB128C using a 4 – 3 T subtraction (as described in section 2.8). The positive magnetic susceptibility observed at low field in a) and b) is attributed to a minuscule ferromagnetic impurity in both cases

Linear regression of the 300 K *M vs H* isotherm in the linear (high-field) region was used to extract χ_{meas} values for $Sr_2CuO_2Cu_2Se_2$ and $Ba_2CuO_{2-x}Cu_2Se_2$, which were corrected for core electron diamagnetism to determine whether there was a significant Pauli paramagnetic susceptibility and then used to derive $N(E_F)$. The analysis is shown in Table 6.9. It should be noted that the tabulated χ_D for Se^{2-} is known to be uncertain, due to its variable polarisability in different compounds, adding another layer of uncertainty to these calculations.

The refined composition of $Ba_2CuO_{2-x}Cu_2Se_2$ from SCXRD analysis (x ~0.5) would suggest that $Ba_2CuO_{2-x}Cu_2Se_2$ is diamagnetic with only Cu^I d^{10} ions, but the derived χ_P (i.e. the residual susceptibility after correcting for core electron diamagnetism) is not zero, so for direct comparison with $Sr_2CuO_2Cu_2Se_2$, it is assumed in Table 6.9 that $Ba_2CuO_{2-x}Cu_2Se_2$ may be Pauli paramagnetic.

Table 6.9 Comparison of the density of states at the Fermi level of $Sr_2CuO_2Cu_2Se_2$ (JNB112B) and $Ba_2CuO_{2-x}Cu_2Se_2$

Sample	JNB112B	JNB128C
Compound	$Sr_2CuO_2Cu_2Se_2$	$Ba_2CuO_{2-x}Cu_2Se_2$
χ_{meas} ($\times 10^{-6}$ emu mol^{-1})	-48.6(5)	-141(1)
χ_D ($\times 10^{-6}$ emu mol^{-1})	-193	-208
χ_P ($\times 10^{-6}$ emu mol^{-1})	+144	+67
$N(E_F)$ (orbital states eV^{-1} per formula unit)	2.23	1.04

The obtained $N(E_F)$ values for both $Sr_2CuO_2Cu_2Se_2$ and $Ba_2CuO_{2-x}Cu_2Se_2$ are relatively low, but the value is significantly lower for $Ba_2CuO_{2-x}Cu_2Se_2$, consistent with greater filling of the conduction band (discussed further in section 6.8). *M vs H* isotherms were measured for $Ba_2CuO_{2-x}Cu_2Se_2$ (JNB128C), at 5 and 100 K (see Fig. 6.12). The isotherm of the sample at 5 K is curved, reminiscent of a ferromagnet approaching saturation, were it not that the moment is so low. As stated above, it is possible that JNB128C contains a "hard" ferromagnetic impurity with a low (below 100 K) T_C, which would account for the small saturated moment. This impurity would be paramagnetic at 300 K and may therefore contribute to χ_P. It remains unclear whether $Ba_2CuO_{2-x}Cu_2Se_2$ is purely diamagnetic or whether it has a small Pauli susceptibility.

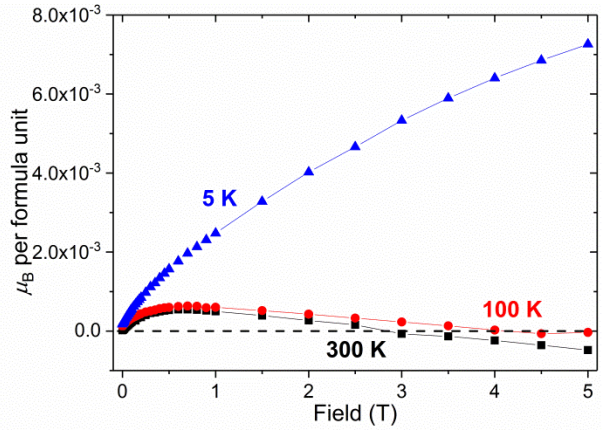


Fig. 6.12 M vs H isotherms of $Ba_2CuO_{2-x}Cu_2Se_2$ (JNB128C) measured at 5, 100 and 300 K

6.6 Bulk resistivity measurements

The bulk resistivity of both $Sr_2CuO_2Cu_2Se_2$ (JNB112B) and $Ba_2CuO_{2-x}Cu_2Se_2$ (JNB128C) were measured as sintered pellets using the four-connection-probe method outlined in section 2.9.

6.6.1 $Sr_2CuO_2Cu_2Se_2$

The resistivity of $Sr_2CuO_2Cu_2Se_2$ (JNB112B) is 0.34(1) Ω cm at 300 K. Fig. 6.13 shows that this rises slowly on cooling. This behaviour does not correspond with the classic behaviour of either a metal or an insulator (described in section 2.9). The material appears to have a small resistivity, in the range of a relatively poorly conducting metal. It is possible the increase in resistivity on cooling arises from partial localisation of the orbitals, which would increase the resistivity of the compound as temperature decreases. The resistivity increase is comparatively small, suggesting that this effect is small.

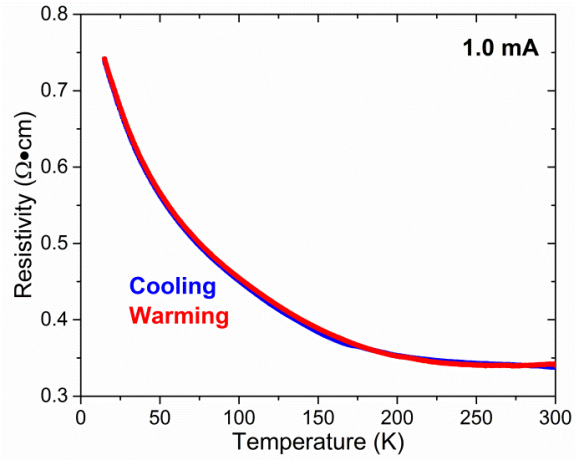


Fig. 6.13 Bulk resistivity of $Sr_2CuO_2Cu_2Se_2$ (JNB112B) as a function of temperature, measured with a constant current of 1.0 mA

6.6.2 $Ba_2CuO_{2-x}Cu_2Se_2$

The resistivity of $Ba_2CuO_{2-x}Cu_2Se_2$ (JNB128C) is much larger than that of the Sr analogue and rises exponentially on cooling from 300 K (Fig. 6.14, see inset for direct comparison of the two compounds). This is characteristic of semiconductor behaviour. However, a broad feature is observed in the resistivity in the region 25 – 50 K, in which there is an unexpected dip in the resistivity. This suggests that there is an electronic transition in the compound at this temperature. This corresponds closely with an observed discontinuity in the lattice parameters when the sample is measured via VT PXRD. It is unknown if this is an intrinsic property or if it a feature arising from the impurities present in the sample. This merits further investigation were a purer sample of $Ba_2CuO_{2-x}Cu_2Se_2$ synthesised.

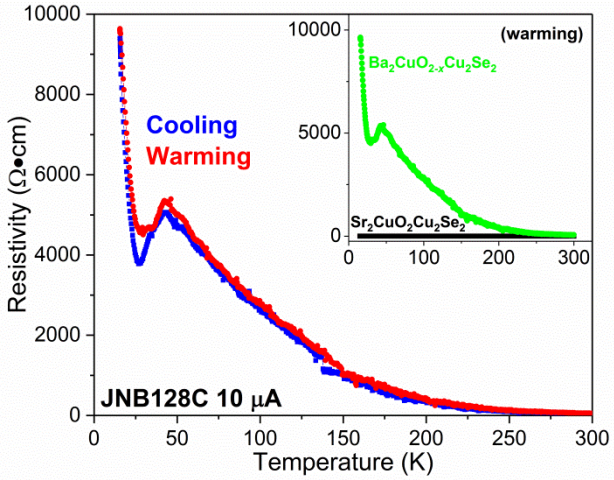


Fig. 6.14 Bulk resistivity measurement of $Ba_2CuO_{2-x}Cu_2Se_2$ (JNB128C), measured using a constant current of 10 μA; the inset compares the bulk resistivity of $Sr_2CuO_2Cu_2Se_2$ (JNB112B) and $Ba_2CuO_{2-x}Cu_2Se_2$ (JNB128C) when measured on warming using the same axes

6.7 Oxygenation of $Ba_2CuO_{2-x}Cu_2Se_2$

Analysis of the VT PXRD data at high temperature (section 6.4.2) suggested that the oxygen vacancies in $Ba_2CuO_{2-x}Cu_2Se_2$ could be filled by oxidation of the phase, resulting in a contraction in lattice parameter *c* and an expansion in lattice parameter *a*. This was investigated by heating small quantities of $Ba_2CuO_2Cu_2Se_2$ under an active flow of oxygen.

Four parent samples of $Ba_2CuO_{2-x}Cu_2Se_2$ (JNB271, JNB292, JNB305 and JNB336) were used in this investigation, all prepared on a 5 g scale using an identical method. BaO, Cu and Se were ground in a molar ratio of 2:3:2 and prepared as described in section 2.1.1. The reactants were heated to 650 °C at 10 °C min^{-1} for 48 h. The sample was allowed to cool in the furnace, before the product was isolated. Sample purity was assessed by in-house PXRD.

In order to oxygenate these samples, small quantities of powder were loaded into alumina boats, which themselves were placed in a large silica tube fitted with end-caps in the glovebox. The endcaps had Young's taps attachments to allow the controlled flow of gas. The tube was then placed in a split-tube furnace and O_2 was flowed over the reactants using the setup shown in Fig. 6.15. The furnace was heated to a temperature and for a duration determined by the selected reaction conditions. The tube was cooled to RT in air before the O_2 was removed from the tube using a dynamic vacuum. The sample was ground and isolated in the glovebox before analysis by laboratory PXRD. Often multiple heatings were used in an attempt to obtain a single $Ba_2CuO_{2-x}Cu_2Se_2$ phase. The various conditions used are shown in Table 6.10.

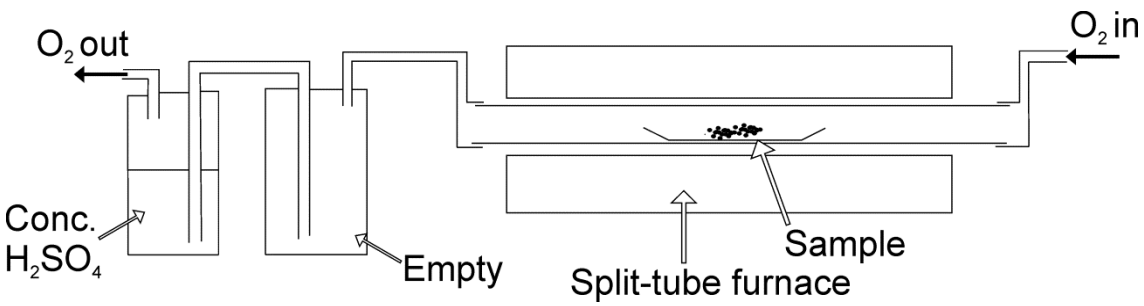


Fig. 6.15 The setup used for the oxygenation of $Ba_2CuO_{2-x}Cu_2Se_2$

Table 6.10 Reaction conditions used in oxygenation reactions of $Ba_2CuO_{2-x}Cu_2Se_2$

Sample	Parent	Mass (g)	Heating temperature (°C)	Duration (h)
JNB285	JNB271	0.50	250	4
JNB286	JNB271	0.50	200	1
JNB287	JNB271	0.50	200	4
JNB291	JNB271	0.50	230	6
JNB293	JNB292	0.50	245	1
JNB314	JNB305	0.50	200	76 (over 4 heat cycles)
JNB320	JNB305	2.00	200	~100 (over 5 heat cycles)
JNB337	JNB336	3.00	200	146 (over 4 heat cycles)

It was found that heating above 200 °C (JNB285, JNB291, JNB293) or for too long (JNB337) caused a large proportion of $Ba_2CuO_{2-x}Cu_2Se_2$ to decompose to $BaSeO_3$. The best quality sample obtained was JNB314, which appeared to have reached completion using laboratory PXRD, but Rietveld refinement against a PSD scan (from the I11 beamline) showed that the sample clearly consisted of at least two phases of $Ba_2CuO_{2-x}Cu_2Se_2$, as shown in Fig. 6.16. The refined lattice parameters of this sample are compared with those of JNB128C (as-synthesised $Ba_2CuO_{2-x}Cu_2Se_2$) in Table 6.11.

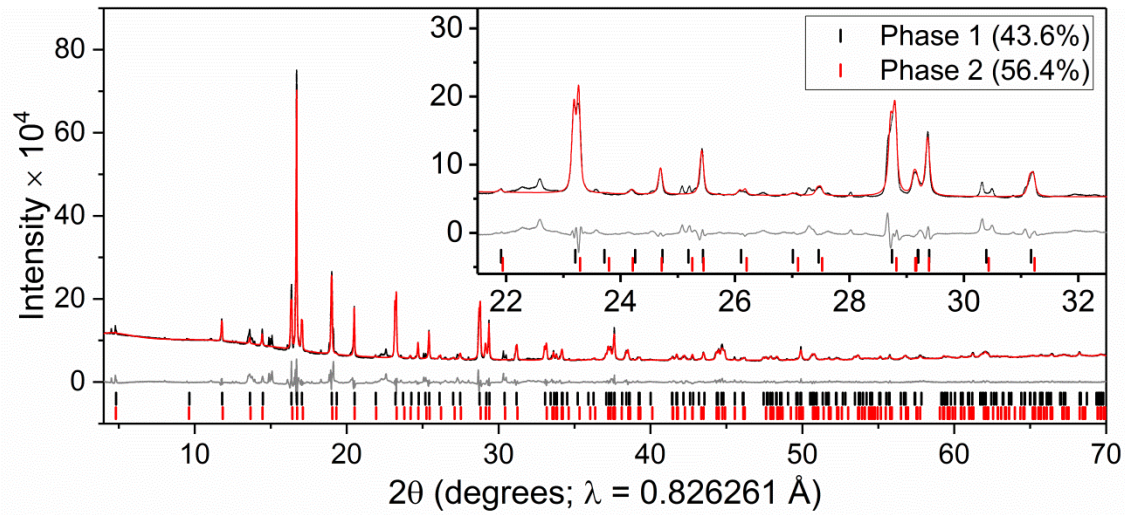


Fig. 6.16 Rietveld refinement against a synchrotron PXRD pattern of JNB314 (oxygenated $Ba_2CuO_{2-x}Cu_2Se_2$) measured using the PSD at the I11 beamline, the inset emphasises the double-peaked nature of the diffraction pattern

Table 6.11 Comparison of the lattice parameters of JNB128C (as-synthesised $Ba_2CuO_{2-x}Cu_2Se_2$) and JNB314 (O_2-flow treated $Ba_2CuO_{2-x}Cu_2Se_2$), parameters obtained from Rietveld refinement against synchrotron PXRD data obtained from the PSD at the I11 beamline

Sample	JNB128C (as-synthesised)		JNB314 (O_2 flow treated)	
Radiation	X-ray, λ = 0.825855 Å		X-ray, λ = 0.826261 Å	
Diffractometer	PSD, I11			
Phase	1	2	1	2
Phase fraction (wt%)	70.2(2)	29.8(2)	43.6(3)	56.3(3)
a (Å)	4.11742(6)	4.11244(7)	4.10785(9)	4.09338(8)
c (Å)	19.7250(3)	19.7865(5)	19.6662(8)	19.7001(6)
Volume ($Å^3$)	334.40(1)	334.63(1)	331.86(2)	330.09(2)

The comparison of the lattice parameters in Table 6.11 shows that although attempts to produce a single-phase of "O_2-rich" $Ba_2CuO_{2-x}Cu_2Se_2$ were not successful, a clear reduction in the lattice parameters (both *a* and *c*) has been achieved in both the phases present in JNB314. This provides evidence that oxygen has been absorbed. Further analysis is hampered by the two-phase nature of the sample.

It is possible that the method used to isolate the compound, in which the sample was put under vacuum after the reaction, may have caused some partial re-reduction of the compound by O_2 loss, resulting in the two-phase behaviour. An *in-situ* experiment, in which $Ba_2CuO_{2-x}Cu_2Se_2$ was measured (using diffraction), while heating under an active flow of O_2, would be informative. Neutron diffraction would be particularly useful for this because the neutron coherent scattering length of O (5.803 fm)[161] is of a more comparable size to the other elements in the compound, offering better contrast than would be achieved via PXRD.

The synchrotron PXRD pattern of JNB314 was originally measured 2 months after the sample was synthesised. The same sample was then measured 6 months after this (8 months after synthesis) to check if the sample had annealed over time. The sample was found to be the same within reasonable errors, suggesting that the sample does not anneal or decompose under inert conditions over a mid-length timescale.

As it was found to be difficult to obtain a single "oxygen-rich" phase using a simple O_2-flow, attempts were made to oxidise the compound by filling the oxygen vacancies with F^- ions, using XeF_2 as the fluorinating agent. It was found that even lightly grinding XeF_2 with $Ba_2CuO_{2-x}Cu_2Se_2$ resulted in an extremely exothermic reaction and subsequent PXRD analysis revealed the presence of BaF_2 in the sample.

Small samples of JNB320 were subject to various conditions in an attempt to cycle the compound back to being a mainly "oxygen-poor" phase. The conditions attempted were: heating under dynamic vacuum, heating in moist O_2, heating in the presence of an aluminium oxygen-getter and heating with NaH. In each case the reaction either led to decomposition of the sample (normally to $BaSeO_3$) or no reaction was observed.

6.8 **Discussion**

If the composition of $Ba_2CuO_{2-x}Cu_2Se_2$ is taken to be $Ba_2CuO_{1.5}Cu_2Se_2$, as concluded from SCXRD analysis, and the oxidation state of Se is assumed to remain -2, then the isovalent substitution of Ba for Sr has caused a change in the formal oxidation state of Cu from Cu^{II} (in $Sr_2CuO_2Cu_2Se_2$) to Cu^{I} (in $Ba_2CuO_{1.5}Cu_2Se_2$). However, it is likely that in $Sr_2CuO_2Cu_2Se_2$ partial oxidation of Se^{2-} has occurred, consistent with the similar energies of the Cu 3d and Se 4p bands.

Magnetometry and bulk resistivity measurements suggest that $Sr_2CuO_2Cu_2Se_2$ is most likely a poor metal, with a net Pauli paramagnetism and a conductivity considered low for a metal; $Ba_2CuO_{2-x}Cu_2Se_2$ has an even lower residual paramagnetism (possibly effectively zero) and appears to behave like a semiconductor, suggestive of a filled conduction band. An explanation for these observations is shown tentatively in schematics of the possible band structures of these compounds in Fig. 6.17. Here it demonstrated that the filling of the valence band would lead $Ba_2CuO_{2-x}Cu_2Se_2$ to be a diamagnetic semiconductor, which is consistent with observations from the resistivity measurements and the observation that the magnetic susceptibility is much smaller than for $Sr_2CuO_2Cu_2Se_2$ and close to the value expected for the diamagnetism of the core electrons.

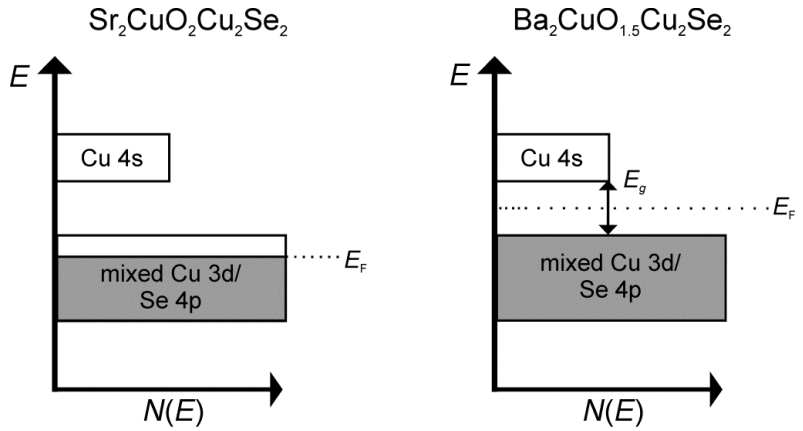


Fig. 6.17 Schematic of the proposed band structures of $Sr_2CuO_2Cu_2Se_2$ and $Ba_2CuO_{1.5}Cu_2Se_2$ near E_F

The difference in the electron count of $Sr_2CuO_2Cu_2Se_2$ and $Ba_2CuO_{1.5}Cu_2Se_2$ is presumably induced because Ba^{2+} (1.49 Å) is significantly larger than Sr^{2+} (1.32 Å),[117] causing increases in the *a* and *c* lattice parameters and therefore in the Cu(1)-O and Cu(1)-Se bond distances, as shown in Table 6.12.

Table 6.12 Comparison of selected bond lengths of $Sr_2CuO_2Cu_2Se_2$ (JNB112B) and $BaCuO_{2-x}Cu_2Se_2$ (JNB128C); values obtained from Rietveld refinement of synchrotron PXRD data

Compound	$Sr_2CuO_2Cu_2Se_2$	$Ba_2CuO_{2-x}Cu_2Se_2$*
Sample	JNB112B	JNB128C
Cu(1)-O	1.99106(2)	2.05871(3)
Cu(1)-Se	3.1784(5)	3.472(1)
Cu(1)-Se/Cu(1)-O	1.5963(3)	1.6865(5)

*majority phase of as-synthesised JNB128C

It is likely that the increase in the Cu(1)-O distance in $Ba_2CuO_{2-x}Cu_2Se_2$ compared with $Sr_2CuO_2Cu_2Se_2$ disfavours the oxidation of Cu. As shown in the schematic in Fig. 6.17, it is likely that both Cu(1) and Se are oxidised to some extent in $Sr_2CuO_2Cu_2Se_2$, but computational calculation of the electronic structure of this compound is necessary to understand this behaviour and therefore the key difference between the two compounds.

6.9 Conclusions

The synthesis of two novel compounds: $Sr_2CuO_2Cu_2Se_2$ and $Ba_2CuO_{2-x}Cu_2Se_2$ has been reported. It has been shown that, while $Sr_2CuO_2Cu_2Se_2$ is fully stoichiometric, $Ba_2CuO_{2-x}Cu_2Se_2$ has an oxygen occupancy of approximately 0.74(5). It has also shown that this compound is then reactive with respect to oxygenation by heating in the

presence of O_2. Further work is required to produce a phase-pure sample of $Ba_2CuO_{2-x}Cu_2Se_2$.

While the magnetic character of these compounds appears to be superficially similar to one another, their electrical resistivity is very different, where $Sr_2CuO_2Cu_2Se_2$ has a relatively low resistivity in the metallic range, albeit with a factor of two increase in the resistivity on cooling to 10 K, $Ba_2CuO_{2-x}Cu_2Se_2$ has a resistivity approximately 10^4 times larger. A transition is also observed in the resistivity data of $Ba_2CuO_{2-x}Cu_2Se_2$ at ~50 K, but further work is required to understand if this transition is intrinsic to $Ba_2CuO_{2-x}Cu_2Se_2$ or related to the behaviour of an impurity in the sample. Re-measuring the bulk resistivity using a phase-pure sample (were it possible to synthesise one) would elucidate this.

Reconstructed precession images of the SCXRD data for $Ba_2CuO_{2-x}Cu_2Se_2$ revealed structured diffuse scattering. This is highly suggestive of short-range ordering of the oxygen vacancies. The use of electron diffraction or a total scattering experiment may assist in further identifying the nature of this ordering.

Comparison of $Sr_2CuO_2Cu_2Se_2$ and $Ba_2CuO_{2-x}Cu_2Se_2$ has shown that isovalent substitution of the alkali-earth metal in compounds of this structure type is non-trivial. Presumably the large change in lattice parameters, enforced by the large change in the size of the alkali-earth metal ion, forces the observed changes in composition. Future investigation of the solid-solution $Sr_{2-y}Ba_yCuO_{2-x}Cu_2Se_2$ may show that the Cu oxidation state can be controlled by the average size of the alkali-earth metal.

Chapter 7

7 Synthesis and characterisation of $Sr_2NiO_2Cu_2Se_2$

7.1 Introduction

The synthesis of $Sr_2NiO_2Cu_2S_2$ was first reported by Otzschi *et al.* with no further analysis performed due to poor sample purity.[47] Smura reported the synthesis of this compound, with phase purity of ~90 wt%, which was sufficient for physical measurements to be performed. Further sample purification appeared to be prevented by the thermodynamic favouring of the formation of $SrSO_4$ at temperatures higher than 500 °C, as was found to be the case for $Sr_2CuO_2Cu_2S_2$.[58]

The changes in lattice parameters and magnetic susceptibility of $Sr_2NiO_2Cu_2S_2$ as a function of temperature show that the compound exhibits unusual behaviour (Fig. 7.1).[13, 58] This unusual behaviour has been attributed to the electronic behaviour of the Ni^{2+} ion as a function of temperature.[13, 58]

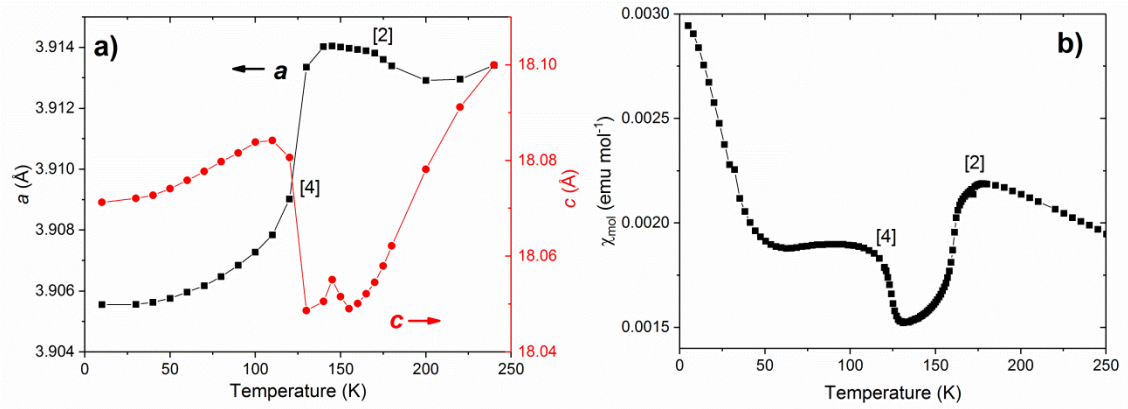


Fig. 7.1 a) refined lattice parameters and b) magnetic susceptibility of $Sr_2NiO_2Cu_2S_2$ as a function of temperature; numbers in square brackets refer to the temperatures of the proposed transitions in Fig. 7.2. Data obtained from ref. 58.

Smura hypothesised that $Sr_2NiO_2Cu_2S_2$ undergoes several electronic transitions on cooling, including a high-spin-to-low-spin transition in the Ni^{2+} ion.[58] These are shown schematically in Fig. 7.2.[58] Apart from the contraction of *a* and the expansion of *c* around 120 K, evidence for a transition to a low-spin state comes from the fact that there is no long-range-ordered magnetic moment according to low-temperature neutron diffraction in $Sr_2NiO_2Cu_2S_2$.

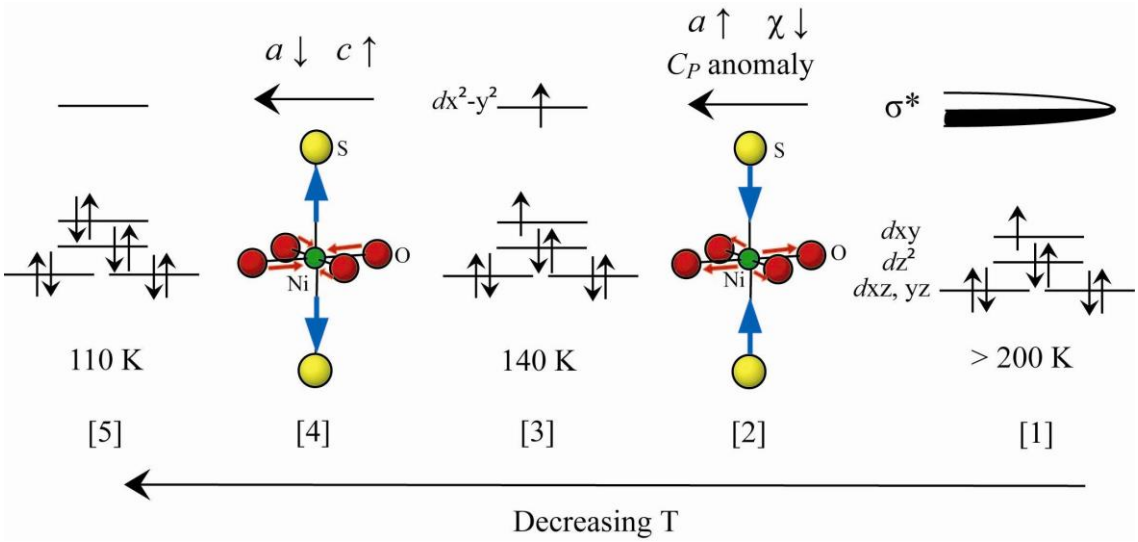


Fig. 7.2 Schematic of the proposed electronic changes that occur in $Sr_2NiO_2Cu_2S_2$ as a function of temperature; image obtained from ref. 58

In the work in this chapter, it was found that $Sr_2NiO_2Cu_2Se_2$ could be synthesised with considerable more ease than $Sr_2NiO_2Cu_2S_2$, once an appropriate synthesis temperature was used. This result closely mirrors the relative stabilities of $Sr_2CuO_2Cu_2S_2$ and $Sr_2CuO_2Cu_2Se_2$ (see chapter 6).

$Sr_2NiO_2Cu_2Se_2$ also exhibits unusual behaviour on cooling, as shown by variable temperature (VT): powder X-ray diffraction (PXRD), powder neutron diffraction (PND), magnetic susceptibility and bulk resistivity measurements. While superficially some of this behaviour is similar to that observed for $Sr_2NiO_2Cu_2S_2$, there are significant differences that are discussed in detail. The root causes of many of the described features remain unknown.

It is also shown that $Sr_2NiO_2Cu_2Se_2$ is active with respect to reaction with I_2 at low temperatures, in a manner not dissimilar to that described for $Sr_2MnO_2Cu_{1.5}S_2$ in section 3.2 and the Co analogues (Chapter 5). However, there appear to be differences in this case. The preliminary results of this analysis are shown.

7.2 Synthesis and composition of $Sr_2NiO_2Cu_2Se_2$

All samples targeting $Sr_2NiO_2Cu_2Se_2$ were synthesised by weighing out SrO, Ni, Cu and Se in the molar ratio 2:1:2:2 and preparing them as described in section 2.1.1. The samples were then heated to the synthesis temperature for 24 – 48 h and either quenched in ice-water or allowed to cool in the furnace, depending on the reaction conditions selected.

Producing a phase-pure sample of $Sr_2NiO_2Cu_2Se_2$ initially proved much more difficult than for $Sr_2CuO_2Cu_2Se_2$ (see Chapter 6). It was later found that this is because low synthesis temperatures (500 °C) were being used, which favoured the formation of compounds of the composition $Sr_2Ni_{1-x}Cu_xO_2Cu_2Se_2$, with substantial amounts of Cu in the oxide layer, leading to the formation of significant quantities of nickel-containing impurities, mainly as $Ni_{1-x}Cu_x$ alloys. This is shown in the Rietveld plot of JNB107 (Fig. 7.3), a sample synthesised at 500 °C. SrO and SrSe are also present because the reaction is incomplete.

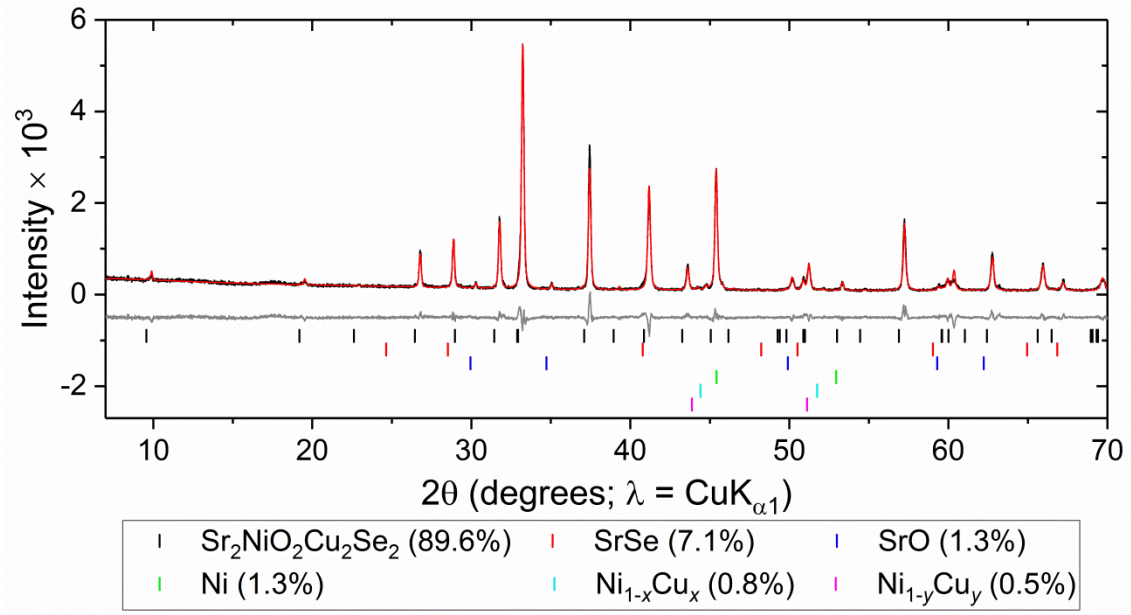


Fig. 7.3 Rietveld plot of JNB107 (nominally $Sr_2NiO_2Cu_2Se_2$), measured using the PANalytical Empyrean diffractometer

It was found that using a higher synthesis temperature, first 650 °C, then 850 °C produced samples that both contained fewer impurities and also had a smaller *c* parameter and larger *a* parameter than those obtained at lower temperatures. This feature was identified as the presence of a greater amount of Ni in the oxide layer as higher temperatures were used. This assumption is corroborated by the comparison of samples where the target compound was $Sr_2NiO_2Cu_2Se_2$ at various synthesis temperatures with samples where the solid solution $Sr_2Ni_{1-x}Cu_xO_2Cu_2Se_2$ was targeted. The synthesis conditions of these compounds are tabulated in Table 7.1 and the *c/a* ratio compared in Fig. 7.4. The ramp rate used was 10 °C min^{-1}. Samples that were heated to 850 °C were first heated to 400 °C for 15 h to prevent vaporisation of elemental selenium. Samples where quenching was used were found to have less peak asymmetry, suggesting that the sample was more homogeneous.

Table 7.1 Synthesis conditions of various compounds of $Sr_2Ni_{1-x}Cu_xO_2Cu_2Se_2$

Sample	Mass synthesised (g)	Target Ni:Cu ratio	Synthesis temperature (°C)	Duration (h)	Quenching used?
JNB107	3.0	1:2	500	100	No
JNB195	1.0	1:2	650	2 × 48	No
JNB231	1.0	1:2	850	24	No
JNB267B	3.0	1:2	850	24 then 16	Yes
JNB260	1.0	0.8:2.2	850	24	No
JNB259	1.0	0.6:2.4	850	24	No
JNB258	1.0	0.4:2.6	850	24	No
JNB257	1.0	0.2:2.8	850	24	No
JNB112B	5.0	0:3	500	2 × 48	No

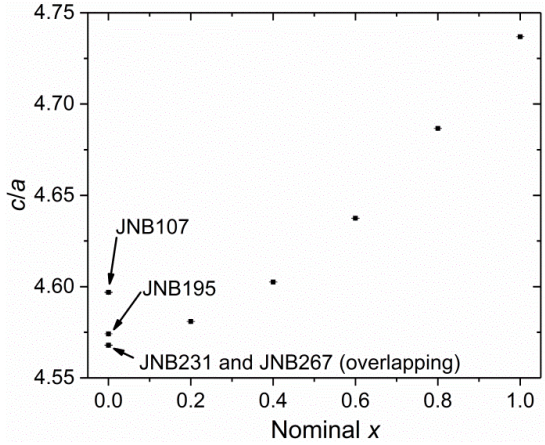


Fig. 7.4 c/a ratio as a function of the nominal value of x in $Sr_2Ni_{1-x}Cu_xO_2Cu_2Se_2$. Lattice parameters derived from Rietveld refinement against synchrotron PXRD data (obtained using the PSD at the I11 beamline), except for JNB107, the lattice parameters of which were obtained from Rietveld refinement against data from the in-house PANalytical Empyrean diffractometer. The error bars are smaller than the points on the graph

Examination of the *c/a* ratios of these compounds (Fig. 7.4) suggests (by extrapolation to the main trend line) that the approximate composition of JNB107 (synthesised at 500 °C) is $Sr_2Ni_{0.7}Cu_{0.3}O_2Cu_2Se_2$ and JNB195 (synthesised at 650 °C) has approximate composition $Sr_2Ni_{0.9}Cu_{0.1}O_2Cu_2Se_2$. It is believed that JNB231 and JNB267B (synthesised at the higher temperature of 850 °C) both largely consist of a metal oxide layer fully occupied with Ni and these were the samples used for further analysis. The clear relationship between the proportion of Cu in the oxide layer and the *c/a* ratio arises due to the unusually elongated structure of $Sr_2CuO_2Cu_2Se_2$ compared with $Sr_2NiO_2Cu_2Se_2$ (which bears much closer resemblance to the related analogues $Sr_2CoO_2Cu_2Se_2$ and $Sr_2ZnO_2Cu_2Se_2$), discussed further in Chapter 8.

7.2.1 Room temperature powder X-ray diffraction and powder neutron diffraction of JNB267B

The structure and composition of JNB67B ($Sr_2NiO_2Cu_2Se_2$) was probed using synchrotron PXRD and high-resolution PND measurements at room temperature (RT). Both these measurements indicated that at RT $Sr_2NiO_2Cu_2Se_2$ adopted the *I*4/*mmm* space group. Attempts to model the Ni site as a disordered site containing both Cu and Ni in the PND data resulted in a refined Cu occupancy on this site of 0.00(2), suggesting that this site consists solely of Ni. The coherent neutron scattering lengths of Ni and Cu (10.3 fm and 7.718 fm respectively)[161] are sufficiently different that this feature would be expected to be resolved from PND. Rietveld refinements of this data are shown in Fig. 7.5 – Fig. 7.7 and the refined parameters are compared in Table 7.2.

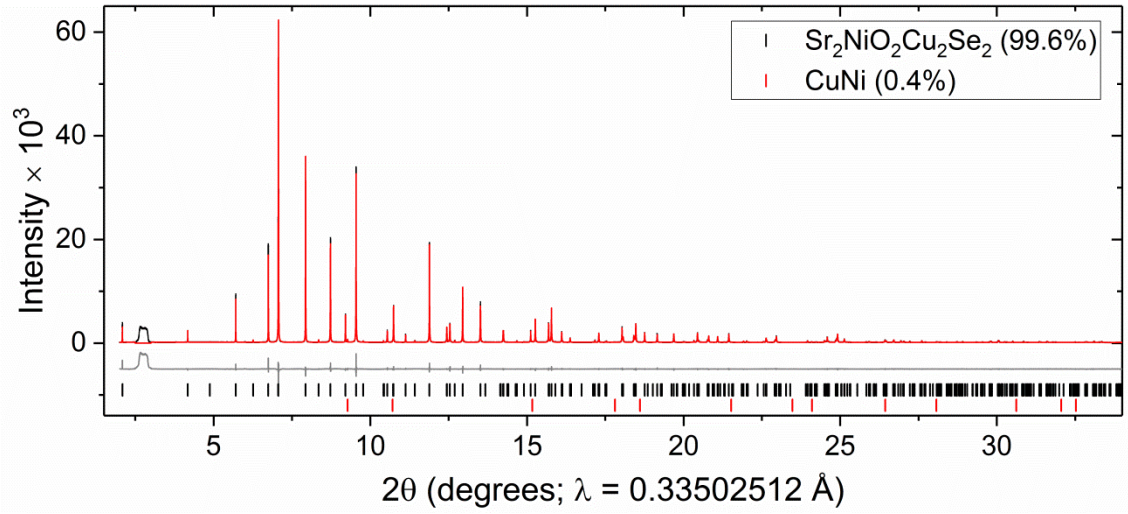


Fig. 7.5 Rietveld plot of $Sr_2NiO_2Cu_2Se_2$ (JNB267B) measured at RT using ID22

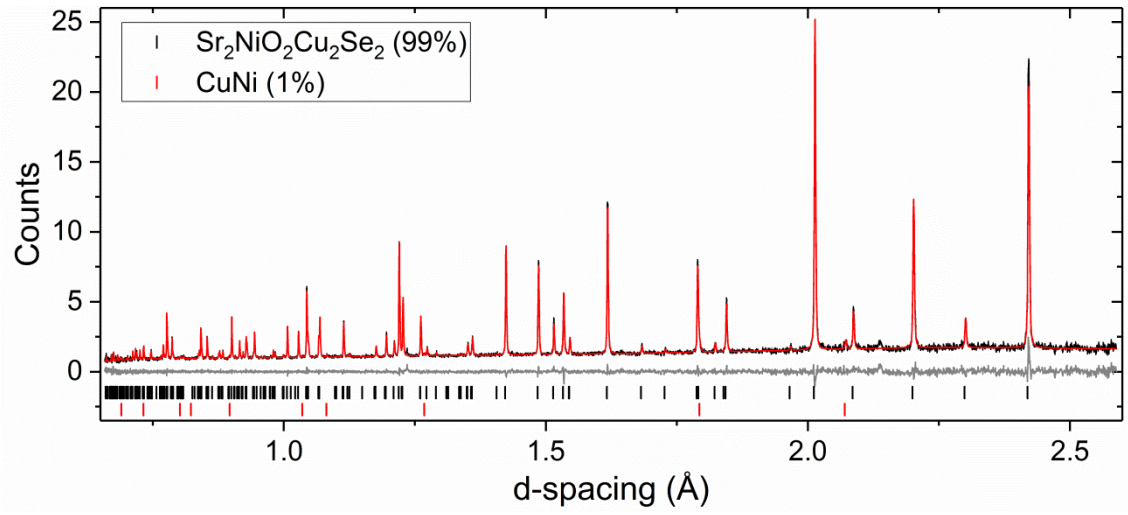


Fig. 7.6 Rietveld plot of $Sr_2NiO_2Cu_2Se_2$ (JNB267B) measured at 300 K using the backscattering (168°) bank of HRPD

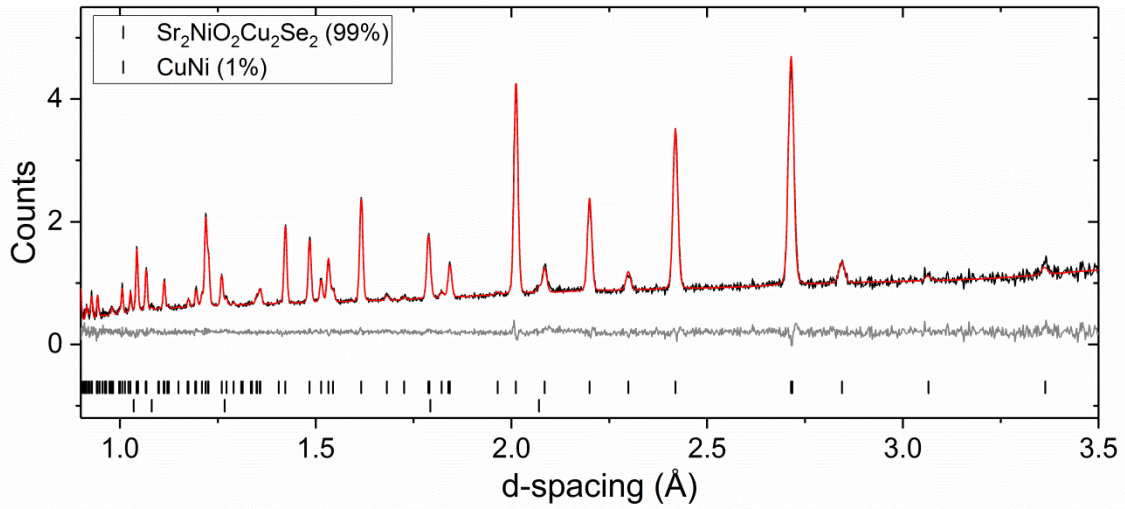


Fig. 7.7 Rietveld plot of $Sr_2NiO_2Cu_2Se_2$ (JNB267B) measured at 300 K using the 90° bank of HRPD

Table 7.2 Selected refined parameters of JNB267B ($Sr_2NiO_2Cu_2Se_2$) from synchrotron PXRD (measured using ID22) and PND (measured using HRPD) both at RT

Sample	JNB267B	
Compound	$Sr_2NiO_2Cu_2Se_2$	
Radiation	X-ray, λ = 0.33502512 Å	Neutron, ToF
Diffractometer	ID22	HRPD
Temperature (K)	RT	300
Purity (wt%)	99.60(1)	99.12(5)
Impurities	CuNi (0.4 wt%)	CuNi (0.88(5) wt%)
Space group	*I*4/*mmm*	
a (Å)	4.026467(7)	4.02354(4)
c (Å)	18.40611(4)	18.3922(2)
Volume (Å^3)	298.408(1)	297.749(6)
z(Sr)	0.41258(2)	0.41239(9)
z(Se)	0.16757(2)	0.16760(6)
Sr U_{11} (Å^2)	0.0061(1)	0.0087(6)
Sr U_{33} (Å^2)	0.0075(2)	0.010(1)
Ni U_{11} (Å^2)	0.0041(3)	0.0077(6)
Ni U_{33} (Å^2)	0.0263(6)	0.024(1)
O U_{11} (Å^2)	0.011(2)	0.009(1)
O U_{22} (Å^2)	0.007(1)	0.009(1)
O U_{33} (Å^2)	0.013(2)	0.015(1)
Cu U_{11} (Å^2)	0.0183(2)	0.0184(6)
Cu U_{33} (Å^2)	0.0192(3)	0.019(1)
Se U_{11} (Å^2)	0.0079(2)	0.0084(6)
Se U_{33} (Å^2)	0.0132(3)	0.015(1)
R_{wp} (%)	7.475	4.467
χ^2	1.514	1.069

7.3 Magnetometry and resistivity measurements

7.3.1 Magnetometry measurements

It was found that the small amount of $Cu_{1-x}Ni_x$ present in the sample of $Sr_2NiO_2Cu_2Se_2$ (JNB231) prevented accurate determination of the magnetic susceptibility at low fields. The *M vs H* isotherm of this sample at 300 K was linear above ~5000 Oe, suggesting that the ferromagnetic impurity had saturated. Therefore, a 3 T/4 T subtraction was used to obtain an accurate intrinsic magnetic susceptibility measurement for the oxide selenide. The magnetic susceptibility of JNB231 as a function of temperature is compared with that of $Sr_2NiO_2Cu_2S_2$ (data obtained from ref. 58) in Fig. 7.8.

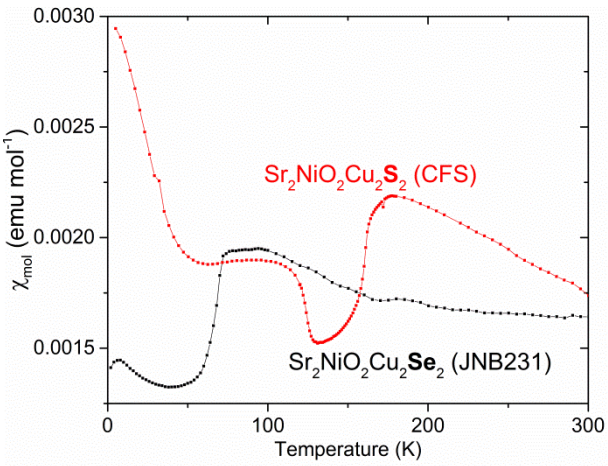


Fig. 7.8 Magnetic susceptibility of $Sr_2NiO_2Cu_2Se_2$ (JNB231), measured using a 4 – 3 T subtraction (as described in section 2.8) compared with the magnetic susceptibility of $Sr_2NiO_2Cu_2S_2$ (obtained from ref. 58)

Several features are apparent in the magnetic susceptibility curve of $Sr_2NiO_2Cu_2Se_2$. There appears to be a sharp transition at 50 – 70 K, marking a sharp drop in magnetic susceptibility as temperature decreases. There is also a small, relatively broad, cusp apparent at 170 – 190 K, superimposed on the general rise in χ_{mol} as temperature decreases between 300 K and 100 K. The inverse susceptibility is non-linear in the whole region 5 – 300 K, so Curie or Weiss constants cannot be extracted.

This behaviour appears qualitatively somewhat similar to that of $Sr_2NiO_2Cu_2S_2$ (also shown in Fig. 7.8). However, there are clearly significant differences in the magnetic behaviour. There are no features in the magnetic susceptibility behaviour of $Sr_2NiO_2Cu_2S_2$ associated with an antiferromagnetic transition and there are some sharp transitions in the magnetic susceptibility curve of $Sr_2NiO_2Cu_2S_2$ not present in

$Sr_2NiO_2Cu_2Se_2$. This is suggestive of clear differences in their behaviour, requiring further investigation.

7.3.2 Resistivity measurements

The bulk resistivity of JNB231 ($Sr_2NiO_2Cu_2Se_2$) was measured on a pellet sintered to 850 °C using the method outlined in section 2.9. The resistivity of JNB231 (shown in Fig. 7.9, compared with the magnetic susceptibility) decreased as temperature decreased, suggesting that the compound had metal-like properties. A hump, with hysteresis dependant on whether the sample was being measured on cooling or heating is apparent in the temperature range 160 –215 K. This compares closely with the small cusp apparent in the magnetic susceptibility curve. Surprisingly, there is no feature in the conductivity curve that corresponds to the sharp transition in the magnetic susceptibility (~70 K).

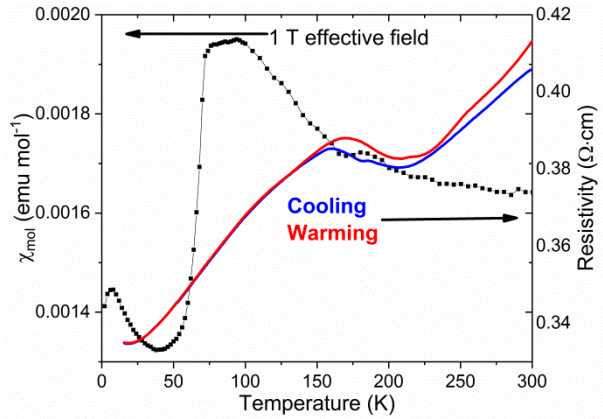


Fig. 7.9 Bulk resistivity of $Sr_2NiO_2Cu_2Se_2$ (JNB231), measured in a constant current of 10 mA as a function of temperature (15 – 300 K). This is compared with the magnetic susceptibility of the same compound, measured as previously described

The hump in the resistivity is thought to arise from the antiferromagnetic ordering of $Sr_2NiO_2Cu_2Se_2$; this is corroborated by the small cusp apparent in the magnetic susceptibility measurement and by variable temperature PND measurements, described in section 7.4.

7.4 Variable temperature diffraction

7.4.1 Changes in lattice parameters

As discussed in section 7.1, Smura found that the transitions observed in the magnetic susceptibility measurements of $Sr_2NiO_2Cu_2S_2$ were accompanied by discontinuities in the lattice parameters of this compound when it was measured using PND.[58] Therefore,

a similar experiment was performed on $Sr_2NiO_2Cu_2Se_2$ to see if similar changes in the lattice parameters accompanied the unusual transition observed in the magnetic susceptibility measurements.

$Sr_2NiO_2Cu_2Se_2$ (JNB267B) was measured using HRPD in the temperature range 5 – 300 K using the following setup: 2.05 g of $Sr_2NiO_2Cu_2Se_2$ (JNB267B) was packed into a 2 mm deep square aluminium cell with 40 mm × 40 mm vanadium windows (described as a "slab can"). A heating element and thermocouple were inserted into the sides of this cell. This setup was used because it allows for more efficient control of the temperature than a standard cylindrical vanadium can – in this setup the cryostat stays cold and heating is directly on the sample. The sample was measured on warming. The refined lattice parameters from this experiment are shown in Fig. 7.10.

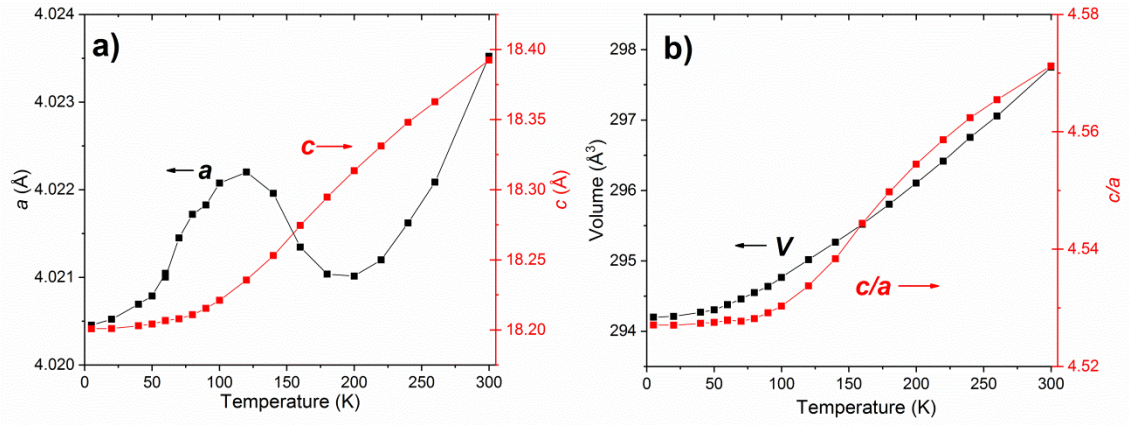


Fig. 7.10 Refined lattice parameters of $Sr_2NiO_2Cu_2Se_2$ (JNB267B) obtained from Rietveld refinement against HRPD data a) compares the change in a and c as a function of temperature and b) compares the change in unit cell volume and the c/a ratio as a function of temperature. In each case the error bars are smaller than the points on the graph

It appears from these data that, in contrast to $Sr_2NiO_2Cu_2S_2$, no discontinuities are observed in the *c* lattice parameter on cooling, which contracts on average significantly more than the *a* lattice parameter (1.04% and 0.08% respectively over the whole temperature range). The shapes of the volume and *c*/*a* curves are therefore dominated by the change in *c*, because *a* remains comparatively static as temperature is reduced. *a* changes in a non-trivial way on cooling, comparing closely to the magnetic susceptibility behaviour of this compound, as shown in Fig. 7.11. It also appears that the rate of reduction in *c* increases as the temperature where the anomaly in the

resistivity measurement is observed is approached; this increase in rate of decrease in *c* is maintained above ~100 K.

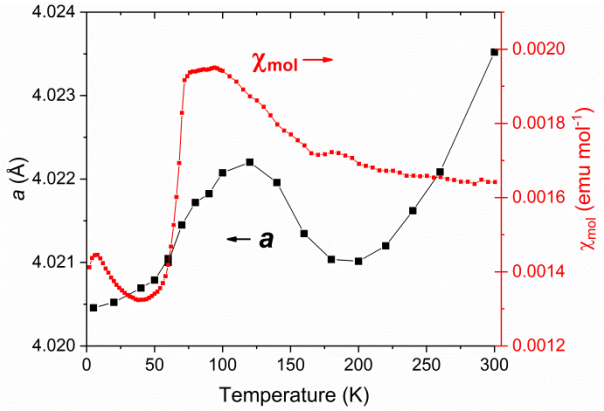


Fig. 7.11 Comparison of the lattice parameter a of $Sr_2NiO_2Cu_2Se_2$ (JNB267B) derived from Rietveld refinement against HRPD data (error bars are smaller than the points on the graph) and the magnetic susceptibility of $Sr_2NiO_2Cu_2Se_2$ (JNB231), measured using a 3 T/4 T subtraction (see section 7.3.1)

This comparison shows that the local minimum in *a*, ~200 K, closely corresponds to the cusp in the magnetic susceptibility, identified as T_N. There also appears to be a relationship between the sharp transition in χ and the temperature around 100 K at which *a* begins to decrease again on cooling after passing through a local maximum. As *a* is defined as double the Ni-O bond length, this provides evidence that the unusual magnetic susceptibility behaviour is caused by electronic transitions which affect the Ni-O bond length.

7.4.2 Observation of peak splitting

VT PXRD measurements were also performed on JNB267B ($Sr_2NiO_2Cu_2Se_2$) using ID22. In order to measure the sample, it was ground with boron in a 2:1 mass ratio and packed into a 0.7 mm diameter borosilicate capillary in an argon atmosphere. Prior to mounting the capillary, the end of the capillary was snapped off in a helium-filled glovebag and the end stuffed with vacuum grease. This was done to minimise beam heating effects that have been observed when samples are cooled below the boiling point of argon (87 K).[61] Particular care was taken because previous work performed on the ID31 beamline (as the diffractometer system at ID22 was known prior to being moved) erroneously attributed these beam heating effects to real electronic transitions.[162-164] JNB267B ($Sr_2NiO_2Cu_2Se_2$) was treated as air sensitive during every stage from synthesis onwards.

The high-resolution obtainable using ID22 led to the identification of subtle peak-splitting as a function of temperature. This peak splitting was apparent in several peaks, but appeared largest in the 017 peak (when indexed using an *I4/mmm* cell), shown in Fig. 7.12. Because the focus was on the low temperature region, and the availability of time on I11 at Diamond for the region above 100 K, data were not collected in the region RT – 140 K.

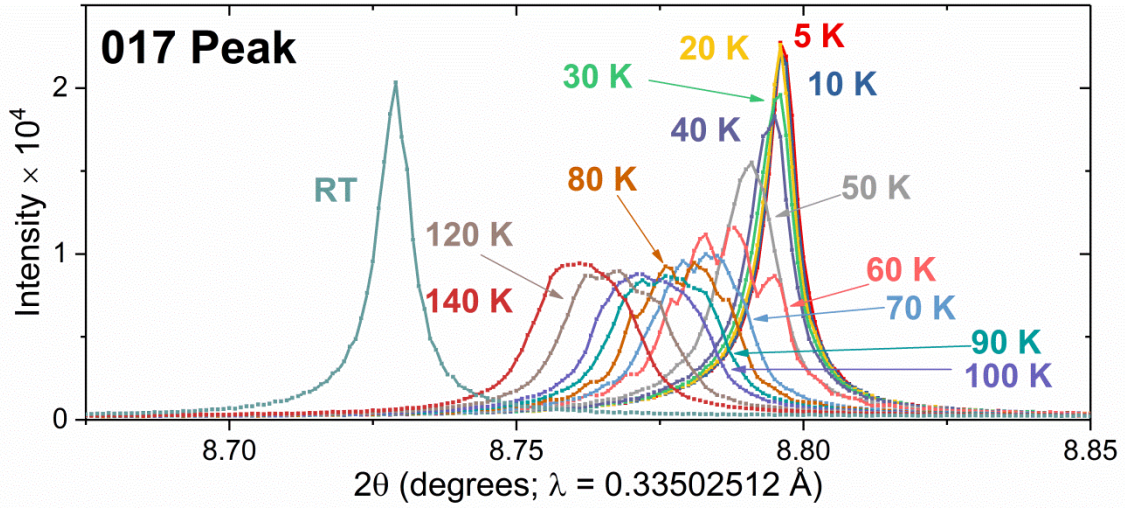


Fig. 7.12 Raw PXRD patterns of $Sr_2NiO_2Cu_2Se_2$ (JNB267B) measured at various temperatures using the ID22 diffractometer, the 017 peak is emphasised

The data shown in Fig. 7.12 show that the 017 peak is undistorted at RT, significantly broader at 140 K and continues to broaden on cooling, until at 60 K the peak appears to be split into at least four distinct peaks. However, unusually for a symmetry-lowering distortion, when the sample was cooled below 60 K, the distortion appeared to disappear, so that when the sample was measured below 40 K, it appeared to have *I4/mmm* symmetry. Note that the peaks continue to shift to higher angle on cooling, suggesting no beam heating of the sample occurs.[61] It may be that the observations are dependent on the order in which the measurements were collected: the sample was cooled to 5 K and measured on heating in 5 – 20 K steps up to 140 K and the RT measurement was collected on a separate capillary. The possible implications of this will be discussed further later.

The extent of the peak splitting is shown in Fig. 7.13, a Rietveld plot of JNB267B measured at 60 K and indexed using a single phase with *I4/mmm* symmetry.

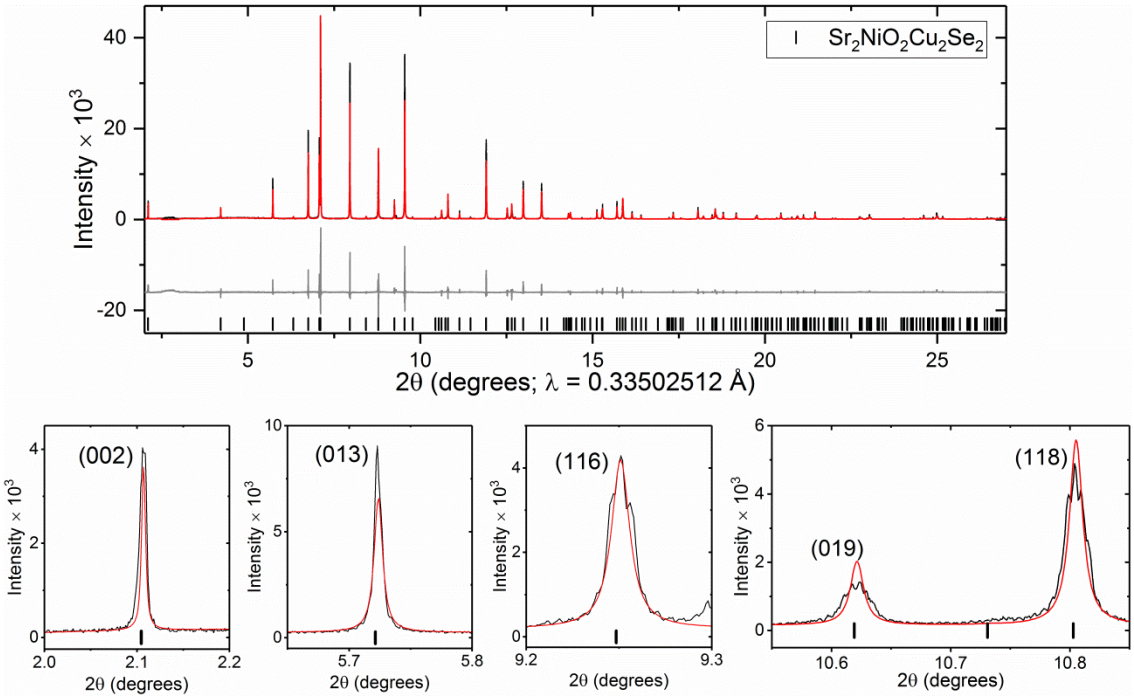


Fig. 7.13 Rietveld plot of $Sr_2NiO_2Cu_2Se_2$ (JNB267B) measured using ID22 at 60 K and fitted using a single I4/mmm model, the 002, 013, 116, 019 and 118 peaks are magnified to emphasise regions where the model fits poorly

Four possible causes of this peak splitting were investigated:

1. the sample contains multiple similar phases of compounds with composition close to $Sr_2NiO_2Cu_2Se_2$ which reach maximal divergence at 60 K prior to converging;
2. that splitting arises from a symmetry-lowering distortion;
3. the peak splitting observed is an artefact of the experiment;
4. the peak splitting arises from a photon-induced electronic transition.

These possibilities are discussed in turn.

7.4.2.1 *Multiple phases*

As was shown in section 7.2.1, JNB267B ($Sr_2NiO_2Cu_2Se_2$) appears to be single phase at RT. However, it is believed that the way in which the lattice parameters of $Sr_2NiO_2Cu_2Se_2$ change with temperature are extremely sensitive to the precise composition of the compound, as will be shown when the I_2 treated samples are discussed (section 7.6).

JNB195, a sample with target composition $Sr_2NiO_2Cu_2Se_2$ and synthesis temperature of 650 °C, was also measured on ID22 as a function of temperature. As discussed in

section 7.2 (see particularly Fig. 7.4), it was concluded that this sample had approximate composition $Sr_2Ni_{0.9}Cu_{0.1}O_2Cu_2Se_2$. This sample appeared to be single-phased at RT, but when cooled to lower temperatures significant peak-splitting, characteristic of the presence of at least two phases, was observed, as shown in Fig. 7.14.

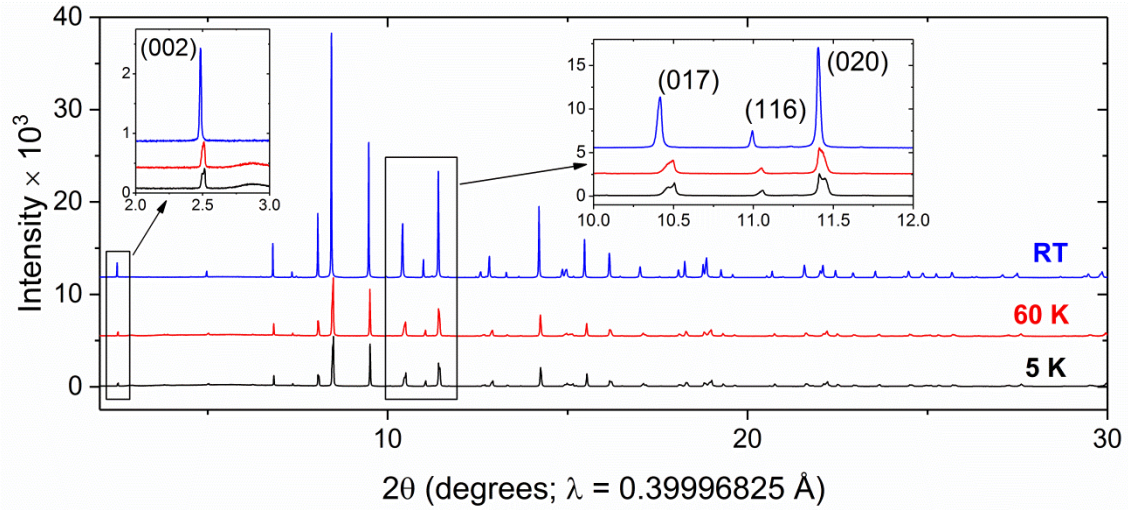


Fig. 7.14 Stacked raw PXRD patterns of JNB195B ($Sr_2NiO_2Cu_2Se_2$, synthesis temperature 650 °C) measured using ID22 at 5 K, 60 K and RT. The insets emphasise the splitting of the 002, 017, 116 and 020 peaks due to the presence of multiple similar phases

When this sample JNB195B ($Sr_2Ni_{1-x}Cu_xO_2Cu_2Se_2$, synthesis temperature 650 °C) is approximated as two phases, a reasonable approximation (see Rietveld plot in Fig. 7.15), the lattice parameters are most divergent at the lowest temperature (5 K, see Fig. 7.16). This suggests that if JNB267B ($Sr_2NiO_2Cu_2Se_2$, synthesis temperature 850 °C) is also multi-phase; it does not primarily arise from Ni-Cu mixing in the oxide layer, since in this sample significant peak-splitting is not observed below ~50 K.

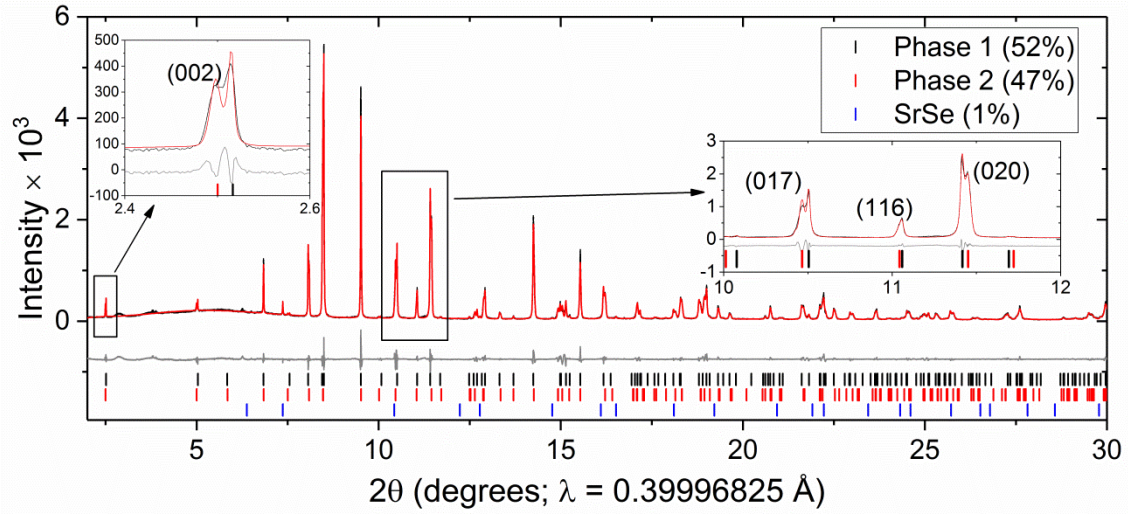


Fig. 7.15 Rietveld plot of JNB195B ($Sr_2NiO_2Cu_2Se_2$ with synthesis temperature 650 °C), measured at 5 K using ID22, insets emphasise the fit to the 002, 017, 116 and 020 peaks

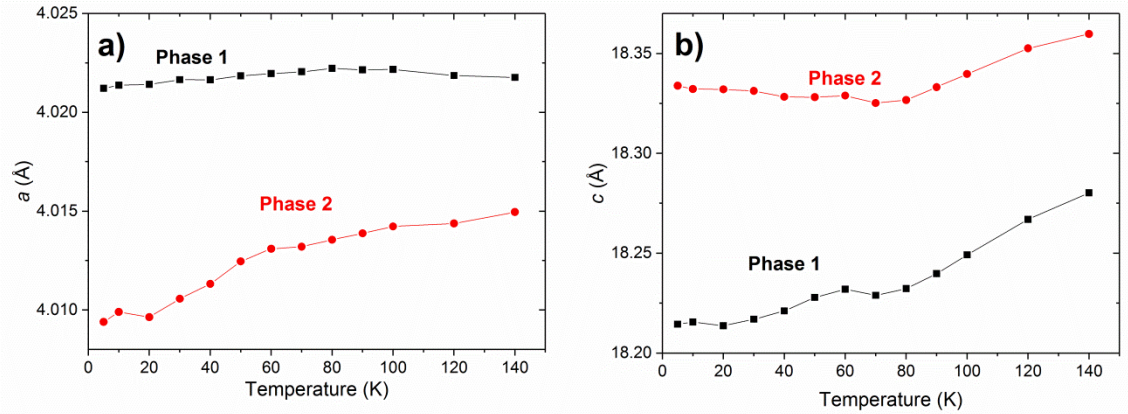


Fig. 7.16 Lattice parameters of JNB195B ($Sr_2NiO_2Cu_2Se_2$) as a function of temperature when the data obtained from ID22 is modelled using two phases. The error bars calculated from the Rietveld refinement are smaller than the points on the graph

However other changes to the composition of this compound from the ideal $Sr_2NiO_2Cu_2Se_2$ stoichiometry are possible (as shown in section 7.6) and the lattice parameters may behave differently with respect to temperature, therefore attempts were made to model the PXRD pattern of JNB267B at 60 K as multiple phases of *I*4/*mmm* symmetry with slightly different lattice parameters.

In these Rietveld refinements, the results of refining four similar $Sr_2NiO_2Cu_2Se_2$ phases were compared with the results of refining the data against a single $Sr_2NiO_2Cu_2Se_2$, both with and without the addition of Stephen's tetragonal anisotropic broadening terms.[154] When multiple phases were modelled, the atom positions, atom displacement parameters and peak-shape were refined, but constrained to be the same in every phase. Anisotropic broadening terms were not used when multiple $Sr_2NiO_2Cu_2Se_2$ phases were

used in the model. The results are shown as Rietveld plots in Fig. 7.17 and the lattice parameters of the phases are tabulated in Table 7.3.

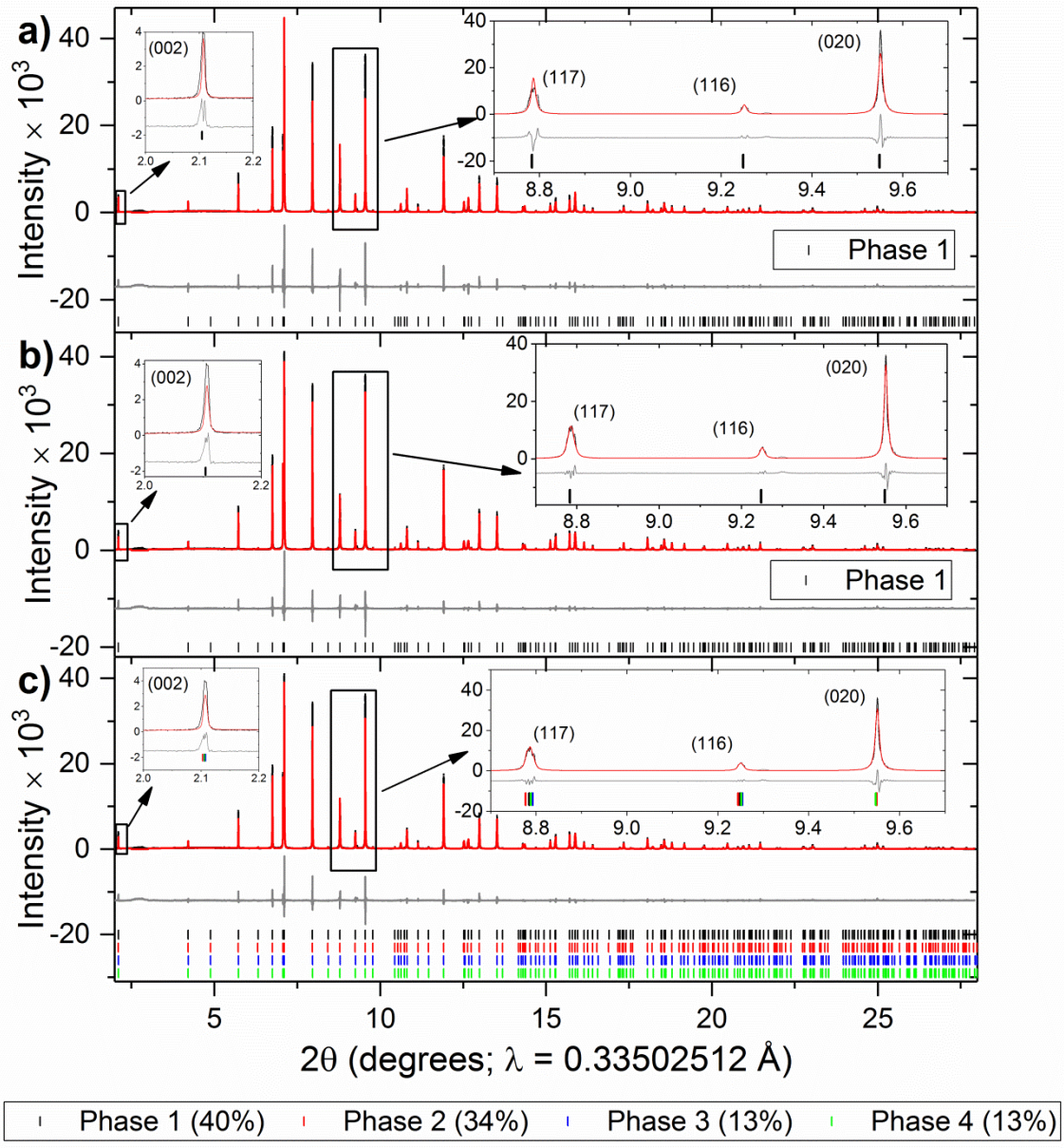


Fig. 7.17 Rietveld refinement against synchrotron (ID22) PXRD data of $Sr_2NiO_2Cu_2Se_2$ (JNB267B) when measured at 60 K, a) using a single phase without anisotropic broadening terms; b) using a single phase with anisotropic broadening terms and c) using four similar phases (no anisotropic broadening terms)

Table 7.3 Lattice parameters and fit parameters obtained from refinement against synchrotron PXRD data of $Sr_2NiO_2Cu_2Se_2$ (JNB267B) when measured at 60 K using ID22, using different refinement models

Refinement model	Single phase, no anisotropic broadening	Single phase, with anisotropic broadening	Four similar phases
a (Å)	4.02523(2)	4.02521(1)	4.02539(6) 4.02471(4) 4.0258(1) 4.0256(2)
c (Å)	18.2410(1)	18.24231(9)	18.2394(3) 18.2616(2) 18.2147(6) 18.226(1)
Volume (Å^3)	295.549(3)	295.567(2)	295.807(6) 295.21(2) 295.36(4)
R_{wp} (%)	18.560	13.286	13.968
χ^2	2.860	2.048	2.153

Table 7.3 shows that the simultaneous refinement of four similar phases improves the fit to the data, but not as much as when tetragonal anisotropic broadening terms are added. Anisotropic broadening terms work well modelling the data because the peak splitting is most prevalent in peaks where $l \neq 0$. However, as the structure of the peak splitting can be observed, as emphasised in Fig. 7.18, anisotropic broadening cannot be a good description of the structure, despite giving a reasonable average.

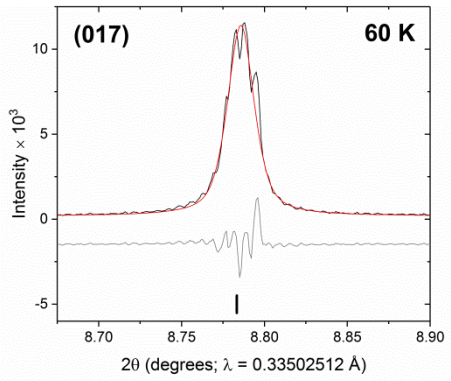


Fig. 7.18 Rietveld plot of the 017 peak of $Sr_2NiO_2Cu_2Se_2$ (JNB267B) using a single-phase model, with Stephen's anisotropic broadening terms incorporated,[154] showing that the anisotropic broadening terms do not account for the splitting observed in the peak. The sample was measured at 60 K, using ID22

The lattice parameters of the four similar phases that were refined are compared in Fig. 7.19. They show that the refined relationship is that as *a* increases, *c* decreases. This relationship is qualitatively similar to the relationship observed between samples when

$Sr_2NiO_2Cu_2Se_2$ is treated with I_2 (section 7.6), but is quantitatively different: a linear fit to the relationship between *a* and c of the refined phases here gives a gradient of -38(4), the gradient for the samples treated with I_2 is -20.0(7).

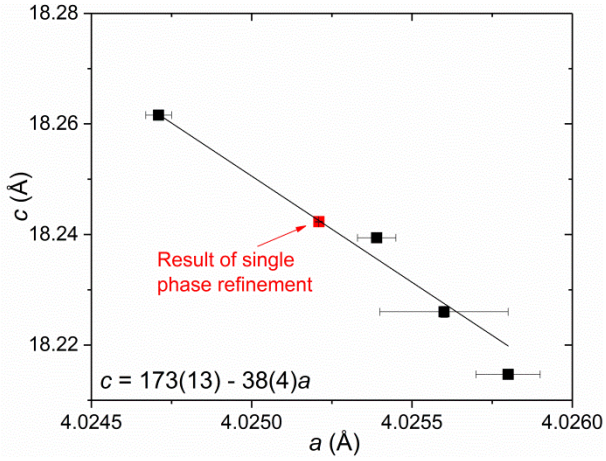


Fig. 7.19 Comparison of the refined lattice parameters when the PXRD data obtained from measuring $Sr_2NiO_2Cu_2Se_2$ (JNB2678B) at 60 K using ID22 was modelled with four similar phases. A linear fit is also shown

7.4.2.2 *Symmetry-lowering distortion*

The peak splitting appears to increase to a maximal amount on cooling to 60 K, below which the splitting appears to be suppressed. It is possible that this arises from a symmetry lowering distortion which is suppressed by the electronic transition that causes the sharp feature in the magnetic susceptibility curve near this temperature (section 7.3.1). Therefore ISODISTORT,[112] interfaced with TOPAS[99] was used in an attempt to index the peak-splitting as if it were a symmetry-lowering distortion.

No superstructure peaks appear on cooling, so expansion of the unit cell could be excluded from the analysis. Therefore the standard cell for $Sr_2NiO_2Cu_2Se_2$ was reduced to *P*1 symmetry and the possible strain modes analysed. It was found that two strain modes caused the desired distortion: These have the symmetry labels $GM5^+$(a) and $GM5^+$(b). The $GM5^+$(a) strain distortion is shown schematically in Fig. 7.20, along with its effect on the 017, 116 and 020 peaks.

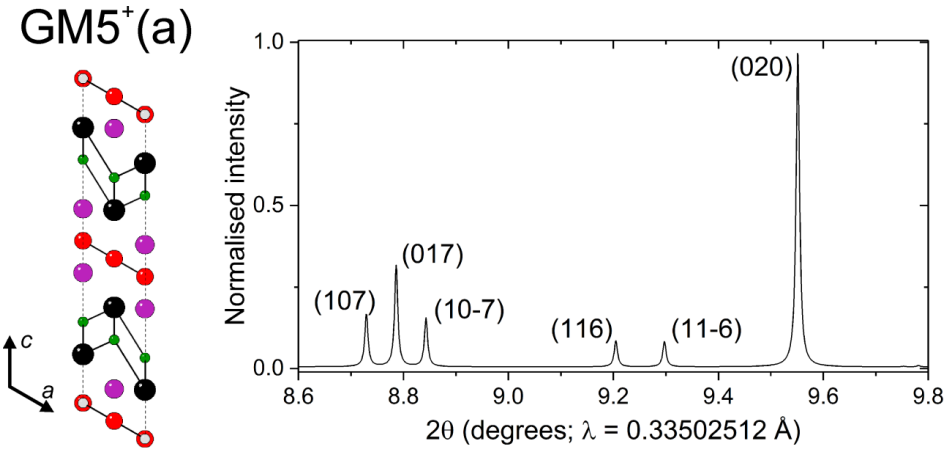


Fig. 7.20 Schematic of GM5$^+$(a) distortion and a predicted PXRD pattern exhibiting the effect of this distortion on the 017, 116 and 020 peaks (indexed using the I4/mmm model)

GM5$^+$(b) is equivalent to GM5$^+$(a), both representing a monoclinic distortion. GM5$^+$(a) represents a distortion in β, while GM5$^+$(b) represents a distortion in α. The 017 peak clearly divides into at least four separate peaks and the 116 into at least three separate peaks. This suggests that the putative distortion is the result of the relaxation of both symmetry modes, causing a triclinic distortion, as shown schematically in Fig. 7.21.

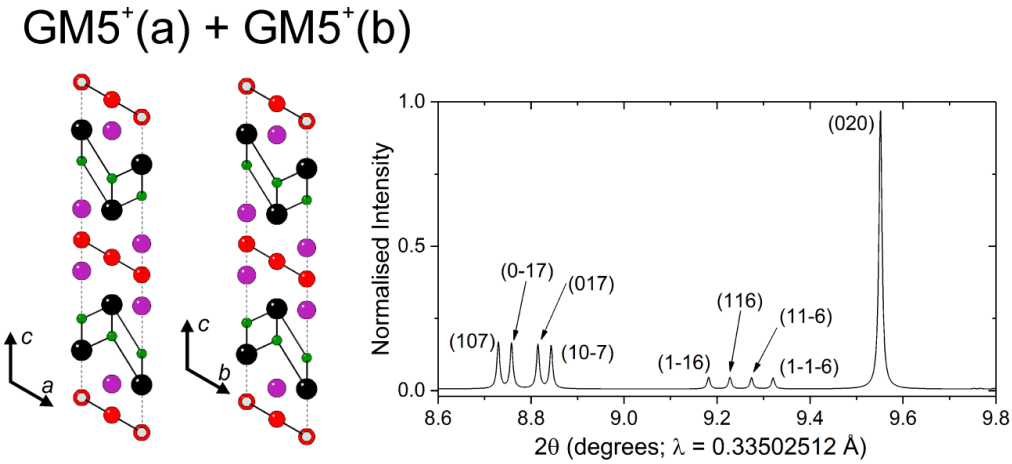


Fig. 7.21 Schematic of the combined effect of the GM5$^+$(a) and GM5$^+$(b) strain modes used concurrently and the effect of these modes on the 017, 116 and 020 peaks (indexed using the I4/mmm model), providing GM5$^+$(a) ≠ GM5$^+$(b)

It was found that when the strain modes were allowed to freely refine, they tended towards zero. Therefore, a representative fit where the best visual fit to the peaks was achieved by multiple iterations is shown in Fig. 7.22, with the values from this fit tabulated in Table 7.4.

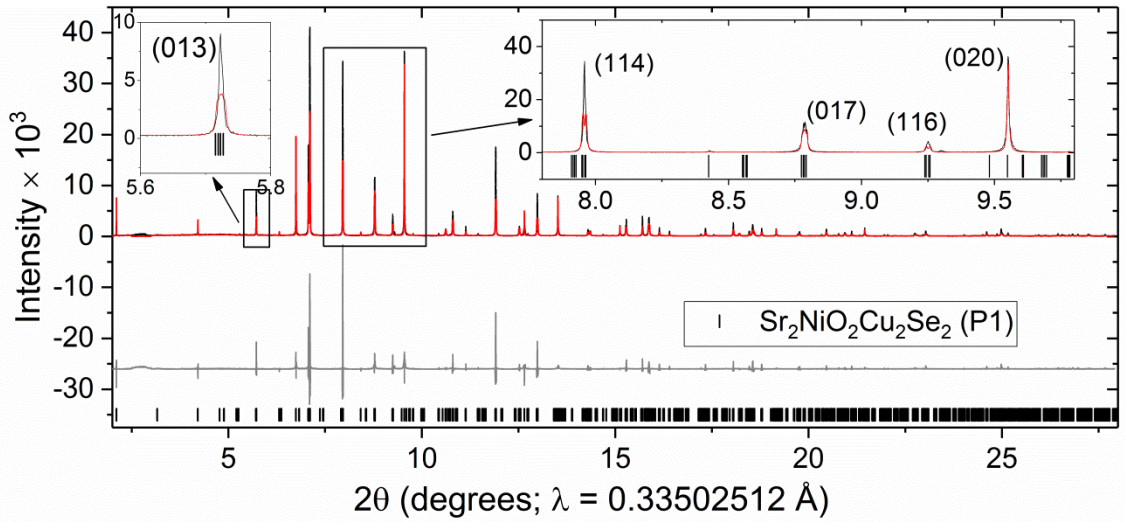


Fig. 7.22 Rietveld plot of $Sr_2NiO_2Cu_2Se_2$ (JNB267B) measured using ID22 at 60 K, indexed using a triclinic distortion

Table 7.4 Parameters used to index $Sr_2NiO_2Cu_2Se_2$ (JNB267B) measured using ID22 at 60 K, using a triclinic distortion; fit statistics are also shown

Space group	*P*1
a (Å)	4.025203
b (Å)	4.02521
c (Å)	18.242273
α (°)	90.12965
β (°)	89.95949
γ (°)	90.0000
Volume (Å^3)	295.565
R_{wp} (%)	30.265
χ^2	6.491

These results show that the quality of the fit is not good. Although use of the distortion strain modes gave a reasonable fit to most of the peaks that show a structured splitting, it significantly reduces the quality of the fit with several peaks (such as the 114 peak) that show little or no splitting. It is also noted that use of these strain modes does not result in splitting of the 00*l* peaks, so the asymmetry in the 00*l* peaks (which is quite significant, see Fig. 7.23) is not fitted better using this method.

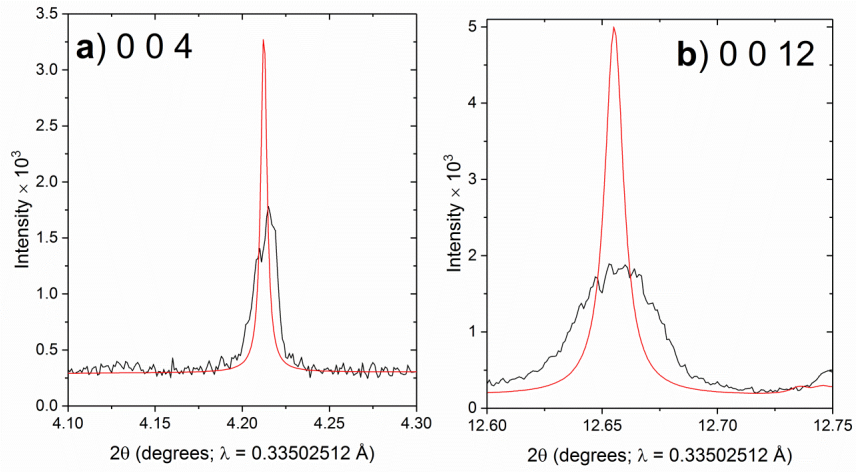


Fig. 7.23 Showing the asymmetry of two 00l reflections a) 0 0 4 and b) 0 0 12

7.4.2.3 *Experimental artefact*

A third possibility is that this observed peak splitting is an experimental artefact, potentially arising from an uneven temperature distribution in the capillary or uneven capillary packing. As previously stated, beam heating has been reported to cause unusual effects on samples measured at low temperature using the previous incarnation of ID22, ID31 (the same diffractometer system was formerly mounted on the ID31 station of the ESRF synchrotron), therefore care should be taken to exclude the possibility of the effects from experimental artefacts before overanalysing the data.[61]

This sample was measured as part of a two day experiment, during which samples of $Sr_2CoO_2Cu_{2-x}S_2$ were also measured (as discussed in section 5.2.5). The capillaries of these samples were prepared (opened in a He-filled glovebag to prevent beam heating below the boiling point of Ar) and measured (on heating from 5 K) in the same way as $Sr_2NiO_2Cu_2Se_2$ (JNB267B). This unusual peak splitting was not observed in the samples of $Sr_2CoO_2Cu_{2-x}S_2$, suggesting the effect is dependent on sample-identity, not experimental error.

Moreover, two different capillaries of JNB267B were measured during this experiment, both were prepared in the same way (described above) and the same type of peak splitting was observed, albeit to a slightly lesser extent in the second case (see Fig. 7.24). The differences between these two measurements are discussed at greater length in section 7.4.2.4.

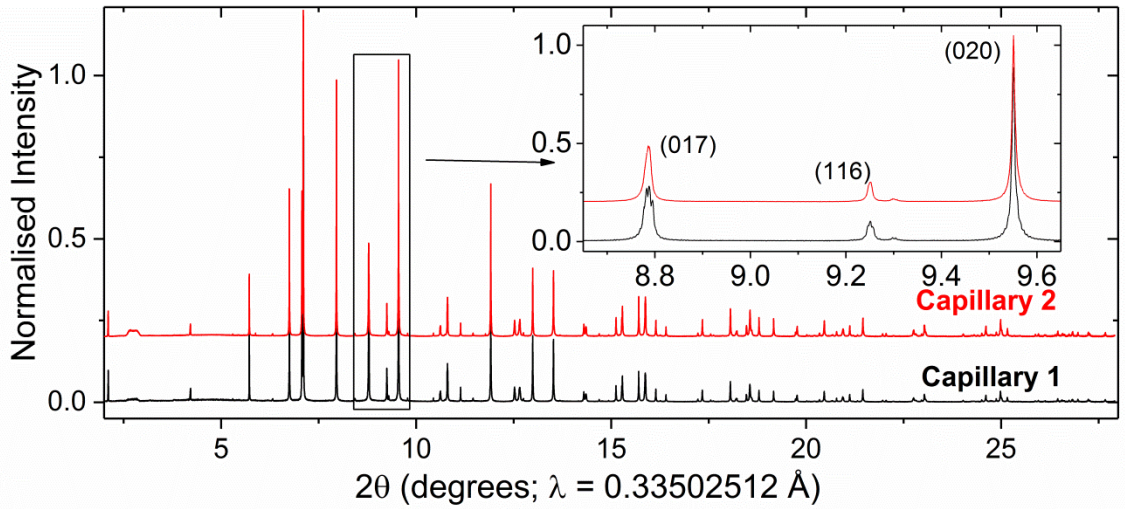


Fig. 7.24 Comparison of the raw PXRD patterns of two different capillaries of $Sr_2NiO_2Cu_2Se_2$ (JNB267B) measured at ~60 K using ID22

Attempts were made to see if the peak splitting could be observed using data obtained from HRPD (PND) and the I11 beamline (PXRD), in order to confirm the observed effects. The higher resolution MAC detector was used in an attempt to observe peak splitting using the I11 beamline at temperatures down to 100 K.

The highest resolution databank of HRPD is the backscattering bank ($160 \leq 2\theta\,(°) \leq 176$), with nominal resolution $4 \leq \Delta d/d \times 10^{-4} \leq 5$ and d-spacing range 0.6 – 4.6 Å. The 017 peak position is ~2.19 Å, well within the range of this bank. It is also possible to refocus data obtained from the backscattering bank, using just the inner part of the detector and therefore the highest part of the angular range ($174.5 \leq 2\theta\,(°) \leq 175.5$). This improves the resolution, by reducing the uncertainty in θ (see section 2.4), but at significant cost to the intensity, reducing the signal-to-noise ratio, because the solid angle of this inner part of this detector bank close to $2\theta = 180°$ is necessarily small. Fig. 7.25 compares the 5, 60 and 300 K data using both the standard backscattering bank and the inner part of the detector bank. No significant peak splitting or broadening is observed in these data.

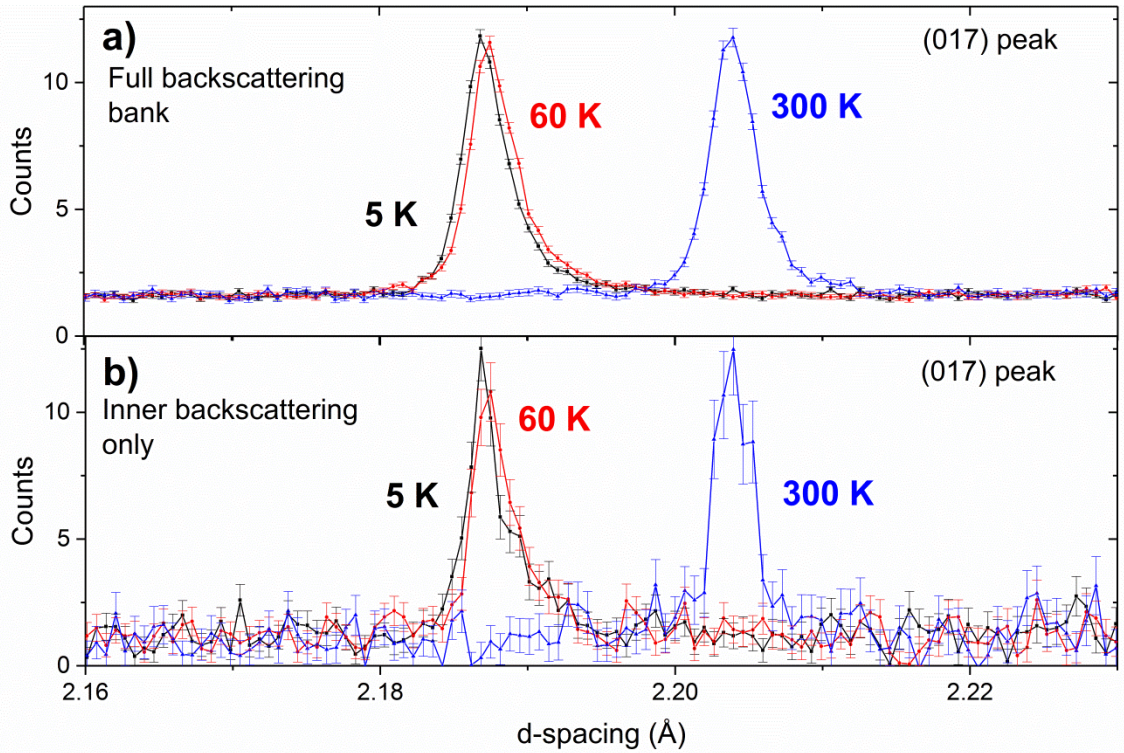


Fig. 7.25 Comparison of the 017 peak of $Sr_2NiO_2Cu_2Se_2$ (JNB267B) measured using HRPD at 5 K, 60 K and 300 K. a) shows the full backscattering bank data and b) shows the inner-angle focussed backscattering data

The 017 peak was fitted using a single Lorentzian peak function in order to quantitatively compare the full-width-half-maximum (FWHM) of the peak at different temperatures. The obtained fits are shown in Fig. 7.26, with the calculated FWHM. This data shows that, although the absolute value of the FWHM is larger at 60 K than both 5 and 300 K when both the full and inner-angle focussed backscattering bank data are treated, the values are well within three standard deviations of each other and therefore cannot be considered to be significantly different from one another. Although, it is possible that repeating this measurement with longer collection times and therefore improving the signal-to-noise ratio of the inner-angle-focussed data may lead to the observation of a significant change in the FWHM of these peaks.

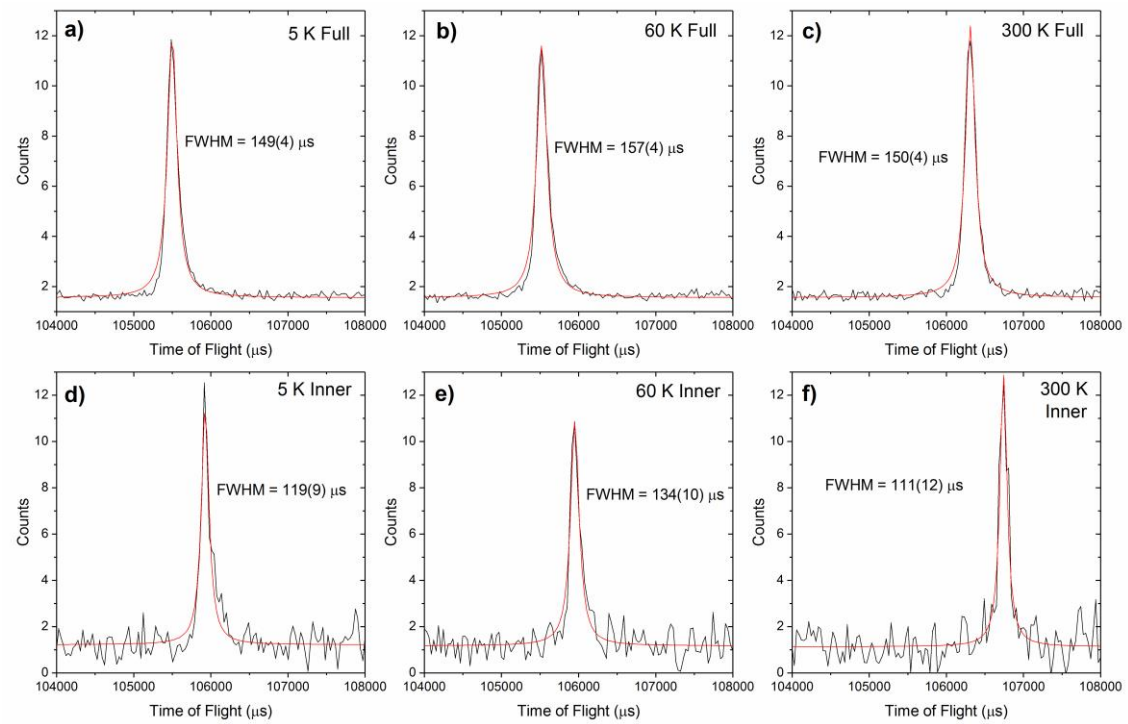


Fig. 7.26 Results of a Lorentzian peak fit to the 017 peak of $Sr_2NiO_2Cu_2Se_2$ (JNB267B), when measured using both the full backscattering bank (full) and the inner-angle focussed backscattering data (inner) at 5, 60 and 300 K

The lack of significant peak broadening is confirmed by examination of the refined FWHM values of the 017 peak as a function of temperature, using values obtained from peak fitting both the full and inner-angle-focussed backscattering bank datasets. Fig. 7.27 clearly shows that the errors are larger than any changes observed (error bars here are one standard deviation).

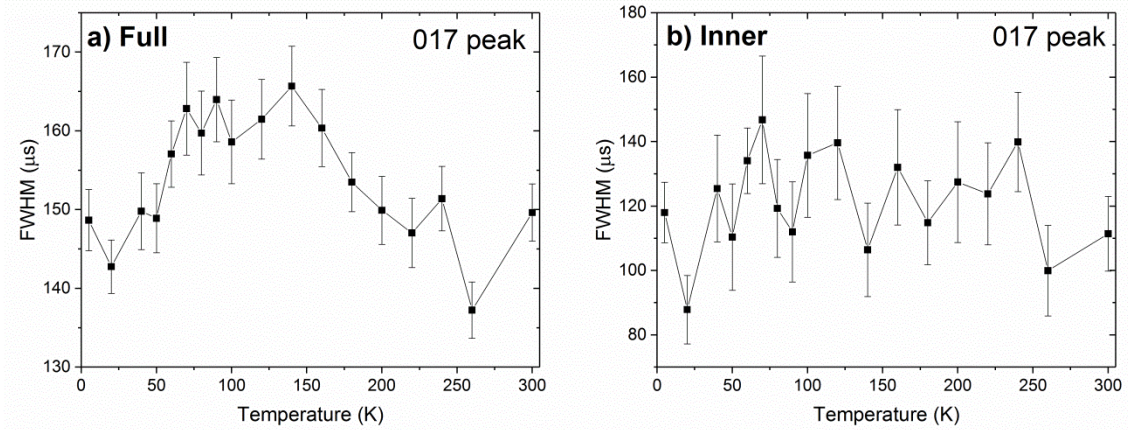


Fig. 7.27 Refined FWHM values of the 017 peak of $Sr_2NiO_2Cu_2Se_2$ obtained from Lorentzian peak fitting of data collected from measurement of JNB267B using the a) full backscattering bank and b) inner-angle focussed backscattering bank of HRPD at various temperatures

The resolution of the PSD (Mythen detector) at the I11 beamline was judged to be too low for subtle peak splitting to be observed. Therefore JNB267B (packed undiluted into a 0.3 mm diameter capillary) was measured using the MAC detector for 20 min at four temperatures: RT, 210 K, 150 K and 100 K. Each time the sample was quenched from RT to the measurement temperature. Although the full structure of the peak splitting was not obvious at 100 K using ID22, substantial peak broadening was evident (see Fig. 7.12), which should be observable with the resolution of the MAC detector. However, Fig. 7.28 shows that no significant peak broadening appears to occur in the MAC data.

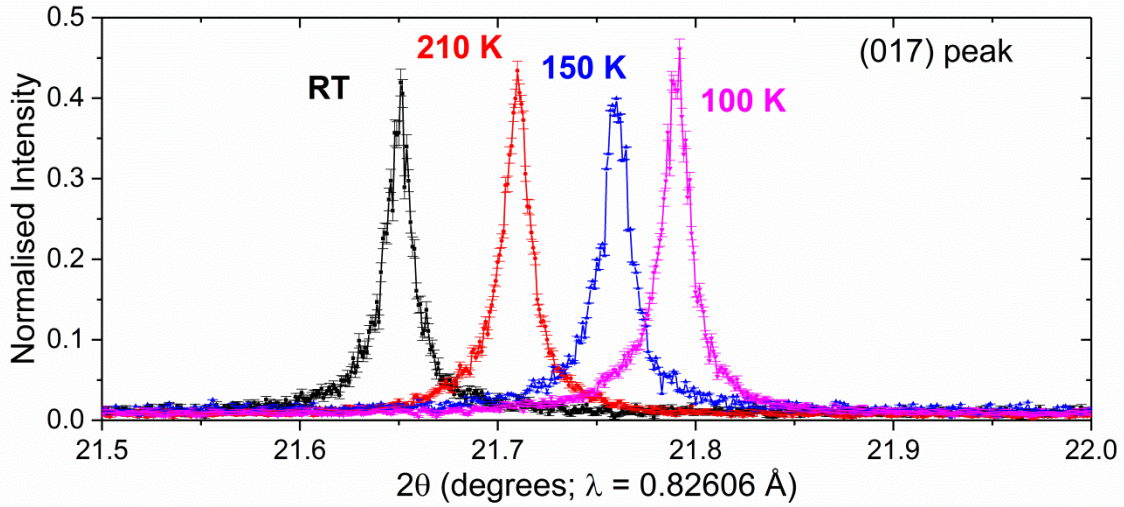


Fig. 7.28 Comparison of the 017 peak of $Sr_2NiO_2Cu_2Se_2$ (JNB267B) measured using the MAC detector at the I11 beamline at various temperatures

To quantitatively measure if any peak broadening could be observed in the data collected using the MAC data, the 017 peak was fitted using a Lorentzian peak-shape function, in an analogous way to the treatment of the HRPD data. No significant change in the calculated FWHM values was observed, as shown in Fig. 7.29.

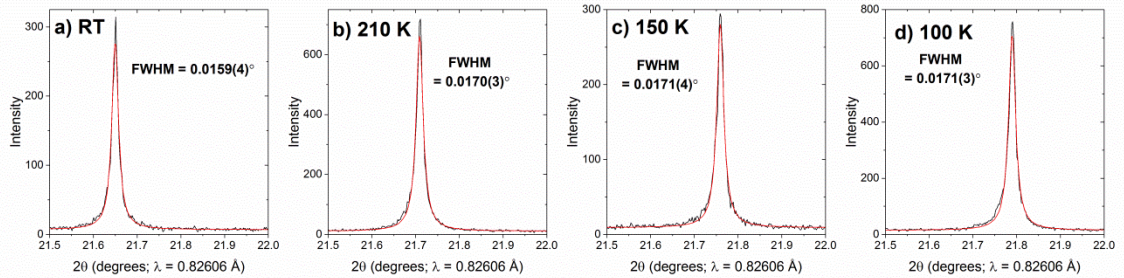


Fig. 7.29 Single peak fits to the 017 peak of $Sr_2NiO_2Cu_2Se_2$ for the sample JNB267B measured using the MAC detector at the I11 beamline at a) RT, b) 210 K, c) 150 and d) 100 K, with associated FWHM values.

This is surprising, comparison of the 017 peak of JNB267B at 100 K, measured using ID22, I11 and HRPD and shown as a function of Q ($2\pi/d$) (see Fig. 7.30) suggest that the broadening of the 017 peak should be visible in the MAC and HRPD data, but it is not. A possible reason for this is discussed below.

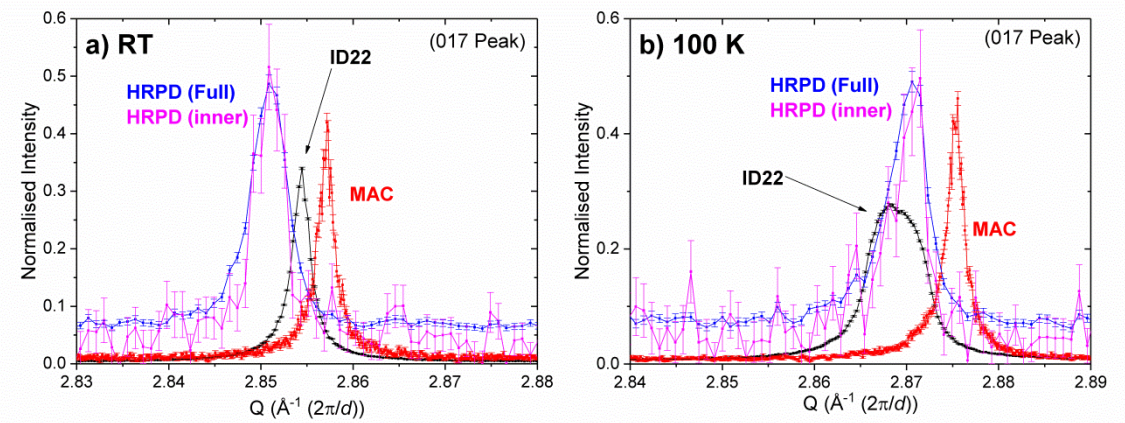


Fig. 7.30 Comparison of the 017 peak of $Sr_2NiO_2Cu_2Se_2$ for the sample JNB267B for data collected using ID22, the MAC detector of I11 and HRPD (using both the full backscattering bank and the inner-detector array) at a) RT and b) 100 K

7.4.2.4 *Photon-induced electronic transition*

If the peak-splitting observed is not an experimental artefact, it is surprising that the effect has not been observed in the other diffraction measurements (MAC and HRPD). The X-ray beam that was used at ID22 is particularly high energy (λ = 0.33502512 Å, E = 37.0 keV) and these high-energy photons may have induced an electronic transition in the sample.

There is precedent for X-ray induced electronic transitions in the literature. Some examples are: an antiferromagnetic-to-ferromagnetic transition in $Pr_{0.7}Ca_{0.3}MnO_3$;[165, 166] a high-spin-to-low-spin transition in the Prussian blue analogue $CsFe^{II}[Cr^{III}(CN)_6]$[167] and disordering of the charge-ordered dimerization in $CuIr_2S_4$.[168-170]

$Pr_{0.7}Ca_{0.3}MnO_3$ contains mixed-valent Mn^{3+}/Mn^{4+} ions in the ratio 7:3. These charge and orbital order below T_{CO} ~ 180 K, and the spins order antiferromagnetically below T_N ~ 140 K. However, below T_C ~ 120 K a small ferromagnetic component along the a axis is observed on the Mn ions, which increases on cooling. It was found that the application of a high-energy beam at low temperatures (15 – 20 K) disrupted the charge ordering, causing growth of the metallic, ferromagnetic phase.[165, 166]

The Fe^{II} ion in $CsFe^{II}[Cr^{III}(CN)_6]$ undergoes a high-spin-to-low-spin transition on cooling from 270 K to 190 K, as shown by magnetic susceptibility measurements. It was found that if the lattice parameters of the compound were measured as a function of X-ray illumination time at 265 K (a temperature expected to be high-spin), a phase with lattice parameters corresponding to the low-spin phase grew in rapidly.

$CuIr_2S_4$ is another example of a mixed-valent compound (Ir^{3+}/Ir^{4+} in a 1:1 ratio) that exhibits charge and orbital order, with dimers of Ir^{4+} ions separated by a metal-metal distance of ~3.0 Å.[170] X-ray illumination at low temperatures disrupts the charge ordering without destroying the dimer relationship between pairs of Ir^{4+} ions in the short range.[168] Kiryukhin *et al.* showed that the X-ray induced transition did not necessarily lead to disorder, but could lead to new ordering schemes. An incommensurately ordered scheme was identified that has not been observed in the absence of X-ray or electron illumination.[169]

These examples show that X-ray induced transitions can have multiple, often non-intuitive effects, but is often strongly correlated with transitions that are also observed as a function of temperature. The examples also show that in powder samples incomplete conversion (the presence of two or more phases) is possible. If X-ray illumination were inducing a transition in $Sr_2NiO_2Cu_2Se_2$, then it is likely that it would cause a small change in lattice parameters, which would appear as peak-splitting in a powder sample.

It is also likely that the relative phase fraction of the different phases in the sample would be highly related to the length of time and temperature that the sample had been exposed to the beam. As stated in section 7.4.2.3, two capillaries of $Sr_2NiO_2Cu_2Se_2$ (JNB267B) were measured at ID22 for different lengths of time and small differences in the results were achieved. Here the differences between these capillaries are reviewed to further understand if X-ray exposure has induced a transition. At the time of the experiment, the amount of X-ray beam exposure was not under investigation; therefore the amount of beam exposure is somewhat unsystematic.

Table 7.5 and Table 7.6 show the temperatures and scan durations that the two capillaries of $Sr_2NiO_2Cu_2Se_2$ (JNB267B) were measured. Capillary 1 was cooled to 5 K and measured at increments on warming to 140 K, capillary 2 was cooled to 50 K and

measured at increments on warming to 67 K. The sample was not subject to X-ray illumination when the sample was not being measured.

Table 7.5 PXRD scans collected of capillary 1 of $Sr_2NiO_2Cu_2Se_2$ (JNB267B) as a function of temperature at ID22

Measurement	Temperature (K)	Scan time (min)
ch4997_JNB267_5K	5	25 (aborted)
ch4997_JNB267_5K_new	5	25
ch4997_JNB267_10K	10	aborted
ch4997_JNB267_10K_new	10	13
ch4997_JNB267_20K	20	13
ch4997_JNB267_30K	30	13
ch4997_JNB267_40K	40	13
ch4997_JNB267_50K	50	13
ch4997_JNB267_60K	60	13
ch4997_JNB267_70K	70	13
ch4997_JNB267_80K	80	13
ch4997_JNB267_90K	90	13
ch4997_JNB267_100K	100	13
ch4997_JNB267_120K	120	13
ch4997_JNB267_140K	140	13

Table 7.6 PXRD scans collected of capillary 2 of $Sr_2NiO_2Cu_2Se_2$ (JNB267B) as a function of temperature at ID22

Measurement	Temperature (K)	Scan time (min)
ch4997_JNB267_2ndcap_50K	50	13 (Aborted)
ch4997_JNB267_2ndcapi_50K	50	13
ch4997_JNB267_53K	53	13
ch4997_JNB267_55K	55	13
ch4997_JNB267_57K	57	13
ch4997_JNB267_59K	59	13
ch4997_JNB267_61K	61	13
ch4997_JNB267_63K	63	13
ch4997_JNB267_65K	65	~5

The two tables (Table 7.5 and Table 7.6) show that capillary 2 was irradiated significantly less than capillary 1. This may explain the observed differences in peak behaviour, shown for the 017 peak in Fig. 7.31.

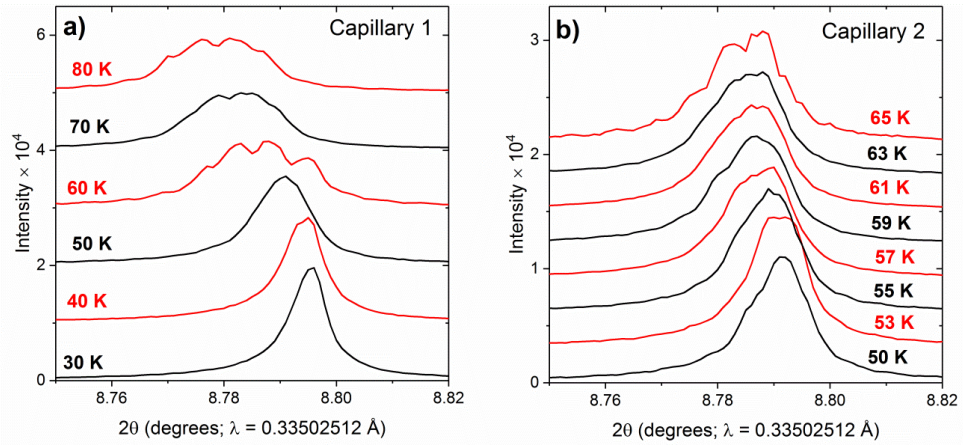


Fig. 7.31 Comparison of the changes in the 017 peak of $Sr_2NiO_2Cu_2Se_2$ (JNB267B) that occur in the two capillaries measured as a function of temperature. Successive diffractograms offset from the origin for clarity

7.4.2.5 *Conclusion*

It is thought to be unlikely that the low temperature peak splitting arises from an experimental artefact, as it is thought unlikely that the splitting would appear in similar ways in two different capillaries. It also appears to be unlikely that a temperature-dependent symmetry-lowering distortion causes the observed peak-splitting. This makes it most likely that multiple similar $Sr_2NiO_2Cu_2Se_2$ phases are observed in the PXRD pattern.

The working hypothesis is that this multiple phase behaviour is the result of X-ray-illumination induced effects, causing the formation of phases with different lattice parameters. However, further experiments are required to confirm this hypothesis and if it is the case, to determine if this behaviour results from a reversible electronic transition or irreversible "beam damage". Of particular note is that the peak splitting behaviour is not observed on data using I11. It is possible that the energy of the X-rays at I11 (15 keV) is insufficient to induce this transition. An experiment which measured the behaviour of $Sr_2NiO_2Cu_2Se_2$ in the range $5 \leq T\,(\mathrm{K}) \leq 160$ at two or more wavelengths of substantially different energies would test this. It is also possible that the I11 samples, which were quenched from RT, with a long time gap between each measurement, were illuminated for an insufficiently long time for peak broadening behaviour to be observed. A further experiment could be to cool a sample of $Sr_2NiO_2Cu_2Se_2$ to 60 K, start a sequence of short scans (~5 min) and observe changes in the sample as a function of X-ray illumination time. The sample could subsequently be

"annealed" at RT before re-measuring the sample at 60 K to determine if beam damage or a reversible transition has occurred.

7.5 Powder neutron diffraction to probe magnetic ordering

2.50 g of $Sr_2NiO_2Cu_2Se_2$ (JNB267B) was loaded into a cylindrical vanadium can (sealed with an indium gasket) and measured at various temperatures using OSIRIS. The measured raw PND patterns are shown in Fig. 7.32. While a full *d*-range was measured when T = 5, 100 and 170 K, when T = 120, 140 and 160 K the sample was only measured in the region $4.1 \leq d$ (Å) ≤ 6.1.

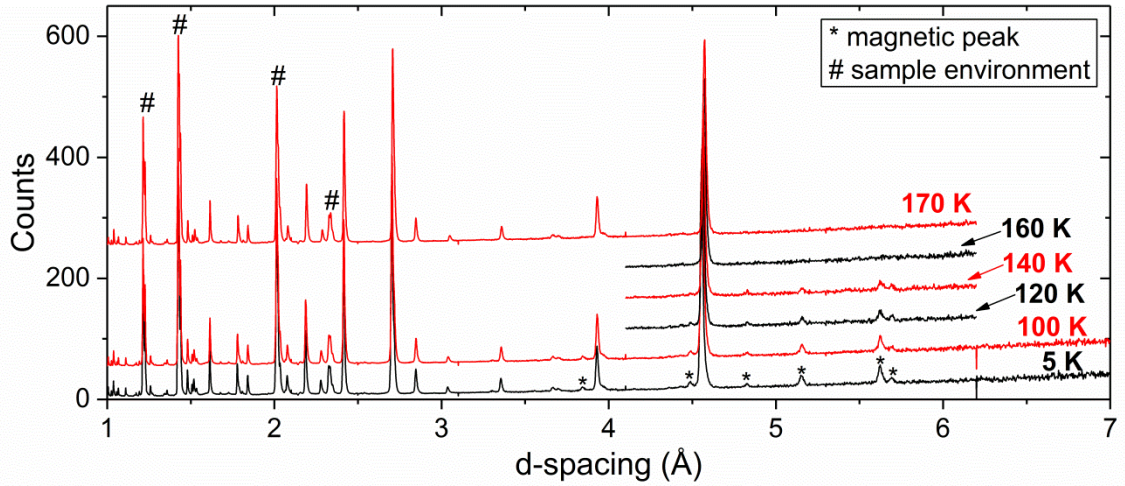


*Fig. 7.32 Offset PND patterns of $Sr_2NiO_2Cu_2Se_2$ (JNB267B) measured using OSIRIS at various temperature, peaks identified as magnetic are emphasised with * symbols. The four main peaks arising from the sample environment (primarily the Al-tailed cryostat) are indicated by # symbols*

Fig. 7.32 shows that some peaks appear in the PND patterns that were not present in the PXRD patterns at the same temperatures and so have been identified as magnetic peaks. These magnetic peaks disappear above 160 K, which closely correlates with the small cusp in the magnetic susceptibility measurements and the feature in the conductivity measurement, allowing positive connection of these features with the Néel temperature (T_N). Interestingly, there is little visual difference between the PND pattern of $Sr_2NiO_2Cu_2Se_2$ (JNB267B) measured at 5 K and 100 K, that is above and below the temperature where the sharp transition is observed in the magnetic susceptibility curve. Smura identified a similar-looking transition in $Sr_2NiO_2Cu_2S_2$ as a high-spin-to-low-spin transition in $Sr_2NiO_2Cu_2S_2$ (where square planar Ni^{2+} is low spin, and therefore diamagnetic, at low temperature), partly due to the lack of any magnetic Bragg peaks.[58]

The presence of magnetic ordering below the transition shows that this cannot be the case for $Sr_2NiO_2Cu_2Se_2$.

All the magnetic peaks could be indexed using a $\sqrt{2}a \times \sqrt{2}a \times 2c$ expansion of the unit cell. The cell symmetry was solved by distortion of symmetry modes in ISODISTORT,[112] originally in magnetic space group $P1$ (1.1).

As was the case for $Sr_2CoO_2Cu_2Se_2$ (section 5.2.4.2), it was found that refinement of both the mP*n* (where n = 3, 4) and mX$^+$*n* (where n = 4, 5) magnetic modes was required to model the magnetic intensity. However, unlike $Sr_2CoO_2Cu_2Se_2$, it was found that only one of mX3$^+$(a) or mX4$^+$(a) was required. A magnetic space group that allowed refinement of the mP4(a) and mX3$^+$(a) was therefore searched for, yielding the $P_C4_12_12$ (92.117) magnetic space group. The possible symmetry mode combinations are shown in the schematic in Fig. 7.33.

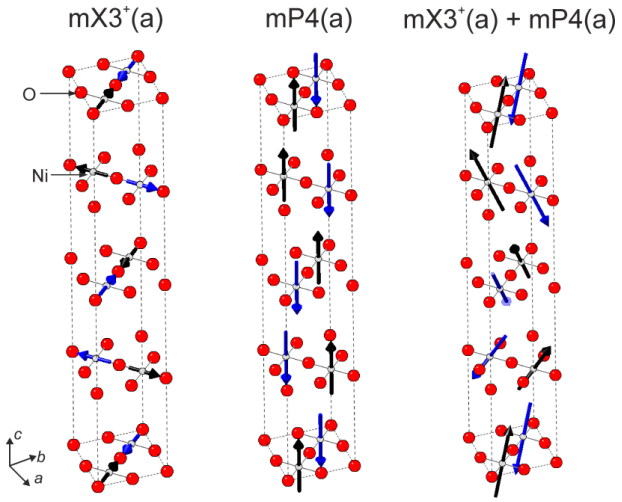


Fig. 7.33 Schematic of the possible magnetic modes of $Sr_2NiO_2Cu_2Se_2$ in the $P_C4_12_12$ (92.117) magnetic space; Sr, Cu and Se atoms have been excluded for clarity

This was found to fit the magnetic intensity well. The Rietveld plot is shown in Fig. 7.34, with a plot of refined intensity as a function of temperature. The refined magnetic moment at 5 K is tabulated in Table 7.7. The magnetic moment was also refined as a function of temperature; the large errors in the refined moment at 120 and 140 K arise because only a small part of the *d*-spacing range was measured.

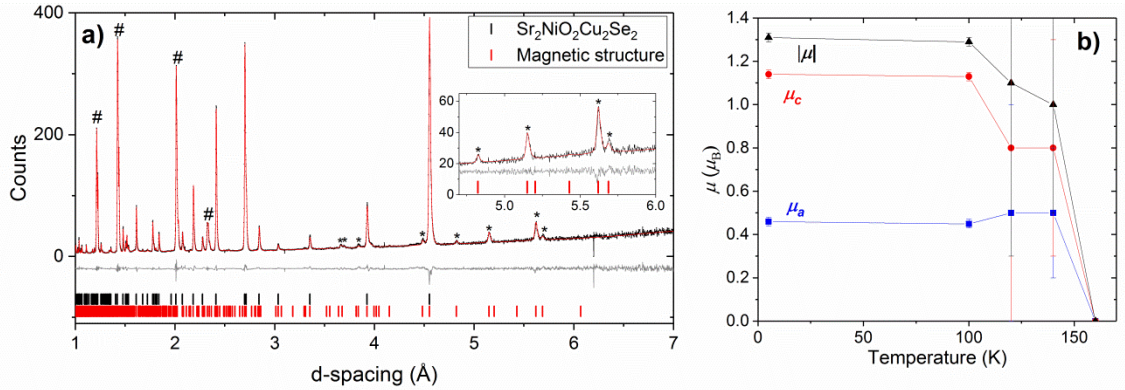


*Fig. 7.34 a) Rietveld plot of $Sr_2NiO_2Cu_2Se_2$ (JNB267B) measured at 5 K using OSIRIS, * and inset emphasise magnetic peaks; # symbols indicate the four main peaks arising from the sample environment (primarily Al-tailed cryostat) b) refined magnetic moment as a function of temperature, the line is a guide to the eye*

Table 7.7 Refined magnetic moments of Ni atoms in $Sr_2NiO_2Cu_2Se_2$; data obtained by combined refinement against PND data of $Sr_2NiO_2Cu_2Se_2$ (JNB267B) measured at 5 K using OSIRIS and HRPD

	μ_a (μ_B)	μ_b (μ_B)	μ_c (μ_B)	$\lvert\mu\rvert$ (μ_B)
Ni (0.75, 0.75, 0.75)	0.46(2)	0.46(2)	-1.14(2)	1.31(2)
R_{wp} (%)	4.461			
χ^2	1.322			

The refined ordered moment of nickel in $Sr_2NiO_2Cu_2Se_2$ (1.31 μ_B) is below the value that might be expected from high-spin Ni^{2+} (d^8, 2 μ_B), but this might be accounted for by considering the ordered moment may be reduced by the effects of covalency. The refined moment is the same within error at 100 K as it is at 5 K, and no reorientation of the moment is observed to accompany the sharp transition that appears in the magnetic susceptibility measurement at ~70 K. $Sr_2NiO_2Cu_2Se_2$ thus behaves as a metallic compound with a large localised moment on Ni. This suggests that the high conductivity probably arises from holes in the Se4p-Cu3d band rather than from the electrons NiO_2 layers. Further measurements and calculations are probably required to explore this further.

7.6 Treatment of $Sr_2NiO_2Cu_2Se_2$ with I_2

$Sr_2NiO_2Cu_2Se_2$ is isostructural with $Sr_2CoO_2Cu_2Ch_2$ (where *Ch* = S, Se, see section 5.2) and $Sr_2MnO_2Cu_{1.5}S_2$ (see section 3.2), therefore $Sr_2NiO_2Cu_2Se_2$ was stirred in a solution of I_2/MeCN in order to see if this induced a change in lattice parameters that might suggest deintercalation of Cu, as it did with $Sr_2CoO_2Cu_2Ch_2$ and $Sr_2MnO_2Cu_{1.5}S_2$. This was not expected to be successful because it was believed that Ni^{2+} would be more

resistant to oxidation than Co^{2+}. However, a significant change in lattice parameters was in fact observed. This section describes the measured changes that accompany treatment of $Sr_2NiO_2Cu_2Se_2$ with I_2.

7.6.1 Method

Two samples of I_2-treated $Sr_2NiO_2Cu_2Se_2$ were synthesised and studied: JNB318 and JNB319B. To synthesise these samples two separate 5 g batches of parent $Sr_2NiO_2Cu_2Se_2$ were synthesised in a similar manner to that described in section 7.2 for JNB267B (sample analysed using VT PND and PXRD): SrO, Ni, Cu and Se were weighed out in the molar ratio 2:1:2:2 and prepared as described in section 2.1.1. The sample was then heated to 400 °C for 15 h (ramp rate: 10 °C min^{-1}) then the sample was heated to 850 °C (also 10 °C min^{-1}), after 24 h the tubes were quenched in ice-water, isolated in the glovebox and phase purity checked by in-house PXRD. Table 7.8 compares the lattice parameters of these samples with those of JNB267B, showing that the lattice parameters are the same within reasonable estimates of error.

Table 7.8 Comparison of the lattice parameters of three samples of $Sr_2NiO_2Cu_2Se_2$, prior to reaction with I_2

Sample	JNB267B	JNB315B	JNB315A
Daughter sample	-	JNB319B	JNB318
Diffractometer	PSD (I11)	Bruker d8	Bruker d8
a (Å)	4.02653(2)	4.02415(8)	4.02493(9)
c (Å)	18.39373(8)	18.4035(4)	18.4061(5)
Volume (Å^3)	298.216(3)	298.02(1)	298.18(2)
R_{wp} (%)	1.982	6.166	7.070

JNB318 was synthesised by reacting 4.00 g of parent $Sr_2NiO_2Cu_2Se_2$ with 1.5 molar equivalents of I_2, as described in section 2.1.3. The reaction was filtered after 3 days. JNB319B was synthesised by reacting 4.00 g of parent $Sr_2NiO_2Cu_2Se_2$ with 0.1 molar equivalents of I_2 and filtered after 3 days. Analysis by PXRD revealed that the lattice parameters of this sample were very similar to that of the parent. Therefore 3.7 g of JNB319B was reacted again under the same conditions, producing a sample with lattice parameters intermediate between JNB267B and JNB318 (as shown in Fig. 7.35)

7.6.2 Room temperature powder X-ray diffraction

As with other compounds which have been tested with respect to their reactivity with I_2, the changes in the compounds were observed in the first instance by changes in the lattice parameters, as is shown in Fig. 7.35.

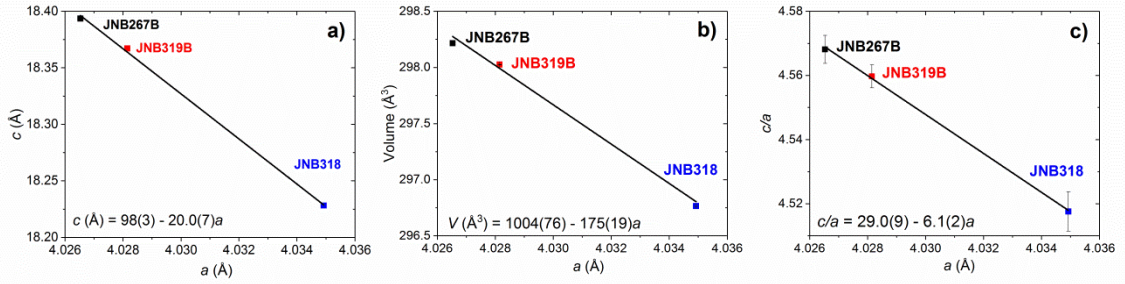


Fig. 7.35 Comparison of a) lattice parameter c; b) unit cell volume and c) c/a ratio as a function of lattice parameter a for three samples of I_2 treated $Sr_2NiO_2Cu_2Se_2$. Values obtained from refinement against data measured using the PSD on the I11 beamline, in a) and b) the error bars are smaller than the points on the graph

The behaviour of $Sr_2NiO_2Cu_2Se_2$ on treatment with I_2 is markedly different to that of the Co and Mn analogues. Although *c* decreases as the degree of oxidation increases (assuming that JNB318 is more oxidised than JNB319B), *a* increases as the degree of oxidation increases. This causes a large reduction in the *c/a* ratio. The decrease in unit cell volume, even as *a* increases shows that the reduction in *c* is significantly larger than the increase in *a*.

It was also observed from the raw PXRD patterns that the peaks in JNB318 are significantly broader than those of JNB267B or JNB319B (Fig. 7.36), particularly those peaks where $l \neq 0$.

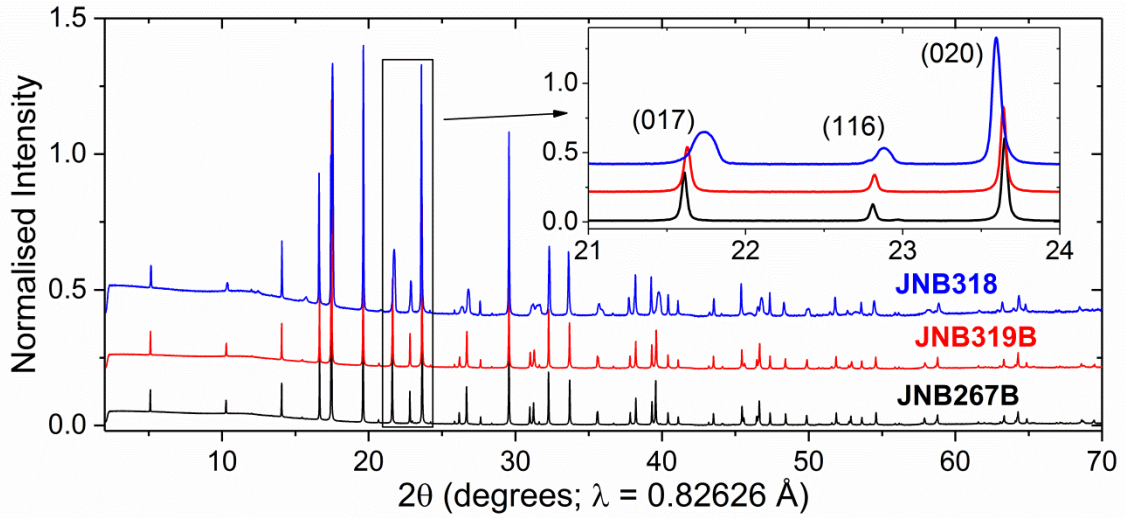


Fig. 7.36 Stacked raw plots of JNB267B (parent $Sr_2NiO_2Cu_2Se_2$), JNB319B and JNB318 (both I_2 treated $Sr_2NiO_2Cu_2Se_2$ samples measured using the PSD of the I11 beamline; inset emphasises the 017, 116 and 020 peaks

This peak broadness in JNB318 is attributed to a small phase-width in the sample, which it is possible is inherent to most-oxidised samples of $Sr_2NiO_2Cu_2Se_2$. The use of

Stephen's anisotropic tetragonal peak broadening terms[154] significantly improved the fit to the PXRD data for this sample, as is shown in the Rietveld plots in Fig. 7.37.

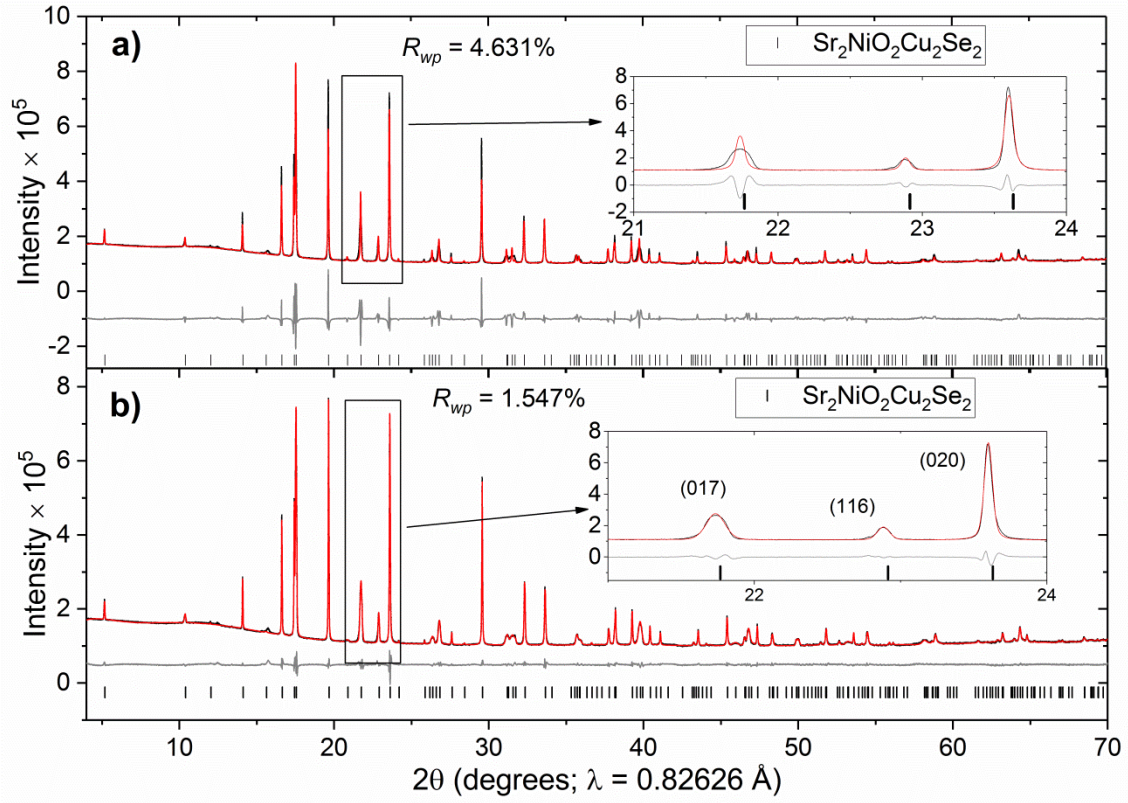


Fig. 7.37 Rietveld plots of JNB318 (I_2 treated $Sr_2NiO_2Cu_2Se_2$) measured using the PSD on the I11 beamline when a) no anisotropic broadening terms are used and b) when Stephen's tetragonal anisotropic broadening terms[154] are used

7.6.3 Room powder neutron diffraction

RT high-resolution PND was employed in an attempt to understand the changes in composition that occur on treatment of $Sr_2NiO_2Cu_2Se_2$ with I_2. ~3 g of JNB318 and JNB319B were loaded into separate vanadium cans under inert conditions and measured for 2 h at RT using HRPD. Despite the high quality data obtained, no trend in the fractional occupancies of any of the atomic sites was found. Refinement against the PND data for JNB318 was hampered by the peak broadness described above.

7.6.4 Air sensitivity

The effect of exposing JNB318 (I_2 treated $Sr_2NiO_2Cu_2Se_2$) to air was observed in order to further understand the properties of the I_2 treated samples of $Sr_2NiO_2Cu_2Se_2$.

The following experimental procedure was used: the PXRD pattern of the sample was measured using the Bruker d8 Advance, first under an argon atmosphere (in an air-tight sample holder) and subsequently when the sample had been exposed to air for 4 and

22 h. Each time the sample was measured under otherwise equivalent conditions for direct comparison of the raw PXRD patterns and lattice parameters. The results are shown in Fig. 7.38.

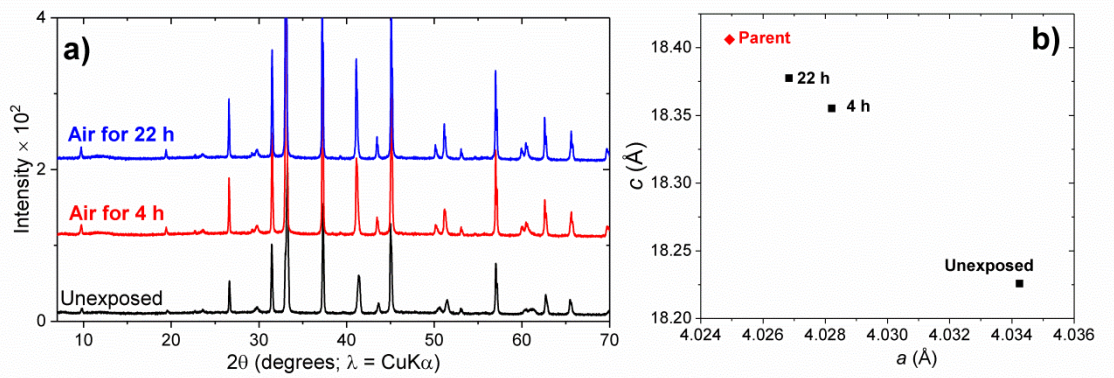


Fig. 7.38 The results of exposing JNB318 (I_2 treated $Sr_2NiO_2Cu_2Se_2$) to air: a) comparison of raw PXRD plots (measured using the Bruker d8 Advance) and b) the refined lattice parameters (the error bars are smaller than the points on the graph)

The results of this experiment show that exposing the sample to air causes the sample to return to a composition close to that of parent $Sr_2NiO_2Cu_2Se_2$, as shown by the change in lattice parameters (Fig. 7.38 b)) and the sharpening of the peak-shapes (Fig. 7.38 a)), so they more closely resemble the parent material. This offers some evidence that the anisotropic broadening of the peaks in I_2-treated $Sr_2NiO_2Cu_2Se_2$ is an inherent feature.

7.6.5 Magnetometry measurements

The magnetic susceptibility of JNB319B and JNB318 was measured using a 3 T/4 T subtraction for direct comparison of these compounds with the magnetic susceptibility measured for JNB231 (parent $Sr_2NiO_2Cu_2Se_2$), the results are shown in Fig. 7.39.

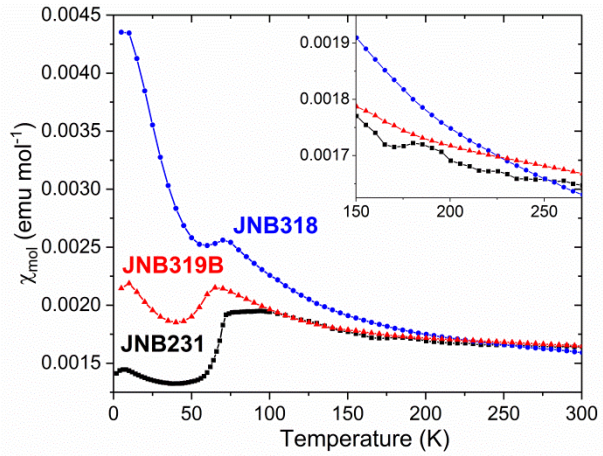


Fig. 7.39 Magnetic susceptibility of JNB231 (parent $Sr_2NiO_2Cu_2Se_2$), JNB319B (intermediate $Sr_2NiO_2Cu_{2-x}Se_2$) and JNB318 (most-deintercalated $Sr_2NiO_2Cu_{2-x}Se_2$), measured using a 4 T – 3 T subtraction (as described in section 2.8)

It was found that the greater the degree of oxidation, the less pronounced the transition in the magnetic susceptibility below 100 K became, indicative that oxidation suppresses this transition. The size of the low temperature "Curie-tail" also increases. This data corroborates the VT PXRD data (see below), which shows that the discontinuities in the lattice parameters are suppressed by oxidation as well.

The broad cusp in JNB231 that indicates T_N (~170 K) does not appear to be present in the magnetic susceptibility curves of JNB319B or JNB318, suggesting that long-range magnetic ordering is suppressed by oxidation. However, low-temperature PND measurements would be required to confirm this observation.

7.6.6 Variable temperature powder X-ray diffraction

JNB318 (I_2-treated $Sr_2NiO_2Cu_2Se_2$) was measured using VT PXRD with both the PSD (I11 beamline) and ID22 over the temperature range 5 – 300 K so that the changes in lattice parameters could be compared with those of JNB267B (parent $Sr_2NiO_2Cu_2Se_2$) and correlated with the magnetic susceptibility data obtained.

No peak splitting was observed in JNB318 using ID22, though this could be due to the lower resolution arising from the broad-peaked nature of diffraction patterns of JNB318 – at every temperature measured the peaks of JNB318 were broader than the broadening and peak-splitting observed in the parent (JNB267B). The refined lattice parameters of JNB318 are compared with JNB267B in Fig. 7.40. The differences in the lattice parameters between the data collected on ID22 and the PSD of the I11 beamline are most likely due to systematic differences in the calibration of the two instruments. The peak-splitting observed in the ID22 measurements of JNB267B may also have an effect.

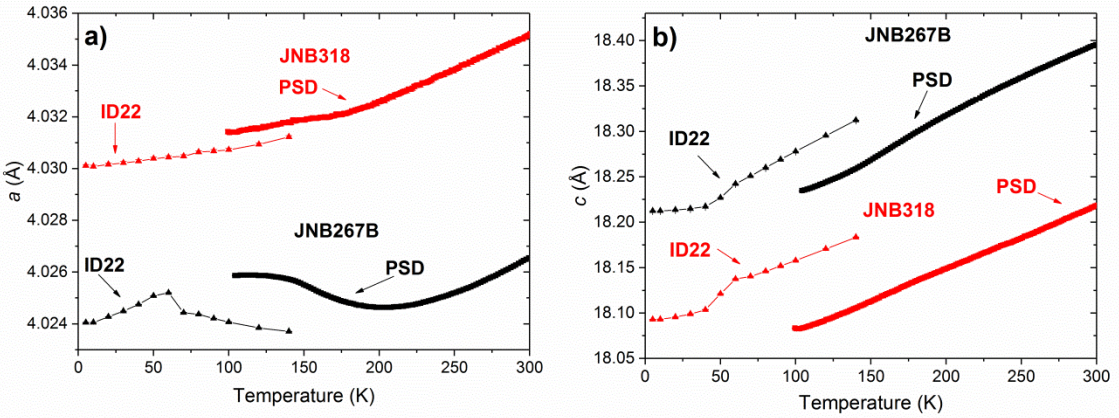


Fig. 7.40 Refined a) a parameter and b) c parameter of JNB318 (I_2 treated $Sr_2NiO_2Cu_2Se_2$) and JNB267B (parent $Sr_2NiO_2Cu_2Se_2$) as a function of temperature; data obtained from sequential Rietveld refinement against data measured using ID22 and the PSD at the I11 beamline. The error bars, as calculated from Rietveld refinement are smaller than the points on the graph

Fig. 7.40 shows that the discontinuities observed in the *a* lattice parameter as a function of temperature in parent $Sr_2NiO_2Cu_2Se_2$ (JNB267B) are greatly suppressed in JNB318 (I_2-treated $Sr_2NiO_2Cu_2Se_2$). This closely reflects the observed trend in the magnetic susceptibility data.

7.6.7 Discussion

$Sr_2NiO_2Cu_2Se_2$ has been shown to react with I_2/MeCN, however the precise outcome of the reaction is not yet clear. It is reasonable to assume that the reaction results in the oxidation of the Ni^{2+} ions, although X-ray absorption near-edge spectroscopy (XANES) would be required to confirm this. Interestingly, this reaction leads to expansion of lattice parameter *a* and therefore the Ni-O bond distance. This is in contrast to the reduction in *a* observed on oxidation of $Sr_2MnO_2Cu_{1.5}S_2$ (section 3.2) and the Co-containing analogues (Chapter 5).

The nature and extent of this oxidation needs to be further understood. Energy dispersive X-ray spectroscopy (EDX) could be used to determine the changes in composition, but the large error associated with this technique (as seen in section 5.3.2.3 for $Sr_2CoO_2Ag_{2-x}Se_2$) may mean that subtle changes in composition cannot be detected. This might particularly be considered to be the case because the change in unit cell volume observed for $Sr_2NiO_2Cu_2Se_2$ (1.45 $Å^3$) is significantly smaller than that observed for $Sr_2CoO_2Ag_{2-x}Se_2$ (4.56 $Å^3$) or $Sr_2CoO_2Cu_2Se_2$ (3.33 $Å^3$). Assuming that the compositional change in $Sr_2NiO_2Cu_2Se_2$ on oxidation was the removal of copper and that the relationship between Cu occupancy and volume was the

same as for $Sr_2CoO_2Cu_2Se_2$, the maximal volume change observed in the oxidised $Sr_2NiO_2Cu_2Se_2$ samples (JNB318) would correspond to a ~2% Cu deficiency ($Sr_2NiO_2Cu_{1.96}Se_2$).

7.7 Conclusions

In this chapter the synthesis of $Sr_2NiO_2Cu_2Se_2$ was reported. It was found that a high synthesis temperature was required to synthesise a compound with stoichiometric Ni in the oxide layer. Magnetic susceptibility and VT diffraction measurements revealed that a transition, assumed to be electronic in character, occurs in this compound at ~70 K. However, PND measurements with high resolution at (relatively) high *d*-spacing ranges reveal that the compound is magnetically ordered at 5 K, showing that the electronic transition cannot be a complete high-spin-to-low-spin electronic transition.

Furthermore, the presence of long-range antiferromagnetic order shows that the Ni electrons are localised, but bulk resistivity measurements show that the compound is metallic, suggesting delocalised bands. It is possible that $Sr_2NiO_2Cu_2Se_2$ has both localised Ni moments and a partially-filled valence band, possibly arising from the Se 4p states. Computational calculations, such as density functional theory (DFT) calculations, may provide an insight into the cause of the transition observed at ~70 K and the coexistence of antiferromagnetic order and metallic behaviour.

The peak-splitting behaviour, observed using high-resolution VT PXRD, is thought to be the result of an X-ray-induced change in the sample, which causes the presence of multiple phases in a powder sample. However, this hypothesis requires further experiments to confirm if there is a relationship between illumination time and the observed peak-splitting behaviour.

It was also found that $Sr_2NiO_2Cu_2Se_2$ is active with respect to oxidation by I_2. This reaction alters the lattice parameters of the compound, implying that a change in composition has occurred. However, the precise nature of this reaction is unknown, requiring further work.

Chapter 8
8 Summary

This thesis focussed on the structure, magnetic behaviour and chemistry of compounds with composition $A_2MO_2X_2Ch_2$ (*A* = Sr, Ba; *M* = Mn, Co, Ni, Cu, Zn; *X* = Cu, Ag; *Ch* = S, Se, Te). These compounds are all based on the $Sr_2Mn_3Sb_2O_2$ structure type,[40] but have diverse properties, as demonstrated in this thesis.

Chapter 3 investigated the properties of some manganese-containing analogues. Work on the reaction of $Sr_2MnO_2Cu_{1.5}S_2$ with I_2 was continued, showing that this removes Cu, producing a compound with composition $Sr_2MnO_2Cu_{1.33}S_2$. This compound is incommensurately modulated with $\mathbf{q} \sim 0.24\mathbf{a^*}$ and space group $Xmmm(\alpha 00)00s$, where *X* is an unconventional centring vector. The incommensurate modulated structure differs from the average structure in two primary ways: the fractional Cu occupancy orders in a harmonic wave function and the $[Sr_2MnO_2]$ blocks are displaced transverse to the layers (in the *c*-direction), so that the Sr atoms are closer to the S atoms when the Cu occupancy is low, minimising under-bonding.

Evidence was also found for a Cu/vacancy-ordering structure (region "*B*") distinct from both the parent (region "*A*") and the most-deintercalated (region "*C*") structures at Cu occupancy values intermediate between region "*A*" and "*C*". However, this ordering structure appeared to generate very few, low intensity peaks, hampering the resolution of this structure.

The magnetic behaviour of $Sr_2MnO_2Cu_{1.5-x}S_2$ was probed as a function of *x*, using a combination of magnetic susceptibility and powder neutron diffraction (PND) measurements. The magnetic structures of samples of region "*A*" and region "*C*" were confirmed to be those previously reported in the literature, while a third magnetic ordering region was found in region "*B*". Two samples that contained compounds with lattice parameters assigned to region "*B*" were measured: JNB054 and JNB311. In both of these two samples two magnetic peaks were assigned to the region "*B*" structure, at $d \sim 5$ and $10.5 - 11$ Å. However, the positions of the peaks in the two samples were different enough that it is possible that the magnetic structure is incommensurately modulated, with a slightly varying **q**-vector as a function of composition.

The reaction of $Sr_2MnO_2Cu_{1.5}S_2$ with iodine was investigated *in situ* by powder X-ray diffraction (PXRD) in Chapter 4. It was found that the reaction occurred at a reasonable rate at temperatures as low as 240 K, albeit the rate was much reduced. Performing the reaction at three different temperatures allowed the activation energy, E_a, to be estimated as ~46(5) kJ mol^{-1}. More importantly, performing the reaction below the Cu vacancy ordering temperature of the region "*A*" structure (~250 K) allowed the changes in the Cu/vacancy ordering to be probed in real time. It was shown that there was a region where neither the region "*A*" nor the region "*C*" Cu vacancy ordering scheme applied, possibly because the system passed through a composition with no long-range order. No region "*B*" peaks appeared in this experiment (although work in Chapter 3 showed that these are very weak), preventing any further characterisation of region "*B*".

Work in Chapter 3 had shown that several samples synthesised with Cu occupancy values close to the boundary between regions "*B*" and "*C*" were two-phased. This was attributed to a small phase-gap between the two regions and was searched for in the *in-situ* data by analysis of the peak-shapes as a function of time. It was found that the resolution of the data was not high enough to resolve the peaks, but the peaks that were analysed (112, 015 and 114 indexed using the *I4/mmm* cell) were most broad, as shown by their full-width-half-maxima (FWHM), at approximately the point in the reaction when the phase-gap might be expected. This may be evidence of a phase-gap, but is not conclusive because other factors, such as strain effects may also have caused the peak broadening.

Investigating this reaction *in situ* at the I12 beamline provided the opportunity to design and test equipment intended to maximise the productivity of the allocated beam-time. This development of equipment divided into two strains: developing a reaction vessel for the reliable remote mixing of reactants and developing an efficient cooling method with minimal contribution to the background.

Two reaction vessels were used, one that was developed by Sedlmaier *et al.*, based on the powder tipping into the solvent (the "powder tip")[76] and one that was developed as part of the work of this thesis, which was based on the solution tipping into the powder (the "solution tip"). The "solution-tip" vessel was developed because it was found that when solvents with higher boiling points than ammonia were used, significant amounts of powder stuck to the walls on tipping when using the "powder-tip" vessel. This was

attributed to solvent on the walls of the vessel, causing the powder to also stick to the walls, reducing the amount of powder in the path of the beam.

Unfortunately, the Y-shape of the "solution-tip" vessel made it difficult to align in the X-ray beam, so the datasets described in this thesis were collected using the original "powder-tip" vessel. However, a third method of remote reactant mixing is suggested, based on mixing reactants by injection of the solution. This method was not used previously by Sedlmaier *et al.* because the high vapour pressure of ammonia required the use of a single piece of glassware.[76] This is not a consideration with solvents such as acetonitrile. An injection method would circumvent many of the problems encountered with the "powder-tip" and "solution-tip" vessels.

Conventionally, reactions are cooled using a liquid-coolant bath, which is itself cooled by either a chiller system or some solid coolant, such as (water) ice or dry-ice, dependent on the reaction temperature required. This is a problem for *in-situ* reactions because the large amounts of amorphous media involved can absorb radiation and generally contribute to the background. If the walls of the coolant bath contain crystalline material, they may also contribute peaks to the obtained PXRD pattern, further deteriorating the quality of the data. Therefore, a cooling method using cold argon was investigated. This method was generally a success, able to cool the reaction vessel to the required temperatures with reasonable stability and with minimal contribution to the background. However, the efficiency of this method could be improved by reducing the volume cooled by the gas and making the gas-cooled bath more gas-tight. Using an injection-based mixing technique would make both these goals more achievable.

The I_2 reaction was also investigated with several Co-containing compounds: $Sr_2CoO_2Cu_2S_2$, $Sr_2CoO_2Cu_2Se_2$, $Sr_2CoO_2Cu_2Se_{1.6}S_{0.4}$ and $Sr_2CoO_2Ag_2Se_2$. Unlike the manganese-containing analogues, where the only compound in the series found to be reactive with I_2 was $Sr_2MnO_2Cu_{1.5}S_2$, all these compounds reacted with I_2, albeit to different extents. Significantly more Cu could be removed from $Sr_2CoO_2Cu_2S_2$ than its Se-containing analogue, but the greater influence on the degree of oxidation achievable was found to be the identity of the coinage-metal ion. ~0.5(2) equivalents of Ag could be removed from $Sr_2CoO_2Ag_2Se_2$, which resulted in the formation of a sample with stacking faults, modelled as the displacement of layers in all three Cartesian directions,

rather than an Ag/vacancy ordering structure. This was attributed to a localised inhomogeneity in the Ag content, suggesting that the mobility of the Ag ions may be relatively low in the most-deintercalated compound. Annealing small samples of $Sr_2CoO_2Ag_{2-x}Se_2$ led to decomposition, rather than removal of stacking faults.

The magnetic behaviour of these compounds as a function of oxidation was also compared. It was found that for $Sr_2CoO_2Cu_2S_2$, $Sr_2CoO_2Cu_2Se_2$ and $Sr_2CoO_2Cu_2Se_{1.6}S_{0.4}$, the magnetic structures of the oxidised samples were largely the same as those found for their parent structures, but with reduced intensity of the magnetic peaks, attributed primarily to a reduced ordered magnetic phase fraction. This is the behaviour expected from the doping of a small amount of Co^{3+} into the Co^{2+} sites, introducing magnetic disorder.

Investigation of the magnetic behaviour of $Sr_2CoO_2Cu_{2-x}Se_2$ as a function of oxidation also allowed re-evaluation of the magnetic-ordering scheme proposed by Smura for this compound. Smura proposed that the magnetic peaks in this compound arose from the coexistence of two magnetic structures in a single nuclear structure. In this thesis, a new magnetic ordering behaviour has been proposed, based on a single magnetic structure. This magnetic structure does not give quite as good a fit to the magnetic intensity as the Smura two-phase model (R_{wp} 4.139% *vs* 4.095%), but is thought to be a more realistic representation of the ordering behaviour. Further studies, using a diffractometer which is high resolution at a large range of *d*-spacings, such as WISH, may be useful in further understanding the magnetic behaviour of this compound. Studying the magnetic ordering of this compound as a function of temperature may also provide further information.

The magnetic behaviour of most-deintercalated $Sr_2CoO_2Ag_{1.5(2)}Se_2$ appears to be complex. In contrast to the parent material ($Sr_2CoO_2Ag_2Se_2$), magnetometry measurements reveal that $Sr_2CoO_2Ag_{1.5(2)}Se_2$ has a ferromagnetic-like transition at ~70 K, with a large spin-glass element that freezes below ~30 K. It is possible that the ferromagnetic-like behaviour arises from itinerant ferromagnetism, but further studies, such as conductivity measurements and field-dependent AC magnetic susceptibility measurements are required to confirm this.

The manganese-containing analogue of most-deintercalated $Sr_2CoO_2Ag_{2-x}Se_2$, $Sr_2MnO_2Ag_{1.5}Se_2$ on the other hand was found to have a comparatively simple magnetic

structure – the *A*-type magnetic structure, based on ferromagnetic alignment of spin within the [MnO_2] planes and antiferromagnetic alignment between the planes. This magnetic structure is identical to that observed in the Cu analogue $Sr_2MnO_2Cu_{1.5}Se_2$.[107] The detailed structural and magnetic analysis of $Sr_2MnO_2Ag_{1.5}Se_2$ was made possible by the use of I_2/MeCN to remove SrSe and Ag crystalline impurities after solid state synthesis. Boskovic and Jin *et al.* had previously found that $Sr_2MnO_2Ag_{1.5}Se_2$ could not readily be made phase-pure using a purely solid-state route.[57, 60]

The synthesis, structure and magnetic behaviour of two novel telluride containing compounds is reported in this thesis: $Sr_2MnO_2Cu_{1.8}Te_2$ (Chapter 3) and $Sr_2CoO_2Cu_2Te_2$ (Chapter 4). The low temperature PND pattern of $Sr_2MnO_2Cu_{1.8}Te_2$ revealed a Warren-shaped magnetic peak, characteristic of short-range two-dimensional magnetic ordering. This might be modelled by the antiferromagnetic superexchange of Mn^{2+} ions, regularly interrupted by Mn^{3+} ions in the [MnO_2] planes.

The magnetic structure of $Sr_2CoO_2Cu_2Te_2$ was found to be very similar to the magnetic structure of $Sr_2CoO_2Cu_2S_2$, based on the $\sqrt{2}a \times \sqrt{2}a \times c$ expansion of the nuclear cell, with magnetic spins directed in the plane. Unlike $Sr_2CoO_2Cu_2S_2$ and $Sr_2CoO_2Cu_2Se_2$, the magnetic structure of $Sr_2CoO_2Cu_2Te_2$ was studied as a function of temperature using PND, revealing a small reorientation of the magnetic spin in the *ab*-plane on warming. Synchrotron PXRD measurements suggested that the compound may be slightly Co deficient, but the results remained inconclusive. The use of PND using a diffractometer that is optimised for low *d*-spacing measurements, such as HRPD or GEM, would be useful to confirm this observation.

Two compounds containing Cu in the oxide layer have been reported for the first time: $Sr_2CuO_2Cu_2Se_2$ and $Ba_2CuO_{2-x}Cu_2Se_2$. These compounds are related by the substitution of the alkali-earth metal but have very different properties. $Sr_2CuO_2Cu_2Se_2$ is stoichiometric and magnetic susceptibility measurements revealed that the compound was a Pauli paramagnet with density of states at the Fermi level, $N(E_F)$ = 2.23 orbital states eV^{-1} per formula unit in the oxide layer, consistent with the bulk conductivity measurements showing that the compound has a conductivity corresponding to that found for a poor metal (0.34(1) Ω cm at 300 K). By contrast, single-crystal X-ray diffraction revealed that $Ba_2CuO_{2-x}Cu_2Se_2$ was oxygen deficient, with refined composition approximately $Ba_2CuO_{1.5}Cu_2Se_2$, corresponding to the oxidation state of

the Cu ions in the oxide layer being +1. It was thought that this would make $Ba_2CuO_{1.5}Cu_2Se_2$ a diamagnetic semiconductor. This appears to be the case, but full analysis of the properties of this compound was hampered by the appearance of unindexed impurities in samples of this compound that could not be eliminated by varying the length or temperature of the reaction. Further work is required to make this compound phase-pure.

It was also found that the oxygen content of $Ba_2CuO_{2-x}Cu_2Se_2$ could be increased by reacting the compound with a flow of $O_{2(g)}$ at ~200 °C. While partially successful, as shown by the decrease in lattice parameters on the reaction with O_2, attempts to make a single-phased, high-oxygen-content product failed. Further work is required on this reaction.

Attempts to synthesise $Sr_2NiO_2Cu_2Se_2$ revealed that at low temperatures there was competition for the formation of compounds with Cu in the oxide layer. Therefore, the comparatively high temperature of 850 °C, combined with quenching to low temperature, was required to form a product that contained only Ni in the oxide layer. $Sr_2NiO_2Cu_2Se_2$ was found have unusual behaviour as a function of temperature, as evidenced by both magnetic susceptibility and variable temperature powder diffraction measurements. A sharp rise in the magnetic susceptibility is observed on warming at 50 – 70 K. The electronic cause of this feature is not yet accounted for. A similar transition in $Sr_2NiO_2Cu_2S_2$ was assigned to a high-spin-to-low-spin transition on cooling, but that cannot be the case for $Sr_2NiO_2Cu_2Se_2$ because PND measurements showed that an antiferromagnetic ordering occurs in $Sr_2NiO_2Cu_2Se_2$, with T_N ~ 160 K and ordered Ni moments of 1.4 μ_B that appears to be unchanged above and below this feature in the magnetic susceptibility measurements. The use of computational calculations may provide insights into the energetically-favourable interactions that could be considered.

Interestingly, some peak-splitting was observed in the diffraction pattern of $Sr_2NiO_2Cu_2Se_2$, maximising at ~60 K, when the sample was measured by PXRD on the high-flux, high-energy beamline ID22 at the ESRF, but not when the sample was measured by PND. After consideration of the alternatives, this peak-splitting has been assigned as most likely due to some photon-induced electronic transition or to beam damage, hence splitting cannot be observed in high-resolution PND data. However,

further low temperature PXRD experiments, measuring the diffraction pattern as a function of time illuminated and also possibly as a function of X-ray wavelength (and therefore photon energy), would be required to understand this transition fully.

This thesis has expanded the number of known compounds of the $A_2MO_2X_2Ch_2$ series, but in particular, by synthesis of $Sr_2CuO_2Cu_2Se_2$ (Chapter 6) and $Sr_2NiO_2Cu_2Se_2$ (Chapter 7), the $Sr_2MO_2Cu_2Se_2$ series (where M = Mn, Co, Ni, Cu and Zn). This allows comparisons in the changes in structural parameters of this series across the period to be made, as shown in Fig. 8.1.

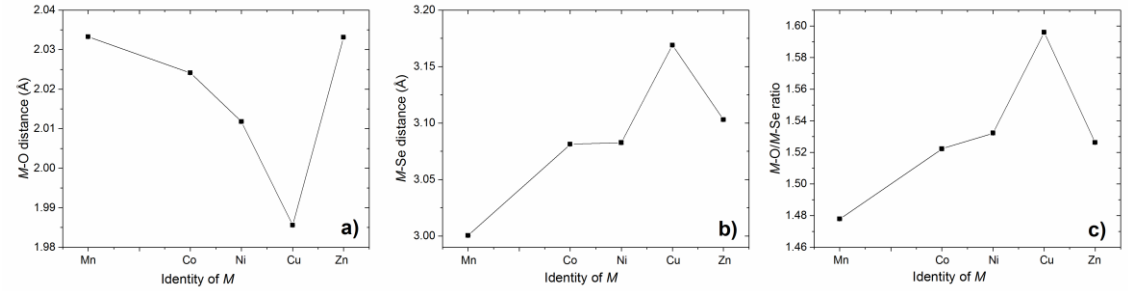


Fig. 8.1 Changes in the a) M-O distance; b) M-Se distance and c) M-O/M-Se ratio as a function of the identity of the transition metal, M in the formula $Sr_2MO_2Cu_2Se_2$ (except Mn, where the refined composition is $Sr_2MnO_2Cu_{1.5}Se_2$). Values are obtained from room temperature PND data: $Sr_2MnO_2Cu_{1.5}Se_2$ from ref. 107; $Sr_2CoO_2Cu_2Se_2$, $Sr_2NiO_2Cu_2Se_2$ and $Sr_2NiO_2Cu_2Se_2$ from this thesis and $Sr_2ZnO_2Cu_2Se_2$ from ref. 63. In each of a), b) and c) the error bars are smaller than the points on the graph

The graphs in Fig. 8.1 show that only very small changes to the transition metal environment occur across the period. This suggests that the most significant factor in determining the geometry of these compounds is the identity of the other ions in the compound. The large changes that occur on replacing Cu with Ag were shown in sections 3.3 and 5.5 for M = Mn and Co respectively; the effects of replacing Sr with Ba were discussed at length in Chapter 6; and the effects of replacing Se with S and Te were shown in Chapter 3 and Chapter 5 for M = Mn and Co respectively.

It is noted that the Mn-Se distance in $Sr_2MnO_2Cu_{1.5}Se_2$ is relatively short, this is likely related to the increased oxidation state (+2.5) of Mn in this species. The increased oxidation state presumably leads to increased Mn-Se interactions and therefore a shortening of the Mn-Se distance. The transition metal environment of $Sr_2CoO_2Cu_2Se_2$ and $Sr_2NiO_2Cu_2Se_2$ appear to be very similar to one another, this is considered further evidence that (at least at room temperature) the Ni^{2+} ion in $Sr_2NiO_2Cu_2Se_2$ is high-spin d^8. If the Ni^{2+} ion were low-spin, then the Ni^{2+} environment would be expected to be

significantly closer to square-planar. It is this behaviour that is observed in $Sr_2CuO_2Cu_2Se_2$: the Cu-Se distance is comparatively long and matched by a rather short Cu-O distance, leading to a significantly distended octahedral environment. This behaviour is reminiscent of the Jahn-Teller distortion of d^9 Cu^{2+}, suggesting that the Cu ion in the oxide layer of $Sr_2CuO_2Cu_2Se_2$ has indeed at least partially oxidised beyond Cu^+. Computational calculation of the electronic structure of this compound may provide further insight into this behaviour.

As stated in the introduction, the $A_2MO_2X_2Ch_2$ compounds provide a rich playground of transition metal environments based on the distended octahedral site. The presence of the chalcogenide ions has the general effect of stabilising lower oxidation states than are generally observed in related oxide phases, such as the perovskites. This leads to interesting chemical and physical properties, which, as has been shown, can be controlled by chemical substitutions and oxidation of the transition metal ion using soft chemistry.

References

1. J. Bardeen, L. N. Cooper and J. R. Schrieffer, *Physical Review*, 1957, **108**, 1175-1204.
2. J. G. Bednorz and K. A. Müller, *Zeitschrift für Physik B Condensed Matter*, 1986, **64**, 189-193.
3. Y. Kamihara, T. Watanabe, M. Hirano and H. Hosono, *Journal of the American Chemical Society*, 2008, **130**, 3296-3297.
4. M. S. Whittingham, *Journal of The Electrochemical Society*, 1976, **123**, 315-320.
5. K. Mizushima, P. C. Jones, P. J. Wiseman and J. B. Goodenough, *Materials Research Bulletin*, 1980, **15**, 783-789.
6. J. B. Goodenough and Y. Kim, *Chemistry of Materials*, 2010, **22**, 587-603.
7. W. G. Zeier, A. Zevalkink, Z. M. Gibbs, G. Hautier, M. G. Kanatzidis and G. J. Snyder, *Angewandte Chemie International Edition*, 2016, **55**, 6826-6841.
8. W. Eerenstein, N. D. Mathur and J. F. Scott, *Nature*, 2006, **442**, 759-765.
9. K. Maeda, *Journal of Photochemistry and Photobiology C: Photochemistry Reviews*, 2011, **12**, 237-268.
10. A. J. Jacobson, *Chemistry of Materials*, 2010, **22**, 660-674.
11. C. N. R. Rao and B. Raveau, *Accounts of Chemical Research*, 1989, **22**, 106-113.
12. J. Z. Sun and A. Gupta, *Annual Review of Materials Science*, 1998, **28**, 45-78.
13. S. J. Clarke, P. Adamson, S. J. C. Herkelrath, O. J. Rutt, D. R. Parker, M. J. Pitcher and C. F. Smura, *Inorganic Chemistry*, 2008, **47**, 8473-8486.
14. S. G. Ebbinghaus, H.-P. Abicht, R. Dronskowski, T. Müller, A. Reller and A. Weidenkaff, *Progress in Solid State Chemistry*, 2009, **37**, 173-205.
15. Y. Tsujimoto, K. Yamaura and E. Takayama-Muromachi, *Appl. Sci.-Basel*, 2012, **2**, 206-219.
16. C. Stock and E. E. McCabe, *Journal of Physics: Condensed Matter*, 2016, **28**, 453001.
17. S. D. N. Luu and P. Vaqueiro, *Journal of Materiomics*, 2016, **2**, 131-140.
18. H. Hiramatsu, H. Yanagi, T. Kamiya, K. Ueda, M. Hirano and H. Hosono, *Chemistry of Materials*, 2008, **20**, 326-334.
19. S. Muir and M. A. Subramanian, *Progress in Solid State Chemistry*, 2012, **40**, 41-56.
20. L. I. Alexander, *Russian Chemical Reviews*, 2010, **79**, 1.
21. M. Palazzi, *Comptes Rendus De L Academie Des Sciences Serie Ii*, 1981, **292**, 789-791.
22. K. Ueda and H. Hosono, *Thin Solid Films*, 2002, **411**, 115-118.
23. V. Johnson and W. Jeitschko, *Journal of Solid State Chemistry*, 1974, **11**, 161-166.
24. K. Ueda and H. Hosono, *Journal of Applied Physics*, 2002, **91**, 4768-4770.
25. H. Hiramatsu, K. Ueda, H. Ohta, T. Kamiya, M. Hirano and H. Hosono, *Applied Physics Letters*, 2005, **87**, 211107.
26. E. E. McCabe, D. G. Free and J. S. O. Evans, *Chemical Communications*, 2011, **47**, 1261-1263.
27. H. Hiramatsu, K. Ueda, T. Kamiya, H. Ohta, M. Hirano and H. Hosono, *Journal of Materials Chemistry*, 2004, **14**, 2946-2950.

28. C. M. Ainsworth, C.-H. Wang, H. E. Johnston, E. E. McCabe, M. G. Tucker, H. E. A. Brand and J. S. O. Evans, *Inorganic Chemistry*, 2015, **54**, 7230-7238.
29. E. E. McCabe, D. G. Free, B. G. Mendis, J. S. Higgins and J. S. O. Evans, *Chemistry of Materials*, 2010, **22**, 6171-6182.
30. S. Broadley, Z. A. Gál, F. Corà, C. F. Smura and S. J. Clarke, *Inorganic Chemistry*, 2005, **44**, 9092-9096.
31. M. Valldor, U. K. Rossler, Y. Prots, C. Y. Kuo, J. C. Chiang, Z. W. Hu, T. W. Pi, R. Kniep and L. H. Tjeng, *Chemistry-a European Journal*, 2015, **21**, 10821-10828.
32. E. J. T. Salter, J. N. Blandy and S. J. Clarke, *Inorganic Chemistry*, 2016, **55**, 1697-1701.
33. T. Sambrook, C. F. Smura, S. J. Clarke, K. M. Ok and P. S. Halasyamani, *Inorganic Chemistry*, 2007, **46**, 2571-2574.
34. W. Liu, K. T. Lai, K. Eckhardt, Y. Prots, U. Burkhardt and M. Valldor, *Journal of Solid State Chemistry*, 2017, **246**, 225-229.
35. C. Delacotte, O. Pérez, A. Pautrat, D. Berthebaud, S. Hébert, E. Suard, D. Pelloquin and A. Maignan, *Inorganic Chemistry*, 2015, **54**, 6560-6565.
36. S. F. Jin, Q. Huang, Z. P. Lin, Z. L. Li, X. Z. Wu, T. P. Ying, G. Wang and X. L. Chen, *Physical Review B*, 2015, **91**, 094420.
37. F. Han, D. Wang, C. D. Malliakas, M. Sturza, D. Y. Chung, X. Wan and M. G. Kanatzidis, *Chemistry of Materials*, 2015, **27**, 5695-5701.
38. S. J. Cassidy, M. Batuk, D. Batuk, J. Hadermann, D. N. Woodruff, A. L. Thompson and S. J. Clarke, *Inorganic Chemistry*, 2016, **55**, 10714-10726.
39. K. T. Lai, A. C. Komarek, M. T. Fernández-Díaz, P.-S. Chang, S. Huh, H. Rosner, C.-Y. Kuo, Z. Hu, T.-W. Pi, P. Adler, V. Ksenofontov, L. H. Tjeng and M. Valldor, *Inorganic Chemistry*, 2017, **56**, 4271-4279.
40. E. Brechtel, G. Cordier and H. Schafer, *Zeitschrift Fur Naturforschung Section B-a Journal of Chemical Sciences*, 1979, **34**, 777-780.
41. W. J. Zhu and P. H. Hor, *Journal of Solid State Chemistry*, 1997, **130**, 319-321.
42. W. J. Zhu, P. H. Hor, A. J. Jacobson, G. Crisci, T. A. Albright, S. H. Wang and T. Vogt, *Journal of the American Chemical Society*, 1997, **119**, 12398-12399.
43. W. J. Zhu and P. H. Hor, *Journal of Solid State Chemistry*, 1997, **134**, 128-131.
44. G. Hyett, N. Barrier, S. J. Clarke and J. Hadermann, *Journal of the American Chemical Society*, 2007, **129**, 11192-11201.
45. Z. A. Gál, O. J. Rutt, C. F. Smura, T. P. Overton, N. Barrier, S. J. Clarke and J. Hadermann, *Journal of the American Chemical Society*, 2006, **128**, 8530-8540.
46. W. J. Zhu and P. H. Hor, *Journal of Solid State Chemistry*, 2000, **153**, 26-29.
47. K. Otzschi, H. Ogino, J. Shimoyama and K. Kishio, *Journal of Low Temperature Physics*, 1999, **117**, 729-733.
48. L. Cario, A. Lafond, T. Morvan, H. Kabbour, G. André and P. Palvadeau, *Solid State Sciences*, 2005, **7**, 936-944.
49. Z. Han, J. Shifeng, G. Liwei, S. Shijie, L. Zhiping and C. Xiaolong, *Chinese Physics B*, 2016, **25**, 026101.
50. J. Wilson, MChem, University of Oxford, 2008.
51. M.-L. Liu, L.-B. Wu, F.-Q. Huang, L.-D. Chen and I.-W. Chen, *Journal of Applied Physics*, 2007, **102**, 116108.
52. D. O. Scanlon and G. W. Watson, *Chemistry of Materials*, 2009, **21**, 5435-5442.
53. N. Barrier and S. J. Clarke, *Chemical Communications*, 2003, DOI: 10.1039/b209747h, 164-165.
54. O. J. Rutt, DPhil, University of Oxford, 2007.

55. M. David, MChem, University of Oxford, 2012.
56. T. Lunt, MChem, University of Oxford, 2016.
57. J. Boskovic, MChem, University of Oxford, 2007.
58. C. F. Smura, DPhil, University of Oxford, 2008.
59. T. Zhou, Y. Wang, S. Jin, D. Li, X. Lai, T. Ying, H. Zhang, S. Shen, W. Wang and X. Chen, *Inorganic Chemistry*, 2014, **53**, 4154-4160.
60. S. Jin, X. Chen, J. Guo, M. Lei, J. Lin, J. Xi, W. Wang and W. Wang, *Inorganic Chemistry*, 2012, **51**, 10185-10192.
61. C. F. Smura, D. R. Parker, M. Zbiri, M. R. Johnson, Z. A. Gál and S. J. Clarke, *Journal of the American Chemical Society*, 2011, **133**, 2691-2705.
62. S. J. C. Herkelrath, DPhil, University of Oxford, 2009.
63. S. Broadley, MChem, University of Oxford, 2005.
64. K. Ueda, S. Hirose, H. Kawazoe and H. Hosono, *Chemistry of Materials*, 2001, **13**, 1880-1883.
65. S. J. C. Herkelrath, I. Saratovsky, J. Hadermann and S. J. Clarke, *Journal of the American Chemical Society*, 2008, **130**, 14426-14427.
66. K. Ueda, K. Takafuji and H. Hosono, *Journal of Solid State Chemistry*, 2003, **170**, 182-187.
67. D. O. Charkin, A. V. Akopyan and V. A. Dolgikh, *Russian Journal of Inorganic Chemistry*, 1999, **44**, 833-837.
68. G. H. Chan, B. Deng, M. Bertoni, J. R. Ireland, M. C. Hersam, T. O. Mason, R. P. Van Duyne and J. A. Ibers, *Inorganic Chemistry*, 2006, **45**, 8264-8272.
69. M. J. Pitcher, C. F. Smura and S. J. Clarke, *Inorganic Chemistry*, 2009, **48**, 9054-9056.
70. E. Chong, MChem, University of Oxford, 2011.
71. J. Lim, MChem, University of Oxford, 2012.
72. F.-C. Hsu, J.-Y. Luo, K.-W. Yeh, T.-K. Chen, T.-W. Huang, P. M. Wu, Y.-C. Lee, Y.-L. Huang, Y.-Y. Chu, D.-C. Yan and M.-K. Wu, *Proceedings of the National Academy of Sciences*, 2008, **105**, 14262-14264.
73. J. Guo, S. Jin, G. Wang, S. Wang, K. Zhu, T. Zhou, M. He and X. Chen, *Physical Review B*, 2010, **82**, 180520.
74. T. P. Ying, X. L. Chen, G. Wang, S. F. Jin, T. T. Zhou, X. F. Lai, H. Zhang and W. Y. Wang, *Scientific Reports*, 2012, **2**, 426.
75. M. Burrard-Lucas, D. G. Free, S. J. Sedlmaier, J. D. Wright, S. J. Cassidy, Y. Hara, A. J. Corkett, T. Lancaster, P. J. Baker, S. J. Blundell and S. J. Clarke, *Nature Materials*, 2013, **12**, 15-19.
76. S. J. Sedlmaier, S. J. Cassidy, R. G. Morris, M. Drakopoulos, C. Reinhard, S. J. Moorhouse, D. O'Hare, P. Manuel, D. Khalyavin and S. J. Clarke, *Journal of the American Chemical Society*, 2014, **136**, 630-633.
77. J. A. Alonso and M. J. Martinez-Lope, *Journal of the Chemical Society, Dalton Transactions*, 1995, DOI: 10.1039/DT9950002819, 2819-2824.
78. M. Crespin, P. Levitz and L. Gatineau, *Journal of the Chemical Society, Faraday Transactions 2: Molecular and Chemical Physics*, 1983, **79**, 1181-1194.
79. P. Levitz, M. Crespin and L. Gatineau, *Journal of the Chemical Society, Faraday Transactions 2: Molecular and Chemical Physics*, 1983, **79**, 1195-1203.
80. M. A. Hayward, M. A. Green, M. J. Rosseinsky and J. Sloan, *Journal of the American Chemical Society*, 1999, **121**, 8843-8854.

81. O. J. Rutt, G. R. Williams and S. J. Clarke, *Chemical Communications*, 2006, 2869-2871.
82. S. Indris, J. Cabana, O. J. Rutt, S. J. Clarke and C. P. Grey, *Journal of the American Chemical Society*, 2006, **128**, 13354-13355.
83. B. N. Figgis and M. A. Hitchman, *Ligand Field Theory and Its Applications*, Wiley, New York, 2000.
84. J. B. Goodenough, *Physical Review*, 1955, **100**, 564-573.
85. J. B. Goodenough, *Journal of Physics and Chemistry of Solids*, 1958, **6**, 287-297.
86. J. Kanamori, *Journal of Physics and Chemistry of Solids*, 1959, **10**, 87-98.
87. J. A. Mydosh, *Spin glasses : an experimental introduction*, Taylor & Francis, London; Washington, DC, 1993.
88. P. Adamson, DPhil, University of Oxford, 2010.
89. H. Cohen, MChem, University of Oxford, 2012.
90. A. L. Patterson, *Physical Review*, 1934, **46**, 372-376.
91. D. Sayre, *Acta Crystallographica*, 1952, **5**, 60-65.
92. J. Karle and H. Hauptman, *Acta Crystallographica*, 1950, **3**, 181-187.
93. G. Oszlanyi and A. Suto, *Acta Crystallographica Section A*, 2004, **60**, 134-141.
94. S. P. Thompson, J. E. Parker, J. Potter, T. P. Hill, A. Birt, T. M. Cobb, F. Yuan and C. C. Tang, *Review of Scientific Instruments*, 2009, **80**, 075107.
95. J.-L. Hodeau, P. Bordet, M. Anne, A. Prat, A. N. Fitch, E. Dooryhee, G. Vaughan and A. K. Freund, 1998.
96. M. Drakopoulos, T. Connolley, C. Reinhard, R. Atwood, O. Magdysyuk, N. Vo, M. Hart, L. Connor, B. Humphreys, G. Howell, S. Davies, T. Hill, G. Wilkin, U. Pedersen, A. Foster, N. De Maio, M. Basham, F. Yuan and K. Wanelik, *Journal of Synchrotron Radiation*, 2015, **22**, 828-838.
97. J. E. Daniels and M. Drakopoulos, *Journal of Synchrotron Radiation*, 2009, **16**, 463-468.
98. H. Rietveld, *Journal of Applied Crystallography*, 1969, **2**, 65-71.
99. A. A. Coelho, *TOPAS Academic Version 5*, Coelho Software, Brisbane, Australia, 2012.
100. V. Petricek, M. Dusek and L. Palatinus, *Zeitschrift für Kristallographie*, 2014, **229**, 345-352.
101. Agilent, *CrysAlis PRO*, Agilent Technologies Ltd, Yarnton, Oxfordshire, UK, 2014.
102. P. W. Betteridge, J. R. Carruthers, R. I. Cooper, K. Prout and D. J. Watkin, *Journal of Applied Crystallography*, 2003, **36**, 1487.
103. L. Palatinus and G. Chapuis, *Journal of Applied Crystallography*, 2007, **40**, 786-790.
104. H. Nowell, S. A. Barnett, K. E. Christensen, S. J. Teat and D. R. Allan, *Journal of Synchrotron Radiation*, 2012, **19**, 435-441.
105. S. Elliott, *The Physics and Chemistry of Solids*, Wiley and Sons, Chichester, UK, 1998.
106. P. A. Cox, *The electronic structure and chemistry of solids*, Oxford University Press, Oxford, 1987.
107. P. Adamson, J. Hadermann, C. F. Smura, O. J. Rutt, G. Hyett, D. G. Free and S. J. Clarke, *Chemistry of Materials*, 2012, **24**, 2802-2816.
108. S. Mori, C. H. Chen and S. W. Cheong, *Nature*, 1998, **392**, 473-476.
109. D. R. Parker and S. J. Clarke, unpublished work.

110. J. N. Blandy, A. M. Abakumov, K. E. Christensen, J. Hadermann, P. Adamson, S. J. Cassidy, S. Ramos, D. G. Free, H. Cohen, D. N. Woodruff, A. L. Thompson and S. J. Clarke, *APL Materials*, 2015, **3**, 041520.
111. J. N. Blandy, J. C. Boskovic and S. J. Clarke, *Journal of Solid State Chemistry*, 2017, **245**, 61-66.
112. *ISODISTORT: ISOTROPY Software Suite, iso.byu.edu*.
113. J.-H. Her, P. W. Stephens, Y. Gao, G. L. Soloveichik, J. Rijssenbeek, M. Andrus and J.-C. Zhao, *Acta Crystallographica Section B*, 2007, **63**, 561-568.
114. E. E. McCabe, C. Stock, E. E. Rodriguez, A. S. Wills, J. W. Taylor and J. S. O. Evans, *Physical Review B*, 2014, **89**, 100402.
115. A. L. Goodwin, M. G. Tucker, M. T. Dove and D. A. Keen, *Physical Review Letters*, 2006, **96**, 047209.
116. D. B. Litvin, *Magnetic Group Tables: 1-, 2- and 3-Dimensional Magnetic Subperiodic Groups and Magnetic Space Groups*, International Union of Crystallography, 2013.
117. R. Shannon, *Acta Crystallographica Section A*, 1976, **32**, 751-767.
118. B. E. Warren, *Physical Review*, 1941, **59**, 693-698.
119. B. E. Warren and P. Bodenstein, *Acta Crystallographica*, 1966, **20**, 602-605.
120. S. L. Brock, N. P. Raju, J. E. Greedan and S. M. Kauzlarich, *Journal of Alloys and Compounds*, 1996, **237**, 9-19.
121. L. L. Zhao, S. Wu, J. K. Wang, J. P. Hodges, C. Broholm and E. Morosan, *Physical Review B*, 2013, **87**, 020406.
122. T. Kanashiro, Y. Kishimoto, T. Ohno and Y. Michihiro, *Solid State Ionics*, 1990, **40–41, Part 1**, 308-311.
123. M. Oliveria, R. K. McMullan and B. J. Wuensch, *Solid State Ionics*, 1988, **28–30, Part 2**, 1332-1337.
124. G. R. Williams, A. J. Norquist and D. O'Hare, *Chemistry of Materials*, 2006, **18**, 3801-3807.
125. G. G. Amatucci, J. M. Tarascon and L. C. Klein, *Journal of the Electrochemical Society*, 1996, **143**, 1114-1123.
126. A. S. Andersson, B. Kalska, L. Häggström and J. O. Thomas, *Solid State Ionics*, 2000, **130**, 41-52.
127. W. Paulus, H. Katzke and R. Schöllhorn, *Journal of Solid State Chemistry*, 1992, **96**, 162-168.
128. S. M. Clark, P. Irvin, J. Flaherty, T. Rathbone, H. V. Wong, J. S. O. Evans and D. O'Hare, *Review of Scientific Instruments*, 1994, **65**, 2210-2213.
129. S. J. Moorhouse, N. Vranješ, A. Jupe, M. Drakopoulos and D. O'Hare, *Review of Scientific Instruments*, 2012, **83**, 084101.
130. Y. Wu, M. I. Breeze, G. J. Clarkson, F. Millange, D. O'Hare and R. I. Walton, *Angewandte Chemie International Edition*, 2016, **55**, 4992-4996.
131. G. R. Williams, S. J. Moorhouse, T. J. Prior, A. M. Fogg, N. H. Rees and D. O'Hare, *Dalton Transactions*, 2011, **40**, 6012-6022.
132. J. Filik, A. W. Ashton, P. C. Y. Chang, P. A. Chater, S. J. Day, M. Drakopoulos, M. W. Gerring, M. L. Hart, O. V. Magdysyuk, S. Michalik, A. Smith, C. C. Tang, N. J. Terrill, M. T. Wharmby and H. Wilhelm, *Journal of Applied Crystallography*, 2017, **50**, 959-966.
133. A. P. Hammersley, *FIT2D V9.129 Reference Manual V3.1, ESRF Internal Report, ESRF98HA01T*, 1998.
134. S. Bruckner, *Journal of Applied Crystallography*, 2000, **33**, 977-979.

135. P. Thompson, D. E. Cox and J. B. Hastings, *Journal of Applied Crystallography*, 1987, **20**, 79-83.
136. M. Avrami, *The Journal of Chemical Physics*, 1939, **7**, 1103-1112.
137. M. Avrami, *The Journal of Chemical Physics*, 1940, **8**, 212-224.
138. M. Avrami, *The Journal of Chemical Physics*, 1941, **9**, 177-184.
139. B. V. Erofe'ev, *Comptes rendus (Doklady) de l'Académie des sciences de l'URSS*, 1946, **52**, 511-514.
140. J. D. Hancock and J. H. Sharp, *Journal of the American Ceramic Society*, 1972, **55**, 74-77.
141. A. M. Fogg, S. J. Price, R. J. Francis, S. O'Brien and D. O'Hare, *Journal of Materials Chemistry*, 2000, **10**, 2355-2357.
142. S. M. Clark, J. S. O. Evans, D. O'Hare, C. J. Nuttall and H.-V. Wong, *Journal of the Chemical Society, Chemical Communications*, 1994, DOI: 10.1039/C39940000809, 809-810.
143. S. J. Cassidy, DPhil, University of Oxford, 2015.
144. L. Harris, MChem, University of Oxford, 2011.
145. G. Shirane, *Acta Crystallographica*, 1959, **12**, 282-285.
146. G. Aeppli and D. J. Buttrey, *Physical Review Letters*, 1988, **61**, 203-206.
147. G. Aeppli, D. R. Harshman, D. Buttrey, E. Ansaldo, G. P. Espinosa, A. S. Cooper, J. P. Remeika, T. Treltoft, T. M. Riseman, D. R. Noakes, B. Ellman, T. F. Rosenbaum and D. L. Williams, *Physica C: Superconductivity*, 1988, **153–155, Part 3**, 1111-1114.
148. C. S. Knee and M. T. Weller, *Physical Review B*, 2004, **70**, 144406.
149. K. Yamada, M. Matsuda, Y. Endoh, B. Keimer, R. J. Birgeneau, S. Onodera, J. Mizusaki, T. Matsuura and G. Shirane, *Physical Review B*, 1989, **39**, 2336-2343.
150. D. E. Cox, A. I. Goldman, M. A. Subramanian, J. Gopalakrishnan and A. W. Sleight, *Physical Review B*, 1989, **40**, 6998-7004.
151. S. Skanthakumar, J. W. Lynn, J. L. Peng and Z. Y. Li, *Physical Review B*, 1993, **47**, 6173-6176.
152. J. I. Budnick, B. Chamberland, D. P. Yang, N. Ch, A. Golnik, E. Recknagel, M. Rossmanith and A. Weidinger, *EPL (Europhysics Letters)*, 1988, **5**, 651.
153. J. B. Goodenough, *Magnetism and Chemical Bond*, Interscience, New York/London, 1963.
154. P. W. Stephens, *Journal of Applied Crystallography*, 1999, **32**, 281-289.
155. A. A. Coelho, *TOPAS Academic Version 6*, Coelho Software, Brisbane, Australia, 2016.
156. M. D. Vannette and R. Prozorov, *Journal of Physics: Condensed Matter*, 2008, **20**, 475208.
157. M. D. Vannette, S. L. Bud'ko, P. C. Canfield and R. Prozorov, *Journal of Applied Physics*, 2008, **103**, 07D302.
158. A. Prasher, MChem, University of Oxford, 2013.
159. Y. B. Park, D. C. Degroot, J. L. Schindler, C. R. Kannewurf and M. G. Kanatzidis, *Chemistry of Materials*, 1993, **5**, 8-10.
160. G. A. Bain and J. F. Berry, *Journal of Chemical Education*, 2008, **85**, 532.
161. V. F. Sears, *Neutron News*, 1992, **3**, 26-37.
162. J. Arvanitidis, K. Papagelis, S. Margadonna, K. Prassides and A. N. Fitch, *Nature*, 2003, **425**, 599-602.
163. S. Margadonna, J. Arvanitidis, K. Papagelis and K. Prassides, *Chemistry of Materials*, 2005, **17**, 4474-4478.

164. S. Margadonna, K. Prassides, M. Chondroudi, J. R. Salvador and M. G. Kanatzidis, *Chemical Communications*, 2005, DOI: 10.1039/B511606F, 5754-5756.
165. D. E. Cox, P. G. Radaelli, M. Marezio and S. W. Cheong, *Physical Review B*, 1998, **57**, 3305-3314.
166. V. Kiryukhin, D. Casa, J. P. Hill, B. Keimer, A. Vigliante, Y. Tomioka and Y. Tokura, *Nature*, 1997, **386**, 813-815.
167. D. Papanikolaou, S. Margadonna, W. Kosaka, S.-i. Ohkoshi, M. Brunelli and K. Prassides, *Journal of the American Chemical Society*, 2006, **128**, 8358-8363.
168. H. Ishibashi, T. Y. Koo, Y. S. Hor, A. Borissov, P. G. Radaelli, Y. Horibe, S. W. Cheong and V. Kiryukhin, *Physical Review B*, 2002, **66**, 144424.
169. V. Kiryukhin, Y. Horibe, Y. S. Hor, H. J. Noh, S. W. Cheong and C. H. Chen, *Physical Review Letters*, 2006, **97**, 225503.
170. P. G. Radaelli, *New Journal of Physics*, 2005, **7**, 53.
171. T. Janssen, J. L. Birman, F. Denoyer, V. A. Koptsik, J. L. Verger-Gaugry, D. Weigel, A. Yamamoto, S. C. Abrahams and V. Kopsky, *Acta Crystallographica Section A*, 2002, **58**, 605-621.
172. S. van Smaalen, *Incommensurate Crystallography*, Oxford University Press, Oxford, 2007.
173. *International Tables for Crystallography* Kluwer Academic Publishers, Dordrecht/Boston/London, 3 edn., 2006.
174. P. M. de Wolff, T. Janssen and A. Janner, *Acta Crystallographica Section A*, 1981, **37**, 625-636.
175. S. C. Miller and W. F. Love, *Tables of Irreducible Representations of Space Groups and Co-Representations of Magnetic Space Groups*, Pruett, Boulder, 1967.
176. B. J. Campbell, H. T. Stokes, D. E. Tanner and D. M. Hatch, *Journal of Applied Crystallography*, 2006, **39**, 607-614.

The following book was used in the discussion on the magnetic behaviour of solids (Chapter 1):

1. N. A. Spaldin, *Magnetic materials: fundamentals and applications*, Cambridge University Press, Cambridge, 2 edn., 2011

Appendix A
A. Incommensurate Crystallography

The diffraction pattern of an incommensurately modulated crystal has two distinct sets of reflections: main reflections and satellite reflections. The main reflections can be indexed using a standard three-dimensional (3D) unit cell, but the satellite reflections cannot.

The average structure of an incommensurately modulated crystal may be solved by simply disregarding the satellite reflections. However, to fully describe the structure of the crystal the satellite reflections must be indexed and their intensity accounted for. This requires the use of additional dimensions. Incommensurately modulated crystals with up to three additional dimensions are possible, but the incommensurately modulated crystal described in this thesis (see section 3.2.3) was indexed using a (3+1)D description, so this discussion will be limited to (3+1)D cases.

Reflections in four-dimensional reciprocal superspace are described by:

$$\mathbf{H} = h\mathbf{a^*} + k\mathbf{b^*} + l\mathbf{c^*} + m\mathbf{q} \tag{A.1}$$

where m is the fourth-dimension equivalent of the indices h, k, l and $\mathbf{q}$ is a vector:

$$\mathbf{q} = \alpha\mathbf{a^*} + \beta\mathbf{b^*} + \gamma\mathbf{c^*} \tag{A.2}$$

When the structure is incommensurately modulated (as opposed to commensurately modulated), one or more of α, β, γ is an irrational number. Satellite reflections, where $m \neq 0$ are much weaker than the main reflections and intensity drops off quickly as a function of satellite order $|m|$, so it is common that only first or second order satellite reflections are of sufficient intensity to be observed.

When the unit cell parameters (including **q)** have been indexed, the reflections are analysed for systematic absences in order to find the space group. The number of possible space groups increases rapidly with the increasing number of dimensions, as shown in Table A.1.

Table A.1 Comparison of the number of possible space groups for 1 – 6 dimensions; data obtained from ref. 171

Number of dimensions	Possible number of space groups
1	2
2	17
3	219*
4	4783*
5	222018*
6	28927922*

*excluding enantiomeric pairs

However, in incommensurate crystallography the number of space groups is restricted somewhat by the constraint that the point group of the *n*-dimensional space group must be isomorphous with the point group of three-dimensional space. These space groups relevant to incommensurate crystallography are termed *superspace groups*; the number of superspace groups in each dimension is shown in Table A.2.

Table A.2 Number of superspace groups in each dimension, here enantiomeric pairs are treated as separate space groups, data obtained from ref. 172

Number of dimensions	Possible number of space groups
3+1	756
3+2	3335
3+3	11764

The (3+1)D superspace groups have been tabulated with their reflection conditions in *International Tables for Crystallography Volume C*.[173] The anatomy of a (3+1)D superspace group is shown for the example *Xmmm*(*α00*)00*s* in Fig. A.1.

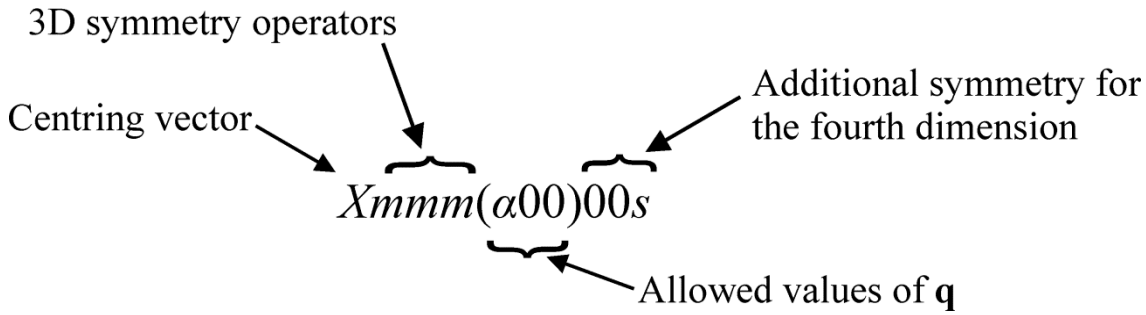


Fig. A.1 Anatomy of a superspace group symbol

The centring vector is analogous to those found in three-dimensional space groups (*P*, *A*, *B*, *C*, *F*, *I*, *R*), but the addition of an extra dimension allows the use of centring vectors with a non-zero fourth component, with naming conventions that may be found in *International Tables for Crystallography Volume C*.[173] The symbol *X*, used in Fig. A.1, represents a non-conventional centring vector, which must then be defined

explicitly. The "suffix" of the superspace group symbol represents the additional symmetry that can occur in the fourth dimension. This additional symmetry can be conceptualised as the (3+1)D superspace equivalent of screw axes and glide planes.[172-174]

The position, occupancy and thermal displacement parameters of the atoms in an incommensurately modulated crystal are solved by consideration of the positions in both superspace and physical three-dimensional space. Conversion between the two is achieved by considering the atom at point **x** in physical space and the atom at point $\mathbf{x}_s$ in superspace. To make it easier to extend these parameters to higher dimensions, the three-dimensional coordinates *x*, *y*, and *z* are termed x_1, x_2 and x_3 respectively and the unit cell parameters *a*, *b*, *c* are termed a_1, a_2 and a_3 respectively.

$$\mathbf{x} = x_1a_1 + x_2a_2 + x_3a_3 \tag{A.3}$$

$$\mathbf{x_s} = x_{s1}a_{s1} + x_{s2}a_{s2} + x_{s3}a_{s3} + x_{s4}a_{s4} \tag{A.4}$$

Synthesis of x_{s1}, x_{s2}, x_{s3} is trivial, but x_{s4} requires further consideration:

$$x_{s1} = x_1 \qquad x_{s2} = x_2 \qquad x_{s3} = x_2 \qquad x_{s4} = t + \mathbf{q}\cdot\mathbf{x} \tag{A.5}$$

where *t* is a parameter that runs parallel to a_{s4} and is defined in the regime $0 \leq t < 1$. *t* may be conceptualised as the phase of the modulation, so the atom positions and fractional occupancy at any point in real space will correspond to a value of *t*. For this reason changes in the atom positions and occupancy are often represented as a function of *t*.

The position of an atom in an incommensurately modulated structure ($\mathbf{r_{n\nu}}$) is described by (for a (3+1)D structure):

$$\mathbf{r_{n\nu}} = \mathbf{r_\nu^0} + \mathbf{n} + \mathbf{u_\nu}[\mathbf{q}(\mathbf{n} + x_{s4})] \tag{A.6}$$

where $\mathbf{r_\nu^0}$ is the average position of atom ν and **n** represents lattice translations. $\mathbf{u_\nu}$ is the periodic function that describes the change in the atom positions x_1, x_2 and x_3 along x_{s4}. It is possible to use several different types of function to describe the modulation function $\mathbf{u_\nu}$: saw-tooth, zig-zag or a Fourier series of harmonic functions. The choice of function used is dependent on the character of the modulation. This may be found

through a combination of trial-and-error and examination of Fourier maps of electron density along x_{s4}.

For the compound in region "*C*" $Sr_2MnO_2Cu_{1.33}S_2$ it was found that the best fit to the data was obtained by use of a Fourier series of harmonic functions. These functions are defined by:[100]

$$\mathbf{u}_{\boldsymbol{v}} = \sum_{i=1}^{l} \boldsymbol{A}_i \sin[2\pi\mathbf{q}_i \cdot (\mathbf{n} + x_{s4})] + \sum_{i=1}^{l} \boldsymbol{B}_i \cos[2\pi\mathbf{q}_i \cdot (\mathbf{n} + x_{s4})] \qquad \text{(A.7)}$$

in each of x_1, x_2, x_3. A_i and B_i are the amplitudes of the sin and cos displacement waves respectively and i is the order of the Fourier series. By convention, to prevent over-parameterisation of the data, the order of the Fourier series is truncated to the order of the satellite reflections observed (m). The modulation of thermal displacement parameters (ADPs) is precisely analogous to the modulation of atom position.

The formulae for occupation modulation parameters are similar to that for position:

$$p_{nv} = p_v^0 + p_v[\mathbf{q}_i(\mathbf{n} + x_{s4})] \qquad \text{(A.8)}$$

where p_{nv} is the fractional occupancy of the n^{th} cell and p_v^0 is the average fractional occupancy. p_v represents the occupational modulation function and as with the position modulation function, the best choice of function is structure dependent. Common options are the Crenel function or a truncated harmonic Fourier series. The truncated harmonic Fourier series takes the form:[100]

$$p_v = \sum_{i=1}^{l} p_{s,i} \sin[2\pi\mathbf{q}_i \cdot (\mathbf{n} + x_{s4})] + \sum_{i=1}^{l} p_{c,i} \cos[2\pi\mathbf{q}_i \cdot (\mathbf{n} + x_{s4})] \qquad \text{(A.9)}$$

where $p_{s,i}$ and $p_{c,i}$ are the amplitude of the sin and cos displacement waves respectively.

Appendix B

B. Magnetic structures and Symmetry-Mode Distortion Analysis

Magnetic structures within this thesis were solved with the use of ISODISTORT to perform symmetry-mode distortion analysis.[112] Symmetry-mode distortion analysis was also used to probe possible causes of the peak-splitting observed in $Sr_2NiO_2Cu_2Se_2$ (see section 7.4.2.2).

ISODISTORT is an extremely powerful tool that uses the concepts of group theory to present a list of options predicated on the breaking of various symmetry elements, by breaking the symmetry of a structure down to a series of physically irreducible representations (irreps).

The user inputs the undistorted crystallographic information file (CIF) and selects the distortions to be analysed (displacements, occupancy, magnetic vectors, strain) based on prior knowledge. If an expansion of the unit cell (as often occurs with magnetic structures) has occurred and is known, then this can also be inputted into the dataset prior to analysis of the available irreps. The effect of either individual or combined irreps on both the crystal structure and simulated diffraction patterns can be observed using Java™ applets.

If the available combination of modes is thought to be appropriate for further analysis, the symmetry-mode-active structure can be imported into TOPAS[99] for direct Rietveld refinement. This way, the magnitude of a symmetry distortion can be refined directly, allowing complex distortions, which may have conventionally required the use of many parameters, to be refined using just one or two parameters.

B.1 Symmetry mode labels

ISODISTORT assigns labels to each irrep, which provide information about the type of distortion used. Two representative examples obtained from $Sr_2MnO_2Ag_{1.5}Se_2$ (undistorted space group: *I*4/*mmm*) are shown below:

GM3-[Mn1:a:dsp]A2u(a) (B.1)

mM3+[Mn1:a:mag]A2g(a) (B.2)

The first part of the label is the presence or absence of a small letter "m", this letter represents that the symmetry mode is magnetic. The second part is either one or two capital letter, in this case "GM" and "M", these symbols represent the *k*-point, in this case (0, 0, 0) and (1, 1, 1). Pairs of letters are Romanised transliterations of Greek letters (here "GM" for Γ). The number and "+" or "-" signs further define the irrep according to the Miller-Love (ML) scheme.[175]

The information in square brackets indicates the atom label "Mn1", its Wyckoff position "*a*" and the type of distortion "dsp" for displacement and "mag" for magnetic (also available is "occ" for occupancy; a strain mode simply says "strain" without reference to atoms or square brackets). The next part of the symbol represents the Wyckoff site point-group irreps, recognisable from those used in molecular spectroscopy (A2u for A_{2u}). The final letters in brackets "(a)" are used to distinguish irreps that would otherwise have identical labels.

In this this thesis, for ease of comparison with the irreps presented by ISODISTORT, the linear, transliterated form used by ISODISTORT is retained. However, since in each case the atom type and the type of distortion under investigation is clear from the text and diagrams, a shortened irrep symbol is presented, as shown below for the two examples above respectively:

$$GM3^{-}(a) \tag{B.3}$$

$$mM3^{+}(a) \tag{B.4}$$

This is a linear variation of the notation devised by Miller and Love. Care should be taken, because the same irrep labels are not directly comparable between different parent space groups.[176]

B.2 Magnetic space groups

Once the active irreps have been found, a higher symmetry space group can be searched for using ISODISTORT.[112] Magnetic structures comprise not just atoms, but also magnetic spin, represented by vectors with a direction. The ordering of these vectors leads to a further symmetry element that can be broken, *time reversal*. The incorporation of this new symmetry element requires a new set of space groups, the Shubnikov or magnetic space groups. There are 1651 three-dimensional magnetic space

groups (contrast with 230 three-dimensional conventional space groups). A full list of these space groups may be obtained from Litvin.[116]

The default magnetic space group scheme adopted by both TOPAS and ISODISTORT is the Belov-Neronova-Smirnova (BNS) scheme. The BNS scheme is therefore used in this thesis. As with conventional, three-dimensional space groups, each BNS magnetic space group is assigned a number. These are given in each case to prevent confusion.

Appendix C

C. Magnetic structures of $Sr_2CoO_2Cu_{2-x}Se_2$ and $Sr_2CoO_2Cu_{2-x}Se_{1.6}S_{0.4}$ modelled using model 1

Section 5.2.4 describes the various magnetic structures that can be used to model the magnetic intensity of $Sr_2CoO_2Cu_2Se_2$ and its derivatives. Model 3, using the $mX3^+(a)$, $mX4^+(a)$ and mP4(a) modes in magnetic space group P_C4_1 (76.11) was chosen as the model that was thought to most closely model the real magnetic structure. However, model 3 does not give as good a fit to the data as model 1, which modelled the magnetic intensity using the $mX2^+(a)$, $mX3^+(a)$, $mX4^+(a)$, mP4(a) = mP4(b) and mP5(a) modes in magnetic space group $P1$ (1.1). Therefore, for completion, the results of fitting the data when model 1 was used are also presented here for all samples of $Sr_2CoO_2Cu_{2-x}Se_2$ and $Sr_2CoO_2Cu_{2-x}Se_{1.6}S_{0.4}$ that were measured using powder neutron diffraction (PND) as part of the work of this thesis.

All parameters apart from the change of magnetic model were kept the same, so that the results from model 1 and model 3 may be compared directly.

C.1 $Sr_2CoO_2Cu_{2-x}Se_2$

The refined magnetic moments obtained for each Co ion when model 1 was used is shown in Table C.1 – Table C.3 for the $Sr_2CoO_2Cu_{2-x}Se_2$ series and the fit to the data using model 1 and model 3 is compared in Fig. C.1.

Table C.1 Results of Rietveld refinement of the magnetic structure of JNB102 ($Sr_2CoO_2Cu_2Se_2$) using a combined refinement against HRPD/OSIRIS data at 5 K, refined using model 1 (all reasonable magnetic symmetry modes relaxed)

Sample	JNB102			
Composition	$Sr_2CoO_2Cu_2Se_2$			
Atom	μ_a (μ_B)	μ_b (μ_B)	μ_c (μ_B)	$\lvert\mu\rvert$ (μ_B)
Co1 (0, 0, 0)	1.84(3)	-4.02(5)	1.1(2)	4.55(6)
Co2 (0.5, 0.5, 0)	-1.84(3)	4.02(5)	-1.1(2)	4.55(6)
Co3 (0, 0.5, 0.25)	3.20(6)	-2.65(3)	1.1(2)	4.30(6)
Co4 (0.5, 0, 0.25)	-3.20(6)	2.65(3)	-1.1(2)	4.30(6)
Co5 (0, 0, 0.5)	1.84(3)	-1.29(5)	0.1(2)	2.25(4)
Co6 (0.5, 0.5, 0.5)	-1.84(3)	1.29(5)	-0.1(2)	2.25(4)
Co7 (0, 0.5, 0.75)	0.47(6)	-2.65(3)	0.1(2)	2.70(3)
Co8 (0.5, 0, 0.75)	-0.47(6)	2.65(3)	-0.1(2)	2.70(3)
R_{wp} (%)	4.095 (*cf.* model 3: 4.139)			
χ^2	2.208 (*cf.* model 3: 2.231)			

Table C.2 Results of Rietveld refinement of the magnetic structure of JNB171 ($Sr_2CoO_2Cu_{1.94}Se_2$) using a combined refinement against HRPD/OSIRIS data at 5 K, refined using model 1 (all reasonable magnetic symmetry modes relaxed)

Sample	JNB171			
Composition	$Sr_2CoO_2Cu_{1.94}Se_2$			
Atom	μ_a (μ_B)	μ_b (μ_B)	μ_c (μ_B)	$\|\mu\|$ (μ_B)
Co1 (0, 0, 0)	1.58(3)	-3.09(6)	1.5(1)	3.78(7)
Co2 (0.5, 0.5, 0)	-1.58(3)	3.09(6)	-1.5(1)	3.78(7)
Co3 (0, 0.5, 0.25)	2.75(7)	-1.92(3)	1.5(1)	3.68(7)
Co4 (0.5, 0, 0.25)	-2.75(7)	1.92(3)	-1.5(1)	3.68(7)
Co5 (0, 0, 0.5)	1.58(3)	-0.74(6)	0.0(1)	1.75(4)
Co6 (0.5, 0.5, 0.5)	-1.58(3)	0.74(6)	-0.0(1)	1.75(4)
Co7 (0, 0.5, 0.75)	0.40(7)	-1.92(3)	0.0(1)	1.96(3)
Co8 (0.5, 0, 0.75)	-0.40(7)	1.92(3)	-0.0(1)	1.96(3)
R_{wp} (%)	3.804 (*cf.* model 3: 3.826)			
χ^2	2.020 (*cf.* model 3: 2.032)			

Table C.3 Results of Rietveld refinement of the magnetic structure of JNB104 ($Sr_2CoO_2Cu_{1.89}Se_2$) using a combined refinement against HRPD/OSIRIS data at 5 K, refined using model 1 (all reasonable magnetic symmetry modes relaxed)

Sample	JNB104			
Composition	$Sr_2CoO_2Cu_{1.89}Se_2$			
Atom	μ_a (μ_B)	μ_b (μ_B)	μ_c (μ_B)	$\|\mu\|$ (μ_B)
Co1 (0, 0, 0)	0.97(4)	-2.18(8)	0.6(2.1)	2.5(5)
Co2 (0.5, 0.5, 0)	-0.97(4)	2.18(8)	-0.6(2.1)	2.5(5)
Co3 (0, 0.5, 0.25)	1.93(8)	-1.22(4)	0.6(2.1)	2.4(5)
Co4 (0.5, 0, 0.25)	-1.93(8)	1.22(4)	-0.6(2.1)	2.4(5)
Co5 (0, 0, 0.5)	0.97(4)	-0.27(8)	-0.6(2.1)	1(1)
Co6 (0.5, 0.5, 0.5)	-0.97(4)	0.27(8)	0.6(2.1)	1(1)
Co7 (0, 0.5, 0.75)	0.02(8)	-1.22(4)	-0.6(2.1)	1(1)
Co8 (0.5, 0, 0.75)	-0.02(8)	1.22(4)	0.6(2.1)	1(1)
R_{wp} (%)	4.074 (*cf.* model 3: 4.084)			
χ^2	2.003 (*cf.* model 3: 2.009)			

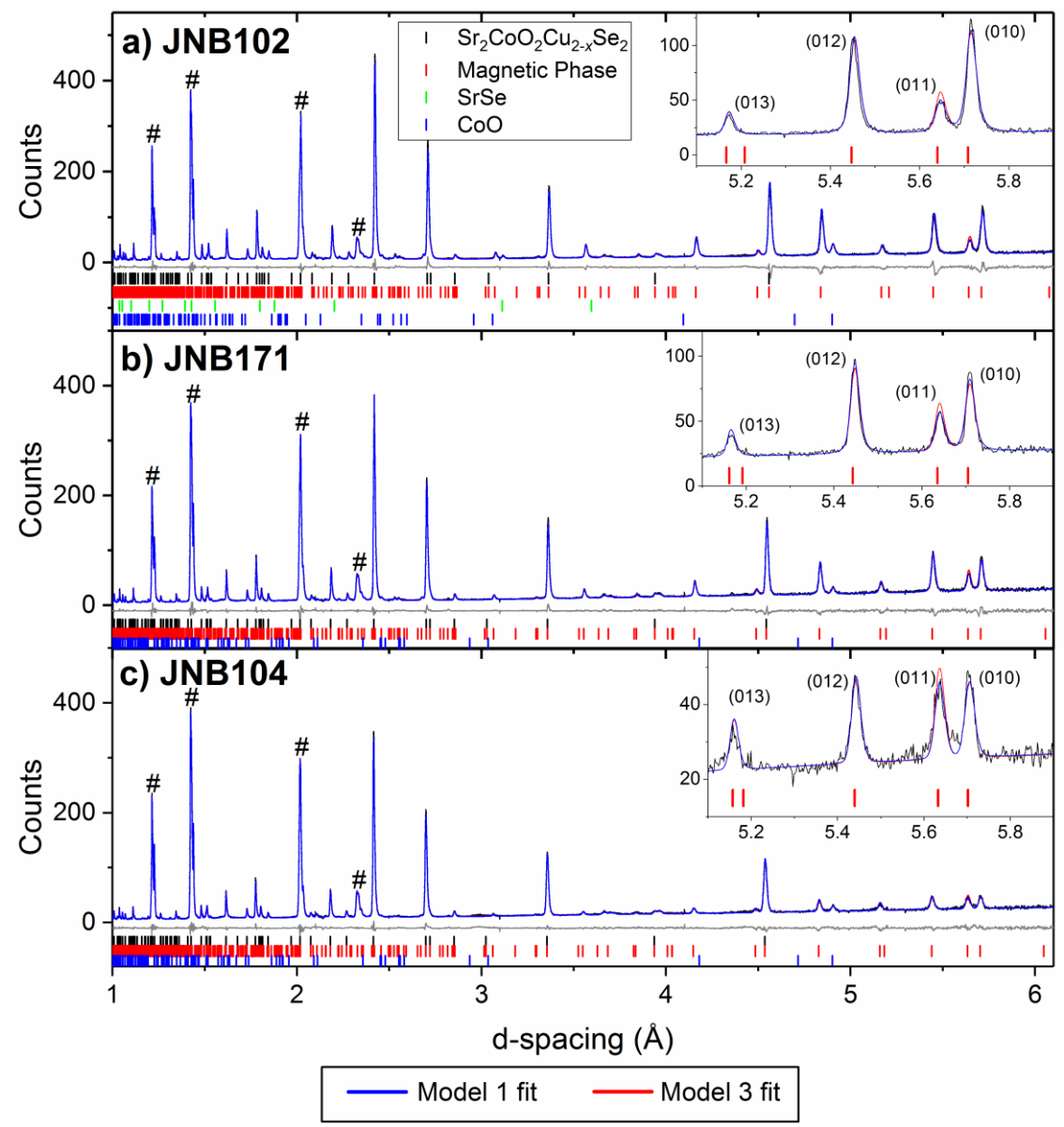


Fig. C.1 Comparison of the fits to the magnetic structure of a) JNB102 ($Sr_2CoO_2Cu_2Se_2$) b) JNB171 ($Sr_2CoO_2Cu_{1.94}Se_2$) and c) JNB104 ($Sr_2CoO_2Cu_{1.89}Se_2$) when model 1 and model 3 are used to fit the data; the difference curve given is that for the model 1 fit

C.2 $Sr_2CoO_2Cu_{2-x}Se_{1.6}S_{0.4}$

The refined magnetic moments obtained for each Co ion when model 1 was used is shown in Table C.4 – Table C.6 for the $Sr_2CoO_2Cu_2Se_{1.6}S_{0.4}$ series and the fit to the data using model 1 and model 3 is compared for each sample in Fig. C.2.

Table C.4 Results of Rietveld refinement of the magnetic structure of JNB236A ($Sr_2CoO_2Cu_2Se_{1.6}S_{0.4}$) using a combined refinement against HRPD/OSIRIS data at 5 K, refined using model 1 (all reasonable magnetic symmetry modes relaxed)

Sample	JNB236A			
Composition	$Sr_2CoO_2Cu_2Se_{1.6}S_{0.4}$			
Atom	μ_a (μ_B)	μ_b (μ_B)	μ_c (μ_B)	$\|\mu\|$ (μ_B)
Co1 (0, 0, 0)	0.1(6)	-3(2)	1.3(2)	3(2)
Co2 (0.5, 0.5, 0)	-0.1(6)	3(2)	-1.3(2)	3(2)
Co3 (0, 0.5, 0.25)	3.2(6)	0(2)	1.3(2)	3.5(6)
Co4 (0.5, 0, 0.25)	-3.2(6)	-0(2)	-1.3(2)	3.5(6)
Co5 (0, 0, 0.5)	-0.7(2)	0.1(6)	-0.7(2)	3(2)
Co6 (0.5, 0.5, 0.5)	0.7(2)	-0.1(6)	0.7(2)	3(2)
Co7 (0, 0.5, 0.75)	-0.7(2)	-3.1(6)	-0.7(2)	3.2(6)
Co8 (0.5, 0, 0.75)	0.7(2)	3.1(6)	0.7(2)	3.2(6)
R_{wp} (%)	3.191 (*cf.* $I_ab a2$ (45.240) model: 3.181)			
χ^2	1.324 (*cf.* $I_ab a2$ (45.240) model: 1.319)			

Table C.5 Results of Rietveld refinement of the magnetic structure of JNB245B ($Sr_2CoO_2Cu_{1.91}Se_{1.6}S_{0.4}$) using a combined refinement against HRPD/OSIRIS data at 5 K, refined using model 1 (all reasonable magnetic symmetry modes relaxed)

Sample	JNB245B			
Composition	$Sr_2CoO_2Cu_{1.91}Se_{1.6}S_{0.4}$			
Atom	μ_a (μ_B)	μ_b (μ_B)	μ_c (μ_B)	$\|\mu\|$ (μ_B)
Co1 (0, 0, 0)	0.81(7)	-2.42(9)	2.0(1)	3.2(1)
Co2 (0.5, 0.5, 0)	-0.81(7)	2.42(9)	-2.0(1)	3.2(1)
Co3 (0, 0.5, 0.25)	2.0(1)	-1.21(5)	2.0(1)	3.1(1)
Co4 (0.5, 0, 0.25)	-2.0(1)	1.21(5)	-2.0(1)	3.1(1)
Co5 (0, 0, 0.5)	0.81(7)	-0.00(9)	-0.1(1)	0.81(7)
Co6 (0.5, 0.5, 0.5)	-0.81(7)	0.00(9)	0.1(1)	0.81(7)
Co7 (0, 0.5, 0.75)	-0.4(1)	-1.21(5)	-0.1(1)	1.28(6)
Co8 (0.5, 0, 0.75)	0.4(1)	1.21(5)	0.1(1)	1.28(6)
R_{wp} (%)	2.911 (*cf.* model 3: 2.925)			
χ^2	1.261 (*cf.* model 3: 1.267)			

Table C.6 Results of Rietveld refinement of the magnetic structure of JNB244 ($Sr_2CoO_2Cu_{1.84}Se_{1.6}S_{0.4}$) using a combined refinement against HRPD/OSIRIS data at 5 K, refined using model 1 (all reasonable magnetic symmetry modes relaxed)

Sample	JNB244			
Composition	$Sr_2CoO_2Cu_{1.84}Se_{1.6}S_{0.4}$			
Atom	μ_a (μ_B)	μ_b (μ_B)	μ_c (μ_B)	$\|\mu\|$ (μ_B)
Co1 (0, 0, 0)	0.1(6)	-1.8(4)	1.6(2)	2.4(3)
Co2 (0.5, 0.5, 0)	-0.1(6)	1.8(4)	-1.6(2)	2.4(3)
Co3 (0, 0.5, 0.25)	1.7(6)	-0.1(4)	1.6(2)	2.4(4)
Co4 (0.5, 0, 0.25)	-1.7(6)	0.1(4)	-1.6(2)	2.4(4)
Co5 (0, 0, 0.5)	-0.6(2)	0.1(6)	-0.6(2)	1.6(4)
Co6 (0.5, 0.5, 0.5)	0.6(2)	-0.1(6)	0.6(2)	1.6(4)
Co7 (0, 0.5, 0.75)	-0.6(2)	-1.5(6)	-0.6(2)	1.6(5)
Co8 (0.5, 0, 0.75)	0.6(2)	1.5(6)	0.6(2)	1.6(5)
R_{wp} (%)	2.892 (*cf.* model 3: 2.924)			
χ^2	1.364 (*cf.* model 3: 1.379)			

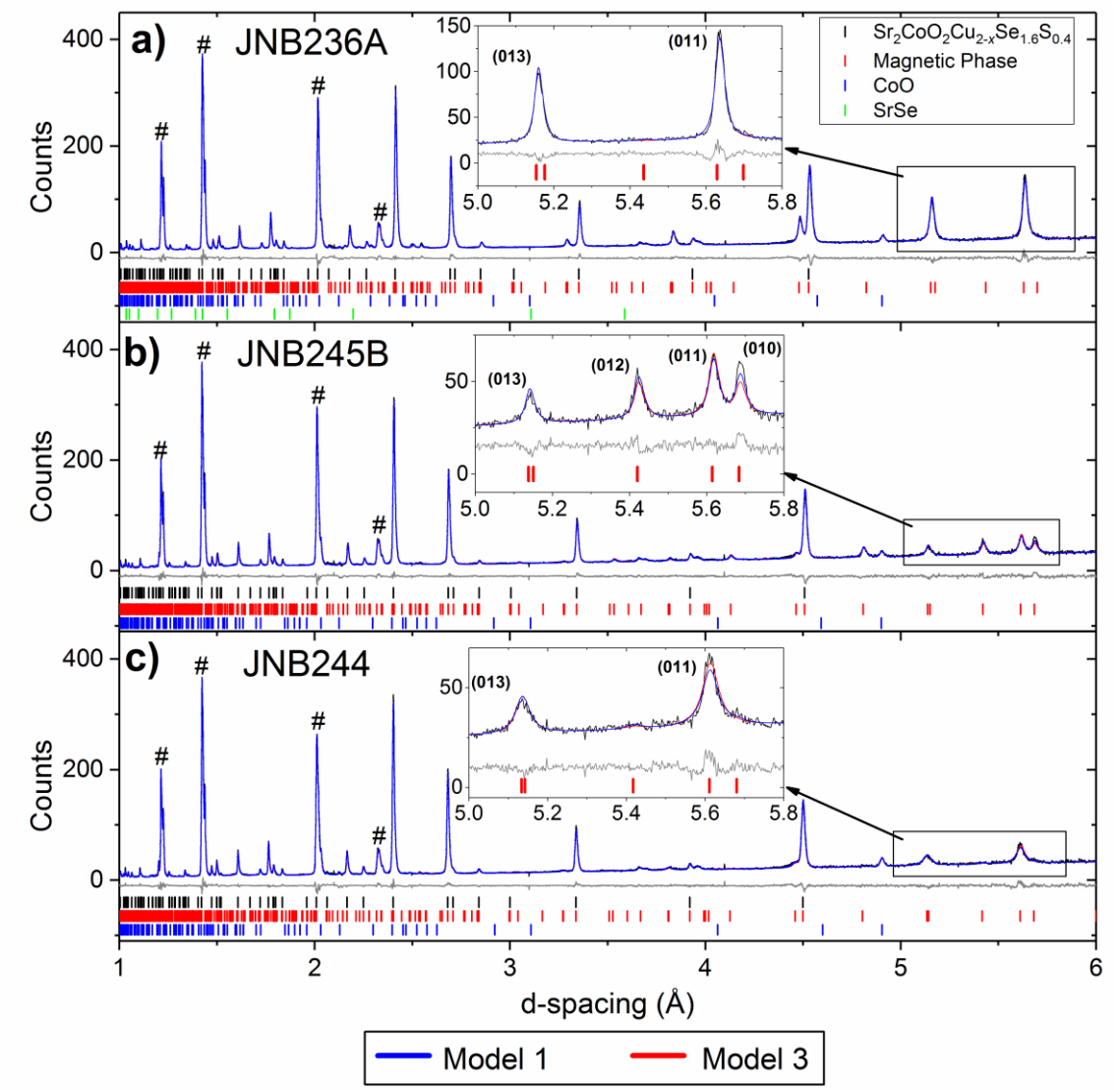


Fig. C.2 Comparison of the fits to the magnetic structure of a) JNB236A ($Sr_2CoO_2Cu_2Se_{1.6}S_{0.4}$) b) JNB245B ($Sr_2CoO_2Cu_{1.91}Se_{1.6}S_{0.4}$) and c) JNB244 ($Sr_2CoO_2Cu_{1.84}Se_{1.6}S_{0.4}$) when model 1 and model 3 are used to fit the data; the difference curve given is that for the model 1 fit

Appendix D

D. Energy Dispersive X-ray Spectroscopy of $Sr_2CoO_2Ag_{2-x}Se_2$

Energy dispersive X-ray spectroscopy (EDX) was performed on two samples of $Sr_2CoO_2Ag_{2-x}Se_2$: JNB010 (parent $Sr_2CoO_2Ag_2Se_2$) and JNB130 (most-deintercalated $Sr_2CoO_2Ag_{2-x}Se_2$). These samples were prepared using the following method; first the powders were dispersed in hexane using an ultrasonication bath, then small amounts of the suspension were dropped onto a copper transmission electron microscope (TEM) grid, with a lacey carbon film. As parent $Sr_2CoO_2Ag_2Se_2$ is considered air-stable, the sample of JNB010 was prepared in air. The sample of JNB130 was prepared inside an argon-filled glovebag to prevent contamination by air.

EDX analysis was then performed using the JEOL JEM-2100 with Dr N. P. Young. Particles were picked out; measured using EDX and then a transmission electron microscope (TEM) image recorded. Each EDX measurement was performed on a different particle. The atomic molar percentages, obtained from integration of each EDX spectra measured, are shown in Table D.1 for JNB010 and Table D.2 for JNB130, while the TEM images of the particles from which each EDX spectra was collected is shown in Fig. D.1 (for both JNB010 and JNB130).

Table D.1 Atomic molar percentages of each element collected for each EDX measurement of JNB010 (nominal composition $Sr_2CoO_2Ag_2Se_2$)

Sample	JNB010				
Spectrum	Sr (%)	Co (%)	O (%)	Ag (%)	Se (%)
1	20.8	17.5	7.24	33.6	20.86
2	25.93	14.33	9.8	24.07	25.78
3	23.57	12.82	12.79	27.01	23.82
4	23.14	13.6	10.86	27.23	25.17
5	22.95	17.31	11.51	25.82	22.4
6	21.94	18.99	13.43	24.59	21.05
Mean(su)	23(2)	16(2)	-	27(3)	23(2)
Mean(su) (excluding outliers)	24(1)	15(2)	-	26(1)	24(2)

Table D.2 Atomic molar percentages of each element collected for each EDX measuremnt of JNB130 (nominal composition $Sr_2CoO_2Ag_{2-x}Se_2$)

Sample	JNB130				
Spectrum	Sr (%)	Co (%)	O (%)	Ag (%)	Se (%)
1	30.28	16.22	6.34	17.48	29.66
2	13.57	8.07	49.63	14.7	14.03
3	25.03	14.2	14.33	20.4	26.04
4	25.03	14.53	13.94	19.28	27.23
5	20.75	12.69	22.51	20.15	23.9
6	25.48	14.37	13.91	18.4	27.84
Mean(su)	23(5)	13(3)	-	18(2)	25(5)
Mean(su) (excluding outliers)	22(5)	13(2)	-	19(2)	24(5)

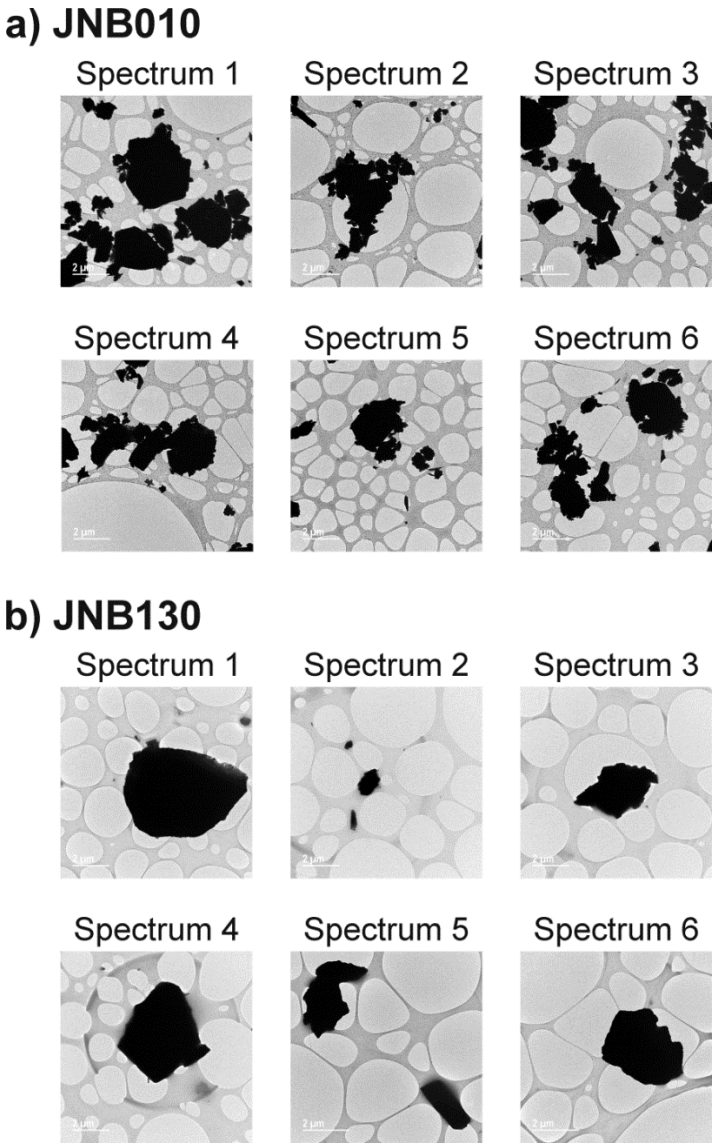


Fig. D.1 TEM images of the particles used to collect the EDX spectra of a) JNB010 (parent $Sr_2CoO_2Ag_2Se_2$) and b) JNB130 (most-deintercalated $Sr_2CoO_2Ag_{2-x}Se_2$)